LDRD Annual Report

Laboratory Directed Research and Development

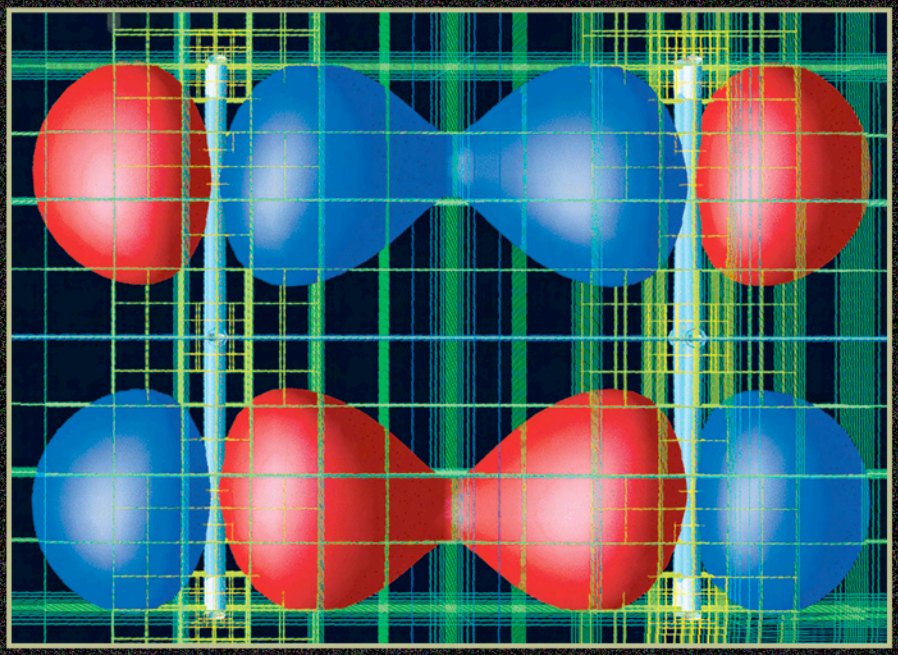

OAK RIDGE NATIONAL LABORATORY
MANAGED BY UT-BATTELLE FOR THE DEPARTMENT OF ENERGY

FY 2004

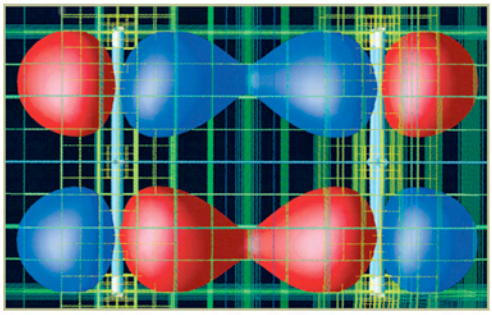

On the cover: *The adaptively refined mesh and isosurfaces for a molecular orbital of the benzene dimer. Note that the boxes are larger between the molecules where the orbital varies slowly but smaller near nuclei where the orbital varies rapidly. From the report, "Advanced Computational Methods," by R. J. Harrison et al.*

DOCUMENT AVAILABILITY

Reports produced after January 1, 1996, are generally available free via the U.S. Department of Energy (DOE) Information Bridge:

Web site: http://www.osti.gov/bridge

Reports produced before January 1, 1996, may be purchased by members of the public from the following source:

National Technical Information Service
5285 Port Royal Road
Springfield, VA 22161
Telephone: 703-605-6000 (1-800-553-6847)
TDD: 703-487-4639
Fax: 703-605-6900
E-mail: info@ntis.fedworld.gov
Web site: http://www.ntis.gov/support/ordernowabout.htm

Reports are available to DOE employees, DOE contractors, Energy Technology Data Exchange (ETDE) representatives, and International Nuclear Information System (INIS) representatives from the following source:

Office of Scientific and Technical Information
P.O. Box 62
Oak Ridge, TN 37831
Telephone: 865-576-8401
Fax: 865-576-5728
E-mail: reports@adonis.osti.gov
Web site: http://www.osti.gov/contact.html

ORNL/PPA-2005/1

Oak Ridge National Laboratory

LABORATORY DIRECTED RESEARCH AND DEVELOPMENT PROGRAM

FY 2004 ANNUAL REPORT

March 2005

Prepared by
OAK RIDGE NATIONAL LABORATORY
P.O. Box 2008
Oak Ridge, Tennessee 37831-6285
managed by
UT-BATTELLE LLC
for the
U.S. DEPARTMENT OF ENERGY
under Contract DE-AC05-00OR22725

CONTENTS

INTRODUCTION

The Oak Ridge National Laboratory (ORNL) Laboratory Directed Research and Development (LDRD) Program reports its status to the U.S. Department of Energy (DOE) in March of each year. The program operates under the authority of DOE Order 413.2A, "Laboratory Directed Research and Development" (January 8, 2001), which establishes DOE's requirements for the program while providing the Laboratory Director broad flexibility for program implementation. LDRD funds are obtained through a charge to all Laboratory programs.

This report describes all ORNL LDRD research activities supported during FY 2004 and includes final reports for completed projects and shorter progress reports for projects that were active, but not completed, during this period. The FY 2004 ORNL LDRD Self-Assessment (ORNL/PPA-2005/2) provides financial data about the FY 2004 projects and an internal evaluation of the program's management process.

ORNL is a DOE multiprogram science, technology, and energy laboratory with distinctive capabilities in materials science and engineering, neutron science and technology, energy production and end-use technologies, biological and environmental science, and scientific computing. With these capabilities ORNL conducts basic and applied research and development (R&D) to support DOE's overarching national security mission, which encompasses science, energy resources, environmental quality, and national nuclear security. As a national resource, the Laboratory also applies its capabilities and skills to the specific needs of other federal agencies and customers through the DOE Work For Others (WFO) program. Information about the Laboratory and its programs is available on the Internet at <http:// www.ornl.gov/>.

LDRD is a relatively small but vital DOE program that allows ORNL, as well as other multiprogram DOE laboratories, to select a limited number of R&D projects for the purpose of

- maintaining the scientific and technical vitality of the Laboratory,
- enhancing the Laboratory's ability to address future DOE missions,
- fostering creativity and stimulating exploration of forefront science and technology,
- serving as a proving ground for new research, and
- supporting high-risk, potentially high-value R&D.

Through LDRD the Laboratory is able to improve its distinctive capabilities and enhance its ability to conduct cutting-edge R&D for its DOE and WFO sponsors.

To meet the LDRD objectives and fulfill the particular needs of the Laboratory, ORNL has established a program with two components: the Director's R&D Fund and the Seed Money Fund. As outlined in Table 1, these two funds are complementary. The Director's R&D Fund develops new capabilities in support of the Laboratory initiatives, while the Seed Money Fund is open to all innovative ideas that have the potential for enhancing the Laboratory's core scientific and technical competencies. Provision for multiple routes of access to ORNL LDRD funds maximizes the likelihood that novel and seminal ideas with scientific and technological merit will be recognized and supported.

Table 1. ORNL LDRD Program

	Seed Money Fund	Director's R&D Fund
Purpose	Supports core competencies	Supports laboratory initiatives
Year established	1974	1983
Funding cycle	Continuous	Annual
Proposal review	Proposal review committee	Initiative review committees
Project budget	≤ $125,000	≤ $800,000
Project duration	12 to 18 months	24 to 36 months
LDRD outlay	20%	80%

The ORNL LDRD program recognizes that the R&D staff generally initiate new ideas, peer review of proposals is an essential component, and management has a role in fostering projects that are aligned with the strategic directions of the Laboratory. All proposals to the ORNL LDRD program undergo peer review and must be approved by the Deputy Director for Science and Technology and concurred by DOE before funding can be provided.

Director's R&D Fund

The Director's R&D Fund is the strategic component of the ORNL LDRD program and the key tool for addressing the R&D needs of the Laboratory initiatives. The initiatives, which are the focus of the Laboratory Agenda, ORNL's strategic plan developed in collaboration with DOE, are the critical areas on which the Laboratory must concentrate if it is to be prepared to meet future DOE and national requirements for science and technology.

The success of an initiative, which generally lasts 3–5 years, depends to a large extent on the Laboratory's ability to identify and nurture cutting-edge science and

technology on which enduring capabilities can be built. To do this, ORNL uses the resources of the Director's R&D Fund to encourage the research staff to submit ideas aimed at addressing initiative-specific research goals. Each spring, after conducting a review of the initiatives with the Laboratory's senior technical managers, the Deputy Director for Science and Technology issues a call for proposals to the scientific and technical staff. The call emphasizes specific research priorities selected by management as critical to accomplishing the Laboratory's initiatives. To select the best and most strategic of the submitted ideas, the Deputy Director establishes a committee for each initiative to review the new proposals and ongoing projects associated with it. The committees are staffed by subject matter experts including external members from the academic community and senior technical managers.

Proposals to the Director's R&D Fund undergo two rounds of review. In the first round, the committees evaluate preliminary proposals and select the most promising for development into full proposals. In the second round, the committees review the new proposals and ongoing projects that are requesting second- or third-year funding. After the reviews are completed, the committees provide funding recommendations to the Deputy Director for Science and Technology, who develops an overall funding strategy and presents it for approval to the Leadership Team, ORNL's executive committee headed by the Laboratory Director. All projects selected for funding must also receive concurrence from DOE.

In FY 2004, $11.7 million was allocated to the Director's R&D Fund to support 57 projects, 31 of which were new starts (Table 2). About 90% of the fund's annual allocation is awarded to projects at the beginning of the fiscal year. The remainder, about 10%, is held in reserve primarily to support research projects of new R&D staff members being recruited to address strategic Laboratory needs.

Table 2. FY 2004 ORNL LDRD Breakdown by Fund

	Director's R&D Fund	Seed Money Fund
Costs	$3.62 million	$11.70 million
Number of projects	57	59
Number of new starts	31	35
Number of continuing projects	26	24
Average total project budget	~$419,000	~$104,000
Average project duration	24 months	16 months

Director's R&D Fund Research Priorities

In requesting proposals for FY 2004, the Laboratory's senior R&D managers developed a set of research priorities for the Laboratory initiatives in advanced grid technologies, advanced materials, fission to fusion, hydrogen infrastructure, national security, neutron sciences, systems biology, and terascale computing and simulation science. Brief descriptions of these initiatives and their associated research priorities for FY 2004 are provided below. The levels of investment in each initiative are summarized in Fig. 1, and an index of projects by initiative is provided on p. 305.

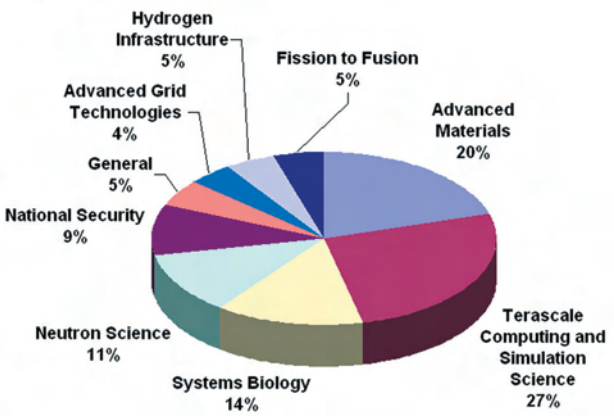

Fig. 1. Level of Director's R&D Fund investment in the Laboratory-wide initiatives for FY 2004.

Advanced Grid Technologies

The objective of the advanced grid technologies initiative is to establish ORNL as a leader in addressing problems of national importance in electricity transmission, distribution, and reliability with the goal of helping to ensure a reliable, secure grid. As a first step toward this goal, the Laboratory set the following research priorities:

- revolutionize the power grid by deploying new materials, processes, and modeling for components and devices;
- strengthen the grid by developing fast-responding, distributed-generation, and responsive-load technologies that will respond when an emergency is imminent; and
- build a new long-term research program in high-performance computer modeling, simulation, and visualization of the grid on a regional scale.

Advanced Materials

The intent of advanced materials initiative is to establish ORNL as a leading interdisciplinary center for nanoscale science, engineering, and technology (NSET) performing forefront research and providing unique facilities, such as the Center for Nanophase Materials Science, for understanding the synthesis, fabrication, structure, and properties of nanoscale materials and systems. NSET is an area that is expected to provide breakthrough opportunities in many fields

central to DOE's missions, including materials science, biotechnology, processing science, energy, environmental technology, information technology, and national security. The initiative's research priorities for FY 2004 were nanocatalysis, nanobiotechnology, and the development of capabilities for the controlled synthesis of nanomaterials and nanostructures, resulting in functionality for nanoscale systems.

Fission to Fusion

The objective of the fission to fusion initiative is to establish ORNL as the main provider of new technologies to support the expanded developmental use of nuclear and fusion technologies to supply the power needs of the world and lead in the development of one or more experimental facilities. New technologies are needed for next-generation demonstrations and missions such as the International Thermonuclear Experimental Reactor (ITER), the International Fusion Materials Irradiation Facility (IFMIF), DOE's advanced gas reactor/nuclear hydrogen demonstration, and NASA's nuclear reactor–powered space probes. To address those technological issues for which ORNL is uniquely positioned to provide a leadership role, the Laboratory developed the following research priorities for FY 2004:

- fission and fusion relevant materials,
- innovative nuclear fuels technology,
- advanced inspection technologies for coated particle fuel, and
- advanced modeling and analysis techniques for design of reactors or fuel fabrication facilities.

Hydrogen Infrastructure

The intent of the hydrogen infrastructure initiative is to establish ORNL as a recognized national leader in materials sciences and engineering needs for fuel cells, hydrogen production and delivery, hydrogen combustion engines, and research on sensors. The initial objective is to demonstrate a short-term path to improved hydrogen production and improved energy density in materials for hydrogen storage and to enable the transition to fuel cell vehicles and a hydrogen economy as a natural progression of events. With these objectives in mind, the Laboratory established research priorities focused on the development of

- sensors for hydrogen technologies,
- low-temperature and novel combustion regimes for hydrogen internal combustion engines, and
- new materials and systems for lightweight high-energy density storage devices.

National Security

A principal thrust of the National Security initiative is to position ORNL to support the missions of the Department of Homeland Security (DHS) to protect the nation against further terrorist attacks and to respond quickly when such threats do materialize. ORNL is therefore developing leading-edge capabilities that can be used to combat terrorism. The major outcome of this effort is to assist the DHS in its efforts to examine specific threats and deter or mitigate their effects; to develop the tools for early warning; to identify materials used in the event of an attack; and to work with local, state, and regional first responders, public safety, and emergency management officials to provide them the scientific tools they need to do their jobs better and more efficiently. To help achieve these objectives, the FY 2004 research priorities were

- development of detection technologies for biological, chemical, and high-explosive countermeasures;
- analysis tools for critical infrastructure protection;
- detection and interdiction technologies to prevent the importation or transportation of a radiological or nuclear device within our borders; and
- new analytical methods and tools for sensor fusion and the synthesis/analysis of text, imagery, sensor measurements, and other information.

Neutron Sciences

The Spallation Neutron Source (SNS) and the upgrades at the High Flux Isotope Reactor (HFIR) that will be completed as part of the Laboratory initiative in neutron sciences offer a unique opportunity for ORNL and the nation to demonstrate world leadership in this area. The success of these projects (and their impact on ORNL) depends critically on the ability to develop the full potential of these new scientific tools and to integrate neutron sciences into research programs across the Laboratory. Thus, the intent of this initiative is to establish ORNL as the world's foremost center for neutron sciences, providing unprecedented capabilities for understanding the structure and properties of materials and macromolecular systems and the fundamental physics of the neutron. In FY 2004, this initiative focused on three research priorities that are essential to leadership in neutron sciences: novel applications of neutron scattering, novel instrumentation concepts, and new approaches to facilitate development of higher-power spallation neutron sources.

Systems Biology

The initiative in systems biology addresses the strategic needs of the DOE Genomics:GTL and related programs at other agencies that focus on gaining a molecular-level understanding of biological processes. In FY 2004, the research priorities for this initiative were (1) characterization and imaging of molecular machines and (2) molecular ecology. Understanding how molecular machines operate at the molecular level will unlock the capability to control and deploy useful molecular

processes conducted by microbes and apply them to DOE mission needs. This will require the development of new biological, analytical, and computational tools to facilitate the high-throughput analysis of protein complexes. The research priority in molecular ecology was aimed at facilitating the science of complex and adaptive biological systems by interrogating and modeling ecosystems at multiple scales. The expected outcomes were (1) new experimental and computational methods for analyzing community metagenomes and (2) initial development of tools for detecting and simulating the response of whole ecosystems to all factors of global change.

Terascale Computing and Simulation Science

The intent of terascale computing and simulation science initiative is to establish ORNL as a world leader in capability computing as a tool for scientific discovery. The initiative recognizes the importance of computing infrastructure and scientific computing in addressing key R&D issues of DOE's missions. As the development of supercomputers continues, advances in processing power must be complemented by advances in computing, communications, and information tools and technologies. At the same time, the dramatic advances in the power and performance of computers are opening new pathways to the modeling and simulation of physical systems and providing new insights into a host of complex science and engineering problems. In FY 2004, the research priorities for this initiative focused on three areas:

1. scientific applications to create new models for fusion energy, biology, nanoscience, physics, materials science, chemistry, and climate;
2. mathematics and computer science including distributed and cluster computing, mathematical analysis, scalable numerical algorithms, mesh generation and discretization technology, petascale data analysis, and data visualization; and
3. middleware development for easy-to-use, reliable, high-performance, and secure access to data and tools.

Seed Money Fund

The Seed Money Fund complements the Director's R&D Fund by providing a source of funds for innovative ideas that have the potential of enhancing the Laboratory's core scientific and technical competencies. It also provides a path for funding new approaches that fall within the distinctive capabilities of ORNL but outside the more focused research priorities of the major Laboratory initiatives. Successful Seed Money Fund projects are expected to generate new DOE programmatic or Work-for-Others sponsorship at the Laboratory.

Proposals for Seed Money Fund support are accepted directly from the Laboratory's scientific and technical staff (with management concurrence) at any time of the year. Those requesting more than $20,000 ($125,000 is the maximum) are reviewed by the Proposal Review Committee (PRC), which is comprised of 11 scientific and technical staff members representing each of the Laboratory's research divisions and the LDRD manager (chair). To assist the committee, each proposal is also peer reviewed by two Laboratory staff members selected by the LDRD manager. Proposals requesting $20,000 or less are not reviewed by the PRC but are peer reviewed by a research staff member selected by the LDRD manager. All Seed Money Fund proposals receiving a favorable recommendation are forwarded to the Deputy Director for Science and Technology for approval and require DOE concurrence.

In FY 2004, $3.6 million of the LDRD program was apportioned to the Seed Money Fund to support 59 projects, 35 of which were new starts (Table 2). The distribution of Seed Money Fund support by science and technology area is shown in Fig. 2. The assignment of projects to specific areas is not meant to be definitive as many projects are cross-cutting and could be assigned to more than one category.

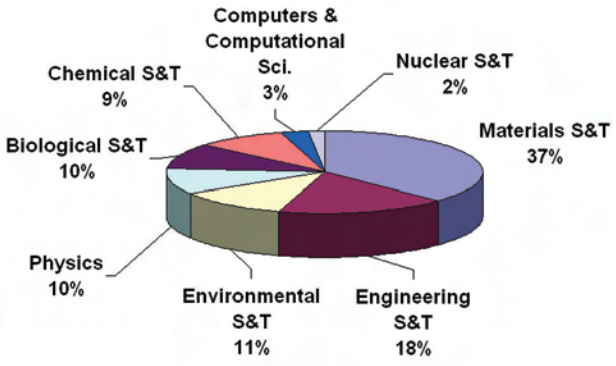

Fig. 2. Distribution of Seed Money by science and technology area for FY 2004.

Report Organization

The report is divided into eight broad areas of science and technology that underlie the programmatic and Work for Others activities at ORNL. Within each of these areas, the projects are grouped by fund (i.e., either the Director's R&D Fund or the Seed Money Fund). Within each fund grouping are the final reports and progress reports in that order. A list of Director's R&D Fund projects by initiative, an author list, and a project list are included at the back of this document.

MATERIALS SCIENCE AND ENGINEERING

Director's R&D Fund

Enhanced Performance and Energy Savings through Ultrahigh Magnetic Field Processing of Ferromagnetic Materials

G. M. Ludtka,[1] R. A. Jaramillo,[1] R. A. Kisner,[2] D. M. Nicholson,[3] J. B. Wilgen,[2]
G. Mackiewicz-Ludtka,[1] G. M. Stocks,[1] T. R. Watkins,[1] and P. N. Kalu[4]
[1]*Metals and Ceramics Division*
[2]*Engineering Science and Technology Division*
[3]*Computer Science and Mathematics Division*
[4]*National High Magnetic Field Laboratory, Florida State University*

The goal of this project was to validate and demonstrate the use of ultrahigh magnetic fields as a materials processing tool for developing novel microstructures and energy savings. Because the application of a large magnetic field favors the formation of ferromagnetic phases over paramagnetic phases, magnetic field processing provides a tool for manipulating microstructural evolution in several ferrous materials. Experiments performed with several steels have shown that magnetic fields can accelerate and augment austenite decomposition during continuous cooling and isothermal transformations. Data indicates that transformation temperatures are increased by 3°C/Tesla, which corresponds to a ~12.6-J/mol/Tesla shift in free energy for 1045 steel. It has been demonstrated that for a constant cooling rate, a 30-Tesla magnetic field can change the transformation mechanism from martensitic for the ambient condition to diffusive with the ultrahigh magnetic field. The ability to isothermally cycle the $\alpha \leftrightarrow \gamma + Fe_3C$ transformation was demonstrated by cycling the magnetic field between 0 and 30 Tesla at 750°C. These results support the hypothesis that ultrahigh magnetic field processing is a viable processing parameter for developing improved and unique microstructures and, therefore, properties in carbon steels.

Introduction

This research endeavor developed the basis for an innovative and revolutionary processing technology that will create an entirely new research initiative for materials and materials process development. The magnetic field processing technology has both scientific and industrial relevance with potential annual energy savings ranging from 14 trillion BTUs for single heat treatment applications to many times that number when considering the complete manufacturing and application life cycle. This project has demonstrated and quantitatively documented the influence of ultrahigh (B>5 Tesla) magnetic fields on phase equilibria and transformation kinetics for ferromagnetic materials. To validate the concepts of this proposal, experiments were conducted at the National High Magnetic Field Laboratory (NHMFL) on several ferromagnetic alloy systems. Novel microstructures with enhanced performance have resulted that will enable the implementation of new and lighter-weight materials. This will lead to major energy savings and environmental benefits for the heat treatment and transportation sectors.

Prior research suggests that critical temperatures such as Ae1 and Ae3 can be modified significantly by a large magnetic field (Choi 2000). Because austenite is paramagnetic and ferrite is ferromagnetic, the application of the magnetic field favors the formation of the ferrite and destabilizes the austenite. The thermodynamic contribution to the Gibbs free energy of the magnetic field increases linearly with the applied field once the phase constituents have reached their magnetic saturation. The theory suggests that the change in free energy is limited only by the availability of an ultrahigh magnetic field.

A parallel computation effort using modern thermodynamic calculations was conducted to calculate the contribution to the free energy of the alloy phases that results from the application of these large magnetic fields. Based on the guiding principles established by this modeling effort, new compositions with their phase equilibria and new processing paths will be predicted and verified experimentally. By successfully demonstrating this novel materials and process development concept, a fundamental understanding and predictive capability of ultrahigh magnetic field processing technology will be gained. This will also result in significant future program development and funding opportunities from several major resources. In addition, deployment of this technology will be a major step towards achieving national goals of "materials by design."

Technical Approach

Experiments were performed using a 32-mm-diameter bore-resistive magnet with a 33-Tesla maximum field strength at the NHMFL. A key component of the experimental work was the ability to heat and cool the specimen within the spatial constraints imposed by a

32-mm-diameter magnet bore. To address this issue, a custom-designed induction heating coil coupled with a gas purge system for atmosphere control and specimen cooling was fabricated for experiments. The system was designed such that the specimen is located in the center of the bore mid length and can be rapidly heated to 1100ºC and maintains the high temperature for extended periods of time. Temperature measurement and control was obtained by attaching a type "S" (Pt-10%Rh) thermocouple to the specimen. An argon gas purge was used to minimize high-temperature oxidation and a helium gas quench was applied for accelerated cooling. Such a system allows for the entire thermal cycle or any portion of it to be exposed to a high magnetic field.

Previous work suggests that a large magnetic field will destabilize a paramagnetic phase relative to a ferromagnetic phase in a two-phase system (Choi 2000). Therefore, steels represent a material class that is an ideal candidate for ultrahigh magnetic field processing. Because steels can be heat treated to produce a large range of microstructures during austenite decomposition, various heat treatments associated with the austenite decomposition process were investigated. These experiments involved heating the specimen to a temperature in which the microstructure is fully austenitic. The austenitization treatment was followed by cooling at different rates to room temperature or cooling to a predetermined temperature and allowing the austenite to decompose isothermally. The magnetic field was applied during the entire cooling portion of the experiment for continuous cooling and during the isothermal hold and subsequent quench for the isothermal experiments. In all cases, an experiment was performed with the magnetic field applied and a companion experiment was performed for the exact same thermal history without the magnetic field. This allowed for a direct comparison between experiments where the magnetic field was the only variable. For isothermal experiments, metallographic examination was required to determine the effect of the magnetic field. However, for the cooling rates used in continuous cooling experiments, the release of latent heat due to austenite composition produced a recalescence easily observed in temperature data. Such data provided information for quantifying the shift in transformation temperature associated with the application of a large magnetic field. From these measurements an estimate of the change in free energy due to the magnetic field could be made.

Once the effect of the magnetic field on the free energy was quantified, these estimates were employed in computational thermodynamics calculations for predicting new phase diagrams accounting for the effect of a magnetic field. By comparing phase diagrams calculated with a magnetic field to traditional phase diagrams, processing paths for generating novel microstructures can be identified. In this project, the calculated phase diagrams identified regions in temperature-chemistry space where the magnetic field could be used to isothermally cycle transformations between the paramagnetic and ferromagnetic phases. These calculations along with quench dilatometry data were used to estimate an optimum temperature for isothermally cycling a phase transformation in 1045 steel. This temperature should be greater than the Ae1 but low enough that when a 30-Tesla magnetic field was applied, a majority of the austenite would transform to ferrite. Then the magnetic field would be removed, and the newly formed ferrite would reverse transform back into austenite. Such a processing strategy could be used to refine the microstructure without developing the undesirable microstructure gradients typically present during temperature cycling for the same purpose.

Results and Discussion

Initial results were aimed at reducing the amount of retained austenite in a 52100 steel. Specimens were annealed at either 850°C or 900°C and rapidly quenched to room temperature. A magnetic field was applied either during the quench or at room temperature after quenching. Subsequent X-ray analysis revealed that the amount of retained austenite was reduced from approximately 35% volume fraction without the field to less than 20% and, for some cases, less than 10% retained austenite. These results are the first data that show the magnetic field can be used to transform retained austenite at room temperature. These results are significant in that they suggest that a magnetic field can be used in lieu of cryo-quench treatments designed to reduce/eliminate retained austenite.

Another 52100 experiment involved cooling at a moderate rate with and without a magnetic field and comparing the measured thermal recalescence and resulting microstructures. For the case run at ambient field, a subtle thermal recalescence was observed below 200°C, suggesting a martensitic transformation. The experiment was repeated except that a 30-T magnetic field was applied prior to the onset of cooling. In this case, a thermal recalescence was initiated at ~620°C, indicating that a transformation had occurred. Subsequent SEM analysis revealed a pearlitic microstructure and confirmed that the application of a 30-T magnetic field had changed the transformation mechanism from a low-temperature diffusionless transformation to a high-temperature diffusive transformation. Additional experiments were performed using 10- and 20-Tesla fields, and intermediate transformation temperatures were obtained. This result indicates that for a fixed chemistry and cooling rate, a magnetic field can be applied to select a desired microstructural constituent. This is significant because

the need for "furnace cooling" and/or an additional heat treatment cycle can be eliminated by applying the magnetic field to obtain a non-hardened material.

Similar cooling experiments were performed with a 1045 steel. However, in the 1045 steel, the application of the magnetic field did not alter the transformation mechanism but increased the transformation temperature and ferrite content of the final microstructure. Because of these results, it was deemed reasonable to use temperature measurements to estimate the shift in transformation temperature due to a magnetic field. Again, a single alloy and cooling rate were applied in experiments where only the magnetic field strength was altered. These data estimated a 3.0°C/Tesla shift in transformation temperature due to a magnetic field. Also, a simple thermodynamic analysis was performed to estimate a shift of 12.6 J/mol/Tesla as the relation between free energy and the applied magnetic field. The estimate for change in free energy is important in that it allows for the effect of the magnetic field to be accounted for in computational thermodynamics calculations. Figure 1 is a pseudo-binary phase diagram calculated using ThermoCalc, Fe-DATA database (Saunders) for the 1045 steel chemistry used in these experiments. The figure displays two sets of data. The dashed line diagram was calculated using standard calculation procedures. For the solid-line phase diagram, the free energy of the ferrite was reduced 360 J/mol to simulate the effect of a 30-Tesla magnetic field. The figure illustrates the dramatic influence a ultrahigh magnetic field has on traditional alloy thermodynamics. The Ae1 and Ae3 temperatures are increased considerably along with the stability of the ferrite phase at higher temperatures. It is important to note that the magnetic field results should be considered an upper bound analysis because the calculation does not account for the decrease in magnetism of the ferrite at temperatures above the curie temperature.

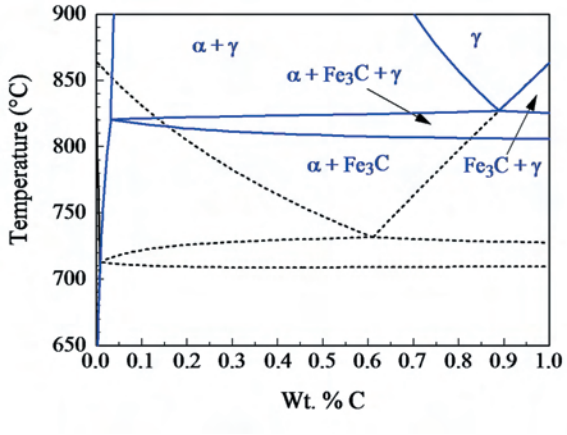

Fig. 1. Pseudo binary phase diagrams for 1045 steel calculated with ThermoCalc Fe-DATA database. The dashed line is the diagram without a magnetic field. The solid line is the diagram with the ferrite free energy decreased by 360J/mol to simulate a 30-Tesla magnetic field.

Regarding Figure 1, one observation is that the calculation shows there is a region where the $\alpha \leftrightarrow \gamma + Fe_3C$ transformation can be completely reversed, isothermally, by simply applying and removing a 30-Tesla magnetic field. To investigate this possibility, a 1045 sample was held at 750°C while the magnetic field was cycled between 30 Tesla and ambient. Samples were quenched after each portion of the cycle to capture the evolution of the microstructure. Although complete transformation reversal of the microstructure was not obtained, the resulting microstructures do show that a significant portion of the microstructure did undergo isothermal transformation cycling. These data illustrate that ultrahigh magnetic field processing is potentially a tool for microstructural refinement by way of transformation reversal.

As demonstrated in this project, ultrahigh magnetic fields are a viable materials processing tool for developing customized microstructures and reducing energy consumption. The induction heating/gas cooling system developed for this project is state of the art in terms of rapidly heating and cooling samples within the confines of a magnet bore. The data generated by this system convincingly show that a large magnetic field can be used to augment and accelerate austenite decomposition in steels. This has been illustrated by altering the transformation mechanism in 52100 steel and raising the transformation temperature 3.0°C/Tesla in 1045 steel. The 1045 results indicate a 12.6-J/mol/Tesla effect on the free energy, and computational thermodynamics calculations suggest that a magnetic field may be used to isothermally cycle transformations between paramagnetic and ferromagnetic phases. This technique is a potential method for refining microstructure to obtain bulk nanocrytalline grain size.

Benefits

This work was motivated by the need to reduce energy consumption and develop new environmentally friendly processes for the ferrous metals industry. Because ultrahigh magnetic fields can significantly alter phase transformation kinetics in steels, they provide a means to cut energy requirements by eliminating cryo-quench treatments, time- and energy-consuming furnace cool processes, and additional heat treatments that may be necessary to develop a softer microstructure in preparation for machining processes. Because steel is an ideal candidate for ultrahigh magnetic field processing, the potential savings in this high-volume industry is enormous. It is envisioned that the commercial application of this technology will use superconducting magnets due to their relatively low costs and availability. This research has shown a significant effect at field strengths less than

20 Tesla, and this makes the application of superconducting magnets viable. Superconducting magnets are desirable because of the low energy required to charge them, and once charged, they are an environmentally benign processing tool.

With further development, this technology has the potential to evolve into a processing tool with significant commercial value. Therefore, to date, one patent has been published (Ludtka patent 2004) and an additional patent application has been filed (Ludtka patent application 2004) regarding ultrahigh magnetic field processing.

In addition to the energy savings and environmental friendliness, ultrahigh magnetic field processing has shown the potential for developing new microstructures with increased strength and enhanced performance. The additional thermodynamic driving force provided by the magnetic field can be used to refine microstructures, such as pearlite, and develop high-strength pearlite. Also, it has been shown that grain refinement may be achieved by isothermally cycling the magnetic field, inducing transformation cycling. These additional benefits could potentially help the transportation industry and have military applications by creating steels with enhanced performance and properties.

References

Choi, J-K., H. Ohtsuka, Y. Xu, and W-Y Choo. 2001. "Effects of a Strong Magnetic Field on the Phase Stability of Plain Carbon Steel," *Scripta Mater.* **43**, 221–226.

Saunders, N. "Mg-DATA, a database for thermodynamic calculations for Mgalloys," Thermotech Ltd., Surrey Technology Centre, The Surrey Research Park, Guilford, Surrey GU2 7YG, U.K.

Ludtka, G. M. 2004. "Method for residual stress relief and retained austenite destabilization," United State Patent 6,773,513.

Ludtka, G. M., G. Mackiewicz-Ludtka, R. A. Kisner, J. B. Wilgen, R. A. Jaramillo, and D. M. Nicholson. 2004. "Magnetic field processing for developing and customizing microstructures and properties in materials," United State Patent application S-96,666.

Materials Science of Nanostructured Carbons and Graphites

T. D. Burchell,[1] C. L. Fu,[1] N. C. Gallego,[1] J. Howe,[1] M. Miller,[1]
D. Geohegan,[2] W. Shelton,[3] J. Calo,[4] D. D. Edie,[5] and Y. Basova[5]
[1]*Metals and Ceramics Division*
[2]*Condensed Matter Sciences Division*
[3]*Computer Science and Mathematics Division*
[4]*Brown University*
[5]*Clemson University*

The hydrogen adsorption behavior of a series of nanostructured carbons was studied. No evidence was found of significant hydrogen adsorption on the carbons at ambient temperature. However, modeling studies suggested that metal catalyst particles play a crucial role in facilitating adsorption. Consequently, the work was focused on the experimental determination of the role of the metal catalyst in the interaction of hydrogen on the carbons. The influence of catalyst morphology on the interaction between C and H was examined using samples of pure and impure nanotubes and activated carbons and fibers with and without dispersed metal catalyst. Hydrogen adsorption at low pressure (2 MPa) was performed. Advanced characterization methods (e.g., HRTEM, XRD, XPS, and STEM) were applied to study the catalyst morphology and dispersion within the carbon nanostructure. The modeling studies indicated that hydrogen storage could be substantially increased if the high potential energy barrier associated with the initial stage of intercalation of H_2 molecules can be overcome (i.e., through a proactive rather than reactive expansion of the graphite lattice). In this context, catalytic metal particles should both help expand the interlayer spacing and provide an electronic interaction that lowers the energy of sorption of H_2 molecules on carbon surfaces adjacent to the metal particles. Sorption of the initial H_2 molecules promotes additional lattice expansion, and further sorption of hydrogen is facilitated.

Introduction

Carbon materials exhibit unique and interesting properties because of structural or molecular phenomena occurring at the nanoscale. Moreover, it has been widely reported that carbon nanostructures, such as single walled nanotubes, can adsorb H_2 to significant levels at ambient temperature. The objectives of this work were (i) the characterization of the nanostructure of a range of carbon materials, (ii) assessment of the hydrogen storage capability of nanostructured carbons, (iii) the development of mathematical models that describe the "real" carbon structure and the interaction of H_2 with carbon and catalysts, and (iv) the application of those models to assess the nanostructure features that control and influence the interactions of the carbon with the H_2. A major emphasis of this work was the examination of metal-doped carbon fibers which we obtained through a collaborative effort with Clemson University.

Technical Approach

This project sought to explore the role of nanostructure in H_2 storage on carbons. Experimental (advanced structural characterization and measurement of H_2 isotherms) and theoretical (both ab initio calculation of potential H_2/carbon-surface/metal-catalyst interactions and reverse Monte-Carlo simulations of the carbon nanostructure) approaches were adopted. Characterization data provided a basis for the development of simulation of nanoporous carbon structures. Small-angle neutron scattering (SANS) data demonstrated that light gas interactions occur predominantly in the nano-dimensioned pores (i.e., <3 nm in width). Hydrogen adsorption isotherms at ambient and liquid N_2 (77 K) temperatures, over the pressure range 0–2 MPa, were obtained using a Hiden "Intelligent Gravimetric Analyzer" (IGA) system, which integrates computer-controlled measurements of weight change, pressure, temperature, gas flow, and gas composition (by mass spectrometry analysis).

Modeling data suggested that the combination of highly nanoporous activated carbon and a finely dispersed metal catalyst might offer the best chance for H_2 storage on carbon. Consequently, through a collaborative effort with Clemson University, the project focused on nanostructured activated carbon fibers with dispersed Pd metal particles in the size range 2–20 nm. Three independent methods of structure analysis, X-ray diffraction (XRD), X-ray photoelectron spectroscopy (XPS), and scanning transmission electron microscopy (STEM) provided information on the nature of the Pd nanoparticles in the Pd-doped activated carbon fibers and how they may be associated with the formation of structural defects in the fibers and, consequently, increased H_2 uptake.

Results and Discussion

Hydrogen Storage

The H_2 adsorption behavior of a broad selection of nanoporous carbons was determined utilizing the IGA system. None of the samples tested showed significant H_2 uptake at ambient temperature (typically < 0.2 wt % uptake). The greatest hydrogen uptake at ambient temperature was ~0.3 wt %, obtained on a wood-based activated carbon; the same sample exhibited a H_2 uptake in excess of 8 wt % at 77 K.

Given that ab initio calculations suggested that the presence of a metal catalyst on the carbon surface promotes the adsorption of hydrogen, ORNL partnered with Clemson University to study the hydrogen storage capacity of metal-containing activated carbon fibers (ACF). Several Pd-containing ACFs were produced and evaluated. We obtained a 2 wt % hydrogen uptake at ambient temperature and a pressure of ~2 MPa (285 psia) on an ACF containing 4 wt % Pd. This was an order-of-magnitude improvement over the hydrogen storage capacity of ACF prepared without Pd (Fig. 1). The enhanced uptake of hydrogen corresponded to a H-to-Pd atomic ratio of about 50:1, substantially greater than could be accounted for by hydride formation alone, for which the H-to-Pd ratio would be about 0.8:1 under comparable conditions of temperature and pressure (Lewis 1967). It should be emphasized that the manner in which the Pd-doped ACF was prepared distinguished it from other activated carbon materials doped with a metal catalyst. In contrast to the conventional method of post-treating (impregnating) an activated carbon material with a catalyst, the Pd-doped ACF was prepared by melt spinning, carbonizing, and subsequently activating an isotropic pitch (Bahl et al. 1998; Oberlin et al. 1998) precursor material preloaded with a dissolved Pd salt. Reduction of the salt-to-Pd metal occurred at temperatures below that at which carbonization of the precursor commenced.

The data shown in Fig. 1 exhibited a very unusual form of adsorption hysteresis: the desorption branch of the hydrogen isotherm is not only located well below the adsorption branch but is clearly of a different type. Both qualitatively and quantitatively, these results could be reproduced at will using fresh samples of the Pd-doped ACF. When, however, a sample of the Pd-doped ACF was subjected to repetitive hydrogen adsorption/desorption cycling, the second and subsequent uptakes of hydrogen were considerably less; namely, about 0.2 wt %. We speculate that the unusual hysteresis loop is due to a latent structural change induced in the Pd-doped carbon upon exposure to hydrogen at progressively increasing pressure. The structural change was not manifested until the pressure in the system was reduced below that of the maximum attained (about 2 MPa), when release of hydrogen from the Pd-doped ACF resulted in a progressive collapse of what is tentatively referred to here as a metastable carbon hydrogen structure; that is, at a given pressure, the carbon could no longer store the same amount of hydrogen reached during the adsorption cycle.

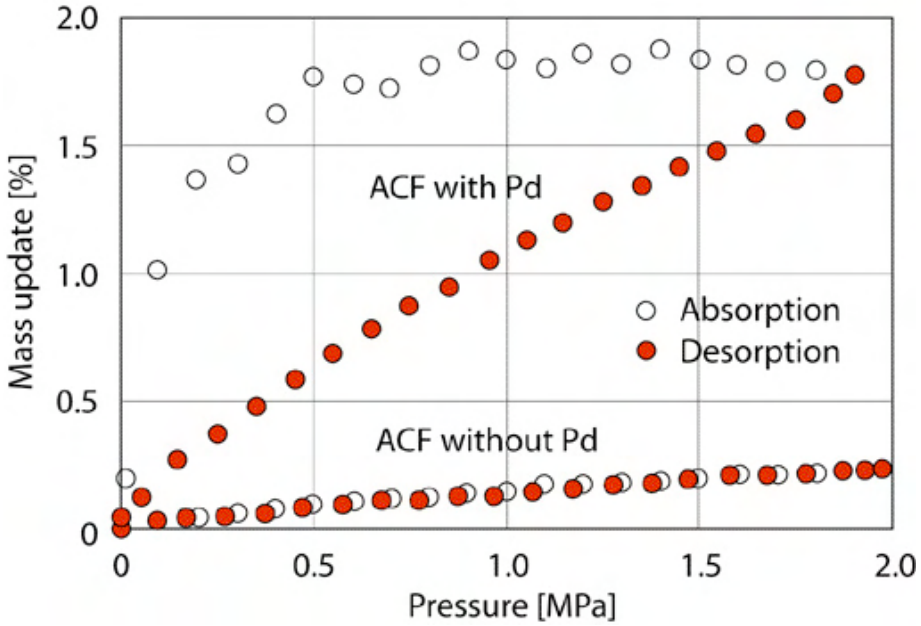

Fig. 1. Hydrogen isotherms at ambient temperature for ACF and Pd-loaded ACF. These ORNL data demonstrate an order-of-magnitude enhancement of hydrogen storage induced by the presence of Pd in the activated carbon fibers.

This finding is disturbing in the context of developing a viable hydrogen storage system but is intriguing from a fundamental standpoint. Certainly, it begs the questions of what structural changes are being induced in the Pd-doped activated carbon fiber during hydrogen adsorption, and how they can be stabilized to maintain a reversible and high level of hydrogen storage on the carbon.

The adsorption data indicate that the mechanism of hydrogen storage on the Pd-doped ACF was fundamentally different from that for gas adsorption on microporous carbon materials or for hydride formation. In this context, it is proposed that the role of the Pd nanoparticles comprises one or both of the following:

- As a catalyst: Pd nanoparticles dissociate molecular hydrogen to atomic H, which can migrate, via activated surface diffusion, across the carbon surfaces and between graphene layers.
- As a defect former: Pd nanoparticles generate local defects in the pitch precursor, which survive the carbonization and activation stages to become the sites for hydrogen storage.

Characterization of Nanostructured Carbons

Three independent methods of structure analysis provided information on the nature of the Pd nanoparticles in the Pd-doped activated carbon fibers and how they may be associated with the formation of structural defects in the fibers: (i) X-ray Diffraction (XRD) data indicated that amorphous PdO was the dominant phase present after the stabilization stage, and that it was reduced to Pd metal during the stages of stabilization and carbonization of the fiber (Basova and Edie 2004). Peaks attributable to crystalline Pd were observed in the XRD of the carbonized and activated fibers, in addition to the broad peak associated with turbostratic structures of carbon. (ii) X-ray Photoelectron Spectroscopy (XPS) characterization of Pd-loaded ACF revealed evidence of carbon particles on the Pd surface. For virgin samples of the Pd-loaded ACF, the Pd/C ratio in the outer surface layers was about half of that expected (based on the bulk composition), indicating preferential "wrapping" of Pd nanoparticles by resilient carbon structures. After Ar sputtering of the sample, the Pd/C ratio in the surface layer increased (but did not attain the bulk value) and the O/C ratio was lowered. (iii) Scanning Transmission Electron Microscope (STEM) analysis of the Pd-loaded ACF after sorption and desorption of hydrogen revealed that the Pd particles were largely spherical in shape, with sizes ranging from about 2 to 20 nm. The smallest nanoparticles, although not revealed in the secondary electron image, became visible in the Z-contrast image. Further studies of the same ACF sample using ORNL's aberration-corrected STEM revealed domains of local short order together with larger domains of disordered carbon. However, it is not clear at this point what the relationship is between the short order domains and metal particles.

Theoretical Modeling: Metal-Promoted H_2 Adsorption on Graphite Surface

Metal particles on defect-free carbon surfaces promote adsorption of hydrogen, but the effect varies from metal to metal. Using first-principles methods, we have modeled the binding interactions of hydrogen molecules on a graphite surface in the presence and absence, respectively, of Pd atoms. In the absence of Pd, H_2 molecules interact weakly with the graphite surface (adsorption energy is only -0.09 eV) and the H-H bond length is unaffected by the surface. Therefore, adsorption of hydrogen on graphite is unlikely at ambient temperature. In the presence of Pd, however, H_2 molecules bind preferentially to Pd atoms stabilized on the graphite surface, with a binding energy as high as -1.36 eV. The H-H bond strength is weakened (length increases by 17% with respect to free H_2), and therefore H_2 adsorption is promoted.

A single Pd atom on a graphite surface will not dissociate H_2 molecules. However, a single Pd atom will promote adsorption of multiple H_2 molecules through direct electronic interaction between Pd and H_2. If the Pd particles are well dispersed, the direct Pd-H_2 interaction increases hydrogen uptake, but this alone cannot explain the relatively high level of hydrogen uptake observed experimentally for the Pd-doped ACF. As the number of atoms in a Pd particle increases, the catalytic activity of the Pd particle should approach that of a Pd metal surface, resulting in dissociation and adsorption of H atoms on the Pd (Mitsui et al. 2003; Lovvik et al. 1998). Dissociated H atoms are either chemisorbed on the Pd surface or migrate into the carbon lattice through surface/interlayer diffusion.

On a defect-free graphite surface, atomic hydrogen has an adsorption energy of 1.0 eV/H (relative to the energy of free atomic hydrogen), which is less than half of the binding energy of the H_2 molecule (4.7 eV, or 2.4 eV/H). Thus, hydrogen atoms would spontaneously break away from a defect-free graphite surface to form H_2 molecules. If hydrogen atoms are intercalated between the graphene sheets, they would similarly recombine because of the higher stability of the H_2 molecule. However, if hydrogen sorption on graphite is assisted by electronic interactions with nearby metal particles or lattice defects, hydrogen atoms are more likely to be stable on the graphite surface or between graphene layers. Hydrogen atoms bound at low-gas-phase concentration serve as "seeds" for the hydrogen recombination process as the

hydrogen concentration is increased. It is also possible that these "seeds" are the nucleation centers for further hydrogen uptake if a collective stabilization of hydrogen chemisorption processes proves to be feasible.

Theoretical Modeling: Metal-Assisted Hydrogen Intercalation between Graphene Sheets

Molecular simulation studies reported in the literature (Cracknell 2001) indicate that H_2 in the vicinity of edge sites on graphite dissociates into H atoms, which bond to the terminal positions. This increases graphite interlayer spacing, which possibly leads to the insertion of more hydrogen. In pure graphite, the graphene layers are stacked too closely together for hydrogen molecules to fit between; that is, in the dilute limit, H_2 molecules are energetically unstable between the graphene sheets. At higher H_2 concentrations, however, a large number of H_2 molecules can be stabilized in the graphite lattice because they induce a dramatic expansion of the lattice. Significantly, our modeling data indicate that a substantial decrease in the H_2 sorption energy together with a large expansion in the graphite interlayer spacing occurs at low H/C atom ratios; i.e., $H/C < 0.2$. Our modeling results indicate that a bound state is formed at high H_2 concentration between graphene sheets, but the geometry of the intercalated H_2 molecules has yet to be optimized. Nevertheless, the energy of H_2 sorption between graphene layers cannot exceed 0.2 eV/H_2 (i.e., twice the sorption energy of H_2 on a single pure graphite surface). It is unclear at this time whether this is too small for H_2 sorption at ambient temperature.

Benefits

Through the work reported here, we have shown the fascinating H_2 sorption behavior of Pd-doped nanostructured carbon fibers. Moreover, we have successfully achieved a harmonization of modeling and characterization to develop hypotheses to explain the observed H_2 adsorption behavior of nanostructured carbon in the presence of metal nanoparticles. As a result of the insights gained from this LDRD project, we were invited to submit a proposal to the DOE BES program in the area of H_2 storage science. The proposal addresses the BES long-term program targets in the area of design, modeling, fabrication, and characterization, at the nanoscale level and with atomic precision, of novel materials for energy-related applications. Specifically, the project is directed towards elucidation of the atomistic mechanisms of metal-assisted hydrogen storage in nanostructured carbons. Partly through this LDRD project, ORNL, in partnership with Clemson University, is uniquely qualified to investigate the atomistic mechanisms through a crosscutting, interdisciplinary approach that capitalizes on existing strengths; namely, synthesis and testing of nanostructured carbons, sub-angstrom resolution electron microscopy, neutron scattering, and theoretical modeling.

References

Lewis, F. A. 1967. *The Palladium Hydrogen System*. Academic Press, London.

Bahl, O. P., et al. 1998. "Manufacture of Carbon Fibers." In *Carbon Fibers*, pp. 1–84. Marcel Dekker, New York.

Oberlin A., S. Bonnamy, and K. Lafdi. 1998. "Structure and Texture of Carbon Fibers." In *Carbon Fibers*, 85–160. Marcel Dekker, New York.

Mitsui, T., et al. 2003. "Dissociative Hydrogen Adsorption on Palladium Requires Aggregates of Three or More Vacancies." *Nature*. **422**, 705.

Lovvik, O. M., and R. A. Olsen. 1998. "Adsorption Energies and Ordered Structures of Hydrogen on Pd(111) from Density-functional Periodic Calculations." *Physical Review B.* **58**, 10890.

Cracknell R. F. 2001. "Molecular Simulation of Hydrogen Adsorption in Graphitic Nanofibres." *Physical Chemistry Chemical Physics*. **3**, 2091.

Aberration-Corrected, Ultra-High-Resolution Electron Microscopy for Atomic-Level Characterization of the Structure and Chemistry of Nanophase Materials

S. J. Pennycook,[1] M. V. del Arco,[1] L. F. Allard,[2] I. M. Anderson,[2] and D. A. Blom[2]
[1]*Condensed Matter Sciences Division*
[2]*Metals and Ceramics Division*

The goal of the LDRD project was to develop the necessary theoretical and computational groundwork for the simulation and interpretation of atomic-scale images and spectra enabled by two ORNL scanning transmission electron microscopes (STEMs) equipped with aberration correctors. These unprecedented instruments have provided a unique test of and challenge for existing theories for electron scattering within solids. This LDRD has placed ORNL in a clear and unchallenged leadership position in the field of STEM, in an excellent position to lead future major projects.

Introduction

In the last few years, the ability to correct the aberrations in electron microscope lenses has more than doubled the achievable spatial resolution, a greater advance than in the previous two decades. It was predicted that this would allow the imaging of individual atoms within materials and on their surfaces, and the imaging of light atoms adjacent to heavy atoms. This experimental advance would require the parallel development of new simulation techniques, to account for the larger convergence angles used in aberration-corrected probes, and also for spectroscopic imaging, in which the achievement of atomic resolution has long been controversial. All these goals have been met; in particular, the project recently achieved a new world record, the first direct imaging of a crystal lattice at sub-Angstrom resolution, reported in *Science* (Nellist, Chisholm et al. 2004). In addition, an unexpected advantage of aberration correction has been discovered, the ability to image in three dimensions (3D), which overcomes the historic limitation of the microscope in providing a two-dimensional view of a 3D world, and could revolutionize the way electron microscopy is done in the future.

Technical Approach, Results, and Discussion

Over the three years prior to the start of this proposal, aberration correctors manufactured by Nion were installed on the two ORNL STEMs. Resolution of the 100-kV STEM improved from 2.2 Å uncorrected to 1.2 Å after correction, and presently this machine achieves 0.9 Å resolution. On the 300-kV STEM, the resolution increased from 1.3 Å uncorrected to 0.9 Å corrected, and presently, through improvement of instrumental stabilities, it has further improved to the 0.6 Å mentioned above. This achieves the theoretical capability of the electron-optical system. The goals of this project were primarily to develop the simulation methods to match the new instrumental capabilities and to scope out new advances that may lead to future research initiatives. The theoretical methods involved development of means for the simulation of images based on both coherent and incoherent scattering, and for both elastic and inelastic scattering. Codes were to be developed based on the Bloch wave method that we had previously used to study image formation in the Z-contrast mode, and also on multislice methods that were more popular elsewhere, using the absorptive potential and frozen-phonon algorithms. Simulation and experiment would be compared in the new regime of sub-Angstrom resolution to demonstrate leadership on both the experimental and theoretical fronts.

Development of reliable techniques for simulation of single-atom images in nanostructured materials. A Bloch wave analysis of the imaging process was extended to the larger apertures available with present and next-generation aberration-corrected STEMs. The image indeed becomes a direct image of the 1s Bloch states, as proposed by us previously based on analytical approximations to the image, but the non-1s portion of the incident probe becomes increasingly important with increasing aperture angle. Theory showed that this portion of the probe can be focused at a specific depth within a specimen, even a crystal aligned to a low index zone axis where strong electron channeling occurs (via the 1s state portion of the probe). Nevertheless, it appears feasible to use the non-1s portion of the probe to perform depth sectioning, giving three-dimensional reconstruction. Simulations have confirmed that the depth resolution increases with increasing aperture angle, but also that it is not negated by the tendency of electrons to channel along atomic columns. The simulations have led to the realization that both types of behavior are seen for any given probe, the ratio depending on aperture angle. Channeling dominates for small angles, the depth sectioning effect for large

angles. Experimental verification of this behavior is described in the next section. We have also initiated the frozen phonon multislice algorithm, which is more efficient for some purposes and have extended the code to sub-Ångstrom probes and to include inelastic excitation as required for simulating electron energy loss spectroscopy (EELS) images.

Development of 3-D tomography at atomic resolution and sensitivity. Based on the insights from the image simulations described above, we have investigated the possibility of selecting atoms at different depths simply by focusing on them directly. Experimentally we have already achieved 2-nm depth resolution using a 0.7 Å probe, while maintaining sensitivity to individual La atoms on the surface of gamma-alumina support (Wang, Borisevich et al. 2004). Images on 3D-supported catalyst samples also maintained single-atom sensitivity and allowed the reconstruction of the 3D shape of the support. More strikingly, depth sectioning was applied to a $Si/SiO_2/HfO_2$ alternative gate dielectric specimen, and individual Hf atoms could be seen inside the narrow 1-nm SiO_2 layer, as shown in Fig. 1. It is clear that the Hf atoms are not attached to the Si substrate, a key issue in the field because of possible effects on carrier mobility in the Si gate region. This result marks a landmark achievement in semiconductor characterization, one of the stated goals for the industry, the identification of individual atoms with 3D atomic resolution, with previously no known solution. Simulations show that our current system will be limited to about 2-nm resolution, but the next generation STEM anticipated from the future TEAM program should improve this to 1 nm, and depth resolution at the atomic level would be possible in a future-generation instrument with an additional factor of two increase in aperture angle.

Development of electron energy loss spectroscopy with ultimate sensitivity and resolution. Individual atoms have been detected and identified spectroscopically within a bulk material for the first time by EELS. The sample was La-doped $CaTiO_3$, specially grown in ORNL, comprised of lightly doped layers spaced 10 nm apart. The experiment was performed on the 100-kV STEM where the depth resolution is larger than the thickness of the specimen. Nevertheless, dynamical simulations allowed the atom depth to be determined to an accuracy of a few nm by comparing the calculated and experimental EELS images. With increasing atom depth, as a result of beam broadening, signals from adjacent columns increase relative to that from the column that contains the dopant atom. This shows that reliable techniques are now available both for simulating both Z-contrast imaging and element-specific spectroscopic imaging, one of the major tasks of this project. A *Physical Review Letter* was published showing agreement between experiment and simulation at atomic resolution (Varela, Findlay et al. 2004).

Assessing the potential of aberration-corrected STEM for dynamics and in-situ imaging. Apart from the 3D sensitivity, another unexpected benefit of aberration correction is that conventional phase contrast images of high quality can now be obtained in STEM mode by the use of a small axial detector. It has long been realized through the principle of reciprocity that such a detector will in theory produce an identical image to that produced by a conventional TEM with parallel illumination, but such images have previously been too noisy to be of any practical use. Now, with aberration correction, the size of the axial aperture can be enlarged substantially and high-quality images result. Phase contrast imaging can now be achieved in the STEM along with simultaneous Z-contrast imaging. This is a major advance for imaging nanomaterials. Carbon nanotubes are a perfect example where imaging of the light carbon structure is best done with phase contrast, whereas Z-contrast is the ideal way to image catalyst atoms. Beam currents are sufficient for high-quality movies to be made with frame rates of just a few seconds. One could therefore envisage an in situ STEM designed to image the growth of carbon nanotubes in situ.

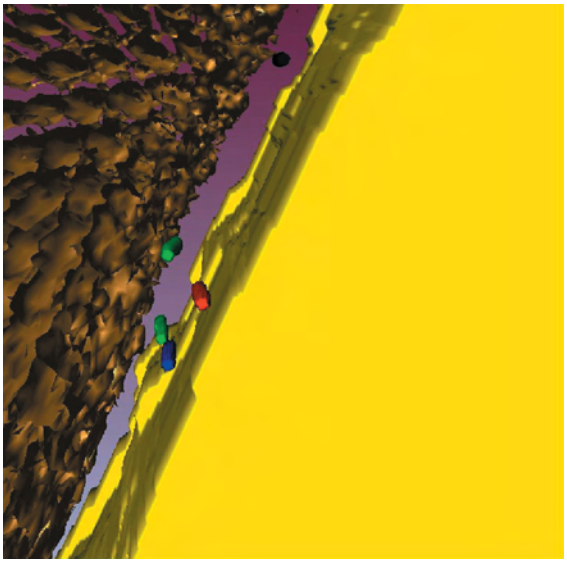

Fig. 1. Snapshot of a three-dimensional representation of the $Si/SiO_2/HfO_2$ interface created by setting thresholds on intensity values from the through-focus series. The Si substrate was colour coded in gold, whereas the HfO_2 film is marked solid yellow. Single Hf atoms in the interface layer are colour coded separately in green, black, red, and blue, according to depth. Note that even some surface roughness of the HfO_2 film is observable at the interface with the SiO_2 layer. Results are submitted to Science.

Benefits

This LDRD has cemented a dominant leadership position for ORNL in the field of STEM. Not only do we fully reap the benefits of the instrumental upgrades of our 100- and 300-kV STEMs, but we now have the theoretical leadership and image simulation capability to match. Interactions have been established with numerous leading groups worldwide, with two visiting Japan Society for the Promotion of Science Fellows, a Wigner Fellow, and a Humboldt Fellow. Their work has resulted in high-visibility publications as cited above, and several more (Pennycook, Lupini et al. 2003; Diebold, Foran et al. 2004; McBride, Kippeny et al. 2004; Shibata, Pennycook et al. 2004) with numerous talks at international meetings. This could not have been achieved without the LDRD project.

References

Diebold, A. C., B. Foran et al. 2004. "Image formation in the high-resolution transmission electron microscope - Authors' response," *Microscopy and Microanalysis* **10**(4), 399–400.

McBride, J. R., T. C. Kippeny et al. 2004. "Aberration-corrected Z-contrast scanning transmission electron microscopy of CdSe nanocrystals," *Nano Letters* **4**(7), 1279–1283.

Nellist, P. D., M. F. Chisholm et al. 2004. "Direct sub-angstrom imaging of a crystal lattice," *Science* **305**(5691), 1741.

Pennycook, S. J., A. R. Lupini et al. 2003. "Aberration-corrected scanning transmission electron microscopy: the potential for nano- and interface science," *Zeitschrift Fur Metallkunde* **94**(4), 350–357.

Shibata, N., S. J. Pennycook et al. 2004. "Observation of rare-earth segregation in silicon nitride ceramics at subnanometre dimensions," *Nature* **428**(6984), 730–733.

Varela, M., S. D. Findlay et al. 2004. "Spectroscopic imaging of single atoms within a bulk solid," *Physical Review Letters* **92**(9), 095502.

Wang, S. W., A. Y. Borisevich et al. 2004. "Dopants adsorbed as single atoms prevent degradation of catalysts," *Nature Materials* **3**(3), 143–146.

Biologically Driven Controlled Synthesis and Directed Assembly of Nanophase Inorganic Materials

M. L. Simpson,[1] M. J. Doktycz,[2] T. E. McKnight,[3] and N. Samatova[4]
[1]*Condensed Matter Sciences Division*
[2]*Life Sciences Division*
[3]*Engineering Science and Technology Division*
[4]*Computer Science and Mathematics Division*

University Collaborators
D. E. Morse,[1] G. S. Sayler,[2] and J. J. Collins[3]
[1]*University of California, Santa Barbara*
[2]*University of Tennessee Center for Environmental Biotechnology*
[3]*Boston University*

The major goal of this project was to "learn the rules" of biologically driven controlled synthesis and directed assembly and eventually to apply these rules to the creation of engineered nanophase material systems. We focused ORNL's and our collaborator's unique capabilities in biology, computation, and synthesis of nanoscale materials on the mechanisms of biology that manipulate energy, information, and materials with spatial and temporal specificity on the nanoscale. Our work included functional studies to identify, characterize, model, simulate, and engineer the biomolecular mechanisms useful for the controlled synthesis and directed assembly of inorganic materials. While there are 60 different inorganic minerals produced by organisms from bacteria to humans, we focused on "silicateins" (silica proteins) that can be harnessed to direct the nanofabrication of other technologically important materials such as titanium dioxide, zinc oxide, and gallium oxide. This provided an appropriate model system to focus the science of this LDRD project while providing the potential of highly significant technology results. Our work included the following components: identifying/describing molecular processes useful for controlled synthesis and directed assembly of inorganic materials to create inorganic nanostructures abiotically; the analysis and simulation of natural gene/biochemical circuit and network topologies that control synthesis and direct assembly at the nanoscale in biological systems; and the creation of synthetic gene/biochemical networks for the engineered control/mimicking of biologically driven controlled synthesis and directed assembly.

Introduction

The central premise of this work is graphically represented in Fig. 1. With a precision of nanostructural control that far exceeds present human capabilities, biological systems fabricate a remarkable diversity of three-dimensionally organized materials. In contrast to the conditions of industrial manufacture, these biological syntheses occur under mild physiological conditions of low temperatures, ambient pressures, and near-neutral pH. On the far right in Fig. 1, a microscale silica structure with nanoscale features is shown. The diatom *Diploneis*, a single-cell marine organism, fabricates this structure. Since different structures are fabricated by different varieties of diatoms, clearly the plans, material transport, and control systems leading to each of these nanostructures are encoded in the genome. The arrow that points from the DNA to the nanostructure represents a set of complex processes that provide for the transport of material, energy, and information at the nanoscale that leads to the controlled synthesis and directed assembly of nanophase material systems. It is these processes, pathways, and complex network topologies that we investigated and began to integrate into the research agenda of the Center for Nanophase Materials Science.

As there are more than 60 different inorganic minerals produced by organisms from bacteria to humans, we could look at a wide variety of biological systems that synthesize inorganic nanophase materials. However, in the laboratory of one of the collaborators in this work (Morse), it was recently discovered that "silicateins" (silica proteins) can be harnessed to direct the nanofabrication of other technologically important materials such as titanium dioxide, zinc oxide and gallium oxide (the later potentially serving as a precursor to the gallium nitride family of wide bandgap semiconductors). This provided an appropriate model system to focus the science of this LDRD project while providing the potential of highly significant technology results. To take advantage of this opportunity, we organized our work around the following three thrust areas:

1. Molecular processes useful for controlled synthesis and directed assembly of inorganic materials
2. Natural gene/biochemical circuit and network topologies that control synthesis and direct assembly at the nanoscale in biological systems and synthetic gene/biochemical networks for the engineered control/mimicking of biologically driven controlled synthesis and directed assembly.
3. Exploration of the use of synthetic nanoscale elements to control genetic/biochemical systems.

Technical Approach and Results

Molecular processes useful for controlled synthesis and directed assembly of inorganic materials

As part of this project in Dan Morse's lab, Paul Curnow and Michi Izumi worked on the genetic manipulations of the silica proteins (silicateins), which has proved to be tougher and slower than we had anticipated. However Curnow, who has special expertise in membrane proteins, succeeded in creating a genetic fusion of the gene coding for silicatein with a gene that codes for a transmembrane protein that is expressed on the surface of *E. coli* bacterial cells. He has demonstrated that the silicatein is actually displayed (in about 10,000 copies per cell) on the surfaces of the recombinant bacteria, and that it remains active. Izumi has succeeded in getting the cells to produce significantly elevated quantities of silicatein. The problem she is now addressing (with recent considerable progress) is the purification of the protein in workable quantities and with sufficient stability to enable material synthesis research. These developments provide us vital tools for biologically driven controlled synthesis and directed assembly using silicatein materials.

In advance of having sufficient quantities of silicateins, we have been working with poly-L-lysine (PLL) as a mimic of silicaten function. We demonstrated the use of poly-L-lysine to promote the synthesis of silica in neutral, aqueous solution and when immobilized onto a silicon support structure under similar conditions (Coffman 2004). Both reagent jetting and conventional photolithography techniques were used to pattern the templating polymer. Spots created by reagent jetting led to the creation of silica structures in the shape of a ring that may be a result of the spotting process. Photolithographically defined poly-L-lysine spots led to thin laminate structures after exposure to a dilute aqueous silicic acid solution. The laminate structures were nanostructured and highly interconnected. Photolithographic patterning of (3-amino propyl)trimethoxysilane, a reagent that mimics the lysine functional group, led to similar silica coatings even though low-molecular-weight materials do not promote silica synthesis in solution. This result highlights the importance

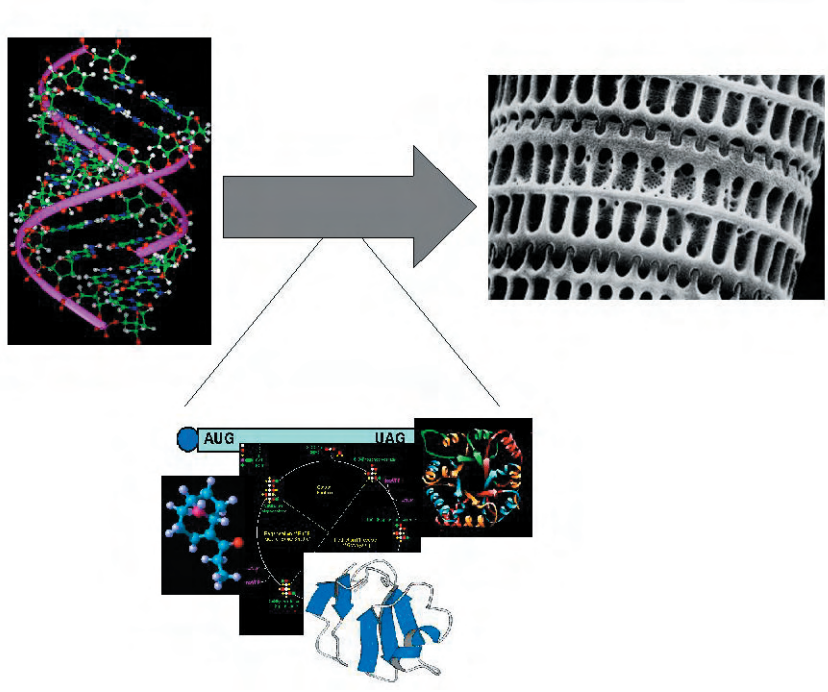

Nanoscale features in the silica wall of the marine diatom *Diploneis* (length 50 μm)

Fig. 1. A complex set of processes lead from a biochemical "plan" (i.e., DNA) to the finished product: a microscale structure with precisely ordered nanoscale features. Within these processes are the "rules" for the control of material, energy, and information transport on the nanoscale that drive the controlled synthesis and directed assembly of nanophase material systems.

of functional group arrangement for templating and promoting the synthesis of inorganic materials. The described surface patterning techniques offer a route to integrate conventional silicon patterning technologies with biologically based material synthesis. Such combined fabrication techniques enable controlled assembly over multiple length scales and an approach to understanding interfacial silica synthesis as occurs in natural systems. This work provides a firm base for the deployment of the silicateins in synthetic material systems.

Natural gene/biochemical circuit and network topologies that control synthesis and direct assembly at the nanoscale in biological systems and synthetic gene/biochemical networks for the engineered control/ mimicking of biologically driven controlled synthesis and directed assembly

Synthetic Gene Circuits: A major obstacle to generate highly complex function using synthetic gene circuits is the requirement of long ("deep") logic cascades. Many electronic circuits are constructed as deep logic cascades where signals are serially processed as they pass from the output of one module to the input of the next, and functional complexity grows as the cascade becomes longer. However such architecture is not favored in gene networks, perhaps due to the very slow dynamics of cascaded transcriptional circuits, which would lead to long transit times for information processed through a deep cascade. Rather, it seems that complex gene networks employ a "broad and shallow" architecture where multiple logic functions are integrated into the cis-regulatory elements and information is processed in parallel instead of serially. In this project the Collins' lab leveraged existing complexity by deploying a synthetic circuit as an interface between natural pathways that serve as input (signal detection) and output (response) modules (Kobayashi 2004; Simpson 2004). The role of the synthetic circuit was not the de novo creation of complexity but rather was to customize the function of existing complexity by controlling the connection between pathways.

The genetic toggle switch (Gardner 2000) was used for this intermediate layer of synthetic circuitry. The toggle switch is unique among the suite of synthetic gene circuits as it implements a memory function, and the Collins lab used this property to produce a circuit that implemented epigenetic inheritance leading to a persistent phenotypic alteration in response to transient signals. That is, signals of limited duration latched in place responses at the individual cell level that determined group behavior of this cell's progeny long after the signal subsided. This was convincingly demonstrated by a circuit coupling the SOS response pathway that is activated by single-stranded DNA (input) and a pathway leading to biofilm formation (i.e., biologically driven controlled synthesis). Transient DNA damage induced by chemical or physical stresses latched the toggle switch into a stable state that led to biofilm formation many cell cycles after application of the input signal.

Analysis, Modeling, and Simulation: This portion of the work was centered on the analysis, modeling, and simulation of gene circuits and networks. Toward this goal we developed the following software tools: (1) ESS (Exact Stochastic Simulator) is an optimized Gillespie simulator; (2) BioSmokey is a tool for manipulation and conversion of time series data from any SBML-compatible analysis tool; (3) An Octave agent that allows commands from the Octave open-source mathematical software to be implemented from within our software environment; (4) BioSpreadsheet provides a tabular interface for entering chemical reactions and expresses the resulting model as SBML (BioSpreadsheet also serves as an integrated stochastic simulation platform that implements the ESS, BioSmokey, and Octave agents described above); and (5) BioGrid is a distributed computing environment that distributes individual ESS simulations across a cluster of machines with the resulting increase in simulation speed scales proportionally with the number of machines (McCollum 2004). BioGrid also allows the user to conveniently scan model parameters, initial conditions, and random number seeds by automatically generating the requisite SBML and providing a convenient summary of the results. Underutilized computational resources can be exploited to run the numerous stochastic simulations needed to develop a statistically representative phenotype. Our approach is similar to and complementary to previous work with Netsolve, Condor, and Globus.

In addition to software development, we have begun exploring custom hardware as another promising approach to accelerate stochastic simulations. Our approach exploits Field Programmable Gate Arrays (FPGA), which consist of multiple PowerPC processors connected to a large portion of reconfigurable logic on the same integrated circuit, enabling a design that is optimized for performing stochastic simulations (Simpson 2004a; Cox 2003). A simulation experiment making very limited use of reconfigurable computing resulted in a 20× decrease in required simulation time. A more comprehensive implementation of this scalable approach, utilizing the newest FPGAs recently obtained by the University of Tennessee (Xilinx Virtex II Pro XCV2P30), may potentially provide orders-of-magnitude reduction in simulation time by exploiting additional parallelism.

We have begun applying our software tools to the LuxI/R quorum sensing system in Vibrio fischeri 7 as a model system of cell-cell communication required for large-scale biologically driven controlled synthesis. We have calibrated the model to bioluminescence

data in the literature and are now revising the model and doing additional calibrations of the model based on RT PCR data collected in our labs. One interesting hypothesis that has arisen from our work to date is that the stochastic processes may assist cells in sensing a quorum 7. Individual cells periodically become induced for short periods of time, during which time they produce larger quantities of autoinducer than is warranted for the given cell population. If several cells in the same area become induced at approximately the same time, the local concentration of autoinducer can exceed the threshold level needed to sustain induction, thereby creating a "seed quorum" that will begin to recruit nearby cells to the induced state.

Our work also focused on the development of frequency domain analysis of stochastic processes in gene circuits and networks (Cox 2003; Simpson 2003). We have applied the analysis to the most fundamental processes in biology including transcription, translation, protein dimerization, and regulation though binding of transcription factors to operator regions of DNA (Simpson 2004a; Simpson 2003; Simpson 2004b). The frequency domain approach that we have developed shows promise for several reasons. First, inspection of the resulting equations reveals intuitive relationships between kinetic parameters and circuit functionality. Secondly, the preservation of the noise frequency distribution allows the propagation of noise in downstream circuit elements to be considered. Finally, this approach appears to have good potential for yielding faster simulations since in the frequency domain, the approximate equations (e.g., Langevin equations) can be applied to situations outside those where it is normally thought to be valid (Gillespie 2000). We have begun to extend this approach to develop modular CLE models for commonly occurring circuit motifs such as those recently identified (Shen-Orr 2002).

Exploration of the use of synthetic nanoscale elements to control genetic/biochemical systems

This research focus pursues the application of vertically aligned carbon nanofibers (VACNFs) as a key element in the practical realization of arrays of passively addressed intracellular probes, actuators, and material delivery vectors, specifically in this project to interact with biological processes that direct synthesis and assembly of nanoscale materials. Starting in a previous project, but directed here toward the goals of this project, we demonstrated that arrays of VACNFs provide a unique opportunity for relatively long term (>3 weeks) molecular manipulation of the intracellular- and even nuclear domains of viable mammalian cells (McKnight 2003; McKnight 2004).

In our initial studies, VACNFs were modified with either nonspecifically adsorbed or covalently tethered plasmid DNA, and these nanofibers were introduced in a parallel fashion into the intracellular domains of large numbers (1000s) of viable cells. Following insertion, cells were left resident (i.e., interfaced) upon the VACNF array, where they were found to be able to recover and proliferate. Further, cells that were impaled with the plasmid-derivatized nanofibers were able to express the gene harbored in the plasmid. The expression of the tethered plasmid DNA indicated that not only was the fiber surface functionally available to the intracellular machinery but it was even available to specific sub-cellular machinery (i.e., when the nanofiber with the covalently tethered plasmid DNA was inserted into the nucleus, DNA replication and transcription were allowed to occur successfully).

Specific to this work was the demonstration of tethered-plasmid transcription. This system provided an element of control over the biochemical manipulation of the targeted cells that no other gene delivery method can offer. This level of control was achieved because the tethered genes were immobilized on the nanofiber scaffold, and as a result, the genes were not able to freely diffuse, nor were they segregated to progeny during cellular division (both cells released from a fiber and the progeny cells not impaled by fibers did not express the exogenous gene). We hypothesize that the level of control over nanofiber-mediated molecular manipulation of cells may be significantly increased by integrating nanofiber elements into functional electronically and electrochemically capable systems. In this project we began developing individually addressable nanofiber-based electrochemical probes for electroanalytically interrogating extremely small volumes (500 zeptoliter, 5×10^{-19} liter) around and ultimately within cells. In addition to imaging, these instrument systems provide an exciting platform for intracellular manipulation and the control of material synthesis and assembly pathways. The results of this work is documented in several publications (McKnight 2003; McKnight 2004a; McKnight 2003a).

Benefits

This project directly addresses central issues of nanoscience, nanotechnology, and nanobiotechnology. The focus on controlled synthesis and directed assembly of inorganic materials is especially relevant to the research programs of the DOE-BES supported Center for Nanophase Materials Sciences and to the Nanosynthesis FWP (ERKCM38-01). In addition, the biocomputation aspects of this project are relevant to DOE Advanced Scientific Computing Research (ASCR) missions. The work in this LDRD project has made a direct impact on a newly begun (FY 2005) ASCR research program (jointly

funded at ORNL and PNNL). Portions of this work are closely related to DARPA, NIH, and NSF programs. An NIH proposal related to this work is now under review.

References

Coffman, E. A., A. V. Melechko, D. P. Allison, M. L. Simpson, and M. J. Doktycz. 2004. "Surface patterning of silica nanostructures using bio-inspired templates and directed synthesis," *Langmuir* **20**, 8431–8436.

Cox, C. D., et al. 2003. "Analysis of Noise in Quorum Sensing," *Omics* **7**, 317–334.

Gardner, T. S., C. R. Cantor, and J. J. Collins. 2000. "Construction of a genetic toggle switch in *Escherichia coli*," *Nature* **403**, 339–342.

Gillespie, D. T. 2000. "The Chemical Langevin Equation." *Journal of Chemical Physics* **113**, 297–306.

Kobayashi, H., et al. 2004. "Programmable cells: Interfacing natural and engineered gene networks," *PNAS* **101**, 8414–8419.

McCollum, J. M., G. D. Peterson, C. D. Cox, and M. L. Simpson. 2004. "Accelerating gene regulatory network modeling using grid-based simulation," *Simulation-Transactions of the Society for Modeling and Simulation International* **80**, 231–241 (2004).

McKnight, T. E., et al. (2003). In *Nanotechnolog*y 551–556 (2003).

McKnight, T. E., et al. (2003a). "Effects of microfabrication processing on the electrochemistry of carbon nanofiber electrodes," *Journal of Physical Chemistry B* **107**, 10722–10728.

McKnight, T. E., et al. (2004). In *Nano Letters* 1213–1219.

McKnight, T. E., et al. (2004a). In *Journal of Physical Chemistry B* 7115–7125.

Shen-Orr, S. S., R. Milo, S. Mangan, and U. Alon. "Network motifs in the transcriptional regulation network of Escherichia coli." *Nature Genetics* **31**, 64-68 (2002).

Simpson, M. L., C. D. Cox, and G. S. Sayler. 2003. "Frequency domain analysis of noise in autoregulated gene circuits," *Proceedings of the National Academy of Sciences of the United States of America* **100**, 4551–4556.

Simpson, M. L. 2004. "Rewiring the cell: synthetic biology moves towards higher functional complexity," *Trends in Biotechnology* **22**, 555–557.

Simpson, M. L., C. D. Cox, G. D. Peterson, and G. S. Sayler. 2004a. "Engineering in the biological substrate: Information processing in genetic circuits," *Proceedings of the IEEE* **92**, 848–863.

Simpson, M. L., C. D. Cox, and G. S. Sayler. 2004b. "Frequency domain chemical Langevin analysis of stochasticity in gene transcriptional regulation," *Journal of Theoretical Biology* **229**, 383–394.

Nanoscale Control of Collective Phenomena Using Artificially Structured Materials

H. N. Lee, H. M. Christen, and D. H. Lowndes
Condensed Matter Sciences Division

This project focused on finding new physical phenomena at the nanoscale in artificial oxide multilayers of dielectrics and ferroelectrics and manipulating their resulting properties at the atomic scale. We demonstrated for the first time the growth of ultra-high-quality ferroelectric-dielectric superlattices by a high-pressure pulsed laser deposition technique. These superlattices were grown with layer-by-layer control, yielding a*s-grown* samples with compositionally abrupt interfaces, atomically smooth surfaces, and excellent ferroelectric behavior. The atomic-scale control of the combining of dissimilar materials produces striking property enhancements as well as fascinating new combinations of desired properties.

Introduction

Advanced modern epitaxial growth techniques have enabled the synthesis of nearly perfect thin films, superlattices, etc., by the atomic-scale control of surfaces and interfaces. This enables the formation of artificial oxide superlattices that do not exist in bulk forms. The challenge associated with fabricating such structures, that is, the deliberate and controlled deposition of up to hundreds of individual layers, remains a formidable task, for which the principal technique used has been high-vacuum molecular beam epitaxy (MBE) (Schlom 2001). However, the MBE technique cannot utilize high oxygen background pressures for growing insulating oxides, consequently yielding improper oxidation or inappropriate physical properties due to incorrect oxygen stoichiometry. Pulsed laser deposition (PLD) has long been regarded as an effective method for synthesizing various oxide heterostructures, but obtaining atomically sharp interfaces has been difficult in the comparatively high-pressure processes needed to maintain oxygen stoichiometry. In this work, for the first time, we have focused on achieving atomic-scale control by high-pressure PLD of hundreds of individual perovskite layers of barium titanate ($BaTiO_3$), strontium titanate ($SrTiO_3$), and calcium titanate ($CaTiO_3$), so called three-component superlattices (TCSs).

Furthermore, a shortage of electrically conducting oxide substrates and our still-limited understanding of the stability and growth mechanisms of conducting-film electrodes have hindered the electrical characterization of oxide superlattices. In this project, we have also investigated the thermal stability of high-quality strontium ruthenate ($SrRuO_3$) thin films (with atomically flat surfaces exhibiting only single unit-cell terrace steps) under various oxygen pressures and temperatures and have mapped out the stable growth regime of oxide films, in general, on conducting $SrRuO_3$.

Technical Approach

As a first step, atomically flat, single-stepped surfaces were prepared on commercial $SrTiO_3$ substrates by using combined chemical (buffered hydrogen fluoride etch) and thermal treatments (at 1100–1200ºC in air). Then, epitaxial $SrRuO_3$ films were grown by PLD on the single-stepped (001) $SrTiO_3$ substrates using a KrF excimer laser (λ = 248 nm) at 700ºC in 100 mTorr O_2. As shown in Fig. 1(a),

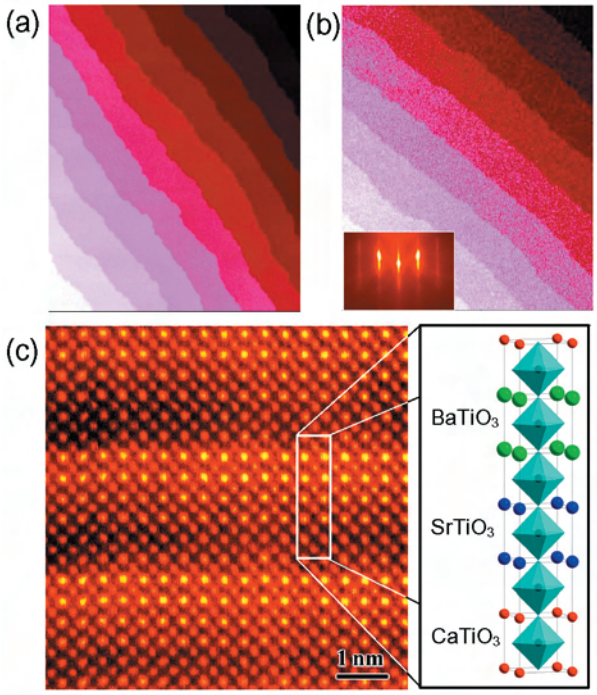

Fig. 1. Atomic-scale flatness and compositional abruptness in surfaces and interfaces of a conducting $SrRuO_3$ film and an artificial superlattice grown by PLD. AFM topographic images (image size: 4 × 5 μm²) with single terrace steps (~0.4 nm) of (a) a $SrRuO_3$ film on $SrTiO_3$ and (b) a 200-nm-thick $(BaTiO_3)_2/(SrTiO_3)_2/(CaTiO_3)_2$ superlattice. (b) Cross-sectional Z-contrast image of compositionally abrupt interfaces in $(BaTiO_3)_2/(SrTiO_3)_2/(CaTiO_3)_2$; the schematic shows its atomic structure.

the single terrace steps on the $SrRuO_3$ film surface are a direct replica from these of the $SrTiO_3$ substrate. The TCSs were also grown by PLD at ~700ºC in 10 mTorr O_2 (i.e., within the above-determined stability region) using sintered stoichiometric $CaTiO_3$ and $BaTiO_3$ targets, and a single-crystal $SrTiO_3$ target. The laser repetition rate and laser fluence were kept at 10 Hz and 2 J/cm^2, respectively. The deposition of each individual unit cell was monitored via the intensity oscillations of the specular spot in the reflection high energy electron diffraction (RHEED) pattern.

Results and Discussion

Our development of techniques to control PLD at the atomic scale has enabled us to synthesize completely artificial oxide crystals with specific, designed-in properties and thicknesses of up to 2500 of the constituent perovskite unit cells. The three key elements of our approach are a reduction in the amount of material deposited per laser pulse, the integration of continuous in situ monitoring by RHEED, and the preparation of atomically flat substrate surfaces. In order to grow atomically flat conducting layers, we employed $SrRuO_3$, which has a low lattice misfit (0.6%) with $SrTiO_3$ single crystals. Although $SrRuO_3$ represented a perfect structure in the as-grown state and remained stable at temperatures as high as 720ºC when annealed in moderate oxygen ambients (>1 mTorr), higher temperature anneals at lower pressures results in the formation of islands, pits, and metallic Ru due to the decomposition of $SrRuO_3$. Using in-situ RHEED, we have determined a stability map [temperature (25 ~ 800ºC), pressure (10^{-7} ~ 10^{-2} Torr)] defining the region suitable for subsequent film-growth on $SrRuO_3$ that remains perfect. The observations are consistent with a thermally activated decomposition process having an activation energy of 88 kJ/mol (Lee 2004a).

This atomically flat conducting $SrRuO_3$ layer has been applied to grow new artificial titanate materials, by using single unit-cell (~4 Å thickness) layers of perovskites such as $BaTiO_3$, $SrTiO_3$, and $CaTiO_3$ to synthesize monolithic periodic heterostructures through their systematic repetitive stacking. The PLD method can be used to produce materials designed in advance to exhibit specific desired physical properties. Most significantly, materials that lack inversion-symmetry (Sai 2000) —and thus display a rich variety of physical properties not normally found in nature—have been formed, as shown in Figs. 1(b) and (c). As one can see in Fig. 1(c), a superlattice alternatively stacked with two unit cells (~0.8 nm in thickness) of $BaTiO_3$, $SrTiO_3$, and $CaTiO_3$ clearly contains compositionally abrupt interfaces without any intermixing and well demonstrates our establishment of an atomic-scale growth capability. Moreover, these materials display strong intrinsic ferroelectric properties in their as-grown state; that is, unlike MBE, they do not require a post-growth treatment to obtain the desired combination of highly electrically insulating and ferroelectric behaviors (Lee 2004b). In addition, we have also realized the atomic scale control of collective phenomena by designing the superlattices differently. For example, it has been a long-standing challenge to realize experimentally the ferroelectric polarization enhancement by strain, as theoretically predicted (Neaton 2003).

By constructing TCSs, we found that the coupling induced by elastic interactions at heterointerfaces plays a significant role for strain-enhanced polarization (Lee 2004b). By using different stacking sequences of layers to vary the degree of asymmetry, we also found that the strongest polarization enhancement is achieved by the proper balancing between two competing requirements: (1) the $BaTiO_3$ layers must be thick enough to contain a sufficient amount of non-interfacial TiO_6 octahedra but (2) thin enough to remain fully strained. This produces a maximum increase of the polarization by 50% in a TCS of $(BaTiO_3)_4/(SrTiO_3)_2/(CaTiO_3)_2$, over that of a pure $BaTiO_3$ film, despite the low volume fraction of only 50% $BaTiO_3$.

This investigation of atomic-scale precision TCS structures leads to two significant observations: (1) the use of three-component materials, as dictated by the need for near-perfect lattice matching to the substrate, reveals the subtle effects of elastically coupled heterointerfaces with a non-inversion symmetric environment. (2) These structures have allowed for the first time the experimental verification of theoretical predictions of strain-enhanced ferroelectric polarization of $BaTiO_3$, even in structures containing a relatively small volume-fraction of $BaTiO_3$. Together with the advance in pulsed laser deposition accomplished by this work, these results illustrate how physical properties of materials can be improved and modified on the atomic length scale.

Benefits

Oxide heterostructures with apparently high crystalline quality have been grown previously only by MBE, but these are typically poor electrical insulators—probably because of oxygen non-stoichiometry—and thus offer limited practical benefits. Bringing high-pressure PLD to the level of atomic-layer control and demonstrating the synthesis of much thicker and highly insulating transition metal oxides eliminate the difficulties with MBE and additionally yields great flexibility for the design of artificial materials exhibiting new combinations of properties.

This work is a significant step toward long-sought "designer materials" and leads to investigations of unprecedented physical properties and that are expected to have a wide range of applications. Such materials are

highly relevant to DOE missions and will impact many federal agencies because of their potential usefulness for sensors, actuators, and related devices. Thus, they may contribute to the entire range of security, energy, environmental, and science applications.

References

Lee, H. N., H. M. Christen, M. F. Chisholm, C. M. Rouleau, and D. H. Lowndes. 2004a. "Thermal stability of epitaxial SrRuO3 films as a function of oxygen pressure." *Appl. Phys. Lett.* **84**, 4107–4109.

Lee, H. N., H. M. Christen, M. F. Chisholm, C. M. Rouleau, and D. H. Lowndes. 2004b. "Strong polarization enhancement in asymmetric three-component ferroelectric superlattices." *Nature* (submitted).

Sai, N., B. Meyer, and D. Vanderbilt. 2000. "Compositional inversion symmetry breaking in ferroelectric perovskites." *Phys. Rev. Lett.* **84**, 5636–5639.

Neaton, J. B., and K. M. Rabe. 2003. "Theory of polarization enhancement in epitaxial $BaTiO_3/SrTiO_3$ superlattices." *Appl. Phys. Lett*. **82**, 1586–1588.

Schlom, D. G., et al. 2001. "Oxide nano-engineering using MBE," *Mater. Sci. Eng. B* **87**, 282–291.

Materials Needs for Successful Implementation of Lean NO_x Treatment Technology

C. K. Narula
Metals and Ceramics Division

The regulatory requirements for diesel emissions (excluding particulates) can be met by deploying NO_x trap systems (LNT) for exhaust treatment; however, the performance of LNTs deteriorates rapidly. The understanding of microstructural changes in LNT materials and development of new materials that can withstand harsh conditions of lean exhaust and regeneration cycles is necessary for the deployment of LNTs. In summary, our studies on microstructural changes in supplier catalysts upon aging on (1) a pulsator at Ford (2) dyano at Ford, and (3) Ford vehicles in gasoline DISI engines in Europe show that precious metal sintering and barium migration cause performance deterioration in NO_x trap materials. We have prepared model LNT catalysts and studied their microstructural changes in lean diesel and rich diesel conditions at 500ºC for 4 hours in an ex-situ reactor that allows us to treat TEM samples directly in simulated exhaust.

Introduction

The introduction of diesel engine or lean-burn engine-based passenger vehicles depends on a successful development of a strategy to treat nitrogen oxides (NO_x) emissions, since a catalyst (or a combination of catalysts) that can convert NO_x into inert gases under oxidizing conditions over a complete range of exhaust temperature does not exist. In the nineties, OEMs and their suppliers focused on lean NO_x technology for treatment of diesel engine exhaust and exhaust from gasoline engines operating under lean conditions (Shelef 1995). There was quite an excitement over the discovery of effective Cu-ZSM-5 and Pt/alumina catalyst combinations for the diesel temperature range (Adams 1996) and Ag/alumina catalysts for high temperatures (Miyadera 1993; Narula 2001). Despite years of research, a catalyst or a combination of catalysts has not been found that can treat exhaust from these engines in the complete range of operating temperatures. Instead of waiting for the serendipitous discovery of a new lean NO_x catalyst, researchers shifted focus towards strategies such as urea/hydrocarbon SCR (selective catalytic reduction) (Lambert 2001), low-temperature plasma catalysis (Panov 2001), and NO_x trap technology (Johnson 2002). While urea SCR technology has been shown to be capable of treating NO_x over the entire range of temperatures for diesel-powered small vehicles, it is not considered viable at this time because the infrastructure to deliver urea and diesel simultaneously at fueling stations will not be in place. The low-temperature plasma catalysis process did not mature in time and is out of contention for deployment. The NO_x trap technology (LNT) was first proposed by Toyota in 1994 (Katoh 1994). At present LNT is the most likely candidate for early deployment provided materials issues can be solved to make LNT's durable and functional for U.S. and European driving conditions so that vehicles remain in compliance over the entire lifetime.

Technical Approach

In order to determine microstructural changes that take place in NO_x trap materials, we carried out an exhaustive study of supplier samples that have been aged in the laboratory on (1) a pulsator at Ford (2) dyano at Ford and (3) vehicles in gasoline DISI engines in Europe. The aging protocols for rapid laboratory and dyano aging of LNTs under diesel exhaust conditions are being developed, and we plan to analyze samples aged under diesel conditions. Since diesel exhaust temperatures are less than those of gasoline exhaust, we expect microstructural changes to occur gradually as compared with the changes under gasoline exhaust conditions.

The study of microstrucutral changes during LNT operation by any of the above methods is time consuming and expensive. Also, one can only get snapshots of microstructural changes at the end of test run of aging because of the cost associated with aging sample. In order to monitor microstructural changes at various stages of rapid aging protocols, we designed an ex-situ reactor system capable of dynamic lean or rich diesel or gasoline simulated exhaust conditions at a flow rate of 100cc/min and temperature range of 25–600ºC. We also prepared model catalyst systems that can be rapidly examined for microstructural changes in the ex-situ reactor and laboratory bench-top reactor. We are upgrading the ex-situ reactor to introduce rich pulse capability during lean operation. This will enable us to duplicate LNT operating condition. The updated reactor system will be able to operate in 25–1000ºC temperature range.

Results and Discussion

The results on our study of microstructural changes in supplier catalysts and model catalysts are summarized in the following sections.

Microstructural Changes in LNT Materials of Supplier Lean NO_x Traps: Over last two years, we determined the microstructural changes that occurred in a supplier lean NO_x trap system (based on Pt/BaO-Al_2O_3 and CeO_2-ZrO_2 materials) upon aging on (1) a pulsator at Ford, (2) dyano at Ford, and (3) Ford vehicles in gasoline DISI engines in Europe.

- After pulsator aging, lean and rich aged samples showed that the sintering of platinum particles occurs during aging, and barium migrates into ceria-zirconia layer. Both of these factors reduce platinum-barium oxide surface area where NO_x adsorption and reduction takes place during lean and rich cycles, respectively. The stoichiometric aging also leads to the migration of barium into ceria-zirconia layer, but the sintering of platinum is less severe.
- The dyano-aged samples showed extensive sintering of platinum and its migration in ceria-zirconia layer. The sintering of rhodium was also observed. The migration of barium into ceria-zirconia and the sintering of precious metal component could explain the deterioration of performance.
- The analysis of on-vehicle-evaluated samples after 32 km and 80 km showed that bulk of the sintering of precious metals occurred in the stages of on-vehicle aging.

These results primarily show precious metal sintering and barium migration to be the cause of performance deterioration in NO_x trap materials in gasoline engine exhaust conditions.

Model Catalyst Materials with Improved Thermal Durability: The complexity of the LNT described above warrants a complex model system that can be analyzed and evaluated in laboratory. Improvements in the model system then can be implemented in the full-size catalyst that can be tested on a vehicle. While at Ford, CKN started addressing the thermal durability of LNT materials. He found that a model system [10%CeO_2-ZrO_2-90%(2%La_2O_3-98%BaO·6Al_2O_3)] retains its beneficial surface properties even after thermal aging at 1050°C. This material can be prepared as follows:

1. Impregnation of $Ba(NO_3)_3$ on commercial high-surface-area alumina, pyrolysis, and sintering at 750ºC.
2. Impregnation of step 1 material with lanthanum nitrate, pyrolysis, and sintering at 750ºC.
3. Ball milling step 2 material with commercial high-surface-area CeO_2-ZrO_2.

As a next step, we impregnated this powder with 1% platinum and investigated Pt distribution on the powder. The electron micrograph shows that Pt particles are about 1 nm in size. For comparison and to study the effect of base metal oxides on LNTs, we prepared the following two model catalysts:

- Pt/Al_2O_3: The Pt/alumina was prepared by the impregnation method using H_2PtCl_6 salt. The X-ray powder diffraction shows broad diffraction peaks for alumina and no peaks due to Pt as expected due to small particle size of Pt in freshly prepared sample.
- (2%Pt, 5%MnO_2—93%[10%CeO_2-ZrO_2-90%(2%La_2O_3-98% BaO·6Al_2O_3)]): The model catalyst was synthesized by impregnating 2%Pt,-97%[10%CeO_2-ZrO_2-90%(2%La_2O_3-98% BaO·6Al_2O_3)] with manganese nitrate and subsequent decomposition.

The microstructural changes in model catalysts (Pt/Al_2O_3), (2%Pt-98%[10%CeO_2-ZrO_2-90%(2%La_2O_3-98%BaO·6Al_2O_3)]), and (2%Pt, 5%MnO_2—93%[10%CeO_2-ZrO_2-90%(2%La_2O_3-98% BaO·6Al_2O_3)]) after thermal treatment at 500, 600, 700, 800, and 900ºC, lean treatment at 500ºC for 4 hours, and rich treatment at 500ºC were followed with X-ray powder diffraction (XRD) and transmission electron microscopy (TEM). Here lean and rich treatment refers to exposure of sample in ex-situ reactor (described previously) to diesel lean and diesel-rich conditions. A summary of changes in precious metal (Pt) is presented in Table 1.

A. Thermal Treatment: Thermal treatments of samples were carried out at 500, 600, 700, 800, and 900ºC in a bench-top furnace in air.

- Pt/Al_2O_3: In XRD patterns of Pt/Al_2O_3, diffraction peaks due to Pt particle size start to grow in 500–900ºC range. The calculated Pt particles sizes (using Scherrer formula, assumes spherical particles) are 3.4, 17.1, 26.1, and 39.5 nm at 600, 700, 800, and 900ºC, respectively. At 500ºC, the alumina is a mixture of γ-alumina and hydrated γ–alumina. At 800ºC, a broad peak assignable to alpha phase can be seen. At 900ºC, the diffraction peaks due to α– and γ–alumina are observed. TEM of fresh sample shows that the Pt particle size is in 1- to 1.2-nm range. This particle size grows to 2-4 nm on thermal treatment in a furnace at 500ºC for 4 hours.
- (2%Pt-98%[10%CeO_2-ZrO_2-90%(2%La_2O_3-98%BaO·6Al_2O_3)]): In XRD patterns, diffraction peaks due to Pt particle size start to grow in 500–900ºC range. The calculated Pt particles sizes (using Scherrer formula, assumes spherical particles) are 2.6, 21.3, 37.2, and 48.4 nm at 600, 700, 800, and 900ºC, respectively. TEM of fresh sample shows that

the Pt particle size is ~1 nm. This particle size grows to 1–2 nm on thermal treatment in a furnace at 500ºC for 4 hours.

- ($2\%Pt,\ 5\%MnO_2$—$93\%[10\%CeO_2$-ZrO_2-$90\%(2\%La_2O_3$-$98\%\ BaO{\cdot}6Al_2O_3)]$): In XRD patterns, diffraction peaks due to Pt particle size start to grow in the 500–900ºC range. The calculated Pt particles sizes (using Scherrer formula, assumes spherical particles) are 20.7, 27, and 34 nm at 700, 800, and 900ºC, respectively. TEM of fresh sample shows that the Pt particle size is ~1 nm. This particle size grows to 1–2 nm on thermal treatment in a furnace at 500ºC for 4 hours.

B. Lean and Rich Treatment: The aging of model catalysts was carried out in our ex-situ reactor system under lean or rich diesel exhaust conditions at 500ºC for 4 hours [CO, CO_2, H_2, HC, NO_x, H_2O, flow rate 100cc/min] showed some sintering of Pt particles. However, the sintering is significantly less than that observed on thermal aging at 500ºC in air. It is important to note that our samples are exposed to lean or rich conditions and lack of control on space velocity due to very small amount of catalyst leads to NO_x absorber saturation conditions. The saturation condition persists throughout our treatment.

Diesel Lean Treatment

- Pt/Al_2O_3: TEM of fresh sample shows that the Pt particle size is in 1- to 1.2-nm range. This particle size grows to 8–10 nm on lean treatment in an ex-situ reactor at 500ºC for 4 hours.
- ($2\%Pt$-$98\%[10\%CeO_2$-ZrO_2-$90\%(2\%La_2O_3$-$98\%BaO{\cdot}6Al_2O_3)]$): TEM of fresh sample shows that the Pt particle size is ~1 nm. This particle size grows to 1–2 nm on lean treatment in ex-situ reactor at 500ºC for 4 hours.
- ($2\%Pt,\ 5\%MnO_2$—$93\%[10\%CeO_2$-ZrO_2-$90\%(2\%La_2O_3$-$98\%\ BaO{\cdot}6Al_2O_3)]$): TEM of fresh sample shows that the Pt particle size is ~1 nm. This particle size grows to 2–3 nm on thermal treatment in an ex-situ reactor at 500ºC for 4 hours.

Diesel-Rich Treatment

- Pt/Al_2O_3: TEM of fresh sample shows that the Pt particle size is in 1- to 1.2-nm range. This particle size grows to 2–4 nm on rich treatment in an ex-situ reactor at 500ºC for 4 hours.
- ($2\%Pt$-$98\%[10\%CeO_2$-ZrO_2-$90\%(2\%La_2O_3$-$98\%BaO{\cdot}6Al_2O_3)]$): TEM of fresh sample shows that the Pt particle size is ~1–1.2 nm. This particle size grows to 1.5–3.5 nm on rich treatment in an ex-situ reactor at 500ºC for 4 hours.

Table 1. Summary of changes in precious metal (Pt)

Sample			Treatment Conditions		
	Fresh	Thermal Treatment (XRD of Powders)	Thermal treatment at 500ºC on ex-situ reactor	Treatment under Lean Conditions on ex-situ reactor	Treatment under Rich Conditions on ex-situ reactor
Pt/Al_2O_3	1–1.2 nm	600ºC, 3.4 nm 700ºC, 17.1 nm 800ºC, 26.1 nm 900ºC, 39.5 nm	2–4 nm	8–10 nm	2–4 nm
Model NO_x Trap Catalyst I: $2\%Pt$-$98\%[10\%CeO_2$-ZrO_2-$90\%(2\%La_2O_3$-$98\%BaO.6Al_2O_3)]$	1–2 nm	600ºC, 2.6 nm 700ºC, 21.3 nm 800ºC, 37.2 nm 900ºC, 48.4 nm	1–2 nm	1–2 nm	1.5–3.5 nm
Model NO_x Trap Catalyst II: $2\%Pt,\ 5\%MnO_2$—$93\%[10\%CeO_2$-ZrO_2-$90\%(2\%La_2O_3$-$98\%\ BaO.6Al_2O_3)]$	1–2 nm	700ºC, 20.7 nm 800ºC, 27.0 nm 900ºC, 34.0 nm	1–2 nm	2–3 nm	1–2 nm

- ($2\%Pt, 5\%MnO_2$—$93\%[10\%CeO_2$-ZrO_2-$90\%(2\%La_2O_3$-$98\% BaO{\cdot}6Al_2O_3)]$): TEM of fresh sample shows that the Pt particle size is ~1 nm. This particle size grows to 1–2 nm on rich treatment in an ex-situ reactor at 500ºC for 4 hours.

Benefits

Catalysis is a major thrust area for DOE EERE FreedomCAR and Vehicle Technologies (OFCVT). The ability to prepare, characterize, and evaluate new LNT materials under this program complements the DOE-EERE-funded diesel programs at NTRC on evaluation of LNT and HTML involvement in several catalysis-related efforts generally addressing the changes that occur at micro-structural level in collaboration with Ford, Cummins Engines, Caterpillar, etc.

References

Adams, K. A., J. V. Cavatio, and R. H. Hammerle. 1996. "Lean NO_x Catalysts for Diesel Passenger Cars: Investigating Effects of Sulfur and Space Velocity," *Appl. Catal. B* **10**, 57.

Johnson, T. V. 2002. "Diesel Emission Control: 2001 in Review," SP-1674 (2002).

Katoh, K., T. Kihara, M. Asanuma, M. Totoh, and N. Shibagaki. 1994. "Development of NO_x storage-Reduction 3-Way Catalyst System for Lean-burn Engines," *Toyota Tech. Rev.* **44**(2) 30.

Lambert, C. K., J. Vanderslcie, R. H. Hammerle, R. C. Belair. 2001. "Application of Urea SCR to Light Duty Diesel Vehicles," SP-1641.

Miyadera, T. 1993. "Alumina-supported Silver Catalyst for SCR of Nitric Oxide with Propene and Oxygen-Containing Organic Compounds," *Appl. Catal. B* **2**, 19.

Narula, C. K., H.-W. Jen, H. S. Gandhi. 2001. "Sol-Gel Alumina Membrane for Lean NO_x Catalysts & Method of Making Same," US Patent 6,232,253.

Panov, A. G., R. G. Tonkyn, C. H. F. Peden, J. W. Hoard, M. L. Balmer. 2001. "Selective Reduction of NO_x in Oxygen Rich Environment with Plasma Assisted Catalysis: the Role of Plasma and Reactive Intermediates," SP-1639.

Shelef, M. 1995. "Selective Catalytic Reduction of NO_x with N-Free Reductants," *Chem. Rev.* **95**, 209–225.

Production of Hydrogen Using Nuclear Energy and Inorganic Membranes

B. L. Bischoff,[1] C. W. Forsberg,[2] L. D. Trowbridge,[2] and L. K. Mansur[1]
[1]*Metals and Ceramics Division*
[2]*Nuclear Science and Technology Division*

The sulfur family of thermochemical processes is the leading candidate worldwide for production of hydrogen (H_2) using nuclear energy. These processes which thermocatalytically crack water into hydrogen and oxygen consist of a series of chemical reactions where all the chemicals are recycled in the process except for water. The processes are potentially efficient, scalable, and use no expensive chemical reagents. These processes have one major disadvantage: high operating temperatures (800 to 900°C). The high-temperature chemical reaction common to all of these cycles is the equilibrium thermal decomposition of sulfuric acid. The deployment of these processes can be facilitated provided the reaction temperatures can be lowered by 200°C+ by separating SO_3 from other sulfuric acid decomposition products such as O_2, H_2O, and SO_2. The goal of this project was to conduct proof-of-principle experiments and associated analysis to demonstrate the potential for inorganic membranes in SO_3 separation. We have explored the development of inorganic membranes that promote the separation of O_2, H_2O, and SO_2 from SO_3, under simulated conditions. We also propose a model that could describe the separation of multiple species from a multicomponent gas stream. We summarize preliminary data on the separation efficiency of the product gases from SO_3.

Introduction

The leading candidates for low-cost, large-scale H_2 production using heat from a nuclear reactor are thermochemical processes where a set of chemical reactions converts water to H_2 and O_2. Three of the four highest-rated processes (sulfur-iodine, hybrid sulfur, and sulfur bromine) take place at 850ºC at ~10 bar (Brown et al. 2003). The highly endothermic (heat-absorbing) gas-phase reaction in these processes is

$$2H_2SO_4 \leftrightarrow 2H_2O + 2SO_3 \leftrightarrow 2SO_2 + 2H_2O + O_2\ (850°C)\ . \qquad (1)$$

Detailed studies have shown that the required peak temperatures need to be ~850ºC for near-complete dissociation of SO_3. After the high-temperature dissociation reaction, the resulting chemical stream must be cooled. The SO_2 must be separated out and sent to the next chemical reaction, and the unreacted sulfuric acid (formed by recombination of SO_3 and H_2O) is reheated and recycled. Unless the chemical reactions go almost to completion, the process is very inefficient and uneconomical due to the energy losses in separations and the heat exchangers to heat and cool all the unreacted reagents.

A major challenge to thermochemical H_2 production is the high temperature required for efficient H_2 production, which is at, or perhaps exceeds, the limits of reactor technology. The 850°C process temperature implies that the peak nuclear reactor temperature needs to be higher in order to account for temperature losses in heat exchangers between the reactor coolant and chemical plant. If this temperature could be lowered to 700ºC, current (LaBar 2002) and advanced (Forsberg et al. 2004) designs of high-temperature nuclear reactors could be used for H_2 production. This is attainable provided the reaction equilibrium can be shifted in favor of SO_3 dissociation via SO_2 removal. We proposed an inorganic membrane separation process to separate SO_2, H_2O, and O_2 from the SO_3 at 650 to 750°C.

The impetus to use inorganic membranes comes from our extensive experience with gas separation membranes starting with separation of uranium isotopes by gaseous diffusion. In recent years, we have developed several new inorganic membranes for commercial applications. We have evaluated several of these membranes to separate SO_2, H_2O, and O_2 from SO_3. This report describes the unique experimental equipment fabricated for these separations and preliminary experimental results.

Technical Approach

The rationale for our experimental work is based on the classical thermodynamic equation for SO_3 dissociation equilibrium reaction:

$$K(T) = [SO_2]_2\ [O_2]/[SO_3]_2\ , \qquad (2)$$

where

- $K(T)$ = equilibrium constant (a constant at any temperature but increases with temperature)
- $[SO_2]$ = gas-phase concentration of SO_2
- $[O_2]$ = gas-phase concentration of O_2
- $[SO_3]$ = gas-phase concentration of SO_3

As indicated by Eq. (2), as SO_2 and O_2 are removed from the catalyst bed, more of the SO_3 must dissociate to reestablish equilibrium. If a large fraction of both the O_2 and SO_2 were removed, the concentration of the SO_3 must decrease even further to satisfy the equilibrium condition.

A parametric study was conducted to determine the potential benefit of O_2 and SO_2 removal on the conversion of SO_3 to SO_2. Using a thermochemical equilibrium modeling program, the equilibrium conversion as a function of temperature was calculated, assuming an initial quantity of 100 moles of H_2SO_4. Calculations assumed that the reaction reached equilibrium in the first (theoretical) stage. It was assumed that a membrane selective for oxygen removed all of the O_2, leaving behind the SO_3 and SO_2 which were allowed to come to equilibrium again (stage 2). The O_2 was again removed, and this process was repeated through six stages. The residual SO_3 at 700°C (21.6 moles) using an O_2 selective membrane is approximately equal to the residual SO_3 at equilibrium at 850°C (21.13 moles) with no membrane separation. For a membrane reactor, lengthening the membrane tubes would increase the continuous removal of reaction products (i.e., effectively increasing the number of hypothetical batch removal stages).

Lastly, the effect of the removal of both O_2 and SO_2 was studied. It was assumed that a membrane now selective for the removal of both O_2 and SO_2 was employed. The O_2 and SO_2 were removed, and the SO_3 was allowed to dissociate and come to equilibrium again (stage 2). This was repeated as before through six stages where only 2.08 moles of the SO_3 remained.

Based on these results, we evaluated a variety of membranes for their effectiveness in shifting the SO_3 equilibrium at low temperatures.

Results and Discussion

Membrane separation processes operate by having a higher partial pressure of the transported gas on one side of the membrane and lower partial pressure of that gas on the other. The relative rates of transport of different molecules through the membrane determine the capability of the membrane to separate different gases. The precise transport mechanism that is dominant for each gas depends on a variety of physical factors including temperature *T,* transmembrane pressure *P,* molecular mass *m,* pore diameter d_p, molecular size and shape, pore surface composition, pore morphology, and mutual interactions between molecules traversing the membrane.

The most important characteristic feature of membranes that dictates the dominant transport mechanism is the pore diameter. Generally, for pore diameters >2 nm, important transport mechanisms include Knudsen diffusion and surface transport, together with molecular diffusion and viscous flow (Poiseuille or laminar flow) at larger pore diameters. For pore diameters about 1 nm and smaller, other mechanisms become operable and are covered by the term nanopore diffusion.

Nanopore diffusion is a term that encompasses several distinct mechanisms that take place in nanometer-diameter pores. For separation of larger molecules from smaller molecules, the membrane may function effectively as a molecular sieve by blocking transport of the larger molecules through the membrane, thus resulting in high separation factors. For smaller molecules, the transport exhibits thermally activated behavior—as the temperature is increased, the permeance increases exponentially, rather than decreases as in Knudsen diffusion. One thermally activated mechanism that is understood is termed gas translational diffusion. It is also referred to as thermally activated Knudsen diffusion, where again molecules jump between pore walls but with an activation barrier that must be overcome in order to make a diffusion jump. This thermally activated characteristic is similar to the diffusion of defects or atoms in the solid state in the presence of traps (Mansur 1981), with activation energy E_d. This is physically plausible, because the lower limit on size of a pore must correspond to interatomic spacing in the solid state. In the $d_p \sim$ 1-nm regime, separation factors >100 are possible. For example, Uhlhorn and coworkers (1992) report that a separation factor > 200 has been measured for a mixture of H_2 and C_3H_6 gases using a supported amorphous silica membrane with a pore diameter of approximately 1 nm.

The performance of a membrane is measured by two parameters: permeance and selectivity. The permeance is defined as volumetric flow rate of the pure gas in question per unit of membrane area per unit of transmembrane pressure. The selectivity or ideal separation factor is defined as the ratio of the permeances of two pure gases. The separation factor for a mixture of two gases is defined as $[y/(1-y)]\ [(1-x)/x]$. Here, y is the concentration of the fastest-permeating component on the permeate side of the membrane and x is the concentration of the fastest-permeating component on the feed side. The product of the separation factor and permeance is often taken as the figure of merit by which to judge a particular membrane–gas mixture combination.

For O_2/SO_3 separations, high operating temperatures are required. This defines the type of physical separation system that is required—nanopore diffusion. Nanopore separations improve with temperature. We expect this phenomenon to occur also for SO_2 and O_2 if the membrane has properly sized pores. That is, we expect to design a membrane in which the O_2 and SO_2 permeances increase dramatically with temperature while the SO_3 permeance stays more or less constant, with temperature resulting in high separation factors at high temperatures.

A membrane test system was designed and fabricated. The system was designed to measure the permeance of pure gases, including N_2, O_2, SO_2, and SO_3, as a function of temperature and pressure. The permeance of water was not investigated. Since operating temperatures are relatively low with regard to sulfuric acid decomposition, it was decided to avoid any problems that could result if residual water in the membrane or elsewhere in the system were to come into contact with SO_3 and form H_2SO_4. The system was constructed of materials that are compatible with the operating temperatures and gases employed in this system. Because SO_3 is not gaseous at room temperature, the piping, valves, and gauges were heated by heat tape throughout the complete system where there is a possibility that the gas would be at high enough pressures to condense. The membrane holder and membrane were enclosed in a clam-shell heater capable of temperatures of approximately 900°C. Both the upstream and downstream pressures were controlled and monitored independently from each other to give maximum flexibility in varying total pressure as well as transmembrane pressure. Lastly, all of the heat zone temperatures, pressures, and gas flow data were continuously collected and monitored by a computer.

The initial membrane testing was completed by measuring the permeance of pure gases (N_2, O_2, SO_2, and SO_3) as a function of temperature and pressure. The gas flow per unit surface area is measured as a function of pressure drop and temperature. The mutual interactions among gas molecules and of the gas mixture with the membrane will be investigated in the future.

Testing was completed on the first membrane. This membrane was prepared by applying a thin porous oxide layer to a metallic support tube. The average pore size was determined to be approximately 0.8 nm. Using independent gas measurements, its pore size was estimated to be between 0.6 and 0.8 nm. Because of concerns with SO_3 condensation, only O_2 permeance was measured at room temperature and SO_3 permeance was only measured at 133°C. The results are shown in Fig. 1. The plots show the permeance versus the sum of the pressures on the high and low pressure sides of the membrane (ΣP). The data at high ΣP can have both a molecular and viscous flow component. When the data are extrapolated to $\Sigma P = 0$, the permeance should be a more accurate representation of molecular flow. This set of data had too much noise to get a valid extrapolation to $\Sigma P = 0$. Although the data had some noise due to minor initial control problems and the gas flows were very close to the lower detection limits, the bottom chart indicates that the permeance of O_2 increased by a factor of almost 2.5 from room temperature to 133°C. This observation is consistent with thermally activated diffusion observed previously for He and H_2 and believed to be due to nanopore diffusion. The SO_2 data also show an increase in permeance with temperature. The top graph shows the permeance of all three gases at approximately 133°C. By calculating the ratio of the average permeances, the selectivities (ideal separation factors) of O_2 and SO_2 over SO_3 are approximately 2.3 and 2.2, respectively. If an equal mixture of O_2 and SO_3 were fed to this membrane, a separation factor of 2.3 would result in a permeate having an oxygen concentration of approximately 70%, with the remaining being SO_3. To produce a permeate stream having less than 5% SO_3 would require a separation factor greater than 20. The flow of O_2 was significantly reduced

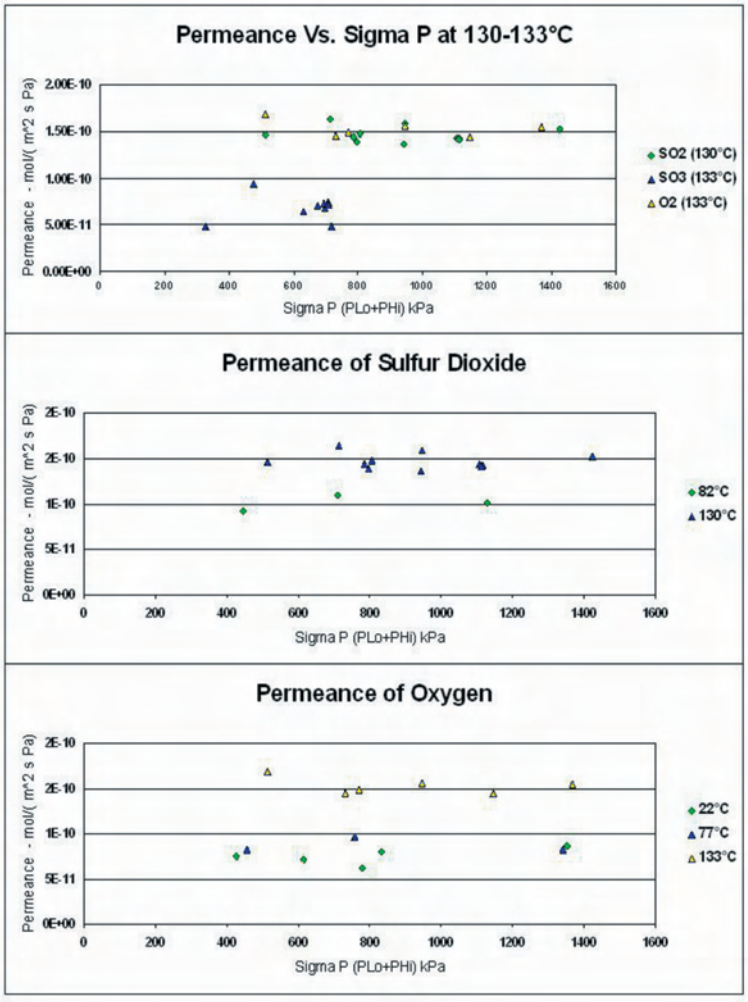

Fig. 1. Results of pure gas flows through membrane 101501.

after the membrane was subjected to SO_3. Although the SO_3 was above its condensation temperature in the membrane, significant gas adsorption probably occurred, which would substantially block the pores to flow of O_2.

Benefits

This LDRD project demonstrated through proof-of-principle experiments that it is possible to separate O_2 and SO_2 from SO_3 using inorganic membranes. We have shown that this separation can reduce peak operating temperatures in the sulfur family of thermochemical cycles. It is expected that further improvements to the membranes in terms of pore size control and chemical and thermal stability will have a major impact on the Office of Nuclear Science and Technology's Nuclear Hydrogen Initiative.

As a result of the work performed in this LDRD project, follow-on funding was secured to continue this development work. This project, funded through the Office of Nuclear Science and Technology's Nuclear Hydrogen Initiative (NHI) started in late FY 2004 and is expected to continue through at least FY 2006. Also, as an indirect result of this work, an additional project was funded through the NHI to evaluate the effectiveness of ORNL's inorganic membranes to separate steam from hydrogen in a high-temperature electrolyzer.

References

Brown, L. C., et al. 2003. *High Efficiency Generation of Hydrogen Fuels Using Nuclear Power*, GA-A24285, General Atomics, San Diego, California, June 2003.

La Bar, M. P. 2002. "The Gas Turbine–Modular Helium Reactor: A Promising Option for Near Term Deployment," Proceedings of International Congress on Advanced Nuclear Power Plants, Embedded Topical American Nuclear Society 2002 Annual Meeting, Hollywood, Florida, June 9–13, 2002, GA-A23952.

Forsberg, C.W., et al. 2004. "Maximizing Temperatures of Delivered Heat from the Advanced High-Temperature Reactor," Proceedings 2004 International Congress on Advances in Nuclear Power Plants (ICAPP '04), Embedded topical 2004 American Nuclear Society Annual Meeting, Pittsburgh, Pa., June 13–17, 2004.

Mansur. L. K. 1981. "Effective diffusion coefficients of point defects in impure materials," *Acta Met*. **29**, 375–381.

Uhlhorn, R. J. R., et al. 1992. "Gas Transport and Separation with Ceramic Membranes. Part I. Multilayer Diffusion and Capillary Condensation. and Part II. Synthesis and Separation Properties of Microporous Membranes," *Journal of Membrane Science* **66**, 259–287.

Boron-Nitrogen Polymers/Boron Nitride System for Hydrogen Storage

C. K. Narula,[1] J. M. Simonson,[2] and R. T. Paine[3]
[1]*Metals and Ceramics Division*
[2]*Chemical Sciences Division*
[3]*University of New Mexico*

Hybrid systems of borazane polymer impregnated on high-surface-area boron nitride can potentially provide efficient, reversible hydrogen storage, offering a superior alternative to known solid-state hydrogen storage approaches. To realize this potential, a low-cost method to prepare high-surface-area boron nitride powders and simple, low-cost pathways for reversible hydrogenation of boron-nitrogen polymers must be found. We initiated this work with the preparation of model compound, a mixture of two isomers, 1(e),3(e),5(e)- and 1(e),3(e),5(a)-Trimethylcycloborazane. This model compound releases 4.49% H_2 at 80ºC and additional 4.7% H_2 at 260ºC (w/w ≈ v/v since density is ~1). The model compound was impregnated into high-surface-area boron nitride that was prepared in two steps. In the first step, we used an aerosol reactor with commercially available trialkylborate compounds and ammonia to form BN_xO_y spherical particles with oxygen levels less than 8 wt %. Brief calcination of these particles in NH_3 gave smooth spherical morphology particles of BN. The hydrogenation of this system is being investigated.

Introduction

The hydrogen-fuel cell car concept articulated by President Bush hinges on the development of a viable system for storing hydrogen at high volumetric and mass densities. The DOE and the FreedomCAR program have established detailed criteria for solid-state storage of hydrogen on a vehicle. At present no known storage materials meet these criteria.

Hybrid systems of borazane polymer impregnated on high-surface-area boron nitride can potentially provide efficient, reversible hydrogen storage, offering a superior alternative to known solid-state hydrogen storage approaches. To realize this potential, a low-cost method to prepare high-surface-area boron nitride powders and simple, low-cost pathways for reversible hydrogenation of boron-nitrogen polymers must be found. We propose a new class of composite materials for hydrogen storage based on catalytic hydrogenation-dehydrogenation of low-molecular-weight boron-nitrogen polymers impregnated in high-surface-area boron nitride. This system will provide two complementary mechanisms for storage and release of hydrogen: hydrogenation-dehydrogenation of the boron-nitrogen polymer and physisorption on high-surface-area boron nitride. Project goals include demonstration of new capabilities for hydrogenation of novel boron-nitrogen polymers and assessment of catalytic routes to improve efficiency in hydrogenation-dehydrogenation cycles.

Technical Approach

We addressed the technical challenges of developing on-board storage with high specific energy and energy density, simple and economical cycling (discharge/recharge capacity), and safety through a hybrid storage system incorporating both hydrogen sorption and chemical-hydride storage media. We proposed a new class of composite materials—low-molecular-weight boron-nitrogen compounds (chemical hydride storage media) impregnated in high-surface-area boron nitride (hydrogen sorption).

Composite Material I—Borazane-Impregnated Boron Nitride: The molecular compound borazane contains 13.9% hydrogen and can release 6.9% of hydrogen via a borazane-borazine chemical transformation. The high-surface-area boron nitride powders can store and release ~2% hydrogen. The hydrogen storage limits for this system are ~2–6.9% (0% borazane to 0% boron nitride) at low temperatures. Since the density of borazane is 0.96 ± 0.01 g/cm^3, the volumetric hydrogen storage is not significantly different.

Borazane, $B_3N_3H_{12}$, which is the B-N analogue of cyclohexane, can undergo facile chemical hydrogenation–dehydrogenation. In the 1960s, Schaeffer et al. showed that borazane can be prepared from hydrochlorination and sodium borohydride reduction of borazine, $B_3N_3H_6$ (Dahl 1961).

$$[H_2N{\cdot}BH_2]_3 \rightarrow [HN{\cdot}BH]_3 \xrightarrow[NaBH_4]{HCl} [H_2N{\cdot}BH_2]_3$$

Borazane reverts to borazine on heating at 200ºC. Thus, the hydrogenation-dehydrogenation pathway involved:

- hydrochlorination of borazine to B-trichloro-borazane,
- borohydride reduction to borazane, and
- thermal degradation to release hydrogen and conversion back to borazine

Thus, borazane-impregnated boron nitride can be viable hydrogen storage system. Here, high-surface-area boron nitride will be the borazane carrier as well as the borazine adsorber.

***Composite Material II—Boron Nitrogen Polymer–Impregnated Boron Nitride*:** This system retains most of the hydrogen storage capacity (~6.0%), but the primary advantage of this system is that media remain in solid state through hydrogenation-dehydrogenation cycle. This eliminates the need to separate hydrogen from volatile dehydrogenated borazane (i.e., borazine). While borazane polymers have not been explored, the borazine-ring-encompassing polymers are quite common (Narula 1987; Paine 1990; Narula 1995). A typical polymer synthesized directly from B-trichloroborazine and hexamethyldisilazane is shown in Fig. 1.

These polymers can also be subjected to Schaeffer's protocol of hydrochlorination and reduction for hydrogen storage because the reaction chemistry will occur on the borazine rings. Such borazane polymer will contain ~12.9% hydrogen and will eliminate ~6% hydrogen during low-temperature dehydrogenation.

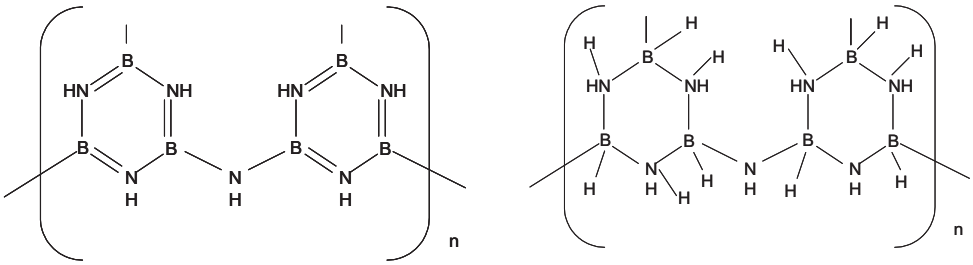

Fig. 1. A typical polymer synthesized directly from B-trichloroborazine and hexamethyldisilazane.

These systems can provide a viable alternative to known solid hydrogen storage media. We emphasize that unlike boranes, explored as rocket fuels in the 1960s, the boron nitrogen compounds of borazane type are stable under ambient conditions in the absence of moisture. Trimethylborazanes, prepared in Riley Schaeffer's laboratory, were stored in screw cap bottles and were available for study by the authors of this proposal after 20 years of storage.

A detachable cartridge containing these composites can be integrated into the fueling systems. The consumer will replace the spent cartridge at refueling stations, and spent cartridges will be taken to a central facility for recharging (hydrogenation).

Results and Discussion

We initiated this work with the preparation of model compound, a mixture of two isomers, 1(e),3(e),5(e)- and 1(e),3(e),5(a)-Trimethylcycloborazane by the method reported previously by Narula et al. (Narula 1986)

$$H_3B{\cdot}THF + CH_3NH_2 \rightarrow CH_3N(H)_2{\cdot}BH_3 \xrightarrow[-H_2]{\Delta} [CH_3N(H)BH_2]_3$$

The decomposition temperature of trimethyl-cycloborazane was determined to be 250ºC at atmospheric pressure.

$$[CH_3N(H)BH_2]_3 \rightarrow [CH_3NBH]_3 + 3H_2$$

This model compound releases 4.49% H_2 at 80ºC and additional 4.7% H_2 at 260ºC (w/w ≈ v/v since density is ~1). The model compound was impregnated into high-surface-area boron nitride that was prepared in two steps. In the first step, we used an aerosol reactor, schematically shown in Fig. 2, with commercially available trialkylborate compounds and ammonia to form BN_xO_y spherical particles with oxygen levels less than 8 wt % (Pruss 2000). Brief calcination of these particles in NH_3 gave smooth spherical morphology particles of BN.

The hydrogenation of this system is being investigated. This will be followed by investigation of borazine/BN composite and poly(borzinyl)amine/BN composite systems.

Benefits

The U.S. Department of Energy, Office of Hydrogen, Fuel Cells, and Infrastructure and Office of FreedomCAR and Vehicle Technologies have embarked on a Presidential Initiative to develop a hydrogen-powered fuel cell

automobile. The goals of the program include very high energy efficiency and nearly zero harmful emissions. If the hydrogen is produced from non-petroleum feedstock, the program offers the potential of increased national security via less dependency on imported oil. While there are many technological barriers in this program, there is consensus that sold-state storage of hydrogen at high densities (e.g., ~10% by weight of the fuel storage system) is the critical barrier. Although extensive literature indicates many materials, systems, and approaches have been examined, there is no clearly defined path to reaching the DOE hydrogen storage goals. It is important to mention that our model system can provide up to 9.2% H_2 (excluding the weight of system for on-board installation).

This research specifically addressed the development of a viable chemical hydride system for on-board storage of hydrogen with the potential to meet all the requirements listed by DOE and the FreedomCAR program.

References

Dahl, G.H., and R. Schaeffer. 1961. "Studies of Boron-Nitrogen Compounds. III. Preparation and Properties of Hexahydroborazole, $B_3N_3H_6$," *J. Am. Chem. Soc*. **83**, 3032.

Narula, C. K., J. F. Janik, E. N. Duesler, R. T. Paine, R. O. Schaeffer. 1986. "Convenient Synthesis, Separation and X-ray Crystal Structure Determination of E,E,E-1,3,5-Trimethyl Cycloborazane and E,E,A-1,3,5-Trimethyl Cycloborazane," *Inorg. Chem.* **25**, 3346.

Narula, C. K., R. O. Schaeffer, R. T. Paine, A. Datye, W. F. Hammetter. 1987. "Synthesis of BN Ceramics from Poly(borazinyl)amine," *J. Amer. Chem. Soc*. **109**, 5556.

Narula, C. K. 1995. *Ceramic Precursor Technology and Its Applications*, Marcel Dekker, New York.

Paine, R. T., and C. K. Narula. 1990. "Synthetic Routes to Boron Nitride," *Chem. Rev*. **90**, 73.

Pruss, E. A., G. L. Wood, W. J. Kroenke, and R. T. Paine. 2000. "Aerosol Assisted Vapor Synthesis (AAVS) of Spherical Boron Nitride Powders," *Chem. Mater.* **12**, 19–21.

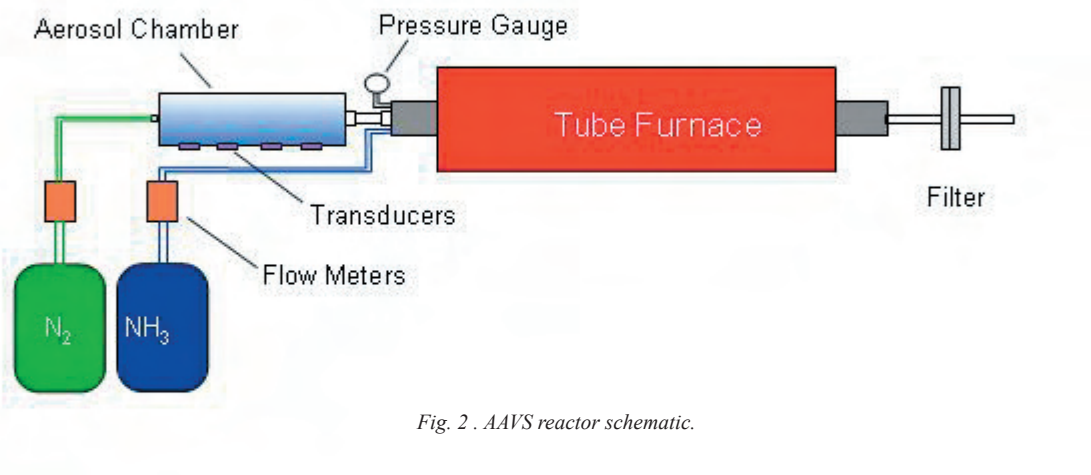

Fig. 2 . AAVS reactor schematic.

Nanorods for Energy and Photonics

D. B. Geohegan,[1] Z. Pan,[2] I. N. Ivanov,[3] B. Hu,[3] D. H. Lowndes,[1] J. W. Mays,[2] A. A. Puretzky,[3]
S. Dai,[2] H. M. Christen,[1] C. M. Rouleau,[1] G. Eres,[1] and V. Meunier[4]
[1]*Condensed Matter Sciences Division*
[2]*Chemical Sciences Division*
[3]*The University of Tennessee*
[4]*Computer Science and Mathematics Division*

This project targets the controlled synthesis of transparent, conducting nanorods to enable applications in energy and photonics. It also targets methods for rapid optical assessment of nanorod properties and methods for the fabrication of prototype composites. Nanorods are among the most scientifically interesting nanostructures and the most important technologically since (unlike quantum dots) the confined transport of electrons, ions, and photons over long (microns) distances permits crucial addressability for microscale electronics and photonics and efficient charge migration over long distances for energy-related applications. This project enables a concerted program in the controlled synthesis, characterization, and application of these advanced materials.

The overall approach involves the development of methods to synthesize transparent, conducting nanorods and their assemblies by generally vapor-phase growth techniques and rapid optical characterization techniques to survey their electronic structure and photonic properties. Ultimately, vertically aligned nanorods will be grown at discrete, deterministically placed locations on substrates through patterning of individual catalyst dots via lithography. However, first the synthesis conditions of the optimal nanorod crystal structure and functional properties must be determined through the synthesis of loose nanorods or nanorod forests on substrates. Techniques for the manipulation, alignment, and fabrication of loose nanorods into assemblies with functional properties must be accomplished.

In the first year of this project, major accomplishments were achieved in each of five task areas. First, the growth of crystalline nanorods of ZnO, In_2O_3, SnO_2, and their doped variants were investigated by the vapor-liquid-solid (VLS) technique and by catalyst-free methods. For the catalytic growth of ZnO nanowire forests, an entirely new strategy was developed involving the first use of a semiconductor, Ge, as the catalyst. This approach enabled deterministic growth of ZnO nanowires on patterned substrates at precise Ge-dot locations. Research will continue into doping the nanorods to optimize their electrical conductivity. Doping of ZnO nanorods was investigated and correlated with fluorescence maps which categorize the photoluminescence of the nanorods as a function of the excitation wavelength. This method provides the technique to rapidly assess dopant levels of various nanorods. Finally, single-wall carbon nanotubes were fabricated into percolation networks for use in organic light-emitting diodes (OLED's). The nanorod networks doubled the efficiency of the devices in forward bias mode, permitting reverse electroluminescence for the first time, as well as significantly lowering the turn-on voltage.

The work in this project was identified by Battelle Memorial Institute (BMI) as one of the key application areas for future commercialization after their survey of technology development at ORNL. Transparent conductive coatings lend functionality to every application from OLEDs to military cockpits to floor coatings. Initial findings from this project on OLED development were proposed to DOE's NETL for improved solid state lighting. DARPA's MTO office invited the PI to participate in two workshops based upon the work in this project. Several notable publications were accomplished in this project during the first year. As a result, both follow-on-funding possibilities as well as fundamental science recognition were achieved in this project.

A Revolutionary Infrared Nanoscale Processing Approach

R. D. Ott,[1] C. A. Blue,[1] D. A. Blom,[1] R. B. Dinwiddie,[1] B. Radhakrishnan,[2] A. S. Sabau,[1]
T. R. Watkins,[1] and J.W. Harrell[3]
[1]*Metals and Ceramics Division*
[2]*Computer Science and Mathematics Division*
[3]*University of Alabama, Department of Physics*

Oak Ridge National Laboratory (ORNL) has high-density infrared plasma arc technology and a technique called pulse thermal processing (PTP) that approaches heating rates and power densities of lasers with a 4000% larger footprint (processing area); this capability allows the process to be scaled for production. The controlled synthesis of FePt nanoparticles for ultrahigh-density magnetic recording has been chosen as a case study. Being able to transform disordered face-centered-cubic (fcc) FePt nanoparticles to an ordered face-centered-tetragonal (fct) L10 structure without sintering the nanoparticles could result in more than a 200% increase in storage density.

ORNL, for the first time, has demonstrated the ability to control diffusion on the nanomaterial scale utilizing broad-area rapid IR heating. This approach results in the phase transformation of FePt nanoparticles from a disordered A1 structure to an ordered L10 structure while inhibiting nanoparticle sintering. The significance of this research project lies in the ability to understand and control the diffusion within the nanoparticles system. The capability to precisely control diffusion on this scale becomes extremely important when attempting to functionalize nanomaterials such as nanoparticles and thin-films for microelectronic devices. Having the ability to control phase transformations, grain growth, grain boundary refinement, sintering and crystallization on the nanoscale is key for next-generation magnetic media storage, photovoltaics, and thin-film transistors for flat panel displays. Once knowledge of this interaction begins to be understood for one material system, the foundation is set for carrying the knowledge to other functional nanomaterial systems.

Results to date have been encouraging and show good ordering and high coercivity measurements. IR imaging has been utilized to provide real-time temperatures of the surface of the nanoparticles, which allows validation of the theoretical processing model. This model is established with finite-difference methods and is based on the thermal properties of the nanoparticles, substrate, and processing environment. By an iterative process, the model has been refined, leading to a better understanding of the temperature profile within the nanoparticle layer and the underlying silicon substrate. Further refinement of the model is under way to establish better correlation between measured temperatures and processing parameters so that precise control over the phase transformation can be obtained.

The programmatic opportunities relating to this research are numerous. There has been tremendous interest generated by the results thus far and the potential for this technique to be utilized in numerous material systems. Within DOE, the Office of Science and Basic Energy Science have programs that would benefit from this research. The Defense Advanced Research Projects Agency (DARPA) Microsystems Technology Office (MTO) is highly interested in the technology for photovoltaic applications as well as for thin-film transistors (TFT) for flat panel displays. A collaboration has been established with Dr. Rommel Noufi at National Renewable Energy Laboratory (NREL) to investigate increasing the collection efficiency of next-generation copper-indium-gallium-diselenide (CIGS) photovoltaic materials, opening the possibility for future funding from EERE for photovoltaic research. The potential to control the degree of sintering of the ceramic nanoparticles on a Kapton polymer substrate has been demonstrated.

Profiling Spin Injection at the Atomic Scale

J. Shen,[1] H. H. Weitering,[1,2] X. G. Zhang,[3] and L. C. Feldman[1,4]
[1]*Condensed Matter Sciences Division*
[2]*The University of Tennessee*
[3]*Computer Science and Mathematics Division*
[4]*Vanderbilt University*

The objective of this project is to demonstrate a highly innovative experimental approach to profile spin transport across the interface using *cross-sectional spin-polarized scanning tunneling microscopy* (CSSP-STM). In the first year, we have made outstanding progress in setting up the CSSP-STM, which includes challenging tasks of setting up cross-sectional STM, spin-polarized STM, and finally a technical combination of the two. High-quality images with atomic resolution have been obtained in the cross-sectional STM, while magnetic domain images have been obtained by the spin-polarized STM. In addition, we have successfully grown and characterized various ferromagnetic/semiconductor heterostructures, which are essential for measurements by CSSP-STM.

Spintronics is widely anticipated to benefit many branches of society: information technology, strategic systems, space technology, and perimeter defense (sensors). However, researchers still face many challenges at the most fundamental level, the materials level! The greatest challenge of all is to transfer spin-polarized electrons from a ferromagnetic material into a non-ferromagnetic semiconductor without substantially degrading the polarization (spin injection). The second problem is to detect such spin polarization or, better yet, to obtain a complete spatial profile of the electrochemical potential of the spin-up and spin-down electrons.

Our objective is to create a novel tool that enables accurate profiling of spin polarization and injection efficiency for a wide range of materials and interfaces. We have named this cross-sectional spin-polarized scanning tunneling microscopy or CSSP-STM. Our goal is to achieve quantitative spin-injection measurements using the CSSP-STM. The specific tasks include setting up cross-sectional STM, spin-polarized STM, and finally the combined CSSP-STM. In addition, we need to develop the synthesis capabilities for spin-injection samples and the theoretical tools for analyzing the CSSP-STM data.

To date, we have made outstanding progress in all these areas. High-quality images with atomic resolution have been obtained in the cross-sectional STM, while the most difficult technical challenge for the spin-polarized STM (i.e., magnetic tip preparation) has been successfully addressed. We expect the later will soon be patented and then move into the commercial sector where it could readily convert all ultrahigh vacuum STMs from the market-dominating company (Omicron) into spin-polarized STMs. Preliminary results on magnetic domain structures of low-dimensional films have been obtained by the spin-polarized STM. In addition to the progress in CSSP-STM, we have also successfully grown various high-quality ferromagnetic/semiconductor heterostructures, which are essential for spin injection measurements by CSSP-STM.

Our team is an exemplary partnership among Oak Ridge National Laboratory (ORNL), The University of Tennessee, Knoxville, and Vanderbilt researchers that can put the ORNL Center for Nanophase Materials Sciences (CNMS) on the map as the prime Department of Energy facility for spintronics research. The proposed technology and instrumentation will be one of a kind and because of its versatility, it is destined to become one of the most successful user facilities at CNMS. It will be an important characterization tool for a broad range of spintronic materials and devices, including semiconductor electronics, molecular electronics, soft materials (plastic spintronics), radiation hardened devices, and possibly sensors that can be utilized for perimeter defense and unexploded ordinance detection. Each of these areas is of vital interest to the United States economy and the security of the nation. Hence, there is no doubt that this program will become a major asset for the laboratory in terms of scientific recognition and leadership in key areas such as information technology and homeland security.

Complex Oxides with Frustrated Orbital Ordering

T. Egami,[1] G. M. Stocks,[1] and D. G. Mandrus[2]
[1]*Metals and Ceramics Division*
[2]*Condensed Matter Sciences Division*

Capability for accurate structural determination at a nanometer scale is a key prerequisite for the successful development of nanotechnology and nanoscience. However, there is a gap in the capability coverage for the range of 0.5 ~ 20 nm. The goal of this project is to develop the method of atomic pair-density function (PDF) analysis with pulsed neutrons to fill this gap. The success of this project will greatly expand the role of neutron scattering in nanotechnology and nanoscience and achieve a synergy between the Spallation Neutron Source (SNS) and the Center for Nanophase Materials Sciences (CNMS). We focus on $LiNiO_2$ and related compounds with orbital frustrations, carry out neutron scattering studies, and develop theories based upon first-principles calculations.

Capability for accurate structural determination at a nanometer-scale is a key prerequisite for the successful development of nanotechnology and nanoscience. However, at this moment there is a dearth of techniques that can accurately determine the nanometer range local atomic structure in the bulk. Surface nano-structures can be determined using tunneling probes, such as STM and AFM. However, they are either powerless or misleading for bulk materials with nano-scale local variations. Small-angle neutron scattering (SANS) is effective in the length scale exceeding several tens of nanometers, while electron microscopes give an image averaged over the film thickness. Local probes, such as EXAFS and NMR, provide information on the nearest, and at best second, neighbor atoms. This results in a gap in the structural characterization capabilities of the range 0.5–20 nm.

This project sets out the goal of filling this gap. This will be achieved by applying the method of atomic pair-density function (PDF) analysis. The PDF describes the distribution of distances between atoms in the system and has been used for the structural studies of liquids and glasses. While the PI (T. Egami) championed its use in the study of crystals with disorder, by using pulsed neutrons and synchrotron radiation as a probe (Egami and Billinge 2003), it has been applied so far only to the analysis of local structure up to 0.5–1 nm. The purpose of this project is to extend the capability of this method to the study of nano-scale non-periodic structure in the range 1–20 nm. For this purpose new software and theories need to be developed and tested on real materials. As the object to apply this method, we chose a group of layered complex oxides including $LiNiO_2$, for which we recently discovered rich nano-structure, which appears to come from the orbital frustration. Frustrated systems are collecting much attention today because of the possibility of discovering new phenomena that may translate to development of new functional materials

The results obtained this year include the following: (1) Inelastic correction to the PDF, a very significant improvement over the currently used correction method, the Placzek correction. (2) Determination of the Local structure of $LiNiO_2$, including the observation of the local Jahn-Teller (JT) distortion, formation of the trimer structure, and understanding of the origin of the nano-scale domains. (3) Single-crystal X-ray diffraction of $LiNiO_2$ that showed local shifts in position, consistent with the local distortion. (4) Theoretical calculation of the electronic band structure using the local density approximation (LDA) for a simplified NaCl-type structure resulted in a metal as expected, demonstrating the effect of strong electron correlation to produce an insulator with orbital ordering. (5) Observation of the local structure of superconducting cobaltate with water by pulsed neutron PDF, which suggested an important role of water in superconductivity. (6) Local structure of $LiVO_2$ studied by neutron PDF, which is well explained by the similar trimer model as the $LiNiO_2$.

The success of this project will greatly enhance the PDF technique and make it applicable to structural characterization of nano-materials critical for catalytic, energy, and other functional applications. It will add to the strength of ORNL to attract funding in the area from DOE and other agencies. It also will achieve a synergy between the Spallation Neutron Source (SNS) and the Center for Nanophase Materials Sciences (CNMS).

References

Egami, T., and S. J. L. Billinge. 2003. *Underneath the Bragg peaks: Structural analysis of complex materials*. Pergamon Press, Elsevier Science, Oxford.

Development of In Situ Neutron Diffraction Capabilities for Studies of Deformation and Fracture Behavior under Hydrogen-Rich Environments

C. R. Hubbard,[1] H. Choo,[1,2] J. W. Pang,[1] G. Sarma,[3] S. Pawel,[1] and P. Nash[4]
[1]*Metals and Ceramics Division*
[2]*University of Tennessee*
[3]*Computer Science and Mathematics Division*
[4]*Illinois Institute of Technology*

This project integrates neutron diffraction with mechanical metallurgy, corrosion science, and modeling to (1) develop in-situ ND experimental facilities and protocols for characterization of structural materials under realistic and extreme conditions at the High Flux Isotope Reactor (HFIR); (2) conduct experiments to advance fundamental understanding of in-situ microstructure evolution and deformation mechanisms of structural materials under stress in "hydrogen-rich" environments; and (3) initiate computational modeling of environmental effects through mesoscale deformation modeling to investigate interactions between plasticity and environment.

Sub-critical flaw growth phenomena involving a cooperative interaction between a static stress and the environment are referred to collectively as environment-assisted cracking. For example, corrosion fatigue, a combined environmental and mechanical damage mechanism, is one of the most abundant damage processes in structural materials. Recent thrust towards the "hydrogen economy" could significantly expand the attention to such problem.

The current LDRD project focuses on the investigation of hydrogen embrittlement in structural materials, and specific R&D objectives include the following: (1) develop a load frame and electrochemical environmental cell for in-situ neutron-scattering studies; (2) using neutron scattering, advance the fundamental understanding of deformation and fracture in response to applied stress under hydrogen-rich environments; (3) develop and validate computational deformation models that include environmental effects; and (4) expand user research opportunities at HFIR and SNS.

First, a dedicated load frame for the NRSF2, the new second-generation Neutron Residual Stress mapping Facility at HFIR, was designed and constructed. The load frame can apply uniaxial load up to 5000 lbf (15 kN) for in-situ deformation studies (tensile, compressive, and potentially low-cycle fatigue). In addition, a dedicated environmental cell is being developed to be used combination with the load frame at NRSF2 for hydrogen charging, cathodic protection, and corrosion research. The new capabilities will provide a unique, high-impact research tool for the corrosion/mechanical-behavior/modeling communities.

Second, preliminary in-situ neutron diffraction studies were performed to investigate the interplay between the internal strain and the mechanism of hydride formation around the crack tip in a polycrystalline zirconium alloy (Zircaloy-4). Neutron diffraction results show significant changes in lattice strain profiles in front of the crack tip after electrochemically charging the specimen with hydrogen. Three systematic neutron diffraction measurements are in progress: (1) effect of hydrogen on the microstructure and lattice dilation, (2) effect of hydrogen on the deformation behavior, and (3) effect of hydrogen on the fatigue and fracture behavior. The success of this task will advance the fundamental understanding of the microstructure, deformation, and fracture micro-mechanisms of structural materials under hydrogen-rich environment.

Third, a polycrystal finite-element model is being developed to simulate the deformation and fatigue behavior of metals in the presence of environmental effects at the mesoscopic length scale using the unique supercomputing capabilities at ORNL. In this simulation, the finite-element discretization is applied directly to the individual grains of the microstructure, and plastic deformation by slip is modeled using constitutive laws based on crystal plasticity. Efforts are under way to incorporate elasticity into the current viscoplastic constitutive model so that direct comparisons with the neutron diffraction measurements can be made. The proposed attempt to extend the modeling capability to investigate the effect of environment such as hydrogen on the deformation behavior will represent a significant advance in the state of the art in microstructure modeling.

Development of experimental and modeling expertise and advances in fundamental understanding of science issues regarding hydrogen embrittlement problem will benefit major industrial sectors including energy (heat exchangers and piping systems), transportation (hydrogen storage, transmission and conversion), civil infrastructure (steel bridges, reinforcements, water/gas/oil piping systems), nuclear (reactor piping and pressure vessels), and aerospace (fuselage, wing).

Quantum Circuit Modeling for Nanoelectronics

X. Zhang,[1] S. Pantelides,[2,3] V. Meunier,[1] Z. Lu,[1] M. Evans,[4] J. Bernholc,[1,5] and R. D. Schrimpf[3]
[1]*Computer Science and Mathematics Division*
[2]*Condensed Matter Sciences Division*
[3]*Vanderbilt University*
[4]*Massachusetts Institute of Technology*
[5]*North Carolina State University*

In recent years, nanoscale electronic devices (molecules or semiconductor nanostructures) have been extensively investigated as a new frontier beyond conventional microelectronics. We and our collaborators have pioneered the simulation of transport properties of individual nanodevices. Ultimately, nanodevices must be integrated as components of active electronic circuits, and the simulation of the circuit as a whole remains a key milestone in developing applications. The fundamentals of quantum circuit modeling are strikingly different from the issues encountered in classical circuit modeling, where one assumes a simple picture of constant currents in the wires between devices, which in turn are modeled using approximate solutions of the Boltzmann transport equation (each conventional device is represented by a classical equivalent circuit-in-a-box, within which the relevant elements are obtained by simulating the device using the Boltzmann equation). In a quantum circuit, the wires are too short for conventional modeling to apply and should be treated by the Boltzmann equation as well, by building proper interface between the wires and the quantum devices via appropriate boundary conditions. Conversely, the quantum devices themselves must be treated with full quantum mechanics. Our initial success during the first year in modeling charge dynamics and in constructing a one-dimensional Boltzmann model for a carbon nanotube device proves the viability of our approach and prepares us for further progress in this groundbreaking initiative.

Conventional microelectronics is already confronting the nanoscale, where quantum phenomena are inevitable. The industry is still at a stage of designing around quantum phenomena, for example, by seeking alternative insulators with high dielectric constant in order to enable thinner gate-dielectric films and avoid disastrous tunneling (leakage currents). Nevertheless, the time is approaching fast that nanoscale devices will have to exploit quantum phenomena instead of avoiding them. Experimentalists have been fabricating and measuring this type of nanodevices, such as single-electron transistors or individual molecules, in which quantum mechanical effects play a decisive role, unveiling new and interesting phenomena that can be exploited in applications. Successful designs of nanoelectronics require a valid model to connect the quantum device elements into a circuit, much like the classical circuit model for semiconductor devices. This is a critical step in turning the advances in nanoscience into practical applications. Yet very little has been done in this area. There has been virtually no research in the direction of a quantum mechanics–based model for interconnects that connect quantum devices. Although at this early stage of nanoelectronics technology it is far from clear what kind of devices, whether molecular, atomic, ultrathin film, or magnetic, will be ultimately successful in terms of commercial applications, the utility for the quantum circuit model is clearly defined independently of the specific implementations of the quantum devices. Thus, we have a unique window of opportunity to grab the leadership and make ORNL the center of this emerging area of R&D.

We and our collaborators have been at the forefront of theoretical research aiming to simulate the transport properties of nanodevices, both molecular devices and ultrathin-film structures. This project is about the next step, namely, the simulation of circuits that contain nanodevices and is the first attempt to address this problem. We propose to implement the first codes ever for modeling circuits consisting of quantum devices such as individual molecules (the wiring in molecular circuits must be modeled at the semiclassical level using the Boltzmann equation, that is, with the sophistication that is currently used to model conventional devices). We will set up a hierarchy of codes for circuit modeling that conforms to standard industrial practices.

We have made significant progress in formulating a framework for the theory of charge dynamics. This is a crucial step for going beyond the steady-state solution available in the state-of-the-art quantum transport theory. We have formulated an effective Hamiltonian allowing the separate treatment of the quantum device from electrodes. We have tested the effective Hamiltonian on a few simple problems, and shown that it reproduces correctly important aspects of quantum devices such as

the Kondo effect, and the dynamic charge fluctuation of a quantum dot. One of the encouraging successes in this effort is that we were able to solve analytically the charge and spin oscillation of a quantum dot connected to a single electrode and found nearly perfect agreement with the numerical solutions in the literature.

We have developed a one-dimensional Boltzmann transport code for Bloch electrons to perform the proof-of-concept test on model quantum circuits. The test system we chose was a double carbon nanotube intramolecular junction, a system of three carbon nanotubes connected though two constrictions, each one formed around the introduction of one single pentagon-heptagon pair. This pair of defects allows for a seamless junction in which each atom conserves its threefold sp^2 coordination. The conducting carbon nanotubes are characterized by two conduction channels at the Fermi energy. Full electronic quantum transport calculation based on Landauer formalism obtained the total resistance as a function of the separation between the two junctions (i.e., length of the central tube). The result shows an oscillation reflecting the quantum interference between incoming and outgoing electron wave functions reflected on the constriction. Interestingly, the Boltzmann approach yields a constant resistance that is equal to the average of the quantum solution over many oscillations and independent of the separation. As expected, the total resistance is equal to the simple direct sum of the resistance of the two junctions when there is no scattering in the electrodes. As we mentioned in the original proposal, we expect that the total resistance will deviate from Ohm's law when there is scattering in the electrodes and the two conduction channels are asymmetric. This highly encouraging proof of principle opens the route to larger-scale, systematic studies of nanoscale (molecular) devices and how they can be incorporated in a realistic practical circuitry. Further developments will include an intermediate model, which will constitute a natural bridge between Boltzmann and Landauer approach. More specifically, we intend on developing the so-called "S-matrix combination" approach that allows for the extension of the scattering approach to either coherent or incoherent transport, to be compared to Landauer and Boltzmann, respectively.

We have refined the existing quantum transport model to enable the calculation of the transmission and reflection coefficients for individual Bloch states. This provides the input parameters for the Boltzmann model calculations.

Characterization of Spin Structure and Spin Dynamics of Nanostructure Assemblies Using In-Field Scanning Electron Microscopy with Polarization Analysis

J. F. Wendelken,[1] J. Shen,[1] S. Dai,[2] and Z. Gai[3]
[1]*Condensed Matter Sciences Division*
[2]*Chemical Sciences Division*
[3]*Peking University, Beijing, China*

In data storage and spintronics devices, nanostructured magnetic materials must have their magnetization direction reversed by application of an external field. The performance of the materials critically relies on the dynamics of the magnetization reversal, which can be imaged using the in-field Scanning Electron Microscope for Polarization Analysis (in-field SEMPA) developed at the MPI-Halle in Germany. Zheng Gai, who has outstanding experience in both nanoscale magnetism and instrumentation, will join Oak Ridge National Laboratory (ORNL) and will develop this technique to operate under higher magnetic fields and with improved spatial resolution. These capabilities will become a major tool for the study of scientific issues regarding magnetization reversal and spin injection.

In a recent Office of Science Strategic Plan, key emphasis is placed on understanding new properties at the nanoscale and in the corresponding development of facilities for probing atomic and molecular processes. Nanoscale magnetic phenomena will play a key role in the continued development of magnetic data storage devices and future spintronics-based devices. This project is focused on the creation of a unique capability at ORNL and the Center for Nanophase Materials Sciences (CNMS) for the characterization of a broad range of nanomagnetism materials and devices.

The effect of spatial confinement on magnetic domain structures will be observed using in-situ growth of magnetic monolayer films, wire arrays, and dot assemblies of the same material on a common substrate. We will then identify the thermal stability of nanoscale spin structures to understand the mechanisms of magnetization reversal with domain images taken at various fields using a unique SEMPA that allows for imaging with an in-plane magnetic field. Magnetostatic coupling in nanodot assemblies with controlled aerial densities will be observed, which will allow separation of dipole-dipole coupling effects from the less-understood substrate-mediated exchange interactions. Finally, the effects of spin-polarized current on magnetic domain structures and magnetization reversal in nanowires will be explored.

In the first stage of this project, preliminary work at ORNL has proceeded to develop the technology for growth of magnetic nanostructures, which will be implemented in the SEMPA system. The most important capability developed is the ability to control both the size and spacing of magnetic iron dots on a surface. This has been done for a system consisting of iron nanodots on a Cu(111) surface using the synthesis technique of buffer layer–assisted growth. In this technique, a molecular beam epitaxy source is used to deposit atoms on a substrate that has been first covered with a layer of frozen inert gas at a temperature of about 30 K. The low-surface free energy of this inert surface leads to the formation of clusters, which are then deposited on the substrate after slowly warming the substrate to remove the inert gas layer. Detailed recipes have been developed that allow the control of both the iron dot size and spacing by varying both the buffer layer thickness and the total iron deposition amount. These recipes will be transferred to the SEMPA system, which has facilities for in-situ growth.

Completion of this program will further establish ORNL as a center for the study of nanoscale magnetism and will provide a significant and unique capability for the CNMS.

MATERIALS SCIENCE AND ENGINEERING

Seed Money Fund

Nanoelectronic Devices Made from Doped Nanofibers

J. B. O. Caughman,[1] M. L. Guillorn,[2] D. B. Beach,[3] V. I. Merkulov,[2] L. R. Baylor,[1] and L. Allard[4]
[1]*Fusion Energy Division*
[2]*Engineering Science and Technology Division*
[3]*Chemical Sciences Division*
[4]*Metals and Ceramics Division*

The purpose of this project was to understand and develop a process for depositing doped carbon-based nanofibers that can be used to make nanoelectronic devices in a way that will be useful for large-scale manufacturing. The concept is based on the growth of vertically aligned nanofibers using a high-density plasma-enhanced chemical vapor deposition technique that allows for control of gas-phase and surface chemistry. In contrast to current growth methods, our approach is to modify the electrical properties of the nanofibers by substitutional doping of boron and/or nitrogen to produce metallic or semiconducting doped carbon-based nanofibers. The electrical characteristics of individual nanofibers were determined by measuring the current flowing through the fiber as a function of applied voltage across the fiber. Our approach for growing nanofibers has potential advantages over current methods in terms of controlling electrical properties of individual nanofibers, controlling the geometry of the growth, and the potential use as a practical method for realizing vertical integration of dense arrays of nanoelectronics. While we had trouble incorporating boron or nitrogen into the nanofibers, we were successful in understanding and demonstrating a growth technique that is applicable to large-scale manufacturing. This work resulted in an *Applied Physics Letters* publication where we showed the ability to control and understand the process parameters leading to nanofiber growth.

Introduction

There has been much research in the growth of carbon-based nanotubes and nanofibers. Because of their interesting electrical and physical properties, they have numerous applications, including nanoelectronics, hydrogen storage, and field emission devices. The nanoelectronics application was the focus of this project.

Numerous researchers have used various techniques to use carbon nanotubes or silicon nanowires to make logic devices out of transistors or diodes made from individual molecules (Kong 2002, Derycke 2001, Huang 2001). While these results are impressive, there is a large disconnect between current approaches and the practical implementation of nanoelectronics on a large scale. The electrical properties are mostly determined from the physical size of the nanotube, which is very difficult to control, especially on a large scale. Our approach was to control the electrical properties by controlling the composition of a nanofiber, which is conceptually easier to do. Note that nanotubes are composed of concentric cylinders of carbon atoms, while nanofibers consist of concentric cones of carbon atoms. Our main objective was to develop and understand a process for growing doped carbon-based nanofibers that can be used to make nanoelectronic devices in a way that will ultimately be applicable to manufacturing.

The basis for controlling the properties of nanofibers is tied to the method of growth. Growth techniques include laser ablation, arc discharge, thermal chemical vapor deposition (CVD), and plasma-enhanced chemical vapor deposition (PECVD). For nanoelectronic applications, patterned arrays of vertically aligned nanotubes or nanofibers are desirable. It has been shown that nanotubes and nanofibers will grow in the direction of an applied electric field. Because of the electric field provided by the plasma sheath in contact with the substrate surface during growth, a PECVD method is an attractive choice for growth of these vertically aligned structures. Several PECVD methods have been used for growth of nanofibers, including microwave discharges, direct current (dc) or radio-frequency (RF) glow discharges (Merkulov 2002), and inductively coupled discharges (Delzeit 2002).

Technical Approach

Our approach for PECVD of nanofibers uses an inductively coupled plasma source that operates at a much lower neutral pressure of ~50 mtorr, in contrast to the other methods used to date, which have operating pressures of 2–10 torr. Inductively coupled plasma sources are attractive because they are fairly simple in construction (no external magnets) and have been demonstrated to be applicable for large-area processing (>300 mm), which is desirable for large-scale manufacturing. Low-pressure operation, which has been recently demonstrated for diamond deposition at pressures below 100 mtorr, is potentially advantageous because of the improvement in plasma uniformity as the pressure is decreased.

Details of the system and initial growth results can be found in a recently published paper (Caughman 2003). The PECVD process in this work uses an inductively coupled plasma source operated at 13.56 MHz. The source coil consists of a 15-cm-diam flat spiral coil (six turn) separated from the chamber vacuum by a 20-cm-diam, 2.5-cm-thick fused quartz window. The chamber is made from stainless steel and is 30 cm in diameter. A 4.4-cm-diam heated substrate, equipped with RF biasing at 13.56 MHz, is located 20 cm below the window. Typical RF-induced self-biases of –50 to –200 V were used during growth. The optical emission from the plasma was measured with a Czery-Turner spectrometer with a 1-m monochrometer, and the mass spectrum was measured through a small sampling orifice with a differentially pumped Pfifer Prisma80 mass spectrometer. The plasma light passed through a quartz viewport and was fed to the monochrometer via fiber optic cable.

Both forests of nanofibers and isolated nanofibers have been grown on silicon substrate samples using nickel as a catalyst. For the forest growth, continuous nickel thin films (15 nm thick) were deposited on a buffer layer of tungsten-titanium alloy (100 nm thick) to prevent formation of nickel silicide. For the isolated nanofiber growth, a pattern of 100-nm-diam nickel dots (10 nm thick) were defined by electron beam lithography and deposited on a 10-nm-thick titanium buffer.

Acetylene (C_2H_2) or methane (CH_4) was used as the carbon source gas, and hydrogen (H_2) was used as the etchant gas. The plasma source was typically operated at 50 mTorr with a source RF power level of 1 kW. Hydrogen flow was varied from 30 to 150 sccm, and acetylene or methane flow was varied from 5 to 50 sccm. The nickel catalyst was exposed to a pure hydrogen plasma for ~6 min to remove any native oxide that may have formed. The growth temperature was ~700°C. The growth rate obtained was 30–50 nm/min, based on measuring the nanofiber height divided by the growth time. The vertically aligned carbon nanofibers (VACNFs) were analyzed using a Hitachi S4700 scanning electron microscope (SEM) with X-ray energy dispersive spectroscopy (EDS) and a Hitachi HR-2000 transmission electron microscope (TEM).

Results and Discussion

Our research has focused on understanding of the growth of vertically aligned carbon-based nanofibers and how to change their composition. We have conducted experiments to determine the role of various parameters on the growth results, modeled some of the process chemistry, performed electrical characterization of the nanofibers, and have explored nanofiber growth with boron addition to the plasma (from diborane).

Many parameters influence the growth and structure of vertically aligned carbon nanofibers (VACNFs), including the gas composition, the substrate bias, and the growth temperature. As the acetylene-to-hydrogen flow ratio increases, the production of the carbon-depositing species increases relative to the production of the atomic-hydrogen etching species, which affects the morphology of the nanofibers. For a hydrogen-rich plasma (low acetylene flow), the large level of atomic hydrogen flux reduces the amount of carbon deposited on the sidewalls of the VACNFs during growth by chemical etching of the carbon, which leads to a cylindrical nanostructure, as shown in Fig. 1(a). A TEM of a typical nanofiber is shown in Fig. 1(b). The graphitic planes spaced at 0.34 nm are clearly shown in the figure. The nanostructure of the VACNFs grown with the carbon-rich condition indicates an increase in condensable carbon species on the sidewalls of the nanofiber. The increase in the depositing species relative to the chemical etching species is a contributor to a cone-like morphology, as shown in Fig. 1(c), along with a TEM of the fiber in Fig. 1(d). Another contributor to this cone-like morphology is physical etching. The increase of acetylene relative to hydrogen in the plasma will likely lead to an increase in the average mass of the ions bombarding the surface, which may lead to more physical damage of the nanofibers during growth. Thus, the amount of physical etching taking place would be expected to be higher for the carbon-rich condition, while the amount of chemical etching would be lower.

The role of substrate bias is related to ion energy, which controls the physical etching that takes place during VACNF growth. We have discovered that a minimum

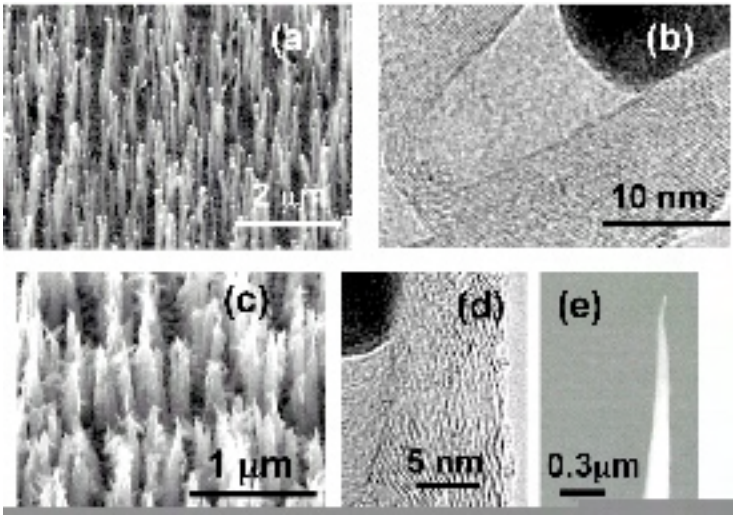

SEM images of carbon nanofibers showing forest of nanofibers grown in (a) hydrogen-rich plasma, (c) carbon-rich plasma, and (e) isolated nanofiber grown in hydrogen-rich plasma. TEM images taken near the catalyst base for the hydrogen-rich plasma (b) and the carbon-rich plasma (d).

amount of substrate bias is required to grow fibers. If the ion energies are too low (<50 volts), then a layer of carbon builds up on the surface and VACNF growth stops. We have also discovered that growth temperature is important. If the growth temperature gets too high, then the carbon-containing gas (acetylene of methane) will substantially decompose on the substrate surface and inhibit VACNF growth. There is a balance between growth temperature and gas flow.

The operating pressure used in these experiments (50 mtorr) is significantly lower than in most PECVD processing of carbon-based nanofibers (2–10 torr), which leads to a difference in plasma chemistry. It is likely that the contribution from gas-phase reactions relative to chamber surface reactions will be very different at the lower pressure. For example, the mean free path for acetylene neutral collisions is ~2 mm at 50 mtorr compared to 0.01 mm at 10 torr. The longer mean free path will lead to slower reaction rates for gas-phase interactions and reduced production of complex hydrocarbon species. Plasma surface interactions also contribute to the plasma chemistry, as can be seen in the optical emission and mass spectrometer data, where numerous hydrocarbon species are the result of atomic hydrogen interactions with the carbon-coated chamber surfaces.

We have also done some modeling work to help understand our experimental results. The mechanisms of reactions in plasmas are relatively complex, because the excitation energy is generally quite high relative to individual chemical bonds, so that a number of reaction pathways are available. To account for the species observed spectroscopically and taking into account the reactions likely to occur in an inductively coupled plasma environment (neutral species rather than charged species), several reaction mechanisms have been proposed. These mechanisms were used as input for a stochastic mechanism simulator program, Chemical Kinetics Simulator (IBM). This program allows the use of ensembles of 100,000 molecules with relatively short (less than 1 min) simulation times on a PC. Relevant gas-phase kinetic data was obtained from the NIST website (http://kinetics.nist.gov/index.php). Reaction of radicals with surfaces was assumed to be gas-kinetic (1×10^{-9} $cm^3/mol \cdot sec$).

Results of the calculation help to explain some of the observed changes in chemical composition due to gas-phase reactions. The simulations showed that steady state (rates of formation equals rates of consumption) is reached in ~ 30 msec at 50 mtorr of total pressure. The simulations were extremely sensitive to the concentration of atomic hydrogen. High concentrations of atomic hydrogen (high plasma power or high H/C ratios) lead to the formation of stable hydrocarbon species that presumably do not lead to film growth at 700ºC. Conversely, low plasma power and low H/C ratios lead to greater formation of CH_2 and CH species. Methane/hydrogen mixtures produce lower concentrations of CH_2 and CH species than do acetylene/ hydrogen mixtures. These preliminary simulations indicate that there is more than sufficient time for the formation of higher hydrocarbons and that a more extensive mechanism may be required to properly simulate the chemistry observed. It is clear that there are several surface reactions that take place, as evidenced by the hydrocarbons produced by atomic hydrogen interactions mentioned above, that need to be incorporated to more fully understand the experimental results.

The electrical characterization of the non-doped VACNFs was done. We have measured the VACNF conductivity by using a four-point probe technique. We found that the VACNFs are conducting (metallic), with a conductivity similar to graphite at 1 mΩ-cm, which is similar to that measured for VACNFs grown with a DC PECVD technique by Mike Simpson's group at ORNL.

While we were successful in understanding more of the growth process, we were not successful in getting boron to be incorporated into the nanofibers. For growing boron-containing VACNFs, we added dilute diborane to the system (four percent in hydrogen). Although the plasma was quite effective at dissociating the diborane, with the utilization measured to be roughly 80 percent, the boron simply coated the nanofibers and was not incorporated into the carbon matrix. The amount of boron in the plasma strongly influences the growth results. If the diborane flow rate was greater than roughly 5 percent of the acetylene flow, the surface was coated with boron and nanofiber growth stopped. For diborane flows of less than 5 percent of the acetylene flow, forests of nanofibers were grown, but the boron was not incorporated into the nanofiber. It is suspected that gas-phase reactions of boron and carbon may be necessary for incorporation to occur, which is much more likely to happen at higher pressures (>200 Torr). In the absence of reaction with a hydrocarbon fragment, boron may form volatile hydridoborane clusters that are not incorporated in the growing film.

Benefits

There is potential for numerous benefits for DOE and potential for follow-on funding from this project. While the doping of the nanofibers using this technique has not yet been successful, the growth of VACNFs using our approach has worked well. The area of nanoscience is of great interest to DOE, and the knowledge that we gained from this work has helped us to understand the growth mechanisms of nanofibers. Potential applications of interest include nanoelectronics, field-emission devices, hydrogen storage, and super-hydrophobic materials. We are currently planning to continue development of the

growth technique as part of a recently renewed project with DARPA. In addition, we have recently been approached about collaboration with a private company for validation of chemistry models to explain our processing results.

References

Kong, J. et al. 2002. "Applied chemical profiling of single nanotubes: Intramolecular p-n-p junctions and on-tube single electron transistors." *Physics Letters* **80**, 73.

Derycke, V. et al. 2001. "Carbon Nanotube Inter- and Intramolecular Logic Gates." *Nano Letters* **1**, 454.

Huang, Y. et al. 2001. "Logic Gates and Computation from Assembled Nanowire Building Blocks." *Science* **294**, 1313.

Merkulov, V. I. et al. 2002. "Control Mechanisms for the Growth of Isolated Vertically Aligned Carbon Nanofibers." *J. Phys. Chem. B* **106**, 10570.

Delzeit, L. et al. 2002. "Growth of multiwall carbon nanotubes in an inductively coupled plasma reactor." *J. Appl. Phys*. **91**, 6027.

Caughman, J.B.O. et al. 2003. "Growth of vertically aligned carbon nanofibers by low-pressure inductively coupled plasma-enhanced chemical vapor deposition." *Applied Physics Letters* **83**, 1207.

Nanocrystalline Giant Magnetostrictive Materials for Microactuator Applications

C. T. Liu,[1] J. A. Horton,[1] and J. H. Zhu[2]
[1]*Metals and Ceramics Division*
[2]*Tennessee Technological University*

This project focused on the development of nanocrystalline giant magnetostrictive (GMS) materials for next-generation microactuators which will exhibit large displacement, actuating force/energy density, low actuating and saturation magnetic fields, rapid response, and compatibility with Si microfabrication. The project demonstrated that the amorphous state in the $(Tb,Dy)Fe_2$-based system could be stabilized by either combined alloy design/melt spinning or ball milling. Furthermore, bulk amorphous and nanocrystalline samples have been synthesized by powder consolidation and controlled annealing. The nanocrystalline GMS materials exhibited much higher magnetostriction and/or magnetostrictive strain coefficient at low magnetic field, compared to commercial GMS material Terfernol-D.

Introduction

Terfenol-D, based on a ternary Laves phase system with composition of stoichiometric $(Tb_xDy_{1-x})Fe_2$, is the most widely used commercial magnetostrictive material, with strains about 0.2% (or 2000 ppm) in a field of 10,000 Oe at room temperature (Clark 1980). One important issue related to the application of magnetostrictive materials in many emerging technologies such as microelectromechanical systems (MEMS) is to increase the magnetostriction at low magnetic field and to lower the saturation field. Recent study indicated that stabilization of the amorphous state in $(Tb,Dy)Fe_2$ via alloying additions (such as boron) and rapid cooling could significantly reduce the saturation field (Duc 2000, Fujimori 1993). Even though amorphization has been found to reduce the saturation field of $(Tb,Dy)Fe_2$ significantly, it has an adverse effect in decreasing the maximum magnetostrictive strain. What is really desirable for microsystem application is to increase the magnetostrictive strain coefficient and maximum magnetostrictive strain while maintaining the low saturation field through some innovative approach. In this project, nanocrystalline magnetostrictive materials based on $(Tb,Dy)Fe_2$ are studied to achieve such a combination of properties.

Technical Approach

To achieve the desirable performance for the magnetostrictive materials, we proposed to form nanocrystalline $(Tb,Dy)Fe_2$ with a grain size of 1–10 nm in an amorphous matrix by nanocrystallizing amorphous $(Tb,Dy)Fe_2$ alloys through controlled annealing. The rationale for this approach is the amorphous matrix, and the nano-scale crystalline phase will reduce the magnetoelastic anisotropy of the material, thus retaining the low saturation magnetic field of the amorphous alloy. The reduction of grain size to nano-scale range will improve magnetic softness of the alloys; for example, coercivity and hysteresis will decrease dramatically.

Since the magnetostrictive properties correlate well with the crystal size, it is important to develop scientific bases to control the grain size of these materials. One very attractive way to control the grain size of the crystalline materials is to first stabilize the amorphous state of the material, followed by controlled crystallization to get the desirable nano-scale grain size via thermal treatments. This approach requires a fast cooling rate or enhanced glass formability to obtain a supercooled liquid state.

Recent studies indicate that three metallurgical factors strongly affect the glass-forming ability of bulk amorphous alloys (Inoue 2000):

1. multi-component systems consisting of more than three consituent elements;
2. significant difference in atomic size ratios above 12% among the three main constituent elements;
3. negative heats of mixing among the three main constituent elements.

According to the physical metallurgy principles required for forming amorphous structures, additional elements with tiny atomic size such as B and C, small atom size such as Co and Ni, and large atom size such as Zr and Al, have been added to $(Tb,Dy)Fe_2$ system to achieve the large difference in atomic sizes among the main constituent elements. With careful control of alloying elements, it was expected that the glass-forming ability of the $(Tb,Dy)Fe_2$ phase would be enhanced, and amorphous $(Tb,Dy)Fe_2$-based ribbons or bars could then be formed by melt-spinning or melting/casting.

Once the formation of amorphous structure had been accomplished, controlled heat treatments were conducted

to crystallize the materials to obtain nanocrystalline structures. By controlling the annealing temperature/time, it was expected to be possible to get extremely fine, nano-scale structures with the crystalline phase distributed in an amorphous matrix, or a mixture of several crystalline phases.

Results and Discussion

To develop amorphous (Tb,Dy)Fe_2-based alloys with enhanced glass formability, a large number of alloys with various alloying additions were arc-melted and drop-cast into 0.5- to 5-mm-diameter copper molds, using high-purity starting materials, with the purpose of getting bulk amorphous cylindrical bars. However, even though about 100 different alloys were made, it was found that none of them was amorphous after drop casting, indicating the difficulty in retaining amorphous structures in this type of materials. The reason for such difficulty is not clear at this stage, even though we postulate that the Tb element we used in alloy-making was not very pure (possibly oxygen impurity), which might reduce the glass formability of the alloys. Because of the difficulty in getting amorphous materials via melting/casting, two alternative methods were used instead to get amorphous pellets for study. The first method was to prepare the amorphous ribbons by melt-spinning, followed by pulverizing of the ribbons into powders and consolidation of the powders by cold pressing to form amorphous pellets. The second method was to pre-mix the alloys by melting/casting, followed by high-energy ball milling of the alloys to get amorphous powders and subsequent consolidation of the powders to form amorphous pellets.

A series of alloy compositions were identified which retained amorphous structure after melt-spinning. The alloy compositions are based on the multi-component system of $Tb_{30}Fe_{(70-a-b-c)}B_aC_bY_c$, where B and C are small atoms compared to Tb or Fe, and Y is a reactive element added to scavenge oxygen and nitrogen in the alloys. The optimal contents of B and C have been identified. Transition metals such as Co and Ni were also added, which did not noticeably affect the glass-forming ability of the alloys. The amorphous ribbons were then pulverized in a milling machine in a glove box to get amorphous powders for consolidation. Alternatively, it was found that after high-energy ball milling of pre-alloyed $TbFe_2$ powders for 10 h, amorphous powders were obtained, based on X-ray diffraction results. The amorphous powders were cold pressed at 1 GPa to form dense pellets.

Annealing study of the amorphous pellets indicated that after crystallization at 500ºC for 1 h, a crystalline Laves phase is formed from the amorphous matrix The precipitates were very fine, and the sizes were in the range of 5–50 nm. Based on results on ribbon samples, heat treatment at higher temperature (e.g., 600ºC for 1 h) fully crystallized the material.

Magnetostriction measurements of the ribbons after different heat treatments were conducted, and it was observed that the saturation magnetostriction strain was 280 ppm for the amorphous ribbon, while heat treatment of 400ºC for 1 h decreased the saturation magnetostriction slightly, yet increased the initial magnetostrictive strain coefficient. Heat treatment of 500ºC for 1 h increased the saturation magnetostriction significantly, up to the strain level of 500 ppm at high fields, possibly due to the formation of nanocrystalline microstructure. Further increase in annealing temperature decreased, instead of increased, the saturation magnetostriction.

Compared to the commercial GMS material Terfernol-D as well as cast $Tb_{30}Fe_{(70-a-b-c)}B_aC_bY_c$, the nanostructured $Tb_{30}Fe_{(70-a-b-c)}B_aC_bY_c$ pellet obtained by heat treatment at 500ºC for 1 h showed significantly higher magnetostrictive strain at low magnetic field, as shown in Fig. 1. This clearly indicated that the amorphous/nanocrystalline structure was advantageous over the large-grained crystalline structure in the GMS materials. Due to the limitation of time/resources, the magnetostriction measurement of ball-milled, nanocrystalline $TbFe_2$ pellets has not been measured at this stage. It is expected that even higher magnetostrictive strain at low magnetic field will be obtained in this material.

In conclusion, the new alloy ribbon or pellets, after a 500ºC–1 h nanocrystallization treatment, possessed higher magnetostriction and initial magnetostrictive strain coefficient and required smaller magnetic field for actuation, compared to the same alloys in the amorphous, as-cast, or fully crystallized conditions. The developed materials outperform the current commercial alloy Terfernol-D at low magnetic fields.

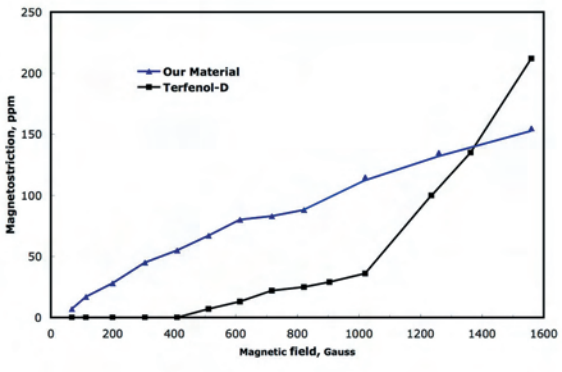

Fig.1. Comparison of magnetostriction of nanostructured $Tb_{30}Fe_{(70-a-b-c)}B_aC_bY_c$ pellet—our material (after 500ºC for 1-h annealing) and commercial GMS material Terfenol-D.

Benefits

With the initial success of syntheses of amorphous and nano-structured GMA materials via melt-spinning or ball milling and the demonstration of the outstanding performance of the nanostructured GMA materials, we plan to pursue further study to obtain bulk amorphous GMS materials via melting/casting. The potential use of GMS materials for MEMS devices and other technologies is expected to attract the interest of a variety of funding agencies including DOE, NSF and DOD. For example, DOE transportation programs are potential funding sources, because sensors and actuators are used extensively in automobile applications. Also, Dr. Zhu will pursue some funding from NSF to conduct some fundamental study on glass formability in this class of materials.

References

Clark, A. E. 1980. *Magnetostrictive Rare Earth-Fe_2 Compounds*, *Ferromagnetic Materials*. Vol. 1, ed. By E. P. Wohlfarth, North-Holland.

Duc, N. H., K. Mackay, J. Betz, Z. Sárközi, and D. Givord. 2000. "Magnetic and Magnetostrictive Properties in Amorphous $(Tb_{0.2}7Dy_{0.73})(Fe_{1-x}Co_x)_2$ Films," *J. Phys.: Condens. Matter* **12**, 7957–7968.

Fujimori, H., J. Y. Kim, S. Suzuki, H. Morita, and N. Kataoka. 1993. "Huge Magnetostriction of Amorphous Bulk (Sm,Tb)Fe_2-B with Low Exciting Fields," *J. of Magnetism and Magnetic Materials* **124**, 115–118.

Inoue, A. 2000. "Stabilization of Metallic Supercooled Liquid and Bulk Amorphous Alloys," *Acta Mater.* **48**, 279–306.

Development of a New High-Temperature Proton-Electron Mixed Conductor for Hydrogen Separation

E. A. Payzant, S. A. Speakman, R. D. Carneim, and T. R. Armstrong
Metals and Ceramics Division

High-temperature ion transport membranes (proton conductors) are presently limited in availability and performance. The pyrochlore-perovskite binary systems, $La_2Zr_2O_7$-$SrZrO_3$, $La_2Zr_2O_7$-$LaYO_3$, $La_2Zr_2O_7$-$LaCeO_3$, and $La_2Zr_2O_7$-$SrCeO_3$, were studied as potential high-temperature proton conductors. The end-point oxides have relatively low proton conductivities; however, these pyrochlore–perovskite binary systems include at least one phase boundary between the two end-point compositions which might enhance the proton conductivity. Rapid synthesis and characterization techniques were utilized to screen a large number of initial compositions, followed by X-ray diffraction and dc conductivity measurements to develop empirical relationships between structure and conductivity. Neutron diffraction analysis of the most promising samples provided additional structural detail. The solubilities of Sr in $La_2Zr_2O_7$ and La in $SrZrO_3$ were low, less than 0.1. The solubility of Zr in $LaYO_3$ was less than 0.25, and the solubility of Y in $La_2Zr_2O_7$ was less than 0.375. In $La_2Zr_2O_7$, Y substituted for both La on the A-site and Zr on the B-site, reducing its effectiveness as a dopant. Y-doped $La_2Zr_2O_7$ and Zr-doped $LaCeO_3$ had the greatest conductivities, though no electrical conductivity exceeded 5×10^{-4} S/cm at the target temperature of 600°C in any of the samples studied herein.

Introduction

Ion transport membranes (ITMs) composed of proton conducting materials are a critical component for future fuel processing and energy production systems, as well as ancillary technologies such as sensors and electrolyzers. Proton conducting ITMs are necessary to extract absolutely pure hydrogen from mixed gas streams in the processing of fossil fuels and other petroleum and petrochemical processes. Microporous membranes can meet a large portion of hydrogen separation needs; however, at best they are only 99% selective towards hydrogen and cannot produce the unadulterated hydrogen feed required by many industries. Only ITMs have the ability to extract pure hydrogen from a mixed gas stream. The best candidate ITM materials for hydrogen separation at high temperatures are proton-conducting ceramic oxides; however, a viable ceramic-based ITM has not yet been developed and current high-temperature ion transport membranes are limited in availability and performance. Most either have low conductivities (e.g., $SrZrO_3$-based materials) or are highly susceptible to chemical attack by contaminants such as sulfur (H_2S) and CO_2 (e.g., $BaCeO_3$-based materials).

Technical Approach

The purpose of the proposed research was to develop a practical high-temperature (HT) proton conductor based on possible enhancement of proton conductivity near appropriate phase boundaries. New materials were developed in the lanthanum zirconate–strontium zirconate–lanthanum yttrate system, which has proton-conductive pyrochlore or perovskite end members, as shown in Fig. 1. This system was selected based on its potential for new ternary compositions that meet the expectation of developing high conductivity requirement for a practical HT proton conductor. This novel approach relies on a combination of defects and interfaces to enhance the proton conductivity. Rapid synthesis and characterization techniques were utilized to screen a large number of initial compositions, followed by conductivity measurements, structural characterization, and modeling.

A glycine-nitrate method was used to produce fine precursor powders for testing. Nitrate solutions of the appropriate cations were mixed with glycine fuel and then combusted. The resulting fine precursor was calcined at 900°C for 1 hour, pressed into pellets, and sintered at either 1000°C for 96 hours, 1500°C for 2 hours, or 1500°C for 15 hours, as required for densification. Compositions were synthesized in the following series: $(La_{1-x}Sr_x)ZrO_{3.5-x/2}$, $La(Zr_{1-x}Y_x)O_{3.5-x/2}$, $La(Zr_{1-x}Ce_x)O_{3.5-\delta}$, $(La_{1-x}Sr_x)(Zr_{1-x}Ce_x)O_{3.5-x/2}$, and $La_{0.95}Y_{0.05}ZrO_{3.5}$. The first series allowed evaluation of A-site substitution of La^{3+} by Sr^{2+} with corresponding introduction of oxygen defects. The second series allowed evaluation of B-site substitution of Zr^{4+} by Y^{3+} with corresponding introduction of oxygen defects. The third series allowed evaluation of B-site substitution of Zr^{4+} by Ce^{4+} without introduction of oxygen defects. The fourth series allowed evaluation of simultaneous A-site substitution of La^{3+} by Sr^{2+} and B-site substitution of Zr^{4+} by Ce^{4+}, and the last series allowed evaluation of the effects of Y^{3+} substituting for La^{3+} on the A-site instead of for Zr4+ on the B-site.

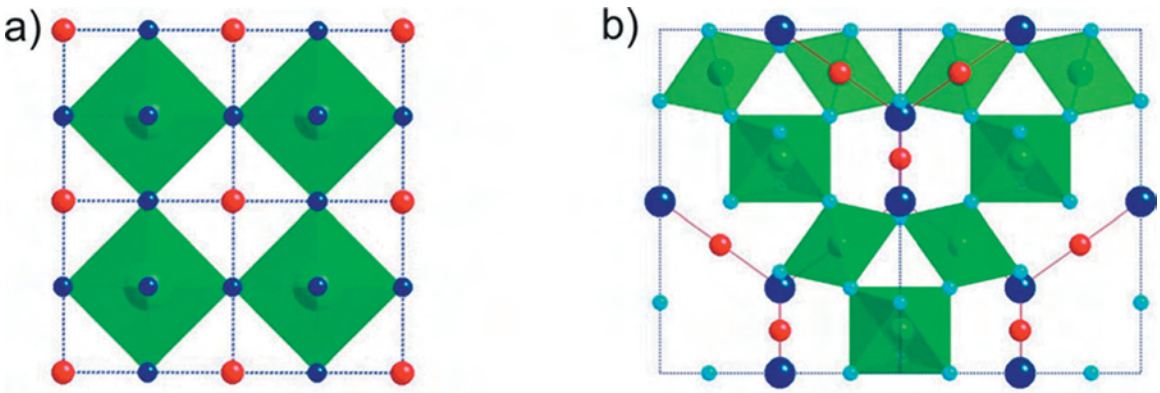

Fig. 1. Crystal structures of (a) lanthanum yttrate perovskite and (b) lanthanum zirconate pyrochlore.

Results and Discussion

X-ray diffraction (XRD) was used to analyze the amorphous precursor, calcined, and sintered powders. XRD patterns were collected with a Scintag PADV and/or a Panalytical X'Pert Pro diffractometer using Cu-Kα radiation. Lattice parameters were determined by collecting an XRD pattern from the sintered powder intimately mixed with standard reference material (SRM) 640c, Si, was used to calibrate samples consisting predominantly of perovskite phases; SRM 660a, LaB_6, was used to calibrate samples consisting predominantly of pyrochlore phases to minimize Bragg peak overlap. Peak positions were determined by profile fitting individual diffraction peaks with pseudo-Voigt functions. The calibrated peak positions of the sample were analyzed with a cell refinement algorithm to determine the unit cell lattice parameters.

The electrical conductivities of sintered discs were measured in air at temperatures from 300 to 900°C using a four-point van der Pauw technique, using two Keithley 6517A electrometers and an Agilent 34970A switch unit. One electrometer simulated a current source, applying voltages (V_{appl}) of ±10, 5, 2.5, 1.25, and 0.675 V and measuring the corresponding current (I_{source}) across two electrodes, while the second electrometer measured the resulting potential (V_{obs}) across the two parallel electrodes. The eight measurements made at different V_{appl} were analyzed for linearity and reproducibility. The linear portion of the $I_{source}V_{obs}$ curve was then used to determine the resistance. These measurements were repeated for four configurations of the electrodes M, N, O, and P: $I_{MN}V_{OP}$; $I_{NO}V_{PM}$; $I_{OP}V_{MN}$; and $I_{PM}V_{NO}$. The measurements of $I_{MN}V_{OP}$ and $I_{OP}V_{MN}$ were averaged together to produce R_A; likewise $I_{NO}V_{PM}$ and $I_{PM}V_{NO}$ were averaged together to produce R_B. The resistivity (ρ) for a pellet of thickness d was then solved from the equation:

$$\exp\left(-\frac{\pi d}{\rho}R_A\right)+\exp\left(-\frac{\pi d}{\rho}R_B\right)=1 \qquad (1)$$

These measurements were made in a Thermolyne F21130-33 tube furnace at different temperatures. The sample temperature was measured with a thermocouple that was independent of the one used to control the furnace. The resulting data of conductivity and temperature were used in an Arrhenius analysis to determine the activation energy (E_A) and pre-exponential geometric factor (σ_o) according to the equation:

$$\sigma_{ion}=\frac{\sigma_o}{T}\exp\left(-\frac{E_A}{kT}\right) \qquad (2)$$

In summary, new materials in the lanthanum zirconate–strontium zirconate–lanthanum yttrate systems were produced by combustion synthesis using a glycine nitrate process followed by X-ray diffraction analysis to screen a large number of initial compositions. An automated apparatus for measurement of high-temperature electrical conductivity in controlled atmospheres was developed with which the conductivities of 22 different compositions were determined at temperatures between 30°C and 900°C in air. Recent modifications to this system have enabled measurements to be made in controlled gas environments including inert (argon) and reducing (argon-hydrogen). Atomistic modeling of the compositional end members using the GULP code yielded reasonable correspondences to the measured structures and properties.

As hypothesized, improved conductivities, though smaller than required for the applications, have been realized in doped pyrochlore compositions, although it has not yet been determined whether this improvement is in proton or oxygen ion conductivity. The number of

Summary of Conductivity Measurements

Composition	Activation Energy (eV)	log σ_o (S/cm)	Conductivity at 600 °C (x 10^{-5} S/cm)
$SrZrO_3$	0.466	4.008	0.75
$La_{0.125}Sr_{0.875}ZrO_{3.0625}$	0.520	4.119	0.18
$La_{0.25}Sr_{0.75}ZrO_{3.125}$	0.424	3.539	0.92
$La_{0.375}Sr_{0.625}ZrO_{3.1875}$	0.389	3.580	2.98
$La_{0.5}Sr_{0.5}ZrO_{3.25}$	0.393	3.960	6.18
$La_{0.75}Sr_{0.25}ZrO_{3.375}$	0.372	4.146	18.3
$La_{0.875}Sr_{0.125}ZrO_{3.4375}$	0.363	4.149	24.2
$LaZrO_{3.5}$	0.376	3.712	5.91
$LaZr_{0.96}Y_{0.04}O_{3.48}$	0.335	3.841	28.1
$LaZr_{0.92}Y_{0.08}O_{3.46}$	0.351	4.016	25.5
$LaZr_{0.875}Y_{0.125}O_{3.4375}$	0.387	4.427	21.7
$LaZr_{0.75}Y_{0.25}O_{3.375}$	0.404	4.503	15.7
$LaZr_{0.625}Y_{0.375}O_{3.3125}$	0.435	4.646	8.50
$LaZr_{0.5}Y_{0.5}O_{3.25}$	0.437	4.479	5.46
$LaZr_{0.375}Y_{0.625}O_{3.1875}$	0.471	4.460	1.83
$LaZr_{0.25}Y_{0.75}O_{3.125}$	0.544	5.030	0.72
$LaZr_{0.125}Y_{0.875}O_{3.0625}$	0.536	4.642	0.38
$LaYO_3$	0.431	4.609	8.64
$La_{0.75}Ca_{0.25}Y_{0.75}Zr_{0.25}O_3$	0.511	3.510	0.06
$La_{0.95}Y_{0.05}ZrO_{3.5}$	0.390	4.148	10.5
$LaZr_{0.75}Ce_{0.25}O_{3.5-d}$	0.479	4.481	1.48
$LaZr_{0.5}Ce_{0.5}O_{3.5-d}$	0.483	5.408	11.2
$LaZr_{0.25}Ce_{0.75}O_{3.5-d}$	0.489	6.089	44.6
$La_{0.5}Sr_{0.5}Zr_{0.5}Ce_{0.5}O_{3.25-d}$	0.529	6.658	48.2
$La_{0.25}Sr_{0.75}Zr_{0.25}Ce_{0.75}O_{3.125-d}$	0.518	5.778	8.91

charge carriers was nearly constant over the lanthanum zirconate–lanthanum yttrate system and in the lanthanum zirconate–strontium zirconate system, with improved conductivity resulting from a reduction of the energy barrier in the solid solutions. In contrast, the activation energies were nearly constant in the cerium-doped lanthanum zirconate system, with improved conductivity resulting from the creation of additional charge carriers in the solid solutions.

Neutron scattering experiments were run on the NPDf beamline at LANSCE to quantify the oxygen vacancy distribution and assist in resolving the cation site occupancies, since neutron diffraction is much more sensitive to oxygen in the presence of heavy ions than XRD. High-resolution neutron diffraction data was collected on six compositions, which enabled both Rietveld (long-range structure) and Pair-Distribution Function (short-range order) analyses to be made.

Benefits

New proton-conducting high-temperature membranes are an important technology for improving energy efficiency and advancing the development of the "hydrogen economy." This work is relevant to technology programs in the Office of Fossil Energy (NETL) and the Office of Energy Efficiency and Renewable Energy (Hydrogen, Fuel Cells, and Infrastructure). Additionally the materials science aspect of this project relates to the mission of the Office of Science. Improved hydrogen separation materials have potential benefit for military (DOD) and space (NASA) applications and have the potential to attract industrial interest in partnering through DOE or ATP (Dept of Commerce) programs.

References

Speakman, S.A., et al. 2004. "Development of proton conductors using pyrochlore-perovskite phase boundaries," *Journal of Materials Engineering and Performance* **13**, 303–308.

Selective Area Chemical Vapor Deposition of Carbon Nanotube Films Using Seeded Molecular Beams

G. Eres
Condensed Matter Sciences Division

Exploration of new growth techniques for carbon nanotubes is important because they provide access to previously unexplored regions of the complex carbon nucleation parameter space leading to the synthesis of novel carbon nanotube structures. This project explores carbon nanotube growth from a new growth environment consisting of small carbon-containing molecules entrained in a molecular beam. A study of carbon nanotube growth from 12 different carbon-containing molecules revealed that acetylene is an order of magnitude more efficient than the nearest precursor, acetone, and several orders of magnitude more efficient than its hydrocarbon cousins. Acetylene is highly efficient in carbon network formation because its molecular structure facilitates direct incorporation into the carbon network. The other precursors must first produce acetylene-like species through gas-phase intermediates. The availability of a direct pathway for transformation of a carbon-containing molecule such as acetylene into carbon nanotubes allows exploration of the role that kinetic processes play in the synthesis process. These studies are enabled by the unprecedented versatility of the molecular beam environment which allows independent external control of all the major growth variables in carbon nanotube growth. The molecular jet experiments reveal that the incidence rate of acetylene molecules at optimal catalyst particle size is a key factor in the formation of single-wall carbon nanotubes and dense vertically aligned arrays in which they are the dominant component. The threshold for vertically aligned growth, the growth rate, the diameter, and the number of walls of the carbon nanotubes are systematically correlated with the acetylene incidence rate and the substrate temperature.

Introduction

The goal of this project was to control carbon nanotube (CNT) properties by using the molecular beam growth environment. For a kinetically controlled growth process such as CNT growth, the kinetics determines not just the growth rate but also the properties such as the diameter, the length, the density, and the type of the CNT. The key advantage of the molecular beam growth environment is that it decouples the most important growth parameters, the mass input (incident flux) and the energy input (substrate temperature) from each other (Eres 1998). Now that these important growth variables are independent of each other, they can be externally controlled and in conjunction with the catalyst nanoparticle characteristics used to tailor the CNT properties. The substrate temperature and the incident flux were used to optimize the conditions for nucleation of single-wall (SW) CNTs and vertically aligned (VA) arrays of SWCNTs, the highly sought-after structures that are difficult to synthesize. Two important original discoveries made in this project were essential for the success of this project. First, the discovery that acetylene molecules are direct precursors to SWCNT growth—meaning that CNT growth by incorporation of carbon from acetylene occurs without the need for intermediate reaction steps—enabled direct control of the CNT synthesis pathway. The second important discovery is that the flux of acetylene molecules plays a critical role in determining not just the properties of individual CNTs but the conditions for formation of CNT structures such as VA-SWCNT arrays. The use of a direct precursor in CNT growth has numerous advantages, including higher growth efficiency, lower growth temperature, and fewer undesirable side products.

Technical Approach

The catalyst particle size is a critical, and by some accounts the decisive, variable in SWCNT growth (Moisala 2003). A standard approach in CNT synthesis studies is to study the relationship between the particle size and the CNT diameter. This approach is dictated by the prevalent model of CNT growth according to which CNT growth occurs by carbon precipitation from molten metal catalyst particles (Kanzow 1999). This model provides a satisfactory explanation if the feedstock is provided by vaporized carbon such as in arc-synthesis and pulsed laser vaporization. However, when carbon originates from molecular species, this model fails to account for the specific nature of the fragmentation and decomposition of the carbon-containing molecules that clearly must precede CNT growth. In this project we explored the role of variables other then the particle size, such as the nature of the carbon source gas molecules, the flux of the growth species, and the substrate temperature. The molecular beam approach provides a growth environment in which these variables can be separated from each other and controlled independently.

Chemical vapor deposition (CVD) is regarded as the only viable technique for synthesis of CNTs (Dai 2001).

CVD of carbon is a complex process that despite several decades of fundamental studies and practical use is still poorly understood. The complexity of CVD stems from the fact that the mass flow and the heat flow are coupled with the kinetics in the CVD reactor (Smith 1995). This growth environment is conducive to numerous secondary gas-phase reactions that are difficult to control or suppress. Such a growth environment clearly lacks the control capabilities that are required for nanoscale synthesis. In contrast, in the molecular beam environment the carbon-containing molecules rarely undergo more than a single collision with the substrate because the size of the sample is negligible compared to the area of the chamber walls. Under these conditions, secondary gas-phase reactions are eliminated and CNT growth occurs directly from the impinging molecules (Eres 1998). The principal requirement for molecular beam growth is that the CNT growth reaction be confined to the surface and that a direct pathway for transformation of source molecules into CNTs be available.

The molecular beam was first used to identify molecules that directly lead to CNT growth. The molecular beam was generated by a high-pressure gas expansion through a 100-μm-diameter nozzle orifice.The source gases were used in the form of a 2% mixture in 10% H_2 and 88% He. Source molecules that are liquids at room temperature were entrained in a carrier gas and were introduced through a bubbler. In this case, the carrier gas consisted of a 10% H_2 and 90% He gas mixture. A total of 12 different carbon source molecules were used. The carbon deposit from each of these molecules was characterized using Raman spectroscopy, scanning electron microscopy (SEM), and, when necessary, transmission electron microscopy (TEM). Based on these measurements, acetylene was identified as the most efficient direct building block for CNT formation. Kinetic studies exploring the role of the incidence rate and the substrate temperature in formation of CNTs and CNT structures were conducted using acetylene molecules entrained in hydrogen and helium carrier gas.

Results and Discussion

The absence of a deposit from a particular molecule in CNT growth was interpreted to mean that carbon incorporation occurred through intermediate reaction products. The reaction intermediates form by secondary gas-phase reactions, which were suppressed in the molecular beam environment. The discovery that carbon incorporation from acetylene occurred directly without the need for gas-phase intermediates is the key result of this project. The availability of a direct precursor to CNT growth enabled the subsequent studies of the kinetics of formation of SWCNTS and the unique structures of VA-SWCNT films.

SWCNT growth from 12 different carbon-containing molecules was explored. Four of the molecules, methane, ethylene, acetylene, and propylene, were small hydrocarbons; two, benzene and xylene, were aromatic hydrocarbons; five were oxygen-containing organic compounds; and the twelfth compound was CO. The five oxygen-containing organic compounds consist of three alcohols, methanol, ethanol and propanol, and acetone and diethylether. Acetylene was an order of magnitude more efficient than the nearest precursor, acetone, and several orders of magnitude more efficient than its hydrocarbon cousins typically used in CVD growth of CNTs. Surprisingly, oxygen-containing small carbon molecules were more efficient precursors than the hydrocarbons containing the same number of C atoms. The type of the oxygen bonding to C made no observable difference in the CNT yield. However, CO produced no CNT growth. This result is not unexpected because CNT growth from CO requires that C be liberated by a secondary gas-phase reaction before CNT growth can occur.

It was demonstrated for the first time in this project that the molecular flux is the key factor that enables high-density nucleation, which is necessary for vertically aligned growth. VA-SWCNT films were only grown from acetylene, and only above a certain incidence rate. The threshold flux for VA-SWCNT film growth was 2×10^{18} molecules/cm^{2}s. Below this flux, SWCNT films grew in the form of random mats. Above this flux the growth rate and other properties of the VA-CNT films were governed by the flux. Vertically aligned growth enabled us for the first time to determine the conversion efficiency of acetylene molecules. From the growth rate, the flux and the packing density of the VA-SWCNT films we calculate a conversion efficiency of acetylene into CNTs of 10^{-2}. Raman spectroscopy shows that at a fixed substrate temperature, the diameter of the CNTs decreases with incidence rate. Subsequently, it was found that smaller diameter CNTs can be grown by increasing the flux, even when the substrate temperature is rising. In contrast, increasing the substrate temperature at fixed flux was found to produce larger diameter CNTs. The significance of these results is in the fact that the decrease in the CNT diameter occurred under nominally constant particle size conditions that were maintained by the fixed substrate temperature. Note that these trends are in contrast with the notion that the particle size dictates the CNT diameter, as implied by the diffusion model.

SWCNT growth and VA-SWCNT growth occurred in a narrow temperature window from 560 to 700ºC. Note that 560 ºC is the lowest reported temperature for SWCNT growth. The reduction in the growth temperature was made possible by the new understanding of the growth mechanism of CNTs that was acquired in this project. It was discovered that the presence of hydrogen atoms plays

an important role and that an optimal amount of hydrogen must be maintained in the growing network in order to sustain continued growth of CNTs from hydrocarbons. The hydrogen atoms represent the active sites in the growing network. Molecular mass growth occurs by a two-step process consisting of hydrogen abstraction and the addition of acetylene. The amount of hydrogen in the growing network is determined by a dynamic equilibrium between the incident flux and the hydrogen desorption rate. The loss of hydrogen at higher temperatures by molecular hydrogen desorption results in termination of CNT growth. This trend can be counterbalanced by increasing the flux. We are currently experimenting with other control mechanisms for maintaining the necessary amount of hydrogen in the growing network.

Benefits

This seed money project, along with producing a novel and versatile growth technique, opened a new research area in fundamental studies of CNT synthesis. The advanced control capabilities enabled the growth of the highly sought-after and very valuable VA-SWCNT films. An invention disclosure describing the method of carbon structure deposition using molecular beams was submitted to the ORNL Technology Transfer Office. The VA-SWCNTs are ordered structures with highly anisotropic properties and are attractive for numerous applications. These structures conduct both heat and electricity far better along the tube axis than perpendicular to it. SWCNTs are superior to the more defective structures of multiwall CNTs and are better heat conductors than diamond. Material structures with such directional properties are attractive for a large number of applications including field emitters, fuel cell electrodes, heat transport, advanced composites, and EMI shielding. We are currently working on optimizing the growth technique for practical applications. We have made contacts with program managers from several funding agencies and are aggressively pursuing external funding from DARPA, ATP, NASA, NIH, and private industry.

References

Eres, G. 1998. "Application of Supersonic Molecular Jets in Semiconductor Thin Film Growth," *Critical Reviews in Solid State and Materials Science*. **23**, 275.

Dai, H. 2001. "Nanotube Growth and Characterization," pp. 29–53 in *Carbon Nanotube Synthesis Structure, Properties and Applications*, Springer, Berlin.

Kanzow, H. and A. Ding. 1999. "Formation Mechanism of Single-Wall Carbon Nanotubes on Liquid-Metal Particles," *Physical Review B* **60**, 11180.

Moisala A., A. G. Nasibulin, and E. I. Kauppinen. 2003. "The Role of Metal Nanoparticles in the Catalytic Production of Single-Walled Carbon Nanotubes—a Review," *Journal of Physics: Condensed Matter* **15**, S3011.

Smith D. L. 1995. "Chemical Vapor Deposition," pp. 307–369 in *Thin-Film Deposition Principles and Practice*, McGraw-Hill, New York.

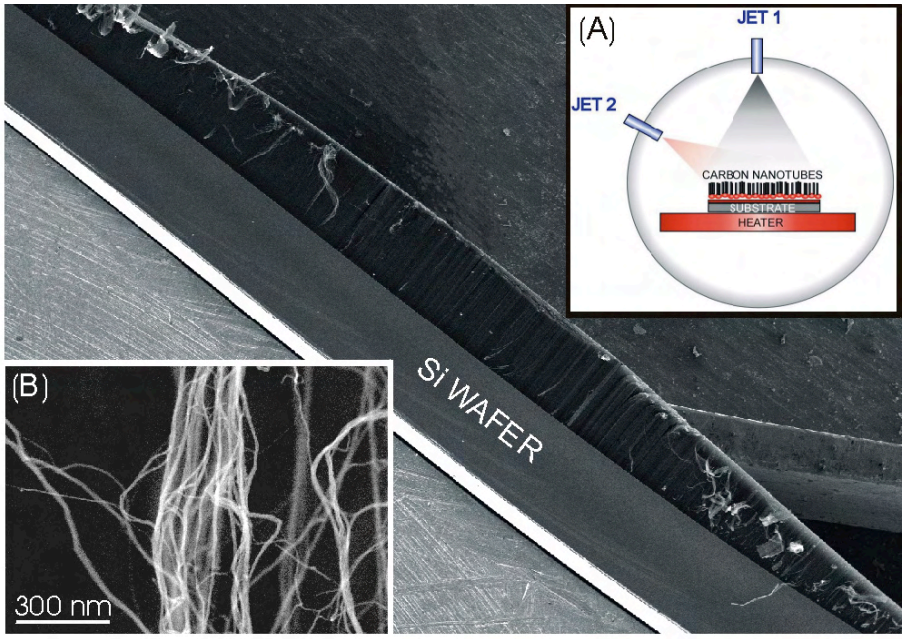

Fig. 1. Low-resolution SEM image of a molecular jet-grown CNT film. The curvature in the film surface is produced by the acetylene distribution in the molecular jet. Inset (A) shows a schematic drawing of the molecular jet apparatus. Acetylene is supplied by Jet 1. Jet 2 is used for introducing an oxygen beam for use with weakly active catalyst films. Inset (B) shows a high-resolution SEM image of a dislodged bundle with individual SWCNT bundle diameters on the order of 10 nm.

High-T_c Silicon-Compatible Ferromagnetic Semiconductors

H. H. Weitering, J. Shen, and Z. Zhang
Condensed Matter Sciences Division

Semiconductor "spintronics" holds great promise for novel, faster devices that consume much less power than conventional electronics and that may even facilitate quantum bit or "qubit" operations for quantum computing. The control of the electron spin in semiconductor devices is still at a conceptual stage, however, awaiting the science and engineering breakthroughs to create new materials and technologies. This project focused on the experimental realization of novel, silicon-compatible ferromagnetic materials with high ferromagnetic ordering temperatures which could serve as the spin injector or spin detector in silicon-based spintronic devices. The project resulted in the realization of (1) an epitaxial Mn_5Ge_3/Ge(111) ferromagnetic heterostructure for spin-injection; (2) ferromagnetic nanostructures of antiferromagnetic FeGe; and (3) discovery of a new growth procedure for Mn-doped Ge with high ferromagnetic T_C. These novel material systems represent an important scientific advancement in the area of magnetic semiconductors and nano-magnetism, with significant ramifications for spintronic applications in a silicon-compatible environment.

Introduction

The revolution of spin-based electronics ("spintronics") in materials physics is likely to impact our lives in ways reminiscent of the early days of the transistor and microelectronics industry (Wolf 2001). Unlike current microelectronic devices, spintronic devices utilize both carrier spin and charge to carry or store information. Spin is a purely quantum phenomenon which lends itself elegantly to the logic of "ones" and "zeroes." One example of a spintronic device is the "spin valve," a layered structure of magnetic and non-magnetic metal films, which is now widely used in read heads for magnetic hard disk drives. The discovery of high-temperature ferromagnetism in diluted magnetic semiconductors in the late 1990's has defined a radically new avenue in spintronics research. If spintronic devices can be made from semiconductors, that is, if semiconductors could be made magnetic, then in principle we could build spin amplifiers and integrate electronic, opto-electronic, and magneto-electronic functionality on a single device. We may even think of injecting spin-polarized currents into semiconductors and controlling the spin state of the charge carriers, which may allow quantum bit operations for quantum computing. This project focused on identifying novel materials systems and heterostructures for spin injection devices that are compatible with mainstream Si technology (Park 2002).

Technical Approach

There are two ways to realize spin injection. One of these is to fabricate a ferromagnetic-metal/semiconductor (MS) heterostructure; the other is to use a dilute magnetic semiconductor (DMS) as the spin aligner. The former method is often hampered by chemical intermixing or lattice mismatch at the MS interface, which usually results in significant loss of spin polarization. The large "conductivity mismatch" between the metal and semiconductor furthermore limits the spin injection efficiency for "transparent" MS contacts. Low Curie temperatures (T_C) limit the latter method using a DMS. We pursued both avenues. High-T_C ferromagnetic heterostructures on Ge(111) and Ge(100) substrates have been realized in our laboratory, using low-temperature molecular beam epitaxy (Zeng 2003, Zeng 2004). The structures were investigated using a wide variety of structural, electrical, and magnetic characterization techniques. Density functional theory (DFT) calculations were performed to calculate the total-energy-minimized structures, Mn-diffusion barriers, and scanning tunneling microscope (STM) images. This project was carried out in collaboration with scientists from the University of Tennessee (J. R. Thompson), Vanderbilt University (L. C. Feldman), Wayne State University (B. Nadgorny), Naval Research Laboratory (S. C. Erwin), Harvard University (E. Kaxiras), and the Chinese Academy of Sciences in Beijing (E. G. Wang). A parallel theoretical study was performed by Fishman and collaborators, using dynamical mean field theory, to investigate the influence of magnetic frustration on the ferromagnetic transition temperature in DMS materials.

Results and Discussion

Epitaxial Ferromagnetic Mn_5Ge_3(0001) on Ge(111), with L. C. Feldman, S. C. Erwin, and B. Nadgorny)

We report on a novel ferromagnetic epitaxial metal/semiconductor interface with high Curie temperature and good potential for spin injection in a silicon-compatible geometry, namely, ferromagnetic Mn_5Ge_3(0001) thin

films on Ge(111) (Zeng 2003, Zeng 2004). The crystalline quality, surface topography, and thermal stability of the films allow for epitaxial growth of Ge on top of Mn_5Ge_3 so that epitaxial trilayers or "spin valves" and multilayer structures have been realized. Note that in contrast to germanides, silicides either have low T_C or are not ferromagnetic at all. Drawing the logical parallel to the promise of epi-silicides for Si-based microelectronics, ferromagnetic epi-germanides may hold great potential for germanium-based spintronics.

The Mn_5Ge_3 films were fabricated by depositing 40-nm Mn onto Ge(111) in ultrahigh vacuum and subsequent annealing at 150ºC for several minutes. The crystal structure suggests $Mn_5Ge_3(0001)//Ge(111)$. Scanning tunneling microscope (STM) images display large terraces with a $(\sqrt{3} \times \sqrt{3})$ R30° honeycomb structure, which perfectly agrees with the theoretical image of the Mn-terminated $Mn_5Ge_3(0001)$ surface, using first-principles DFT; see Fig. 1(a). X-ray diffraction θ-2θ scans only show Mn_5Ge_3 (0002) and (0004) reflections besides the Ge(111) and (333) reflections, which confirms the $Mn_5Ge_3(0001)//Ge(111)$ epitaxial relationship. Rutherford backscattering spectrometry and ion-channeling experiments confirmed the stoichiometry and epitaxy of the film.

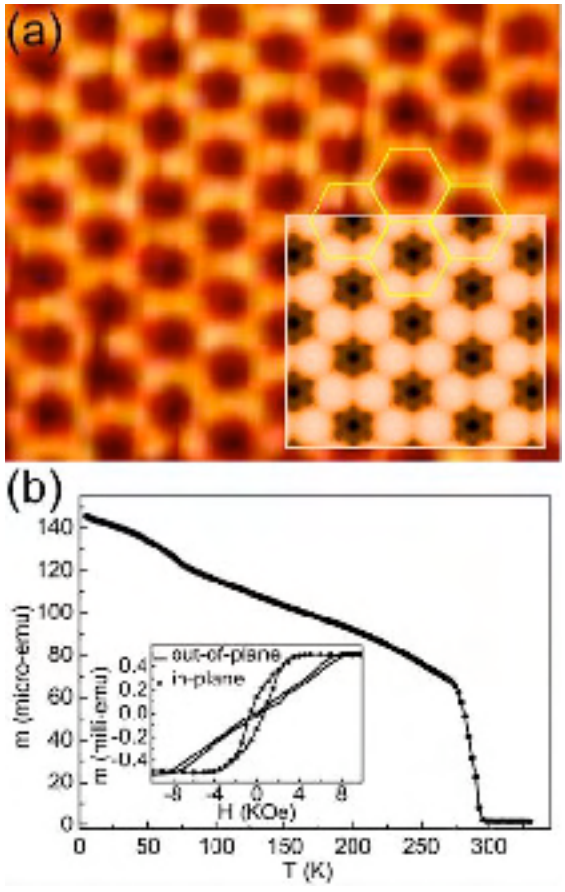

Fig. 1. (a) 5.3-nm × 4.5-nm filled-state STM image from the surface of a $Mn_5Ge_3(0001)$ thin film. The inset in (a) is the simulated filled-state image from DFT. (b) Remanent magnetization as a function of temperature. The inset in (b) shows the ferromagnetic hysteresis loop at 5 K.

Magnetic properties were measured with a SQUID magnetometer. Figure 1(b) shows the temperature-dependent remanent magnetization. It reveals a T_C of about 295 K. Hysteresis loops at T = 5 K with in-plane and out-of-plane field orientations are shown in the inset. The easy axis is in-plane, which is most likely due to the shape anisotropy. The multiplet splitting of the Mn 3*s* core level in X-ray photoelectron spectroscopy indicates an average magnetic moment of $2.7\mu_B$ per Mn atom, which is in almost perfect agreement with the spin-resolved band structure calculations and SQUID measurements. The residual resistivity of the film is 4.0 μΩ·cm, only slightly higher than the residual resistivity of transition-metal silicides such as $CoSi_2$ (2.6 μΩ·cm). The spin-polarization of this material is of the order of 40% (at 2 K), comparable to that of a 3*d* transition metal. The spin polarization of this material was measured using point contact Andreev reflection, in collaboration with Prof. Boris Nadgorny at Wayne State University.

Ferromagnetic Nanocrystals of Antiferromagnetic FeGe

Attemps to fabricate Fe_5Ge_3 films with T_C = 485 K have not been successful. Instead, epitaxial nano-crystals of FeGe were formed on Ge(111). The nano-crystals assume a quasi one-dimensional shape as they grow exclusively along the <110> direction of the Ge(111) substrate, culminating in the monoclinic modification of FeGe. The uni-directional growth results from a close match between the Ge-atom spacing along $<110>_{Ge}$ and monoclinic *b*-axis of FeGe. Whereas monoclinic FeGe is antiferromagnetic in the bulk, the nanocrystals are surpisingly strong ferromagnets below ~250 K with an average magnetic moment of 0.8 μ_B per Fe atom (at 5 K).

Bulk FeGe exhibits an interesting variety of structures and magnetic properties. It crystallizes in three different polymorphs. The cubic polymorph is an antiferromagnetic metal with a Dzyaloshinskii-Moriya type spin spiral, while the hexagonal and monoclinic polymorphs exhibit complex, modulated spin structures with a net antiferromagnetic magnetization. The FeGe nanocrystals, on the other hand, appear to be strongly ferromagnetic. Their structure and shape gradually evolves as a function of annealing temperature, culminating in the formation of long nanowires that can be identified as the monoclinic polymorph of FeGe. We find that the Ge(111) substrate plays a key role in stabilizing ferromagnetism in monoclinic FeGe. The substrate not only serves as a template for uni-directional growth but also imposes

a small tensile strain along the growth direction of the nanocrystals. This tips the subtle balance of competing exchange interactions into a collective ferromagnetic response. These FeGe nanoparticles present a first example of volume ferromagnetism in nanoparticles of an antiferromagnetic compound.

Contrasting Growth Modes of Mn on Ge(100) and Ge(111) surfaces: Subsurface Segregation Versus Intermixing, with E. G. Wang and E. Kaxiras

We have carried out a comparative study of the energetics and kinetics involved in Mn growth on Ge along the (100) and (111) orientations, using extensive first-principles total energy calculations within DFT (Zhu 2004). The main findings are intriguing both from the point of view of fundamental growth science and for improved understanding of the system as a DMS. First, we have shown that, along the (100) orientation, the growth of Mn proceeds in a subsurface mode, characterized by their easy access to, and strong preference for, interstitial sites located between the two topmost Ge layers. Strikingly, such a "subsurfactant action" is preserved even during epitaxial growth of additional Ge capping layers, as shown by the existence of easy kinetic pathways for the dopants trapped in deeper layers to float toward the subsurface sites. In contrast, during growth along the (111) orientation, Mn can easily diffuse into the bulk via interstitial sites. These findings have important implications within the context of dopant control via growth manipulation and post-annealing in dilute magnetic semiconductors. Our preliminary growth experiments showed that the subsurfactant mechanism produces significantly higher Curie temperatures ($T_C > 400$ K).

Dynamical Mean Field Study of Magnetism in $Ga_{1-x}Mn_xAs$, with K. Aryanpour, J. Mereno, M. Jarrell, and R. S. Fishman

We employed the dynamical mean field approximation to perform a systematic study of magnetism in $Ga_{1-x}Mn_xAs$ DMS. The model incorporates the effects of the strong spin-orbit coupling on the J = 3/2 GaAs valence bands and of the exchange interaction between the randomly distributed magnetic ions and the itinerant holes. The ferromagnetic phase transition temperature T_C is obtained for different values of the impurity-hole coupling J_C and of the hole concentration n_h at the Mn doping of $x = 0.05$. We also investigate the temperature dependence of the local magnetization and spin polarization of the holes. By comparing our results with those for a single band Hamiltonian in which the spin-orbit coupling is switched off, we conclude that the spin-orbit coupling in $Ga_{1-x}Mn_xAs$ gives rise to frustration in the ferromagnetic order, strengthening recent findings (Zaránd 2002).

Benefits

In May of 2003, Dr. John H. Marburger, Director of Office of Science and Technology Policy within the Executive Office of the President, highlighted the promise of spintronics and nanomagnetism in his address at the BES 2018 symposium entitled "The Promise of Nanotechnology." One of his four most promising avenues for discovery is "the taming of the electron spin degree of freedom." Marburger's remarks were likely more than just a timely coincidence. With the advent of the Center for Nanophase Materials Sciences (CNMS), ORNL has the unique opportunity to assume the leadership role in developing novel materials and groundbreaking technologies that involve magnetism and spin transport. This project presented an important first step toward establishing in-house expertise and capabilities to produce such extraordinary materials. So far, the project has resulted in three publications while several publications are still pending. Combined with our long-standing expertise in nanomagnetism and spin-polarized tunneling, this project has laid the groundwork for a vigorous spintronics program within the CNMS with excellent prospects for future funding.

Spintronics is a major research area for the DOE and other federal agencies. Within the first year, this project produced a novel heterostructure for spin injection in a silicon compatible geometry and produced a powerful strategy toward enhancing the ferromagnetic ordering temperature in a dilute magnetic semiconductor. These accomplishments represent major contributions toward solving the bottleneck issues for spintronics research and technology.

References

Wolf, S. A., D. D. Awschalom, R. A. Buhrman, J. M. Daughton, S. von Molnár, M. L. Roukes, A.Y . Chtchelkanova, and D. M. Treger. 2001. "Spintronics, A Spin-Based Electronics Vision for the Future." *Science* **294**, 1488–1492.

Park, Y. D., A. T. Hanbicki, S. C. Erwin, C. S. Hellberg, J. M. Sullivan, J. E. Mattson, T. F. Ambrose, A. Wilson, G. Spanos, and B. T. Jonker. 2002. "A Group-IV Ferromagnetic Semiconductor: Mn_xGe_{1-x}." *Science* **295**, 651–654.

Zaránd, G., and B. Jankó , 2002. *Phys. Rev. Lett.* **89**, 047201

Zeng, C, S. C. Erwin, L. C. Feldman, A. P. Li, R. Jin, Y. Song, J. R. Thompson, and H. H. Weitering. 2003. "Epitaxial Ferromagnetic Mn_5Ge_3 on Ge(111)." *Appl. Phys. Lett.* **83**, 5002–5004.

Zeng, C., W. Zhu, S. C. Erwin, Z. Zhang, and H. H. Weitering. 2004. "Initial stages of Mn adsorption on Ge(111)," *Phys. Rev.* **B 70**, 205340.

Zhu, W., H. H. Weitering, E. G. Wang, E. Kaxiras, and Z. Zhang. 2004. "Contrasting growth modes of Mn on Ge(100) and Ge(111) surfaces: Subsurface segregation versus intermixing." *Phys. Rev. Lett.* **93**, 126102.

An Innovative Technique for Bi-Material Interface Toughness Research

J. J. Wang,[1] I. G. Wright,[2] K. C. Liu,[2] M. J. Lance,[2] S. Sengupta,[3] and R. Xu[3]
[1]*Nuclear Science and Technology Division*
[2]*Metals and Ceramics Division*
[3]*Vanderbilt University*

In general, the weakest link in bi-materials occurs at the interface between dissimilar materials, such as the interface between a thin film and its substrate. In order to make multi-layered electronic devices or structural composites with a long-term reliability, the fracture behavior of these interfaces must be known. Unfortunately, none of the state-of-the-art testing methods for evaluating interface fracture toughness fully conform to fracture mechanics theory, as is evident in existing data that show severe scatter and procedure-dependence in thin-film evaluation methods. This project addresses the problems associated with this deficiency and offers an innovative testing procedure for determination of interface fracture toughness applicable to thin-film coating materials in general. An innovative technology for measuring interface toughness was demonstrated for oxide scales formed on high-temperature alloys of MA956. The estimated interface fracture toughness of alumina scale and MA956 substrate is 3.7 N-m/m², and the estimated equivalent Mode I fracture toughness is 1.1 MPa$\sqrt{m}$. This innovative technique is expected to greatly assist the development of coating materials with improved protective capabilities and provide a reliable method for use in assessing material performance.

Introduction

Microelectromechanical Systems (MEMS) evolved from the technology of silicon microfabrication and introduced the concept of micro-sized mechanical "moving" components, with the attendant mechanics of materials problems. This development led to a completely new field of study, called "mechanical properties of thin films." In a completely different field, advances made over the last 30 years in improving the high-temperature capabilities of materials designed for propulsion systems have relied increasingly on advances in thin-film technology. Increasing the power and/or efficiency of propulsion systems requires that they operate at higher temperatures; and the point was reached several years ago where the materials considerations required to provide strength at high temperature are incompatible with those to provide environmental protection. As a result, such systems must rely on coatings or composite structures in which the mechanical and chemical integrity of interfaces are critical to their successful application.

For the case of thin-film materials and other small structures intended for electronic applications, interest is focused on the role of mechanical stress in defect nucleation and growth. Stress typically arises in such materials due to the constraint of epitaxy, a mismatch in coefficients of thermal expansion, or intrinsically as a result of growth processes. Residual stresses and material discontinuities arise naturally from the deposition or growth processes used to produce these films, and further stresses may be imposed from thermal cycling in service and mismatch in coefficients of thermal expansion. These undesirable stresses and other physical effects as a result of service can lead to fracture, delamination, and other modes of damage initiated at the interface(s) (Chadhury 1999, Ray 2000). Thus, the need to understand what governs the mechanical properties of the interfaces between these dissimilar materials becomes important as the mechanical properties of these interfaces ultimately control the reliability of the device and the performance of the composite structural material. The goal of the proposed project is to develop an innovative technology that can be used for interface toughness research. The specific aims of the project are as follows:

- to support innovation in the development and use of materials and coatings by providing reliable methods to use in assessing their performance; and
- to provide the means to develop and use improved (more advanced) materials and coatings through a better understanding of how they behave in practical situations.

Technical Approach

Bi-material systems with property mismatch are encountered in advanced material and nano-technology development. A theoretical framework for analyzing the mechanics of fracture of dissimilar material interfaces was developed by Williams (1959) and subsequently expanded by many others, including Rice and Shih (1964), Bogy (1970), and Huntchson and Suo (1992). A resurgence of interest for quantifying fracture behavior of bi-material systems in terms of fracture toughness and fracture mode mixity is evident from the works reported in

many recent papers. Yet both the fundamental mechanics and experimental techniques capable of systematically characterizing such fracture are incompletely developed because of a lack of appropriate testing procedures that can properly characterize the interfacial mechanical properties.

Spiral Notch Torsion Test (SNTT) methodology, a 2002 R&D 100 Award winner, was developed by some of the present authors (Wang 2000, Wang 2002). The applicability of SNTT has been verified for homogeneous materials and for relatively large test samples (compared to the micrometer-level of thin films). Consequently, the applicability of this concept to thin-film test samples of bi-materials needs to be validated. In this feasibility study, SNTT technology was modified for use in measuring the interfacial toughness of thin, protective oxide scales formed on a high-temperature alloy, Inconel® MA956 (nominally Fe-20Cr-4.5Al-0.5Y2O3) after thermal treatment. This alloy was chosen for its ability to reliably form a uniformly thick, adherent surface film of α-alumina which is very similar to that formed on bond coating alloys used with TBCs, thus avoiding the complication of using coatings. A 10- to 15-μm-thick alumina scale was formed after oxidation in air at 1200°C for 4 hours. Several configurations of proposed SNTT specimens were investigated. Two types of notch configurations, a V-shape and a square U-shape with different aspect ratios, were used.

The experimental set-up is illustrated in Fig. 1a. A circular rod of alloy MA956, machined with a shallow spiral groove, was used as the baseline. This specimen design utilized a 45° pitch angle of the spiral groove under pure torsion to generate opening mode stress along the interface between the oxide and the alloy. The optional fatigue precrack procedure applied to the baseline MA956 sample was also investigated. The details of notch root geometry and the indicated failure initiation sites of an oxide MA956 SNTT sample are illustrated in Fig. 1b. The shaded area of alumina scale indicates the region of thin film that is capable of transmitting resultant force of the principal stress induced by pure torsion loading. The orientation of the crack propagation for the proposed SNTT configuration is material dependent. With (1) thin-film alumina scale of high hardness compared to that of substrate and the compressive residual stress of the thin film (acting normal to the principal stress), and (2) potential notch root blunting or substrate yielding due to high tensile stress fields near the corner of the notch root, a crack is more likely to initiate from the corner of the notch root and to propagate upward (in the orientation of Fig. 1b) along the interface. After the threshold for crack growth along the interface (vertical in Fig. 1b) has been exceeded, the compressive residual stress in the alumina will cause the unsupported portion of alumina scale to buckle (because of the lack of lateral support from the substrate). This hypothesized SNTT failure mode was confirmed from SEM examination of tested SNTT thin-film samples. Furthermore, SEM examination also indicates that numerous flaws exist near the bottom corner of the U-groove, which provide crack starter for the proposed configuration; thus, the required precrack for a valid toughness evaluation is not needed.

Determination of the torque at crack initiation used several techniques concurrently, including acoustic

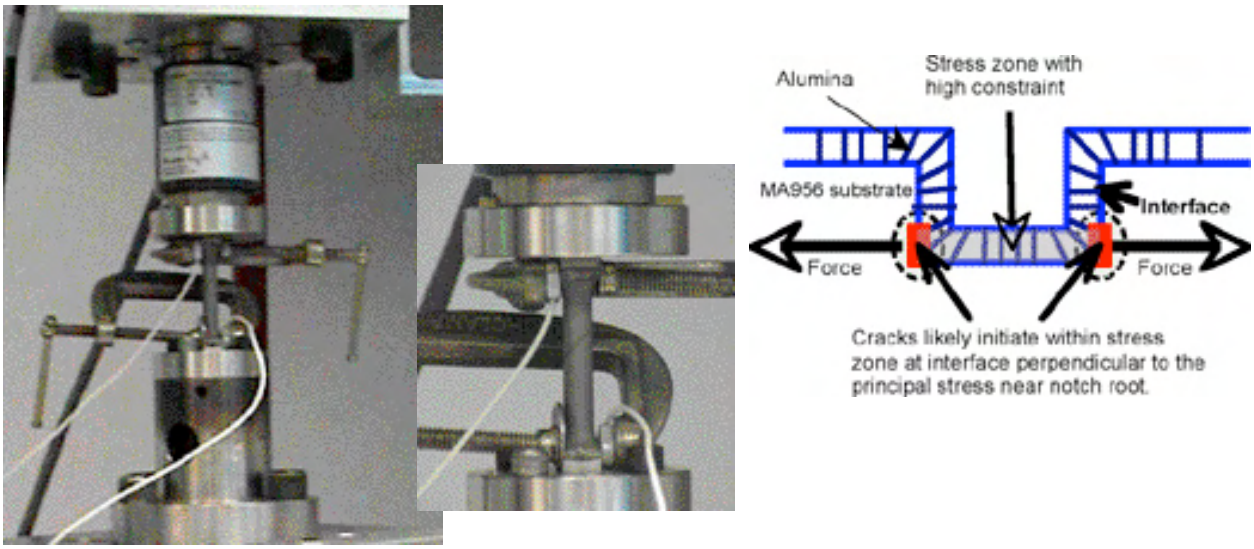

(a) (b)

Fig. 1. Experimental set-up, including acoustic emission sensors attached to the ends of SNTT specimen (a) and schematic diagram of notch root geometry and the associated crack initiation sites (b).

emission and infrared, due to the micro-scale of oxide thickness. In recent years infrared imaging has been applied successfully for detecting and monitoring fatigue crack growth. However, due to the highly insulating nature of the alumina film, the surface temperature profile of the SNTT oxide sample revealed from IR imaging was not useful for detecting or determining evolution of an interfacial crack underneath the alumina film. The acoustic emission technique provided very consistent and distinct signals during the fracture test.

Results and Discussion

Due to the limited availability of alloy MA956, only four SNTT samples were used for exploring the fatigue precrack and fracture behavior for the as-received (non-oxidized) alloy. Of the three SNTT MA956 specimens used for evaluating the fatigue precrack procedures, all fractured during the exploration of the fatigue precrack testing procedure. This fatigue precrack procedure was then used to precrack some of the SNTT baseline samples. One sample used to measure the fracture toughness of MA956 was fractured at 32 N-m with a 0.06-in.-deep crack. Instead of carrying out detailed finite-element analysis for fracture toughness evaluation, the fracture toughness data were estimated and projected from the earlier SNTT fracture toughness data for A302B steel with a/W ratio (crack length to diameter ratio) at about 0.4. The estimated toughness of the as-received MA956 material was about 68.36 MPa $\sqrt{m}$ (62.2 ksi $\sqrt{in.}$).

The technique of Cr^{3+} fluorescence piezospectroscopy was used to measure the stress in the α-alumina film formed by thermal oxidation. All measurements were made at room temperature. The estimated residual stresses from the bulk and side of the U-groove of Specimen No. 3 were used as input of the boundary condition for finite-element analysis of the proposed SNTT thin film model. The measurements gave 3.6-GPa and 2.5-GPa residual stress for bulk alumina scale and alumina scale at the U-groove, respectively. An acoustic emission (AE) system was also used in this research for detecting crack initiation in oxidized SNTT samples under torsional loading. Each AE signal contains background noise. In order to obtain accurate AE test results, these noise sources must be controlled. Use of a suitable "threshold" can filter out background noise and is the prime variable that controls channel sensitivity. Gain has an important effect on energy measurements; also gain has to be set high for high-sensitivity testing. In the current study the threshold was set as 45 dB and the gain was set as 20 dB during the AE data collection. Furthermore, in order to increase the sensitivity of fracture load evaluation, a smaller biaxial load cell (load capacity 200 in.-lb) was installed. A Haver sine function torque loading with displacement control was applied to the oxidized SNTT specimens. Based on AE and torsion test data, the estimated fracture torque at interface crack initiation is 4.63N-m (41 lb-in.).

A three-dimensional finite-element model (FEM) for the proposed SNTT thin film specimen was developed. The PATRAN mesh generator was used to create three-dimensional finite element meshes and the ABAQUS code was used for stress-strain analysis. Prismatic quadratic isoparametric singular elements are used around the crack front. Further modifications were made to these singular elements to facilitate the computational flexibility in linear elastic and non-linear elastic-plastic fracture mechanics analyses. In the former the nodes at the crack tip are constrained to have the same displacement in order to embody the r-1/2 singularity. A major difficulty in constructing a FEM for SNTT thin film samples is to incorporate the relatively large meshes of substrate and the very small meshes of thin film that surround the substrate into one finite-element model. The wide ranges of spectrum of FEM meshes require several layers of transition zones to mitigate the gradient of the adjacent-mesh sizes. Due to a large number of finite elements used for the SNTT thin film model, a minimum of 3 Gb of RAM memory and 14 Gb of scratch disk space is required to carry out stress-strain analysis with the ABAQUS code. Thus, in order to carry out the analytical evaluation within a reasonable timeframe, the finite element analysis was carried out on a supercomputer facility at ORNL. It took about 8,778 sec CPU time and a hard clock time of 4½ hours to complete the finite element analysis. The estimated interface fracture toughness from finite element analysis is 3.7 N-m/m² (0.021 lb-in./in.²) and the estimated equivalent Mode I interface fracture toughness is 1.1 MPa (0.97 ksi).

Benefits

Materials used in processes critical to DOE's missions require a thermal/environmental barrier coating to allow operation at increasingly higher temperatures and harsher environments. Lack of an unambiguous way of quantifying the ability of that coating to adhere to the surface is hindering progress. Measurement of the toughness of the coating-substrate interface, the ultimate weakest link in such systems, is the key to progress. Knowledge of how that toughness is influenced by alloy and coating parameters will greatly aid improved environmental/thermal barrier design.

The drive toward increased performance, efficiency, and reduced environmental pollution in heat engines, energy conversion processes, and many chemical processes involves operation of equipment at higher temperatures, often in increasingly corrosive environments. All construction materials require environmental protection,

and in high-temperature environments the ability of the protective barrier to remain adherent to the surfaces is critical. As a result, measurement of the toughness of the substrate-barrier interface addressed in this project is expected to increase the ability to improve the performance of many of the components needed in, for example, the DOE's Vision 21 and Distributed Generation programs, as well as in DOD programs, to improve liners for combustors and thermal barrier coatings for gas turbine engines, and to develop better thermal protection systems for space vehicles.

References

Bogy, D. B. 1970. "Two Edge-Bonded Elastic Wedge of Different Materials and Wedge Angles under Surface Traction," *J. Appl. Mech.* 38, 377–386.

Chaudhury, Z.A., G. M. Newaz, S. Q. Nusier, T. Ahmed, and R. L. Thomas. 1999. "Chronological Evaluation of Interfacial Damage in TBC due to Thermal Cycling," *J. Mater. Sci*. **34**, 2475–2481.

Evans, A.G., J. W. Hutchinson, and M. Y. He. 1999. "Micromechanics Model for the Detachment of Residually Compressed Brittle Films and Coatings," *Acta. Mater.* 47, 1513–1522.

Hutchinson, J. W. and A. Suo. 1992. "Mixed Mode Cracking in Layered Materials," *Adv. Appl. Mech.* **29**, 63–191.

Ray, A. K. 2000. "Failure Mode of Thermal Barrier Coatings for Gas Turbine Vanes under Bending," *Int. J. Turbo Jet Eng.* **17**, 1–24.

Rice, J. R. and G. C. Sih. 1964. "Plane Problem of Cracks in Dissimilar Media," *J. Appl. Mech.* **32**, 418-423.

Shih, C. F. 1991. "Cracks on Bimaterial Interfaces: Elasticity and Plasticity Aspects," *Journal of Material Science and Engineering* **A143**, 77–90.

Wang, J. A., K. C. Liu, D. E. McCabe, and S. A. David. 2000. "Using Torsion Bar Testing to Determine Fracture Toughness, KIC," *Journal of Fatigue & Fracture for Engineering Materials and Structure* **23**, 45–56.

Wang, J. A., K. C. Liu, and D. E. McCabe. 2002. "An Innovative Technique for Measuring Fracture Toughness of Metallic and Ceramic Materials," *Fatigue and Fracture Mechanics,* **33**, ASTM STP 1417.

William, M. L. 1959. "The Stress Around a Fault or Crack in Dissimilar Media," *Bull. Seismol. Soc. America* **49**, 199–204.

Nanoporous Inorganic Membranes for High Selectivity Hydrogen Separations

L. K. Mansur, B. L. Bischoff, L. E. Powell, and K. D. Adcock
Metals and Ceramics Division

The United States is committed to a future hydrogen economy. Although hydrogen is not available as an elemental resource, it can be dissociated from compounds, such as hydrocarbons or water, by high-temperature chemical reactions. Effective recovery of hydrogen from gas mixtures then becomes a central issue. We have addressed this issue through research on nanoporous inorganic gas separation membranes. Knudsen diffusion, surface transport, and other reasonably well-understood permeation processes operate at membrane pore sizes ranging from several nm to many μm, but unfortunately these processes provide only limited gas selectivity. Recently, we have fabricated experimental inorganic membranes with pore sizes on the order of 1 nm. Proof-of-principle gas permeation experiments have been carried out over a range of temperatures up to 400ºC. The selectivity for hydrogen has been investigated with respect to other gases including propane and carbon dioxide, which were chosen to be relevant to separations required in applications, where various hydrocarbons and combustion products may be present. Selectivity factors up to approximately 30, which are much higher than Knudsen selectivity, have been measured in the temperature range 200–300ºC. Further, the hydrogen permeance increases with increasing temperature. It is concluded that this type of membrane holds high promise for the efficient separation of hydrogen. Further research is recommended on the gas transport mechanisms to provide guidance on how to manipulate processing and fabrication parameters to more fully exploit the high hydrogen separation potential of these membranes.

Introduction

Inorganic membranes have been employed for well over half a century for separating uranium isotopes in the form of UF_6 molecular gas. In the early 1980s, inorganic membranes began to be applied to the separation of particles from fluids and to the separation of mixtures of fluids, both liquids and gases (de Lange 1995; Fain 2000; Ismail 2001; Meixner 1998). Inorganic membranes are now used industrially for separation of gases, catalysis, beverage production, and water purification, for example. Most of the inorganic membranes that have been produced to date have pore diameters of tenths to several micrometers. The smallest pore diameters available in commercial membranes are about 4 nm. Primary permeation and separation mechanisms operating in this regime are Knudsen diffusion and surface transport.

Knudsen diffusion (Knudsen 1909; Burggraaf 1999; Lee 2002) is gaseous diffusion within the pores of the membrane, where the mean free path for molecule-molecule interactions is much larger than the pore diameter. The molecules migrate through the membrane by random straight-line trajectories that are traversed at a velocity dictated by the inverse square root of temperature. One jump is terminated and the next one begun by a collision with a pore wall. In this mechanism there is assumed to be no binding energy with the pore wall. On the other hand, a primary process of surface transport is via a two-step mechanism, where the gas is first adsorbed onto the pore wall and then undergoes surface diffusion in which it hops randomly from surface site to surface site. Because these two separation mechanisms dominate in membranes with pore sizes of several nm and above, such membranes generally have relatively low selectivities for separating gas mixtures (Burggraaf 1996). For example, the maximum separation factor that can be achieved by Knudsen diffusion is limited to the inverse square root of the ratio of molecular masses of the gases to be separated. For a mixture of hydrogen in propane or in CO_2, the selectivity under ideal conditions is limited to less than 5.

From the mid 1980s onward there has been concerted work to decrease the pore sizes of separation membranes to diameters of 2 nm or less.* Membranes with such small pore sizes can have high separation factors for mixtures of gases, which is especially relevant to the recovery of hydrogen. Hydrogen is expected to become of great importance in the future as an energy carrier (National 2002).

Although they are the most highly developed and well-understood separation processes, Knudsen diffusion

*In the separation literature, membranes with pore sizes of 2 nm and less are described as "microporous," in accordance with an IUPAC definition of some years ago (Sing 1985). However, in view of the actual diameter of the pores of order nm, and in harmony with the current major thrusts of U.S. R&D funding agencies in nanoscience, nanoengineering and nanotechnology (NSET), we refer to membranes with pore sizes of order nm as nanoporous.

and surface transport fail to describe permeation and separation processes of gases in inorganic membranes at pore sizes below 2 nm, and especially below 1 nm, where potentially high separation factors can be achieved. Gas transport through inorganic membranes in the nanometer pore size regime is not well understood. Qualitatively it is clear, however, that diffusion through smaller and smaller pores can be visualized to more and more closely approach the regime of solid-state diffusion.

We see gas transport under these conditions as occupying a realm where gaseous diffusion, surface diffusion, and solid-state diffusion converge. Nanoporous membranes hold promise in two areas that are of great interest: (1) high selectivities can be achieved under certain conditions, and (2) the permeance has the potential, as a consequence of thermally activated processes, to increase with temperature rather than decrease as occurs with larger pore membranes.

In this work we have performed proof-of-principle experiments on membranes with pore sizes on the order of nm to explore the potential for high hydrogen separation.

Technical Approach

Experimental Apparatus

We developed capabilities to measure hydrogen separation from hydrocarbon mixtures using nanoporous inorganic membranes. A key step was to acquire the capability to experiment with H_2 and to assess its permeation. Since a main objective was to separate H_2 from a gas mixture relevant to applications, a number of gases were evaluated for inclusion in the work. Propane (C_3H_8) and carbon dioxide (CO_2) were selected. Helium was included also, both for benchmarking with previous work and because it is of interest in itself in connection with our membranes having potential for improved recovery of helium from gas mixtures.

Initially, SF_6 was also included in the work for benchmarking with earlier work. However, part way through the experiments there were indications that SF_6 could be interacting with and modifying the properties of the membranes at the higher temperatures, so measurements using this gas were discontinued. Two existing gas permeation test systems were modified for use with the flammable gases H_2 and C_3H_8. The required safety documentation was completed and approved.

In order to help determine the fundamental operating mechanisms of gas separation, it is essential that data be obtained over a wide range of temperatures, with the maximum temperature as high as possible. Therefore, one of these systems was modified for operation up to and above 400°C. Previous work using this system was limited to temperatures below 275°C. Most of the work was carried out on this system and consisted of sequential permeation measurements on individual gases. The ratios of permeances of the individual gases give the selectivity or ideal separation factor for the membrane in question. In addition, however, this system provides the capability to measure the actual separation of hydrogen from mixtures of two or more gases. Mixed gas measurements were carried out for one membrane during the last phase of the research program reported here. This capability will be utilized in future work.

Test Methodology

Tubular separation membranes were installed within a tubular holder. Gas feed lines, permeate, and retentate lines were attached to the holder within a test system, which was surrounded by a clamshell furnace. Repeated purges with helium gas and controlled heating cycles were applied prior to each test. The specimen membrane was flow tested at a series of pressures for the sequence of gases H_2, He, CO_2, and C_3H_8 for each temperature. For each membrane, at least one set of tests was completed with all four gases, at one temperature per day, for the seven temperatures from 100 to 400ºC in 50ºC increments. Tests at room temperature were also carried out for H_2 and He. The flow through the membrane, from which permeance was calculated, was obtained by measuring the pressure rise with time in a known volume downstream of the membrane. Pressures via transducer voltages and temperatures via thermocouple readings were acquired continuously using computer data acquisition software. These raw data were transferred to a spreadsheet where pressure, flow, and permeance calculations were carried out.

Results and Accomplishments

Measurements

Measurements were carried out on eight different membranes, designated as S1 through S8 in Table 1. The membranes tested consisted of stainless steel tubes supporting various ceramic membrane separation layers. The tube holder was also constructed of stainless steel. Each membrane had different permeance and separation properties based on different processing parameters during membrane fabrication.

Figures 1 and 2 show the permeance and selectivity, respectively, for membrane S2. This is the membrane that showed the highest product of selectivity and permeance for H_2 with respect to C_3H_8. This product is generally accepted as a figure of merit to assess membrane performance. At 200ºC the measured selectivity of hydrogen with respect to propane was 31.39. The corresponding number for helium with respect to propane was 32.69. These numbers are 6.71 and 9.85 times the Knudsen selectivity, respectively,

Table 1. Measured selectivities of eight membranes at temperatures ranging from 100 to 400 °C

	H_2/C_3H_8 Selectivity*						
Membrane	***100 °C***	***150 °C***	***200 °C***	***250 °C***	***300 °C***	***350 °C***	***400 °C***
S1	2.55	4.10	**5.70**	**6.79**	**6.74**	**6.48**	3.37
S2	**18.26****	**19.87**	**31.39**	**22.71**	**10.59**	**6.69**	**5.45**
S3	**6.59**	**8.86**	**9.30**	**11.88**	**8.14**	**6.22**	**4.85**
S4	4.42	3.82	**5.78**	**5.63**	**6.02**	**4.93**	**4.70**
S5	**5.34**	No Data	**5.14**	**5.07**	**5.49**	**5.65**	No Data
S6	**7.73**	No Data	**9.20**	**12.41**	**11.58**	**6.08**	No Data
S7	1.87	3.63	**4.94*****	**5.69*****	No Data	No Data	No Data
S8	2.73	2.65	3.43	4.00	4.46***	No Data	No Data

*Selectivity, the ratio of the permeances of the two gases measured separately, is sometimes also termed the ideal separation factor.

** Values in bold indicate that the ideal separation factor is higher than what is expected from Knudsen diffusion for these two gases (4.69), and unbolded values indicate an ideal separation factor less than predicted by Knudsen diffusion.

***The two highest temperatures for membrane S7 were 175, and 225 °C. The highest temperature for membrane S8 was 275 °C.

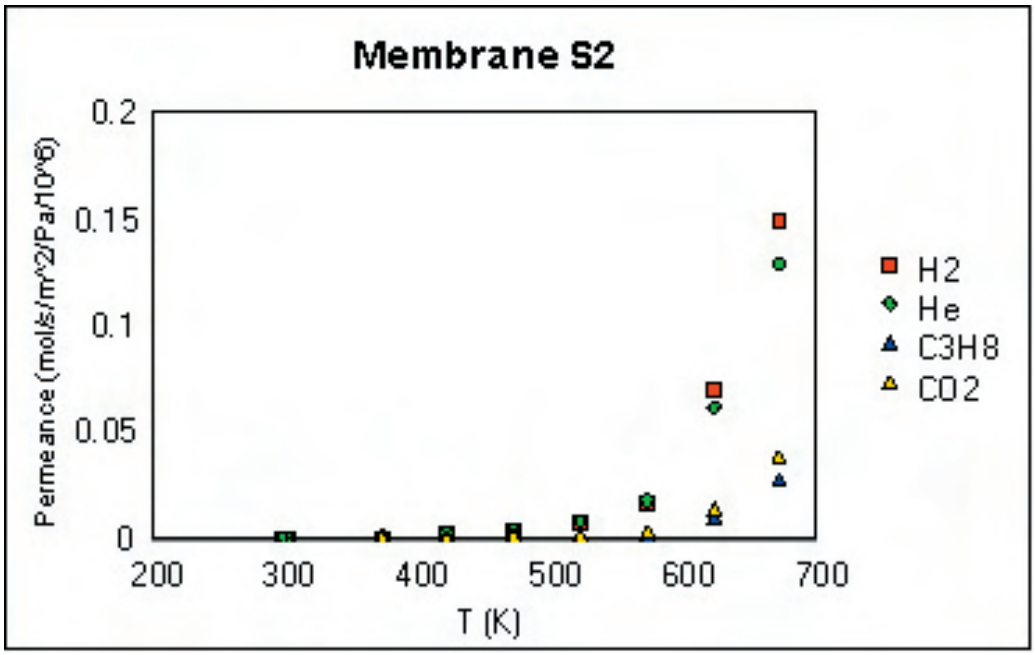

Fig. 1. Measured permeance with respect to temperature. At room temperature, only He and H_2 were measured. At other temperatures, all four gases were measured.

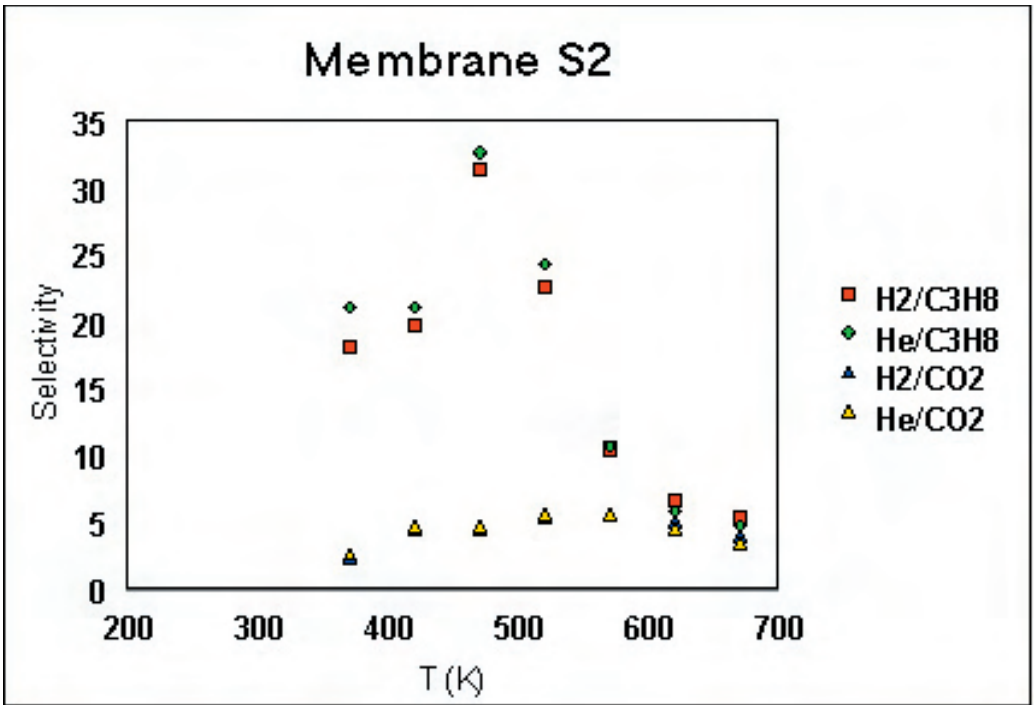

Fig. 2. Selectivity with respect to temperature of the four gas combinations indicated.

and indicate that the pore diameters in this membrane are of order one nanometer. The corresponding permeance at the highest temperature of 400ºC was approximately 1.5×10^{-7} mol/s/m^2/Pa.

There was some variation with time at temperature in the properties of the membranes. This is illustrated in Fig. 3. Here the results of repeated permeation measurements of H_2 on membrane S2 are shown. It is evident that the permeation of hydrogen increased by about 30% between the first and the last measurement at 400ºC.

Analytical Expressions

In order to most effectively analyze the experimental data being accumulated, the dominant operating mechanisms of membrane transport need to be sought. To this end we have distilled parametric dependencies of key mechanisms of gas transport into simple and readily applicable expressions. Key parameters include temperature (T), pressure (P), molecular mass (m), kinetic molecular diameter (d_m), pore diameter (d_p), molecular collision mean free path (λ), and several thermal activation energies. The latter are H_a, the heat of gas adsorption, E_s, the activation energy for surface diffusion, and E_d, the activation energy for nanopore diffusion.

The most important characteristic of membranes that dictates the dominant transport mechanism is the pore diameter or, more precisely, the ratio of the pore diameter to two important physical characteristics of the gas, λ and d_m. Most gases of interest have kinetic molecular diameters between one-fourth and two-thirds of a nanometer. Generally, for pore diameters >2 nm, the important permeation mechanisms in operation are Knudsen diffusion and surface transport, together with molecular diffusion and viscous flow (Poiseuille or laminar flow) at larger pore diameters. For pore diameters of about 1 nm and smaller, other mechanisms which are covered by term "nanopore diffusion," come into operation. Several mechanisms of gas transport through a membrane are summarized in Table 2. Expressions for selectivity and permeance also are given in the table for those cases where the dependencies on important variables can be expressed in simple form without extensive qualifying statements or limiting conditions.

Thermally Activated Behavior

The first thing to note about Fig. 1 is that the permeances increase with increasing temperature. It should be emphasized that if Knudsen diffusion were the dominant mechanism in operation, the permeances would decrease as the inverse square root of temperature. It can also be shown that the permeance for mechanisms that operate by adsorption followed by surface diffusion decreases with increasing temperature. The progressive increase with temperature of permeance for all the gases shown in Fig. 1 indicates the possibility of thermally

Table 2. Characteristic expressions for key membrane gas-transport mechanisms.

Mechanism	Pore Diameter	Selectivity	Permeance
Viscous Flow	$\lambda < d_p$	None	$d_p^2\ P\ T^{-1}$
Molecular Diffusion	$\lambda < d_p$	None	
Knudsen diffusion	$\lambda > d_p$	$m^{-1/2}$	$M^{-1/2}\ d_p\ T^{-1/2}$
Surface Transport	All d_p	Variable	$d_p^{-1}\ P\ \exp[(H_a - E_s)/RT]$
Capillary Condensation	f(P)	Variable	
Nanopore Diffusion	$3\ d_m > d_p$	Highest	$m^{-1/2}\ d_p\ T^{-1/2}\ \exp[-E_d/RT]$

activated behavior. This thermally activated characteristic is similar to the diffusion of defects or atoms in the solid state in the presence of traps (Mansur 1981), with activation energy E_d. Physically this is plausible, because delay time in negotiating the pore and activation energy have a one-to-one correspondence in the sense that they can be directly related to each other in a trapping model. Here now the jump distance is determined by the pore diameter rather than being constrained to a crystal lattice dimension; however, the lower limit on size of a pore must correspond to interatomic spacing in the solid state.

It is of interest to determine the effective activation energies of the increases shown in Fig. 1. The dominant temperature dependence of the expression in the last line of Table 2 is the exponential in the effective diffusion energy E_d. Without losing accuracy over this temperature range for typical activation energies, the expression can be simplified to

$$P_i = A_i \exp(-E_{di} / \mathrm{k}\ T) \qquad (1)$$

where P_i is the permeance of gas i, A_i is essentially a constant for each gas and E_{di} is the effective diffusion activation energy for each gas.

Using this equation we have determined that the effective activation energies for the measurements shown in Fig. 1 range from approximately 40 kJ/mol for propane to 60 kJ/mol for hydrogen. These numbers are approximate. One reason that these are not precise values is apparent in Fig. 3. Although each series of points for hydrogen appears to show the signature exponential shape for thermally activated behavior, it is also true that the last measurement taken at the highest temperature shows about thirty percent greater permeance than the first measurement at that temperature. Further, each measured result shows higher permeance than the one before it at the same temperature. Therefore a minor part of the effective activation energies quoted above is likely due to time-at-temperature changes in the membrane itself, rather than being a true measure of any physical activation barrier for gas transport.

Summary and Benefits

This project has created the capability at ORNL to measure hydrogen permeation through inorganic membranes and its separation from other gases. Membranes of this type have excellent potential for application to separation of hydrogen from hydrocarbons and combustion products. The results obtained show clear potential for accomplishing goals set forth in the "National Hydrogen Energy Roadmap" released by Secretary of Energy Spencer Abraham on November 12, 2002 (National 2002).

Eight membranes were examined, six of which demonstrated selectivity higher than for Knudsen diffusion. Selectivities of hydrogen and helium with respect to propane and carbon dioxide have been demonstrated up to as high as 30.

Analysis has been carried out to express parametric dependencies of key mechanisms of gas transport in simple and readily applicable expressions. The best membranes showed an increase of permeance with increasing temperature, of a form that is consistent with a thermally activated gas transport mechanism. The effective activation energies appear to be relatively high, in the range of 40 to 60 kJ/mol.

It is recommended that future work focus on quantitative understanding of the detailed mechanisms of operation of these membranes in order to further improve their performance. Definitively establishing the relationships between processing parameters and procedures and membrane selectivity, permeance, and stability should be given high priority. This research work provides strong and timely support for a new proposal that may be approved by ORNL for submission in response to the DOE call for proposals distributed in April 2004

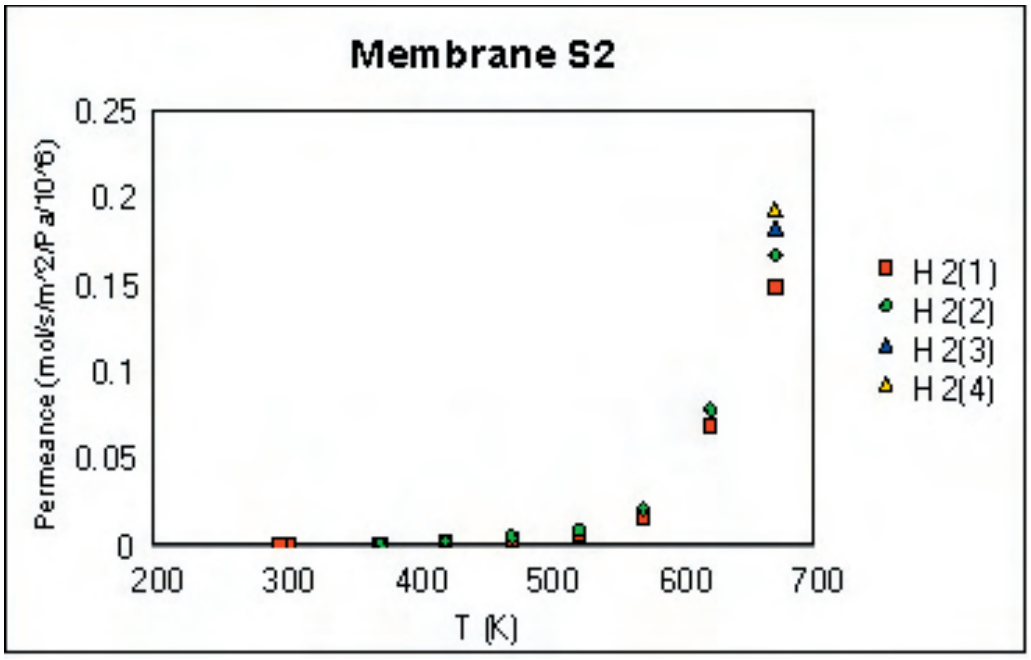

Fig. 3. Results of repeated measurements of H_2 permeance at each temperature. H_2 permeance was first measured at a given temperature and then again after the permeance measurement for each of the other gases, for a total of four H_2 measurements at each temperature.

as Office of Science Notice DE-FG01-04ER04-20, Basic Research for the Hydrogen Fuel Initiative. In particular, five areas of emphasis in this call for proposals are stated, with membranes highlighted specifically as area 2—Membranes for Separation, Purification, and Ion Transport. In addition, at ORNL the EERE, FE and NE programs of the DOE have indicated strong interest in hydrogen separation membrane technology and in fact are planning to support follow-on work to the present program.

References

Burggraaf, A. J. and L. Cot, Eds. 1996. "Fundamentals of inorganic membrane science and technology," *Membrane Science and Technology Series 4*, i–xviii, 1–690 pages, Elsevier, Amsterdam.

Burggraaf, A. J. 1999. "Single gas permeation of thin zeolite (MFI) membranes: theory and analysis of experimental observations," *J. Membrane Sci.* **155**, 45–65.

R. S. A. de Lange, K. Keizer, and A. J. Burggraaf. 1995. "Analysis and theory of gas transport in microporous sol-gel derived ceramic membranes," *J. Membrane Sci.* **104**, 81–100.

Fain, D. E. 2000. "Mixed gas separation technology using inorganic membranes," *Membrane Tech.* **120**, 9–13.

Ismail, A. F. and L. I. B. David. 2000. "A review of the latest development of carbon membrane for gas separation," *J. Membrane Sci.* **193**, 1–18.

Knudsen, M. 1909. "The law of the molecular flow and viscosity of gases moving through tubes," *Ann. Phys*. **28**, 75–130.

Lee, D. and S. T. Oyama. 2002. "Gas permeation characteristics of a hydrogen selective supported silica membrane," *J. Membrane Sci.* **210**, 291–306.

Mansur, L. K. 1981. "Effective diffusion coefficients of point defects in impure materials," *Acta Met.* **29**, 375–381.

Meixner, D. L. and P. N. Dyer. 1998. "Characterization of the transport properties of microporous inorganic membranes," *J. Membrane Sci.* **140**, 81–95.

National Hydrogen Energy Roadmap. 2002. *November 2002 Report on the results of the National Hydrogen Energy Roadmap Workshop*, Washington, D.C., April 2–3, 2002. Report released by Secretary of Energy Spencer Abraham, November 12, 2002.

Sing, K. S. Ed. 1985. "Reporting physisorption data for gas/solid systems (recommendations 1984)," *Pure Appl. Chem.* **57**, 603.

High-Aspect-Ratio Carbon Nanofiber Probes for Scanning Probe Microscopy

M. L. Simpson,[1] M. A. Guillorn,[1] C. Rouleau,[2] D. Hensley,[1,2]
R. J. Kasica,[1] M. Doktycz,[3] and A. Melechko[4]
[1]*Engineering Science and Technology Division*
[2]*Condensed Matter Sciences Division*
[3]*Life Sciences Division*
[4]*The University of Tennessee*

The objective of this project was to develop the first technique for the synthesis of high-resolution high-aspect-ratio scanning probe microscope (SPM) tips that can be implemented in a large-scale fabrication process. This technique is based on the ORNL-developed vertically aligned carbon nanofibers (VACNF) technology. While other methods currently exist for the production of this type of probe tip, the use of the VACNF will surpass these techniques since VACNFs can be synthesized completely deterministically in a wafer scale fabrication process. This allows for thousands of identical tips to be fabricated simultaneously in precise locations with total control over their morphology. A patent application on this technology was submitted at the end of 2003.

Introduction

Scanning probe microscopy (SPM) has become an indispensable tool for the analysis of surfaces and the exploration of general substrate morphology at the nanoscale and microscale. Moreover, SPM techniques have been used to investigate a wide variety of material properties beyond substrate topography. The range of applications spans a vast array of scientific disciplines ranging from solid-state physics to biology, environmental science, to polymer engineering. The currently used methods for producing high-resolution high-aspect-ratio tips for SPM applications are based on processes serial in nature; that is, only a single tip can be fabricated at a time. The goal of this project was to integrate synthesis of vertically aligned carbon nanofibers (VACNFs) with standard cantilever fabrication processes and to characterize the high-aspect-ratio VACNF SPM tips obtained in such method.

Technical approach

We have demonstrated that VACNFs can be synthesized in a completely deterministic manner using a catalytic dc plasma-enhanced chemical vapor deposition process (Merkulov 2002). Features such as the location, length, tip diameter, shape, and chemical composition of VACNFs can be precisely controlled during the synthesis process(Merkulov 2002). Functional microfabricated device structures have been fabricated that exploit both the electrical and mechanical properties of single and multiple VACNF. These structures have been fabricated on a variety of substrates including whole 100-mm-diameter Si, Si-on-insulator (SOI), and quartz wafers. This material meets the required specifications for high-aspect-ratio SPM tips. In addition, it offers a number of other features that may allow it to surpass all other materials presently used in SPM tip manufacturing.

Results and discussion

The fabrication process for microcantilevers with VACNF tips have been developed. Individual processing steps compatible with handling microsctructures with high-aspect-ratio features such as VACNFs have been developed and tested. The cantilevers with VACNF tips has been obtained, thus proving the feasibility of the idea. Figure 1 shows an SEM image of a finished device. The sharpness of the VACNF tips has been improved via changes in the catalyst preparation process. The diameter of the nanofiber coincides with the diameter of the catalyst particle. We have found the techniques to prepare smaller nanoparticles that can be prepared using standard photolithography (Melechko 2003), thus making the complete fabrication an inexpensive and high-throughput method. The devices obtained after optimization of all processing steps have been characterized, and their performance was compared to currently available AFM tips.

Benefits

VACNF-tips are of high interest for application areas that are critical to DOE and NIH. Micro- and nano-

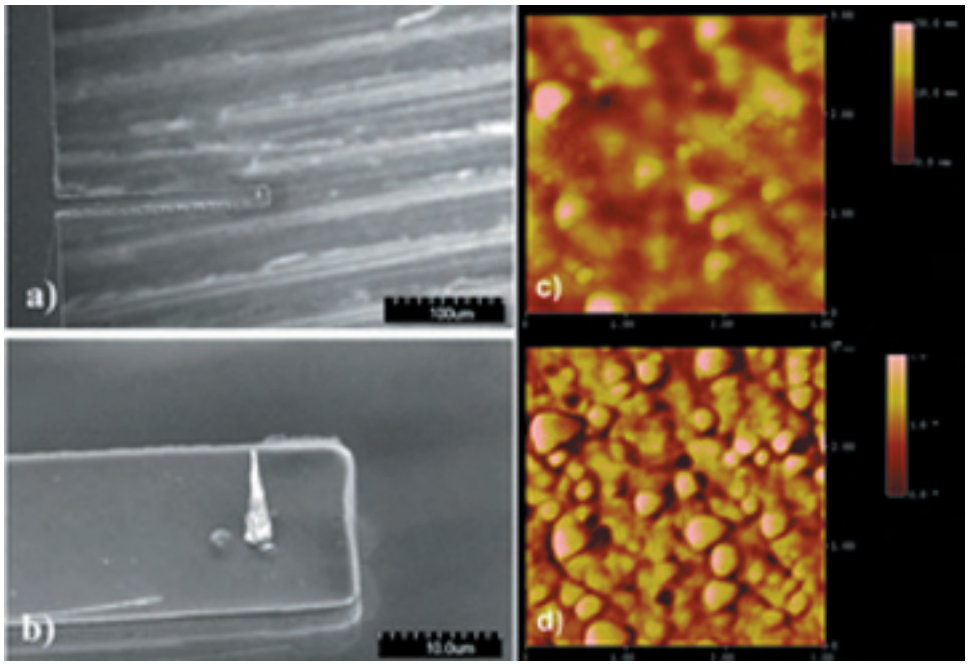

Figure 1. Scanning electron micrographs of a cantilever with a VACNF tips at 45° viewing angle at two different magnifications: (a) 300 × and (b) 3000 ×; (c) and (d) are topography and phase AFM images obtained using VACNF tip on a MFM test sample provided by Digital Instruments.

fabricated structures and complex biological systems, two major research thrust areas at ORNL, possess a varied surface topography that is often best characterized by SPM techniques. However, they can only be imaged accurately with high-resolution high-aspect-ratio tips. The exploration of the applications of the VACNF probe tips in these two target areas as they show significant promise for follow-on funding. In addition to standard AFM function, VACNF-based tips can provide probes for study and manipulate processes inside live cells (McKnight 2003, McKnight 2004a) and electrochemical scanning techniques (McKnight 2004b).

References

Merkulov, V. I., D. K. Hensley, A. V. Melechko, M. A. Guillorn, D. H. Lowndes, and M. L. Simpson. 2002a. "Control mechanisms for the growth of isolated vertically aligned carbon nanofibers," *Journal of Physical Chemistry B* **106**(41), 10570–10577.

Melechko, A. V., T. E. McKnight, D. K. Hensley, M. A. Guillorn, A. Y. Borisevich, V. I. Merkulov, D. H. Lowndes, and M. L. Simpson. 2003. "Large-scale synthesis of arrays of high-aspect-ratio rigid vertically aligned carbon nanofibres," *Nanotechnology* **14**(9), 1029–1035.

McKnight, T. E., A. V. Melechko, G. D. Griffin, M. A. Guillorn, V. I. Merkulov, F. Serna, D. K. Hensley, M. J. Doktycz, D. H. Lowndes, and M. L. Simpson. 2003. "Intracellular integration of synthetic nanostructures with viable cells for controlled biochemical manipulation," *Nanotechnology* **14**(5), 551–556.

McKnight, T. E., A. V. Melechko, D. K. Hensley, D. G. J. Mann, G. D. Griffin, and M. L. Simpson. 2004a. "Tracking gene expression after DNA delivery using spatially indexed nanofiber arrays," *Nano Letters* **4**(7), 1213–1219.

McKnight, T. E. , A. V. Melechko, D. W. Austin, T. Sims, M. A. Guillorn, and M. L. Simpson. 2004b. "Microarrays of vertically-aligned carbon nanofiber electrodes in an open fluidic channel," *Journal of Physical Chemistry B*, **108**(22), 7115–7125.

In Situ Studies of Hydrogen Storage Materials Using Neutron Scattering

C. J. Rawn,[1,2] J. Howe,[1] B. C. Chakoumakos[3]
[1]*Metals and Ceramics Division*
[2]*Materials Science and Engineering Department, University of Tennessee*
[3]*Condensed Matter Sciences Division*

This project concentrated on building a pressure/temperature cell for in situ neutron diffraction studies to answer structural and thermodynamic issues about the role of hydrogen in hydrogen-containing compounds. We have collaborated with personnel from the neutron scattering facility at Chalk River Laboratories to design and construct a new pressure cell for use at different temperature and pressure ranges of interest for the investigation of suitable hydrogen storage materials and to collect neutron diffraction data at ambient conditions on $NaAlD_4$ doped with $TiCl_3$. Secondary phases and an elevated background, most likely caused by incoherent scattering from H that was not exchanged with D during the desorbing and recharging procedure, prevented obtaining statistically significant results concerning the location of the Ti atoms in the atomic structure.

Introduction

Candidate materials for hydrogen storage must demonstrate a reasonable amount of storage capacity that is reversible on a reasonable time scale. In addition, such issues as the operating pressure and temperature range and the degradation of the materials after repeated cycling need to be understood. For fundamental understanding of these issues, characterization of materials with hydrogen-storage potential must be conducted at the atomic level using in situ environments. Neutron diffraction data is advantageous since the scattering power of the deuterium atoms allows their positions in the crystal structure to be determined with equal or greater precision than some of the heavier elements that would dominate structural refinements using X-ray diffraction data. This greater precision for the D positions in a structure determined from neutron diffraction data will result in smaller uncertainties associated with the atomic positions, the atomic displacement parameters, and the bond distances, parameters that are related to many of the physical characteristics that will determine if these materials will prove useful for applications.

Technical Approach

One of the main goals of this proposal was to design and build a high-pressure, high-temperature cell to study hydrogen storage materials with in situ neutron powder diffraction. Studying the safety and technical requirements surrounding the fabrication of such a cell, it became clear that the only way to obtain such a cell was to collaborate with other researchers. To achieve this, we have collaborated with Lachlan M. D. Cranswich and Ian Swainson from the Neutron Program for Materials Research at Chalk River Laboratories (Chalk River, Ontario, Canada).

Fabrication of a cell with a pressure maximum of 10 bar, the instrumentation layout shown in Fig. 1 is currently under way at the Chalk River Laboratories. Through this seed project, we contributed various components and we will have access to the cell once completed and tested. The design of this pressure cell is such that it will work in conjunction with a commercial Cryofurnace, which we currently have available at the High Flux Isotope Reactor (HFIR), for changing the temperature. A Labview data acqusition/control program will regulate the processes. Through our support, by showing our financial commitment via contributing components to the cell and by writing a support letter, the group from Chalk River was able to obtain funding from a capital equipment competition to build a second cell that would be designed to obtain pressures of up to 50 bar.

In addition to the design and fabrication of the pressure cell, we have collected ambient temperature and ambient pressure neutron diffraction data on $NaAlD_4$ doped with the addition of $TiCl_3$, as a catalyst, on the powder diffractometer at the Chalk River neutron scattering facility. There are several explanations in the literature for the location of the Ti within in the crystal structure; however, to date there are conflicting conclusions from a variety of different experiments.

Results and Discussion

Joachim Schneibel (Metals and Ceramics Division, ORNL) synthesized $NaAlD_4$ with $TiCl_3$ from as received $NaAlH_4$ by desorbing the material and recharging it with D_2 gas for the neutron powder diffraction experiment discussed above. Prior to sending the samples to the Chalk River Laboratories, they were characterized by Scott Speakman (Metals and Ceramics Division) using X-ray powder diffraction. The X-ray results indicated that

secondary phases were present in the as-received materials, and additional phases were present after adding the $TiCl_3$ (i.e., NaCl) and repeated desorbing and recharging of the material. It was found that several cycles of desorbing and recharging $NaAlD_4$ were necessary to modify the material and resulted in sharper diffraction peaks. Due to the secondary phases and elevated background, most likely caused by incoherent scattering from H that was not exchanged with D during the desorbing and recharging procedure, no statistically significant results could be obtained on the location of the Ti atoms in the atomic structure. Beamtime is available for the continuation of this project should higher quality samples or samples of another material with promising physical properties become available. These results were presented at the American Crystallographic Associations Annual Meeting (July 2004).

Benefits

This research has helped to increase the staff's expertise in the characterization of hydrogen-storage material systems at the atomic level. In the future, the pressure cells discussed in this report will be available for ORNL researchers to collect in situ studies on hydrogen storage materials in collaboration with scientists from the Chalk River neutron scattering facility. A pre-proposal was prepared for the ORNL internal competition for BES Hydrogen Fuel Initiative call; however, our project was not selected to compete outside ORNL. A second pre-proposal was prepared and submitted to the BES Hydrogen Fuel Cells Initiative call through UT and was not selected for submitting a full proposal. In addition funds were requested but not obtained from the Energy Efficiency and Renewable Energy Program on Hydrogen Storage for supporting a hydrogen storage session scheduled for the American Crystallographic Association's Annual Meeting in 2005.

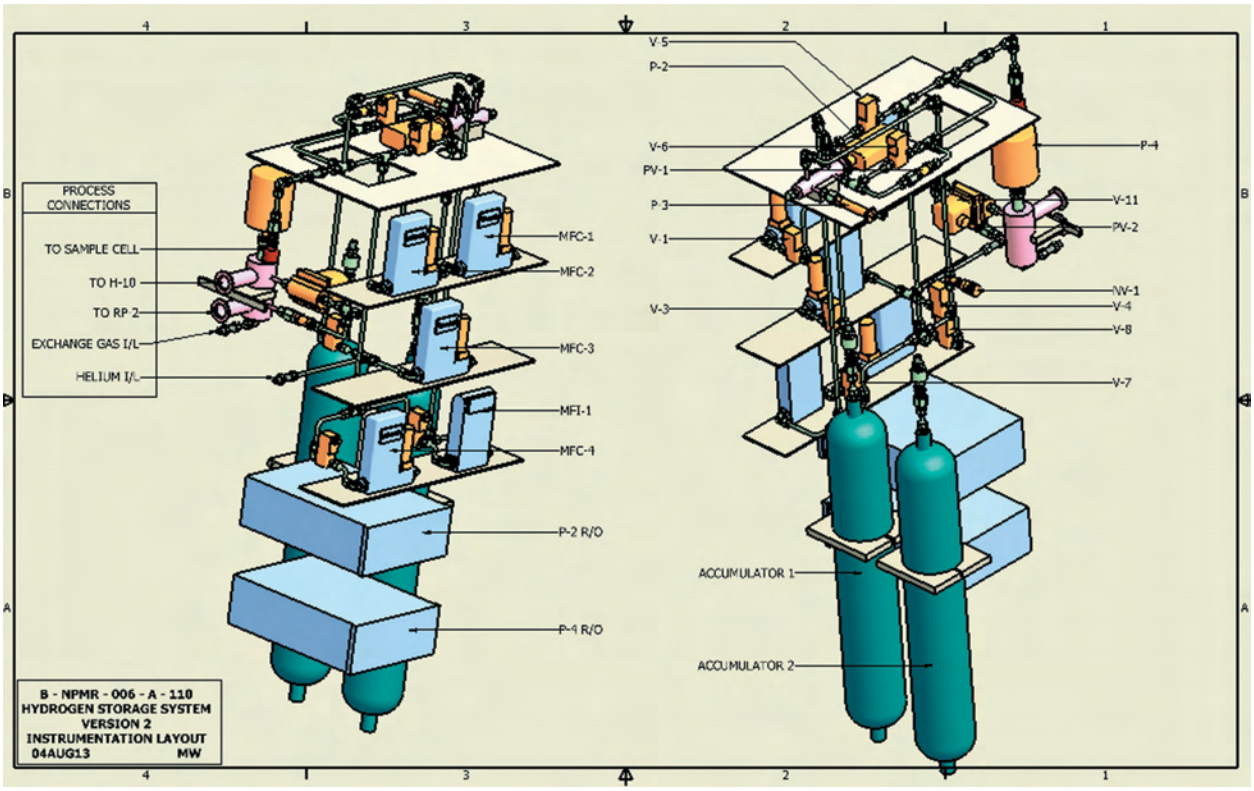

Fig. 1. Instrumentation layout for the 10-bar hydrogen cell currently being constructed at Chalk River Laboratories.

Superionic Electrolyte-Based Fuel Cell Concept for Portable Multi-Fuel Power Sources

I. Kosacki,[1] C. M. Rouleau,[2] P. F. Becher,[1] and D. H. Lowndes[2]
[1]*Metals and Ceramics Division*
[2]*Condensed Matter Sciences Division*

The project focused on the development of oxygen-conducting, highly textured thin films and multilayered structures with enhanced ionic conductivity at relatively low operating temperatures. An enhancement in the in-plane conductivity was observed for CeO_2:20%Sm films that combine high texture and layer thicknesses in the nanometer range. This effect is attributed to the transition from lattice- to interface-controlled diffusivity and also has been observed in CeO_2:20%Sm/CeO_2 superlattices, for which the interfacial area is increased intentionally and significantly as compared to that of a single-layer film. Enhanced ionic conductivity with decreasing layer thickness (referred to as the "thickness effect") was observed for superlattices composed of alternating CeO_2:20%Sm (30 nm) and CeO_2 (20 nm) layers. To demonstrate the advantage of such structures, their performance was assessed for two types of single-chamber solid oxide fuel cells: (1) using a single-layer electrolyte cell and (2) for superlattice electrolytes with different numbers of alternating CeO_2:20%Sm and CeO_2 layers. The results show an enhancement in both power and current densities for the superlattice-based cells as compared with the single-layer electrolyte cell. The high performance of the fuel cells with superlattice electrolytes represents both a scientific and a technical opportunity for developing unique multilayer nanoscaled materials for chemical-to-electrical energy conversion.

Introduction

This project focused on the development of advanced materials for solid oxide fuel cells with exceptionally high efficiencies and reduced operating temperatures. These advanced fuel cells will require new solid electrolytes with both increased ionic conductivity and faster reaction kinetics to attain efficient operation at temperatures of 500–700ºC. The key issue to achieve this goal is the optimization of ionic conductivity, which in conventional oxygen-conducting materials is attributed to mobile oxygen vacancies created by acceptor doping. The oxygen transport in these systems is controlled by the lattice diffusion mechanism and is limited by the ion jump distance, as determined by the material lattice constant. Assessments based on this mechanism suggest a maximum ionic conductivity of 10 S/cm that can only be reached at temperatures close to the melting point (over 2700ºC). Experimental data obtained at temperatures below 1000ºC are in good agreement with these predictions (Kosacki and Anderson 2001a).

To reach higher levels of ionic conductivity at moderate operating temperatures, it is necessary to develop materials in which diffusivity is not limited by the lattice mechanism. A number of studies have shown that this can be achieved by reducing the microstructure (crystalline grain size) into the nanometer range (Kosacki and Anderson 2001b, Kosacki et al. 2002). The introduction of interfaces/grain boundaries has proven to be a powerful way to enhance the ionic transport based on the high diffusivity of the grain boundary regions, which is often 2–3 orders of magnitude greater than lattice diffusivity. Such influences have been reported recently for nanocrystalline CeO_2 and ZrO_2 (doped with either Y or Sc) thin film specimens, and significant enhancements in ionic conductivity were observed (Kosacki and Anderson 2001b, Kosacki et al. 2002). The ionic conductivity of solid electrolytes also can be enhanced by the introduction of a high density of dislocations or interfaces that act as rapid diffusion paths for ionic species. Such an idea has been discussed recently by Maier and coworkers for BaF_2/CaF_2 superlattices for which a substantial increase in ionic conductivity was observed (Sata et al. 2000). Another recent advance in the conceptual design of fuel cell materials was the demonstration that ionic transport can be enhanced in highly textured YSZ thin films deposited onto MgO substrate by controlling their thickness in the nanometer range. An enhancement in the in-plane conductivity was observed for films with thicknesses below 60 nm and is attributed to a transition from lattice- to interface-controlled diffusivity (Kosacki et al. 2004a). It was estimated that the interfacial conductivity could be three orders of magnitude larger than lattice-limited transport (Kosacki et al. 2004b). This observation illustrates the tremendous potential of nanostructured materials and offers new opportunities for the application of highly textured oxide thin films in electrochemical devices including solid oxide fuel cells.

This project sought to determine the potential of nanoscale effects by using single crystal–like oxide thin films. The goal was to exploit our experience with

nanoscale YSZ films by further investigating Sm-doped CeO_2, a premier low-temperature solid electrolyte. We were seeking to take advantage of our discovery of greatly enhanced ionic conductivity in textured YSZ films by demonstrating their applicability to the development of other advanced solid oxide fuel cells materials, capable of operating at temperatures ranging from 400 to 700ºC.

Technical Approach

The practical application of this nanoscaling concept required the development of highly textured CeO_2:20%Sm films for a single-chamber fuel cell as a small portable power source. Epitaxial thin films cannot only exhibit the nanoscale thickness effect but also have the advantage that there are no grain boundaries aligned normal to the current flow to inhibit the in-plane conductivity. We also note that thin-film approaches already have been considered within design concepts for advanced solid oxide fuel cells (Hibido et al. 2000).

The ultimate objectives of the project were (1) to observe the nanoscale thickness effect on the ionic conductivity in epitaxial CeO_2:20%Sm thin films deposited on MgO-substrates and (2) to demonstrate a proof-of-concept fuel cell that operates in the single-chamber geometry at reduced temperatures with increased efficiency and power density. The interfacial effect on ionic conductivity was further exploited by growing CeO_2:20%Sm/CeO_2 superlattices, in which the number of high-conductivity interfacial paths can be increased significantly as compared to a single-layer film.

Highly textured CeO_2:20%Sm single-layer films and CeO_2:20%Sm/CeO_2 superlattice structures were deposited on (001) MgO single-crystal surfaces by pulsed laser ablation of dense polycrystalline CeO_2:20%Sm and CeO_2 targets using a KrF (248-nm wavelength) excimer laser. Typical deposition rates of 0.5 to 1 Å per pulse were achieved at 5 Hz with the MgO substrate mounted on a stage that was heated typically to 700ºC and positioned 5 cm from the target. During the course of this work, the surface preparation of the substrate and the control of oxygen partial pressure during deposition were critical factors in producing high quality films. Prior to deposition, the polished MgO-substrates were etched for 5 seconds in phosphoric acid to reduce the surface roughness below 1 nm. Repeatable and consistent nucleation was achieved on this surface, and the highest level of epitaxy was obtained for specimens which incorporated a thin (~50 nm) undoped CeO_2 buffer layer.

The degree of preferred orientation (texture) of the CeO_2:20%Sm thin films was evaluated by X-ray 2-theta and phi scans. The conductivity measurements were obtained over a temperature range of 400 to 800ºC in an oxygen atmosphere using two-probe impedance spectroscopy. Silver electrodes were used and data was collected with a Solartron 1260 impedance system. Single-chamber fuel cells were fabricated using single-layer CeO_2:20%Sm films and CeO_2:20%Sm/CeO_2 superlattices with different numbers of periods (50, 100 and 200). The fuel cells were operated in 10% propane (air balance) at 600ºC.

Results and Discussion

The analysis of X-ray diffraction results obtained for CeO_2:20%S thin films indicates that the best texture and crystallinity were obtained when (1) an undoped CeO_2 buffer layer was deposited on the MgO substrate and (2) the oxygen partial pressure in the deposition chamber was controlled during the film processing. By employing in situ reflection high-energy electron diffraction (RHEED) during layer deposition, it was determined that at least a 50-nm CeO_2 buffer was required as a transition layer from the MgO lattice constant to that associated with the electrically active cerium oxide. Thin films possessed a very high degree of (001) texture, when deposited at an oxygen pressure of 10 mTorr. In general, the X-ray analysis revealed a four-fold symmetry in (111) phi-scan figures, indicative of a strong cube-on-cube film/substrate relationship. Omega-scans of the (002) reflections showed very small peak widths of 0.3–1.1 degrees, which increased for thinner films. These results indicated the very high degree of both crystallinity and (001) texture of the CeO_2:20%Sm films, which were nearly "ideal" single crystal. The superlattices, however, revealed an additional feature in the degree of texture, which was influenced by the number of superlattice periods. Omega scans of the (002) reflections showed a high degree of out-of-plane orientation with increasing rocking curve widths of 0.69, 1.50, and 4.51 degrees for superlattices with 50, 100, and 200 periods, respectively. A rapid broadening of the (111) phi-scan peaks also was observed for a superlattice with 200-versus-100 periods, which indicated a departure from simple cube-on-cube epitaxy to the formation of 2 or even 3 domains.

In terms of material performance, CeO_2:20%Sm films possessing a high degree of texture were found to have both enhanced ionic conductivity and lower activation energy. The conductivity as a function of temperature and film thickness was determined for highly textured CeO_2:20%Sm films. The data obtained for a 3.36-µm-thick film correlates well with the conductivity reported for bulk single crystals and indicated no scaling effect, which is not surprising given its thickness. The effect of the film thickness was observed for 85- and 20-nm-thick specimens. This data showed that the in-plane conductivity of CeO_2:20%Sm exhibited a nanoscale-thickness effect with the highest conductivity recorded for a film thickness of 20 nm, which is more than one order of magnitude higher than for bulk crystalline specimens.

The observed thickness effect on the ionic conductivity was exploited in CeO_2:20%Sm/CeO_2 superlattices, which enhance the effect by increasing the interfacial area versus that achieved in a single-layer film. The material performance was assessed in a single-chamber solid oxide fuel cell, which was constructed using the superlattice thin films with selected numbers of CeO_2:20%Sm/CeO_2 periods. The performance of these cells, along with a single-layer cell, is presented in Fig. 1. As can be seen, the steady-state open circuit voltage is around 0.6 V when the cell was operated at 600ºC in 10% propane (air balance) gas mixture.

The insets within the figure present discharge curves and power/current density curves as determined for both a CeO_2:20%Sm single layer and CeO_2:20%Sm/CeO_2 superlattices with 50 and 100 periods of solid electrolytes. The internal resistances of the cells were determined from the linear part of voltage-current characteristics. The results showed that these resistances are reduced as desired with the increasing number of the superlattice periods. In the case of a superlattice film with 100 periods, the internal resistance is nearly 6 times lower than that for the CeO_2:20%Sm single-layer film. This reduction in the superlattice internal resistance leads to an increase in the power density that can be achieved. As can be seen in Fig. 1, a power density of only 20 mW/cm² was obtained for a 3.36-µm-thick single-layer film, which is in good agreement with data recently reported for a 1-mm-thick CeO_2:20%Sm microcrystalline electrolyte (Stefan et al. 2004). On the other hand, a value of 70 mW/cm² was achieved for the CeO_2:20%Sm/CeO_2 superlattice with 100 periods, which illustrates the potential of nanoscaled thin-film oxygen conductors for energy conversion.

Benefits

As demonstrated in this project, highly textured CeO_2:20%Sm thin films with thicknesses < 80 nm exhibit significantly enhanced ionic conductivity. The highest conductivity value (1 S/cm at 800ºC) was observed with a 20-nm-thick film, which is over one order of magnitude larger than that for bulk single crystals. Increased conductivity was also observed in superlattice structures with alternating 30 nm CeO_2:20%Sm and 20 nm CeO_2 layers for which the increased interfacial area results in substantial increases in conductivity. These advanced nanoscale ionic conductors were also evaluated as solid electrolytes in single-chamber solid oxide fuel cells. The results reveal that the cell performance is improved

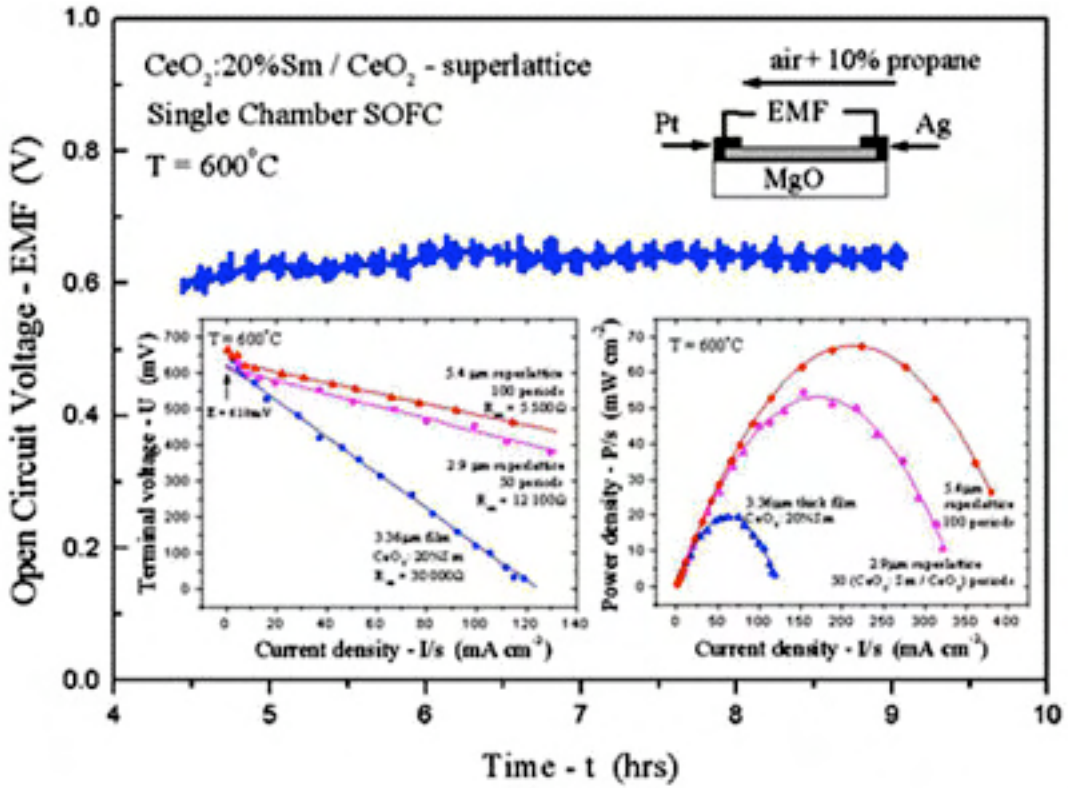

Fig.1 Time-dependent open circuit voltage of single-chamber solid oxide fuel cell using a CeO_2:20%Sm/CeO_2 superlattice electrolyte operated at 600ºC. The inset presents the schematic of the fuel cell and its performance curves for I-V discharge and power density, as determined for a single-layer CeO_2:20%Sm thin film and for superlattices with 50 and 100 CeO_2:20%Sm/CeO_2 periods.

significantly by the use of the superlattice electrolyte. In addition, considerable understanding was gained of factors influencing the thin-film quality that can be achieved by the laser ablation process, which now allows us to reliably fabricate highly textured CeO2:Sm and superlattice CeO2:20%Sm/CeO2 structures that exhibit novel ionic conductivity behavior.

The advanced concepts for oxide electrolytes developed within this project can have a major impact on various fuel cell programs (e.g., the DOE Fossil Energy fuel cell program). Novel nanoscale solid electrolytes offer a promising option for single chamber fuel cells operating at temperatures below 700ºC. These findings should also benefit the DARPA Micro Power Generation and the Palm Power programs.

References

Hibino, T. K., A. Hashimoto, T. Inoue, J-I Tokuno, S-I Yoshida, and M. Sano. 2000. "A Low-Operating Temperature Solid Oxide Fuel Cell in Hydrocarbon-air Mixtures," *Science* **288**(5473), 2031–2033.

Kosacki, I., and H. U. Anderson. 2001a. "Mixed Conductivity in Nanocrystalline Oxide Thin Films," Electrochemical Society Proceedings, vol. 2001–8, The Electrochemical Society, Inc., Pennington, N.J., pp. 238–251.

Kosacki, I., and H. U. Anderson. 2001b. "Grain Boundary Effects in Nanocrystalline Mixed Conductors," pp. 3609–3617 in *Encyclopedia of Materials: Science and Technology*, vol. 4, Elsevier Science Ltd., N.Y.

Kosacki, I., H. U. Anderson, Y. Mizutani, and K. Ukai. 2002. "Nonstoichiometry and Electrical Transport in Sc-doped Zirconia," *Solid State Ionics* **152–153**, 431–438.

Kosacki, I., C. M. Rouleau, P. F. Becher, J. Bentley, and D. H. Lowndes. 2004a. "Surface/Interface-Related Conductivity in Nanometer Thick YSZ Films," *Electrochemical and Solid-State Letters* **7**(12), A459–A461.

Kosacki, I., C. M. Rouleau, P. F. Becher, J. Bentley, and D. H. Lowndes. 2004b. "Nanoscale Effects on the Ionic Conductivity in Highly Textured YSZ Thin Films," *Solid State Ionics* (in press).

Sata, N., K. Eberman, K. Ebert, and J. Maier. 2000. "Mesoscopic Fast Ion Conduction in Nanometer-scale Planar Heterostructures," *Nature* **408**, 946–948.

Stefan, I. C., C. P. Jacobson, S.J. Visco, and L. C. De Jonge. 2004. "Single Chamber Fuel Cells: Flow Geometry, Rate and Composition Consideration," *Electrochemical and Solid State Letters* **7**(7), A198–A200.

Alkali Silicate and Related Glasses as Novel Hydrogen Storage Materials

L. R. Riciputi,[1] D. R Cole,[1] L. M. Anovitz,[1,2] B. L. Armstrong,[3] P. F. Britt,[1] M. Fayek,[1,2] and J. Pickel[1]
[1]*Chemical Sciences Division*
[2]*University of Tennessee*
[3]*Metals and Ceramics Division*

Experiments were undertaken to determine if hydrogen, dissolved incongruently in glass at low temperatures after exposure of the glass to water vapor, could be released from the glass with heating and to determine if hydrogen evolved during heating. Several glass compositions were studied, and time-series hydration and dehydration experiments were conducted. Secondary ion mass spectrometry (SIMS) analysis confirms that hydrogen is added to the glass without uptake of oxygen and furthermore demonstrates that the hydrogen is released from the glass with heating. Coupled Thermogravimetric Mass Analysis and Mass Spectrometry (TGA-MS) analysis indicates mass loss from gases evolved upon heating measured approximately wt 3–5%. The TGA-MS technique did not have the sensitivity to definitively measure hydrogen evolution from the glasses, but the suggestion of hydrogen (or labeled deuterium) release was present in a number of experiments. These results suggest that hydrogen can be rapidly stored and released from alkali-silicate and related glasses and that these materials may provide an alternate hydrogen storage material.

Introduction

We have discovered that at low temperatures, water apparently dissolves incongruently in glass, exhibiting a large uptake of hydrogen without concomitant addition of oxygen, suggesting that silicate-like glasses might be used for storing large amounts of hydrogen. The EERE Hydrogen Strorage Technical Team expressed significant interest in the potential of this technology but posed several fundamental questions to be addressed before further consideration of funding to develop the proposed concept. Three were related to verification of the observations, including (a) if the glass is being exposed to steam and only H_2 enters the glass, can you measure the O_2 that should be generated by this process; (b) can we measure the rate of H_2 outgassing, and thus the rate at which H_2 may be delivered; and (c) what are the effects of pressure on the rate and extent of H_2 uptake, and one was related to the potential of the method; (d) by varying pressure, temperature and, most importantly, glass composition, how much additional improvement may be achievable in the volumetric and gravimetric energy densities?

With these questions in mind, we undertook the following:

(1) Obtain a more chemically varied suite of glasses to examine glass composition controls.
(2) Undertake a series of hydration and dehydration experiments on powders and solid blocks of the glass materials.
(3) Use a new SIMS methodology to improve the precision of oxygen and hydrogen analysis to more definitively address the hydrogen uptake question, and to examine dehydration experiments.
(4) Use TGA-MS to study the weight loss and composition of gases evolved during heating of hydrated glasses to try to identify degassing of hydrogen.

Technical Approach

We expanded our efforts beyond the natural Pachuca obsidian glass used in our original experiments. Additional materials included NBS620, a soda-lime glass; NBS1411, a borosilicate glass, and two ORNL-prepared lithium magnesium silicate glasses, 16Li10Mg74Si and 50Li10Mg40Si (where the numbers refer to mol % Li_2O, MgO, and SiO_2). Samples of each glass were ground into wafers ~2 mm thick, polished on both sides, cleaned and cut into blocks 2–3 mm on a side. Powdered samples of each glass composition were also prepared

Two sets of time-series hydration experiments were performed in saturated water vapor. The first, in which the glasses were hydrated at 200°C for two weeks used all four glass compositions. The second, run at 150°C for two days, used all the glasses except Pachuca obsidian, using normal or deuterated water. Subsets of the hydrated blocks were then heated under dry conditions (150ºC) to prepare time-series samples for SIMS analysis to determine if the hydrogen was released from the samples.

SIMS analyses were performed using a Cs^+ primary beam and monitored H^-, O^-, $^{18}O^-$, $(^{18}O+H)^-$ (mass 19), $^{30}Si^-$ secondary ions with extreme energy filtering of 300 eV. The ~6 nA primary ion beam was rastered over a 125- × 125-µm area. An electron flood gun was used to neutralize the positive charge buildup on the sample surface and enhance secondary ion emission. The masses

were normalized relative to $^{30}Si^-$ and plotted versus depth. There are several advantages using a Cs^+ primary beam and a 300-eV energy offset: (1) both H and O can be monitored within the same analytical session, with no effects from O implantation, and (2) hydride interferences are reduced or eliminated.

Initial TGA-MS experiments used the standard configuration, with TGA and MS instruments connected by a fused-silica capillary tube which is surrounded by a larger, heated tube (200ºC). However in later experiments, the capillary was removed from the shroud, and 12 inches were placed in a low-temperature Dewar so water could be trapped prior to the MS. Samples of approximately 60 mg (where possible to maintain consistency) were heated in 100-µL ceramic pans under an inert gas, usually argon (Air Liquide 99.999%), although nitrogen was used for certain experiments with D_2O hydrated materials so that mass signal 20 might be observed. An oxygen trap was place in the gas line. Factors which affected the sensitivity of the instrument such as position of the capillary with respect to the pan, heating rate, and MS sampling rate were optimized to increase the sensitivity of the instruments to low-molecular-weight gases.

Results and Discussion

The results of the first experiments, performed at 200°C for two weeks, were dramatic. Except for the Pachuca sample, each glass showed significant swelling, surface and interior opacity, and, in some cases, the cubes had stuck together or split, indicating tremendous material uptake over a short period of time. This made all of the synthetic glasses unsuitable for SIMS analysis, and another experiment was performed at lower temperatures and for shorter times (150°C for 2 days). The results of this experiment were suitable for SIMS analysis, and all sample blocks and powders were sealed in small plastic or glass bottles and stored in a freezer until analyses could be performed.

SIMS analyses were performed on both hydrated and dehydrated glasses using the new Cs^+ primary beam analytical protocol. The results on hydrated samples confirmed our earlier observations—that significant amounts of hydrogen are being added to the glass without addition of significant oxygen. Our observations on the dehydration experiments are even more important. They indicate that the excess hydrogen has been completely removed from the glass, demonstrating that hydrogen can be released at rates and temperatures similar to the hydrogen uptake.

Our attempts to use TGA-MS to monitor evolution of hydrogen and other gases from hydrated glasses as a function of heating were technically challenging, and in the end, the results were intriguing but not conclusive. A number of analytical problems were encountered. These included the relatively small signals expected from these samples coupled with the poor sensitivity of the mass spectrometer for hydrogen and deuterium and interferences from the large amounts of water that were adsorbed on the powdered glass surfaces and in the system itself. The presence of adsorbed water proved particularly problematic, as decomposition of water during the ionization process in the mass spectrometer itself could lead to "false" hydrogen signals. We made modifications to both our experiments (using deuterium to provide labeled tracer that could be distinguished from background hydrogen) and to the analytical procedures, including extending purge times and incorporating a cold trap before the gases were inlet to the mass spectrometer to purge the off-gas of water. The cold-trap worked to purge most of the water from the gas flow but, unfortunately, resulted in a far less stable baseline for hydrogen and deuterium, making it much more difficult to conclusively distinguish the expected hydrogen signal from noise fluctuations. Even after all of these steps were taken, signals at mass 3 (HD) were observed in many of the experiments using deuterated materials, suggesting that hydrogen/deuterium exchange was occurring in the analytical system. This was confirmed using D_2O or H_2O standards and could only be eliminated after purging the system with argon for 3–4 days. We have to conclude that the TGA-MS method does not meet the requirements for sensitivity necessary for reliably and definitively measuring hydrogen/deuterium evolution at the low levels required for this project. This is not particularly surprising, as we proposed to build more sophisticated experimental equipment allowing in-situ measurement of hydrogen/deuterium in the full project, but TGA-MS offered the only potential route for meeting the Seed Money Committee's challenge.

In spite of the technical problems with the TGA-MS, our efforts did result in a number of intriguing observations. Mass loss stemming from evolution of adsorbed water or D_2O (measured during purge stage) varied from 0.2% for obsidian to ~40% for NBC620. Mass loss from gases evolved upon heating measured approximately 3–5% (of original pre-purge weight) for all samples. Mass spectral results indicated a significant loss of entrapped/absorbed water upon commencement of the heating ramp (after purge period). Although much smaller than the water signals, peaks indicating hydrogen/deuterium evolution from the glass were observed in some samples. As discussed above, definitive interpretation of these results is complicated by analytical considerations and the fact that we are near the limit of detection for the system, but the results are encouraging and consistent with the SIMS results.

To summarize, our results are consistent with our original contention that alkali-silicate-like glasses may provide a novel hydrogen storage material, but we have

been unable to definitively prove the release of actual hydrogen gas due to experimental limitations with available equipment. The SIMS results indicate that hydrogen can both be input and released from the glass at approximately the same rate, on a time scale of minutes at the nanoscale. There was not enough resource to carry out time-series SIMS analyses to allow definitive release rates to be determined, but the experiments required were conducted so samples are ready and can be analyzed if additional funding is provided. While not definitive, the TGA-MS results suggest that hydrogen may be evolved from the glasses, but more sensitive methods (beyond the scope of Seed Money funding) will be required to obtain quantitative and reproducible data.

Benefits

Our results suggest that hydrogen can be stored and released from alkali-silicate glasses. This observation has important implications for hydrogen production and, in particular, hydrogen storage. Using silicate glasses may overcome many of the limitations of current hydrogen storage technologies because it is a low-cost, lightweight medium for high-capacity(~3 wt % and higher) hydrogen storage. Such a system could have a tremendous impact on advancing the deployment of hydrogen fuel transportation vehicles (such as fuel cell or hydrogen IC engine vehicles), or in other applications requiring remote power production and supply (e.g., military/IC). Our work has also resulted in a better understanding of the fundamental mechanisms of hydration processes and transport in glasses.

Biaxial Flexure Test of Multilayers

C. H. Hsueh
Metals and Ceramics Division

Biaxial flexure tests have been used extensively to determine the strengths of monolithic brittle materials. On the other hand, they have not been used to determine the strengths of multilayer structures as analytical solutions for calculating strengths in such systems are not available. In order to characterize the biaxial strength of multilayers, we have developed an analytical model to derive the general closed-form solutions for the elastic stress distributions in multilayered disks subjected to biaxial loading and used finite-element analyses to verify our results. Not only do our closed-form solutions provide a basis for evaluating the biaxial strength of multilayered systems, they also show that fracture can initiate from any layer under tension depending upon the strength of the individual layers and the stress distribution.

Introduction

Multilayered structures have extensive applications as microelectronic, optical, structural, and biological components. To ensure the functionality and reliability of multilayered systems, it is essential to understand the geometrical and material factors that influence their strength. Uniaxial strength tests, such as three- or four-point bending of bars, have been used extensively in the past to determine the strength of brittle materials. However, the measured strength depends on both the surface and the edge finishing conditions, and it is very difficult to eliminate undesirable edge failures (Wachtman 1972, Ritter 1980). On the other hand, biaxial flexure tests involve supporting a thin plate on three or more points near its periphery and equidistant from its center and loading a central portion. The area of maximum tensile stress thus falls at the center of the plate surface, and the measured strength is independent of the condition of the plate edges. Also, components are generally subjected to multiaxial loading during service applications, and biaxial strength data are more useful than the uniaxial strength data for component design. As a result, biaxial flexure tests, such as ball-on-ring (or ball-on-three-ball), ring-on-ring, and piston-on-three-ball tests, are becoming increasingly popular as a means of measuring the strength of brittle materials (Shetty 1980). However, the stress analyses for biaxial flexure tests are very complex even for monolithic materials, and the existing solutions are limited to the case of monolithic materials. While finite-element analysis (FEA) provides a powerful means for analyzing stress fields in complex multilayered systems, it suffers from the drawback that it is a case-by-case study and computation must be performed for each change in geometrical parameters and material properties. Hence, in order to determine the biaxial strength of multilayer systems, it is essential to develop an analytical model to analyze this problem. Here, we derived a closed-form solution to relate the strength to the fracture load for multilayered disks tested in biaxial flexure and verified our analytical results by FEA.

Technical Approach

A thin multilayered disk is considered. A diametrical section through the axis of symmetry of the multilayered disk is shown schematically in Fig. 1(a). The disk consists of n layers with individual thicknesses t_i where the subscript i denotes the layer number with layer 1 being at the bottom of the disk. The cylindrical coordinates r, θ, and z are used. The bottom surface of layer 1 is located at $z = 0$, the interface between layers i and i+1 is located at h_i, and the top surface of layer n is located at $z = h_n$. With these definitions, h_n is the thickness of the disk, and the relation between h_i and t_i is described by

$$h_i = \sum_{j=1}^{i} t_j \quad (i = 1 \text{ to } n) \ . \tag{1}$$

The disk is subjected to a biaxial flexure load, and the case where the interfaces between layers remain bonded during the test is considered. The stress distributions in multilayered disks can be determined from the force and moment equilibrium conditions coupled with the existing solutions for monolayered disks, and the results are briefly described below. The detailed description of the derivations has been submitted for publication (Hsueh 2004a, Hsueh 2004b).

The radial and tangential stresses, σ_r and σ_θ, in monolayered disks subjected to biaxial flexure have been derived (Shetty 1980). We found that the solutions for multilayered disks can be obtained from those for monolayered disks by replacing the position of the neutral surface and the flexural rigidity of the specimen, such that the radial and tangential stresses in the i-th layer, σ_{ri} and $\sigma_{\theta i}$, are

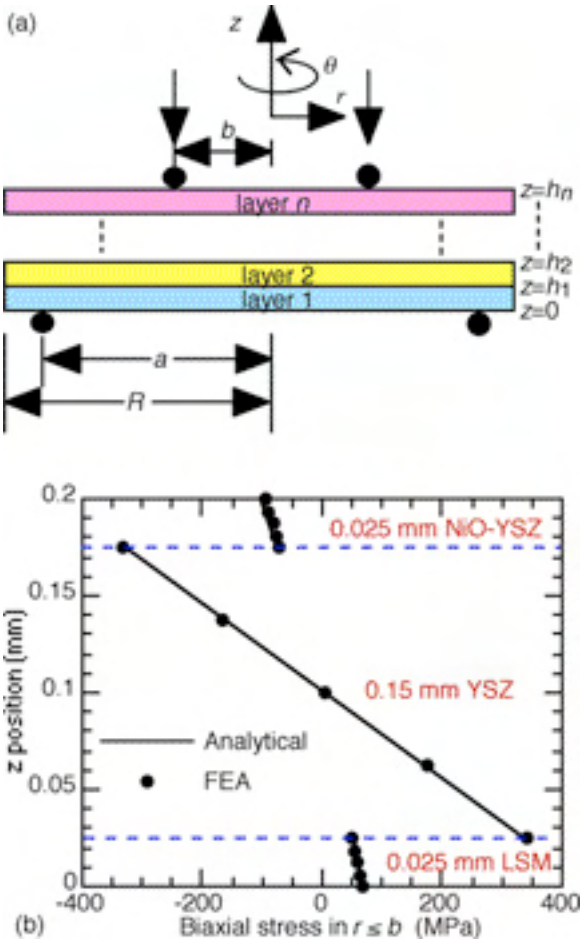

Fig. 1. (a) Schematic of the diametrical section through the axis of symmetry of a multilayered disk subjected to ring-on-ring tests, and (b) biaxial stresses, σ_{ri} (=$\sigma_{\theta i}$), in the region of $r \leq b$ through the thickness of an LSM/YSZ/NiO-YSZ trilayered disk subjected to ring-on-ring tests showing the comparison between analytical and FEA results.

$$\sigma_{ri} = F_i \sigma_r \text{ and } \sigma_{\theta i} = F_i \sigma_\theta \quad (i = 1 \text{ to } n). \tag{2}$$

The modification factor, F_i, is given by

$$F_i = \frac{E_i h_n^3}{12\left(1-\nu_i^2\right)D} \quad (i = 1 \text{ to } n), \tag{3}$$

where E and ν are Young's modulus and Poisson's ratio, respectively, and D is the flexural rigidity of the multilayer, such that (Hsueh 2004b)

$$D = \sum_{i=1}^{n} \frac{E_i t_i}{1-\nu_i^2}\left[h_{i-1}^2 + h_{i-1}t_i + \frac{t_i^2}{3} - \left(h_{i-1} + \frac{t_i}{2}\right)z_n\right] . \tag{4}$$

The position of neutral surface, z_n, is involved in Eq. (4), and it is given by (Hsueh 2004b)

$$z_n = \sum_{i=1}^{n} \frac{E_i t_i}{1-\nu_i^2}\left(h_{i-1} + \frac{t_i}{2}\right) \Big/ \sum_{i=1}^{n} \frac{E_i t_i}{1-\nu_i^2} . \tag{5}$$

For the case of ring-on-ring tests, the specimen is supported by an outer ring and loaded with a smaller coaxial inner ring. The approximate analytical solutions for stress distributions in monolayered disks have been obtained, and the maximum stresses occur in the central region, such that (Shetty 1980)

$$\sigma_r = \sigma_\theta = \frac{-3P\left(z - \frac{h_n}{2}\right)}{2\pi h_n^3}\left[2(1+\nu)\ln\left(\frac{a}{b}\right) + \frac{(1-\nu)(a^2-b^2)}{R^2}\right]$$

(for $r \leq b$), (6)

where P is the load, and a, b, and R are the radii of outer ring, inner ring, and the disk, respectively. When Eq. (6) is extended to the multilayer case, ν should be regarded as the average Poisson's ratio of the disk, such that

$$\nu = \frac{1}{h_n}\sum_{i=1}^{n} \nu_i t_i \quad . \tag{7}$$

The stress distributions in the central region of multilayered disks subjected to ring-on-ring tests are

$$\sigma_{ri} = \sigma_{\theta i} = \frac{-3F_i P(z - z_n)}{2\pi h_n^3}\left[2(1+\nu)\ln\left(\frac{a}{b}\right) + \frac{(1-\nu)(a^2-b^2)}{R^2}\right]$$

(for $r \leq b$ and $i = 1$ to n). (8)

Depending upon the comparison between the strength of the individual layers and the stress distribution through the thickness of the multilayer during loading, cracking can initiate from any layer that is under tension. Using Eq. (8), the biaxial strength of multilayered systems can be obtained from the fracture load.

Results and Discussion

Specific results are calculated using materials properties pertinent to a typical solid oxide fuel cell (SOFC) trilayer subjected to ring-on-ring loading in order to elucidate the essential trends. The SOFC trilayer consists of $La_{0.75}Sr_{0.2}MnO_3$ (LSM) cathode layer of 25-μm thickness (E = 35 GPa, ν = 0.25), yttria-stabilized zirconia (YSZ) electrolyte layer of 150 μm thickness (E = 215 GPa, ν = 0.32), and NiO-YSZ anode layer of 25-μm thickness (E = 55 GPa, ν = 0.17). The specimens have a radius R of 25 mm. The supporting and the loading rings have radii of a = 19 mm and b = 4.75 mm, respectively, and a load P of 10 N is applied to the specimen through the inner loading ring. Both the analytical and FEA results are calculated.

For the LSM/YSZ/NiO-YSZ trilayered disk, modeling is performed such that LSM is the tensile layer, that is, layer 1 in Fig. 1(a). The biaxial stress, $\sigma_{ri} = \sigma_{\theta i}$, in the region of $r \leq b$ and through the specimen thickness is shown in Fig. 1(b). The stress is linear through the

thicknesses in each individual layer; however, because of different elastic properties among the three layers, the stress is discontinuous at the interfaces and the stress gradients are different among the three layers. Good agreement between the analytical and the FEA results validates the present closed-form solutions for multilayers. In this trilayer-case, the greatest tension does not occur at the tensile surface of the specimen; instead, it exists at the lower surface (closest to exterior tensile surface) of the middle layer. This is because the YSZ layer is much stiffer than the LSM layer. Depending upon the comparison between the strength and the maximum tension in each layer, cracking can initiate in the inner layer instead of at the tensile surface of the specimen. Also, detailed comparison between analytical and FEA results shows that the analytical solutions slightly under-predict the magnitude of stresses in the YSZ layer and over-predict the magnitude of stresses in both the LSM and the NiO-YSZ layers. This is because the difference in Poisson's ratio between layers is ignored for analytically determining the position of the neutral surface as an average Poisson's ratio of the trilayer v [see Eq. (7)] is used. While the NiO-YSZ layer has the biggest difference between v_i and v among the three layers, it incurs the biggest discrepancy between the analytical and FEA results. Further analyses show that this discrepancy can be compensated by multiplying stresses given by Eq. (8) by a factor $(1+v_i)/(1+v)$ (Hsueh 2004b).

Benefits

Our closed-form solutions enable researchers to measure strength of multilayers using biaxial flexural tests which, in turn, will strengthen ORNL's position as a leader in characterizing multilayer strength. Depending upon the strength of the individual layers and the stress distribution through the thickness of the multilayer during testing, cracking can initiate from any layer under tension. Measurement of biaxial flexural strength of multilayered systems is important for environmental barrier coatings in the DOE Distributed Energy Resources Program. It is also important for the development and design of SOFCs. Specifically, because the electrodes in an SOFC are very porous in order to allow gas transport during applications, they cannot self-sustain to allow strength measurements, and a multilayered structure is required.

References

Hsueh, C. H., M. J. Lance, and M. K. Ferber. 2004a. "Stress distributions in thin bilayer discs subjected to ball-on-ring tests," submitted to *J. Am. Ceram. Soc*.

Hsueh, C. H., C. R. Luttrell, and P. F. Becher. 2004b. "Modeling of multilayered disks subjected to biaxial flexure tests," submitted to *J. Appl. Phys.*

Ritter, J. E., Jr., K. Jakus, A. Batakis, and N. Bandyopadhyay. 1980. "Appraisal of biaxial strength testing," *J. Non-Cryst. Solids* **38/39**, 419–424.

Shetty, D. K., A. R. Rosenfield, P. McGuire, G. K. Bansal, and W. H. Duckworth. 1980. "Biaxial flexure tests for ceramics," *Am. Ceram. Soc. Bull.* **59** (12) 1193–1197.

Wachtman, J. B., W. Capps, and J. Mandel. 1972. "Biaxial flexure tests of ceramic substrates," *J. Mater.* **7**, 188–194.

Alanates for High-Capacity Hydrogen Storage

J. H. Schneibel,[1] D. S. Easton,[2] S. Babu,[1] and S. A. Speakman[1]
[1]*Metals and Ceramics Division*
[2]*Consultant, Metals and Ceramics Division*

The improvement in the decomposition kinetics of Na_3AlH_6 milled with $TiCl_3$, as compared to Na_3AlH6 prepared by decomposition of $NaAlH_4$ milled with $TiCl_3$, has been studied. The hydrogen desorption of sodium and lithium alanates ($NaAlH_4$ and $LiAlH_4$) ball-milled with more stable sodium borohydride and lithium borohydride ($NaBH_4$ and $LiBH_4$), in addition to a $TiCl_3$ catalyst, has been examined by temperature-programmed desorption. During ball-milling, $LiAlH_4$ with 2 mol% $TiCl_3$ decomposes into Li_3AlH_6. Additions of $NaAlH_4$, $NaBH_4$, and $LiBH_4$ prevent this decomposition, even in concentrations as small as 2 mol%. Investigations are under way to determine whether this effect is related to improved thermodynamic stability or to slower decomposition kinetics.

In its quest for a reduced dependence on foreign oil supplies as well as a cleaner environment, the Bush administration has proposed the FreedomCar (Freedom Cooperative Automotive Research) project. Its long-term goal is to develop technologies for hydrogen-powered fuel cell cars and trucks. This investigation focuses on a particularly important issue of this project, namely, hydrogen storage. The objective is to develop storage materials which can absorb and desorb large amounts of hydrogen (e.g., 10 wt%) at near-ambient conditions.

Alanates (i.e., materials containing AlH^{4-} ions, such as for example $LiAlH_4$) are prepared by high-energy ball milling of powder precursor materials. Small quantities of elements or compounds with catalytic activity are added to improve the absorption/desorption kinetics ("micro-alloying"). Macro-alloying (i.e., ≈1 wt% and above) is carried out with the aim of shifting the absorption/desorption conditions closer to ambient temperatures and pressures.

The decomposition of Na_3AlH_6 milled with $TiCl_3$ occurs at lower temperatures than that of Na_3AlH_6 prepared by decomposition of $NaAlH_4$ milled with $TiCl_3$. Thermal programmed desorption experiments, in which the temperature is slowly ramped up while the hydrogen desorption is monitored, have been carried out to verify this effect. Interestingly, desorption studies carried out by in situ x-ray analysis with a time resolution of approximately 1 minute indicated that additional $NaAlH_4$ formed during the initial decomposition of Na_3AlH_6 into NaH, Al, and H_2. Thermodynamically, this result is not expected. While the reasons are not yet understood, our result illustrates the complexity of the decomposition of alanates.

The thermal programmed desorption of binary mixtures of sodium alanate ($NaAlH_4$), lithium alanate ($LiAlH_4$), sodium borohydride ($NaBH_4$) and lithium borohydride ($LiBH_4$) was studied. The mixtures were produced by ball-milling, and in each case 2 mol% $TiCl_3$ was added to improve the kinetics of decomposition. $NaAlH_4$ is more stable than $LiAlH_4$, and $NaBH_4$ and $LiBH_4$ are more stable than the alanates. Generally, the desorption temperatures of $NaAlH_4$ were not influenced significantly by alloying. $LiAlH_4$ doped with $TiCl_3$ decomposes into Li_3AlH_6 during ball-millling. Additions of $NaAlH_4$, $NaBH_4$, and $LiAlH_4$ as small as 2 mol% prevent this decomposition from occurring. It is not clear yet whether this is due to a slowing down of the kinetics of decomposition, or whether the mixtures are thermodynamically more stable than $LiAlH_4$-2 mol% $TiCl_3$. Hydrogen charging of the decomposition products (Li_3AlH_6, LiH and Al) has not been successful to date. In order to improve the success of hydrogen charging, a new experimental approach has been developed. It consists of ramping up the temperature in vacuum until decomposition occurs, applying the maximum hydrogen pressure allowable for our system (200 atm), and slowly ramping down the temperature. Drops in the pressure at a specific temperature will indicate hydrogen absorption at that temperature.

If improved hydrogen storage capacities can be obtained, and if absorption and desorption occur at close-to-ambient conditions, this project will benefit the Energy Efficiency and Renewable Energy (EERE) program of DOE.

Enhancing Performance of Hydrogen Storage Materials through Nanoscale Design

V. K. Sikka,[1] G. Muralidharan,[1] N. C. Gallego,[1] T. M. Besmann,[1]
T. J. Huxford,[1] and M. P. Paranthaman[2]
[1]*Metals and Ceramics Division*
[2]*Chemical Sciences Division*

Insufficient gravimetric capacities and slow hydriding/dehydriding kinetics have been recognized as hurdles to be overcome in the quest for future hydrogen storage materials. The objective of this project is to examine a novel approach for enhancing the hydriding/dehydriding kinetics based on the use of nanometer-thick films. The feasibility of this approach will be studied by depositing films of Mg on the surfaces of a material with a large surface area and examining the hydriding/dehydriding characteristics of the resulting material. Improved kinetics and lower operating temperatures are benefits anticipated as a result of using this approach.

Background and Objective

Hydrogen storage materials are of great interest for the new national and international interest in the hydrogen economy. Based on the potential use of hydrogen storage materials in automotive applications, a storage criteria of 9 wt % of hydrogen has been set as a national goal and there are many efforts under way to develop such materials. In addition to meeting the gravimetric capacity, such materials should also be capable of adsorbing and desorbing the hydrogen at temperatures less than 100ºC at pressures of 1–10 atm. A number of metal hydrides have been studied for their potential use as hydrogen storage materials. Such studies have shown that slow kinetics of the hydriding/dehydriding reaction, high temperatures required to absorb/release the hydrogen, or insufficient storage capacities limit the use of metal hydrides.

A number of approaches, such as physical and chemical treatments, have been carried out to improve the hydriding and dehydriding kinetics of metal hydrides with limited success. Our approach to addressing this problem is based on developing a general scheme for improving the hydriding/dehydriding kinetics of all hydrogen storage materials of interest. We plan to use Mg as a model material for developing and demonstrating our concept. In addition to improving the hydriding/dehydriding kinetics using this methodology, our objective is to also achieve reduced operating temperatures in the range of 100–150ºC in such films.

Technical Approach

The core theme of our approach is the use of thin films of hydrogen storage materials with thicknesses less than 50 nm. A significant benefit in using such films is that diffusion is required only over very short distances when the surfaces of the thin films are exposed to the gas. In addition, to achieve sufficient gravimetric storage capacity, the internal surfaces of a foam-like material with a large surface area and an interconnected pore structure that is permeable to the surrounding gas medium has to be coated with the thin film that can store hydrogen. The combined use of large surface area materials as a template and that of thin film hydrogen storage material is unique and novel.

Results to Date

Significant advances have been made in the deposition of thin films this year. Both flat substrates and porous materials have been used as the substrate. Experiments on physical and chemical vapor deposition of Mg films were carried out. Physical vapor deposition was carried out by annealing the substrates along with a source of magnesium vapor. Auger electron spectra clearly show the presence of Mg, along with oxygen on the sample surface, confirming that Mg was indeed deposited on the surfaces. Chemical vapor deposition using Mg precursor [Bis(cyclopentadienyl)magnesium $(C_5H_5)_2Mg$] was carried out under different processing conditions, and the results of the deposition are currently being evaluated.

Hydrogen adsorption-desorption studies were carried out on porous material treated with Mg vapor (physical vapor deposition) by exposure to hydrogen gas at a pressure of about 1 atm and various temperatures. Experiments have proven that with appropriate pretreatment, hydrogen can be adsorbed reversibly in the samples, constituting a significant accomplishment. Untreated samples exposed to similar conditions did not show any significant adsorption of hydrogen under similar conditions. Further work is necessary to increase the hydrogen storage capacity and to evaluate and improve the kinetics of adsorption/desorption and will be part of the work this year. Data obtained will be presented to support an existing invention disclosure.

Benefits

Hydrogen storage and delivery materials are of significant interest to DOE and other federal agencies such as DARPA. If this scheme is successful, engineering hydrogen storage materials based on Mg with gravimetric capacities up to 9.3 wt % may be feasible, thus satisfying both the existing and future DOE criteria. There is also the additional advantage that, if necessary, this methodology can be applied to other hydrogen storage materials.

Selectively Enhanced Adatom Diffusion

Z. Zhang,[1] B. Wu,[1] L. C. Feldman,[2] and P. I. Cohen[3]
[1]*Condensed Matter Sciences Division, ORNL*
[2]*Vanderbilt University*
[3]*Department of Electrical and Computer Engineering, University of Minnesota*

The central idea in this project is selectively enhanced adatom diffusion (SEAD). When a laser beam is incident on a growth system, the laser frequency can be tuned to resonantly excite a specific adatom-substrate bond. Once excited, such adatoms become more mobile and easier to desorb, consequently altering the film growth kinetics. The key feature of this excitation is its selectivity: for a system consisting of different bonds, one can tune the laser frequency to excite only the desired one, leaving the rest unchanged. The different bondings can come from multiple species in the depositing materials or distinct geometric confinements. However, the feasibility of this appealing idea is yet to be firmly established due to possible complications from other physical processes in a real growth system. The goal of this proposal is to validate the principle of SEAD with extensive theoretical modeling and calculations by focusing on a prototype model system, the chemical vapor deposition (CVD) growth of silicon. Since the system is widely used in manufacturing Si-based devices, the success of our project will have immediate impact on real-life applications. Furthermore, once validated, the SEAD idea may find important applications in other growth systems as well.

In thin-film growth under laser radiation, the laser can influence the growth process in two different ways. One is laser-induced thermal excitation; that is, laser power is absorbed by the substrate and converted into thermal energy. The film growth is then affected by an increase in the substrate temperature. The other is resonant excitation. This happens when the laser couples strongly to the bonding between adatom and substrate. In this case, the adatoms can be vibrationally excited to a higher level and become more mobile and easier to desorb since the diffusion barrier is effectively reduced by the photon energy. One key difference between these two mechanisms is the selectivity of resonant excitation. In a system of film growth, there can be various bondings between adatom and substrate when the deposition material consists of multiple species or when the adatoms of the same kind experience different local geometric arrangements. With resonant excitation, the laser can be tuned to selectively excite only a specific bonding between adatoms and substrate. The consequence is that only desired adatoms are excited and become more mobile and easier to diffuse along the surface while the rest are essentially unaffected. We call it selectively enhanced adatom diffusion (SEAD). The goal of this project is to demonstrate the feasibility of SEAD in film growth and its potential applications through extensive theoretical modeling and calculations. We will accomplish this by focusing on the model system of chemical vapor deposition (CVD) growth of silicon.

Our study includes two steps. First, we use rate equation approach, with realistic system parameters and laser characteristics, to estimate the efficiency of selectively enhanced desorption of hydrogen adatoms on a stepped Si substrate under CVD environment. This part of the work has been completed and reported in a recent publication (see below). Secondly, we use first-principles calculations within density functional theory to obtain the elemental kinetic factors involved in CVD growth of Si, such as the diffusion barriers of silane on a H-terminated Si(100) surface and across a step edge. With such important input parameters, we will then carry detailed kinetic Monte Carlo simulations of CVD growth of Si, to examine the feasibility of selectively promoting step-flow growth using the SEAD idea. This is in progress, done in collaboration with Prof. Xingao Gao of Fudan University, Shanghai, China (with a joint doctoral student).

References

Wu, B. P. I. Cohen, L. C. Feldman, and Z. Y. Zhang. 2004. "Controlling film growth with selective excitation: Chemical vapor deposition growth of silicon." *Appl. Phys. Lett.* **84**, 2175.

Zhang, Z. 2004a. Materials Research Society Fall Meeting, Boston, December 2003, "Prediction of nanostructural evolution from first principles."

Zhang, Z. 2004b. Applied Mechanics Colloquium, Harvard University, "An atomistic view of the formation and stability of surface-based nanostructures."

Zhang, Z. 2004c. Workshop on Frontier Topics in Condensed Matter Physics, Zhengzhou University (Zhengzhou, China, July 2004). "An atomistic view of the formation and stability of surface-based nanostructures."

Development of the "Ultimate Scanning Tunneling Microscopy" for the Center for Nanophase Materials Science

R. Jin,[1] J. Wendelken,[1] and E. W. Plummer[2,1]
[1]*Condensed Matter Sciences Division*
[2]*Department of Physics and Astronomy, The University of Tennessee*

Advancing knowledge and understanding the phenomena at the nanometer level requires techniques capable of "seeing" at this scale. The most utilized technique to visualize objects and probe spectroscopy at the nanoscale is scanning tunneling microscopy/spectroscopy (STM/S). The objective of this project is to develop an ultra-sensitive STM with new capabilities that will provide low temperature, high magnetic field, and optical capabilities. To test each of the design features, we propose to study three specific problems of current scientific interest for which the capabilities of low temperature, a high magnetic field, and light are critical.

The objectives of this project is to develop an ultrasensitive scanning tunneling microscope (STM) with low-temperature, high magnetic fields and optical capabilities. In this joint project with the University of Tennessee, we will add a high magnetic environment to the new ultra-stable, low-temperature STM in the Center for Nanophase Material Science (CNMS). As part of the development effort, we will conduct three experiments to test our design and demonstrate the utility of this device: (1) microscopic electronic-phase separations in strongly correlated transition-metal oxides, (2) studies of coupling between magnetic-dot assemblies and nonmagnetic metallic substrates, and (3) magnetic-field-induced quantum critical phenomena.

Preliminary (low-field) experiments will be conducted using the low-temperature STM provided by our collaborators, while our "Ultimate STM" is being constructed.

Development of the special experimental capabilities called for in this project is now well advanced. The new design allowing for a cryogenic STM that rotates with the sample with respect to a high magnetic field has been completed. While the magnet has been ordered, the STM head is being built in house in collaboration with Prof. S. Pan at the University of Houston. The next modification to be designed is provision for optical access to the sample while on the STM stage. This capability will now be incorporated in a second STM head that will operate at 4 K rather than 300 mK as with the first head. The decision to create two separate, but interchangeable, STM heads arises from consideration of the heat load induced by the optical access, the extreme mechanical complexity of the system that would include both a He_3 refrigerator and optical access, and the lack of a clear need to provide both capabilities simultaneously.

To test the STM performance at low temperatures, we have measured scanning tunneling microscopy and spectroscopy of quasi-one-dimensional Li purple bronze ($Li_{0.9}Mo_6O_{17}$) down to 4 K using our collaborator's instrument, which has similar features to ours. The measurements yield highly reproducible spectra at each fixed temperature, indicating that the temperature can be well controlled with reasonable stability. More importantly, our experimental results reveal that the density of states and tunneling amplitude of $Li_{0.9}Mo_6O_{17}$ approach zero at the Fermi energy with a power-law behavior, in complete agreement with theoretical prediction based on the assumption that the material is a Luttinger Liquid. Our finding strongly suggests that the ground state of $Li_{0.9}Mo_6O_{17}$ is a Luttinger liquid rather than a Fermi liquid. A paper for publication is in progress.

The STM is the only tool capable of "seeing" the electronic behavior at the nanometer level. Gaining the skills to fully utilize the new capabilities of our "ultimate STM" in a high-magnetic-field, cryogenic environment will be the key to attracting the best scientists in the world to use the instrument at CNMS.

Real-Space Imaging of High-Frequency Transport on the Nanoscale

S. V. Kalinin,[1] V. Meunier,[2] A. P. Baddorf, [1] M. B. Nardelli,[2] and D. Geohegan[1]
[1]*Condensed Matter Sciences Division*
[2]*Computer Science and Mathematics Division*

Technological and commercial viability of nanoscale electronic devices based both on conventional semiconductors and emerging materials such as carbon nanotubes requires operation at GHz range and higher frequencies. The progress in nanoscale science thus necessitates the development of tools capable of characterization of transport behavior in this high-frequency regime, ideally extendable to THz and optical regimes. The objective of this project is the development of scanning probe microscopy (SPM) approach based on the frequency mixing phenomena that allows real-space imaging of high-frequency transport within a single nanoscale device structure.

The progress in nanoscience and nanoelectronics requires development of techniques capable of characterization of high-frequency transport properties on the nanoscale. The often inhomogeneous nature of transport in the low-dimensional nanoscale systems, including both contacts and defects in carbon nanotubes and oxide nanowires and intrinsic physics of mesoscopic conductors, necessitates spatially resolved transport measurements using variants of scanning probe microscopy techniques. The initial progress in this field was achieved by the development of scanning impedance microscopy (SIM) in 2001 by one of us (SVK). However, SIM is limited by (a) ~2-MHz bandwidth of the optical detector in beam-deflection SPMs and (b) the presence of the linear stray capacitances in the circuit due to cabling, electrodes, etc., such that the system capacitance is

$$C = C_{nano} + C_{stray},\ C_{stray} >> C_{nano}.$$

To extend scanning probe microscopy to imaging high-frequency transport phenomena on the nanoscale, we suggested a novel approach, further referred to as scanning frequency mixing microscopy (SFMM), based on the frequency mixing between two high-frequency signals at frequencies ω_1 and $\omega_1 + \delta\omega$. The non-linear transport behavior at the electroactive interfaces will result in local frequency mixing and generation of difference and sum harmonic of the applied signal. In particular, response at the difference frequency $\delta\omega$ is chosen such as to coincide with primary resonance of the cantilever, providing an amplification of the weak mixed signal. The carrier frequency ω_1 can be chosen arbitrarily high, thus providing access to the high-frequency transport properties. Moreover, this mode of detection is sensitive to the voltage derivative of capacitance dC/dV. In this case, due to linearity of stray capacitances,

$$dC/dV = dC_{nano}/dV + C_{stray}/dV = dC_{nano}/dV,$$

providing direct measurement of the intrinsic capacitance of the device.

As a test of SFMM concept, we have experimentally demonstrated the formation of sum and difference frequency harmonics for single-frequency and double-frequency excitation. It was shown that the measured mixed-frequency signal originates both from the intrinsic nonlinearity of the transport properties of the interface and additional quadratic non-linearity of the capacitive forces used for voltage detection. Using the carefully calibrated standard based on metal-semiconductor interfaces, we have demonstrated the formation of intrinsic mixed-frequency signals (J. Shin et al. 2004. "Nonlinear transport imaging by scanning impedance spectroscopy." *Appl. Phys. Lett.* **85**, 4240), providing a first tool to study non-linear transport behavior at the interfaces. The optimal experimental conditions for the detection of the weak nonlinear harmonics were suggested, and quantitative model for data interpretation was developed. However, the presence of two sources of frequency mixing—interface (intrinsic) and tip-surface junction (extrinsic)—was somewhat limiting the universality of this approach by necessitating complicated quantitative data analysis.

Currently, we have developed a double modulation approach in SFMM that allows the intrinsic mixed-frequency signal to be measured selectively using the additional low-frequency modulation of probe bias. Further work is in progress to establish the guidelines for quantitative interpretation of this mode and explicitly relate the SFMM signal to the non-linear current-voltage and capacitance-voltage characteristics of the interfaces and electroactive elements in low-dimensional nanostructures.

Novel Tunable Ultrafast Nonlinear Optical Switching

W. Wang,[1] B. Gu,[1] G. E. Jellison Jr.,[2] and R. Haglund[3]
[1]*Environmental Sciences Division*
[2]*Condensed Matter Sciences Division*
[3]*Department of Physics and Astronomy, Vanderbilt University*

We proposed to develop a new type of ultrafast optical nonlinear Bragg switch with switching speeds from picoseconds to hundreds of femtoseconds. This report summarizes the Phase I of the project, which focused on the synthesis of the metal quantum dot (Q-dot)-doped silica colloids. It is essential to incorporate 5–10 wt % Q-dots in the silica spheres in order to create a refractive index difference of ~0.01 (necessary to observe the nonlinear effect) between composite silica spheres and the refractive index matched surrounding medium. The ultrafast optical nonlinear switching is fabricated by a new class of highly ordered silica photonic colloidal crystals. The novel three-dimensional photonic crystals are made from ordered metal or semiconductor Q-dot-doped silica particles which diffract light according to the d-spacing between particles. The switching mechanism is a result of ultrafast non-equilibrium electronic and coherent vibrational effects of Q-dots because linear Bragg scattering of the photonic crystal can be suppressed by filling the voids between silica particles with an index-matched dielectric medium. Here we report that we have successfully developed a modified microemulsion technique to synthesize silica spheres with >10 wt % of silver or gold Q-dot inclusions. We systematically studied the reaction conditions and optimized reaction parameters, so that we were able to control resulting particle morphology, size, and size distributions. Additionally, we have successfully fabricated a limited number of photonic crystals using these Q-dot-doped silica spheres, and work is in progress to characterize their nonlinear optical properties.

Introduction

Recently, ultrafast nonlinear response was experimentally demonstrated in two-dimensional (2-D) crystals patterned into planar waveguides. These studies have attracted considerable interests because they offer innovative ways of controlling the propagation and emission properties of light. However, no studies to date have explored the use of electronic nonlinear three-dimensional (3-D) photonic crystals to fabricate ultrafast photo-electronic nonlinear optical switches. In our approach, we drive refractive index changes by using electronic nonlinear properties of metal or semiconductor quantum-dots (Q-dots) in SiO_2 colloids on the ultrafast scale from picoseconds to hundreds of femtoseconds. The inorganic SiO_2 colloid has much higher damage threshold under laser pulse than organic polymer colloids. Using these composite silica nanoparticles, we will be able to prepare materials in which the real part (n_r) of the refractive index is matched while preserving a periodic modulation of the imaginary part (n_i) of the refractive index. This creates revolutionary opportunities for creating advanced photonic materials, and their novel optical nonlinear effects will have applications in optical limiting, computing, and ultrafast optical switching devices.

Experimental and Results

The overall goal of this proposed work is to fabricate semiconductor/metal Q-dot-doped silica photonic crystals, which can optically switch light in the time regime from picoseconds to several hundreds of femtoseconds. These optical switching materials utilize silica colloidal spheres containing semiconductor or metal Q-dots which are refractive index matched to the bulk medium at normal light intensities. However, at high light intensities, the nonlinear dielectric effect of the spheres results in a refractive index mismatch with the medium that causes incident radiation to be diffracted, resulting in a zero transmission. Obviously, the successful fabrication of these optical materials strongly depends on the synthesis of Q-dot-doped silica spheres with sufficient Q-dot inclusions.

Experimentally, the silica colloidal particles were synthesized within a microemulsion prepared by using Igepal CO-720 by mixing with Ag^+ ion (0.5 *M* $AgNO_3$ aqueous solution). After the microemulsion became optically clear, we further add 0.1 mL reductant (hydrazine, N_2H_4), silane coupling agents, and tetraethoxysilane (TEOS). The reaction mixture was continuously stirred for 24 hours till completion. We found that the morphology of the resulting composite silica particles strongly depended on the order and time history of added reagents. Another crucial step was that we added silane coupling agent to enhance the affinity between metal cores and silica shells. In the absence of the coupling agent, only separate metal particles and silica particle formed and co-existed in the microemulsion, and no composite nanoparticles were formed.

When we first add reductant to reduce silver or gold ions in the microemulsion followed by the addition of silane coupling agent and TEOS, silica spheres with a single metal core are obtained [Fig. 1(a)]. If the reductant, coupling agent and TEOS were added simultaneously in slow injection during the reaction, we were able to obtain silica spheres with homogenously dispersed metal Q-dots [Fig. 1(b)]. On the other hand, if a small amount of TEOS was added first, followed by the addition of reductant and coupling agent and stepwise addition of additional TEOS, a metal Q-dot shell could be embedded in the silica spheres to form a silica-metal-silica sandwich structure [Fig. 1(c)].

Upon the completion of the reaction in about 24 hours, the microemulsion was destroyed by adding alcohol, and the composite nanoparticles were separated from the suspension by centrifugation. No absorption from metal colloids could be detected in the supernatant by absorption spectroscopy, suggesting the completion of the reaction. Similarly, no new metal particles formed by adding additional reductants into the supernatant, also indicating no free metal ions left in the reaction medium. These observations demonstrate that all metal nanoparticles are included in the silica spheres. Since a known amount of Ag^+ ion was added in the reaction mixture, we estimate that an inclusion of >13% Ag Q-dots was achieved in the resulting composite silica spheres. By changing the initial concentrations of the reactants, we were able to control resulting particle size and size distributions. Dynamic light scattering measurements showed that these synthesized metal–silica composite spheres have narrow size distribution with a polydispersity of 5–10%.

For the synthesized metal–silica composite nanoparticles, we further grafted $–SO_3^-$ groups on their surface to enhance their surface charge density. After purification, these composite nanospheres readily form a highly ordered structure (i.e., crystalline colloidal arrays or photonic crystals in pure water). The crystalline colloidal array clearly exhibits diffraction property, as shown by the extinction spectra in Fig. 1(d).

We also measured the silica spheres with homogeneously dispersed Ag Q-dot inclusions by Z-scan technique. Z-scan is a single-beam measurement of the phase distortion in the far field, which gives both the sign and magnitude of nonlinear refraction *g* and the nonlinear absorption *b*. Preliminary results shown that the Ag–SiO_2 composite nanoparticles have strong nonlinear response, as it is necessary to create optical nonlinear Bragg switches.

In conclusion, we successfully synthesized metal (Ag and Au)–silica composite nanoparticles with metal Q-dot inclustions at >10 wt %, as outlined in Task 1 of this proposed project. We also were able to control the size, size distribution, and morphology of these synthesized nanoparticles and are therefore ready to move to the Phase II of this proposed work. In FY 2005, we will complete the fabrication of various photonic crystals made with metal–silica composite nanoparticles and the measure their nonlinear optical responses.

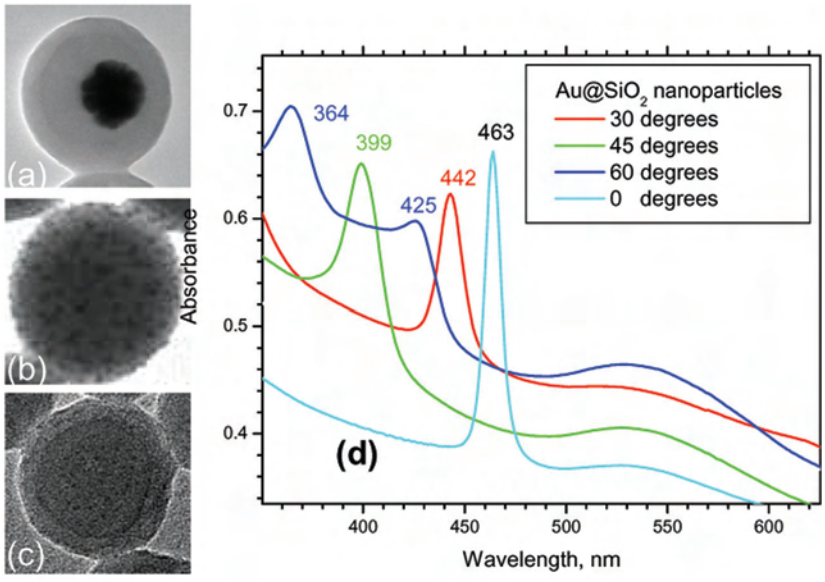

Fig. 1. TEM images of (a) SiO_2 sphere with single Ag core, (b) SiO_2 sphere with homogeneously dispersed Ag quantum dots, (c) SiO_2-Ag-SiO_2 sandwich composite sphere, and (d) extinction spectra of SiO_2 spheres with homogeneously dispersed Au quantum dots at different angles of incident light.

Design and Synthesis of Oriented Guest-Host Nanostructures For Enhanced Membrane Performance

M. Z. Hu,[1] I. Kosacki,[2] V. F. de Almeida,[1] D. A. Blom,[2] and E. A. Payzant[2]
[1]*Nuclear Science and Technology Division*
[2]*Metals and Ceramics Division*

Using ionic-conducting oxide material as a special case, this project plans to demonstrate that the designed orientation and large number of nanograin boundaries/interfaces can be experimentally synthesized to enhance ionic conductivity across a membrane layer. Here we present a novel material design concept and a unique synthesis method for "guest-host" type nanocomposite membranes. Such principal and derived nanostructures could promote a broad range of applications such as in sensors, chemical/gas separations, wastewater cleanup, catalysis, magnetic memory devices, solar cells, and fuel cells.

The objective of the project is to prove the fundamental principle that tailored control of material structure at the nanoscale can be achieved to improve material properties for energy applications. We aim at development of "guest-host" type nanocomposite membranes for which we expect significantly enhanced ionic conductivity.

The proposed approach allows grain-boundary engineering (interface density and orientation, impurity segregation), defect engineering (change of oxygen vacancy concentration), nanostructure tailoring (grain/pore size and alignment), and realization of nanophase stability (nanoscale confinement to restrict grain growth), all of which are critical to improve the properties of solid electrolytes. This work may lead to a new way to develop practical membrane technologies that offers orders-of-magnitude-higher permeability and selectivity, as well as improved thermal stability. Tasks are planned with focus on proof of principle of this proposed concept and the nanomaterials synthesis method.

The project was divided into two fiscal years (FY 2004 and FY 2005). The task for FY 2004 was to focus on the method development for synthesis of good membrane specimens containing the desirable nanocomposite structure. Work was initiated to develop a process using a previously discovered method for synthesis of silica-film substrate containing oriented parallel channels (7.5-nm diameter). We aimed to create oriented mesoporous films with expanded orientation areas that are practical for later conductivity measurements. At the same time we have also been developing a technology for infiltration of yttrium-stabilized zirconia (YSZ) nanophase into the nanopore channels.

The infiltration of dense YSZ nanophase into complete nanochannels (200, 100, 20 nm) of anodized alumina proves to be challenging. Results from multiple experimental trials and back-scattering SEM evaluation show that conventional liquid impregnation at atmospheric pressure cannot overcome the capillary pressure to fill the YSZ (polymer or nanoparticle) liquid precursor into pore channels. However, we have identified a vacuum-impregnation technique and developed a vacuum-infiltration approach that have overcome the capillary pressure resistance, and thus, successfully created segmented solid YSZ nanophases inside the channels of alumina substrate matrices. However, minimization of calcinations-induced volumetric shrinkage of infiltrated YSZ precursor inside the pore channels must be achieved to avoid the segmentation of dense-phase YSZ nanowires in pore channels. Several approaches such as multiple vacuum impregnations are planned in combination with the final touch-up using polymer solution precursor to fill the channels completely with YSZ solid phase. Therefore, a novel YSZ nanoparticle precursor route have been developed to efficiently build up a large mass fraction of desirable YSZ nanophases inside matrix pore channels and will be further developed and evaluated for ionic conductivity in FY 2005.

This nanotechnology project may significantly impact the performance of materials used in fuel cells or solar cells, which would contribute significantly to the energy mission of the Department of Energy (DOE). In addition, the project may also impact DOE's missions in homeland security (sensors) and environmental quality (wastewater treatment and sensors). Furthermore, this project could benefit other agencies such as the Department of Defense (DARPA program), Department of Homeland Security, Office of Naval Research, and Environmental Protection Agency. This project may also provide benefits to U.S. industries such as chemical, petrochemical, pharmaceutical, automobile, and electronics.

A Hybrid Solid-State Process for Joining High-Temperature Materials

Z. Feng, S. A. David, and E. K. Ohriner
Metals and Ceramics Division

Friction stir welding (FSW) is a novel joining process invented about 10 years ago. There has been a tremendous interest and need to further advance FSW technology to joining of high-temperature materials. However, the application of FSW to high-temperature materials is technically challenging. A key issue is related to the inability of the FSW tool to generate sufficient heat to soften the high-temperature materials for extensive material flow and consolidation that are necessary to form a good joint. In this program, we investigate the feasibility of a hybrid process for substantial improvement in welding speed and joint quality, while minimizing the tool wear when welding high-temperature materials.

Today, the FSW process is being used to join low-melting temperature materials, mostly various aluminum alloys. The economical and technological benefits of FSW have been well documented for Al alloys and other low-melting temperature materials. The economical benefits would be much more remarkable if FSW could be applied to high-performance high-melting temperature materials that are very difficult, if not impossible, to fusion weld.

While technically challenging, FSW is inherently suited for joining these difficult-to-fusion-weld materials because of its solid-state nature. The objective of this project is to establish the scientific basis and technical feasibility and to demonstrate the potential advantages of a hybrid FSW process. The research efforts will focus on (1) evaluating and installing an auxiliary heating source to the FSW development system, (2) performing heat flow and stress modeling for selection of critical process parameters and determination of the effectiveness of the hybrid FSW process, and (3) conducting welding trials and post-weld microstructure and property evaluations to prove the feasibility of the hybrid FSW process.

To date, the suitability of two different heating sources for auxiliary heating in FSW has been evaluated. The evaluation included both experimental trials and computational simulation of the heating characteristics and its effects on the stress and deformation process in the FSW process. The data from computational simulation show the possibility for increased welding speed and reduced tool load. Based on these evaluation results, a 4-kW Nd:YAG laser has been chosen for integration with the FSW machine system. The hardware integration is under way and welding trials are planned for FY 2005. Baseline FSW trials on stainless steels and Ti alloys were completed, establishing the baseline process condition against which the hybrid FSW process will be compared.

The economical incentives for fiction stir welding of high-temperature materials are huge, as the process would be a critical technology enabling increased use of many classes of high-performance, high-temperature materials in a number of industry sectors (aerospace, automotive, shipbuilding, power generation–nuclear and fossil, and petrochemical) and government agencies (DOE, DOD and NASA). Examples of potential applications of FSW include the following: (1) joining high-creep-resistant oxide dispersion strengthened steels, vanadium alloys, and dissimilar materials for fusion reactors and other high-temperature applications; (2) repair of irradiation-damaged stainless steel structures in nuclear power plants; (3) construction of ultra-high-strength steel pipelines for energy (hydrogen, natural gas, and liquid petroleum) transmissions; (4) fabrication and repair of aero-engine components made of Ni-based superalloys and mechanically alloyed materials; (5) titanium-alloy intensive aircraft, spacecraft, and Navy ship superstructures; (6) super-austenite alloy (such as Al-6XN) for Navy ship structures; and (7) ultra-high-strength steels for lightweight, high-performance auto vehicle body-structures.

An Energy Efficient Method for Semi-Solid Material Processing

Q. Han,[1] X. Jian,[2] and T. T. Meek[2]
[1]*Metals and Ceramics Division*
[2]*The University of Tennessee*

This project focused on the development of a new method for semi-solid metal (SSM) processing. High-intensity ultrasonic vibrations were used for obtaining a spherical, non-dendritic solidification structure, which is ideal for SSM processing. A novel experimental apparatus was designed and built. Parameters affecting spherical grain formation were studied. These parameters included the casting temperature, the use of grain refiners, and the intensity of ultrasonic vibration. The project demonstrated that extremely small and spherical/non-dendritic grains can be obtained with ultrasonic vibration. The grain size obtained in this project was in the range of 30 to 60 μm, much smaller than 100 μm which is considered as the typical grain size in very well grain-refined aluminum alloys (Greer 2004). The project results represent a technological opportunity for developing a unique low-cost, energy-efficient, and operationally robust method for SSM processing. A patent has been filed recently at ORNL on this method (Han 2004).

Introduction

SSM processing is an emerging technology that offers distinct advantages over other near-net-shape manufacturing processes, such as more homogeneous microstructure, improved die filling during processing, less oxide formation, less porosity and segregation, improved mechanical properties, and less die wear (Flemings 1991). This process is ideally suited for die casting and a number of automotive components. The most widely used industrial process for high-volume production of SSM components is thixocasting (Garat 1998) using the following processing route:

Liquid → Liquid + Solid (electromagnetic stirring and direct chill casting) → Solid Billet → Slug (cut) → Slug (reheated) → Liquid + Solid → Solid Casting (die casting)

The energy and cost savings are enormous if the processing route can be changed to

Liquid → Liquid + Solid → Solid casting,

which is termed rheocasting (Flemings 1976), but rheocasting has not been industrialized (Garat 1998). An ideal route for the rheocasting of SSM would consist of holding the alloy in the liquid state then turning the liquid into a non-dendritic semi-solid structure with required solid fractions for processing. The process has to be a robust, efficient operation under various forming methods, and suitable for mass production.

In earlier research funded by the Industrial Technologies Program (ITP), the U.S. Department of Energy (DOE), we demonstrated in small-size specimens that globular grains can be obtained in aluminum alloys by injecting high-intensity ultrasonic energy into the solidifying ingot (Jian 2004). Based on the success of the DOE-funded project, a novel method for SSM processing using ultrasonic vibrations was suggested. The purpose of this project was to prove the feasibility of the proposed method and to demonstrate SSM processing of A356 alloys using the proposed method. Two tasks were envisioned. These tasks were (1) fabrication of experimental apparatus, and (2) parametric study of the factors affecting spherical grain formation. The goal was to demonstrate that spherical grains could be obtained in ingots of 3 in. in diameter and 5 in. in height, which is one of the sizes of commercial SSM feedstock available in the market. We have obtained spherical grains in the commercial size ingot by combining the use of ultrasonic vibrations and adding grain refiners in the solidifying ingot.

Technical Approach

Details of the proposed method for SSM processing are described in the ORNL patent application (Han 2004). Of the four steps described in the ORNL patent, the critical step involves the use of ultrasonic vibration for the production of non-dendritic or spherical grains throughout the solidifying ingot. Technical approaches were developed based on the following phenomena for producing spherical grains in large-size ingots: (1) the injection of ultrasonic vibration into the melt generates alternating pressures within the melt. The minimum and maximum pressures are given by the following equations (Rozenberg 1973):

$$p_{max} = p_0 + \sqrt{2\rho cI} \quad (1)$$

$$p_{min} = p_0 - \sqrt{2\rho cI} \quad (2)$$

where ρ_0 is the atmospheric pressure, ρ and c are the density and the wave velocity of the melt, respectively, and I is the wave energy density; (2) the instantaneous pressure in the melt induces heterogeneous nucleation of the solid phase as well as a streaming effect that leads to the circulation of the nuclei throughout the melt; (3) the addition of grain refiners promotes heterogeneous nucleation too; and (4) spherical grains, instead of dendritic grains, can be obtained provided enough nuclei can be produced in the bulk melt (Flemings 2002). Based on these phenomena, high-intensity ultrasonic vibrations were injected into the melt from specially designed locations (Han 2004) to generate high alternating pressure and streaming effect; grain refiners were added in the melt to produce a maximum amount of nuclei; metal moulds were used to chill the melt to keep the small nuclei surviving. A systematic study was carried out to investigate the parameters that affect non-dendritic grain formation in industrial size SSM feedstock (3 in. in diameter and 5 in. in height). These parameters included the casting temperature, the amount of grain refiners used, and the intensity of ultrasonic vibration. The commercial A356 alloy (Al–7.0 wt% Si–0.4 wt% Mg–0.1 wt% Fe) was used for the experiments.

Results and Discussion

Experiments were first carried out using a small copper mold, which held up to 250 g of molten A356 alloy, to evaluate the effect of the intensity of ultrasonic vibration and the casting temperature on the solidification structure of the alloy.

Four amplitudes were tested during the experiments, namely 0% (without vibrations), 30%, 50%, and 70% of the nominal 16-μm amplitude of the ultrasonic radiator. (The acoustic intensity is proportional to the square of ultrasonic amplitude.) Molten aluminum was cast into a copper mold at 640ºC and solidified while being subjected to ultrasonic vibration. Experimental results indicated that high acoustic intensity favored the formation of small and spherical grains. Without the vibration, aluminum dendrites were fully developed and the grain sizes were a few millimeters. With the increase of ultrasonic intensity, the primary aluminum grains became less dendritic, more spherical and much smaller. Spherical, non-dendritic grains were successfully obtained when the amplitude was 70% of the nominal amplitude. Furthermore, the size and morphology of the eutectic Si phase were also altered. Rod-like silicon particles were formed under high-intensity ultrasonic vibration instead of plate-like silicon particles that formed without ultrasonic vibration, a result that has not been reported in the literature.

The effect of casting temperature on the solidification structure of A356 alloy was also evaluated. The results indicated that the size of the primary α-Al grains decreased with decreasing casting temperature, reached a minimum of about 30 μm at 630ºC, and then increased lightly with decreasing casting temperature. The results suggest that the mechanism of grain refinement is the formation of non-equilibrium nuclei at temperatures higher than the liquidus temperature of the alloy (615°C). The high instantaneous pressure induced by ultrasonic vibration contributed to the nucleation of the primary aluminum phase above the liquidus temperature of the alloy.

Based on the results obtained using a copper mold, the maximum intensity of ultrasonic vibration and a casting temperature of 630°C were chosen for processing industrial-size A356 alloy ingots of about 3 in. in diameter and 5 in. in height. Image analysis was carried out to measure the size and morphology (roundness of the grains) distribution in the ingot. Results obtained in the larger ingot were consistent with that obtained in smaller casting. Non-dendritic and spherical grains were successfully obtained in the industrial size ingot. The quantitative measurement results are shown in Fig. 1. The grain sizes are in the range between 35 to 55 μm and are quite uniform throughout the ingot. These grains are much smaller than those obtained without the use of ultrasonic vibration. The roundness of the three-dimensional non-dendritic grains was in the range between 0.35 and 0.5. These results suggest that ultrasonic vibrations can be used for making non-dendritic solidification structure that is ideal for SSM processing.

Benefits

This research will serve as the starting point for a new cost-effective and energy-efficient approach for replacing the widely used thixocasting/thixoforming approach. The research will have an important impact on the commercial utilization of semi-solid technologies for the production of high-quality components for automotive applications. The research program was also important for extending the semi-solid technologies to alloys for national defense and aviation industries. Besides, the research can also serve as a starting point for fundamental research on thermodynamics and kinetics of nucleation and crystal growth processes under the influence of ultrasonic vibrations. In particular, ITP of DOE is eager to reduce the high cost and energy consumption associated with the thixoforming processes, which limits the commercial applications of the SSM processes. The DOE Office of Transportation Technology has significant emphasis on

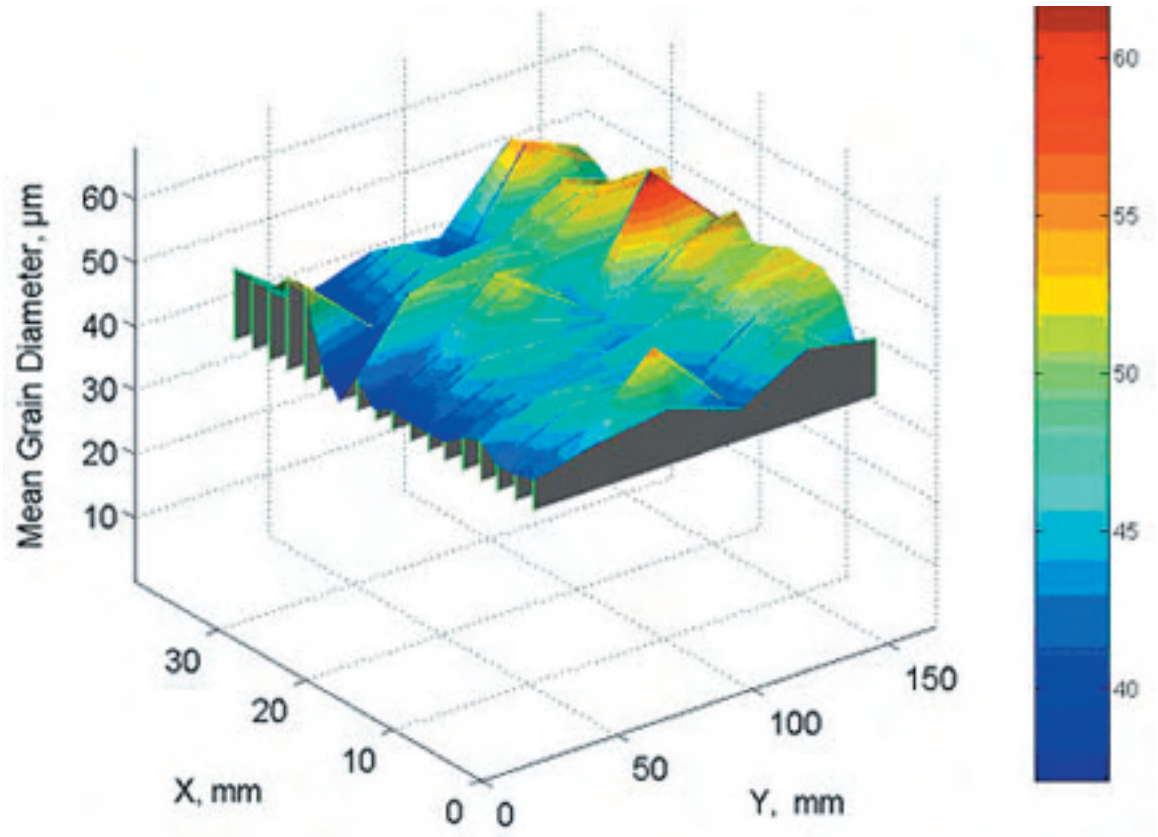

Fig. 1. Grain size distribution in an industrial-size ingot solidified under the influence of high-intensity ultrasonic vibration. The grain size is much smaller than those obtained under normal solidification conditions, usually 100 µm in well grain-refined specimens. The measurement was taken from a radially cut section. The x-axis shows the radial position from the center of the ingot, and the y-axis shows position along the height of the ingot.

materials and technologies for mass reduction. High-property SSM aluminum alloys will find their applications in mass reduction for automotive, aviation, and defense industries.

References

Flemings, M.C. 1991. "Behavior of Metal Alloys in the Semisolid State," *Metall. Meter. Trans.* **22A**, 957–981.

Flemings, M.C., R. G. Riek, and K. P. Young. 1976. "Rheocasting," *Materials Science and Engineering* **25**, 103–117.

Garat, M., S. Blais, C. Pluchon, and W. R. Loué. 1998. "Aluminum Semi-Solid Processing: From the Billet to the Finished Part," pp. xvii–xxxi in *Proceedings 5th International Conference on Semi-Solid Processing of Alloys and Composites*. Eds. A. K. Bhasin, J. J. Moore, K. P. Young, and S. Midson, Golden, Colorado, June 23–25).

Greer, A. A. 2004. "Grain Refinement of Aluminum Alloy," pp.131–145 in *Solidification of Aluminum Alloys*, eds. M. G. Chu, D. A. Granger, and Q. Han. Warrendale, Pa., The Minerals, Metals & Materials Society, 2004.

Han, Q., X. Jian, H. Xu, and T. T. Meek. 2004. "Method and Apparatus for Semi-Solid Material Processing," Docket No. 1372, Oak Ridge National Laboratory.

Jian, X., Q. Han, H. Xu, and T. T. Meek. 2004. "Solidification of Aluminum Alloy A356 Under Ultrasonic Vibration," pp. 73–79 in *Solidification of Aluminum Alloys*, eds. M. G. Chu, D. A. Granger, and Q. Han. Warrendale, Pa., The Minerals, Metals & Materials Society, 2004.

Kirkwood, D. H. 1994. "Semisolid Metal Processing," *International Materials Reviews* **39**(5), 173–189.

Rozenbuerg, L. D. 1973. *Physical Principles of Ultrasonic Technology*, vol. 2, Plenum Press, New York, p. 166.

Sebus, R. and G. Henneberger. 1998. "Optimisation of Coil-Design for Inductive Heating in the Semi-Solid State," pp. 481–487 in *Proceedings 5th International Conference on Semi-Solid Processing of Alloys and Composites*, June 23–25. Eds Bhasin, A. K., J. J. Moore, K. P. Young, and S. Midson, Golden, Colorado.

Spencer, D. B., R. Mehrabian, and M. C. Flemings. 1972. "Rheological Behavior of Sn-15%Pb in the Crystallization Range," *Metall. Trans.* **3**,1925–1932.

Direct Band Gap Semiconductors on Silicon for Solid State Lighting: Si-Based Blue Light-Emitting Diodes

R. McKee
Metals and Ceramics Division

We seek a "cost-effective" method that will facilitate a silicon-based manufacture of high-efficiency blue, green, and yellow light-emitting diodes (LEDs) for solid-state lighting (SSL). Here we identify direct-gap, light-emitting semiconductor compounds that can be fabricated on Si as the materials system for the development of cost-effective SSL. These compounds are tetrahedrally bonded semiconductors: $AgGaS_2$ and $CuInS_2$. They can be epitaxially stabilized on the (001) face of Si, and the band gaps are direct in the blue-to-yellow range. Unlike any other materials system that has been proposed, these compounds are chemically and structurally compatible with silicon and have tunable band-gaps.

Our goal is to demonstrate proof of principle for silicon-based solid state lighting by growing and then getting efficient photoemission out of p-n junctions with chalcogenide heterostructures on silicon. The light will be in the blue-to-yellow wavelength range of the visible spectrum.

The blue-to-yellow wavelength range is currently covered using wide-bandgap GaN, a material that is both expensive to manufacture and difficult to perfect to an acceptable level for energy efficient application. We propose that both of these problems are fixable on silicon with direct gap semiconducting heterostructures that are chemically and structurally compatible with silicon; GaN is not!

We found two special members of the class of chalcogenide compounds (compounds out of Group VI that typically contain S, Se, or Te but not oxygen) that can be stabilized both structurally and chemically on silicon: $AgGaS_2$ and $CuGaS_2$ with indium substitutions on gallium sites to tune the band gaps. The structural matching (lattice parameter and symmetry) uniquely takes advantage of epitaxial stabilization of the CuAu and chalcopyrite polymorphs of the chalcogenide systems. The epitaxial stabilization energy is a significant energy driver for a phase-pure approach towards discriminating against competing polymorphs and defects that are responsible for the unacceptably low quantum efficiency for GaN-based systems.

There are two critical parts of the heteroepitaxy problem that are being investigated. First, a molecular beam epitaxy (MBE) method of layer-sequencing along the [001] direction of the CuAu structured–AgGaS compound is being developed. Second, we are solving the thermodynamic problem of interface-phase stability for the sulfide/silicon system.

The first phase of our work has been to design and construct a sulfur-specific MBE machine to address these critical growth issues. That system is complete and is now being tested and optimized for the p-n junction growth. The next phase will be implementing the growth technology for the p-n junction fabrication.

DOE's Building Technologies Program has a stated goal of 50% energy conservation in electric lighting by 2010. This is a very aggressive objective. Our proposal is a silicon integrated circuit technology, and just like the revolution that integrated circuits are to vacuum tubes, this approach to lighting replacement can be the same. This sulfides-on-silicon LED approach is the enabler for SSL and DOE's goal.

Development of New Nanoparticle-Strengthened Ferritic and Martensitic Steels by Thermomechanical Treatment

R. L. Klueh[1] and N. Hashimoto[2]
[1]*Metals and Ceramics Division*
[2]*University of Tennessee*

Available martensitic steels for power-plant applications (fossil-fired, nuclear fission, and fusion) have upper-temperature limits of ≈620ºC. Higher temperatures are required for improved efficiency. A thermomechanical treatment (TMT) was developed to produce steels strengthened by large numbers of nano-sized nitride particles. Tensile studies indicated nitrogen-containing commercial steels given the TMT have exceptional strengths to 800 ºC. As opposed to the alternative oxide dispersion-strengthened steel for >650ºC operation, which is produced by complicated and expensive processes, the TMT uses conventional processing techniques. Guided by computational thermodynamic modeling, this project seeks new steel compositions and the optimization of the TMT to produce steels for use at >700ºC.

Regardless of fuel (fossil or nuclear), higher operating temperatures are required for power plants for improved efficiency and reduced pollution. Ferritic and martensitic steels are preferred structural materials because of excellent thermal properties relative to alternative materials. Such steels have limitations on operating temperatures; however, and improved elevated-temperature steels are required

In this work, we are using computational thermodynamic modeling as a guide to develop new ferritic and martensitic steels that can be produced by a newly proposed thermomechanical treatment (TMT). These steels will have microstructures with a high number density of nano-sized nitride precipitate particles that impart elevated-temperature tensile and creep strength for use at >700ºC, where no commercial steels are available. A further objective is to demonstrate that the TMT can be applied to commercial nitrogen-containing steels, thus making it possible to use them at higher temperatures and in thinner sections. The TMT will use conventional metal-processing techniques, as opposed to complicated and expensive techniques used on the only alternative high-temperature steels—oxide dispersion-strengthened steels.

To obtain a steel with improved elevated-temperature strength, we developed a TMT where (1) a steel is heated to austenitized (heated to a temperature where steel transforms from a body-centered cubic crystal structure of ferrite to the face-centered cubic structure of austenite) and put precipitates into solution; (2) it is then cooled to a hot-working temperature (750 to 1000ºC); (3) it is hot worked; (4) it is annealed at the hot-working temperature; and (5) it is finally cooled to room temperature. It was hypothesized that dislocations (line defects in the steel) generated by hot working will act as nucleation sites for MX precipitates (where M is vanadium rich with lesser amounts of other elements such as Cr, Mo, Fe, etc., and X is mainly nitrogen with some carbon). The anneal after hot working causes precipitates to grow to suitable size for optimum strengthening. The desired result is a ferrite and/or martensite matrix with a high number density of fine MX precipitates that provide elevated-temperature strength.

Computational thermodynamic modeling was used to predict equilibrium strengthening phases and the amounts of phases expected in different compositions of nitrogen-containing steels that, after a properly chosen TMT, will contain a high number of nano-sized nitride precipitates for elevated-temperature strength. Such compositions are being prepared at Albany Research Center. In the meantime, available nitrogen-containing commercial steels were processed using hot rolling for the TMT. Tensile tests have demonstrated improved strength of these steels over those given a conventional heat treatment. Creep testing to explore optimization of the TMT is in progress. Examination of commercial steel compositions with transmission electron microscopy indicated that the TMT produced a high number density of nano-size particles that impart the improved elevated-temperature strength.

The DOE Office of Fossil Energy is evaluating materials for ultra-supercritical power plants operating at temperatures and stresses significantly above current plants. The DOE Office of Nuclear Energy, Science and Technology is planning a new generation (Generation IV) of nuclear power plants. Ferritic and martensitic steels are preferred materials for these applications, but none are available for temperatures >620 ºC that are needed for improved efficiency. The steels proposed here will fit that need.

BIOLOGICAL SCIENCES AND TECHNOLOGY

Director's R&D Fund

Comprehensive Molecular Probing of Live Biological Cells

T. Thundat,[1] M. J. Doktycz,[1] T. L. Ferrell,[1] R. J. Warmack,[2] T. McKnight,[2] and M. D. Barnes[3]
[1]*Life Sciences Division*
[2]*Engineering Science and Technology Division*
[3]*Chemical Sciences Division*

A novel photon force microscope (PFM) using laser tweezers and nanoprobe optical monitoring was developed for nanofluidics and especially to allow probing and imaging both outside and inside the cell. The PFM probes three-dimensional structures by guiding and monitoring a nanoparticle as an imaging probe. A haptic interface allows force feedback to give the operator a three-dimensional "feel" of interior surfaces and the minute forces that the trapped particle experiences. This unique facility provides information about metabolic pathways and intercellular nano-mechanics, complementing other techniques. This instrument, combined with scanning probe and conventional optical microscopes, will provide an unprecedented perspective of cellular processes, both outside and inside the cell, and will provide invaluable insights and information essential to the success of the DOE Genomes to Life Program and will have benefits in clinical applications, biomedical engineering, and drug discovery .

Introduction

Observing protein complexes in their native environment is necessary for describing cell function in terms of the molecular-level information obtained from genomics and proteomics techniques. Unfortunately, retaining a molecular-level description, while observing on the length scale of a biological cell, presents a significant challenge. Microbes present additional challenges due to their small size, minimal organizational substructure, and impervious cell walls (compared to eukaryotes). Current imaging approaches employ various optical/fluorescent microscopy techniques coupled with appropriate labeling strategies (Ueda 2001, Cook 2002). However, conventional microscopy techniques are limited in their ability to spatially resolve the sub-wavelength-scale complexes we seek to characterize.

Clearly, new and innovative methods will be required to provide the level of detail required to validate complexes in living cells. Scanning probe techniques such as atomic force microscopy (AFM) have offered powerful tools for imaging surfaces. Due to the fact that living cells are 3-D structures, the resolution is limited to the size of the AFM tip; even so, this is of the order of 10 nm or less in physiological liquid. However, imaging inside cells is totally impossible due to the mechanical connection of the instrument with the imaging tip. Therefore, a scanning probe microscope without a mechanical connection to the tip working with extremely small loading forces would be an ideal complementation for the AFM in studies of live cells. The photon force microscope (PFM) would overcome this severe limitation by using a bead tethered by focused light as the probe for imaging inside the cell.

For the PFM, the mechanical cantilever is replaced by the 3-D trapping potential of a focused laser. The possibility to trap and manipulate small micrometer-sized particles with a laser focused into a fluid chamber was first described in 1986 by Ashkin—the same year the first AFM was built (Ashkin 1986). The difference in the refractive index between fluid medium and particle, its diameter, as well as the laser intensity together with its 3-D profile, determines the strength and the 3-D shape of the trapping potential. Depending on the application, this potential, which is harmonic and therefore can be described by a spring constant, can be adjusted by the laser power. Usually the spring constant is two to three orders of magnitude softer than that of the softest commercially available AFM cantilevers. The particles used as tips can be as small as some ten nanometers in the case of high index materials such as metals. The significant step forward from the optical trap of Ashkin to build a PFM is the 3-D detection system for the particle position with respect to the trapping potential allowing the measurement of the value and direction of the force acting on the bead with sub-pico-newton precision on the timescale of microseconds. This makes it possible to use small particles as scanning probe tips that can be moved along a surface to image, or to make interaction force measurements between the particle and other structures.

Technical Approach

The principal effort of the project was to design and construct a user-friendly PFM using laser tweezers and nanoprobe optical monitoring for use in cellular studies. We were aided by a close collaboration with Prof. Heinrich

Hörber (Wayne State University), who invented the technique (Florin 1997). Our PFM design is not based on a commercial optical microscope but rather a custom structure that is more stable and optimizes the use of the instrument. This gave us greatly enhanced mechanical stability, improved optical alignment, and operational flexibility. A simplified schematic depicting the optical arrangement and a photograph of the instrument is shown in the Fig. 1.

The optical trap consists of a high-numerical-aperture objective (1.4 n.a., 100× oil-immersion Zeiss Apoplan) to focus light from a highly stable 1064-nm diode laser. Included in the path from the laser to the objective are a 10× beam expander, to produce the minimum beam waist at the objective focus, and a beam attenuator, to adjust the trapping force. The stage scans the sample in all three dimensions with a closed-loop resolution of roughly 1 nm and is heated to keep cells viable. The trapping wavelength is only weakly absorbed by cells, which can remain viable for extended periods under illumination. Scattered light from the trapped particle is projected through a matched condenser onto a GaInAs quadrant photodiode for readout of particle position in three dimensions at MHz rates. All critical surfaces are finished to λ/10 to eliminate wavefront distortion and enclosed to reduce air turbulence and scattering from dust. To provide for the highest safety and most user-friendly operation, the system was designed with laser beam totally enclosed.

The optics also provides for conventional high-resolution imaging of the sample by illuminating from a tungsten lamp or monochromatic light source through the condenser. Dichroic mirrors are used to separate the white light from the infrared laser light. Using differential-interference-contrast prisms, high-quality optical imaging of cells and the trapped particles can be monitored during trapping. Illumination for fluorescence is provided by a high-speed polychromator (Polychrome) illuminated by a 100-watt arc lamp.

A unique haptic-control feature was added to the instrument with the collaboration of Lonnie Love of the Robotics and Energetic Systems group of ESTD. A three-dimensional joystick controls the particle position, while deviations in its position are interpreted as forces that are applied to the joystick. In this way the user "feels" the forces acting on the particle, whether they originate from viscous drag, cellular-motor kinetics, or obstructions, such as structural features. Three-dimensional information is a unique feature of this microscope and allows probing of interior cavities in all directions.

Results and Discussion

The Zeiss condenser and objective worked well in serving both as a microscope with a resolution of ~λ/2 to observe the probe particles and sample and as a laser-tweezer system for particle trapping and scatter-light projection. Samples were deposited onto a microscope slide and sealed with a cover slip. Focusing was carefully done to a point just inside cover slip. Brownian motion was readily observed for latex probe particles from 100–500 nm. The laser power was adjusted using the

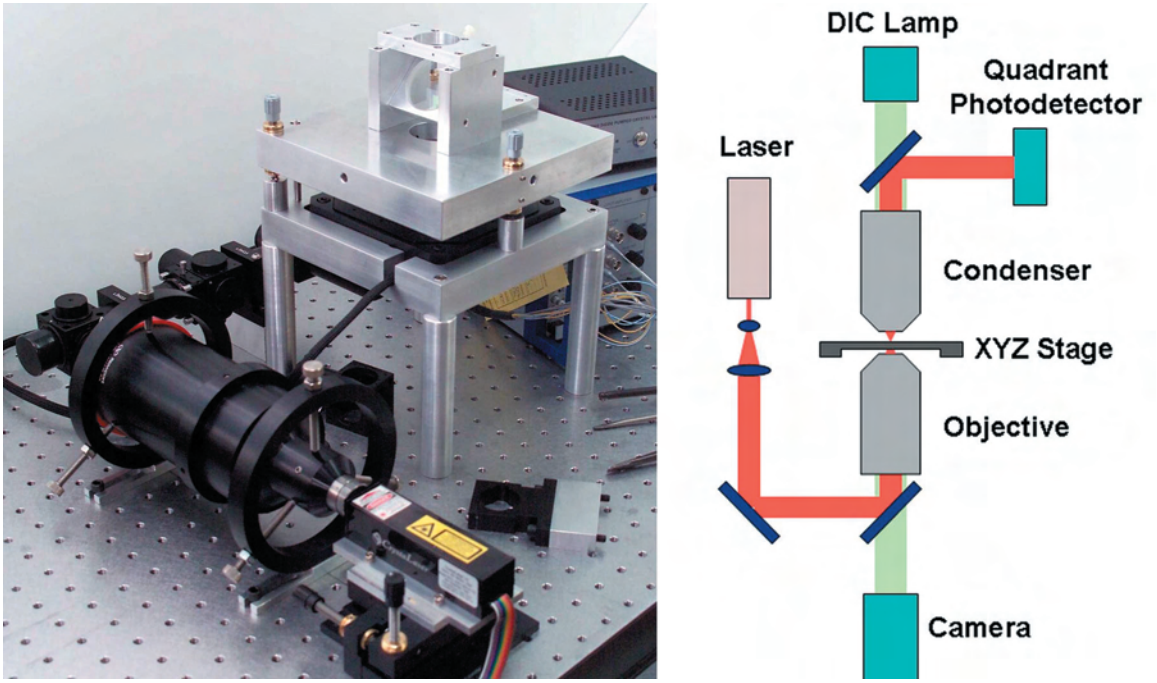

Fig. 1. Simplified schematic of the photonic force microscope and photograph of the system.

attenuator typically to a fraction of the 500 mW available to obtain particle trapping. Trapping was clearly apparent from both the microscope image of the particle and from the characteristic signal from the scattered light onto the quadrant photodiode.

Analysis of the particle motion was performed in real time using custom-written Labview software. The trapping potential of the laser was calibrated by calculating the mean-square displacement of a trapped particle and its autocorrelation using the known viscosity of the fluid. Viscous forces could also be measured by the lag of the particle in moving fluid. Brownian motion provided random scanning while the particle position was plotted in three dimensions. The presence of surfaces distorted the shape of this thermal ellipsoid, so that their topography or force interactions could be mapped. Larger volumes were explored using a raster scan of the stage in two dimensions.

The most interesting and useful feature of the PFM was its haptic control stage. This feature allows the operator to explore three-dimensional objects and voids that are difficult to scan with a raster pattern. Often, the raster scan would move the particle into a surface, and trapping would be lost. Putting the operator into the feedback loop allows the operator to probe a volume in an intelligent fashion.

Benefits

The role of high-resolution imaging has applications directly relevant to DOE's Genomes to Life program. The PFM provides a unique new probe for explorations within the interior of a living cell including imaging force interactions. Such information will greatly enhance our understanding of living cells and the way cells work. Observing protein complexes in their native environment is necessary for describing cell function in terms of the molecular-level information obtained from genomics and proteomics techniques. The tools afforded by this work are also quite relevant to Nanoscale Science, Engineering, and Technology Research (NSET).

This project has applications in several NIH programs, especially to National Institute for Biomedical Imaging and Bioengineering (NIBIB). The ability to real-time imaging of cells to external stimuli has significant applications in clinical applications, biomedical engineering, and drug discovery. The combination of unique nanoprobe techniques with other imaging and probing instrumentation at ORNL opens the possibility of becoming an NIH center that would attract and foster very fruitful collaborations with visiting cellular biologists.

References

Ashkin, A., J. M. Dziedzic, J. E. Bjorkholm, and S. Chu. 1986. "Observation of a single-beam gradient force optical trap for dielectric particles," *Opt. Lett.* **11**(5) 288–90.

Cook, B. N. and C. R Bertozzi. 2002. "Chemical approaches to the investigation of cellular systems," *Bioorgan. Med. Chem*. **10**(4) 829–40.

Florin, E. L., A. Pralle, J. K. H. Hörber, and E. H. K. Stelzer. 1997. "Photonic force microscope based on optical tweezers and two- photon excitation for biological applications," *J. Struct. Biol*. **119**(2) 202–11.

Ueda, M., Y. Sako, T. Tanaka, P. Devreotes, and T. Yanagida. 2001. "Single-Molecule Analysis of Chemotactic Signaling in Dictyostelium Cells" *Science* **864** 7.

Nano/Micro Systems for Advanced Neuronal Interfacing

M. N. Ericson,[1] T. E. McKnight,[1] A. V. Melechko,[2] C. L. Britton, Jr.,[1] J. S. Baba,[1] A. D. McMillan,[3]
G. D. Griffin,[4] M. A. Wilson,[5,6] E. Toh,[5,6] P. S. Khalsa,[7] E. Entcheva,[7] and M. Dichter[8]
[1]*Engineering Science and Technology Division*
[2]*The University of Tennessee*
[3]*Office of the Laboratory Director*
[4]*Life Sciences Division*
[5]*Pittsburgh VA Healthcare System*
[6]*University of Pittsburgh Medical School*
[7]*State University of New York, Stony Brook*
[8]*University of Pennsylvania*

This research is focused on integrating novel nanostructured materials and microelectronics to overcome the existing limitations of conventional neuronal interfacing techniques. We are integrating vertically aligned carbon nanofiber–based electrode architectures with microscale integrated circuits to provide a base technology enabling the realization of highly integrated and functionally specialized miniature neural interface systems. Our approach takes advantage of inherent properties of nanofibers that provide significant improvements over conventional techniques for nerve interfacing, including the ability to insert directly into neural tissue, the ability to electrically address fibers as independent elements, the improved stability of carbon electrodes in neuronal tissue over time, and the ability to pattern and synthesize very-high-resolution stimulus geometries (or pixelation). Full realization of this new technology combining nanoscience, microelectronics, and neuroscience will provide new strategies in neuro-nanomedicine for treatment of individuals struggling with profound neurological impairments.

Introduction

Significant advances have been realized in the area of neuronal interfacing in recent years. Several medically relevant areas are beginning to employ neuronal interfacing as part of their treatment strategy, including functional neuromuscular stimulation of paralyzed muscles or organs, retina stimulation, auditory nerve stimulation, skeletal muscle cardiac assist, spinal cord stimulation for treatment of chronic pain and studying of the nervous system. However, conventional strategies employing mm-scale wire or μm-scale micromachined probes with perimeter interfacing have reached a near limit in sensitivity, size, and probe count due to inherent limitations in the materials and methods used. This research addresses many of the progress-limiting characteristics of conventional probe systems by integrating carbon-based nanoprobes directly with pixelated integrated circuits to provide a new high-density, massively parallel, programmable neuronal interface technology.

Technical Approach

The goal of this LDRD is to develop a prototype pixelated neuronal interfacing system and demonstrate two-way communications (stimulus and monitoring) with neuronal tissue (Fig. 1). To accomplish this goal, three primary focus areas were addressed in the first year of funding: (1) probe array fabrication and integration, (2) pixelated electronics and architectures development, and (3) nanoprobe device characterization. Each of these research areas and associated progress is summarized below.

A key component of this research is the deterministic fabrication of nanoprobes into arrays providing cellular scale, biocompatible, and high-resolution neuronal interfacing. Since temperatures associated with the nanofiber growth process are incompatible with other materials used in the overall implant system, special techniques were developed for fabrication of a nanofiber array that could be separately fabricated and then attached to the chip containing the pixelated integrated circuits for probe interfacing and readout. Typically, high-quality carbon nanofibers are grown at temperatures between 600 and 900ºC. Thus integration of carbon nanofiber synthesis with standard CMOS electronics remains a challenge. To address this need, a new process was developed and successfully implemented for fabricating and placement of arrays on CMOS chips. VACNFs are grown on a sacrificial high-temperature substrate and transferred to the CMOS chip using a bump bonding process at 120°C. For the carrier material, a combination of Mylar, photoresist, and In52 allow was found to have the desired characteristics of tolerance to HF, remaining solid and transparent at soldering temperature, and easily removable at the end

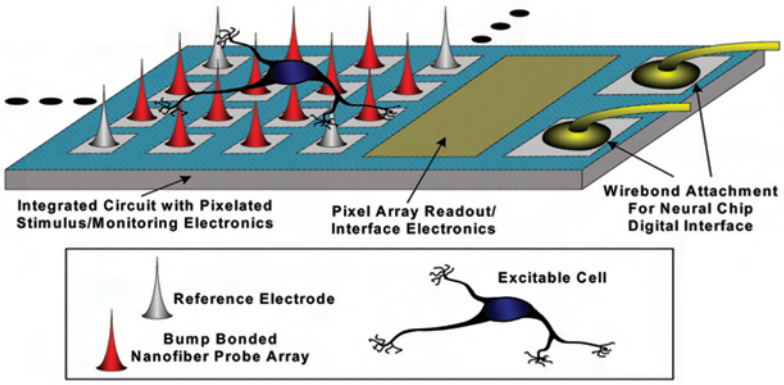

Fig. 1. Advanced neural interface system employing high-density nanofiber probe array bump bonded directly to pixelated probe stimulus/monitoring electronics chip (not to scale).

of the process. We chose not to use NaCl substrates (as originally proposed) as Na is a highly undesirable contaminant in semiconductor microfabrication facilities. In order to test the transfer process before use with an actual CMOS pixelated electronics chip, we prepared fan out chips with Au/Cr contact leads. This process we developed will be used for placement of nanoprobe arrays on CMOS chips in FY 2005.

The final integrated neuronal interfacing system is based on a highly integrated pixelated electronics chip that enables direct localized connection of the low-noise interface electronics with each nano-probe. For monitoring the neuron action potentials, two amplifier approaches were selected and implemented as custom integrated circuits: voltage mode and charge-sensitive mode. The voltage mode approach consists of a low noise preamplifier (3.2 μV_{rms}, 50V/V, 10-kHz bandwidth) followed by a variable gain amplifier (1,2,4,8 V/V). The charge-sensitive mode uses a low noise amplifier with a charge gain of 10 V/pC. Two custom chips were designed, fabricated using a commercially available bulk CMOS 0.5-µm process, and are currently being evaluated. Each chip design has a 4 × 4 array of one of the amplifier approaches (320-µm pitch). The output of each amplifier channel is routed to a perimeter pad for wirebonding/packaging. One of the pixels on each chip was replaced with a stimulus cell allowing external application of a stimulus waveform.

Cell cultures of two excitable cell lines were initiated and maintained throughout this effort period, including rat thoracic aorta smooth muscle, A10, and quail neuroretina, QNR (American Type Cell Culture). Studies were conducted to determine passivation materials compatible with attachment and proliferation of these cell types. Based on these studies, nanofiber arrays comprised of 20 single, dual, or quad-addressable electrodes were fabricated, surface treated, and packaged with these materials. Characterization studies were conducted on these packaged devices, including the electrochemical potential window (often referred to as the "safe" stimulation range for electrophysiology), the specific capacitance, and the electrochemically active surface area of the nanofiber probes (McKnight 2004). In parallel, methods to seed and propagate both QNR and A10 on packaged and operable nanofiber chips were developed and optimized, including evaluation of surface preparation techniques, sterilization methods, passage and feeding schedules, and a variety of handling techniques to promote adhesion and proliferation. Ultimately, neuronal cells were seeded onto nanofiber array chips and cultured for extended periods (up to 6 weeks, at which point experiments were terminated) with electrical/electrochemical probing conducted throughout this period. Using QNR cell culture on nanofiber chips, reproducible firing of neuronal activity was achieved through the nanofiber interface and the same electrode could be used for monitoring the firing response, including observation of the quantum nature of exocytosis of neurotransmitters using fast scan voltammetry and clamped potential amperometry. These stimuli and measurements could be performed even after 3 weeks of continuous cell culture on the nanofiber arrays, providing preliminary evidence that the material composition of our nanofibers is resistant to biofouling effects, which are reported to occur extensively in neuronal environments and are often the limiting factor in long-term electrode interfacing in tissue.

Results and Discussion

All of the necessary elements have been developed and put in place to enable successful completion of the proposed goals. Specifically, we have developed new techniques for both fabrication of a pixelated nanoprobe array and for attachment of the array on an integrated circuit substrate. Using this process, a 4 × 4 array has been fabricated and is on track to be characterized with a neuronal cell culture this FY. Techniques have been

developed for culturing neuronal cells on nanoprobe arrays, and qualitative biocompatibility has been demonstrated. In addition, nanoprobes were used to both stimulate and detect action potentials in a cultured quail neuro-retina excitable cell line using existing arrays. Finally, two different integrated circuits were designed and fabricated that will provide pixelated readout of a 4 × 4 nanoprobe array. These chips will be integrated with our nanoprobe array and used to stimulate and monitor neuronal activity in both neuronal cell culture and peripheral nerve tissue, demonstrating the efficacy of this new approach. Successful completion of these tasks will place the laboratory in a strong competitive position for developing new research programs in this emerging field.

Benefits

We believe that partnering with a strong medical/clinical institution is crucial to the success of this research and to the formation of future programs. Consequently, we have formed three specific collaborations: University of Pittsburgh Medical School (auditory and general medical applications), University of Pennsylvania Department of Neurology (cerebral cortex applications), and the State University of New York, Stony Brook, Department of Biomedical Engineering (peripheral nerve experiments).

Following successful demonstration of the system in both neuronal culture and with peripheral nerves, ORNL-based research programs will be formed around this base technology that is of particular interest to DOE OBER, NIH NIBIB, DARPA, NASA, and DOD. Advanced, highly parallel interfacing strategies will be beneficial to existing and future DOE programs involving retinal interfacing and brain machine interfacing. In addition, it is expected that significant commercial interest will develop resulting in licensing and funding opportunities. Completion of both technical and programmatic objectives will demonstrate the practicality of this new approach and will identify ORNL and its collaborators as leaders in this area and position us favorably for significant future funding from a number of sources.

References

McKnight T. E., A. V. Melechko , M. A. Guillorn, V. I. Merkulov, M. J. Doktycz, D. H. Lowndes, M. L. Simpson. 2004. "Effects of Microfabrication Processing on the Electrochemistry of Carbon Nanofiber Electrodes," *J Phys Chem B* **108**(22), 7115–7125.

Characterizing the Complex Metaproteomes of Microbial Communities

B. Davison,[1] R. Hettich,[2] N. VerBerkmoes,[3] G. Hurst,[2] A. Borole,[1] and F. Larimer[1]
[1]*Life Sciences Division*
[2]*Chemical Sciences Division*
[3]*ORNL-UTK GST Graduate School*

This project seeks to start to develop and demonstrate metaproteome analysis techniques for mixed cultures, establishing the basis for "whole community proteomics". At the end of the project we would expect to have preliminary data to demonstrate that the analytical technology and bioinformatic tools are capable of identifying individual proteins from specific microbes in a mixed culture. Conceptually this is an extension of the use of DNA techniques for "whole community genomics." Data from this LDRD would be used to support proposals for the ultimate application, which is to infer the state of the entire community by detailed proteome monitoring of a single member, a "sentinel" microorganism.

We proposed a research project to extend and demonstrate advanced mass spectrometric technologies and bioinformatics for the comprehensive characterization of microbial communities. The work is being divided into three specific aims: (1) improved "deep" proteome characterization in the presence of other microorganisms, (2) proteome differentiation and bioinformatic analysis of mixed microbial cultures, and (3) "sentinel organism" proteome monitoring in mixed cultures. An important subgoal is to develop improved analysis techniques by adding a third LC dimension to current 2-D LC MS/MS techniques in order to decrease background interferences in these complex peptide mixtures.

We have completed the metaproteome analysis of mixed cultures for task 1 (i.e., the cultures were grown separately and then mixed at the intact cell level). We used *E. coli*, *S. cerevisiae*, *R. pal*, and *S. oneidensis* as model organisms. For the MS-based proteomics, we have verified the four proteomes individually. Mixed samples were run with equal portions of each (25% each); then only the *R. pal* fraction was decreased to 5%, 1%, 0.1%, and 0% of the total. The *R. palustris* was easily identified at 20% and 5%; we are currently analyzing the 1% and below to determine the level of identification and proteome coverage. *R. pal* is also being produced under anaerobic photoheterotrophic, photoautotrophic, and nitrogen fixation conditions. These samples are mixed with the other bacteria to determine if we can distinguish the active metabolism of the *R. pal* cells in the presence of other bacteria. This analysis is ongoing and should be completed by December 2004. Again, the *R. pal* fraction will be varied in the presence of the other distractor organisms.

We have identified clear metabolic function protein markers for different functional metabolisms of *R. pal* (aerobic, phototrophic, nitrogen fixing) in pure culture samples using 2D-LC-MS/MS. The one fundamental challenge of community proteomics is that the statistics of one sequenced microbe favor each protein to have several unique peptides; however, when a full diversity of multiple species is included in the peptide database, the statistics may fail. We have created three proteome databases to test the effect of database size on protein identification. The first database contains only the four test species for this project, the second database is the four test species plus eight other microbial species and a plant species, and the large database contains the test species plus over 260 microbial species with over 1 million protein entries. Now, we are using all three of these databases to search against the experimental MS/MS spectra with SEQUEST and the recent ORNL search algorithm DBDigger. We will use these results to determine what effect large databases and alternative peptide identifier algorithms have on community proteomics.

The results obtained to date are quite encouraging that such an experimental approach might be successful for drilling deep enough into the metaproteome of a microbial community to enable determination of not only the species present but also the functional state of at least the dominant members. This work is highly relevant for the ongoing DOE Genomes-to-Life project, in particular Goal 3 of this program which is focused on comprehensive characterization of natural microbial communities.

Exploring New Methodologies in Detecting Low-Abundance Protein Complexes

Y. Wang,[1] Y. Liu,[1] and G. B. Hurst[2]
[1]*Life Sciences Division*
[2]*Chemical Sciences Division*

While mass spectrometry coupled with liquid chromatography (LC-MS) has been successfully used for identification of abundant protein complexes for DOE's Genomics: GTL program in ORNL, more work is urgently needed to improve affinity purification and identification of low-abundance protein complexes that are of greater biological relevance. The objective of this project is to engineer novel tandem affinity-tagging vectors and to establish purification and elution conditions for enriching low-abundance protein complexes, while eliminating unspecific bound proteins in the range detectable by LC-MS. This work will greatly benefit our current efforts in the identification and characterization of microbial protein complexes in Genomics: GTL project.

The study of complex proteomes is an important research area emerging from genome projects. Currently at ORNL, protein tagging coupled with "shotgun" mass spectrometry (MS) approach has been applied to high-throughput identification of protein complexes in the anoxygenic photobacterium *Rhodopseudomonas palustris*. Although the "shotgun" approach is high-throughput and has great impact on the Genomics:GTL program, it often results in less robust protein identification even by the standard of the most sensitive mass spectrometric approach. This would dramatically compromise the accuracy in protein complex identification. The goal of this project is to establish a high-affinity protein tagging and pull-down system, which, in combination with the advanced high-throughput MS technology, will greatly facilitate the identification of specific-interacting proteins and reduce unspecific contaminants that hinder the identification of authentic sub-stoichiometric components of low-abundance protein complexes.

With these goals in mind, we have so far created the following tandem affinity purification (TAP) vectors: (1) tetracycline regulatable N-terminal tagging vector I: His-tev-strep-4Cys, (2) tetracycline regulatable N-terminal tagging vector II: His-strep-4Cys, (3) tetracycline regulatable N-terminal tagging vector III: ProA-tev-strep-4Cys, (4) C-terminal tagging vector I: 4Cys-strep-tev-His, (5) C-terminal tagging vector II; 4Cys-strep-His, (6) C-terminal tagging vector III: 4Cys-strep-tev-ProA, (7) C-terminal tagging vector IV: strep-4Cys-tev-ProA, (8) C-terminal tagging vector V: His-tev-HA, and (9) C-terminal tagging vector VI: HA-tev-ProA. The tandem affinity purification system allows two-step affinity purification of fusion proteins and can tolerate multiple stringent purification procedures. All the vectors are engineered in the Gateway system, which allows for rapid high-throughput cloning of target genes and are compatible with the Gateway entry clones of *R. palustris genes*; that is, with one step modification, our vectors can be readily used for Genomics:GTL project.

To demonstrate the "proof of principle," we first cloned two mammalian proteins, Trf-2 and Cdc-14 into these vectors. Trf-2 and Cdc-14 are low-abundant, telomere and cell- cycle-related proteins, respectively. We demonstrated that the in-frame 4 Cysteine motif allowed a facile detection of the fusion protein throughout the purification steps. We have optimized the tandem affinity binding, Tev protease cleavage and elution conditions for most of the fusion proteins tested. We compared both batch and column purification with buffers of different stringency. We optimized the buffer compositions for Tev cleavage and protein complex elution, which are often encountered as the most troublesome in obtaining sub-stoichiometric components of low-abundance protein complexes. In FY 2005, our objective is to verify the applicability of our TAP system by identifying the known or novel sub-units of the low-abundance fusion-protein complexes by LC-MS.

Pursuing this research program will not only permit us to solve important biological questions, such as identifying protein complexes important for cellular function, but also bring a new avenue of research to ORNL. Demonstration of improved sensitivity and selectivity in our complete pipeline for protein tagging, expression, purification, identification, and verification of protein complexes will greatly strengthen ORNL's position to secure funding for the proposed Genomics:GTL Facility II for the Characterization and Imaging of Molecular Machines and will benefit the entire proteomics research community.

Genetic Variability in Host Responses to Bioterror Agents

D. K. Johnson,[1] C. T. Culiat,[1] E. J. Michaud,[1] G. Gupta,[2] and M. Altherr[2]
[1]*Life Sciences Division*
[2]*Los Alamos National Laboratory*

ORNL is making mice with mutations in genes that control susceptibility to microbial pathogens in order to study how variations in individual genetic makeup, interacting with environmental factors (e.g., age, gender, diet), create different rates of infection and severity of disease. In collaboration with pathogen biologists at LANL, we are targeting the anthrax receptor (*Atrx1*) that binds anthrax toxin protein, as well as the domain of the immune-system gene *Myd88* critical to pathogen entry into a cell. Resistance will be tested in vitro by LANL in year two using cells from the new mutant mice.

Pathogens or pathogen toxins enter host cells by attaching to proteins on the cell surface. Our goal is to understand the biological mechanisms that control pathogen/toxin attachment and entry in order to develop blocking strategies. By combining the expertise in microbial pathogenesis at LANL with ORNL's ability to target specific mutations in mice, we will develop mouse models for resistance to pathogen attack. These studies will give ORNL credibility in the host-pathogen community and provide preliminary data for large-scale projects to come.

We are generating mice with mutations in two genes being studied by pathogen experts at LANL. One is the anthrax receptor *Atrxl*, the point of entry for anthrax toxin into host cells, and the other, *Myd88*, codes for a cell-surface protein used for entry by a wide variety of bacterial and viral pathogens. Cells from these new mutant mice will be supplied to LANL for exposure in their BSL3 facility to toxins and pathogens to test for resistance. If changes in resistance are observed in vitro, live mice may be used for resistance testing at an approved BSL3 animal facility.

For *Atrx1*, four exons that comprise the primary functional domain have been or are being scanned in ORNL's Cryopreserved Mutant Mouse Bank. Three exons are completed in the genomic DNA bank (4000 DNAs), with one confirmed mutation. Scanning of the fourth exon is just getting under way. In addition, we are preparing a construct for a targeted conditional mutation of the extracellular binding domain of *Atrx1* in order to generate a mouse model that makes a secreted form of this binding domain to competitively bind toxin molecules in the extracellular environment. Scanning of cDNA (rather than genomic DNA) is under way for the *Atrx1* functional domain covered by these four exons.

For *Myd88*, all four exons of the gene have been completely scanned in genomic DNA (4000 DNAs), and a coding-region mutation likely to have a functional impact has been confirmed. LANL will test spleen cells from these mice as soon as their BSL3 facility is operational.

Intracytoplasmic sperm injection for recovery of mutant mice from the CMMB is performed twice each week, and mice carrying four CMMB mutations have been recovered.

We have periodic conference calls with LANL collaborators, and Johnson and Michaud had a very productive visit to LANL in October. We are also fulfilling a request for mutant mice for an NIH intramural researcher working on the human pathogen *Chlamydia*.

Plans for a June 1 submission of a Program Project grant by ORNL and LANL to NIAID are proceeding, as is program development that will lead to NIH- and DHS-supported host-pathogen interaction projects for ORNL's Mouse Genetics Research User Facility; there is strong DOE interest in the development of this User Facility, and homeland security-related projects will be high-quality and high-profile Users. In addition, the Tennessee Mouse Genome Consortium is developing a strategic plan for the involvement of ORNL in a state-wide host-pathogen program. Without this LDRD project, ORNL would have no basis for participation in any of these host-pathogen projects.

High-Throughput Biological Data Analysis and Modeling Tools for Genomes to Life Facilities

N. F. Samatova,[1] A. Gorin,[1] D. Xu,[1,2] B. Park,[1] G. Yu,[1] C. Pan,[1,3] and P. Chandramohan[1]
[1]*Computer Science and Mathematics Division*
[2]*University of Missouri*
[3]*University of Tennessee*

Ultrascale computing and high-throughput technologies, such as genomics, transcriptomics, proteomics, and metabolomics, will revolutionize the way systems biology is conducted. For the first time there is a unique opportunity to build models of molecular interaction at necessary level of detail, and to use ultrascale computation for predictive simulation of their dynamics. With this promise, however, comes the challenge of interpreting and integrating, in a biologically meaningful way, the avalanche of complex data so produced. This project aims to bridge the gap between the high-throughput biological data and the computational and analytical tools that have the capacity to derive from the data the working elements of the cell and to annotate them within functional systems context.

The existing computational tools for systems biology are far less able to characterize and model molecular-scale biological processes from the high-throughput biological data. Our goal is to provide a fresh stream of computational technologies capable of discovering strong functional "clues" from complex and noisy data, and then to integrate them to enable systems level annotation of molecular interactions. Our general strategy is to mine high-throughput and complex biological data to "learn" mathematical relationships among the known data about certain functional clues. These "learned rules" will then be used for predicting functional clues for unknown protein machines in microbial genomes.

During FY 2004, a series of computational tools has been produced from this project. The "de novo PTM" discovers post-translational modifications (PTMs) from tandem MS data (Day et al. 2004). About 80% of PTMs were reproduced when tested on the benchmark set of 54 ribosomal proteins in *R. palustris* generated by a very laborious process. We also developed two mathematical models that each addresses: (1) Given a protein sequence, which residues are interface, surface or core ones? (2) Given two protein sequences that are known to interact, which residue pairs are in direct physical contact? For the former, we devised a statistical model that derives robust confidence for interface or surface residue assignment from a committee of classifiers (Park et al. 2004). The cross-validation for >30,000 residues from 303 protein complexes shows the prediction accuracy of 75% with >70% confidence. For the latter, we created a Markov model to quantitatively describe co-evolution of contacting residue pairs. Our Markov model generates the probability of interaction between two residues from different proteins. An initial evaluation of the model using 6000 SCOP domain-domain interactions shows higher sensitivity to putative interactions and less sensitivity to false interactions.

Our surface patch ranking method finds putative enzyme-substrate specificity-determining residue clusters (Yu et al. 2004). When applied to multiple families of enzymes that are homologous but with different functional subtypes, the method recognizes functional patches that are in considerable agreement with experimental site-directed mutagenesis results. Also, as an initial effort to integrate the extracted functional clues into multi-scale, multi-resolution functional annotation of molecular machines, we developed a knowledge system for supporting high-throughput protein function annotations as well as the KeyGeneMiner method for identification of biochemical process-specific genes.

This project will deliver a capability that will allow researchers to determine a protein function and put it in both a macrocontext of interaction networks and a microcontext of particular residues involved into functions. Thus it will not only address critical computational needs of the DOE Genomes:GTL but also provide many benefits to the biological community by making these capabilities available through the National Leadership-Class Computing Facility.

References

Day, R. M., A. Borziak, and A. Gorin. 2004. "PPM-Chain: new capabilities in de novo peptide identification by tandem MS." Proceedings of the Computational Systems Bioinformatics Conference (CSB2004).

Park, B. H., et al. 2004. "Analysis of protein interaction sites through separated data spaces," in the Proceedings of the Bioinformatics workshop in conjunction with the Fourth SIAM International Conference on Data Mining (SDM'04).

Yu, G.-X., et al. 2004. "In-silico prediction of surface residue clusters for enzyme-substrate specificity," in Proceedings of the IEEE Bioinformatics Conference (CSB2004).

Advanced Plasmonic Sensor Array for Homeland Security

T. Vo-Dinh,[1] G. Griffin,[1] A. Vass,[1] A. Wintenberg,[2] F. Yan,[1] and M. Wabuyele[1]
[1]*Life Sciences Division*
[2]*Engineering Science and Technology Division*

We propose to develop a novel sensing technology based on the Advanced Plasmonic Sensor Array (APSA) concept for rapid and sensitive detection of spectral signatures for both chemical and biological warfare (CBW) agents. Plasmonics refers to the research area of enhanced electromagnetic properties of metallic nanostructures. Excitation of surface plasmons with incident light can produce enormous enhancements of spectral signatures [such as surface-enhanced Raman scattering (SERS) and surface-enhanced fluorescence (SEF)] for ultrasensitive detection of CBW. Specific innovations of the integrated system include (1) an advanced sensing concept based on plasmonics and (2) an array of sensors using nanotechnology-based probes. Results obtained using Raman detection of CBW simulants on silver nanocluster surfaces have been encouraging. Progress has been made in developing polymeric surfaces for optical waveguides for plasmonics sensor arrays. We envision that the APSA system developed during this project could form an important component of the generation-after-next sensor program, as the proposed sensor would "significantly change the detection paradigm."

Introduction

Detection technology is needed for the rapid identification and quantification of the entire suite of CBW agents as well as the detection of precursors, degradation products, and solvents associated with the manufacture and distribution of CBW. Although many analytical techniques have been adapted for such detection purposes, there is still a need for portable devices which can provide rapid early-warning capabilities in the field. We plan to use plasmonics to offer a novel and potentially very sensitive detection technique. The term plasmonics is derived from "plasmons," which are the quanta associated with longitudinal waves propagating in matter through the collective motion of large numbers of electrons. Incident light irradiating these surfaces excites conduction electrons in the metal and induces excitation of surface plasmons leading to enormous electromagnetic enhancement of spectral signatures [such as surface-enhanced Raman scattering (SERS) and surface-enhanced fluorescence (SEF)] for ultrasensitive detection of analytes of interest. This project will lead to a sensitive system with a broad-based sensing capability that can be used within stationary indoor and outdoor field sites as well as on mobile platforms for detecting optical spectral signatures (SERS, fluorescence) of CBW agents. This project will support the following application scenarios for detection in both indoor and outdoor environments: first responder operations, intelligence, CBW threat assessment, early warning, deterrence, and military operation.

Technical Approach

In this project, we propose the use of "enhanced spectral signatures" for CBW detection as an additional approach to detection, because of the tremendous diagnostic power of optical spectral techniques such as Raman and fluorescence. The novel features of the APSA technology include the following:

(1) Advanced sensing concept based on plasmonics (enhanced electromagnetic fields)
(2) Array of senors using nanotechnology-based probes
(3) Combination of bioreceptor recognition and enhanced spectral signatures for detection

We will develop a novel sensor array system based on nanostructured probes capable of producing highly enhanced electromagnetic fields (plasmonics). With the novel selective plasmonics enhancement (SPE) approach, the molecular interactions between the adsorption layer molecules and the plasmonics substrate depend on the chemical nature of the analyte molecules and the adsorption layers.

Results and Discussion

Task 1: Development of Substrate for Plasmonic Arrays

The goal of this task is to investigate and fabricate nanostructures that will permit enhanced field detection (Raman, fluorescence) of model compounds. In this period, we demonstrated a novel approach to preparing plasmon-active substrates based on the formation of silver oxide films and/or Ag nanoclusters on smooth glass surfaces and further illustrated its application for the Raman detection of several CBW simulants such as dimethyl methylphonate (DMMP), pinacolyl methylphosphonate (PMP), diethyl phosphoramidate (DEPA), 2-chloroethyl ethylsulfide (CEES), *Bacillus globigii* (BG), *Erwinia*

herbicola (EH), and *Bacillus thuringiensis* (BT). We have also been working on the preparation of different sizes and shapes (such as spheres, rods, tubes, and cubes) of metallic nanostructures for optimal plasmon enhancement. The preliminary results obtained by Raman spectrometer were very promising.

Task 2. Waveguide for Plasmonic Probe Array

The goal of this task is to develop sampling platforms based on optical waveguides for the plasmonic sensor array. These sensor arrays would be based on polymer-coated APSA sensors and data processing using pattern recognition and chemometric techniques. In this period, we have demonstrated the use of a polymer, that is, poly(vinylpyrro1idone) (PVPL), as a potential durable, effective coating for SERS substrates. Previous studies have demonstrated its permeability to compounds having hydrogen-bonding properties. Because of this permeability, the PVPL coating could be applied in relatively thick layers while still enabling the detection of monocyclic aromatic compounds, including alcohols, carboxylic acids, and various nitrogen-based functional groups, with varying signal enhancement. We began recently to investigate the possibility of making (poly)methyl-methacrylate (PMMA) smooth surfaces using spin-coating, one of the simplest and most common techniques of applying thin films onto solid substrates. The so-prepared polymer substrates enabled us to proceed with studies designed to show unequivocally that energetic charged particles produce surface features on PMMA plastic (Fig. 1).

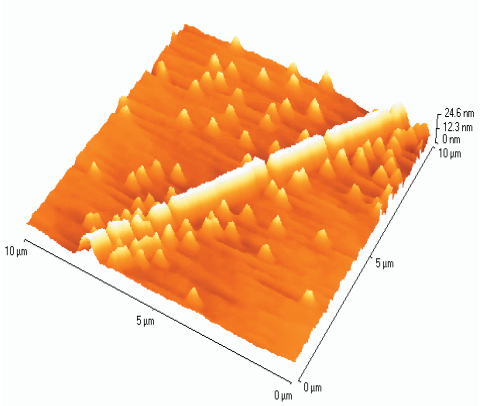

Fig. 1. An AFM image of nanopatterned polymer arrays generated by particle irradiation.Charged particles from an irradiation source were impinged upon the previously prepared PMMA surface and subsequently examined by AFM, tapping mode.

Benefits

The development of this novel "plasmonics-based" detection technology, if successful, will benefit DOE since it will provide a new optical spectral technique which can be applied to a variety of environmental problems associated with energy production, as well as to issues relevant to homeland security. The results of the proposed research will provide critical preliminary results, allowing the investigators to apply for further funding from outside sponsors, such as the Department of Homeland Security (DHS), DOE, the Department of Defense, DARPA, the Department of Justice (DOJ), and the National Institute of Health (NIH).

BIOLOGICAL SCIENCES AND TECHNOLOGY

Seed Money Fund

Biocatalytic Desaturation and Oxidation: A Technology with Multiple Applications

A. P. Borole[1] and C. Y. Hamilton[2]
[1]*Life Sciences Division*
[2]*University of Tennessee*

Desaturase enzymes introduce double bonds in long-chain molecules in a stereospecific and regiospecific manner. These enzymes mainly produce mono and polyunsaturated fatty acids (PUFAs) from long-chain fatty acids and desaturate sterols and other fatty and hydrocarbon molecules as well. The goal of this project was to identify novel desaturase and oxidase enzymes involved in alkane metabolism and fatty acid synthesis in *Rhodococcus* organism. Using the genomic sequence released recently, genes of interest were cloned into *E. coli* and *S. cerevisiae*. Analysis of enzyme activity revealed potentially new products belonging to di- and tri-unsaturated fatty acids of C14, C16, C18, and C20 fatty acids. Since bacterial enzymes have not been reported to produce such fatty acids, this is a novel finding. The clones were screened for activity towards alkane metabolism; however, no activity was observed towards alkanes. Two oxidase genes/operons were also cloned into *S. cerevisiae* and studied for their activity towards alkanes, alkenes and aromatics. The operon represented a protein complex consisting of three enzymes homologous to alkene monooxygenase. Initial screens using 1-octene and toluene have indicated that the complex is not active towards these substrates. The first result can potentially lead to a technology for production of PUFAs via bacterial fermentations, with applications in nutrition, paints, and polymer industries. The oxidase enzymes may be useful in oil and petrochemical industries for production of alkene epoxides, once the substrates are identified. Further work will be pursued by focusing on each application separately.

Introduction

Rhodococcus is known to have several unique metabolic pathways and solvent tolerance properties, which makes it an interesting organism for industrial applications. This organism is capable of growing over a range of temperatures from 5ºC to 40ºC. It has unique alkane and aromatic metabolic pathways suitable for conversion of low-value feedstocks to higher-value intermediates and fine chemicals. It also has enzymes for sulfur-specific conversion of organosulfur compounds, making it applicable for biodesulfurization.

Investigations into the metabolic pathways of the *Rhodococcus* genus can potentially lead to industrial processes for selective oxidation of alkanes and aromatics. It can use alkanes, specifically hexadecane, as the sole carbon source with a high growth rate. There is evidence in the literature that the organism has enzymes capable of desaturation of hexadecane belonging to the Δ9 desaturase class. With the release of the genomic sequence for one of the sp., *Rhodococcus* RHA1, it was possible to use bioinformatics tools to investigate the desaturase enzymes.

There is also evidence in the literature that the organism has temperature-dependent pathways to regulate membrane fluidity, which also use desaturase enzymes for changing structural components of membranes. Preliminary annotation analysis had indicated that sp. RHA1 contained genes homologous to the linoleoyl coA desaturase, which is usually not present in bacteria, but only in higher organisms. Thus, investigation into the desaturase enzymes of this organism was initiated to find these novel desaturases.

The results obtained from the project are encouraging; however, all the project goals were not met. The enzymes involved in alkane conversion were not identified; however, potentially novel fatty acid desaturases were cloned and identified.

Technical Approach

Eight desaturase genes were selected based on homology with known desaturase enzymes. Each of these genes contained a multi-histidine motif necessary for ligating iron to form the dirion catalytic centers. Of the eight enzymes, six were close to the linoleoyl coA desaturase enzyme. The genes were produced by PCR using primers designed for cloning into *E. coli* and *S. cerevisiae* vectors: pCWori and pYES2, respectively. The template used was genomic DNA isolated from *Rhodococcus* sp. RHA1 using Promega's genomic DNA kit for high-GC organisms. A genomic DNA from *Rhodococcus erythropolis* sp. IGTS8 was also used; however, this DNA did not yield significant PCR product.

The PCR product was cloned initially using the pCR2.1-TOPO cloning vector and transferred into *E. coli* DH5α, using the pCWori vector. These clones were investigated for their desaturation potential using

hexadecane and various fatty acids as substrates. Experiments with hexadecane did not show any new products upon GC analysis. There were some (unidentified) peaks in experiments using fatty acids as substrates. A literature survey indicated that *S. cerevisiae* was a better host for assessment of fatty acid desaturation, since it does not produce any PUFAs itself.

E. coli assay experiments were conducted by growing the cells up to an OD600 above 1.0, followed by induction for a period of 24 hours using IPTG as inducer. The cells were then pelleted and resuspended in fresh medium or buffer along with the substrate and incubated for a period of 12–24 hours. The assay mixture was then extracted using hexane as solvent. In case of fatty acids as substrates, the cells were pelleted, freeze-dried, and methylated. The methylation consisted of mixing the cells with 3 mL of methanol containing 1% sodium methoxide, followed by addition of 3 mL 1 *M* NaCL, followed by extraction with 3 mL hexane. The analysis of fatty acids was conducted using a 30-m × 0.53-mm HP innowax column and FID detector. The analysis of hexadecane-experiment extract was conducted using a DB1 column.

S. cerevisiae clones were grown using glucose to an OD600 of 1.0 in a uracil-selection medium, followed by induction using galactose and raffinose medium for 12–24 hours.Two assays were conducted, one using whole cells and one using cell extracts. Hexadecane as well as fatty acids including stearic, oleic, palmitoleic, linoleic acid, and sunflower oil were used as substrates. In experiments with oxidase gene products, toluene and 1-octene were used as substrates and experiments were conducted in 10-mL serum bottles with Teflon-lined septa.

Results and Discussion

The genomic sequence of *Rhodococcus* RHA1 contained significantly high GC content. The PCR reactions failed initially and had to be optimized individually for each gene. This was due to the different melting point for each gene/oligonucleotide pair. Two of the eight desaturase genes could not be PCRed even after five attempts employing different annealing/extension temperatures.

Experiments conducted using *E. coli* as well as *S. cerevisiae* clones showed that fatty acids used as substrates were incorporated into their cell membranes. The fatty acid profile was completely dominated by the substrates showing the ease of incorporation of added fatty acids into cell mass. Some of these fatty acids may be present as triacylglycerols, especially in the yeast; however, the speciation was not done. This result has implications in using microbial hosts for desaturation and may dictate the use of growing vs resting cell cultures for production applications.

In addition to single fatty acids, sunflower oil was also used as a substrate to provide a variety of fatty acids as substrates for conversion. This is almost necessary while screening since the substrates are unknown. A lipase was used in the oil assays to enable breakdown of the triacylglycerols in oil. In the results obtained, three new peaks were obtained when using sunflower oil as the substrate. No new peaks were obtained with the individual fatty acids tested as substrates. This indicates that the substrate for the enzymes were only present in sunflower oil. The new peaks have not been identified yet but were assessed to be di- or tri-unsaturated fatty acids based on their retention times in the GC chromatogram.

When using hexadecane as the substrate, no new peaks were obtained, indicating that none of the six genes encode the alkane desaturase. Further analysis of the genome sequence has identified more than four sequences encoding the peptide ExxHxxHH, which is conserved in Δ9 desaturases; however, these peptide fragments lie outside the predicted orfs based on currently available annotation programs. This implies that *Rhodococcus* may have novel promoter sequences, not known at this time. Alternately, new rules for annotation may have to be developed to identify the genes.

A search for oxidase genes related to hydrocarbon conversion resulted in identification of a complete operon comprising of three genes homologous to alkene monooxygenase, which converts an alkene to an alkene epoxidase. A preliminary annotation of the sequence was available only in April 2004; however, this did not identify the operon explicitly. The oxidase operon was cloned into the yeast and tested; however the two substrates studied, 1-octene and toluene, were not substrates for this protein complex. Monooxygenase enzymes with alkene and aromatic epoxidation have been reported in bacteria and are typically active towards toluene or simple alkenes. Thus, the *Rhodococcus* enzyme may be novel in its specificity.

Benefits

This project was aimed at establishing a groundwork for use of desaturase enzymes and at developing the microbial platform for applications in a number of areas of interest to DOE including biomass conversion (oils derived from plants, etc.), DOE-FE, and DOE-EERE (biocatalytic routes for hydrocarbon conversion). While much work needs to be done, potential enzymes of interest in such applications were identified in this project. Sponsors for further work will be programs supporting fundamental as well as applied work from the Office of Biomass, and EERE.

Two proposals were developed in 2004 to take this work further. One was submitted to DOE OIT in the area of alkane conversion to alkenes and higher alcohols. The reviewers pointed out the need for further fundamental work prior to application development on enzyme characterization and biochemical pathway. The second proposal has been submitted to DOE Office of Biomass requesting funding for demonstrating applicability of desaturase enzymes to conversion of low-value oil feedstocks to higher-value products.

Advanced Diagnostics Algorithm for Cancer Detection Using Hyperspectral Fluorescence Imaging

T. Vo-Dinh,[1] M. Martin,[1] S. G. Kong,[2] and Z. Du[2]
[1]*Life Sciences Division*
[2]*Department of Electrical and Computer Engineering, University of Tennessee*

The objective of the proposed research is to develop a novel advanced computing algorithm (ACA) for real-time, non-invasive diagnosis of skin cancer using a hyperspectral imaging (HSI) system. The application focus involves the study and correlation of fluorescence images of normal and neoplastic tissues. A technical innovation of this project is the combination of an advanced computing algorithm based on principal component analysis (PCA) with a real-time HSI system for detecting small differences in fluorescence profiles of normal and cancer tissues. The PCA provides an effective data representation and feature extraction method for real-time classification of a large amount of spectral signature data. This project selects the skin as the target organ because skin is easily accessible to the instrumental system. Once the systems have been optimized, studies will be performed on laboratory animals for diagnosis. This approach could lead to significant advances in effective and rapid detection of tumors over large areas of organs and in the understanding of cancer in general.

Introduction

Our hyperspectral imaging system captures a series of images, each containing a very narrow (2–5 nm) band of wavelengths, at discrete intervals over the visible spectrum. Since many organic and inorganic materials exhibit unique absorption, reflection, and fluorescence characteristics at particular bandwidths, these hyperspectral images are useful for identifying various materials and phenomena of interest. A hyperspectral image contains spatial information measured at a sequence of individual wavelengths across a sufficiently broad spectral band. This enables hyperspectral imaging to reveal more useful information for material identification than other imaging techniques (Shaw and Manolakis 2002; Landgrebe 2002). Fluorescence is a phenomenon where light is absorbed at a given wavelength by a particular molecular structure followed by the emission of light by that molecular structure at a longer wavelength. The altered biochemical and morphological state of neoplastic tissue may result in changes in the fluorescence spectral characteristics of the tumor tissue. The most definitive test for tumor detection historically has been a biopsy. Hyperspectral imaging offers the possibility for an instant, non-invasive diagnostic procedure based on the analysis of the tissue's spectral properties (Zhang et al. 1999).

Technical Approach

The development of a diagnostic tool using an advanced computing algorithm to detect skin lesions non-invasively in real time would be a major clinical advancement. Our project addresses this critical need in skin cancer detection. In its clinical implementation, the hyperspectral images would be used to aid the clinician during "visual inspection" by providing more accurate, objective information (morphological as well as biochemical) about the target and in identifying malignant lesions. Suspicious lesions that are confirmed to be malignant by the proposed advanced computing algorithm would then be biopsied prior to treatment. The advanced computing algorithm to be investigated in this research involves dimensionality reduction of hyperspectral image data, effective representation and feature extraction of spectral signatures, and classification. The principal component analysis (PCA) technique finds an efficient representation of the data at reduced dimensional feature space. The pattern classifier, based on a neural network algorithm, will be trained to classify skin cancer based on the spectral signatures.

Results and Discussion

ORNL has developed a hyperspectral imaging system capable of fluorescence imaging for tumor detection. As shown in Fig. 1, the HSI system developed at ORNL consists of an imaging fiber probe system for signal collection, an endoscope, an acousto-optic tunable filter (AOTF) for wavelength selection, a laser excitation source, an endoscopic illuminator, a CCD color camera for reflection detection, and an intensified charge-coupled device (ICCD) for fluorescence detection.

Reflection images were acquired using an Olympus endoscopic Illuminator equipped with a 300-W CW Xe arc lamp source. The reflection source was coupled to an Olympus gastrointestinal endoscope equipped with an imaging bundle. Fluorescence spectra and images were acquired using a LSI pulsed Nitrogen laser with a maximum repetition rate of 20 Hz. For fluorescence imaging, the N_2-pumped laser was coupled to a bifurcated fiber probe that was also used to sample point measurements using a miniature fiber optic spectrometer.

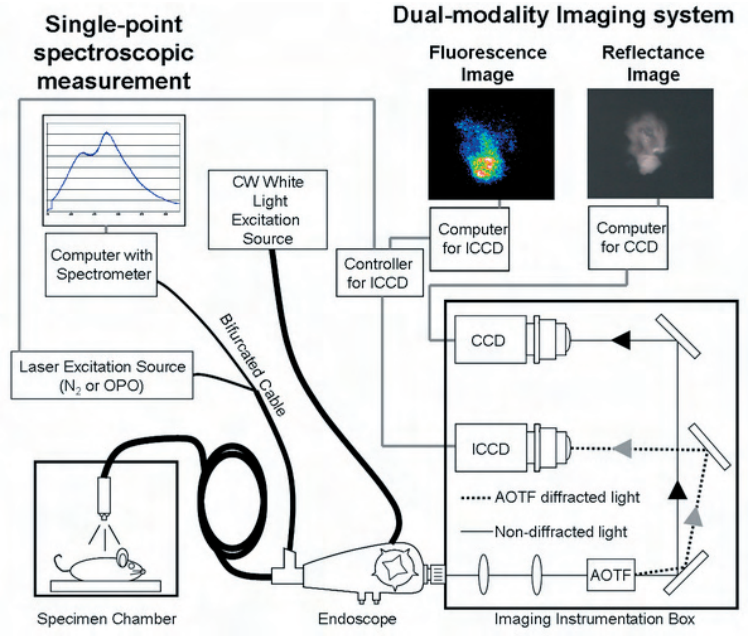

Fig. 1. Hardware component of Hyperspectral Image System.

Hyperspectral fluorescent images have been taken of normal and malignant mouse tissue at ORNL using 21 spectral bands from 440 nm to 650 nm in the visible spectrum. The figure has a size of 128 × 128 pixels and shows a normal tissue area surrounded by tumor tissue of a laboratory mouse. Hyperspectral data typically contains hundreds of contiguous spectral channels. As a result, each hyperspectral sample has an enormous amount of data. However, the large amount of data that must be processed presents significant problems to the end user. These include increased operational complexity and cost, computational burdens, and data transmission bandwidth limitations. In order to overcome these problems, a number of band selection methods were developed. Because not all bands carry the same amount of information, the bands can be ranked according to the significance of their information so data dimensionality reduction can be achieved by removing bands with lesser priorities. Band selection methods identify a subset of the original spectral bands in the fluorescence spectra that contain most of the important characteristics. A proper subset of bands can contain the same information, with less noise, than the complete set of bands. This can lead to both an increase in accuracy and a decrease in computational complexity.

We used all spectral characteristics of the fluorescence spectra as features to train a Support Vector Machines (SVM) classifier. SVM is a new generation learning system based on recent advances in statistical learning theory. We implemented our tumor detection procedure as follows. First, the images were registered by manual registration. Then bands were ranked by the spectral information measure (SIM)-based method. Band selection was applied followed by image registration. Through this result, we found that the fluorescence band at 490 nm provided more information than other bands. This result was consistent with the observation that the actual images image recorded at 490 nm was the clearest one.

We used the mouse data to test the efficiency of the band selection technique. From this work, we found that using only 7 bands, we could achieve good classification accuracy. This result means that, in practice, we do not need to record all 21 spectral image; just 7 spectral images are sufficient for use in data treatment. This data reduction process will save time in acquiring spectral images and performing computation analysis.

Benefits

The development of the Advanced Diagnostics Algorithm for cancer detection using hyperspectral fluorescence imaging will provide benefits to DOE's and NIH's biomedical imaging initiatives. This technique is also of value to DOE as it may provide diagnostic capability to detect early cancerous changes due to exposure to energy-producing processes and substances and thereby allow more effective therapeutic intervention. The results of the research reported here will enable us to make effective application to NIH and other agencies to expand these studies.

Conclusion

This report presents a skin tumor detection method using hyperspectral fluorescence images. Hyperspectral images have proved useful in providing information for detecting tumors. The fluorescence data captured by the hyperspectral imaging system contain a higher level of contrast and thus provide greater possibility of detecting tumors. The classification result shows that the method proposed in this report can efficiently detect tumor and normal tissues. The band selection method can efficiently reduce the size of the hyperspectral image data. The experimental results show that with only 7 bands, we can achieve over 95% accuracy.

References

Shaw, G. and D. Manolakis. January 2002. "Signal processing for hyperspectral image exploitation." *IEEE Signal Processing Magazine* **19**(1), 12–16.

Landgrebe, D. January 2002. "Hyperspectral image data analysis." *IEEE Signal Processing Magazine* **19**(1), 17–28.

Zhang, J., C. Chang, S. Miller, and K. Kang. October 1999. "Optical biopsy of skin tumors." *Proc. 21st Annual Conference on Engineering in Medicine and Biology*. Vol. 2, pp. 13–16.

A Shortcut to Making Mouse Models for Stressor Resistance for Application to Longevity (Aging) and Other Exposure-Biology Research

Y. You
Life Sciences Division

A body of evidence indicates that one of the factors associated with longevity is the ability to deal effectively with stress: even cells derived from long-lived animals exhibit higher stress resistance. This project is to expose mouse embryonic stem (ES) cells to mutagen N-ethyl-N-nitrosourea (ENU) followed by selection of the ES cells for stressor (paraquat)-resistance in culture. ENU causes single-gene mutations in DNA and paraquat (1,1'dimethyl-4,4'-bipyridylium dichloride) generates reactive oxygen species (ROS). ES cells surviving such selections will be characterized, and their germline competency will be evaluated. The objective of this project is to experimentally verify this novel mutagenesis-selection strategy and to create ES cells predicted to give rise to mice with longer life spans.

Using the mouse as a model system to study longevity by genetic approaches has inherent disadvantages: its relatively long life span and associated high maintenance cost. To circumvent this drawback, we designed a genetic strategy to mutagenize ES cells and screen for ROS-resistant ES cells. It was reported that cells derived from long-lived mice display higher resistance to ROS. Therefore mice derived from ROS-resistant ES cells should have higher stress resistance and could live longer. ROS is one type of stressor; therefore, it can be replaced by other stress factors and allow rapid low-cost screens to study cellular response.

The proposed experiments have three stages: (1) mutagenesis, (2) selection, and (3) analysis. Mutations were induced by ENU, a powerful mutagen, on ES cell line EC7.1. The selection was achieved by application of paraquat in the mutagenized ES cell culture which should kill most of the ES cells; only those cells that are resistant to the paraquat, presumably caused by the mutations, could survive. These stressor-resistant ES cells will then be analyzed, and mice will be derived from these stressor-resistant ES cells. It was reported that ROS increased the rate of mitotic crossover, which will cause loss of heterozygosity. This is a desired feature in our experimental strategy so that we can screen for both dominant and recessive mutations.

We analyzed ENU concentration versus ES cell survival rate to determine which ENU concentration will be applied for the ES cell mutagenesis. Freshly prepared ENU at concentration of 0.6 mg/ml in the cell culture media killed 85% of EC7.1 ES cells, whereas 10-day-old ENU stock frozen at -20˚C lost ~6–10% of its potency. We also studied paraquat concentration versus ES cell survival rate to determine what concentration of paraquat will be tested to screen for mutagenized ROS-resistant ES cells. After we obtained such data, ES cells surviving ENU treatment were expanded and cultured with paraquat at 40 μM for 24-hours and then the cells were cultured without paraquat for two weeks. So far we have picked 23 ENU-treated ES cells that survived paraquat screening. During the experiment, we also found that after the ENU-treatment, ES cells were very sensitive to β-mercaptoethanol (β-ME) withdrawal. β-ME is a normal additive to the ES cell media, and it acts as a reducing agent to protect the cells from ROS generated from the environment, presumably through oxygen in the incubator. We also recovered 12 ENU-treated ES cell colonies that survived the ES cell culture media containing no β-ME. All the ES cells survived the ENU-treatment, and the selections were expanded and frozen. DNAs were isolated from these cell lines. We identified and validated two polymorphic MIT markers per mouse chromosome (total 40 polymorphic MIT markers) for genome scanning (by PCR) to identify mitotic crossover events in these ES cells. The next step is to perform the genome scanning for all 35 ES cell lines ($35 \times 40 = 1400$ PCR). We started injection of these ES cells into the blastocysts as well as aggregation of the ES cells with 8-cell-stage embryos to test germline contribution of these mutagenized ES cells.

Creation of Photosystem II Designer Alga for Hydrogen Production

J. W. Lee and B. Evans
Chemical Sciences Division

This project will provide the proof of principle to create a photosystem II (PSII) designer alga for efficient and robust production of hydrogen with temporal separation of oxygen production. By creating such a PSII designer alga, we will be able to simultaneously solve the three associated oxygen problems in the field of photosynthetic hydrogen production: (1) drainage of electrons by oxygen, (2) poisoning of hydrogenase by oxygen, and (3) mixed hydrogen and oxygen gas-product separation and safety issues.

This proof-of-principle project will lead to the creation of our envisioned photosystem II (PSII) designer alga for production of pure hydrogen without the oxygen production so that all of the three oxygen-related problems will be eliminated under hydrogen-producing conditions. It is expected that this study will significantly advance the basic science and produce a preliminary PSII designer alga for enhanced clean hydrogen production. Successful development of such a PSII designer alga will have a significant impact (a 10-fold improvement) on technology development in the field of renewable hydrogen research. Therefore, this project has direct relevancy to DOE's national (energy) security mission by creating a clean and renewable algal hydrogen energy resource. It supports President Bush's Hydrogen Initiative and is in line with the goal of the DOE EERE and BES hydrogen programs.

During this reporting period, we accomplished a DNA-sequence design that could code for the envisioned photosystem II (PSII) suppressor to create the proposed PSII designer alga for enhanced photobiological production of hydrogen (H_2) from water. We are now in the process of chemically synthesizing this DNA material using the sequence design and preparing its transformation into our host alga to demonstrate the proof of principle for the envisioned PSII designer alga in FY 2005. During this period, we also interviewed two postdoctoral candidates and finally found a very good molecular genetics postdoctoral research associate (Dr. Bin Zhao) for this project. Starting on October 5, 2004, Dr. Zhao, has been working full time with us for this project. With this addition of manpower, the progress of this project will be accelerated, and we expect to achieve full project objective during FY 2005.

Development of a Multimode and Multispectral Automated Mueller Matrix Polarization Imaging System for Non-Invasive Skin Cancer Detection and Diagnosis

J. S. Baba,[1] M. N. Ericson,[1] S. S. Gleason,[1] and M. Duvic[2]
[1]*Engineering Science and Technology Division*
[2]*The University of Texas, M. D. Anderson Cancer Center*

Melanoma, the deadliest form of skin cancer, will account for approximately 7600 U.S. deaths this year. Present techniques employed for early detection involve cost-intensive physical examinations and frequently unnecessary tissue biopsies. In an effort to improve patient outcome and reduce cost, researchers at ORNL are developing a non-invasive, non-contact, multimode and multispectral automated Mueller matrix polarization imaging instrument to enable rapid and efficient early detection of melanoma. This instrument will be used at the M. D. Anderson Cancer Center (Houston, Texas) to verify its sensitivity for non-invasive discrimination of human cancerous and non-cancerous lesions, in vivo. Data will be acquired at M. D. Anderson using this new instrument on 20 consenting patients over a period of 6 months.

There is urgent need to develop more reliable instruments for medical diagnostics and treatment that will enable the early detection and treatment of potentially fatal diseases, such as melanoma, while reducing the associated necessary medical resource burden.

Our technique, based on imaging suspect skin lesions with different colors of light (multispectral imaging), provides many significant improvements over current research and clinical methods. For one, by incorporating the use of polarized light, it provides increased structural contrast and detail to improve structural visualization and segmentation. Secondly, by utilizing multispectral images to enhance metabolic contrast of suspect lesions, it improves discrimination based on the increased cellular activity of active tumors. Thirdly, by employing image processing techniques that fuse the multimode data, it will facilitate accurate and automated detection and diagnosis.

Since the project was initiated in March 2004, we have successfully obtained IRB approval to clinically demonstrate our instrument on volunteer human patients, completed system design, and purchased and ordered the necessary system components, of which several are custom optical components. Construction of the instrument has begun in conjunction with system integration and calibration. Once we have completed this step, we will be ready to proceed with the next phase of system quantification before we finally go to the clinic to collect preliminary data on patients.

This project, when completed, will provide a measurable improvement in the discrimination of cancerous and benign skin lesions using a new non-invasive multimode alternative to biopsy. The direct consequence will be improved patient outcome, reduced patient discomfort, and a reduction in the costs associated with skin cancer diagnosis and treatment. The indirect consequence will be the advancement of non-medical fields such as atmospheric science research where a high-resolution multimode and multispectral imaging system would be a useful tool for dynamic studies.

This project fits in with DOE Office of Science's general mission to advance research that improves the quality of life for all Americans, and more explicitly, pursues the goal of DOE Office of Science Medical Science Division (MSD) to develop innovative diagnostic and treatment solutions to critical problems in human health. The success of this research will ultimately lead to the development of a medical instrument that can be transferred to the National Institutes of Health (NIH) for clinical testing or to industry for further development; a stated major objective of the DOE Advanced Biomedical Technology (ABT) Research initiative. Currently, this research directly addresses two NIH-NCI funding areas: (1) Novel Technologies for Noninvasive Detection, Diagnosis, and Treatment of Cancer, and (2) Industry-Academic Partnerships for Development of Biomedical Imaging Systems and Methods That Are Cancer Specific (R21). It also targets NIH-NIBIB objectives. Additionally, this project leverages ORNL's new expertise in the field of biomedical engineering and optics to develop a high-impact instrument with significant clinical application while advancing its initiative to increase collaborations with world-class institutions.

An Image-Based Method for Screening and Diagnosis of Blinding Eye Disease

K.W. Tobin,[1] T. P. Karnowski,[1] and E. Chaum[2]
[1]*Engineering Science and Technology Division*
[2]*University of Tennessee Health Science Center*

Early detection and treatment of prevalent blinding eye disease can have a significant impact on reducing vision loss and blindness worldwide. The objective of this research is to develop, test, and validate a unique image-based retinal screening and diagnostic method that leverages content-based image retrieval (CBIR) technology. In collaboration with the University of Tennessee Health Science Center (UTHSC) Department of Ophthalmology, we are using digital retinal photography and optical coherence tomography to image and automatically quantify specific disease-based changes in the retina. We will develop an extensive image database of retinal disease states for CBIR analysis, and its clinical application will be validated through UTHSC Internal Review Board–approved clinical studies.

Early detection and treatment of prevalent blinding eye diseases including diabetic retinopathy (DR), glaucoma, and age-related macular degeneration (AMD), can have a significant impact on reducing vision loss and blindness worldwide. The primary objective of this proof-of-principle project is to develop, test, and validate a unique image-based retinal screening and diagnostic method that leverages content-based image retrieval (CBIR) technology. In collaboration with the University of Tennessee Health Science Center (UTHSC) Department of Ophthalmology, we will use digital retinal photography and optical coherence tomography to image and quantify specific disease-based changes in the retina. We will develop an extensive image database of retinal disease states for CBIR analysis, and its clinical application will be validated through UTHSC and ORNL Internal Review Board (IRB) approved clinical studies. New image analysis and management methods that can leverage this data have the potential to improve the sensitivity and specificity of ocular diagnosis, and to monitor therapeutic responses to treatment in a robust, objective, and deterministic manner.

We are pursuing three primary research tasks to establish the base method for automated CBIR diagnosis and proof-of-concept. These tasks include establishing a comprehensive database of fluorescein angiography (FA) and optical coherence tomography (OCT) images and associated diagnosis metadata; developing the required image feature extraction, indexing, and diagnosis method; and validating the diagnostic algorithms through a blinded clinical trial.

Our approach to addressing the development of a viable diagnosis method involves implementation of a unique statistical feature description of relevant structure extracted from both the temporal FA image sequences and the associated patient OCT data. A new method for feature mapping to a reduced and case-focused feature set will be implemented based on an exemplar library of diagnosed pathologies. This feature mapping procedure leverages our experience in principle component and linear discriminant analysis. The reduced feature set then becomes the index for each previously diagnosed image in the existing image retrieval engine. Diagnosis is based on a statistical assessment of returned cases. The novel contribution of this effort resides in the unique concept of generating the reduced feature-based index by using the temporal FA and OCT image set. Uniqueness also resides in the proposed method for predicting a diagnosis based on a CBIR engine using an historical database of previously diagnosed human patient data.

This project was initiated in May 2004 and will be concluded in the summer of 2005. Due to the nature of the human data that is being evaluated for this project, it was required that IRB approval be obtained. This was accomplished in June and allowed ORNL to receive anonymized, diagnosed human data from UTHSC. With IRB approval in hand, we worked with Dr. Ed Chaum to assemble a database of 820 FA images representing 331 patients. This dataset comprises our initial image repository and patient context for developing our feature analysis methods. The database is continuing to be augmented with pre-existing data by the UTHSC staff and will be periodically updated at ORNL. Once this dataset was assembled, we visited the Ophthalmology Department at UTHSC to interview Dr. Chaum and his staff and to document the visual attributes of FA imagery that are used to diagnose the various pathologies that this data represent—a necessary step to support our development of appropriate statistical feature descriptions for image indexing, retrieval, and diagnosis.

Subsequent to this working visit and our receipt at ORNL of the pre-existing patient database, we constructed and implemented a database architecture. This database architecture allows us to append the data at later dates and

to incorporate our descriptive feature data for performing image-based queries and diagnostics. In preparation for the next phase of research, we have completed an extensive literature review on the topic of retinal image processing and analysis, primarily as it relates to the identification of anomalous retinal structures and morphology associated with various debilitating pathologies.

This research in biomedical image analysis supports the DOE Office of Science and the area of Biological and Environmental Research. The underlying technology that is being leveraged for this project was developed at ORNL through research supporting the Office of Energy Efficiency and Renewable Energy and the Industrial Technologies Program. This original work was performed in the area of industrial automation and waste mitigation through image-based quality control and is now being applied to the automated diagnosis of blinding eye disease.

It is anticipated that the establishment of a content-based retinal image database in conjunction with the clinical validation of this method for automated retinal diagnosis will provide significant value to a variety of other federal agencies as well. Potential benefactors of this technology include the National Eye Institute (NEI), which continues to support clinical reading centers. Validation of automated diagnostic technology is anticipated to be of interest not only to the NEI but also to the National Institute for Biomedical Imaging and Bioengineering (NIBIB/NIH), which supports research for novel biomedical imaging methods. Other federal agencies that can benefit from this research include the U.S. Army Medical Research and Materiel Command, and its Telemedicine and Advanced Technology Research Center (TATRC). These agencies have a strong interest in innovative technology applied to telemedicine, which is a natural growth area for this research and technology.

CHEMICAL SCIENCES AND TECHNOLOGY

Director's R&D Fund

Self-Organizing Polymers as Biomaterials

P. F. Britt,[1] J. W. Mays,[1,2] J. Pickel,[1] J. Howe,[3] I. Chung,[2] and M. Liu[4]
[1]*Chemical Sciences Division*
[2]*Department of Chemistry*
[3]*Metals and Ceramics Division*
[4]*Department of Materials Science and Engineering, University of Tennessee*

This research project focused on the synthesis, self-assembly, characterization, and properties of amphiphilic block copolymers as potential biomaterials. Many of the properties and function of biological systems can be imitated by using self-organized structures, but there is a lack of fundamental understanding of how the copolymer's architecture affects self-assembly in solution, and property (or function) of the material. A better understanding of the structure-property relationships of amphiphilic block copolymers will lead to the design and synthesis of new functional biomaterials, which have biomedical applications. This project focused on three different synthetic targets utilizing living anionic and controlled radical polymerization techniques. First, linear block copolymers of styrene and ethylene oxide (PS-PEO) and a mixed arm star copolymer of $PS_2(PEO)_2$ were synthesized by living anionic polymerization techniques to investigate the impact of branching on self-assembly. Second, block copolymers of polyacrylic acid-polystyrene and polyacrylic acid-poly(butylstyrene) were prepared by atom transfer radical polymerization techniques (ATRP) to investigate the impact of substitution of the solution-phase aggregation and encapsulation of hydrophobic substrates. Third, well-defined amino acid–based polymers were prepared from acryloyl β-alanine with narrow molecular weight distributions by ATRP methods, and a temperature and pH responsive block copolymer was prepared by copolymerization with N-isopropylacrylamide. This study highlights how the controllable properties of synthetic polymers can be combined with the exceptional functionality, activity, and specificity of biological macromolecules.

Introduction

One of the greatest technical challenges facing chemistry, physics, and materials science today is the controlled synthesis of mesoscopic materials with well-defined properties, and assembly of these materials into macroscopic functional devices. One approach to address this grand challenge involves the synthesis and self-assembly of block copolymers to generate complex architectures with tailored mechanical, optical, electrical, or other physical properties (Bates 1999). Block copolymers can be prepared by living polymerization methods with a high degree of control over the molecular architecture, which in turn controls molecular properties and function (Hong 1999; Coessens 2001). Because of the opportunities that exist for research into materials that mimic the properties and function of biological materials (Förster 2002), this research project focused on the synthesis, self-assembly, characterization, and properties of amphiphilic block copolymers as potential biomaterials. The ultimate goals of this research were to provide ORNL with new opportunities and capabilities in the synthesis and characterization of soft materials for a variety of applications of interest to the Department of Energy (DOE) and the National Institutes of Health (NIH) and to gain insight into the structure-property relationships of amphiphilic block copolymers so that materials (and biomaterials) could be synthesized with tailored structure, property, and function. This research is also directly aligned with the Complex Macromolecular Systems research theme at the Center for Nanophase Materials Sciences (CNMS), and it will help develop the skills and expertise necessary to attract university collaborators to the CNMS and to attract external funding. The synthetic skills developed in this project will also benefit researchers in computational science, to correlate polymer theory with experiments on well-defined polymers, and in neutron science, which needs well-defined deuterated polymers for neutron scattering studies.

Technical Approach

These research tasks are focused on the synthesis and characterization of amphiphilic block copolymers as potential biomaterials. Three different synthetic targets were pursued in parallel utilizing living anionic and controlled radical polymerization techniques. First, nonlinear poly(ethylene oxide)-based block copolymers were synthesized since little prior research has addressed the role of molecular architecture (i.e., branching) on the self-assembly and biocompatibility of these materials. Second, "crew-cut" block copolymers, in which the insoluble polystyrene block is larger than the soluble acrylic acid block, were synthesized by atom transfer

radical polymerization methods (ATRP) to determine how the structure of the core influences the formation and stability of the polymer aggregates in solution, and how it impacts the encapsulation and release of hydrophobic substrates. Since the physical state and properties of the core are largely determined by the glass transition temperature (T_g) of the core-forming block, poly(butyl-substituted styrenes) were investigated since their T_g is below room temperature (i.e., a liquid-like core), while polystyrene has a T_g =100°C (i.e., a glassy core). Third, acryloyl amino acid derivatives were polymerized by ATRP methods to determine if the controllable properties of synthetic polymers could be combined with the exceptional functionality, activity, and specificity of biological macromolecules. Block copolymers were also synthesized with poly(*N*-isopropyl acrylamide), a thermosensitive polymer, and their solution properties studied. The specific accomplishments for each task are described below.

All synthesized monomers and polymers were characterized by standard analytical techniques, which include proton and carbon-13 nuclear magnetic resonance spectroscopy (NMR), and gel permeation chromatography (GPC) with refractive index and light-scattering detection. Conversion was based on monomer consumption and polymer molecular weights, which were determined by NMR, GPC, and gas chromatography. Polymers were purified by multiple precipitations and dialysis. The catalyst from ATRP reactions was removed by passage of the reaction mixture through a short column of silica or alumina. Polymer micelles were characterized by dynamic light scattering, fluorescence spectroscopy, and transmission electron microscopy. Cloud point determinations as a function of temperature and pH were determined by the turbidity of the solution at 500 nm.

Results and Discussion

Polystyrene-Poly(ethylene oxide) Copolymers. Living anionic polymerization techniques were used to make linear block copolymers of styrene and ethylene oxide (PS-PEO) and a mixed arm star polymer of $PS_2(PEO)_2$ to investigate the impact of branching on self-assembly. PS-PEO was prepared in two steps by initiating styrene polymerization with *sec*-butyllithium, followed by capping the living PS chain with excess ethylene oxide. After purification, this polymer was used as a macroinitiator, by reaction with diphenylmethylpotassium, for the polymerization of ethylene oxide in tetrahydrofuran. Many polymers were made in which the measured-number average molecular weights (M_n), determined by NMR and GPC, agreed with the theoretical molecular weights, and polymers with low polydispersities (PDI = M_w/M_n = 1.06) were obtained indicating precise control over the polymer architecture had been achieved. Attempts to prepare $PS(PEO)_2$ by reacting living PS with excess methyltrichlorosilane, followed by removal of excess chlorosilane, and addition of two equivalents of living PEO was unsuccessful. Varying the molecular weight of the PS and PEO from 50,000 g/mol to 10,000 g/mol and increasing the final reaction time up to two weeks did not produce the desired bis-PEO adduct as the dominant product. It was concluded that either the silyl ether linkage was hydrolyzing during workup or the second equivalent of PEO could not access the chlorosilane. A miktoarm star copolymer was successfully synthesized containing two polystyrene and two poly(ethylene oxide) chains attached to a center core of 1,3-bis(1-phenylethenyl)benzene (Liu 2004). Living polystyrene chains (M_n = 6500 g/mol, M_w/M_n = 1.12) were added to 1,3-bis(1-phenylethenyl)benzene (0.5 equivalents), and the resulting anion was quenched with excess ethylene oxide. Under the reaction conditions (lithium counter ion and nonpolar solvent), only one ethylene oxide was added to each living center. After purification by multiple precipitations, the hydroxyl groups were initially reacted with diphenylmethylpotassium, followed by the desired amount of ethylene oxide. The final polymer had M_n = 20,800 g/mol and M_w/M_n = 1.07 with polystyrene arms of M_n = 6500 g/mol and poly(ethylene oxide) arms of M_n = 3900 g/mol. The comparison of the solution-phase behavior of the miktoarm star copolymer vs the linear copolymer is still under investigation via light-scattering techniques.

Polystyrene–Poly(Acrylic Acid) Copolymers. Block copolymers of polystyrene or butyl-substituted polystyrene with poly(acrylic acid) were prepared by atom transfer radical polymerization techniques (ATRP) to determine how the structure of the core influenced the formation and stability of the polymer aggregates in solution, and how this impacts the encapsulation and release of hydrophobic substrates. In general, the preparation of these polymers was slower and more challenging than expected. For each polymer and copolymer, the amount of catalyst, copper bromide (I) and copper bromide (II), ligand, *N, N, N', N', N"*- pentamethyldiethylene triamine, initiator, phenylethyl bromide for styrene and 2-ethyl bromopropionate for *t*-butyl acrylate, solvent, dimethylformamide or acetone, and the reaction temperature and time had to be optimized to obtain a narrow molecular weight distribution. Nevertheless, homopolymers of styrene (PS) and *t*-butyl acrylate (PtBA) were prepared with narrow molecular weight distributions (M_w/M_n = 1.1–1.2) and controlled molecular weights (M_n = 5,000–10,000 g/mol). These macroinitiators were used to prepare block copolymers of PtBA-PS with M_w/M_n of 1.2. Poly(acrylic acid)–polystyrene (PAA-PS) copolymers were prepared by hydrolysis of the *t*-butyl group with trifluoroacetic acid. A series of block copolymers were prepared in which the acrylic acid

block was held constant (79 monomer units), while the polystyrene block was varied from 396 to 61 monomer units (Pickel 2004). The polymerization of three butyl-substituted styrenes was also investigated: *t*-butylstyrene which was commercially available, *n*-butylstyrene prepared from *n*-butylbenzene, and *m*-butylstyrene, prepared from *m*-bromoacetophenone. It was difficult to control the molecular weight and polydispersity of the *p*-substituted polystyrenes by ATRP techniques owing to a predisposition of these monomers to participate in chain transfer reactions. Some degree of control was achieved for the ATRP polymerization of *m*-butylstyrene by using poly(*t*-butyl acrylate) as a macroinitiator, but it was difficult to produce long blocks (>100) of poly(*m*-butylstyrene). A poly(acrylic acid)-poly(*m*-butylstyrene) with block lengths of 79 and 43 monomers, respectively, and low polydispersity (M_w/M_n = 1.1) was prepared by hydrolysis of the *t*-butyl group of the poly(*t*-butyl acrylate)-poly(*m*-butylstyrene) copolymer.

Micelles were typically prepared by dissolving the copolymers in an organic solvent, such as tetrahydrofuran or dimethylformamide, at a concentration of 1–10 mg/mL and slowly adding water to the polymer solution. Successful micelle preparation was indicated by the characteristic faint blue color from scattered light as opposed to a milky color that indicates aggregation. The organic solvent was typically removed by dialysis with water. The micelles were analyzed by fluorescence techniques using pyrene as a hydrophobic probe, dynamic light scattering, and transmission electron microscopy (Pickel 2004). For PAA-PS solutions at pH = 7, dynamic light scattering as well as TEM analysis showed that spherical micelles, ca. 30 nm in diameter, were formed. However, TEM analysis also showed that other morphologies, such as rods and vesicles, were formed, depending on the preparation conditions (Fig. 1). Fluorescence studies allowed the determination of the critical micelle concentration (CMC), partition coefficient, and diffusion coefficients of small hydrophobic probe molecules from the micelles. The CMCs for PAA-PS copolymers (ca. 6 mg/L) and the partition coefficients (K_V ca. 7×10^5) for pyrene were found to be independent of the polystyrene block length. Surprisingly, the poly(acrylic acid)-poly(*m*-butylstyrene) copolymer had a CMC six times larger than the PAA-PS copolymers and a partition coefficient ten times smaller. In addition, the diffusion of pyrene from the hydrophobic core was ca. 7.5 times faster for the *m*-butylstyrene (T_g = - 27°C) than for the styrene (T_g = 100°C) containing copolymer. Although more studies are needed on polymers with different volume fraction of poly(*m*-butylstyrene), this study highlights that the release profile of a micelle can be tuned by altering the structure of the micelle core. These studies are relevant to the design of controlled release drug deliver systems and membranes.

Amino Acid–Based Polymers and Copolymers. Developing the techniques to control the polymerization of amino acid–based monomers is the first step in the synthesis of tailored amino acid–based polymers and copolymers for medical applications. In this study, well-defined acryloyl β-alanine (ABA) polymers with narrow molecular weight distributions were synthesized directly by ATRP methods with various water-soluble initiators. Temperature and pH responsive amphiphilic block copolymers were also prepared by copolymerization of PABA with poly(*N*-isopropylacrylamide) (NIPAAm), a

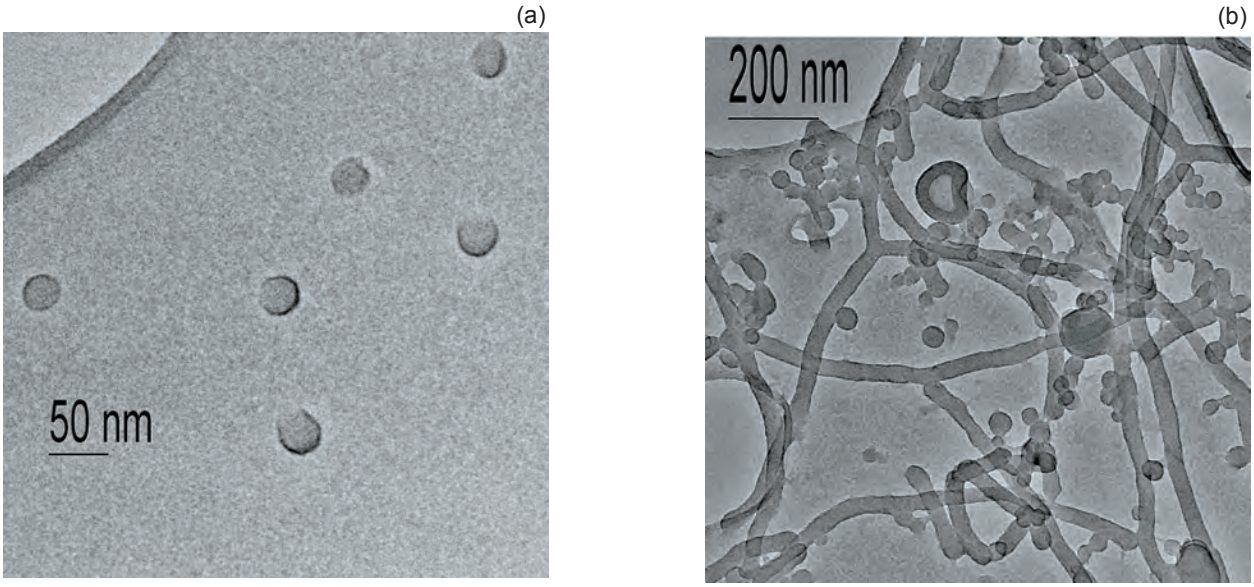

Fig. 1 (a) Transmission electron microscope (TEM) image of spherical micelles from the poly(acrylic acid)-polystyrene block copolymer. (b) TEM image of polymer aggregates, which include spherical micelles, rod-like micelles, and vesicles, from an aqueous solution of poly(acrylic acid)–polystyrene.

thermoresponsive polymer. Amino acid monomers were synthesized by reaction of *beta*−alanine (hydrophilic monomer) or phenylalanine (hydrophobic monomer) with acryloyl chloride. Water-soluble initiators, methoxy heptaethyleneglycol 2-bromoisobutyrate, 2-hydroxyethyl 2-bromoisobutyrate, and sodium 4-bromomethylbenzoate, were synthesized, and the ATRP was studied in aqueous solution or 3:2 water/methanol at room temperature using CuBr/bipyridine catalyst at pH 8 (Chung 2004a).The polymerization of the ABA monomer was surprising fast at room temperature, with over 70% conversion in 10 min. Polymers with M_n = 8,000–18,000 g/mol (by GPC, light scattering, and NMR) were prepared in 90–97% yield with low polydispersities (M_w/M_n = 1.13–1.25). All three initiators afforded good results, but the ethylene glycol-based initiator may be preferred based on biocompatibility considerations.

Block copolymers of PABA and poly(NIPAAm) were synthesized using PABA as the macroinitiator. Initially the polymerization of NIPAAM was optimized in 3:2 water/methanol with CuBr/bipyridine catalyst at room temperature. Polymers with low polydispersities (M_w/M_n = 1.06–1.15) were obtained (by GPC), but the experimental molecular weights were always greater than the theoretical molecular weights, indicating nonideal behavior. Block copolymers of PAMA-PNIPAAm were synthesized (M_n = 11,000–15,000 g/mol and M_w/M_n = 1.1–1.2) and characterized by NMR and light-scattering techniques (Chung 2004b). The solution-phase behavior of the copolymer was sensitive to temperature and pH. In aqueous solution, PNIPAAm shows thermoresponsive behavior, reversibly cycling between a homogeneous solution below 30°C and a heterogeneous solution above 30°C because of the hydrophobicity of the isopropyl groups. Because the block copolymer contains a free carboxylic acid, it also shows a pH-dependent behavior. Above pH 4, an aqueous solution of polymer becomes heterogeneous above 30°C as expected, but below pH 4, the transition temperature decreases to ca. 20°C as a consequence of intramolecular hydrogen bonding between the ABA and NIPAAm chains. A random copolymer of PABA-PNIPAAm produces homogeneous solutions above pH 4, independent of temperature but below pH 4, temperature-dependent aggregation was observed. This study clearly demonstrated that well-defined amino acid–based polymers can be synthesized under relatively mild conditions and that environmentally responsive copolymers can be made that have potential for drug delivery systems.

Benefits

The ultimate goal of this research was to provide ORNL with new opportunities and capabilities in the synthesis and characterization of soft materials for a variety of applications of interest to DOE and NIH and to gain fundamental insight into the structure-property relationships of amphiphilic block copolymers so that materials (and biomaterials) can be synthesized with tailored structure, properties, and function. This research is also directly aligned with the Complex Macromolecular Systems research theme at the CNMS, and it facilitates the development of the skills and expertise that are needed to attract external funding, and to attract external university collaborations. The synthetic skills developed in this project could also be used to produce deuterated macromolecules for neutron scattering experiments at the upgraded High Flux Isotope Reactor and the future Spallation Neutron Source at ORNL. This research will also provide new opportunities in computational science, since theory can be used to predict structure-property relationships in polymers and composites and compare the result to experiments on well-defined polymers. The synthetic skills developed in this project are also of benefit to the carbon nanotube efforts at ORNL in which new opportunities exist in the design of multifunctional polymer-nanotube composites that would be of interest to DOE, National Aeronautical and Space Administration, and defense organizations.

References

Bates, F. S. and G. H. Fredrickson. 1999. "Block Copolymers-Designer Soft Materials." *Phys. Today* **52**, 32–38.

Chung, I., P. F. Britt, D. Xie, E. Harth, and J. Mays. 2004a. "Synthesis of Amino Acid-Based Polymers via Atom Transfer Radical Polymerization in Aqueous Media at Ambient Temperature." *Chem. Commun.* (accepted for publication).

Chung, I., P. F. Britt, and J. W. Mays. 2004b. "Synthesis of Amino Acid Based Block Copolymers via Atom Transfer Radical Polymerization in Aqueous Media at Ambient Temperature." *Polym. Prepr.* (*Am. Chem. Soc., Div. Polym. Chem*.) **45**(1), 1091.

Coessens, V., T. Pintauer, and K. Matyjaszewski. 2001. "Functional Polymers by Atom transfer Radical Polymerization." *Prog. Polym. Sci.* 26, 337.

Förster, S., and T. Plantenberg. 2002. "From Self-Organizing Polymers to Nanohybrid and Biomaterials." *Angew Chem. Int. Ed*. **41**, 688.

Hong, K., D. Uhrig, and J. W. Mays. 1999. "Living Anionic Polymerization." *Curr. Opin. Solid State Mater. Sci.* **4**, 531.

Liu, M., P. F. Britt, and J. W. Mays. 2004. "Synthesis of Amphiphilic Star Copolymer A_2B_2 of Polystyrene and Poly(ethylene oxide)." *Polym. Prepr.* (*Am. Chem. Soc., Div. Polym. Chem.*) **45**(2), 555.

Pickel, J. M. and P. F. Britt. 2004. "Synthesis and Properties of Polymer Micelles Formed from Substituted Polystyrene-Poly(Acrylic Acid) Copolymers." *Polym. Prepr.* (*Am. Chem. Soc., Div. Polym. Chem*.) **45**(2), 240.

Artificial Cellular Receptors: Interfacing Nanostructured Hard and Soft Materials

R. S. Foote,[1] J. M. Ramsey,[2] J. P. Alarie,[2] L. C. Feldman,[3] and J. P. Wikswo[3]
[1]*Chemical Sciences Division*
[2]*University of North Carolina–Chapel Hill*
[3]*Vanderbilt University*

The objective of this project was to explore the possibility of interfacing native biological materials or their synthetic simulants with nanostructured hard solid-state materials to form structures that emulate biological systems. The fundamental concept was to form a nanoscale receptacle from hard materials such as silicon or glass into which transmembrane proteins (e.g., ligand gated ion channels) can be inserted. Ligand gated ion channels have the property that their conductance can be increased or decreased when an appropriate ligand binds with receptors on the ion channel. The coupling of ion channels with a silicon device could result in a nanoscale chemical sensor that can be very robust compared to a cell, the normal receptacle for transmembrane protein assembles. Applications of such devices include environmental sensing of contaminants and chemical and biological warfare agents, in-situ clinical monitoring, and drug discovery.

Introduction

Ion channels are protein assemblies that insert themselves into cellular membranes and selectively control transport of ionic and molecular species across the membrane. These transmembrane proteins are fundamental to biological processes such as cell signal transduction and nerve impulse propagation. Ion channels are presently of great interest because of their role in various disease states and their potential use as selective chemical sensors. The use of ion channels as chemical probes will most likely be manifested through the use of single-ion channels inserted into something akin to a cell wall (e.g., a lipid bilayer). Although planar lipid bilayer experiments are considerably more tractable for drug discovery and chemical sensing applications, they still suffer from the delicacy of the lipid bilayers and the protein assemblies themselves.

Technical Approach

We proposed a possible solution to these robustness issues, while maintaining the attractive features of ion channels as sensors. Synthetic assemblies that emulate ligand-gated ion channels would be developed and interfaced to inorganic materials. The goal was to make the synthetic materials more robust than protein assemblies and the inorganic materials certainly can be more robust, physically and chemically, then planar lipid bilayers. Demonstration of the ability to mate a molecular assembly with a nanostructured inorganic substrate in a controlled fashion would be a fundamental development that could be extended into sophisticated chemical sensing arrays and high-throughput drug screening devices. Chemical sensing devices might include a heterogeneous array of specific ligand-gated ion channels that could be individually addressed to determine the identity and concentration of chemicals that are present in a given environment. Heterogeneous or homogeneous arrays of natural ion channels could be used for high-throughput screening of drug candidates for inhibition or stimulation of ion-channel gating (NIH). It will also be interesting to explore whether nanopores formed in hard materials can be chemically decorated directly to function as gated ion channels.

The ultimate goal of this proposal was to demonstrate a silicon device that displays the properties of a ligand-gated ion channel. The device would include a nanoscale pore into which a synthetic ligand-gated ion channel is inserted and sealed. The device would also provide electrical contact to both sides of the pore so that the ion channel can be electrically biased and the current monitored. The specific goals proposed for a two-year project included:

- top-down fabrication of nanoscale pores (<10 nm) in hard materials such as silicon, silicon oxide, silicon nitride films, etc.;
- bottom-up modification of the pore to further reduce the lateral dimensions and to render its surface hydrophobic;
- design and production of synthetic ligand-gated ion channels to be inserted in the chemically modified nanopores;
- insertion of synthetic gated ion channels into the modified silicon nanopores to form a high impedance seal; and
- demonstration that the assembled hard-soft material device performed as a ligand-gated ion channel.

The following tasks were proposed to achieve these goals: Task 1, nanopore fabrication; Task 2, nanopore surface modification; Task 3, artificial receptor development; and Task 4, artificial receptor insertion and testing.

Results and Discussion

This project was funded for one year. Results for Year 1 were as follows.

Task 1: Buried channel structures where fabricated on SOI substrates using an FIB instrument to open chemical etch windows, followed by chemical etching of intermediate insulating layers to form buried channel structures. An insulator deposition process in the FIB was demonstrated for sealing of buried channel structures. Tetraethoxysilane was injected into the FIB and decomposed to form Si_xO_y material to seal buried channel structures. To expedite the FIB milling of nanopores, thin membranes of SiO_2 and related materials were fabricated that did not require the development of the buried channel structures of specific dimensions. A repeatable method for fabrication of 30- to 40-nm-thick SiO_2 membranes was developed. Nanopores were FIB milled into these membranes with dimensions as small as 40 nm as determined by AFM and SEM imaging. Metrology via TEM imaging was developed and superior to AFM and SEM techniques. Our most notable development under Task 1 was the exploration of electron milling of materials. We were able to mill holes in nanoscale films of amorphous alumina with diameters as small as 1.5 nm (see Fig. 1). This dimension is significantly smaller than those reported by Golovchenko (Li 2001) using FIB milling of silicon nitride. Further materials development efforts will be necessary to probe these alumina nanopores with conductance measurements.

Task 2: We performed a literature study of various methods and believe that interesting approaches include atomic layer deposition and atom transfer radical polymerization. The e-beam milling results also indicated that molecular multilayer films may not be necessary and that monolayer coatings on alumina surfaces may be more useful. Experimental tasks were scheduled for Year 2.

Task 3: An apparatus was assembled that allows scanning electrochemical microscopy (SECM) of ions conducted through nanopores or ion channels. Carbon fiber ultramicroelectrodes (CF-UMEs) 7 μm in size have been fabricated, conditioned, and characterized.

Task 4: An apparatus was acquired and set up for making nanopore conductance measurements. The FIB milled silicon oxide membranes were characterized using conductance measurements. Measurements of surface modified nanopores were scheduled for Year 2.

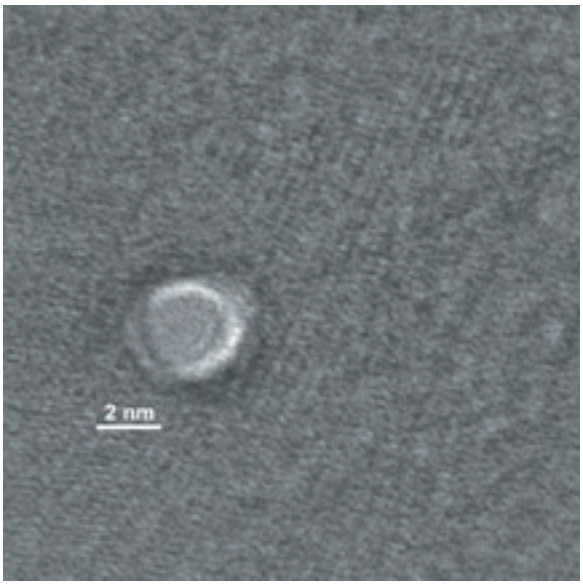

Fig. 1. E-beam milled hole in amorphous alumina film. Diameter ≈ 1.5 nm.

Benefits

Robust chemical sensors are of great importance to homeland security efforts and other environmental monitoring activities (DHS, DARPA, DOE-OBER; Life Sciences, Environmental Remediation, and Medical Applications and Measurement Science, DOE-NA22). Chemical sensing efforts, to date, have suffered from a lack of specificity that ion channel types of recognition events could potentially overcome. Non-intrusive chemical sensors also could find application in biological and medical research. Chemical sensors that can be inserted into animals or patients to determine the concentrations of physiologically important species, without causing discomfort or perturbing the measurements, requires that they be as small as possible. Successful completion of the proposed work would allow chemical probes with submicron dimensions to be developed. Such probes could also find application in single-cell imaging if they can be made minute compared to cellular organelles (DOE-OBER Chemical imaging). The broad range of applications that are possible correspondingly suggests that there will be a large number of potential sponsors to support follow-on efforts of this work. We believe that the relevancy of this project to current DOE and ORNL objectives, as initially proposed, remains high.

References

Li, J., D. Stein, C. McMullan, D. Branton, M. J. Aziz, and J. A. Golovchenko. 2001. "Ion-beam sculpting at nanometre length scales," *Nature* **412**, 166–169.

Advanced Ion Trap Mass Spectrometry for the Detection and Confident Identification of Biological Agents

M. B. Wise,[1] K. J. Hart,[1] D. E. Goeringer,[1] L. J. Hauser[2]
[1]*Chemical Sciences Division*
[2]*Life Sciences Division*

Biological weapons are a significant threat to national security and our armed forces. This project is focused on the development of instrumentation that will provide the ability to rapidly detect and confidently identify low levels of biological agents including bacteria, toxins, and viruses. The technology developed under this funding will permit the biological agents to be identified based on characteristic protein markers using molecular weights and partial amino acid sequence. The measurement approach uses a novel mass spectrometer configuration that includes an electrospray ionization source, a quadrupole ion trap, a linear quadrupole, and a time-of-flight mass analyzer.

The objective of this project is to address the need for instrumentation that is able to rapidly detect and confidently identify low-levels of biological agents including bacteria, toxins, and viruses. The goal is to develop novel methodologies and instrumentation to enable the real-time detection and identification of biological agents. Further, to enhance the utility of the instrumentation, the ability to detect chemical agents will also be incorporated into the system.

The approach that we have selected for biological agent detection is based on protein identification. Because the protein component is likely to be differentiating for all types of biological agents, we will use computational methods to identify proteins that are characteristic of and exclusive to the targeted biological warfare agents. By actually measuring the molecular weight of the protein along with partial amino acid sequences, we will be able to identify the biomarker proteins and hence identify the specific biological agent.

During the first year of this project, both computational and experimental simulations were performed to demonstrate the feasibility of using electrospray ionization mass spectrometry (ESI-MS) for differentiation and identification of biological threat agents in complex mixtures via protein biomarker analysis. These experiments were successful. Also during the first year we completed the conceptual design of a mass spectrometer and associated operational method that promises to be particularly well suited for rapid and sensitive analysis of bio-molecules. This concept consists of a tandem configuration of a three-dimensional RF quadrupole ion trap, a linear RF quadrupole, a time-of-flight (TOF) mass spectrometer, and the associated method of operation. The concept is to extract proteins from biological agents and identify marker proteins based on their molecular weight and partial sequence information. The unique mass spectrometer configuration will permit this to be accomplished very fast without the need to generate a new population of precursor ions, which is a limitation of MS approaches.

Progress during the last 12 months has focused primarily on the construction of a laboratory-based prototype version of the new mass spectrometer configuration. We have successfully demonstrated the ability to generate ESI-ion trap MS spectra of proteins and are in the process of interfacing the TOF spectrometer with the ion trap to acquire MS/MS fragmentation spectra of the proteins. Once proper performance has been established and the hardware has been optimized, we will begin the task of generating pilot data for protein samples that have been derived from biological agent simulants. In addition, we intend to demonstrate the ability to also use this approach for the identification of select chemical agent simulants.

This project has potential for greatly enhancing the current ability to detect biological agents and should be of significant interest to DOD for battlefield and homeland defense applications. In fact, DOD considers mass spectrometry to be one of the most promising tools for biological agent analysis. Further, an instrument with a broad range of biological and chemical agent detection capability will be of utility to any federal agencies involved in homeland security.

Comprehensive Analysis of Microbial Proteomes using Signature Peptides

R. S. Foote,[1] G. B. Hurst,[1] S. J. Kennel,[2] R. S. Ramsey,[3] and J. M. Ramsey[3]
[1]*Chemical Sciences Division*
[2]*Life Sciences Division*
[3]*University of North Carolina–Chapel Hill*

This proposal addresses the need for improved high-throughput methods for microbial proteome analysis in support of the DOE Genomes to Life (GTL) program. Quantitative proteomics data are important to this program to (1) confirm the presence in cells of proteins indicated by the analysis of isolated protein complexes, (2) establish cellular levels of proteins required for complex formation, (3) provide a quantitative database for modeling protein-protein interactions, and (4) allow predictions of the presence of complexes in new organisms based on their protein complements. We propose to isolate and label signature peptides that can be used to comprehensively identify and quantitate proteins in microbial proteomes.

The overall objective of this research is the development of a high-throughput method for comprehensive and quantitative analysis of microbial proteomes. The specific objectives are to (1) simplify proteome analysis by using signature peptides and (2) provide a method for quantitating the parent proteins by combining fluorescence detection of the signature peptides with mass spectrometry analysis.

Methods are being developed to simplify the "bottom-up" approach to proteome analysis, in which trypsin digests of whole protein extracts are analyzed by liquid chromatography coupled with mass spectrometry (LC-MS). The proposed methods involve modifying the proteins and isolating a single signature peptide from each protein in the extract, which can be used to identify and quantitate the parent protein. These methods will reduce the complexity of the digests by a factor of 20 or more and increase the throughput of analysis by a similar factor. The signature peptides are isolated from the C- and/or N-terminus of the proteins. Analysis of the *E. coli* protein database has shown that 98% of its proteins could be identified by the sequence analysis of one or both terminal peptides isolated by the proposed methods. The signature peptides can be fluorescently tagged and separated chromatographically and/or electrophoretically for both optical quantitation and on-line MS analysis for identification of the parent protein.

Preliminary C- and N-terminal peptide isolations were performed on whole protein extracts of *R. palustris,* and LC-MS/MS analysis of the N-terminal peptides demonstrated their recovery. N-terminal peptide isolations were also tested on a model protein mixture. Variations in the procedure were explored to simplify the method and to introduce fluorescent tags into the peptides for quantitation. Experiments with both model and microbial proteins indicated that good recovery of terminal peptides were obtained but that improvements are needed for complete removal of non-terminal peptides.

Microfluidic separations were performed on fluorescently labeled N-terminal peptides from a model protein mixture. Peptides were well resolved by micellar electrokinetic chromatography (MEKC) on chips. Although the relative peptide peaks were consistent with relative protein concentrations, quantitation was complicated by the presence of multiple fluorophores on some peptides and by impurities in the isolation mixture. Methods of labeling peptides with single fluorescent tags will be developed to simplify fluorescence-based quantitation.

The successful development of this approach would significantly enhance the GTL program at ORNL by increasing throughput of microbial proteome analysis. The developed methods would be applicable to a variety of other biological and biomedical problems, including the analysis of altered cellular proteomes in human disease and would benefit research sponsored by NIH as well as DOE.

Development of New Capabilities for Genome-Scale Quantitative Measurements of Protein Complexes

G. B. Hurst,[1] D. A. Pelletier,[2] F. W. Larimer,[2] R. L. Hettich,[1] W. H. McDonald,[1] D. L. Tabb,[2]
I. I. Harruna,[3] K. G. Asano,[1] T.-Y. Lu,[2] T. K. Lankford,[2] A. Savidor,[4] and C. Pan[4]
[1]*Chemical Sciences Division*
[2]*Life Sciences Division*
[3]*Clark Atlanta University*
[4]*Graduate School of Genome Science and Technology*

Identification and characterization of the "machines of life" (protein complexes) in microbes is a major goal of the DOE Genomics:GTL program. Understanding biological function of any such protein complex requires measurement of its concentration in the cell, and the stoichiometry of its subunits. This project includes (1) a new approach to protein complex stoichiometry determination, and (2) development of an optimum strategy for quantitative analysis of protein complexes, both based on state-of-the-art mass spectrometry methods for proteins. This combination of an innovative aim with a more conservative aim will guarantee results that greatly strengthen ORNL's capabilities for high-throughput methods of characterizing protein complexes.

Genome-enabled biology requires new tools for high-throughput, quantitative measurements of proteins and protein complexes. Mass spectrometry (MS) is potentially such a tool, although accurate MS measurement of protein amounts is currently difficult. The DOE-BER Genomics: GTL program recognizes that the next step beyond quantitative protein measurements is the quantitative measurement of protein complexes. There are currently no robust, high-throughput MS-based methods for measuring amounts or stoichiometry of protein complexes.

The first aim of this project is a labeling strategy to attach a multi-purpose chemical "tag" to each protein subunit of a complex. On enzymatic digestion, the tag will remain attached to proteolytic peptides from each subunit of the complex. The tagged peptides will be subjected to liquid chromatography–mass spectrometry (LC-MS) for measurement of masses and fragmentation patterns. This research involves evaluating different chemical entities for each of the functions of the multipurpose chemical tag, including reactivity toward targeted amino acids, uniformity of ionization, affinity purification, and fragmentation to yield a "marker" ion in the tandem mass spectrum.

Our second aim is a strategy that progresses from comprehensive, high-throughput quantitative measurements toward more accurate measurements for targeted proteins or complexes. We culture a reference growth state so as to metabolically incorporate a "rare" stable isotope (^{15}N or ^{13}C). Subsequent growth states will be prepared using the "common" stable isotope form (^{14}N or ^{12}C). Combining equal protein quantities from the archived reference growth state with each sample growth state will allow isotope ratio mass spectrometric measurement of relative amounts of proteins detected in both states. The next step will be to perform absolute quantitative measurements on selected proteins from the "reference" growth state using synthetic peptides as internal standards. These standard peptides will be chosen based on scientific and programmatic interest.

During the first year of this project, significant progress has been achieved in synthesizing two types of reagents for quantitative protein MS. The first type contains a phosphate group, which acts both as a fixed negative charge on the peptide and as a labile group that should yield a low-mass marker fragment in negative-ion tandem mass spectra. A second type of reagent for positive-ion mass spectrometry has also been prepared; this reagent should yield a characteristic benzyl marker ion in the tandem mass spectrum.

Metabolic labeling of *R. palustris* has been performed using ^{14}N and ^{15}N stable isotopes of nitrogen. Initial mass spectrometric characterization of the $^{14}N/^{15}N$ proteome mixture verified successful ^{15}N incorporation, and the ability to observe both ^{14}N and ^{15}N "versions" of ~700 proteins from this organism. Targeted synthetic peptides for use as internal standards have been identified. Software tools are being developed to extract quantitative information based on chromatographic peak areas and relate this to peptide identifications.

Our goal is to demonstrate specific capabilities in quantitative protein mass spectrometry to support DOE's Genomics:GTL Facility for Characterization and Imaging of Molecular Machines. A genome-scale capability for analyzing protein complexes should be attractive to other agencies involved in biological and medical research outside DOE interests. One such potential future beneficiary is the "Building Blocks, Biological Pathways, and Networks" pathway of the NIH Roadmap.

Redefining ORNL's Suite of Protein Analysis Technologies by Adding Flexibility, Analytical Capacity, and Biological Utility

W. H. McDonald
Chemical Sciences Division

To enable ORNL's move to the forefront in the analysis of protein complexes, we must not only strive to increase the throughput of our technologies but also ensure that they are sufficiently flexible and powerful to address more challenging issues associated with modeling complex cellular processes. This will involve keeping a steady supply of new technologies in the development pipeline. Other tagging and purification strategies need to be explored to increase sensitivity, add flexibility to the analysis, and ultimately enable different analytical technologies to be applied. Supporting computational and information system development through both high-quality known data and constructive feedback is also essential for moving the program forward.

The goal of characterizing the "machines of life" is an incredible challenge both biologically and analytically. It will involve keeping a steady supply of new technologies in the development pipeline. Some will prove useful in a medium throughput environment, and a few will be amenable for deployment in high-throughput. Well-vetted sets of protein and peptide standards will provide for rapid and controlled evaluation of new technologies and for instrumentation QA/QC. Supporting computational and information system development through both high-quality "known" data and constructive feedback is also essential for moving the program forward. Finally, the modular nature of our effort needs to be leveraged to bring together our diverse set of capabilities in the most efficient manner possible.

A cornerstone technology for the analysis of proteins is the coupling of high-performance liquid chromatography (HPLC) directly to mass spectrometry (MS). In the Organic and Biological Mass Spectrometry group, there were several strategies used for the coupling these two processes employing both single and multidimensional chromatography. As part of this project, we have implemented another multidimensional separation technique developed in the laboratory of John Yates, MudPIT (Multidimensional Protein Identification Technology). It has proven useful not only for the analysis of protein complexes but also for the analysis of entire bacterial proteomes.

One challenge associated with more efficient collection of mass spectral data is the volume of spectra which must first be analyzed and then synthesized into both an accessible and biologically relevant final output. We have made great strides in the streamlining and integration of our data analysis work flows. By continuing to work with our computational colleagues, we anticipate that we will both extract more insights out of the existing data and refine our future data collection strategies. Realizing the goal of a systems-level understanding of biology will require this constant back-and-forth.

Research and Development for Neutron Structural Biology and Soft Matter Science

D. A. A. Myles
Chemical Sciences Division

We are conducting research and development in structural molecular biology that will build strategic capabilities and competencies and strength at ORNL in neutron scattering applications for the characterization and analysis of target protein complexes in solution and in single crystals. This will include demonstration of neutron structure analysis to locate functionally important hydrogen atom positions in the catalytic sites of enzymes and development of low sample volume, high-throughput characterization techniques for the analysis of multi-molecular complexes using small-angle X-ray and neutron scattering.

We are conducting research and development for the characterization and analysis of target protein complexes in solution and in single crystals. We are analyzing and refining the neutron structure of a fully perdeuterated protein in order to demonstrate the power of neutron diffraction to locate functionally important hydrogen atom positions in enzymes. In order to support our work to develop low-sample-volume, high-throughput scattering techniques for characterization of multi-molecular complexes, we are establishing light scattering and X-ray facilities that will be used for the analysis of proteins and protein complexes in solution.

The techniques and methods developed in this work will allow us to extract meaningful spatial and dynamic information on the structure, function, and often transient interactions of protein systems across the multiple levels of functional organization in the cell. The information derived by neutron and X-ray scattering on the structure/morphology and kinetics of complex formation and interactions in solution are of critical interest in molecular biology and are difficult or impossible to obtain by other techniques.

The tools and capabilities developed will provide ORNL and the user community with a research platform uniquely equipped to tackle complex problems in structural molecular biology. This will be of use and interest to individual researchers and to programs at NIH, NSF, and other agencies that address structural and kinetic analysis of protein complexes. The development of these new neutron and X-ray scattering tools and capabilities for protein and protein complex characterization are aligned with the NIH roadmap, which aims to create centers involving multiple cooperating institutions that bring together innovative combinations of scientific disciplines. In particular, these advanced characterization capabilities would be of interest and benefit to NIH NIGMS Protein Structure Initiative research centers and Centers for Innovation in Membrane Protein Production.

CHEMICAL SCIENCES AND TECHNOLOGY

Seed Money Fund

Controlling Size and Function of Metal Oxide Nanoparticles: Coupling Micellar Nanoreactor Synthesis and Hydrothermal Processing

D. B. Beach, A. J. Rondinone, and D. J. Wesolowski
Chemical Sciences Division

This project involved the development of a two-step process for the formation of crystalline oxide nanoparticles. The first step involved the synthesis of size-selected amorphous oxide nanoparticles followed by a second crystallization step at elevated temperature and pressure under hydrothermal conditions. Size control and uniformity are achieved by relying on the micelle system for the initial particle formation, then taking precautions against nanoparticle aggregation or dissolution during the hydrothermal treatment. Free-standing doped yttrium aluminate nanoparticles were synthesized using this condensation and hydrothermal approach. The average particle size obtained for these particles was 2.5 ± 0.6 nm, or a particle size distribution of 25%. Doped particles fluoresced strongly when excited by near UV light, and fluorescence yield was increased by an order of magnitude using hydrothermal crystallization.

Introduction

Nanoparticles, along with nanowires and nanotubes, are the fundamental building block of nanotechnology (Alivisatos 1997). Nanoparticles display properties which are not necessarily those of discrete atoms or molecules, nor those of bulk solids. In fact, these properties are often tunable over a fairly wide range following scaling laws which are just starting to be understood. Some of the more remarkable properties are listed below:

Optical properties

Semiconducting nanoparticles such as CdS (Murray et al. 1993) with diameters between 1.5 and 10.0 nm emit and absorb light at discrete energies which can be systematically varied by as much as 2 eV from discrete molecules to bulk solid. Quantum confinement within these particles leads to intense, single-energy transitions with very high oscillator strengths. These properties imply that inorganic nanoparticles may be useful as a new class of robust, tunable dye molecules with applications in high-power lasers and long-life light-emitting diodes (LEDs). In addition, if improvements can be made to the size distribution and passivation of the nanoparticle surfaces, it may be possible to use these materials in nonlinear optical devices such as electro-optic modulators.

Electrical properties

The electrical properties of metal and semiconducting nanoparticles are dominated by Coulomb repulsion in these confined systems. Unlike bulk materials, the electron affinity or ionization potential of a nanoparticle is altered by the addition or subtraction of a single charge. A variety of small, single-electron, multi-level devices have been proposed to take advantage of this phenomenon. These devices are perhaps the ultimate development of electronics (Alivasatos 1996).

Phase transitions

Particle size can have a profound effect on fundamental properties such as melting. For example, the melting point of CdS is lowered by 550°C as the particle size is reduced from 3.0 to 1.2 nm. In addition, magnetic phase transitions are simplified because very small particles behave as single magnetic domains giving rise to the phenomenon of superparamagnetism.

Of the various classes of materials, metal oxides show the widest range of properties. For example, small changes in stoichiometry in the copper oxides can result in insulating, metallic, or superconducting properties. Metal oxides suspended in aqueous solvents develop high and pH-dependent surface charge densities that impart unique reactivities toward agglomeration, sorption, and surface catalysis. Oxides also may be paraelectric, ferroelectric, ferromagnetic, and birefringent. Many of the useful optical, electrical, magnetic, and structural properties of nanoparticles are critically dependent on precisely sized and highly uniform particles. Unfortunately, commonly used simple precipitation techniques for syntheses of oxide nanoparticles do not allow size selection or particle size uniformity.

Technical Approach

This project involved the development of a two-step process for the formation of crystalline oxide nanoparticles. The first step involved the synthesis of size-selected amorphous oxide nanoparticles followed by a second crystallization step at elevated temperature and pressure under hydrothermal conditions. The crystal system studied was a monoclinic yttrium aluminate

doped with a several fluorescent rare-earth ions. While this report primarily focuses on yttrium aluminate, this procedure was also successfully tested with zirconia. Because of the general chemical approach used, it should work with a wide range of oxide systems. The chemistry used to condense the nanoparticles was adapted from thin-film techniques, utilizing highly soluble metal alkoxides as the precursors. This approach was selected to make the technique as general as possible, as simple alkoxides (methoxide, isopropoxide) for most metals are commercially available.

Yttrium and aluminum metal alkoxides were reacted with 2-methoxyethanol under argon. The bidentate 2-methoxyethanol replaces the simple alkoxide due to high affinity for the metal center. The product alcohol was distilled off, leaving highly soluble metal methoxyethoxides. Unlike monodentate alkoxides, the solubility of the metal methoxyethoxides can easily reach 1 M concentration. The course of each of the reactions was followed using 13C NMR spectra. The NMR data indicates that ligand exchange is complete and that aluminum and yttrium methoxyethoxides react to form new mixed-metal species. The ratio of yttrium to aluminum was carefully controlled to be 3:5, in an attempt to crystallize the garnet phase of $Y_3Al_5O_{12}$. As a test, a sample of the precursor solution was hydrolyzed and fired in air at 900ºC for 4 h to yield only single-phase garnet $Y_3Al_5O_{12}$.

A solvent/micelle solution was prepared with 50 ml phenyl ether and 1 g freshly distilled oleic acid. The solution was refluxed under vacuum for 30 min to remove moisture. One ml of a 1-M aluminum-yttrium methoxyethoxide solution was injected under argon, at approximately 100ºC. After excess 2-methoxyethanol was removed under vacuum, 2 ml of 30% hydrogen peroxide was injected under argon at 90ºC. The solution, which was brown-yellow, immediately turned pink and then back to light yellow. The solution was allowed to hydrolyze overnight. The solution was then dried under vacuum. Oleyl amine (1 ml) was added to aid solubility during washing. The nanoparticles were precipitated with methanol, redispersed in toluene, then reprecipitated. The nanoparticles were refluxed in DMSO to strip the oleic acid and coordinate the particles, which were then soluble in isopropyl alcohol. The particles were made soluble in water by refluxing the particles in isopropanol/KOH, adding deionized water, refluxing further, then removing the isopropanol under vacuum. The pH was adjusted to 12 with 1 M KOH. Alternatively, the nanoparticles can be made water soluble by dispersion in hexane followed by injection into a solution of methylene chloride and tetramethylammonium-11-aminoundecanoate.

The aqueous nanoparticles were treated hydrothermally in a Teflon-lined stirred reactor based on the Autoclave Engineers model 201e-1473. The particles were subjected to temperatures ranging from 280ºC to 330ºC. Some experiments were conducted at 330ºC and pH 11 in order to grow larger particles for crystal structure determination. The lower temperature experiments produced a mixture of insoluble char, potassium carbonate, and highly soluble nanoparticles. Higher temperatures reduced the amount of organic residue at the cost of slightly reduced pH (from 12 to 11.5). In all experiments, the nanoparticles could be extracted into butanol with acetic acid, thereby removing excess hydroxide, potassium carbonate, and organic residue. One experiment was carried out at a pH of 12 at 500ºC and under 1 KBar of pressure in a gold-bag-lined autoclave. The result was complete elimination of organic residue, yet still highly soluble and dispersed nanoparticles.

X-ray diffraction data of larger nanoparticles following hydrothermal crystallization did not showed the expected garnet phase that the 5-to-3 aluminum-to- yttrium metal stoichiometry should have produced. A monoclinic unit cell with lattice constants similar to θ-yttria can be fit to pattern, but atomic positions cannot be determined. Similar diffraction data were also obtained for the high-temperature, high-pressure materials. The peaks are in the same general position as the monoclinic θ-yttria, so our hypothesis is that these are monoclinic particles. While this is surprising, there is precedence in the literature for both monoclinic yttria and monoclinic alumina. The monoclinic phases form under extremely high temperatures and are higher density than the cubic phases.

Transmission electron microscopy (TEM) was used to analyze nanoparticles produced at 285ºC and pH 12. The particles show clearly visible lattice fringes. While the exact structure is yet to be determined, the cubic garnet phase can clearly be ruled out, consistent with the X-ray data. To determine the degree of size dispersion, two hundred eighty particles micrograph were fit with data analysis software (Igor Pro) and measured, producing an average particle size of 2.5 ± 0.6 nm, or a particle size distribution of 25%.

As these nanoparticles are yttrium aluminate, originally intended to be the garnet structure (YAG), they were doped with rare-earth ions in an attempt to determine suitability for fluorescence applications. Figure 1 shows fluorescence spectra for cerium- and thulium-doped nanoparticles, respectively. The dashed line indicates performance before hydrothermal treatment, when the particles were still amorphous, and the solid line indicates performance after hydrothermal treatment. A large increase in fluorescence yield is indicated. Quantum yield was not measured. The fluorescence decay lifetime for a 5-nm cerium-doped sample treated hydrothermally at 330ºC was measured using a YAG:Nd laser operating at 337 nm. The data were fit to an exponential decay producing a lifetime

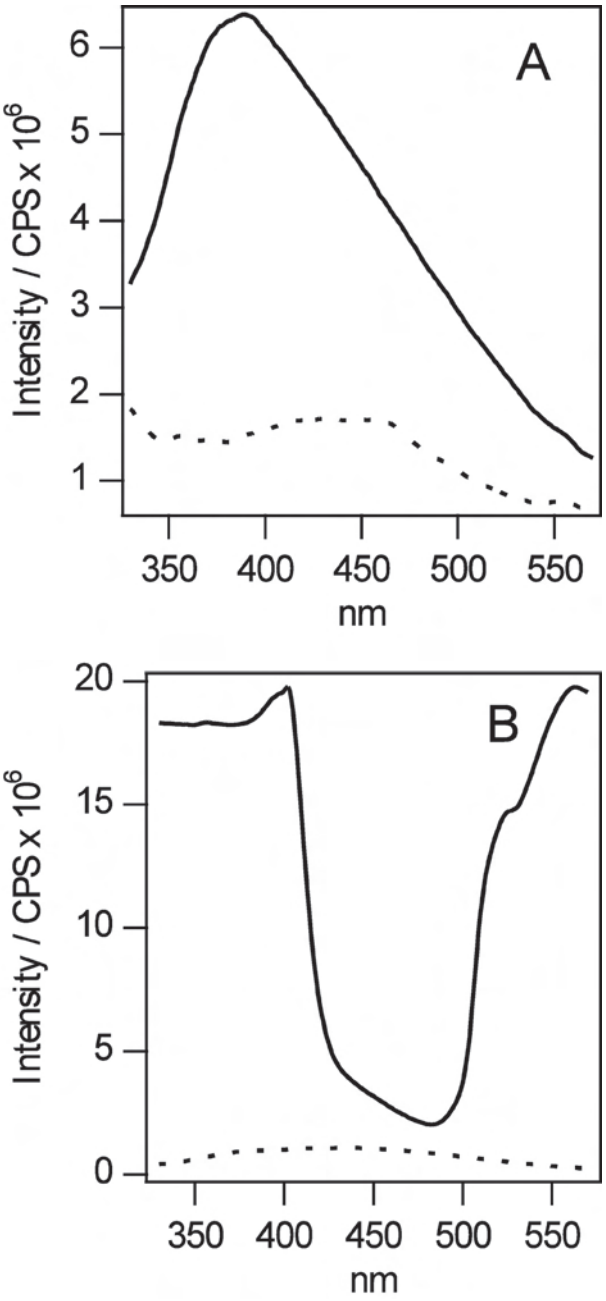

Fig.1. Fluorescence spectra of cerium-doped (a) and thulium-doped (b) yttrium aluminate nanoparticles before (- - - -) and after (——) hydrothermal treatment.

of 19 ns. The lifetime of the decay is much shorter than that of bulk Ce:YAG, consistent with our earlier results on 30-nm Ce:YAG (Allison et al. 2003).

This research was conducted in part with the intention of building optical scintillators, and attempts were made to cast these particles into sol-gel films. Ten milligrams of amorphous nanoparticles were dispersed into a 5-ml tetraethylorthosilane/ethanol (1.0/0.7 wt. fraction) solution. The solution was hydrolyzed with dilute HCl and spun coated into a film. The film was fired at 500ºC for 20 min. The nanoparticles were clearly dispersed throughout the silica matrix and are clearly crystalline. The crystal structure of the nanoparticles was not determined. Work is continuing in this area.

Results and Discussion

While this research has provided some interesting advances, there is much work left to be done. The ultimate goal for nanoparticle research is size control so precise that little or no polydispersity exists. Previous research has demonstrated that polydispersity under 5% is necessary for the formation of self-assembled hexagonal films. The current results of 25%, while not unusual for such small particles, preclude self-assembly. We believe that the reason for the high polydispersity is the nanoparticle condensation step (i.e., hydrolysis). Hydrolysis is achieved by the introduction of water into the micelle system, which could disrupt the micellar nanoreactors or cause micellar aggregation. While another report using aqueous hydrolysis did not indicate micellar aggregation, we feel that the difference in chemical precursors between our work and previous work is sufficient to warrant concern. We are currently in the process of developing non-hydrolytic synthesis techniques that may lower the polydispersity by eliminating the need for hydrolysis (Vioux 1997).

Benefits

The results of this study benefit the DOE by demonstrating a method for making materials that are potentially useful in remote temperature sensing in hostile environments. In addition, the general method of synthesis of doped oxide nanoparticles is applicable to the production of advanced radiation detectors. Finally, rare-earth doped refractory oxide nanoparticles may be used as traceable tagants that would survive under the most severe temperature and radiation environments.

References

Alivasatos, A. P. 1996. “Semiconductor Clusters, Nanocrystals, and Quantum Dots.” *Science* **271**, 933.

Alivisatos, A. P. 1997. “Nanocrystals: Building blocks for modern materials design.” *Endeavour* **21**(2), 56.

Murray, C. B., Norris, D. J., and Bawendi, M. G. 1993. “Synthesis and characterization of nearly monodisperse CdE (E=S, Se, Te) semiconductor nanocrystallites.” *J. Am. Chem. Soc.* **115**, 8706.

Vioux A. 1997. “Nonhydrolytic Sol-Gel Routes to Oxides.” *Chem. Mater.* **9**, 2292.

Allison, S. W., Gillies, G. T., Rondinone, A. J., Cates, M. R. 2003. *Nanotechnology* **14**, 859–863.

Metallic Nanofuels for Vehicles

B. G. Sumpter,[1] S. D. Labinov,[2] D. W. Noid,[1] and D. B. Beach[3]
[1]*Computer Science and Mathematics Division*
[2]*Engineering Science and Technology Division*
[3]*Chemical Sciences Division*

This project addressed the concept of novel, renewable, high-energy-density, non-emission fuels for vehicles based on clusters of metallic nanoparticles and the experimental proof of principles of the outstanding characteristics of the combustion of these fuels. Our results clearly show that due to the high surface-to-volume ratio typical of nanoparticles, complete and fast oxidation, ~500 milliseconds combustion time, occurs at temperatures of 1000–1200 K, completely in the condensed phase. The combustion process leads to near complete retention of the combustion products on a substrate (estimated at 93% complete) and effectively avoids pollution of the air by nitrogen oxides. We have been able to develop this new direction successfully by employing the joint efforts of specialists in chemistry, solid-state physics, energy, transportation, computation, and mathematics.

Background and Introduction

The problem addressed by this project is that of an alternative energy supply system for vehicles that is renewable, non-polluting and has a high energy density. Limited reserves of liquid fossil fuel, security issues due to foreign oil dependence, and the air pollution caused by the burning of fossil fuels are the major drivers for the search for alternative fuels for transportation. We propose the use of engineered clusters of metallic nanoparticles as a fuel for vehicles. When compared to conventional liquids, this metallic fuel features greater energy capacity per volumetric unit, lower flammability, is virtually explosion proof, and does not require any special storage conditions. The combustion products of the metals are solid oxides that can easily be stored and transported to reduction facilities or directly reduced/recycled as part of the engine utilizing the energy produced. Metallic fuel, in spite of all of the advantages just mentioned, has not been used in vehicles with the exception for solid-propellant rocket boosters. Certain unique aspects of metal combustion account for this fact. The process of metal oxidation with gaseous oxygen (air) is accompanied by the formation on the metal surface of an oxide film that prevents oxygen molecules entering into the zone of reaction. The passivating action of the film is increased with increasing film thickness. To avoid this phenomenon, the temperature of reaction has to be above the temperature for oxide film evaporation, about 2500-3000 K for the majority of metals. At this temperature, metal evaporation takes place on the surface and the oxidation reaction progresses in the gas phase. Outside of the high-temperature zone of combustion, the metal oxide is condensed and solidifies, forming particles of solid ash which is carried-over by the air flow and is deposited on the walls of a combustion chamber and other parts of an engine. Obviously, such a fuel is unfit for any conventional engine. The high temperature of metal combustion contributes to intensive formation of nitrogen oxides in the heated air thus adding to atmospheric pollution. Also, there are few structural materials that can stand the high temperature of metal combustion. In summary, the following problems have not yet been solved: (a) the control of the metallic fuel combustion process; (b) the quick decrease or increase of released heat quantity depending on engine load, and (c) systems providing for fuel delivery to a combustion chamber and for ash removal.

Our proposed solution to these problems is to use an engineered metallic fuel cluster composed of individual nano-particles. The underlying basis for this approach is that experimental evidence suggests that the ignition and combustion temperature of metallic particles decreases rapidly with decreasing particle size, while the speed of combustion and intensity of heat release are increased. These desired effects are primarily due to the fact that as the particle size decreases, the surface-to-volume ratio rapidly increases. A cluster of nano-particles should thus be capable of providing the desired combustion properties of intensive and rapid heat release but occur at temperatures below 1600 K in the solid state without significant production of volatile species. The goal of this project was to experimentally verify and test this fundamental hypothesis.

The Results to Date

An experimental apparatus for examining the peak combustion temperature of an engineered cluster of metallic iron nano-particles was designed (see Fig. 1). Following combustion of the metal cluster, the cluster can be removed and examined via microscopy or x-ray diffraction to determine if the combustion produced

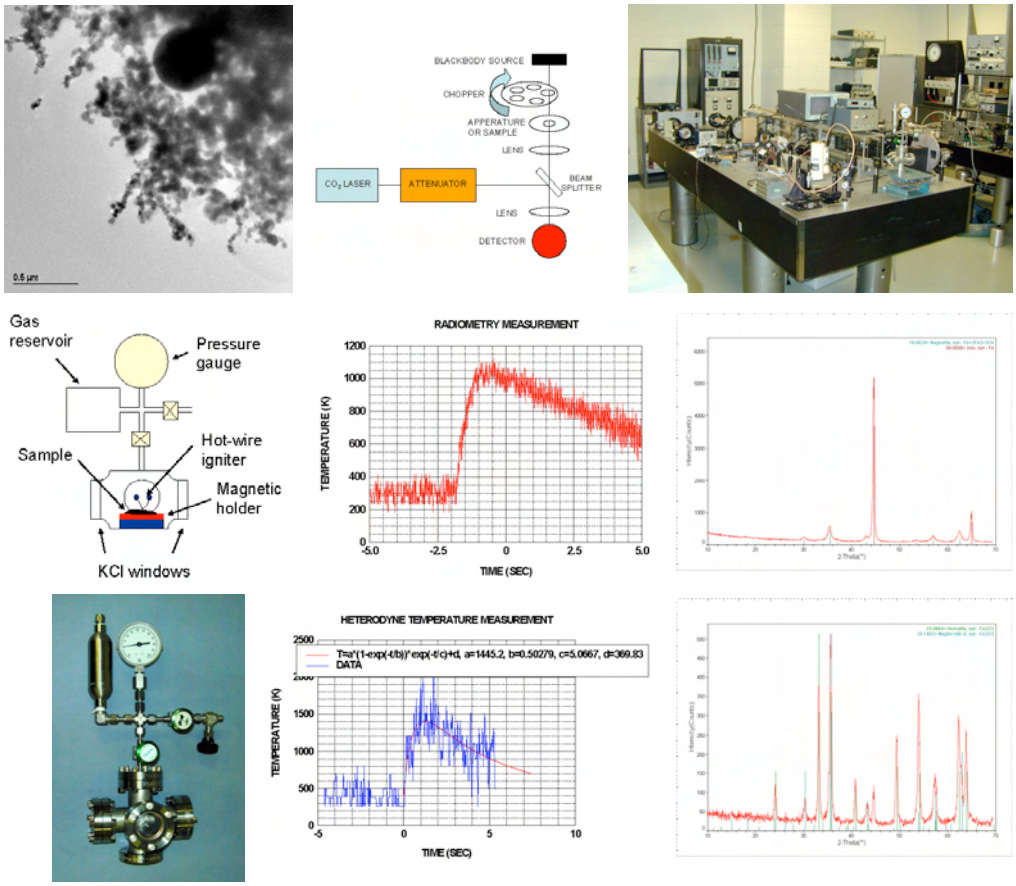

Fig. 1. Experimental apparatus and results for combustion of iron nanoparticale-based clusters. Left side shows TEM of the iron nanoparticles revealing particles with ~50 nm diameter, a schematic of the apparatus designed to perform combustion and reduction and a photograph of this apparatus. Top middle shows a scematic of the laser-based heterodyne device for measuring the temperature of combustion. A photograph is shown at the top right. Bottom middle shows the results obtained from the temperature measurements in both radiometry and heterodyne mode.

significant amounts of volatile products instead of occurring mainly in the solid/condensed phase. The approximate fuel cluster size and shape to achieve the necessary heat flow was determined from computation (see below for details) and a method for experimentally producing this thin disk-shaped pellet composed of iron nano-particles was designed. The experimental method employed was relatively simple. We used commercial grade iron nanoparticles (a TEM of the iron nanoparticles is shown in figure 1; diameters of the particles are ~50 nm) which were sintered on a glass substrate using magnetic forces. The designed iron clusters consisted of ~16 mg/pellet, giving a disk with ~1 mm height and 2 cm in diameter. The glass slide containing the iron cluster can be mounted in the devise (Fig. 1) and placed into an infrared temperature sensor based on heterodyne or radiometric measurements to determine the combustion temperature. The infrared temperature sensor was constructed to specifically monitor time-dependent temperature changes on a sample. This sensor performed two different forms of temperature measurement; one was from a heterodyne measurement of power over a narrow wavelength band (at 10.6 microns) and the other from a radiometric measurement over a broad wavelength band (from 1 to 14 microns). The heterodyne technique is illustrated in Fig. 1. The sensor involves the mixing of infrared radiation from either the blackbody source or a sample and a CO_2 laser tuned to the 10.6-µm wavelength. Because the blackbody source operates at a set temperature, the detectors response can be calibrated for absolute temperature measurements. The focusing optics was aligned through the 2-mm aperture that was replaced with a sample for performing measurements. The high speed response of the mercury-cadmium-telluride (MCT) detector and the integration nature of heterodyne detection allowed measurements to be performed at speeds up to one millisecond. By simply turning off the laser, the device can be used as a radiometric temperature sensor. Again the blackbody source was used for performing absolute temperature measurements, but required integration over

the systems wavelength sensitivity. This was primarily the detectors sensitivity as supplied by the manufacturer.

Multiple samples were tested, and in all cases, combustion proceeded rapidly (~500 ms), generating peak temperatures between 1000 and 1200 K, without the observable production of volatile products. The results for two different samples and measurements are shown in Fig. 1. Both modes of operation clearly demonstrate combustion of the iron cluster occurs rapidly (~500 ms) with a peak temperature in the range of 1000 to 1200 K. The combustion process did not produce any visually notable volatile products or ash. The reproducibility of the process is very good and since the temperature is well below that required to form NOx, it is reasonable to assume there is virtually none formed from the combustion process. Visual observations of the combustion process were quite dramatic as one can clearly follow the wave front of combustion through the cluster by noting the change in color which goes from black to red (Fig. 1 shows a before and after picture of the iron particles that were part of the cluster). As mentioned, there was no observable smoke produced from this process, as opposed to the combustion of magnesium or steel wool, which indicates very little production of volatile species. Additional and more substantial evidence for solid-state combustion was obtained from x-ray diffraction of the iron cluster before and after combustion (Fig. 1) combined with analytical mass determination. These results clearly show that the combustion process oxidizes 93% of the iron into primarily hematite ($Fe2O_3$) and maghemite, only leaving ~7% of the iron in its original state (seen in the x-ray diffraction patterns, peaks at green and blue peaks and supported by analytical mass determination).

Clearly, proof-of-principals for the solid-state combustion of a cluster of iron on a reasonable time scale and with the production of an intense source of heat now has been demonstrated. Still a number of crucial experiments remain: (1) in particular the examination of the combustion process at elevated temperatures and pressures common in combustion chambers; (2) the optimization of the size and shape of the particles/cluster to enhance the combustion process (energy and time scale); (3) reduction of the oxidized metals back to the original metal form; (4) investigation of other metals and alloys; and (5) economic assessment. These experiments are to be addressed in Phase II of this project.

Benefits

The success of this work will lay the foundation for developing the technology for an alternative fuel production and its practical use. It has direct impact on both energy production and environmental quality, two of DOE's main missions. This type of nano-fuel will provide an additional fuel source with a high energy density that combusts with near-zero emission. It can be expected that military, space and specialized vehicles and ships would be the first to make use of such a metallic fuel. For example, fast burning metal nanoparticles could be used to boost the output of a fighter plane's afterburner with significant reduction in fuel weight. Passenger cars, trucks and locomotives converting to metallic fuel will occur gradually.

Hydrogen Production From Naturally Occurring Iron Silicates

D. J. Wesolowski,[1] L. M. Anovitz,[2] J. G. Blencoe,[1] E. M. Ripley,[3] and J. S. Beard[4]
[1]*Chemical Sciences Division*
[2]*University of Tennessee, Knoxville*
[3]*Indiana University, Bloomington*
[4]*Virginia Museum of Natural History, Martinsville*

Rocks containing abundant reduced iron (FeII) silicates are enormously abundant in near-surface terrestrial settings (iron formations, layered ultramafic igneous intrusions) and constitute most of the suboceanic crust. Thermodynamic analysis and evidence from terrestrial and seafloor hot springs indicate that these iron silicates react with water to produce hydrogen gas and oxidized (FeIII) iron minerals. However, the rates of the redox reactions are largely unknown. The purpose of this project was to begin to obtain preliminary data on the rates of hydrogen production by the reaction of water with the most likely candidate minerals and rocks rich in FeII-silicates, namely igneous rocks containing iron-rich olivine (fayalite, Fe_2SiO_4) and sedimentary iron formations rich in greenalite—$Fe_3Si_2O_5(OH)_4$—and minnesotaite—$Fe_3Si_4O_{10}(OH)_2$.

Hydrogen is often referred to as an "energy carrier," rather than a fuel, since unlike coal, oil and natural gas, it does not occur naturally in large accumulations and in sufficiently pure form. However, this is mainly a result of the high reactivity of this gas, and its very rapid diffusion rates, even through tight rock formations. Nevertheless, significant concentrations of dissolved hydrogen have been observed at seafloor hydrothermal vents in the Pacific and Atlantic oceans, that might approach harvestable concentrations. More importantly, engineered systems can be envisioned wherein water is introduced into naturally hot rocks rich in FeII minerals and the hydrogen generated by redox reaction of the water with these minerals in controlled fracture systems could be collected. The most important factor in determining the feasibility of such an endeavor is the rate of reaction of such minerals with water at various temperatures and pressures. The goal of this project was to collect sufficient data to determine whether hydrogen generated from water/rock reactions could conceivably become economically attractive.

In order to determine the hydrogen evolution rates from naturally-occurring minerals and rocks, we modified one of our unique, high temperature pH-monitoring cells to include a hydrogen-permeable membrane fabricated from Pd75Ag25 alloy. The membrane is in the form of a short length of 1/8 inch OD tubing that is 0.006 inches in wall thickness and welded closed at one end. The 'bag' thus formed was filled with alumina powder to provide internal support, topped off with a wad of platinum mess to prevent plugging of the 1/16 inch OD by 0.006 inch ID stainless steel capillary tubing to which the membrane assembly was silver soldered. The capillary tubing penetrated the head of the vessel and is connected to a manifold that permits evacuation and when valved off, permits measurement of the hydrogen pressure within the membrane using Precise Sensors pressure transducers with measurement ranges of 0–100 psi and 0–2000 psi. Only hydrogen can diffuse through the silver-palladium alloy, and the rate of diffusion becomes sufficiently fast at temperatures above about 100ºC that the internal pressure within the membrane closely approaches the external partial pressure of hydrogen in the experimental environment within a few hours. The external pressure is considerably higher, consisting of water vapor in equilibrium with liquid water. A typical experiment consists of the addition of about 10–50 grams of the rock or mineral under study and 50–100 grams of water, placed in a fused-quartz cup within the pressure vessel. The rate of hydrogen gas evolution is monitored as the rate of increase of hydrogen gas pressure, and the calculated mass of hydrogen during reaction of the water at temperatures of 150–350ºC.

Thus far, we have conducted 11 individual experiments, each lasting several weeks. Materials tested thus far have included: (1) a very high FeII olivine (93% fayalite); (2) several olivine concentrates from the Duluth igneous complex in northern Minnesota that contain 50–70% olivine; and a number of samples of the Biwabik iron formation of northern Minnesota that contain 5–40% greenalite and/or minnesotaite. All of these materials produced hydrogen, but only the Duluth Gabbro mineral concentrates evolved more than one atmosphere of hydrogen gas, and this occurred at a temperature of 300ºC and higher. The iron formation samples began evolving hydrogen at 200ºC and higher, but the absolute quantity of hydrogen evolved was considerably less than for the olivine samples. This is nonetheless significant, because olivine is the most abundant iron bearing mineral in the

oceanic crust, and temperatures exceeding 300ºC with a few hundred meters of the seafloor surface are common along the mid-ocean ridges. These seafloor ridges traverse all the world's oceans, and all of the known seafloor hydrothermal vents are found along these ridges.

X-ray diffraction analysis of the run products indicate the formation of serpentine, a hydrous magnesium silicate associated with the reaction of olivine with water. No specific oxidized-iron-bearing phase has been identified, but the brick-red color of the reacted surfaces and the exceedingly fine red colloidal suspension generated indicates formation of amorphous or poorly-crystalline ferric iron oxyhydroxides. In the iron formation experiments, minnesotaite appears to be more reactive than greenalite, and we also observed a reduction in the amount of siderite, a ferrous iron carbonate mineral—$FeCO_3$. A subsequent experiment in which pure siderite was reacted with water and a magnesium-rich olivine resulted in some hydrogen generation, but copious quantities of CO_2 gas. We had hoped that the magnesium-rich olivine with react with the CO_2 to make $MgCO_3$ (magnesite), a commonly-occurring, and highly stable carbonate mineral. Additional tests will be conducted using pH modifiers to promote the formation of magnesite, and we will also investigate the effect of inert salts, such as NaCl, on the rate of hydrogen generation from both olivine and iron formation minerals.

Our preliminary results indicate that rocks that underly large portions of the worlds oceans, and which are abundant in certain large regions of the continents, will produce hydrogen by reaction with water at temperatures of 200–300ºC. Such temperatures are commonly encountered in areas of high geothermal gradient, such as active volcanic terrains and mid-continent rift systems such as central and northern Minnesota in the United States, and the East African rift system. Thus, the potential exists to generate great quantities of hydrogen as a potential fuel for the future. This is clearly a major goal of the Department of Energy, and the U.S. federal government in general.

Cyclopentadienyl Iron Clusters as Nanoscale Building Blocks for Multi-Electron Electrocatalysis

G. M. Brown, P. V. Bonnesen, and D. R. Mullins
Chemical Sciences Division

Proof-of-principle experiments are being conducted for the design, synthesis, characterization, and utilization of novel nanoparticles, based on tetrairon clusters as building blocks, that can function as the charge carrier in catalytic electrochemical reactions. These clusters are attached directly to the surface of electrodes or attached to molecules that are binding sites for substrates. This is a new approach to the design of electrocatalysis involving multielectron electrochemical reactions, and it will be applied to the design of catalysts for the four-electron reduction of oxygen to water. We will synthesize and test a catalyst based on a cobalt porphyrin coordination site and four iron clusters. Tetranuclear iron clusters were attached or sorbed to the surface of carbon electrodes, and an attempt was made to determine the oxidation state of the Fe by in situ X-ray synchrotron spectroscopy methods (XANES). The technological focus of this work is designing "molecular electrodes" capable of carrying out electrochemical reactions that might be more energy efficient ways of effecting chemical transformations in general.

One approach to electrocatalysis involves the attachment of redox active substances to molecules that are selective for the reaction of interest in homogeneous solution to conducting supports. Bifunctional assemblies having the ability to exchange electrons rapidly with the conducting substrate as well as the ability to bind the substrate will be needed. Fundamental scientific research is needed to understand both the reactivity of supramolecular or nanoscale assemblies that are capable of effecting selective chemical transformations driven by electrical energy, and the methodology to construct these assemblies at the required density. We are establishing a research program aimed at developing the chemistry of organometallic clusters as nanoscale building blocks for catalytic reactions. These clusters will be capable of undergoing multiple electron transfer reactions, and they will be used in concert with binding sites for the substrate. In this project, we selected a particularly promising nanocluster ($[CpFe(\mu_3\text{-}CO)]_4$) for a proof-of-principle demonstration to show that attachment of several of these clusters to a catalyst would allow multiple electrons to be transferred to achieve the desired electrocatalytic reaction. Development of electrocatalysis is particularly important in advancing fuel cells and water electrolysis units as alternative energy sources or sources of hydrogen, respectively. Several problems of fundamental technological and scientific interest are the development of effective electrocatalysts for oxygen reduction, water electrolysis (oxygen evolution), and methanol oxidation. Although the electrochemical reactions involved in these three examples are quite different, they do have in common the requirement that reaction of the substrate at the electrode requires that multiple electrons be transferred to achieve an energy efficient process.

The research involves three tasks: (1) the synthesis of model electrocatalytic species incorporating the tetrameric iron clusters, (2) attachment of the nanoclusters to substrate binding sites and electrode surfaces and determination of electrocatalytic properties, and (3) an in situ study of the catalyzed reactions by X-ray spectroscopy methods.

To date we have synthesized the cyclopentadienylironcarbonyl tetramer, $Cp_4Fe_4(CO)_4$, along with $Cp_3Fe_4(CO)_4CpCO_2H$, and $Cp_3Fe_4(CO)_4CpCO_2Ph$. The electrochemistry of these materials was examined in acetonitrile solution. The chemistry for attachment of $Cp_3Fe_4(CO)_4CpCO_2H$ and ferrocenecarboxylic acid to high-surface-area carbon electrodes was investigated. The ferrocene and iron tetramer acids were converted to the acid chlorides, the surface of the carbon electrode was oxidized to create more phenol-like functionalities, and the two were reacted in an effort to chemically bond the iron compound to the surface of the carbon. An electrochemical cell in which the oxidation state of the Fe compound attached to the electrode could be changed while the X-ray near edge absorption spectroscopy (XANES) is simultaneously measured was designed and tested. Electrochemical-XANES experiments were conducted at the National Synchrotron Light Source at Brookhaven National Laboratory. We can clearly see the near edge peak of the Fe compounds, either adsorbed or chemically bound to the carbon electrode, while the electrode is under potentiostatic control using the detection of Fe X-ray emission. However the spectrum of the $Cp_4Fe_4(CO)_4^+$ oxidation product compared to the neutral tetramer does not show a clear shift in peak energy with oxidation state. The intensity of the near edge peak was a factor of ten more intense than observed for normal octrahedrally coordinated iron complexes, and this phenomenon of CpFe complexes will be examined in more detail as time

permits. The method of attachment to the electrode was not as stable as desired, and the formation of esters was abandoned in favor of direct carbon-carbon bonding. We have prepared the porphyrin precursor needed to prepare the cobalt porphyrin adducts with the cyclopentadienylironcarbonyl tetramer. The cobalt porphyrin-iron tetramer complex will be tested for kinetic activity in the reduction of oxygen.

We submitted a preproposal for the DOE BES call for proposals for basic research for the hydrogen fuel initiative, and we were invited to submit a full proposal, which is currently being prepared. The results found in this study are being used as part of the preliminary results in this proposal.

Novel Technologies for Wide-Scale Production of Magnesium and Hydrogen

J. G. Blencoe[1] and S. L. Marshall[2]
[1]*Chemical Sciences Division*
[2]*Electrochemical Systems, Inc., Oak Ridge, Tennessee*

Laboratory experiments are being performed to investigate the possibility that magnesium chloride ($MgCl_2$), magnesium oxide (MgO), and/or magnesium carbonate ($MgCO_3$) can be electrolyzed at 1 atm, T ≤300°C, to form solid magnesium metal (Mg) at the cathode and effervescing gas (Cl_2, or $O_2 \pm CO_2$) at the anode. Key variables are temperature, electrolyte composition, and anodic material (metal/metal alloy, impervious/porous ceramic, crystalline/amorphous carbon). To date, tests have been performed at room temperature with two electrolytes ($MgCl_2$ and choline chloride) using electrodes formed from platinum, silver, and glassy carbon. Results of the work are promising—collectively indicating several important future lines of investigation.

This project seeks to develop new methods for electrowinning magnesium by the reactions

$$MgCl_2 \rightarrow Mg + Cl_2, \quad (1)$$

$$MgO \rightarrow Mg + \tfrac{1}{2}O_2, \text{ and} \quad (2)$$

$$MgCO_3 \rightarrow Mg + CO_2 + \tfrac{1}{2}O_2. \quad (3)$$

Current industrial production of magnesium metal by Reaction 1 involves electrolysis of molten magnesium chloride, producing chlorine gas at the anode. Reaction 2 is induced commercially in two ways: by chemical reduction at high temperatures (>1000°C) using a strong reducing agent (usually silicon or ferrosilicon) and by direct electrolytic decomposition of MgO to Mg and O_2 using an oxide-ion conducting ceramic electrolyte. Reaction 3 is a novel, and as yet untested, means for electrowinning magnesium that relies on the use of an ionic liquid (± an organic solvent) to solubilize and electrolyze the magnesium feedstock (crystalline $MgCO_3$). Since current practices of magnesium electrowinning are very energy intensive and environmentally damaging (by production of various air-borne pollutants, along with copious amounts of CO_2), and because the efficacy of Reaction 3 is, to date, undemonstrated, there is considerable economic and scientific incentive to identify new pathways for magnesium production that are more cost-effective and environmentally sound.

The electrochemical experiments of this project involve the use of a potentiostat/galvanostat—a device that can control either the potential across an electrochemical cell, or the current that flows through it. The potential of the working electrode is measured with respect to a reference electrode, and current flows between the working electrode and a third (counter) electrode. In addition to its simplest possible use as a constant-current power supply to an electrochemical cell, a potentiostat can be used to measure the transient currents resulting from imposition of a time-dependent potential, or the transient potential resulting from driving a time-dependent current through the cell.

We use our electrochemical cells primarily to conduct cyclic voltammetry, which measures the transient current resulting from an applied potential that varies linearly with time between specified limits. Results of the experiments indicate the current-potential characteristics of the anodic and cathodic reactions, which are used to estimate the cell voltage corresponding to the specified current.

Our most significant research activities over the past three months are summarized below.

- A recent journal article reported the extraordinary solvent properties of the deep eutectic mixtures formed between choline chloride (CC) and amides, such as urea, and mono-, di-, tri-, and tetramethyl urea. The fact that the CC-urea eutectic liquid (formed at 12°C) can dissolve silver chloride to 0.66 mol•dm^{-3} suggested to us that it might be possible to dissolve a similar amount of $MgCO_3$ in that liquid (magnesium carbonate has a solubility product in water that is comparable to that of silver chloride). Thus, we prepared the liquid in an inert-atmosphere dry box, and observed no obvious reaction with magnesium metal. However, cyclic voltammetry of this mixture in an electrolytic cell with a glassy-carbon working electrode, a silver quasi-reference electrode, and a platinum wire counter-electrode showed that reduction of urea occurs at a lower potential than that at which Mg^{2+} reduction occurs. In other words, reduction of magnesium ions occurs outside the electrochemical stability window of urea.

- We investigated the possible use of liquid choline hydroxide (COH) as a room-temperature electrolyte. This material is commercially available as a 45% w/w solution in methanol. Unfortunately, it proved impossible to remove the methanol by vacuum distillation. Moreover, COH is far less stable than CC (as evidenced by a strong smell of trimethylamine) and is more reactive towards oxygen (as shown by rapid discoloration). For these reasons, no further work with this material was attempted.
- Experiments were performed to investigate the possibility that solid magnesium could be electrodeposited from solutions of magnesium chloride in dimethyl formamide (DMF). We prepared an ~1 mol•kg^{-1} solution of magnesium chloride in DMF and carried out cyclic voltammetry. The large discrepancy between the anodic and cathodic current transients indicated that the dominant process is the reduction of the solvent rather than reduction of the solute.

While representing failed attempts to achieve the main aim of our research, the foregoing results also suggest other possible methods for electrodepositing solid magnesium at low temperatures. Our future research activities will test the merits of these alternative approaches.

Finally, we note that favorable results from our project would benefit many federal agencies, including the Department of Energy (particularly the Offices of Fossil Energy, Energy Efficiency and Renewable Energy, and Basic Energy Sciences), the Defense Advanced Research Projects Agency, the Environmental Protection Agency, and the National Science Foundation.

COMPUTER AND COMPUTATIONAL SCIENCES

Director's R&D Fund

Scaling Climate Models for Future Computer Architectures

A. S. Bland,[1] J. B. Drake ,[1] X. Liang,[2] P. F. LoCascio,[3] P. K. Nukala,[1] M. C. Smith,[4]
P. H. Worley,[1] J. B. White III,[1] and J. S. Vetter[1]
[1]*Computer Science and Mathematics Division*
[2]*Jackson State University*
[3]*Life Sciences Division*
[4]*Engineering Science and Technology Division*

The 40-TFLOP/s Japanese Earth Simulator (ES40) has challenged the U.S. climate-modeling community and computer industry to accelerate the development of both the models and the computers required to run them, to keep our country competitive in both climate science and policy decisions. This project will characterize the performance of current U.S. models and suggest research areas for improvements. Researchers will use representative kernel codes to understand the factors that limit performance and scalability and then work to mitigate these factors. The second phase will be to instrument and evaluate the latest full climate model, CCSM, to improve its performance. The objective is to prepare ORNL to take advantage of future funding opportunities from DOE to develop and deploy an ultra-scale computer system for the U.S. science community.

Introduction

This project was undertaken to ascertain the validity of the Japanese Earth Simulator centers claims and to define an appropriate path toward leadership class computing for ORNL and the nation. In March 2002, the Japanese Earth Simulator was put into service in Yokohama and posted a LINPACK performance benchmark of 35.86 Tflops, making it the fastest computer in the world. It still held the number 1 position at the end of this project. Furthermore, the Earth Simulator design team targeted high-resolution climate simulation using a particular numerical algorithm and configured the machine to enable a scientific objective. Their 2002 Gordon Bell Prize submission claimed a 26.58-Tflops sustained rate for a global atmospheric simulation at 10-km resolution using the spectral transform method. Since DOE is also committed to high-end climate simulation for global change studies and prediction, the evaluation of these claims was of paramount importance. The LDRD plan duplicated some of the algorithmic work reported by the Japanese, but our target platform was the Cray X1—a vector, massively parallel supercomputer not unlike the NEC SX6 used by the Japanese. We found the claims of the Earth Simulator center credible and determined the size and configuration of similar Cray supercomputers that would be required to compete with the ES for climate simulations. This information was instrumental in the successful bid for a National Leadership Computing Facility (NLCF). In addition, we worked in collaboration with the Japanese to vectorize the leading climate model, the CCSM3, for use on our future Cray system as well as for use on the Earth Simulator.

Technical Approach

The objective of this project is to prepare ORNL to develop and deploy an ultra-scale computer system for the U.S. science community. The approach to this was to scale the components of the Community Climate Systems Model (CCSM) up to the resolution and physical fidelity that is expected to be used on this new class of computer systems and to port these codes to a new generation of high-end computer architectures.

This project has three major technical thrusts:

1. benchmarking performance of a dynamical kernel on a high-resolution model to identify hardware and software issues with current and planned architectures;
2. evaluation and implementation of performance enhancements for global spectral atmospheric models; and
3. in-depth scientific performance study of the CCSM3 at high resolution on IBM p690 and Cray X1 systems.

We developed a model for the computational requirements of the spectral transform method for any problem size. We ran extensive algorithm tuning experiments on the Cray X1 using the Parallel Spectral Transform Shallow Water Model, identifying optimal parallel algorithm settings. We began taking performance measurements for large resolution problems, similar to those run on the Earth Simulator. At this point, we identified a performance problem on the X1 that is still being investigated. The problem appears to be limited to the test code, not to production implementations of the spectral transform algorithm. Unfortunately, final

performance benchmarks are still awaiting resolution of the performance problem.

We redirected efforts from alternative formulations of the spectral transform method to increase focus on vectorization of the CCSM. We iteratively profiled and analyzed the performance of CAM, the atmospheric component model, on the Cray X1, experimenting with alternative approaches to vectorization and optimization. We identified nondeterministic numerics problem and validated the fix. Performance four times that of the IBM p690 cluster was exhibited on the X1 for this as yet incompletely optimized version of CAM (Drake 2004).

In addition to scaling and vectorizing the CCSM3 model, there are other key algorithms for scaling climate models on future computer architectures. As part of this project, we investigated three such areas:

1. novel numerical methods including stereographic projection scheme for Laplacian on the Sphere, long time methods for conservation laws, and dynamic subcycling;
2. performance potential of spherical harmonic transform algorithms on modern architectures; and
3. understanding how reconfigurable computing can be used for accelerating the algorithms of climate models.

Results and Discussion

Results to date show that the Cray X1 architecture is superior to the IBM p690 in both performance and scalability for the CCSM. Future work will focus on completing scaling to T1279L96 resolution for benchmarking and maximizing performance of the full model for high-resolution configurations.

Among the promising numerical algorithms that will likely be used in the next-generation climate models we looked at those used for flow dynamics in the general circulation using the fast Fourier projection methods. The low operation count and predictable memory reference patterns create an opportunity for high performance, taking advantage of specific architectural features. The status of the numerical methods were reviewed and found to be limited by timesteps in both the dynamics and the physics. To address these concerns, we investigated long time step methods for the dynamics and subcyling to decrease the operation count for the physical parameterizations.

One area that showed particular promise was tuning PCM and investigating scalable implementations of communication. PCM was the main coupled climate model for the DOE until the recent release of CCSM3. PCM produced the bulk of model data used in current U.S. climate publications, and it remains a baseline against which new model results are compared. Compared to CCSM3, PCM has lower resolution, parallelism, and complexity, so it is useful for testing system scalability at moderate processor counts.

Initial tests of PCM on the X1 showed that "mpi_sendrecv" was the most expensive procedure, at over 10% of runtime on just eight MSPs. It was called from various procedures in the ocean and ice models that perform nearest-neighbor stencil operations. With the powerful processors of the X1, PCM became latency bound quickly. We replaced the MPI calls with direct memory access in the following ocean and ice procedures, where the chart shows the percentage of runtime for each procedure.

Procedure	MPI	Direct
ninept	9.0%	1.2%
fivept	9.8%	2.2%
neighbors_ice	4.0%	1.3%

The direct memory access was implemented by passing memory addresses using Co-Array Fortran, one of a number of techniques we described in (White 2004).

The tuning of PCM also highlighted some unusual strategies for vectorization. An optimization to the "grcalc" procedure, which performs an inverse Legendre transform, changed an inner loop with variable bounds to a static loop with an "if" statement around the body. This change took "grcalc" from 5.7% of runtime to 1.1%. An inner loop in the procedure "fcd_a2o," which couples the atmosphere and ocean components of the model, required more significant analysis. The loop performed updates on an array based on an index array. When such index arrays have non-repeating elements, the loop can be vectorized. The index array in question, however, had repeating indices, with a variable number of repetitions, between 1 and 130.

We gave the inner loop a stride of the maximum number of repetitions and added an outer loop over offsets across that stride. The inner loop then vectorized, taking the computational impact of "fcd_a2o" from 2.2% to 0.3% of runtime for the test case. We plan to add initialization code that will automatically determine the appropriate stride and perform the same optimization for other procedures in the coupler component.

Tuning PCM is useful in itself because we expect PCM runs as part of a future climate end station. PCM has also given us a convenient platform for testing optimization techniques for larger codes and processor counts, such as for CCSM at high resolution.

The performance of climate codes, including PCM, POP and other kernels, was documented and presented in a variety of forums. In particular, Pat Worley (Worley 2004) made a presentation to a National Academy Study group on our results for the Cray X1. The Cray User

Group meeting, which was hosted by ORNL and Cray in Knoxville, also had several presentations of optimization methods and techniques applied in this project (Drake 2004; White 2004).

As another objective, this project began to explore the use of reconfigurable computing hardware to determine if field-programmable gate arrays (FPGAs) could be productively used to accelerate specific sections of climate models. In this case, work was done to explore different methods for performing FFT algorithms which are a key part of the PSTSWM model. Two different techniques were explored using a new technology from SCR computers that will translate FORTRAN programs into FPGA algorithms. The results are described in (Liang 2004).

Finally, near the end of the project, we began work to compare and evaluate the efficiency of the Cray X1 and other computer architectures on a set of computational biology algorithms known as Biolib. A number of problems with the Cray X1 were identified that prevented completion of this work. We expect to complete the evaluation when the Cray problems are corrected.

Benefits

The major benefit of this project has been to prepare ORNL to successfully compete for the Leadership Computing Facility request from DOE. By beginning this work prior to the call for proposals from DOE, ORNL could readily demonstrate the expertise in vector processing in scaling a major application.

References

Drake, J. B., P. H. Worley, I. Carpenter, and M. Cordery. 2004. "Experience with the Full CCSM," Proceedings of the 46th Cray User Group Conference, Knoxville, Tennessee, May 17–21, 2004.

Liang X., M. Smith, J. Vetter, and A. Bland. 2004. "Balancing FPGA Resource Utilities," in preparation.

White III., J. 2004. "Dangerously Clever X1 Application Tricks," Proceedings of the 46th Cray User Group Conference, Knoxville, Tennessee, May 17–21, 2004.

Worley, P. H. 2004. "Cray X1 Optimization: A Customer's Perspective," Presented to the 46th Cray User Group, Knoxville, Tennessee, May 17–21, 2004.

Advanced Computational Methods

R. J. Harrison, G. I. Fann, A. Khamayseh, and E. D'Azvedo
Computational Science and Mathematics Division

This multidisciplinary project developed, evaluated, and deployed novel numerical methods for the solution of non-linear integral-differential equations and explored novel parallel computing models for next-generation massively parallel computers. Initial application was to computational chemistry, but the resulting methods and tools are widely applicable. Related methods are already being tested in climate simulations by Beylkin and in fusion by Fann. The outcomes of this project include new mathematical and numerical methods, efficient implementations of these algorithms, and application to problems of chemical significance. Results already demonstrate that some of these approaches might have an impact upon chemistry similar to that of the FMM and the FFT.

Introduction

This project aimed to develop some of the fundamental mathematics and computational tools required to make multiresolution techniques practical for computation in three and higher dimensions, and to develop computer science tools to make more productive use of massively parallel computers. In principle, all of chemistry can be understood and predicted from solution of the Schrödinger and/or Dirac equations. In practice, we cannot solve these 3-N dimensional (N, the number of electrons) differential equations and must resort to a variety of approximations. These approximations limit both the accuracy that may be obtained and the size of system that may be studied. By adopting multiresolution methods in multiwavelet bases, we aimed to remove several of these limitations with the objective of enabling more reliable and accurate computations on larger systems and have demonstrated initial success for density functional theory.

Technical Approach

In principle, all of chemistry can be understood and predicted from solution of the Schrödinger and/or Dirac equations. In practice, we cannot solve these 3-N dimensional (N, the number of electrons) differential equations and must resort to a variety of approximations. Conventional computational chemistry adopts the linear combination of atomic orbitals (LCAO) approximation and constructs effective one-electron molecular wave functions from a superposition of atomic wavefunctions. This gives very compact wave functions with desirable physical properties, since molecules are indeed composed of atoms. However, the LCAO approximation is not suitable for high-accuracy calculations, and because the atomic wave functions have extended support, the cost of calculations scales non-linearly with the size of the system. These approximations limit both the accuracy that may be obtained and the size of system that may be studied. Our aim was to remove several of these limitations with the objective of enabling more reliable and accurate computations on larger systems.

The mathematical and numerical methods we employ are multiresolution analysis in multiwavelet bases (Alpert 2002) in the non-standard form (Beylkin 1991) with separated and low-rank representations for operators and/or functions (Beylkin 2002; Harrison 2003; Harrison 2004). Multiresolution analysis (MRA) separates the behavior of functions and operators between length scales, thereby enabling compact and efficient representations with controlled precision. Efficient algorithms exist for the direct computation and application of the inverse and exponential of many important differential operators. The separated representation (Beylkin 2002) of a function (or operator) in many dimensions, to an arbitrary finite precision, is a sum of products of functions of lower (usually one or three) dimension. The number of terms in the sum is referred to as the separation rank and is quite distinct from the operator rank (see the next point). Recently, Beylkin and Mohlenkamp (Beylkin 2002) proved that many interesting operators (e.g., the Schrödinger Hamiltonian, or the Green's function to Poisson's equation) have a separation rank that scales logarithmically as the number of dimensions.

Dr. Khamayseh, an expert in adaptive mesh generation and refinement, examined how standard techniques could be used to improve upon the current refinement approach (Fig. 1), which is strict bisection. Dyadic refinement of boxes is necessary to maintain (most straightforwardly) the multiresolution structure, but instead of dividing a box exactly in two, we may chose a different division to, for instance, place a node at a nearby nucleus. This work was initially motivated by results (Yanai 2004) for analytic derivatives of molecular energies with respect to the position of nuclei – the results are much more accurate if the nuclei are placed at grid nodes. Another motivation was more general boundary conditions, including internal structures.

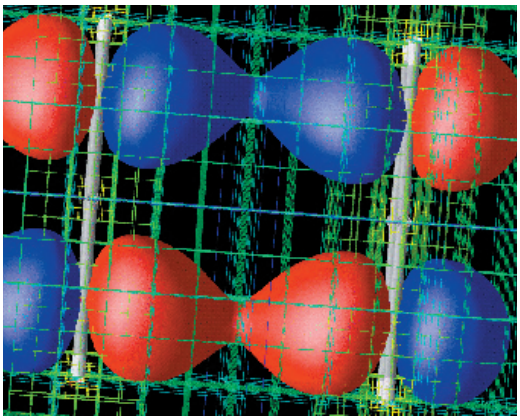

Fig 1. The adaptively refined mesh and isosurfaces for a molecular orbital of the benzene dimer. Note how boxes are larger between the molecules (where the orbital is slowly varying) and how the boxes are small near the nuclei (where the orbital varies rapidly).

To enable and facilitate the development of related algorithms and implementations on next-generation parallel computers, we examined sparse data structures, including many-dimensional trees and sparse matrices, distributed across many processors. These data structures must support one-sided access mechanisms in a non-uniform memory model. In collaboration with Prof. R. Butler (Middle Tennessee State University), we prototyped parallel tools for the support of irregular and hierarchical distributed data structures using one-sided access mechanisms on massively parallel computers. These were built upon both MPI and the Global Array (Nieplocha 1996) and ARMCI libraries that have already been optimized on essentially all current high-performance computers and workstation clusters. They both already exploit shared-memory within SMP nodes.

Results and Discussion

We made major advances in our ability to compute accurately and efficiently with a wide range of operators. The existing prototype code was been significantly enhanced. A 64-bit port has been done to enable large memory calculations on the IBM SP, two new initial guesses were implemented (superposition of atomic densities, and import from GAMESS or NWChem), a Pthread shared-memory parallel version of the important integral operator kernel was developed, a Python wrapper round the MPFR multiple precision library, and a new, much faster Python/C++ tensor class specialized to our needs. The latter was very important since the much greater speed will enable additional optimizations such as aggressive screening during function-function products.

Prof. Ralph Butler (MTSU) who is one of the developers of MPICH and has extensive experience with parallel computing and also Python, was funded by subcontract for research and software development. In collaboration with Dr. Jarek Nieplocha at PNNL, we defined an interface for an active message layer which exposes in a portable fashion existing capability within ARMCI, the transport layer used by Global Arrays and several others packages. The active message interface was designed to enable the manipulation of only remote shared state, whereas other active message interfaces also manipulate remote thread/process private state. This will permit more efficient execution on many platforms including the CRAY-X1. A prototype parallel implementation (shared and distributed memory) has been completed and is now being evaluated. A distributed hash table which can support general data structures, including Python dictionaries, was also prototyped.

Benefits

The strategic opportunity directly addressed by this project was the expressed intention of the DOE and other government agencies to develop computer simulation as a third branch of science on equal footing to experiment and theory. Implicit in this expansion is the need for larger computers, more sophisticated and accurate numerical methods that are capable of solving large problems on large computers, and improved programming paradigms that enable scientists to focus on the science rather than the computer. Another essential component is the training of many more computationally sophisticated scientists, a need that was met in this proposal through the involvement of graduate and postdoctoral students.

References

Alpert, B., G. Beylkin, D. Gines, and L. Vozovoi. 2002. "Adaptive Solution of Partial Differential Equations in Multiwavelet Bases," *Journal of Computational Physics* **182**, 149–190.

Beylkin, G., R. Coifman, and V. Rokhlin. 1991. "Fast Wavelet Transforms and Numerical Algorithms I," *Comm. Pure Appl. Math* **44**, 141–183.

Beylkin, G., and M. J. Mohlenkamp. 2002. "Numerical operator calculus in higher dimensions," pp. 10246–10251 in Proceedings of the National Academy of Sciences, v. 99, 16.

Harrison, R. J., G. I. Fann, T. Yanai, and G. Beylkin. 2003. "Multiresolution quantum chemistry in multiwavelet bases," Lecture Notes in Computer Science, 2660 103.

Harrison, R. J., G. I. Fann, T. Yanai, Z. Gan, and G. Beylkin. 2004. "Multiresolution quantum chemistry: basic theory and initial applications," *J. Chem. Phys.*, in press.

Nieplocha, J., R. J. Harrison, and R. J. Littlefield. 1996. "Global Arrays: A nonuniform memory access programming model for high-performance computers," *The Journal of Supercomputing* **10**, 197–220.

Yanai T., G. I. Fann, Z. Gan, R. J. Harrison, and G. Beylkin. 2004. "Multiresolution quantum chemistry in multiwavelet bases: Analytic derivatives for Hartree-Fock and density functional theory," *J. Chem. Phys.* **121**, 2866.

Creating New Climate Drivers and Interactions in Global Climate Models

D. Erickson,[1] M. Branstetter,[1] M. Sale,[2] W. M. Post,[2] A. King,[2] L. Gu,[2] F. Pan,[2] and S. Hadley[3]
[1]*Computer Science and Mathematics Division*
[2]*Environmental Sciences Division*
[3]*Engineering Science and Technology Division*

This proposal involved the identification of important climate drivers not already present in current climate models. We evaluated a suit of global climate models and implements a range of climate processes/feedbacks and drivers to assess climate prediction improvement. The drivers we perturbed were (1) carbon cycle feedbacks, (2) hydrological cycle feedbacks, and (3) economic feedback responses to climate change. The scientific analysis of the significant feedbacks in the Earth system is key to the reliability and uncertainty estimation of future climate prediction and is critical in making meaningful policy decisions. The programmatic objective was to make ORNL the central DOE institution for computational climate modeling. We implemented temperature acclimation in the PCM-IBIS model, did a variety of soil moisture numerical experiments in the CCSM2, and for the first time, forced an economic model with output from a GCM for the period 2000–2025.

Introduction

The technical R&D objectives of this LDRD were the evaluation and creation of new climate drivers/feedbacks in the climate modeling system. The installation of state-of-the-art global climate models and an assessment of feedbacks and critical biogeochemical physical parameterizations in the global climate models operating on ORNL computational platforms were central to this LDRD. The deliverables are several refereed journal articles, meeting presentations, and a clear delineation of future (2–5 years) research opportunities. This LDRD was intended to position ORNL climate science at the forefront of the U.S. climate modeling efforts.

Technical Approach

We ported the U.S. state-of-the-art global Climate Model (CCSM2) to the CCS/CSM high-performance computing center; evaluated the control run of the CCSM2 (Branstetter and Erickson 2003); and performed a variety of sensitivity tests of the CCSM2. We also, in the last year of the LDRD, moved to using the newest U.S. national model, CCSM3.

An additional milestone is that we have, with colleagues at LLNL, ported the only fully coupled climate-carbon cycle model in the United States to ORNL computers. This allowed us to replicate the results of Cox et al. (2000) and Friedlingstein et al (2001). The effect of acclimation has been coded into IBIS terrestrial biosphere submodel, and an experimental run has been completed (Gardinia and Ryan 2000; Kirschbaum 2000; Lucht et al. 2002; Parton et al. 1987). We also ran three additional test runs of the PCM-IBIS staged to explore new scientific characteristics of the PCM-IBIS.

In the area of hydrologic cycle feedbacks, we began developing new modeling procedures to improve how soil moisture dynamics and lateral transport of water is represented in the CCSM2 code. Our initial computational experiments indicate that the code for soil wetting and drying is not realistic and that there may be errors in the land surface modules of CCSM2. As a result we began to re-code the important parts of the land surface model, including a new simplified algorithm and supporting global data for estimating TOPMODEL baseflow parameters and soil profile characteristics. This new approach is based on work that evaluated a number of different methods for calculating topographic index and flow direction.

Results and Discussion

We have a wide range of accomplishments to report in this final report including several refereed publications published, in press and in preparation. We have successfully included temperature acclimation in the PCM-IBIS global carbon-climate model. An alternative method to the vertical distribution of conductivity of water in soils has lead to a better computed climate. One of the most interesting results of this LDRD is the use of the state-of-the-art USA global climate model, the CCSM2, to drive various energy sector models, including NEMS. This has extended the range of study using climate models past the traditional meteorological discussions of global warming and allows the coupling of environmentally dependent activities such as residential heating and cooling to be computed concurrent with greenhouse gas–induced climate change. This enables the rate and extent of energy production (CO_2 release from energy creating fossil fuels) to evolve in tandem

with global climate change. One example of the portion of this task that assesses the economic impact of climate change is the simulated estimate of the change in cost of energy usage for the period 2000–2020. Specifically, we have grouped the temperature trends, monthly for the period 2000–2020, in the 9 regions of the United States defined by the NEMS model. This climate model output data allows an explicit calculation of the "heating days" and "cooling days" for each region for 20 years of climate change. These heating days and cooling days have been input into the NEMS model, and estimates of the financial implications of the warming patterns will be made. The NEMS and other energy models such as CARMAN and CLIR are also driven with a range of "ensemble" climate predictions from CCSM2. This, for the first time, allows a fully coupled global climate model, the CCSM2, to directly force an economics-based model.

Benefits

Our strategy is initially to build an expertise that is active in global climate modeling science. At the national CCSM2 workshop in Breckenridge, Colorado, in June, 2003, and the CCSM3 workshop in Santa Fe, New Mexico in June, 2004, ORNL also had computational scientists representing our efforts. It is interesting to note that the "theme" of the 2004 CCSM3 workshop was "Biogeochemistry," and that David Erickson is the Task Leader for the SCIDAC-Climate section on Biogeochemistry. We had several lectures, posters, and workshop participation on a variety of climate modeling issues.

Extensive team/partnership building with DOE program sponsors, NASA sponsors, sister DOE national laboratories, and university colleagues has been a focus of this LDRD. We now have a FWP with OBER on numerical ocean circulation models and how those simulations may influence carbon sequestration. King is pursuing collaborations with Jon Foley, University of Wisconsin, author of the IBIS terrestrial biosphere model. We have proposals into NASA, 6 proposals submitted to DOE HQ, and 1 submitted to USAID. This LDRD has created infrastructure and expertise that will be of interest to NSF, NASA, ONR, DOE, NOAA and EPA.

References

Cox , P. M., R. A. Betts, C. D. Jones, S. A. Spall and I. J. Totterdell. 2000. "Acceleration of global warming due to carbon cycle feedbacks in a coupled climate model," *Nature* **408**, 184–197.

Friedlingstein, P., L. Bopp, P. Ciais, J.-L. Dufrene, L. Fairhead, H. LeTreut, P. Monfray, and J. Orr. 2001. "Positive feedback between future climate change and the carbon cycle," *Geophys. Res. Lett*. **28**, 1543–1546.

Gardinia, C. P., and M. G. Ryan. 2000. "Evidence that decomposition rates of organic carbon in mineral soil do not vary with temperature," *Nature* **404**, 858–861.

Kirschbaum, M. U. F. 2000. "Will changes in soil organic carbon act as a positive or negative feedback on global warming?" *Biogeochem*. **48**, 21–51.

Lucht, W., I. C. Prentice, R. A. Myneni, S. Sitch, P. Friedlingstein, W. Cramer, P. Bousquet, W. Buermann, and B. Smith. 2002. "Climatic control of the high-latitude vegetation greening trend and Pinatubo effect," *Science* **296**, 1687–1689.

Parton, W. J., D. S. Schimel, C. V. Cole and D. S. Ojima. 1987. "Analysis of factors controlling soil organic matter levels in great plain grasslands," *Soil Science Society of America Journal*, **51**, 1173–1179.

Biomolecular "Locks and Keys" High Performance Computing for Investigation of Recognition Principles in the Complexes of Biological Macromolecules

A. Gorin, Y. Li, R. Day, and V. Protopopescu
Computational Science and Mathematics Division

Our LDRD project was focused on novel computational capabilities for the modeling of biological macromolecules. Specifically, we explored two important areas: modeling of the biological molecules and complexes using a novel type of the experimental constraints—Residual Dipolar Couplings (RDC); and new algorithms for the search and optimization in the biomolecular conformational space. The main achievements of the project can be summarized as the following: (1) we put forward the Combinatorial Assignment Procedure (CAP)—a new method to incorporate the Residual Dipolar Couplings constraints for the robust NMR resonance assignment and structural characterization of the biological molecules; (2) implemented a library of Markov Chain Monte-Carlo schemas, proposing two new approaches—Accelerated Simulated Tempering (AST) and Accelerated Parallel Tempering (APT); (3) applied APT Monte-Carlo as the search engine for the ab initio protein folding program ROSETTA and demonstrated a significant improvement in the quality of the obtained predictions. Taken together the accumulated capabilities provided the basis for the ORNL participation in several bioscience research initiatives, including NIH Centers for Biomedical Computing and DOE Biopilot Program "Exploratory Data Intensive Computing for Complex Biological Systems." The developed capabilities have formed the foundation for a new biomodeling platform, advanced the state of the art in biomolecular modeling through the merge of novel algorithms and High Performance Computing, and set the future course for robust R&D computational biology program.

Introduction

The successful Genome Projects and the Structural Genomics Initiatives are extending, in a revolutionary way, our knowledge of the elementary components (genes, proteins, etc) of life. The Structural Genomics enterprises and mainstream genomics continue to progress at a fast pace as well, providing formidable challenges for biomolecular simulations. Targets for biomolecular modeling are directly linked to the most important life mechanisms, but the relevant molecular systems are much larger than those modeled in the past and contain several heterogeneous polymers in them (i.e., multiprotein complexes, DNA-protein complexes, ribozimes and small RNAs, RNA-protein assemblies, etc). Formation of the heterogeneous complexes is the central event in most fundamental cellular regulatory pathways: transcription regulation, cell death, replication, etc. For example, failure of the cancer suppressor protein p53 to recognize its DNA binding site is the proven factor in more than 50% of all cancers (Gallou 2001). Biomolecular modeling becomes crucially important for the modern biological research: from rational drug design, where small molecule is fitted into complex binding pockets; through functional characterization driven by protein structure predictions; and up to characterization of the interaction interfaces on protein-protein complexes. A separate and very important role is played by biomodeling software support for the modern high-throughput experiments.

The existing biomolecular modeling tools often have weak capabilities for modeling of the biological complexes, due to the size of the complexes and because of the specific challenges associated with heterogeneous biopolymer complexes (such as the different parameterizations required by diverse biopolymers). Almost all biomolecular modeling requires minimization of the potential energy functions or knowledge-based score potentials, but very few of the existing approaches takes advantage of the recent advances in the mathematics and computer science, for example, in the area of Markov Chain Monte-Carlo optimization techniques. As we show in the It is also well known that biomolecular simulations are delivering especially robust results, when assisted by the experimental constraints guiding the calculations. Yet some of the novel types of the experimental constraints are very complex, and correspondingly the existing algorithms and software implementations do not support them.

In our project we have developed capabilities in two closely related directions: (1) Markov Chain Monte-Carlo algorithms for the conformational space search and (2) combinatorial integration of RDC-based constraints for the structural refinement. Both capabilities are very important for the efforts to model biomolecular complexes and both are not available within the existing simulation tools. For example, Markov Chain Monte-Carlo (MCMC) sampling is fast developing area of statistics and applied mathematics, yet few (if any) of the latest breakthroughs have been utilized in biomolecular computations. MCMC

is also a very natural way to use highly parallel computer architectures and other High Performance Computing architectures.

Even a partial realization of the capabilities described here will create new opportunities in the field. In particular, we may be able to solve structures that are currently not easily accessible to direct experimental tools (such as transmembrane proteins), collect new types of the information (such as movement in the biomolecular complexes), and potentially engineer new properties into existing interaction interfaces. The common threads of our proposal is the modeling of the recognition principles and the ability to manipulate in smart ways with known structural fragments, thus taking advantage of the rapid growth in the structural genomics databases.

The second Genomes-to-Life Call (December 2002) has been solely focused on high throughput experimental technologies. Using ideas and preliminary results developed in the task "Integration of the Residual Dipolar Couplings data" we have formulated a new research program, directly addressing several GTL-2 Research Areas. Our preproposal "NMR methods for quantitative biochemistry" made through the first round of reviews and was selected for the full submission. We continue to accumulate preliminary results in the RDC-related area, developing a new field of ORNL expertise, which has a significant potential both inside GTL framework and beyond it. The current plans for DOE Proteomic Facilities (also known as Proteomics Knowledge Factories) is a strong indication that in the coming future DOE biological research will be centered on cellular molecular machines: mainly protein-protein complexes, but also complexes with RNA, DNA and ligands. The stated aim of the planned Facility II is "to capture significant fraction of all biomolecular complexes present in the bacterial cell." ORNL is leading the bid to host Proteomics Facility II, and the development of computational capabilities for modeling of diverse biological complexes directly contributes to the technological advances essential for this goal.

Research Accomplishments

Research accomplishments of the project can be formulated in the frame of the following closely interconnected tasks: (1) collective variable algorithms forming the backbone of our biomodeling platform, (2) novel Monte-Carlo search sampling methods, and (3) integration of the Residual Dipolar Couplings data into structural refinement.

Implementation of the collective variable algorithms. We have developed and implemented (both in C and in Perl) algorithms for constructing molecular models using collective variables. Specifically, we have completed implementation of several types of helical parameters (local, global, symmetric, and linked to the single rotation axis), dihedral angle variables, including pseudo rotation angles, and routines for the manipulation of the rigid sub fragments (such as secondary structure elements). We have also developed algorithms and subroutines for the force field parameter files (reading, writing, calculating energy components).

Monte-Carlo sampling methods. We have implemented and tested four major types of Markov Chain Monte-Carlo algorithms, namely: (a) Metropolis Monte-Carlo, (b) Simulated Annealing Monte-Carlo, (c) Simulated Tempering, and (d) Weighted Monte-Carlo [1]. The most promising results in terms of convergence speed were obtained with Simulated Tempering. Based on our studies we have proposed a new method—"Accelerated Simulated Tempering Scheme." We construct an alternative ladder that combines temperature and size of step, (t_i, s_i), where $1 = t_1 < t_2 < \ldots < t_m$, and $s_1 < s_2 < \ldots < s_m$. Then, we adjust the original Greyer and Thompson's algorithm by "leaning: the temperature ladder. To this end by set at each ladder asymmetrical transition function, forcing the system to have a lower probability of visiting the higher-level temperature ladders [1].

For the complex landscapes, where it is very hard Greyer and Thompson's parameters accurately, we have proposed Accelerated Parallel Tempering (APT) optimization algorithm [2–3]. APT can be described by the following main principles:

1. Local Monte Carlo moves at each temperature level. The transition probability only depends on the change of in scoring function $E(C_i)$, where C_i is the configuration of the system at temperature level i. The Metropolis-Hastings ratio at temperature level i is computed by

$$w_{Local}(C_i^{old} \rightarrow C_i^{new}) = e^{-\beta_i \Delta_i E} = e^{-\beta_i [E(C_i^{new}) - E(C_i^{old})]},$$

   where $\beta_i = 1 / k_B T_i$ with k_B the Boltzmann constant and T_i the temperature at level i. The new state is accepted with probability $\min[1, w_{Local}[C_i^{old} \rightarrow C_i^{new}]]$.
2. Exchange of systems between two neighbor temperature levels, i and i+1.
   $C_i^{new} = C_{i+1}^{old}$
   $C_{i+1}^{new} = C_i^{old}$
   The exchange is accepted according to the Metropolis-Hastings criterion with probability $\min[1, e^{-\beta i E(Cj) - \beta j E(Ci) - \beta j E(Cj) + \beta i E(Ci)}]$ to maintain the detailed balance condition of every Markov process.
3. The move sizes are adjusted to keep acceptance rate at ~ 0.5 at every temperature layer.

In the APT scheme the moves at high temperature levels intend to have a wide range exploration of the system energy landscape with a higher acceptance rate

while those at low temperature levels explores the local details. With suitably selected parameters, the AST and APT schemes can easily escape entrapment in deep local minima and converge to the target distribution. Our recent computational results in rough high-dimensional objective functions and have confirmed the fast convergence of the schemas. We expect that incorporating various Rosetta fragment moves into APT temperature ladder can lead to a broad exploration of the protein energy landscape and thus eventually improve the resolution of ab initio protein structure prediction. Also, analyzing the Markov Chains in APT scheme may also provide us hints to estimate the convergence of the Rosetta process [3].

Our first attempt of applying Accelerated Parallel Tempering to Rosetta [3], which only incorporates the straight and small moves with a fixed temperature ladder, has already shown significant improvements in some protein structures in Rosetta benchmark. There are significant Ca RMSD shifts (0.5–4Å) in the predicted structures of 1a32, 1cg5, 1elw, 1opd, and 1tuc, while the results of other structures are close to those of original Rosetta (Fig. 1). The results have demonstrated tremendous opportunities to improve prediction accuracy of the protein structures through more advanced sampling technologies, and our APT and AST schemas are primary candidates for the future modeling platforms providing such improvements [1–3].

Integration of the Residual Dipolar Couplings data. Residual Dipolar Couplings (RDC) measurement is one of the most promising new developments in NMR solution techniques. Recently, we have recognized that RDC-based technologies assisted by High Performance Computing can be applied for solving hard problems in structural ribonomics and proteomics [4]. Briefly, the Combinatorial Assignment Procedure (CAP) method works in the following way. RDCs are first measured on a target protein molecule. This leads to the assignment of chemical shift values with a corresponding RDC value. Unlike chemical shifts, the magnitude of a given RDC value reflects the average orientation of the bond vector and hence can readily be related to a given structure. For a given assignment guess, the RDC values will either agree or disagree with the given structure. For the ideal case, the best agreement, measured as the root mean square deviation (rmsd) between measured and 'best-fit' calculated RDCs, will occur for the correct set of assignments. To enhance this unique mapping, one can also work with a group of RDCs (backbone NH and CαHα) that have been correlated using 3D experiments (HNCA, HN(CA)HA) [7]. All possible RDC assignment permutations can therefore be explored for consistency with a given target structure [4–7].

We also have applied the CAP algorithm for the semi-automatic assignment of the protein structures [6,8]. The following aspects of protein-protein interactions have been targeted: (1) reliable and rapid detection of native protein-protein interactions; (2) measurements of binding affinities under as a function of pH, ionic strength, and molecular crowding; (3) mapping of functionally relevant residues at protein-protein interfaces; and (4) spatial characterization of subunit positions in multi-protein complexes. The proposed approach combines novel computational developments with experimental NMR Residual Dipolar Couplings (RDC) methodology and chemical shift perturbations to quantitatively and rapidly characterize protein-protein interactions, efficiently bypassing time consuming requirements of complete structural refinement. Development of the fast and reliable algorithms for protein backbone assignments based on CAP approach is the focus of our future research.

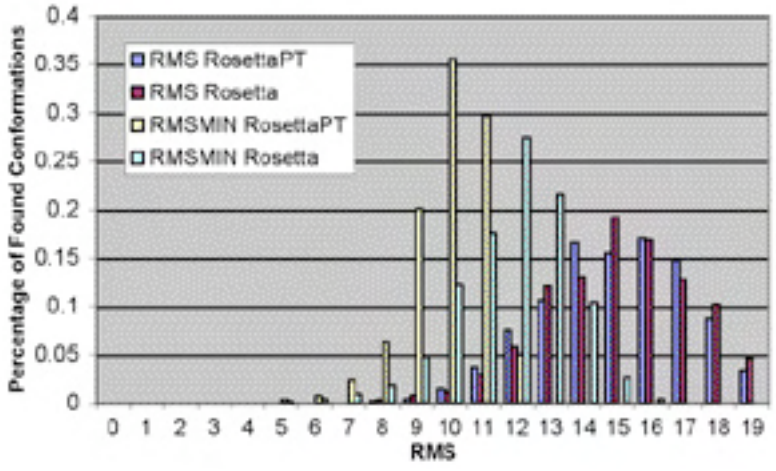

Fig. 1. Root Mean Square Deviation (RMSD) and RMSD for the best structure comparison of 1000 conformations in APT Rosetta and original Rosetta implementation for Protein Data Bank target 1lis.

Benefits

Four full size papers and four conference proceedings were prepared based on the results obtained in our LDRD (see Publications). We have used LDRD ideas to submit a full-scale proposal in response to DOE GTL-2 Call and for DOE Biopilot Program "Exploratory Data Intensive Computing for Complex Biological Systems (one year funding was awarded at the end of FY 2004). We are also actively advancing two additional NIH opportunities related to the proposed NIH Centers for Biomolecular Networks: in collaboration with Genomics Research Institute (University of Cincinnati) and Vanderbilt University (Nashville).

Preliminary results of this LDRD have been used in our recent submission for NIH Center for High Accuracy Protein Structure (five institutions lead by ORNL, PI–Andrey Gorin).

Publications

1. Li, Y., V. A. Protopopescu, and A. Gorin. Accelerated Simulated Tempering. *Physics Letters A*. 2004, 328(4-5), 274–283.

2. Li, Y., C. E. M. Strauss, and A. Gorin (2004). "Parallel tempering in Rosetta practice." Proceedings of ICBA'04 Fort Lauderdale, Florida.

3. Li, Y., and A. Gorin (2003). "An Accelerated Parallel Tempering for Global Optimization in the Complex Conformational Space" (in preparation).

4. Al-Hashimi, H. M., and A. Gorin. Structural genomics of RNA using NMR residual dipolar couplings. *Journal of Applied Genomics and Proteomics*, 2003, 2(1), 3–16.

5. Gorin, A., and H. M. Al-Hashimi. 43rd Experimental Nuclear Magnetic Conference, Savannah, GA (2003). "Automatic RNA assignment using Residual Dipolar Couplings and a Combinatorial Assignment Procedure (CAP)."

6. Gorin, A., and H. M. Al-Hashimi (2003). Keystone Conference 2003: Frontiers Biomolecular NMR "Combinatorial Assignment Procedure—new method for automatic NMR assignment in biopolymers."

7. Zhang, Q., A., Gorin, R. Throolin, and H. M. Al-Hashimi. 43rd Experimental Nuclear Magnetic Conference, Savannah, GA (2003) "Conformational changes underlying dimerization of the DIS RNA domain from HIV-1: Oligomer structure and dynamics from NMR residual dipolar couplings."

8. Gorin, A., and H. M. Al-Hashimi (2003). International Conference Computational Molecular Biology "Computational challenges in rapid characterization of the protein-protein interactions by NMR-based methods."

Towards Common Components for Computational Nanoscience

T. C. Schulthess,[1] M. E. Summers,[2] D. E. Bernholdt,[1] and W. Elwasif[1]
[1]*Computer Science and Mathematics Division*
[2]*Computational Science and Engineering Division*

In order to meet the challenges and take advantage of the opportunities posed by nanoscience, the need for an open source repository of computational materials science codes that are portable, extensible, and well maintained on modern high-performance computing architectures has been identified by several research groups. The costs of building and maintaining such a repository will be prohibitive, unless new approaches are found to integrate legacy code systems in such a repository. Here we have initiated the development of software analysis and modification tools that help integrating semi-automatically legacy codes into modern software environments for computational material science. Recent developments of an object-oriented and generic toolkit for computational materials science have proven an efficient avenue for building future applications codes for nanoscience. We have leveraged these efforts and developed a version of toolkit codes, which are compliant with the Common Component Architecture, an emerging approach to component-based software development, which explicitly recognizes the requirements of high-performance computational science codes. As a demonstration, these tools have been used to implement a simulation system for spin-models that uses the novel Wang-Landau sampling algorithm. Simulations have been performed to develop cost models of the Wang-Landau scheme for various spin models and analyze the parallel scaling behavior.

Introduction

In order to meet future expectations, computational materials science (CMS) must make efficient use of the most advanced high-performance computing (HPC) infrastructure that is available. The strategy for advancing CMS within ORNL's Center for Computational Science (CCS) is through the participation of domain scientists in the development of computational methods, algorithms, and simulation software, as well as early evaluation of new computer hardware. To enable this, a Materials Research Institute within CCS (CCS-MRI) has been created with the mission to build and maintain a community of leading computational materials scientists and to integrate them into the development of high-performance computing infrastructure of the CCS. One of the tasks of the CCS-MRI is to develop a repository of computational materials science codes that are optimized and maintained on CCS's high-performance computing infrastructure. Besides *legacy* electronic structure codes, the repository project includes the *Ψ-Mag* toolkit, a highly extensible generic library of data structures and algorithms that are commonly used in materials simulations. Furthermore, an important part of the SciDAC initiative is the development of a Common Component Architecture (CCA), which aims at providing specification for the development and use of *components* as basic building blocks of high-performance simulation codes. CCA is designed to make the incorporation of existing code and libraries into components straightforward.

The vision pursued by this LDRD project was to combine automated source code analysis and manipulation tools (SCAMT) with the paradigms of the CCA and the generic software design techniques used in the *Ψ-Mag* toolkit, in order to build and maintain the software repository of the CCS-MRI. The SCAMT that were developed here will be used for the maintenances of existing codes as well as the transformation of legacy codes into CCA compliant components. Similarly components of generic libraries, such as *Ψ-Mag*, BOOST (www.boost.org), or ALPS (alps.comp-phys.org), will be made CCA compliant. Future software development in CMS that makes use of these tools will be more efficient and well tailored to high-performance computer architectures. Furthermore, the task of integration and maintenance of external codes and libraries into component-based frameworks is representative of widespread issues faced by CCA in other domains as well.

Technical Approach

The strategy we pursue in this project is to strongly tie the development of software tools to the development of sample applications in computational nanoscience. This makes it possible to develop a core set of tools and expertise needed to build software repositories for computational nanoscience with the limited resources available in an LDRD project. The project consists of three tasks. The first task was concerned with developing a useful SCAMT, specifically it was about developing an open source system of tools that can parse Fortran legacy codes (including Fortran 90 and beyond), generate abstract syntax trees (AST), and do user-oriented operations on these trees. These tools were constantly tested with

existing materials science codes. From a computer science point of view, this task would lead to definition of ASTs that is suitable for codes used in nanosciences, and from the nanoscience point of view, the task is leading to a first set of open source tools that supports scientists analyzing and maintaining large source codes. The second task was concerned with developing an understanding of how to interface generic toolkits that are currently in use in computational nanoscience with the CCA system. The *Ψ-Mag* toolkit, which we chose to work with, is prototypical for modern software libraries that use the generic programming paradigm. Finally, in the third task we analyzed the parallelization of a new Monte Carlo sampling algorithm (Wang 2001a) in order to develop cost models for tools from which we built the simulation codes. The ability to build cost models for generic tools and CCA component will be crucial, if they are to be used efficiently in new simulation frameworks on modern high-performance computing platforms.

Results and Discussion

F77/F90 Parser and user interface for CMS source code analysis. We followed our original plan and developed an open source parser for Fortran 77 and Fortran 90 with which abstract syntax tree (AST) representations of the source codes are built and subsequently used in the analysis tools. The specifications for the AST—there is no commonly accepted standard for ASTs—are being developed along with the analysis tools to optimize the parser systems for the particular requirements of CMS code development and maintenance. Our parser is complete enough to generate ASTs for the codes that are presently used in the CCS-MRI (the particular codes we tested are LSMS, SIC-LSD, FLAIR, and LKKR). For scientists who are working on the CMS codes but are not interested in the bare AST, we have developed a Web-based interface, which displays source code along with the information provided by the AST in terms of pop-up menus and hyper links between source code segments. With this tool, it will be straightforward to isolate parts of legacy codes that are to be used in CCA-compliant components. Making these tools Web based also simplifies collaborative development of CMS software for the CCS-MRI repository over the internet. We have plans to distribute the parser tools and Web interface to the AST on the internet under the name FortranSmart. An example Web interface of the AST of a legacy code that was generated with FortanSmart can be found at URL: http://mri-fre.ornl.gov/codes/LSMS/.

Mapping generic libraries onto CCA-compliant components. The *Ψ-Mag* toolkit is representative for numerous generic libraries based on C++ templates that are gaining importance in CMS. CCA uses the Scientific Interface Definition Language (SIDL) to interface with such libraries. The major issue in the present task was to delineate the parts of the *Ψ-Mag* toolkit that can be mapped onto the CCA-compliant components using SIDL in its present form from those parts that will require modification of SIDL. We have found that it is possible to turn generic classes and functions in the *Ψ-Mag* toolkit into SIDL objects by (1) creating an instance of the *Ψ-Mag* object inside the SIDL implementation and (2) providing a C++ wrapper for each SIDL interface that exactly matches the corresponding *Ψ-Mag* concept. Automation of this process appears straightforward, either through a user-generated specification file that extends SIDL to describe C++ typdefs and templates or through a parser, which is able to extract the appropriate information from the C++ source code. However, a wholesale export of *Ψ-ag* into SIDL is not desirable because generic libraries use templates to provide information about objects they implement at compiler time—CCA presently follows the object-oriented model that uses primarily run time polymorphism. Wael Elwasif (with co-authors Greg Brown, T. C. Schulthess, and D. E. Bernholdt) presented the results of this work under the title "Towards Common Components for Computational Nanoscience" at the Los Alamos Computer Science Institute Symposium (LACSI) in October 2003.

Analysis of the Wang-Landau algorithm with multiple walkers and cost models for generic tools. The Wang-Landau algorithm (Wang 2001b) constitutes a new and efficient sampling scheme to estimate probability distribution, such as the density of states (DOS) used in statistical physics to calculate the partition function. With this new algorithm it is now possible to efficiently estimate the temperature-dependent free energy, which plays a crucial role in various areas of computational nanoscience. We have implemented a new parallel version of the Wang-Landau sampling technique in the *Ψ-Mag* toolkit in a generic way that will allow usage with arbitrary models. Unlike other Monte Carlo methods, the Wang-Landau algorithm requires communication between random walkers at every sampling step; that is, it is not trivially parallel. Since most of the models that will be used with the sampling scheme will themselves be parallelized, it is important to have cost estimates of the different part to allow users to decide how to best allocated the computational resources. Here we have developed cost models for the parallelization of the Wang-Landau scheme using two different classical multi-dimensional spin models that belong to different universality classes (Ising and Heisenberg) for the case study. We find that the mean cost of converging the DOS estimates scales algebraically with the system size with exponent between 2 and 3 depending on the model and system size (see Fig. 1 for the one- and two-dimensional Ising models). The scaling with number of random walkers is linear, for large enough spin system where startup cost can be neglected, only if

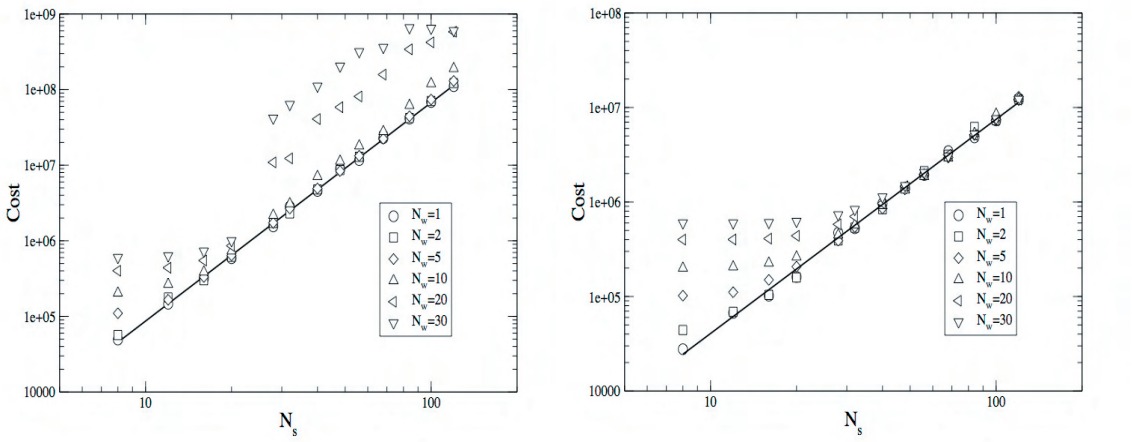

Fig. 1. Mean cost for final estimate of the DOS for the one- (left panel) and two-dimensional (right panel) Ising Models. The solid lines represent a least-squares fit to the data for one walker (Nw =1) and correspond to a cost of S~Ns2.89 and S~Ns2.27 for the one- and two-dimensional model, respectively. In the one-dimensional case with more than 10 walkers, the cost increases compared to one walker.

the dimensionality of the model is larger than one. In the case of the one-dimensional models, we find a significant increase in cost for more than ten random walkers (Fig. 1). Results of this study have been summarized in from of a Technical Report (ORNL/TM-2005/1) (Brown 2004a), and manuscript for submission to a peer-reviewed journal is in preparation. The application of the Wang-Landau algorithm to continuous spin models (such as the Heisenberg model) is in press (Brown 2005).

Benefits

Two major user facilities with significant investments in computational nanoscience, the Nanoscience Theory Institute of the Center for Nanophase Materials Sciences (CNMS-NTI) and the National Leadership Computing Facility (NLCF), are currently under construction at ORNL. Both will rely on software environments that can deliver simulations using the most advanced computational methods for nanoscience, are optimized for high-performance computing platforms, and are accessible to a larger user community. In particular, the plans at the NLCF to build computational end-stations, in which all production computing projects are performed, will require well-managed software repositories. For nanoscience, in particular, which continues to be an emerging field, these repositories will have to be composed of extensible components that can efficiently be recast into new simulation codes as new problems, methods, and algorithms emerge. The tools and expertise we have developed during this LDRD project play a central role in the development of these software repositories.

References

Wang, F., and D. P. Landau, 2001a. "Efficient Multiple-Range Random Walk Algorithm to Calculate the Density of States," *Phys. Rev. Lett.* **86** (10), 2050.

Wang, F., and D. P. Landau, 2001b. "Determining the Density of States for Classical Statistical Models: A Random Walk Algorithm to Produce a Flat Histogram," *Phys. Rev. E* **64**, 056101.

Brown, G., T. C. Schulthess, W. R. Elwasif, and D. E. Bernholdt. 2004. *Multiple Walkers in the Wang-Landau Algorithm*, ORNL/TM-2005/1.

Brown, G., and T. C. Schulthess. 2005. "Wang-Landau Estimation of Magnetic Properties for the Heisenberg Model," *J. of Appl. Physics*, in press.

Distributed Intrusion Detection and Attack Containment for Organizational Cyber Security

S. G. Batsell,[1] N. S. Rao,[2] and M. Shankar[1]
[1]*Computational Sciences and Engineering Division*
[2]*Computer Science and Mathematics Division*

The sheer number and sophistication of cyber attacks are making our nation's critical computer networks increasingly vulnerable. At the same time, these networks are being called upon to play a key role in processing, data storage, monitoring and control of critical infrastructures such as energy, transportation, and finance. Disruption of these networks can have highly damaging affects on our nation. Current cyber security systems are not capable of protecting from all attacks nor providing near real-time response. Host-based intrusion detection systems are not sufficient to protect these networks due to the sheer volume, distributed nature of data, and real-time response requirements. Further they only detect known attacks. We developed an integrated cyber security framework for identifying and containing attacks within an organizational network domain. This framework is distributed, autonomous, and capable of detecting new attacks. It integrates existing cyber security systems and provides a single picture of the entire network, which allows real-time situational awareness of large-scale network systems. It consists of individual components for host-level anomaly detection, attack source localization, and attack containment.

Introduction

Throughout the 1990s, the rise of commercial interest in the Internet has lead to the integration of the information infrastructure as a core component of the United States economy. However, an increasing number of cyber attacks and threats of cyber attacks on our national networks have shown that our energy, transportation, and finance infrastructures are vulnerable with potentially dire consequences. While a significant fraction of these attacks have been ineffective, the cyberspace has become an arena for warfare and acts of terrorism, since it controls various critical infrastructures. Protecting these infrastructures has become a critical and key area of interest for homeland defense.

Current cyber security capabilities have evolved largely as patches and add-ons to the Internet, which was designed on the principles of open communication and implicit mutual trust. It is now recognized that it is no longer sufficient to follow such evolutionary paths and that security must be an integral part of the information infrastructure. Existing intrusion detection systems have evolved as separate ad hoc capabilities and are not sufficient for responding to sophisticated and disguised cyber attacks expected from well-funded terrorist organizations. This created an opportunity to develop a new direction in large-scale and integrated intrusion detection and response systems, which is the main motivation for this project.

Technical Approach

We developed an integrated cyber security framework for identifying and containing cyber attacks at the level of an organizational network domain. This framework consists of three components: intrusion detection, attack source localization, and attack containment. For the first and third components, we utilized the existing methods as well as developed several new components. In particular, we developed novel information fusion methods for host-level anomaly detection and also for network-level diagnosis and attack source identification.

Our integrated framework for intrusion detection and containment provides for scalability by allowing multiple sensor engines to operate in parallel. Single network sensors can only handle small traffic loads and are often limited in their functionality. Only by operating in a distributed fashion can a large-scale approach be successful. This new approach operates in an autonomous manner that allows near-real-time response to events and to ensure that the latest signature updates are available to the sensors as soon as they exist. Current intrusion detection systems are not autonomous and rely on human intervention as a key part of their operation, which makes them orders of magnitude slower than needed. Direct human–in-the-loop operation cannot always effectively counter the newer cyber attacks, particularly at high network speeds. By using an autonomous and distributed framework shown in Fig. 1, the sensor outputs from multiple parts of the administrative network domain can be rapidly correlated.

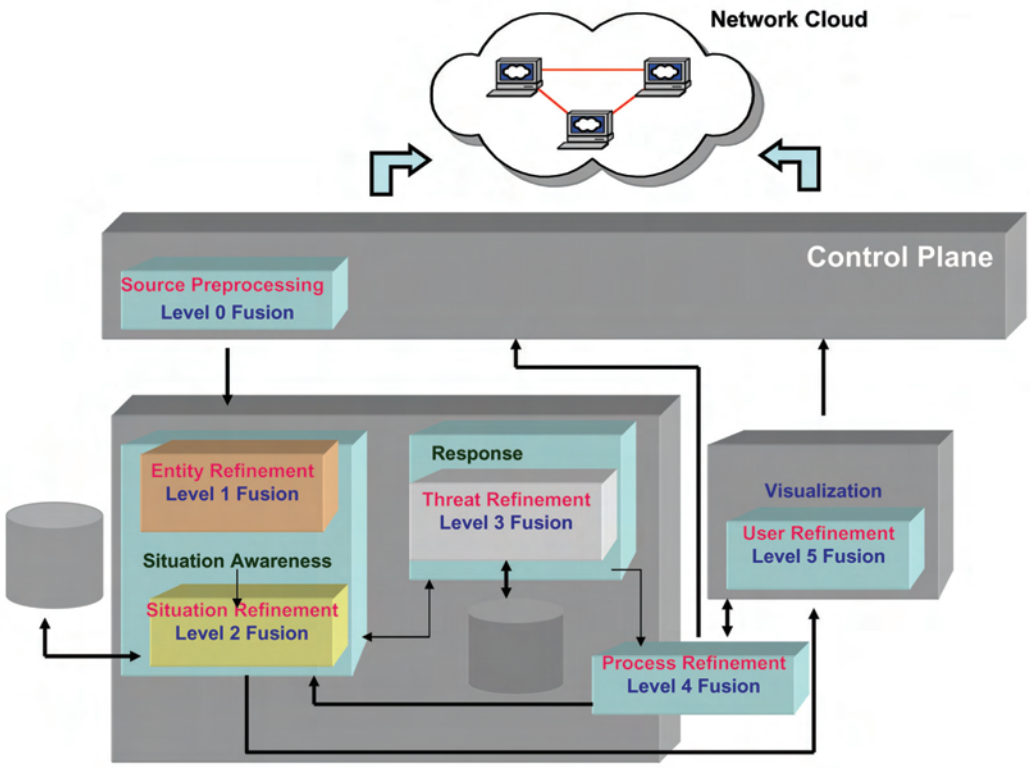

Fig. 1. Distributed framework for integrated cyber security.

Our framework is capable of addressing the routers to set packet filters and the firewalls to block specific ports. Together they form an active response that is activated by the source isolation component. For any suspected attack, its signature is obtained by the detection module together with the physical paths leading to the regions of the attack source. This component activates the filters along the physical paths from the attack source to deny passage rights to the attack packets. Thus the extent of the attack's reach is contained. We investigated two classes of attack containment methods. The first method is suited for attacks that generate low levels of traffic such as unauthorized logins. Here the fusers can readily exchange data with sensors and activate the firewalls closest to the source to filter out the packets from the attack machine. This method, however, does not work in the case of attacks that generate high traffic, such as denial of service attacks. To handle these cases, in this framework the fuser expands the rate controls gradually from the nearby filters to farther ones.

Propagative attacks constitute a growing subclass of cyber intrusions, which rely on steadily compromising hosts and using them as launch pads to attack other hosts. Certain types of worms (e.g., Code Red II) that perpetuate by spreading from host to host belong to this subclass. Coordinated denial-of-service attacks that accumulate zombies into an arsenal of compromised hosts to activate them at a later point, and spam generators that utilize a suite of compromised hosts to send email floods, belong to this subclass. It is important to isolate the origin of attacks, which can potentially distinguish between insider and external attacks. The ability and speed with which such diagnosis can be performed depends on the precise nature of the attack and sensors that detect various attack symptoms. In this paper, we present an abstract framework that utilizes the propagative nature of these attacks to obtain efficient fault source isolation algorithms by utilizing the knowledge (when available) of the sensor activation times and attack propagation times.

The common characteristic of this subclass of cyber attacks of interest to us is that the attack propagates across the network by "infecting" one host or node after another. The other attack characteristics could vary significantly in the type of host compromise, strategy for choosing and attacking hosts, and the generated time and traffic scales. In some worm attacks, the goal is to propagate rapidly, often randomly, in order to infect as many hosts as possible (Weaver et al. 2003; Shankar et al. 2003). This behavior typically results in the classical S-curve of the number of infected hosts: the rate of infection starts slowly during the initial phase, quickly becomes very high as the worm grows in strength, and then tapers off when most of the vulnerable targets are compromised. Zombies that are created for denial-of-service or spam attacks

utilize a more deliberate approach of compromising hosts without generating high traffic levels, and typically spread more slowly. More intelligent worms like Nimda and Code Red II scan the local networks more frequently than they scan remote networks. The lack of knowledge of the enterprise's internal network addresses suggests that such worms would select a strategy of scanning and spreading systematically and not randomly within the enterprise intranet.

We investigated analytical and algorithmic aspects of diagnosing a generic class of propagative attacks that spread across enterprise networks by steadily compromising hosts and then using them to attack other hosts. Certain types of worms, and preparatory phases of coordinated denial-of-service and spam attacks, belong to this class. Symptoms of such attacks are detected at the network sensors by packet signatures and traffic characteristics, and at the hosts by performance degradations and anomalous system behavior. We showed that information about worm propagation times and dynamic sensor activation times can be fused with the network structural information to (a) isolate the regions of network that contain the original attack origin and (b) predict the next set of target hosts. We developed the attack propagation graphs that capture the above three types of information and solved the source isolation and forewarning problems using graph algorithms.

As the attack propagates, its symptoms are detected by the sensors located at the nodes, which could themselves vary in their capabilities and performance. Based on the locations and activation times of the sensors that detect an attack, we showed that source can be isolated within certain regions of the network. We considered two types of sensors deployed to detect the symptoms of cyber attacks, namely, host and network sensors. Host sensors typically detect attacks by utilizing packet signatures, system misbehavior and performance degradations, and anomalous traffic levels to and from the host. Network sensors operate on the traffic streams within the vicinity of routers, switches, and firewalls; they detect attacks by inspecting packet signatures as well as by observing anomaly patterns of individual and aggregate traffic streams. These two types of sensors could provide qualitatively different information, which is typically localized in either case. An enterprise network deploys a combination of host sensors and strategically located network sensors. We developed algorithms to combine the information from various sensors together with the structural connectivity information to isolate the regions that contain the attack origin. In particular, these methods decide if the attack originated outside or within the enterprise; in the former case, firewalls at gateway routers can be activated to drop the attack packets, and in the latter case, appropriate local firewalls can be activated to quarantine the sources. We also developed algorithms to predict the next set of potential target nodes based on the current sensor information so that local firewalls can be activated ahead of time to prevent the further propagation of attack.

The locations of compromised hosts together with the state of sensor activations provide the structural trajectory information about the attack to assist in diagnosis. The sensor activation times together with the estimated attack propagation times provide us the directional information about the attack propagation. We fused the structural and directional information to isolate regions of the network that contain the original attack source. Our methods are effective for attacks that spread deliberately and form the class of topological worms that typically operate in the intranet context as well as for worms that target hosts randomly across the Internet but originate inside the intranet. As is to be expected, the precision of isolation and forewarning depends on: (i) locations of host and network sensors; (ii) network connectivity; and (iii) strategy, propagation times, and sensor activation properties of the attack. In addition, the level of knowledge about each of these items can also have a significant impact both on the algorithms and their precision for isolation and forewarning. We developed propagation graph models that capture the properties (i) and (ii). Using the information about the properties in (iii), we derive a suitable subgraph that will be used both for isolation and forewarning. Such an approach, namely, utilizing a propagative graph for diagnosis, has been used in process plants (Ira et al. 1985), dynamical systems (Rao and Viswanadham 1987), and optical networks (Mas and Thiran 2001). While these systems are quite different from computer networks, they all share certain foundational properties that make it possible to solve origin isolation and forewarning problems. We extended and adapted the methods developed for graph-based systems (Rao 1993a, 1993b) to propagative cyber attacks. These extensions included identifying and defining the relevant properties of computer networks and cyber attacks in the form of a propagation graph and then utilizing the appropriate graph algorithms.

A large number of intrusions such as port scans, login attempts, and buffer overflow attacks can be detected at the hosts by matching the headers and contents of network packets with known signatures. These techniques are fairly mature and are available as freeware, such as snort, and formed some components of our architecture. While these methods detect known attacks, another key issue in intrusion detection today is the ability to detect new attacks. The principal methodology to accomplish this is the identification of anomalies, namely, aberrant deviations from normal behavior, that are hidden within a background of normal activity. Anomaly detection

is crucial against new strategies, for which no known signature exists. We developed a method for detecting the programs running on the hosts with anomalous system calls; in particular, we use histograms of system calls of a program as a signature. A detector is trained on-line on the host using known programs and a small number of attack programs. Such approach has been used previously based on the Basic System Module (BSM) data that contains the system calls made by a program. The methods based on k-nearest neighbor and support vector machines have been used with good success, but both these methods left residual prediction errors.

We developed an information fusion-based approach to train several neural network detectors, wherein these multiple detectors are fused together with a nearest neighbor rule to generate the final answer. Such methods are promising in that they can be shown to perform at least as good as the best among the detectors fused. In fact, a fundamental result in detector theory states that there is no single best detector, but each performs well under different conditions. Our fusion approach achieves the best performance among the available detectors. In practice, however, the fuser has to be appropriately chosen to achieve such performance. We previously developed the nearest neighbor projective fusers that have been shown to outperform the individual detector. For the anomaly detection component of our system, we developed a user configuration on BSM data, which performed better than the earlier methods on DARPA benchmark testset. This configuration employed a linear fuser to first combine 10 sigmoid neural networks and a nearest neighbor rule. Then a meta-fuser based on nearest neighbor projective fusion method (Rao 2002) is deployed to combine the original detectors and the linear fuser. The resultant fused detector can be analytically shown to perform at least as well as the best combination of the detectors. This system achieved zero error on the DARPA benchmark dataset, which is the best performance for this dataset.

Results and Discussion

We developed a distributed and autonomous framework capable of quickly detecting existing and new attacks. It consists of individual components for network and host-level intrusion detection, attack source localization, and attack containment. The detection component is a combination of network and host-based sensors that utilize the sensor data together with the network information to identify the attacks. We developed information fusion method for detecting the host programs with anomalous system calls. We are the first to develop attack source isolation methods for propagative network attacks. The source localization component is activated by a suspected attack and locates the attack source(s) by tracing or reconstructing the physical paths of attack packets. The attack containment component utilizes firewalls and packet filters on various host and network locations to regulate or contain the packet flow from the attack source within the organizational network domain. An implementation of these containment modules will be pursued as a follow-on activity to this LDRD project. These modules together with the ones developed under this project will constitute a comprehensive cyber framework for organization-level security.

Benefits

This integrated framework and the specific unique components developed under this LDRD have significant benefits for any government agency that requires a real-time situational awareness of their network assets. This would include Department of Energy, Department of Defense, Department of Homeland Security, and Department of State. It allows near-real-time detection and response to cyber attack. It further provides an integration platform for cyber defense components to form a single system.

References

Ira, M., K. Aoki, E. Oshima, and H. Matsuyama. 1985. "An algorithm for diagnosis of system failures in the chemical processes," *Comp. Chem. Eng.* **3**, 489–493.

Mas, C., and P. Thiran. 2000. "An efficient algorithm for locating soft and hard failures in WDM networks," *IEEE Journal on Selected Areas in Communications* **18**(10), 1900–1911.

Rao, N. S. V. 1993a. "Computational complexity issues in operative diagnosis of graph-based systems," *IEEE Transactions on Computers* **42**(4), 447–457.

Rao, N. S. V. 1993b. "Expected-value analysis of two single fault diagnosis algorithms," *IEEE Transactions on Computers* **42**(3), 272–280.

Rao, N. S. V. 2002. "Nearest neighbor projective fuser for function estimation," *Proc. Int. Conf. Information Fusion*.

Rao, N. S. V., and N. Viswanadham. 1987. "Fault diagnosis in dynamical systems: A graph theoretic approach," *Int. J. of Syst. Sci.* **18**(4), 687–695.

Shankar, M., N. S. V. Rao, and S. Batsell. 2003. "Fusing intrusion data for detection and containment," Proc. MILCOM.

Weaver N., V. Paxson, S. Staniford, and R. Cunningham. 2003. "A taxonomy of computer worms," WORM.

Image to Intelligence Archive: Intelligent Agent–Based, Large-Scale, Spatial Data Management and Analyses

T. E. Potok,[1] B. L. Bhaduri,[1] K. W. Tobin,[2] P. J. Palathingal,[1] E. A. Bright,[1] P. R. Coleman,[1] S. S. Gleason,[2] T. P. Karnowski,[2] and J. R. Price[2]
[1]*Computational Sciences and Engineering Division*
[2]*Engineering Science and Technology Division*

Scientists and intelligence analysts are interested in quickly discovering new information from the vast amount of available earth observation imagery data. The key issues that arise in this pursuit are first how to manage the vast amount of increasing data, and secondly, how to automate the manual processes that are currently needed to produce and search this type of information. This project demonstrates a solution to these two issues through a novel agent architecture that combines innovative approaches from three distinct research areas: software agents, geospatial data modeling, and content-based image retrieval (CBIR). This system uses intelligent agents to autonomously search for images over the Internet and other physically distributed data sources, analyze the images to develop corresponding description vectors used in searching and retrieval, and finally, process this data using spatial segmentation, feature extraction, and image indexing tools. Results show that this system is capable of significantly reducing the time to find images of interest and the management effort associated with retrieving and updating large amounts of image data. We believe that this system holds tremendous promise in automated imagery analyses and change detection.

Introduction

Enormous volumes of geographical data are analyzed to create scientific, military, and intelligence information. This image information is critical for scientific and national security purposes. There are two significant challenges in analyzing this type of image information. The first is managing the steadily increasing amount of available data. For example, the United States Geological Survey (USGS) has been archiving this type of data and faces exponential near- and long-term growth in digital data. Analysts must manually update this archive with new and better imagery. The second challenge is automating the manual steps that are currently used to create, organize, and search this type of information. Within an image archive, each image must be normalized so that they can be readily merged, compared, indexed for search, stored, and then analyzed depending on the information need.

To address these two issues, we proposed (1) to automatically create and continuously update a geospatial image archive and (2) to automatically georectify, index, and provide rapid search capability over this image archive. Intelligent agent systems have shown in the past to be able to retrieve and manage images in different applications (Christopher 1995; Nolan 2000; Lehmann 2000). We demonstrated an innovative intelligent agent–based system that can autonomously search through distributed image data sources to create and continually update an image archive with new and updated information. These agents also analyze the images using spatial segmentation, feature extraction, image indexing algorithms. The resulting system allows an imagery analyst to quickly search for images based on location, time, and the closeness of images to selected regions and image features. This provides the capability to perform change detection, damage assessment, automatic target recognition, and a wide variety of intelligence, security, and monitoring capabilities.

Technical Approach

The system is comprised of the three main components: software agent technology, geoconformance modeling, and image description and indexing (Fig. 1). The intelligent agent component is responsible for retrieving, storing, and analyzing spatial data from an image. In this system, the software agents search for images on the Internet and store these images and the corresponding metadata about the images. The metadata is information about the image which has been normalizing to work with many different image formats. The agents also create statistical region and feature vectors from the images that are later used for image analysis and retrieval. The vectors are generated from exemplars which represent various geographic regions such as mountainous, agricultural, industrial, highways, power lines, and urban structures. These vectors represent the separation of an image into an indeterminate number of regions using a segmentation procedure that leverages self-similarity of image content. These regions are then described using pixel-based, statistical features. The features vectors separately describe spectral, textural, and structural content within the imagery and provide

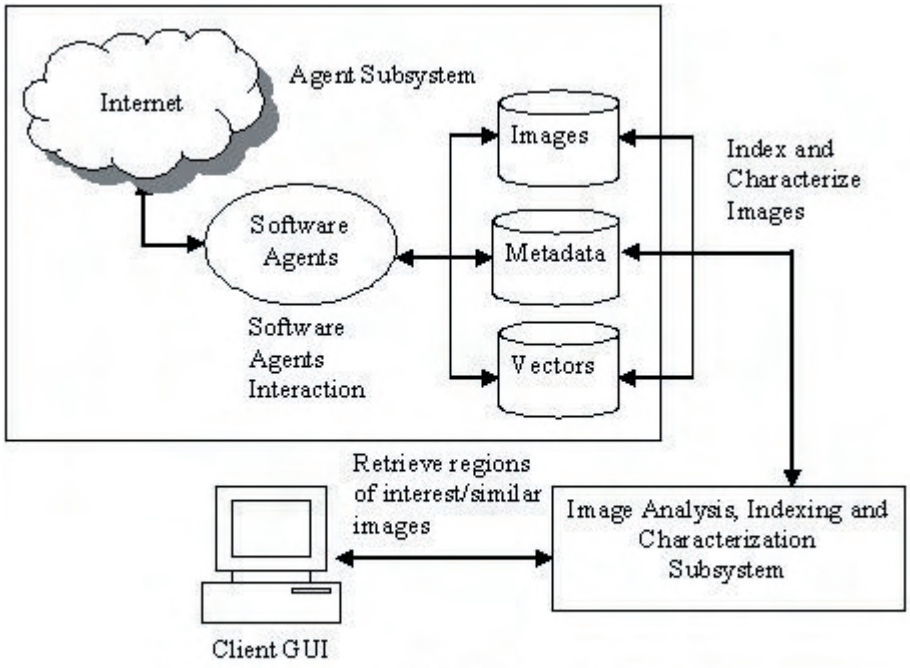

Fig. 1. High-Level Architecture Overview.

independent indexing categories. These vectors are stored in the metadata archive that uses the Directed Indexing Library (DIL) which contain exemplars of different spatial regions that are of interest to the end-user. Finally, a GIS interface is used with DIL to allow a user to find imagery of interest.

Intelligent Agent Subsystem

The intelligent agent system is responsible for gathering, processing, and analyzing information. In our implementation we used the ORMAC (Oak Ridge Mobile Agent Community) framework. This framework has been under development over the course of several agent-based research projects (Potok 2003). ORMAC is a generic agent framework providing transparent agent communication and mobility across any Internet-connected host. There are four main types of agents: (1) a Crawler agent, (2) a Download agent, (3) a Markup agent, and (4) an Extractor agent. The Crawler agents traverse the Internet looking at URL's ending with .edu, .gov and .net. The agents perform a depth-first search looking for images; when an image is found, the link is stored for later download.

The next type of agent is the Download agent. This agent downloads images for all the image links generated by the Crawler agent. This agent coordinates with the image repository to ensure that the image is not already available. If the image is already present in the repository, then the agent checks to see if the image is newer or of a higher resolution than what is already present. This provides automatic update management of the image repository.

The Markup agent creates Extensible Markup Language (XML) files for the downloaded images. These files contain image properties such as height, width, bit planes, etc. In addition, this agent extracts geospatial information such as the images bounding box coordinates from the image. After collecting this information, it builds an XML tagged file for each image in the image repository using all of the above-deduced properties. These XML files are stored in a separate XML Repository.

The final step is for an Extractor agent to create region and feature vectors for each image. The agents monitor the XML repository for newly created files. As new XML files become available, it then begins processing the corresponding image from the image repository. The image is first segmented into 64 × 64 blocks region segments; then a vector file describing each region segment is created by making use of the image properties in the XML file. The vector files generated are stored in the Vectors repository. This process has been demonstrated with agents running in parallel on several machines.

Geospatial Modeling Subsystem

Geographic Information System (GIS) has become the dominant platform that builds, stores, manages, and models massive volumes of spatial data supporting critical decision support systems and logistic applications. However, even in a GIS, developing, updating, and refining data can be a complex and extremely time- and resource-consuming task, given the quantity, as well as quality (resolution), of geographic data is not only increasing exponentially but also is being housed in a

distributed manner (often over the Internet). Most data and models available on the Internet, however, are stored in multiple formats, cover varying spatial extents, and are distributed on widely scattered server sites. This requires each user to search for appropriate data and models and to reformat necessary data before it can be integrated with the models.

A geospatial modeling framework was established to design the Crawler, Download, and Markup software agents. These agents were designed with the specific goal of establishing geoconformity across the image data archive. In general, image data sets for any geographic region are produced and distributed not only in different formats but also in disparate geographic projections and measurement units. Consequently analyses and comparison of multiple data sets become a challenging task for the analyst. The crawler agents were designed to search and identify typical formats of satellite or airborne imagery and their associated geospatial metadata files. Download agents were designed to represent the bounding coordinates of images to a common geographic reference system (Decimal Degrees or Geographic Coordinate System in this project). This was achieved with predefined or user-specified projection and unit specifications based on spatial scale (global, continental, country, or state) and geographic orientation (east-west, north-south, or oblique). Automation of the "information extraction" of spatial data resolution (both in terms of space and time), collecting platform or sensor, and geographic projection systems from common metadata (world files or code embedded in image header) was also incorporated in the download agent structure.

One other focus of the geospatial analysis and modeling was on utilizing traditional remote sensing principles in identifying and defining infrastructural features from earth observation imagery data and creating a logical hierarchy of these features with their associated spatial scales. This was an important first step in developing the scale-dependent training exemplars that were subsequently characterized and indexed in the information archive.

Image Description and Indexing Subsystem

The purpose of the image description and indexing subsystem is to segment, statistically describe, and index large-format image data so that it can subsequently be extracted from the system in response to a user-based query. The numerical feature description and indexing method must also be compatible with and supportive of the agent architecture for locating and providing new data inputs and with the storage and retrieval of associated metadata.

The process begins with using the segments generated by the software agents. Two segmentation methods were investigated over the course the program. The most basic segmentation approach parcelates a large-format image into a regular array of similarly sized regions. The area of these regions is of the order of the size of independent structures at a scale of interest, for example, on the order of the size of farmland fields or urban regions in 30 m data or on the scale of buildings or other man-made structures in 1-m data. The second approach accomplished segmentation using a fractal image description method that identifies region similarity within the image based on the training exemplars maintained in the DIL. In the terminology of fractal description, the original image contains range data, whereas the DIL contains domain imagery (Gleason 2002). The goal is to segment an incoming image into an ensemble of independent, non-overlapping, and non-regular regions that are represented in the DIL, for example, an agricultural region versus an urban region.

After segmentation, each region is independently described by an encoding of the boundary coordinates of the region and by a sequence of features organized into several descriptive groups. In general, these descriptors include spectral features, texture features, and structure features. In this context, the DIL is not only used to define a set of exemplar images for use in segmentation, but the features extracted from these exemplars are also used to provide a feature mapping from a potentially high-dimension feature space to a low-dimension feature space. The goal of indexing is to organize the image features in the database such that a ranked list of approximate nearest neighbors (ANN) can be retrieved without performing an exhaustive comparison with all the records in the database. For our CBIR implementation, this is achieved by generating a binary decision tree of the image features (Tobin 2002). Currently, a total of 332 total features are initially computed: 192 related to color (or intensity) derived from RGB and HSV color-spaces, 108 texture features from local binary patterns and local edge patterns, and 32 features related to structure derived from the distribution of edge orientation directions in an image region. We apply dimensionality reduction techniques to compute a small subset of 8 features comprising linear combinations of the original 332 features—for database search and retrieval.

The number of computed features (332) is excessive for performing fast and efficient database retrievals. Furthermore, it is likely that at least some of these features are redundant, noisy, and/or not useful for retrieval. For this reason, we implement dimensionality reduction by first applying principal component analysis (PCA). We keep only the number of principal components (i.e., linear combinations of original features) necessary to retain 95% of the total energy in the feature vectors. Following PCA, we apply *k*-means clustering to the PCA-reduced

features to group images into 16 clusters, where each cluster corresponds, roughly, to images with similar content. Given these cluster assignments, we next perform weighted linear discriminant analysis on the PCA-reduced features to attain a final dimensionality of only 8 features. These 8 features, comprising linear combinations of the original 332 features, are then used for database search and retrieval.

Results and Discussion

A prototype using software agents, geospatial modeling, and image analysis software was built to demonstrate the ability to manage large volumes of image data and to automate key portions of the image analysis process. We evaluated the system against a set of ortho images from the Oak Ridge Reservation (ORR) area. To demonstrate the ability of the agents to be able to look for newer and better images, a Web server hosting the ORR images was set up on a local machine.

We successfully demonstrated our system on images using 8 bit images from September of 1993. The agent subsystem required approximately 4 hours to download, markup, segment, and then generate feature vectors for 65 images. Next some of the images were replaced by 12 bit images from the same region. The agent subsystem successfully determined that certain images on the Web server were of a higher resolution (12 bit is of a higher resolution than 8 bit). Next some of the images on the Web server were replaced by images for the same region from January of 2004. Again the agent subsystem was successful in determining that certain images on the Web server were newer than what was in the repository. These images were then downloaded, marked up, and segmented, and vectors were generated from these new images. The DIL for this demonstration system was generated by performing principal component analysis (PCA) on the original descriptive feature set. The resulting set of features was clustered using a *k*-means method to locate 16 clusters in the data. Finally, linear discriminant analysis (LDA) was applied to the PCA features using the *k*-means clusters as the DIL training set and a feature set of length 8 was selected to index the image repository for search and retrieval. Effective image retrievals were accomplished on urban, industrial, agricultural, forested, and a variety of other regions demonstrating the potential for streamlining the reduction of data in a large image repository.

In summary, we were able to generate fast and accurate answers to image queries. While comparing this to traditional image retrieval and management systems, the agent approach brings out clear advantages that are easily discernable. The intelligent agent approach provides an automated management and update of the image repository. It also automates the process of normalizing, indexing, and comparing images, providing fast and comprehensive search capabilities that are not currently available.

Benefits

This system demonstrates a capability that currently does not exist in managing and searching large volumes of geospatial image data. This capability can be rapidly applied to help in applications that require immediate and comprehensive searching over an up-to-date and accurate image repository, such as the U.S. Army, the National Geospatial-Intelligence Agency (NGA), or the U.S. Air Force.

References

Christopher, T., and M. William. 1995. "Satellite Image Dissemination via Software Agents," pp. 44–51 in *IEEE Intelligent Systems*.

Nolan, J. J., A. Sood, and R. Simon. 2000. "An Agent-based Architecture for Distributed Imagery & Geospatial Computing," p. 252 in *29th Applied Imagery Pattern Recognition Workshop*.

Lehmann, T. M., B. Wein, J. Dahmen, J. Bredno, F. Vogelsang, and M. Kohnen. 2000. "Content-Based Image Retrieval in Medical Applications: A Novel Multi-Step Approach," pp. 312–320 in Proceedings SPIE 3972.

Potok, T., M. Elmore, J. Reed, and F. T. Sheldon. 2003. "VIPAR: Advanced Information Agents Discovering Knowledge in an Open and Changing Environment", pp. 28–33 in *Proc. 7th World Multiconference on Systemics, Cybernetics and Informatics Special Session on Agent-Based Computing*, Orlando, Fla.

Gleason, S., R. Ferrell, T. Karnowski, and K. Tobin. March 2002. "Detection of semiconductor defects using a novel fractal encoding algorithm," *Design, Process Integration, and Diagnostics in IC Manufacturing,* Proceedings of the SPIE, Vol. 4692.

Tobin, K. W., T. P. Karnowski, L. F. Arrowood, R. K. Ferrell, J. S. Goddard, and F. Lakhani. 2002. "Content-based Image Retrieval for Semiconductor Process Characterization," *EURASIP Journal on Applied Signal Processing*, Special Issue on Applied Visual Inspection Vol. 2002, No. 7.

Cross-Cutting Data and Tools Infrastructure for Genomes to Life Facilities

G. A. Geist,[1] E. C. Uberbacher,[2] N. F. Samatova,[1] and P. F. LoCascio[2]
[1]*Computer Science and Mathematics Division*
[2]*Life Sciences Division*

This project has developed technology for the cross-cutting data infrastructure needs of the proposed Genomes to Life (GTL) facilities. The DOE Genomics: GTL roadmap seeks to establish four GTL facilities over the next decade. Genome-scale collection, analysis, dissemination, and modeling of the vast amounts of data produced by the GTL facilities are the key to success of GTL. Integration and coordination of these activities across the facilities will be extremely critical to ensure high-throughput knowledge synthesis, engage the broader biology community, and to eventually bring genomes to life. The work was divided into two efforts.The first effort created a GTL data integration infrastructure that unified 23 diverse biological databases into a form suitable for study and use across the Genomes to Life community. The second effort developed and deployed a prototype genome and proteome data analysis infrastructure across Oak Ridge National Laboratory, Argonne National Laboratory, and Pacific Northwest National Laboratory using grid standards to make the data available to the biological community.

Introduction

High-throughput GTL facilities, combined with ORNL's leadership-class computing facility, will make it possible to address the ultimate goal of modern biology: to achieve a fundamental, comprehensive, and systematic understanding of life. With this promise, however, comes a problem—the massive quantities and increased complexity of biological data produced by experiments and computations. The GTL facilities plan and GTL workshop reports place considerable emphasis on developing methods for a large community of biologists to analyze petascale biological data sets and develop models and simulations related to complex biological phenomena. The goal of this project is to develop and demonstrate feasibility for a key set of technologies needed to facilitate large-scale analysis and data operations across the GTL facilities in preparation for later data production. These include the development of a shared data infrastructure, data models and schemas, data standards and ontologies, and the development of a prototype shared analysis tools infrastructure and user environments that leverage large-scale distributed data and computing resources. These developments were carried out in collaboration with key partners, Argonne National Laboratory (ANL), Pacific Northwest National Laboratory (PNNL), and Lawrence Berkeley National Laboratory (LBL), who are involved in both GTL facilities planning as well as the recently awarded National Leadership-Class Computing Facility (NLCF). With their help, this research could become an integrating force among the future GTL facilities. Moreover, the software produced and the integration techniques will provide many benefits for the general biology community and form a prototype for an NLCF computational end station in biology.

Technical Approach and Results

Data Integration Infrastructure

It is increasingly evident that a paradigm shift is needed in the development of a data infrastructure, away from dispersed "data collecting" repositories towards a conceptually integrated "knowledge enabling" repository. This project has helped lay the technological groundwork for a distributed but integrated suite of facilities databases, through the cooperative development of data models and database schema prototypes. It identified shared or common data elements, objects, concepts and identifiers that can lead to metadata types that are sharable across the GTL facilities. In this way at the highest level the independent systems can evolve to meet the local conditions of domain experts effectively, while being able to share a common intellectual layer of process and information. In collaboration with the ANL and PNNL sites, this will permit the unique knowledge acquired at each facility to be used across the DOE complex and eventually permit users to mine data from the combined sites. This effort involved regular discussions between the GTL facilities researchers at ORNL, PNNL, ANL, and LBL to define extensible XML-based standards for data models and schemas that meet the needs of the planned GTL facilities and resulted in the following GTL Technical Report: *Compilation and Review of Data Standards and Application to the Genomes to Life Program* by Arkin, Geist, Samatova et al., http://www.genomes2life.org/publications/DataStandards.pdf

We also developed the technology needed to construct an integrated data infrastructure that allows advanced search and queries across a large, diverse set of data sources, including sequence databases (COG,

INTERPRO, SWIS PROT, TIGR, JGI, PFAM, PRODOM, SMART), structure databases (PDB, COILS, SOSUI, PROSPECT), pathway databases (KEGG), protein interaction databases (BIND, DIP, MIPS), and databases of raw mass spec and microarray data. The query language and integrated schema technology that was developed is being leveraged by the Sandia/ORNL GTL project to create a *Synechococcus* encyclopedia containing all the database knowledge in the world about this microbe. This knowledgebase involves the integration of 23 different databases and illustrates the power of this project's technology.

Large-scale Data Analysis and Modeling

Each of the GTL facilities will have a large local infrastructure involved in the manipulation and analysis of experimental data. In concert with the data infrastructure above, a common infrastructure for computational biology analysis services will be a key feature of the GTL facilities complex. We designed an environment based on Web services and grid standards to allow an "opt-in" schema for domain experts from each of the facilities, to be able to have their curated analysis services available transparently to each of the other facilities. In this way each of the GTL facilities will have effectively the entire complement of GTL analysis resources available, for inclusion in internal research processes, thus accelerating the research cycle by importing expert analysis capabilities. The BioGrid we have begun to put into place also has the potential to easily integrate unique leadership-class resources at the NLCF into the scientific environments of biological investigators.

The project developed and deployed a large-scale analysis and modeling environment at our NLCF partner sites, ANL and PNNL (Fig. 1). The environment is based on the Genomic Integrated Supercomputing Toolkit. To encourage adoption by our GTL partners, and potentially the future GTL facilities complex, the environment permits users to customize a tools palette specific for their own use or for a scientific group. The environment also transparently couples each type of biological tool with the computational resource it is tuned for, such as the Cray at the NLCF, the 949 processor Itanium cluster at PNNL, the Pentium clusters at ANL, and the IBM Power 4 at ORNL. A critical part of our success has been allowing partner tools and supercomputing resources into the cross-site analysis environment.

In addition to deploying the BioGrid across ORNL, PNNL, and ANL, we distributed data to this analysis environment as well.

The initial deployment is testing the ability to utilize the local access and scheduling policies to provide the

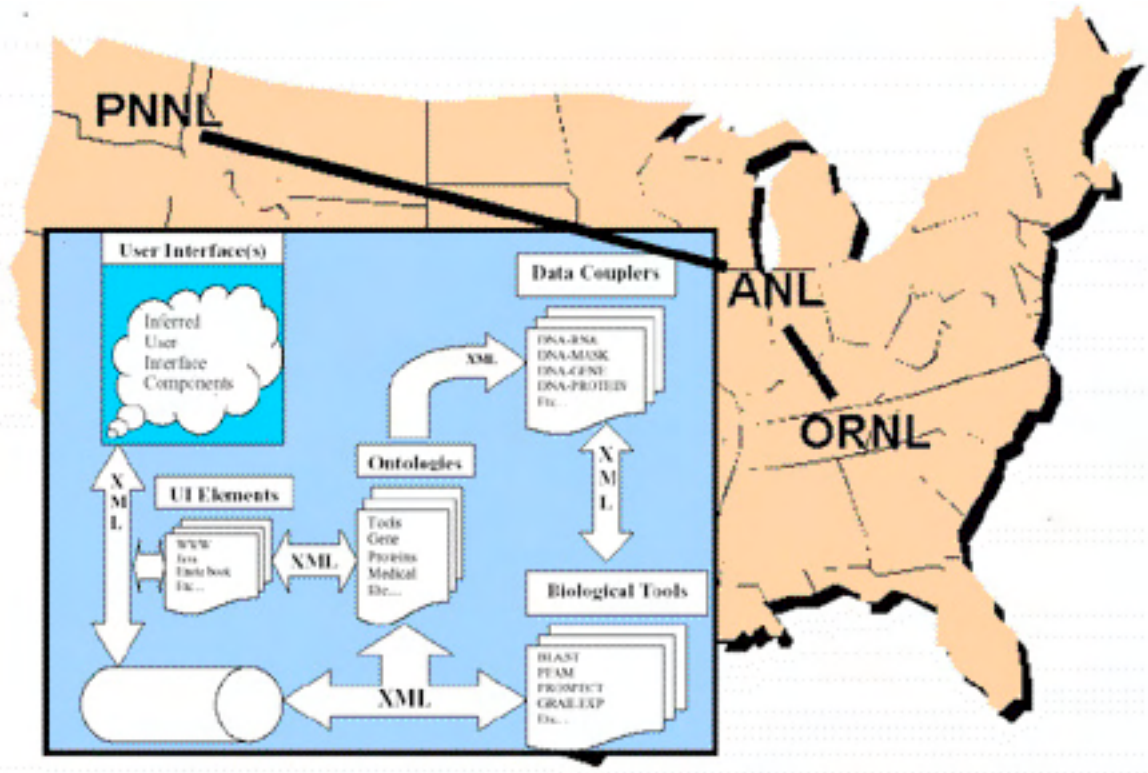

Fig. 1. A common grid-based infrastructure for computational biology analysis has been deployed between key Genomes to Life partners.

basis of an opt-in cooperative framework for large-scale data analysis. An unexpected challenge during the year was the enhanced security requirements enacted across the DOE complex. For example, this involved the use of "SecureID" one-time token passkeys to authenticate users at PNNL. This will become more of an issue in the future with other DOE sites, including ORNL considering SecureID.

Benefits

The DOE OBER facilities plan relies on developing methods for a large community of biologists to analyze the petascale data sets generated by the four GTL facilities. This will require a centralized approach to coordination and planning for data management and support of distributed analysis on supercomputers, clusters, and grid systems. This project has developed prototype technology for advanced queries across diverse biological databases; it has demonstrated large-scale analysis and data operations across the multiple sites that span the nation. These capabilities will be critical when the GTL facilities come on line, but even before then the technologies developed in this project are starting to be used by computational biologist across the nation on projects ranging from Homeland Security to NIH ontology studies.

Comprehensive Fusion Simulation: Component-Based Software Engineering and Evolutionary Time Advancement

L. A. Berry,[1] D. B. Batchelor,[1] D. E. Bernholdt,[2] E. E. D'Azevedo,[2] W. R. Elwasif,[2] W. A. Houlberg,[1] E. F. Jaeger,[1] A. K. Khamayseh,[2] J. A. Kohl,[2] and S. Li[3]

[1]*Fusion Energy Division*
[2]*Computer Science and Mathematics Division*
[3]*Texas A&M, Kinsgsville*

Advances in the simulation of individual fusion physics issues and increases in computer capability have enabled initiating work on integrated simulation [the Fusion Simulation Project (FSP)] of all relevant physics and time and length scales for magnetically confined plasmas. Even so, significant advances in plasma physics, applied mathematics, and computer science will be required to reach the goal of predictive simulation. This project addresses the need for a component-based simulation architecture by using the Common Component Architecture (CCA) and for improved algorithms for radio frequency wave plasma interactions for an integrated simulation of plasma heating and transport.

This project addresses the needs for advances in computer science, applied math, and physics posed by the FSP by developing a time-dependent fusion plasma simulation using component-based software engineering. The simulation will use radio frequency (RF) power for plasma heating and control. High-resolution calculations are needed for this application. The AORSA2D code is capable of such calculations but is presently too slow to allow the ~100s of runs needed for time-dependent input. Thus a more efficient solution must be developed.

The Common Component Architecture (CCA), under development in a DOE/OSCAR SciDAC project, achieves language interoperability in a high-performance, component-based framework. The CCA provides language-independent design as the basis for "componentization" in the module's native language.

AORSA requires the solution to 100,000s of linear equations. Efficient techniques for solving such systems are usually based on iterative techniques, but previous attempts with iteration have not been successful. The simplified physics model used as a "guess" for starting the iteration was too far removed from the desired solution. However, for time-dependent simulations, information from one time step can be used as an improved guess for subsequent solution: thus, the description evolutionary time advancement.

The simulation was designed and implemented with the CCA tools and then tested for functionality and communications. The simulation has four component levels: a driver (Python) for controlling the time flow; physics components (Fortran); coordinate transformations between the incongruent grids of the physics models (Fortran); and a plasma state (C++) for storing results. An effective iterative algorithm based on Krylov techniques was developed for AORSA. If an "exact" solution was used as the initial guess, then convergence was very good for ~ –50% to +100% variations in plasma parameters. This is the same range as found for typical simulations. Thus for the several hundred time steps of a typical simulation, only a few exact solutions will be required with information for the remaining time steps coming from the more efficient iterative solution.

Our experience in using CCA is providing feedback to developers on how to make it a more effective tool for fusion simulation. It is also providing valuable guidance on how to address the computer science issues of the first phase of the FSP. This phase will prototype techniques for implementing the complete set of physics models by integrating a subset that can provide valuable near-term physics. The ability to use AORSA in a time-dependent simulation will allow increased understanding of how to use RF power to heat and control fusion plasmas. Analysis of the ITER (the proposed international burning plasma facility) heating system is one example. The techniques developed for more efficient AORSA solutions are likely applicable to other RF codes, thus enabling additional physics progress.

Bringing Statistical Visualization to the Terascale and Beyond: Visual Analysis in Full Context

G. Ostrouchov,[1] D. B. Batchelor,[2] A. Mezzacappa,[3] and A. Buddana[4]
[1]*Computer Science and Mathematics Division*
[2]*Fusion Energy Division*
[3]*Physics Division*
[4]*University of Tennessee*

While simulation science will routinely produce terascale and petascale data sets, browsing only one percent of one petabyte at ten megabytes per second takes 35 8-hour days! To avoid human bandwidth overload, visualization must be assisted by analysis that selects views of interest and provides the global context for the views. This project concerns bridging scientific visualization (in fusion and astrophysics) and statistical visualization of high-dimensional data. Our progress includes the development of feature sets for qualitative description of volumetric data common in fusion and astrophysics simulation via Morse theory and contour tree computation as well as fast and robust dimension reduction that outperforms principal component analysis. Current activity continues with coupling GGobi, a high-dimensional statistical feature visualization tool, with feature extraction, clustering, and visualization server.

The main objective of this project is to develop statistical analysis and visualization tools to assist scientific visualization of massive data sets in fusion and astrophysics simulation. Our approach has these characteristics: (1) any view of a segment from a massive simulation data set includes a variation context of the full simulation; (2) this context is a reduction of the entire simulation into a feature space that is interpretable with respect to the application; (3) the feature space is obtained in one pass through the data; (4) the feature space is explored with statistics to provide guidance of what is interesting, what is redundant, and how can it be classified; (5) a mapping of the feature space back to the data segments is available to provide fast access to key segments of a massive simulation data set.

Our progress is evident on four fronts: (1) Fusion simulation and astrophysics simulation specific visualization—this involves bridging knowledge between simulation science visualization and statistical visualization and consideration of specific fusion and astrophysics simulation data products. (2) Fast dimension reduction methods for feature extraction from data segments and clustering workload reduction. Here we developed a fast and robust dimension reduction algorithm that outperforms principal component analysis in a heterogeneous data setting. (3) Clustering methodologies for grouping data segments enabling multiscale selection of representative views and identification of rare or extreme events. We have developed flexible clustering methods for massive data sets based on sub-sampling and classification. (4) We leverage infrastructure parallelization of the R statistical computing environment and ASPECT data software for data movement and scientific visualization.

Since most of the data we are considering are volumetric fields, we found that surface coding with Morse theory and Betti numbers provides a qualitative description the topological features of the data, such as maxima, minima, saddle points, voids, and tunnels. A structure known as the contour tree encodes these features for a field of arbitrary dimensionality and provides qualitative information about its topology. Recent results for fast computation of a contour tree make their use possible for moderately sized data sets. Although these fast algorithms were developed for isosurface visualization, they are ideal for our use of coding data topology into high-dimensional feature sets that can be clustered and explored with statistical methods. We use GGobi as an exploration tool for the high-dimensional feature data sets as it provides powerful and interactive projection and brushing methods. It is an open source tool that can be embedded in the open source R data analysis system.

DOE is the premier agency for simulation science research in its energy-related missions, where visualization of the resulting data from such simulations drives scientific discovery and progress. Analysis-driven visualization is critical for exploration of massive data sets whose size prevents effective browsing with scientific visualization alone. The enabling methodology developed under this project has very broad applicability to domains other than fusion science and astrophysics considered here and will benefit research in other domains across most federal agencies. Although one must consider application goals and specifics in each domain, the enabling visual analysis methodology developed under this project can be a major component of any strategy for exploration of massive data sets.

Nanochemistry: The Bridge from Materials to Biological Sciences

B. G. Sumpter, D. W. Noid, R. Harrison, B. C. Hathorn, W. A. Shelton, V. Meunier, and R. Toedte
Computer Science and Mathematics Division

Chemistry at the nanoscale involves the unique properties associated with assemblies of atoms or molecules on a scale between that of the individual building blocks and the bulk material. At this level, quantum effects are usually significant, and innovative ways of carrying out chemical reactions become possible. We propose the development of a computational chemistry effort to examine the dynamics, chemistry, and chemical physics of molecules confined at the nanoscale level. This project will provide new fundamental insight into chemistry and chemical physics of nano-confined systems that could lead to the development of new materials, advances in biotechnology, and modern computational tools bridging chemical, materials, and biological sciences.

ORNL is uniquely positioned to play a key role in making breakthrough advances in nano and biotechnology R&D by integrating advanced computing with physical, chemical, materials, and biological sciences. It is critical that the recent and forthcoming dramatic boosts in supercomputing power be matched by corresponding increases in the capabilities of scientific modeling and simulation codes. We are well positioned to address the rigorous multidisciplinary effort of designing, building, tuning, integrating, and using computer codes to accelerate the solution of emerging or existing complex scientific problems. This LDRD leverages this situation toward developing major breakthroughs in applying and developing computer simulation and modeling methods for examining the complex and unknown chemistry and chemical physics of molecules confined at the nanoscale. The subject proposal, by its very nature of examining the forces of molecular recognition that are critical to self-organization processes as well protein structure, DNA, host-guest complexes, and crystal packing, addresses multiple ORNL thrust areas: advanced materials, biological, chemical, terascale computing, and nanoscale sciences.

We propose the development of a computational chemistry effort to examine the dynamics, chemistry and chemical physics of molecules confined at the nanoscale level, such as inside carbon nanotubes, ordered nano-pores, or nano-particles. By addressing these fundamentally important processes enormous benefits in terms of development of new methods for producing desired materials products and the production/optimization of novel computer simulation and modeling tools are expected.

The proposed/ongoing project has/will stimulate not only novel scientific discoveries but also breakthroughs in modern simulation codes for examining dynamics and chemistry of materials at the nanoscale. The computers in the National Leadership Computing Facility are crucially important for enabling realistic simulation of many physical processes that, for example, require long-time simulations using either classical or ab initio dynamics. In order to develop an understanding of how nano-confinement affects chemistry and chemical physics, we will/have examine several different nano-confined environments: (1) simple carbon nanotubes; (2) carbon nanotube reaction chambers; (3) nano-holes/pores in the surfaces of various materials; and (4) nano-particles. Chemical reaction dynamics and energetics (barrier heights and reaction pathways) of relatively simple molecular species, such as bond dissociation and/or isomerization of small alkanes and phenyl compounds, will be examined in these environments. Comparisons to the analog reactions in the gas or solution phase without nano-confinement can be made to elucidate experimentally observable effects.

We have successfully shown how the transition state of a chemical reaction can be strongly altered by confinement in a carbon nanotube. Two processes were studied: (1) thermal pyrolysis of hydroxy-substituted para-phenylethyl ether, a model of lignin pyrolysis that is important in optimization of renewable resources conversion into higher value products and (2) internal isomerization of hydrogen peroxide. One paper is in preparation and to be submitted to the JACS, and one invited talk was given at the 2004 SETCA meeting. In addition to these accomplishments, we have been able to perform large-scale ab initio quantum calculations for the effects of encapsulating different organic molecules inside carbon nanotubes. These results show, for the first time, clear capability for using organic molecules to achieve n- and p-type doping and complement some very recent experimental measurements. We have also obtained extensive results on how confinement of molecules to nano-sized particles influence the geometric and electronic structure and subsequent excited state properties. One paper has been published, *Macromolecules* (2004), one

paper has been submitted to JACS, and several others are in preparation.

This project is relevant to DOE's programs in basic energy sciences, advanced computing, biology, materials and chemical sciences, and energy resources. It addresses fundamental processes that must be understood in order to bridge materials, chemical, and biological sciences. Chemical physics at the nanoscale is crucial to numerous processes involved in energy production and storage, materials properties, environmental toxicity/fate, catalysis, and chem-bio sensors.

Exploratory Computational Biology for Genomes to Life Facility III

E. Uberbacher,[1] F. Larimer,[1] P. LoCascio,[1] D. Tabb,[1] J. Razumovskaya,[1] Y. Xu,[1]
M. Shah,[1] S. Passovets,[1] A. Gorin,[2] H. Choi,[2] T. Fridman,[2] and R. Day[2]
[1]*Life Sciences Division*
[2]*Computer Science and Mathematics Division*

The purpose of this project is to rapidly develop key computational technologies necessary for the Genomes to Life Facility III "Characterization and Imaging of Molecular Machines." These include (1) computational methods for recognizing and characterizing the interactions of small structural RNAs, (2) computational methods for identifying and predicting the domain structure of membrane proteins, (3) methods for achieving much greater throughput and automation in the analysis of protein interactions using confocal light microscopy, (4) next-generation mass spectrometry data analysis tools for examining protein complexes, and (5) computational methods for constrained protein docking and protein complex geometry modeling using constraints derived from experimental measurements.

The Genomics:GTL Facility III is focused on the "Characterization and Imaging of Molecular Machines", and is ideally suited to ORNL's core strengths in mass spectrometry, structural biology, computational biology and computing. It will leverage the high-performance computing capabilities of the laboratory, the Spallation Neutron Source, and the Center for Structural and Molecular Biology. This project will develop technological capabilities which have been identified as necessary for such a facility.

Understanding the organization, function, dynamics, localization and role of the many thousands of macromolecular complexes in microbial cells will require a combination of many different types of technologies, such as mass spectrometry and imaging, with complementary views of events and interactions. To make mass spectrometry effective, new algorithms are needed that deal with quantitation, post-translational modifications, cross-linking, and peptide identification. Computational methods are needed to interpret confocal image streams and track and classify events. An additional challenge is to develop methods that incorporate experimental constraints to assist protein docking and molecular machine modeling.

In the first year of this project, new mathematics, statistics, and algorithms have been developed which increase the computational discrimination of individual peptides in mass spectrometry. These include (i) an improved scoring function for statistically rigorous match of experimental and theoretical spectra, (ii) de novo identification of ion types in experimental spectra, (iii) improved methods for theoretical fragmentation models, (iv) methods for combining individual peptide hits to estimate significance of a protein hit in a database, and (v) a framework code that incorporates the above functionality (DBdigger). We also constructed a protein docking pipeline, which prototypes some of the computer science solutions that could be used to construct Multi-Level Modeling Platform for constrained docking. The pipeline integrates multiple codes and implements three principal stages of the protein assembly investigation: (1) initial refinement of the docking components; (2) calculations of the potential energy grid and generation of the decoys; and (3) scoring and filtering of the decoys based on synthetic experimental distance constraints.

This LDRD is implementing key technologies for DOE Genomics:GTL and also relevant to environmental or pathogenic microbes, in environmental systems involving microbes and plants and in human disease. NIH, NSF, and DHS have initiatives for which this technology is highly relevant.

Information Analysis and Fusion for Threat-Vulnerability Analysis

R. M. Patton,[1] T. E. Potok,[1] T. F. Gee,[2] and K. W. Tobin[2]
[1]*Computational Sciences and Engineering Division*
[2]*Engineering Science and Technology Division*

We propose an information fusion system for a port security application. The system will be able to (1) autonomously search through distributed information sources, (2) maintain a dynamic data archive, (3) determine the value of a particular piece of information as it relates to other pieces of information, and (4) analyze and fuse the information from different sources and formats to provide for discovery of relationships. Our objective is to provide a threat-vulnerability analysis system that can automatically retrieve and correlate information about worldwide shipping traffic, detect anomalies, and then present this information to an analyst.

The U.S. Department of Homeland Security Technical Intelligence and Information Analysis portfolio lists as a goal to create "new analytical methods and tools for sensor fusion and the synthesis/analysis of text, imagery, sensor measurements, and other information [that] are presented in a scenario-based, analyst-driven computational environment." Our objective is to provide a threat-vulnerability analysis system for port security that can automatically retrieve information about worldwide shipping traffic, correlate this information, detect anomalies, and then present this information to an analyst to view or to query.

The proposed system will utilize intelligent agents that collect information from specific sources. These agents would extract ship locations from weather reports. A set of port agents would be used to gather information from a collection of port Internet sites from across the world, such as Houston, London, etc. Port agents monitoring these sites would gather information about ships within a given port. Next, a set of shipping agents would gather information about shipping lines from individual corporate Internet sites, such as COSCO, K-Line America, etc. Next, a set of image processing agents would gather images of ships in port or at sea. Finally, additional agents could be marshaled to incorporate additional information from other sources.

We are pleased to report the successful achievement of several key milestones identified in the original LDRD proposal. We have focused our efforts on collecting information concerning the Port of San Diego. While our efforts have been specific to this port, the techniques and approach we have used can be generalized to a variety of ports. We have collected approximately 1 million weather reports from various ships over the past several months, 1.7 million images of the Port of San Diego, and daily port schedules for the Port of San Diego for a period of 2 months, as well as information concerning ship inspections performed by the USCG. In addition, preliminary work in identifying ships (under specific environmental conditions) through image analysis has been successful. In specific environmental conditions such as clear daylight, results are very promising. However, other environmental conditions such as fog and rain remain a challenge. We are continuing work in this area to develop robust techniques for handling a wider variety of environmental conditions. The work performed thus far has represented the initial stages of information fusion that is needed to achieve the stated project objective. Our work for the second year of the project is to include the automated fusion of the information collected thus far, the refinement of our image analysis algorithms, and the development of algorithms for threat vulnerability analysis.

The draft DHS program literature clearly states that a significant future challenge will be the development for this type of information analysis and fusion. The proposed work would be of direct interest to both DHS and the U.S. Coast Guard since a strategic objective of both agencies is the protection of maritime infrastructure and the protection of the U.S. Marine Transportation System.

A Neutron Science Portal Infrastructure to Facilitate Remote Access to Spallation Neutron Source Data and Computation

S. Vazhkudai and G. A. Geist
Computer Science and Mathematics Division

The Spallation Neutron Source (SNS) at ORNL is intended to mature into a facility wherein the neutron user community can run their experiments, generate massive datasets, perform analysis and data reduction operations on this data, render and visualize them, and collaborate with other users in the community. Thus, there is the need to bring all of this functionality under one umbrella, which acts as a single gateway where neutron scientists can go to for their needs. In this project, we pursue the development of an object-oriented generic portal framework in cooperation with SNS software group that connects the TeraGrid (a national Grid testbed) to the SNS and provides a template for service composition and development.

As the SNS matures, its users are likely to perform diverse sets of operations including analyses, data reductions, visualization, etc., of massive datasets. These are complex sets of operations, each with their own graphical user interface (GUI) components, associated interfaces, and internal functionality, potentially developed by different groups. There are several benefits in bringing together these services into one fold. First, this would let SNS control the data generated. Second, datasets and operations on them can be annotated with metadata and can thus be made available for future researchers. Third, by way of users coming to SNS for their analyses needs, high-quality, validated software can be provided to the community. Finally, SNS can purchase site licenses for commercial/legacy software and make it available to the community. Our portal effort is a step in that direction and attempts to abstract out software/data management services behind a well-defined user interface

Our technical approach comprises the design and development of a three-tired, service-oriented application portal architecture for the SNS. It consists of an external GUI, internal portal framework, and backend services support. In the GUI, our guiding principle has been to maintain a clean separation of concern between the various components such as analysis, simulation, data, visualization and acquisition. GUI-wise, these components are self-contained and comprise of only a basic set of widgets and controls for essential operations. In the internal portal framework, we cast the various components (data, metadata, analysis, communication, execution environments, etc.) as simple objects with their interrelationships (aggregations, uses, inheritance, etc.), and handle concurrency, session and state management. Finally, in the services arena, we develop several backend services such as metadata/data management and analysis/simulation/visualization execution environments.

Our accomplishments to date include the development of the following portal software components:

- A robust internal design and implementation for the portal framework comprising of well-defined object classes and interfaces
- Framework customization and giving context based on user personalization
- Data management infrastructure, data browsers, and basic operations on data such as view, download, upload, etc., for remote data access
- Portal-Metadata Database conduit infrastructure and basic metadata operations through the portal
- Hyperlinked metadata browser to drill down selective fields in a query to find more information
- Authorization capabilities to provide selective user access to data, metadata, publications, etc.
- Execution environments for launching applications from the portal, constructing sequential pipes of analysis tools and file I/O interfaces for analysis-tool interoperability
- Software repository—interface to repository and mechanisms to upload/download tools
- A robust graphical user interface

At SNS, users from all across the USA will conduct experiments, generate data, and perform computational analyses on these datasets. One of the key requirements for the realization of these goals is a sophisticated software/data management solution. Our portal effort is a step in that direction attempting to abstract services behind a well-defined user interface. Further, several users will likely come from academia. Our portal will be used by these NSF-funded participants as well as participants from other federal agencies. The benefit of the portal is it will make it much easier to access data, compile metadata, and to do analysis on experimental neutron data than has been possible in the past.

COMPUTER AND COMPUTATIONAL SCIENCES

Seed Money Fund

The Global Optimization Problem for Remote Sensing: A Guaranteed, Efficient Solution

J. C. Wells,[1] V. Protopopescu,[1] and C. D'Helon[1]
[1]*Computer Science and Mathematics Division*

We investigated the role of additional information in reducing the computational complexity of the global optimization problem (GOP) and established proof of principle that a broad class of GOPs can be solved efficiently and with a guarantee by exploiting available additional information. Following this approach, we developed GMG—a new algorithm to find the Global Minimum with a Guarantee. This algorithm transforms an originally continuous GOP into a discrete search problem, thereby guaranteeing to find the position of the global minimum in a reasonably short time, commensurate with the amount of additional information. GMG has been validated on a set of standard benchmark functions, and applied on a simple realization of the monocular passive ranging (MPR) problem in remote sensing. This MPR application consists of identifying the precise range of an airborne target (missile, plane, etc.) from its observed radiance. This inverse problem is set as a global optimization problem (GOP) whereby the difference between the observed and model predicted radiances is minimized over the possible ranges and atmospheric conditions. We solved this GOP using GMG and report on the performance of the algorithm here and in a peer-reviewed journal article submitted for publication.

Introduction

Independent of specific approach and algorithmic efficiency, current solutions for continuous GOPs (Horst and Tuy 1993), share a common drawback in that none of them can guarantee that the global minimum will be found in a reasonable time.

We aim to develop a new algorithm that can efficiently solve the continuous GOP arising from monocular passive ranging (Jeffrey 1994) and guarantee the result. MPR determines the instantaneous range to a target relying on remote sensing in the atmosphere, using a single sensor. Our choice of application is motivated by yet unsolved challenges facing National Defense (Missile Defense Agency—MDA), instances of which require the optimal, as opposed to a suboptimal, solution of a GOP. Our work, reported here, has successfully established proof of principle that a broad class of GOPs can be solved efficiently and with a guarantee by exploiting available additional information (D'Helon 2004).

Technical Approach

The new algorithm guarantees to find the global minimum, by systematically using additional information about the error function constructed as the difference between the predicted and observed radiances in MPR. Sufficient additional information may include, for example, the size of the basin of attraction for the global minimum, the separation between the global minimum and the next lowest local minimum, the general shape of the error function and the uncertainties inherent in the sensor measurements. In general, a certain amount of information is available in many applications, but present algorithms either do not or cannot use it. Using this information enables us to map the continuous GOP onto a discrete search, by eliminating all basins of attraction except that of the global minimum.

The performance of our approach has been assessed in terms of a standard set of benchmark objective functions, to show that the new algorithm is often competitive and at times exceeds the performance of present algorithms, even though these existing algorithms are unable to guarantee that the global minimum has been found. The performance of GMG has also been assessed in terms of the amount of additional information sufficient to guarantee that the global minimum is found quickly and accurately.

Results and Discussion

We have successfully implemented GMG to solve continuous GOPs. An authoritative benchmark for calculating atmospheric radiation transmission, MODTRAN (MODTRAN 2004), was used to generate the error function between the predicted and observed radiances in MPR. Multiple minima in the error function were observed for fluctuating ozone profiles, since the ozone density is non-monotonic as the altitude increases. The algorithm was also parallelized on the IBM Power 4 supercomputer within ORNL's Center for Computational Sciences, in order to address independent fluctuations in multiple ozone layers, and thus expand the dimensionality of the error function.

Varying degrees of additional information about the error function were assumed, in order to investigate how much information is needed to eliminate all basins of attraction except that of the global minimum. Our

results prove that the error function available in MPR has sufficient additional information to guarantee that the global minimum is found in a reasonable time. We have investigated the time scaling of the new algorithm, as well as the probability of finding the global minimum, and found that information related to the size of the basin of attraction for the global minimum is of prime importance for an efficient guarantee (D'Helon 2004).

We have compared the performance of GMG with that of the TRUST algorithm (Barhen et al. 1997) for a set of seven standard benchmark functions. The results show that GMG is often competitive with TRUST (Barhen 1997), in terms of the number of function evaluations. Moreover, our approach guarantees that the global minimum will be found, something that TRUST cannot achieve in principle. Thus, in general, a completely conclusive and exhaustive comparison between the two algorithms is not possible. As the number of dimensions grows, GMG exhibits an exponential increase in the number of function evaluations, consistent with the demands of the discrete, ordered search. We emphasize here that the difficulty of this search has been significantly reduced by the effective utilization of available additional information.

Benefits

GMG is applicable to a broad class of continuous GOPs, arising in a wide range of applications that are relevant to strategic ORNL thrusts in national security, materials science, and computational biology. Many of the problems in these areas require precise, guaranteed identification of the global minimum and will benefit from this research. There is also an immediate need and opportunity to apply our algorithm to the challenges facing National Defense. Remote sensing in the atmosphere is currently a critical field of research within strategic and theater missile defense. MPR is a prime example of a problem that will benefit from our optimal GOP solution for accurate ranging, with a guarantee.

References

Horst, R., and H. Tuy. 1993. *Global Optimization*, 2ed. Springer-Verlag, Berlin.

Jeffrey, W., et al. 1994. "Monocular Passive Ranging," IRIS Targets, Backgrounds and Discrimination Conference.

Infrared Clutter Assessment: Radiance and Transmission Models. November 2004. "MODTRAN 4 Software." www.vs.afrl.af.mil/Division/VSBYB/modtran4.html.

Barhen, J., et al. 1997. "TRUST: A Deterministic Algorithm for Global Optimization," *Science* **276**, 1094.

D'Helon, C., et al., 2004. *GMG: A Guaranteed, Efficient Global Optimization Algorithm for Remote Sensing*, ORNL/TM-2004/94, Oak Ridge National Laboratory, Oak Ridge, TN.

ENGINEERING SCIENCE AND TECHNOLOGY

Director's R&D Fund

Zero-Net Power, Low-Cost Sensor Platform

J. E. Hardy,[1] P. D. Ewing,[1] J. E. Christian,[1] R. J. Warmack,[1]
P. G. Datskos,[1] C. L. Britton, Jr.,[1] S. S. Frank,[1] M. Martin,[2]
S. F. Smith,[1] and R. B. Rumbolt[1]
[1]*Engineering Science and Technology Division*
[2]*Environmental Sciences Division*

Numerous national studies and working groups have identified very low-power, low-cost sensors as a critical technology for increasing energy efficiency, reducing waste, and optimizing processes. This research addressed that need by developing an ultralow-power, low-cost sensor platform based on microsensor (MS) arrays that includes MS sensors, very low-power electronics, signal processing, and two-way data communications, all integrated into a single package. MSs were developed to measure carbon dioxide and room occupancy. Advances were made in coatings for detecting carbon dioxide, sensing thermal energy with MSs and capacitive, low-power electronics, robust algorithms were developed for communications within buildings over power lines, and an integrated platform was realized that included gas sensing, temperature, humidity, and room occupancy with on-board communications.

Technical Approach

Microsensor Arrays for Gas Sensing. The sensor chips used in the present studies were fabricated in the Multi-User MEMS Process (MUMPs) at MEMSCAP, Durham, NC. These chips measured 5 mm × 2 mm and contained circular parallel-plate capacitors that could be coated with polymer dielectric material using an ink-jet process. The capacitor plates were made of conductive polycrystalline silicon consisting of a 0.5-µm-thick bottom plate resting on the substrate, a 2-µm air gap that was filled with polymer subsequent to the MEMS fabrication process, and a 2-µm-thick ventilated top plate. The circular capacitor plates were 326 µm in diameter with a 126-µm-diameter central fill hole and had a base capacitance of about 0.3 pF. To minimize the possible flexing of the top plate when the polymer swelled due to absorption of the ethanol or water vapor, the top plate was anchored to the substrate with posts (5 µm square) at approximately 60-µm intervals. The top plate also had an array of 3-µm-square etch holes separated by about 30 µm. These holes were required for removal of a sacrificial silicon dioxide layer during chip fabrication and also to allow analyte vapors to pass through the top plate to interact with the underlying polymer dielectric material during operation. A heater strip encircled the sensors so that the chip could be maintained at 70ºC, the optimum operating temperature. Other sensors on the chips included various cantilevers for testing infrared sensing and interdigitated transducers for an alternative chemical readout.

The MEMS sensors coated with the sol-gel mixture responded to CO_2 with a decrease in capacitance, while capacitance increased with humidity pulses. This is explained by the change in polarity of the interacting dielectric material. Unfortunately, the performance of the sensors coated was more variable than desired. The material was also subject to degradation due to the presence of species such as SO_2 and NO_2, though temperature cycling appears to mitigate oxidization and extend the useful lifetime. The sensitivity of the MEMS sensors is more than adequate for sensing CO_2 for ventilation purposes, but more work is needed to produce reproducible sensors.

Microsensor for Detecting Thermal Energy. One of the goals of this LDRD project was to develop micromechanical infrared sensors for use in combination with chemical sensors. To this end during this LDRD project, we designed and fabricated several types of geometries that included up to nine different infrared detector designs.

The infrared detectors were suspended bimaterial cantilevers made from polysilicon with a gold layer as the bimaterial layer. These cantilevers detectors were capacitively read using a custom analog ASIC. The noise level was about 10–16 farads at a readout rate of 10 KHz.

The detectors were designed to operate in under ambient conditions. A measure of detector performance is the noise equivalent temperature difference (*NETD*). In order for a detector to be able to detect heat from a human, a value of *NETD* of 500 mK or better is required. The predicted *NETD* for the designed detectors was about 20 mK in air and less than 5 mK in vacuum. The temperature fluctuation $NETD_{TF}$ is given by

$$NEDT_{TF} = \frac{8F^2 T_d \sqrt{k_B B G}}{\eta A_d \left(\frac{dP}{dT}\right) 8-12\,\mu m}$$

where F is the f number of the optics, T_d is the detector temperature, A_d is the detector area k_B is the Boltzmann constant, B is the electric bandwidth, G is the thermal conductance, (DP/dT) is the derivative of the black body power with respect to temperature, and η is photon absorption of the detector.

Although these detectors were expected to detect room temperature objects, we were unable, at this time, to detect the heat from a human hand in air or in vacuum. However, these detectors responded to a soldering iron of >150ºC. We expect to achieve detection of room temperature objects even in air by increasing the detector area and eliminating thermo-mechanical noise sources. Designs and new materials have been considered, but time and funding did not allow these to be fabricated nor tested. An off-the-shelf IR motion detector was modified to integrate into the system package, and this plan was successfully implemented.

Ultra-Low Power Electronics. Hardware and software were developed to read various sensors that detect room environmental conditions. The hardware consisted of a circuit board set containing the existing GS2 custom ASIC, a microcontroller to communicate with the host computer via an AC line coupler, and various sensors. The circuit board set included a daughterboard that contains the micro-cantilever sensors and GS2 ASIC and a motherboard that contained the remaining circuitry.

The GS2 ASIC is a mixed-mode capacitive readout chip that is fabricated in the TSMC 0.35µ process. The GS2 ASIC is a full featured capacitive readout chip with 10 inputs and is fully programmable via a 4-wire SPI interface. The ASIC can drive and sample two micro-cantilever sensors simultaneously. The drive circuit has programmable timing and voltage amplitude. An on-chip average of up to 16 samples is available to increase the noise performance. The sampled values are then converted to a digital value by the on-chip 10-bit SAR ADC. The ASIC also contains a thermometer circuit for sensing chip temperature.

The motherboard contained the remaining sensors and electronics and a socket for inserting the daughterboard. The motion detection circuit, a temperature and humidity sensor, and the micro-cantilever heater control electronics are on the motherboard. It also has the electronics that process the signal from the micro-cantilever Si-RTD. This allows sensing the temperature of the micro-cantilevers. A microcontroller handles external communication and interfaces with the ASIC and other sensor electronics. The microcontroller communicates to the PC via the AC line coupler using a simple 2 wire RS232 serial interface. The circuit boards were designed to work independently of the AC line coupler device. Therefore the boards can be interfaced directly to the computer via the PC serial port. Communication speed was set at 2400 baud for the purpose of interfacing to the AC line coupler. However, reprogramming the microcontroller could increase the speeds to the microcontroller limit of 115,000 baud.

LabView software was developed to interface with the microcontroller on the motherboard using the PC serial port. The software allows the user to enter all GS2 configuration data, select the sensors to be read, and the frequency of these readings.

The system data is then collected by the software, displayed on the screen, and saved to the hard drive for further analysis.

The system is capable of reading any of the micro-cantilever sensors, the micro-cantilever temperature, GS2 temperature, ambient temperature and humidity, and any room movement since the last reading. It also has the ability to heat the micro-cantilever device. When tested via direct connection to the PC, the sensor readout system worked very nicely up to 2400 baud. At this communication speed, a complete setup and readout of all sensors was around 7 seconds. No tests were conducted above this speed, but data rates in excess of 115,000 baud should be easily achievable. When connected to the PC via the AC line coupler, the system worked just as well with the exception of the data readout rate being reduced due to the data overhead of the line coupler.

Robust Communications. The intent of this portion of the LDRD program was to develop and demonstrate a highly energy-efficient sensor interface and spread-spectrum radio-frequency (RF) telemetry unit that would typically be deployed in both new and retrofit installations. The very low-power "plug-in" unit would operate using capacitively coupled energy from the single- or three-phase 60-Hz AC power line. A design for this telemetry was completed. Additionally, a spread-spectrum RF protocol (ORNL invention disclosure in process) was developed that was an outworking of emerging ORNL technology (and two currently pending U.S. Patent applications) to address the difficult signal-propagation environment of a home or building AC power distribution system, which is characterized by very high broadband noise levels (largely from brush-type motors), large transient voltages, and wildly varying RF impedance levels (due to intermittent load switching, local line reflections, and disturbances from neighboring users on the grid). Due to funding constraints, this telemetry design could not be implemented, so a survey of lower-performance but commercially available power-line transceiver devices was performed. The most capable one, the IT800D transceiver chip from ITRAN Corporation, was selected for the demo. The IT800D device incorporates a high-performance Data Link Layer (DLL) with a Carrier Sense Multiple Access/Collision Avoidance (CSMA/CA) channel access scheme and a robust physical layer (PHY) transmission protocol which has proven effective in many power-line

data-transmission applications. Custom software was developed to run the host microprocessor to do the data stream buffering demanded by the IT800D. The software implemented a 256-byte FIFO in on-chip RAM. A full-duplex (simultaneous, bidirectional) communication system to transport the sensor array data to the host computer was thus successfully implemented.

Results and Discussions

Significant progress was made on microsensor technology for gas detection and thermal energy detection. A coating was developed that had the range and sensitivity to measure carbon dioxide for building/office ventilation control, energy optimization, and personnel health. To obtain a reasonable response time, the sensor required heating to 700ºC, which is easy to do, but this meant the ultra-low power goal had to be compromised. Long-term stability remained an issue for further research.

The microsensor research for thermal energy detection led to an increase in the understanding of thermal noise sources and microfabrication issues. A first-of-a-kind capacitive readout thermal cantilever was developed that could detect hot object over 1500ºC. Design and materials changes were identified to further increase sensitivity and remain areas for additional research to reach the initial goal of human detection.

Ultra-low power electronics development proceed very well and readout and signal conditioning electronics met all project goals of integrating gas-sensing and thermal energy detection with the same capacitive electronics. An algorithm was developed to increase the robustness of signal communications over power lines in buildings, and a low-cost line couple was created by modifying off-the-shelf units.

Finally, an integrated platform was developed that simultaneously measured carbon dioxide, humidity, temperature, and room occupancy. The platform also included communications and power delivery from existing power lines. This integrated low-power, multi-sensor array is pictured in Fig. 1.

Benefits

This project is relevant to DOE in several mission areas including Building Technologies, Industrial Technologies-IOF-Sensors and Controls, and Fossil & Fuel Cell Energy technologies. The zero-power, low-cost sensor platform will allow more extensive monitoring of processes as well as environmental conditions for personnel health and comfort. The research into low-power electronics and multi-sensor arrays advance measurement science that is an enabling technology for most DOE programs. This project has applications to Department of Defense programs and Homeland Security programs. Collaborations and proposals have been created with Seacoast Science, Rockwell Scientific, RA Bedell Co., and QUALCOMM. Proposals that include this technology have also been delivered to NASA, DOE, and DHS. One invention disclosure is being filed, and two papers were written. At least two more papers will be developed in FY 2005.

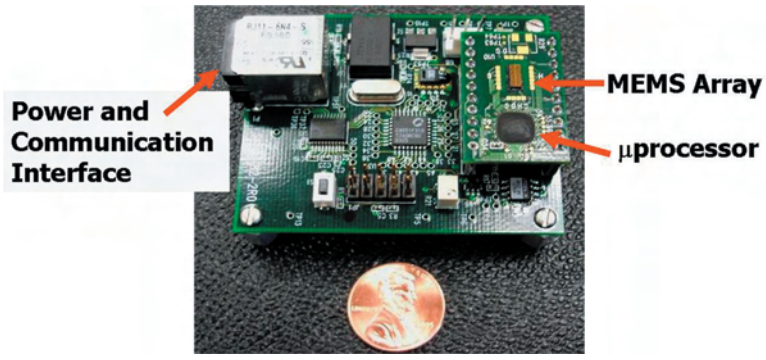

Fig. 1. Low-power, low-cost microsensor array platform.

NeutroMegas: A Pixel Detector for Neutron Imaging

C. L. Britton,[1] W. Bryan,[1] A. Wintenberg,[1] B. Warmack,[1] T. McKnight,[1] S. Frank,[1]
R. Cooper,[2] N. Dudney,[3] and G. Veith[3]
[1]*Engineering Science and Technology Division*
[2]*Spallation Neutron Source*
[3]*Condensed Matter Sciences Division*

A bright neutron source such as the SNS places extreme requirements on detectors such as the highly desirable characteristics of excellent 2-D spatial imaging and high dynamic range. Present imaging detectors have either shown position resolutions that are less than acceptable or they exhibit excessive paralyzing dead times due to the brightness of the source. A new detector concept known as MICROMEGAS (MICROMEsh GAseous Structure) has been developed at CERN in Geneva for high-energy-physics charged-particle tracking applications and has shown great promise for handling high data rates with a rather low-cost structure. If properly developed, this detector platform has features that could revolutionize neutron imaging. We have developed a novel detector using the MICROMEGAS concept by creating NeutroMegas, the first pixelated, high-rate detector for 2-D neutron imaging. This has not been successfully accomplished anywhere else, although it has been a goal for researchers. This is an outstanding contribution to the overall detector instrumentation effort for the neutron community and would establish Oak Ridge as a leader in the search for next-generation neutron detectors.

Introduction

The goal of this LDRD was to develop a prototype high- (position) resolution, low-dead-time NeutroMegas detector. In order to accomplish our goals, two key projects have been undertaken. One focused on the development of the detector structure and readout electronics, while the other was directed towards converter foil research. The detector structure portion of this project will entail building and testing both a 1-D (strip) and 2-D (pixel) detector. Initially a 1-D strip format will be developed (Andriamonje 2002, Stephan) since it allows easy electronics readouts, while our long-term goals will be to produce a true pixilated 2-D detector.

Technical Approach

We have fabricated a detector prototype, shown in Fig. 1, whose anode structure was formed on a quartz substrate using micro-fabrication techniques. A regular array of 73-µm-tall separator columns was formed by chemically etching the photo-patterned surface. A shadow mask was then aligned to permit 250-µm-wide chromium anode strips to be evaporated between the columns. Adjacent strips were spaced 1 mm apart and were alternately connected to vacuum feedthroughs in the aluminum chamber. A 1000-line-per-inch, 7-µm-thick nickel grid was placed atop the anode structure. A 3-mm insulator was then used to space a boron- or lithium-coated aluminum converter plate away from the grid.

The main objective of the neutron converter work has been to develop the synthetic techniques required to fabricate the converter foils as well as understanding and manipulating the chemical or electrochemical stability of these foils. This is essential to successfully building a stable, high-efficiency detector. To this end we have been very successful in meeting our goals.

Converter films consisting of naturally abundant elements have been prepared utilizing a variety of physical deposition techniques. Due to the air and moisture sensitivity of these materials, all film growths were carried out in a deposition system contained within an argon-filled dry box. Thin films of boron (1–2 µm) and gadolinium (1–2 µm) have been prepared utilizing rf and

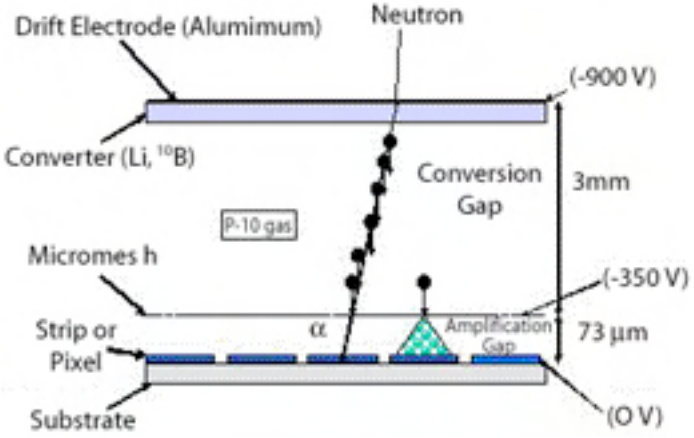

Fig. 1. Neutron detector concept.

d.c. sputtering techniques, respectively, while lithium films were synthesized by thermally evaporating elemental Li (3–100 μm). These thickness ranges were chosen from the literature for reasonable detector efficiency. The deposition conditions were optimized (i.e., argon pressure, power, distances between the targets and substrates, rate and choice of substrates) in order to minimize the film impurities as well as reduce any potential mixing of the reactants due to the energetic nature of the deposition process. By optimizing the deposition conditions, we have effectively reduced the impurity content to below 5 at %.

In summary, we have established the synthetic conditions required to prepare these foils, investigated a series of Li-substrate interactions, initiated a series of long-term studies to address the inter-diffusion between the converter constituents, and determined the stability of the converter to the detector gases.

Results and Discussion

Because the detector has worked so well in a short period of time, we have had opportunity to do extensive testing on the detector. Our testing includes the following:

1. ***Critical voltage ($\acute{\varepsilon}_{crit}$) testing***—We temporarily replaced the converter element inside the detector with an ^{241}Am source to simulate a "point" source of alpha particles instead of using neutron-induced alphas for preliminary testing. This allowed us to evaluate both the detector structure under various voltages and the data acquisition system with a known stable source of particles. The critical voltage $\acute{\varepsilon}_{crit}$ is the voltage when electron multiplication begins for a given gas and detector geometry (Knoll 2000). Calculations for our geometry at 1 atm of P-10 predicted a value of $\acute{\varepsilon}_{crit}$ = 350 V for our multiplying grid voltage. Our measurements showed a value of approximately 330 V, demonstrating excellent agreement with the design value.

2. ***Detector position mapping with ^{241}Am***—With the data acquisition system (DAQ), we simultaneously read out each of the six instrumented channels of strips in two different modes. Mode 1 was a conventional asynchronous multi-channel analyzer (MCA) mode in which any channel that gets an event at any time was converted and histogrammed (analogous to having six independent MCAs). For these tests, the source was located above the instrumented detectors in the approximate center.

3. ***^{252}Cf testing (neutron testing)***—Data were taken for several coatings including 1- to 2-μm boron and 26-μm lithium. Mode 2 of the DAQ allowed us to stop and read all channels when one of the strips had an event that exceeded its threshold. This allowed position determination of an incident neutron in 1-D. Data was collected using external ^{252}Cf (in Lucite to thermalize the neutrons) as a neutron source with a 1-μm-thick boron converter plate. The DAQ was configured in Mode 1 for integrating counts. Some adjacent strips show charge sharing which we expected from earlier Monte-Carlo analyses.

4. ***2-D array development and ^{252}Cf Testing (neutron testing)***—In the second year, we developed 2-D arrays of the pads that allow true position-sensitive detection of neutrons. A 4 × 4 array of pads was designed, fabricated and implemented. A new 16-channel data acquisition system was also developed that records the data for each pad individually. We took array data with the new setup and found that indeed the detector was functioning as desired.

Benefits

We now have a working 2-D pixel detector. This has already attracted interest from instrument scientists at the Spallation Neutron Source and is expected to be used as a beam monitor and as a transmission monitor in some of the proposed experiments. In addition, a variant of this detector is being considered by another experiment at SNS.

We are also working with North Carolina State University (NCSU) on a variant of the Neutromegas for the fundamental physics beamline. The variant will utilize helium as the fill gas.

In addition, partly because of the NeutroMegas project, we have a three-year FWP with DOE jointly with BNL to work on a neutron drift detector.

References

Andriamonje, S., D. Cano-Ott, A. Delbart, J. Derre, S. Diez, I. Giomataris, E. M. Gonzalez-Romero, F. Jeanneau, D. Karamanis, A. Lepretre, I. Papadopoulos, P. Pavlopoulos, and D. Villamarin. 2002. "Experimental studies of a Micromegas neutron detector," *Nuclear Instruments and Methods A* **481**, 120.

Stephan, A. C., R. G. Cooper, and L. F. Miller. "Monte Carlo studies of a Micromegas neutron beam monitor," accepted for publication in *Nuclear Instruments and Methods A*.

Knoll, G. F. 2000. *Radiation Detection and Measurement*, 3rd ed., John Wiley and Sons, pp. 162–173.

Ensuring the Communications Infrastructure for the Electric Grid of the Future

W. W. Manges,[1] G. O. Allgood,[2] T. J. McIntyre,[1] M. R. Moore,[1]
S. G. Batsell,[2] D. T. Rizy,[1] T. Kuruganti,[3] and M. Shankar[2]
[1]*Engineering Science and Technology Division*
[2]*Computational Sciences and Engineering Division*
[3]*University of Tennessee, Knoxville*

The events of August 14, 2003, and September 11, 2001, underscore the vulnerability of the current U.S. critical infrastructure. Whether instigated by hardware misoperation or failure, operator error, or intentional damage, events like these are leading decision makers to call for upgrades or even complete reinvention. DOE's GridWise and GridWorks programs as well as proposals from the Consortium for Energy Infrastructure for Digital Society (CEIDS) (Consortium 2003) all hinge on improving performance through improved sensors, controls, and communications. The level of performance expected from the communications infrastructure has little analytical basis to support the assumptions. Currently available modeling and simulation (M&S) tools don't provide the necessary fidelity and node density for these real-time, high-reliability communication systems (Buckner et al. 2001, Newman et al. 2002). This research began a path to create a new set of algorithms, tools, and software designed to support needs for the national energy grid and provide a prototype model illustrating the application of the tool-set to a representative grid. The new paradigm links, in an analytical, deterministic way, the performance of the grid with the requirements of the communications infrastructure that supports the grid. The influence matrix (Jacobian) derived here paves the way for future analysis that can link long-term and short-term stability of the grid to non-deterministic behavior in the communications infrastructure. Stochastic models of the communications systems have failed to provide the fidelity needed for the detailed analysis required for predicting and mitigating system failure.

Introduction

Ubiquitous sensing and computing is sweeping through application after application from home automation to battlefield situation awareness. The electric power grid is now being considered for a revolutionary make-over to take advantage of the efficiency gains offered by low-cost, pervasive sensor and control architectures. The latest from network researchers, called "Internet-scale Data Acquisition and Control" (Ambrosio 2002, Noecker 2002), is a machine-to-machine (M2M) communications paradigm. Experience on the internet, though, raises serious concern with issues about the robustness under load and security of the communications infrastructure necessary to support important national resources like the power grid.

This project set out to develop a suite of tools necessary to support high-fidelity, high-density modeling and simulation of the communications infrastructure needed for the stability of the electric power grid. We built our team from ORNL experts in sensors and controls, the electric energy grid, communications networks, cybersecurity, and modeling and simulation. We solicited participation from outside experts in current grid stability issues and in determining the directions likely for the future of the grid. The ultimate goal was to develop the tools and then make them available as part of an ORNL User Facility at the Center for Computation Sciences. As the team began to develop the low-level tools and research the relationship between communications and grid control stability, we realized that this relationship needed an analytical basis before real progress could be made. Control stability, with respect to sensor latency, is well understood, but little background work was available on which to base our study of control stability with respect to communications latency and the "jitter" in that latency due to the non-deterministic nature of TCP/IP, the current standard for network communications. For our tools to be relevant, we needed a way to model the communications-stability relationship in a way that would allow modelers to study, not only current protocols (TCP/IP, etc) but also project or anticipate new ones or replacements. Current state of the art in network deployment is "can you hear me now" where a network is planned, based on stochastic forecasts, and then adjusted as the network shows signs of under reach and instability. Better M&S for the communications infrastructure would allow better design and implementation of both communications and grid measurement and control strategies. The project began the study of the analytical relationship between communications and control but was terminated before the tool suite reached a level of maturity suitable for general use. Our hope is to continue the work as new funding

becomes available, especially as the need continues to grow and is getting more urgent as the power grid moves towards a self-healing paradigm.

The DOE has shown interest, recently, in projects that concentrate on the potential energy savings available if the grid controls can exert influence over highly varying industrial loads (like aluminum pot lines) in a time frame that reduces power regulation requirements. Control over these loads requires a communications infrastructure that is reliable and timely. Our research showed that tools could be provided for assessing the potential "real" benefits available when the entire system is considered, including the communications infrastructure requirements.

Technical Approach

The team developed a "canonical" grid segment on which to base the models. We then determined what measurements and control actions would necessary during both normal and abnormal situations. The initial grid segment had to be sufficiently constrained so as to allow meaningful progress to be made but simultaneously needed to support expansion in all dimensions: (1) spatial as the model grew to cover more of the distributed network with denser and denser nodes (measurements) and (2) temporal as the sampling and operational requirements became more demanding (and perhaps automated).

Modeling and simulation of communication systems has gained growing interest as the dependence on them has exploded in all application domains. ORNL's broad and deep expertise in this area was brought to bear on the grid stability issue through team members with similar experience with DOD and specific tools used in other fields. The OPNET modeling tool is the defacto standard for high-fidelity modeling and simulation of communications infrastructures at levels 3 and higher in the International Standards Organization (ISO) Open Systems Interconnect (OSI) 7-layer network architecture standard. For layers 1 and 2, MatLab is more expedient. Combining these two tools into an integrated tool kit to include bit-wise fidelity permits the study of the relationships among the entities that constitute performance in a real-time (or near real-time) communications network: (1) reliability, (2) throughput, (3) security, and (4) latency. Among these, latency appeared to be the most important and the least understood in relating grid stability to communications and control.

Current modeling and simulation tools are based on one of two paradigms: (1) stochastic processes including queuing theory or (2) complex, non-linear processes including self-similar convergence and game theory. Our approach of using high-fidelity, high-density data communications and networks modeling and simulation provides the first attempt at tools that can be prescriptive as well as descriptive. These new tools can provide answers to questions such as the following: (1) What happens to the communications network during the outages caused by a thunderstorm sweeping through the region? (2) What happens to the grid control as the responsiveness of the network (latency) deteriorates under peak load? (3) Will a new component, subsystem, architecture, or philosophy improve or degrade performance and why? (4) What is likely to happen to the performance of the grid if purposely attacked and how will the operators know? Furthermore, it can be used to determine the communications needed to have a self-healing grid that continuously monitors system and equipment health and makes continuously control adjustments to maintain a high level of reliability, security, and stability.

Results and Discussion

A key finding of the research in our 2004 effort was the analytical relationship between communications system properties and control stability. The payoff has been an increased understanding by subject matter experts in the area of grid stability and real-time control of critical grid parameters like VARs, frequency, and load. Figure 1 below illustrates how the matrix "J" represents the influence coefficients in the inside control loop and a second "J" matrix describes the influence of the communications network performance parameters on control stability. The inner loops represent the "tight" controllers on the grid itself, and the outer loop represents the new architectures being implemented that involve wide-area control to facilitate "islanding," the "self-healing grid," and load controls. Many individuals and organizations have expressed interest in pursuing that as a separate study from the development of modeling and simulation tools.

The GridWise program (a public-private partnership) (Lightner 2002, Mazza 2005) represents the state of the art in R&D for optimizing grid performance to anticipate and respond to real-time conditions as such providing "load-as-spinning-reserve." This research investigates the potential available for cost and energy savings if the grid can be made more cost responsive—all the way down to having individual appliances decide to reduce power usage or turn off all together when the cost exceeds preset limits. To realize this potential, the communications from the energy management system to generation and to load must be seamless and virtually instantaneous. The consequences of communication problems like unpredictable latencies, excessive drops in throughput at critical times, and link flooding due to intentional and unintentional intervention, loss of communication paths, and noise must be evaluated against "ideal" performance.

"Hacking" into the nation's infrastructure has become a critical national security issue. Current tools for evaluating performance, security, and reliability are

completely uncoupled from reality so none of the current research can investigate the coupling between/among these aspects that truly characterize the network. Our approach provides the first serious attempt at assessing how improving security with getting sensing and control impacts latency and performance and vice versa. New initiatives in DHS and DOE-OEA are targeting technologies to determine if, in fact, an attack is occurring and the extent of the attack. The communications infrastructure for supporting this new goal is just now being developed. Our approach supports the assessment of the viability of alternative designs and their dependence on local and wide area communications.

Specific outcomes of the research, as it currently stands, include the following:

1. A Generic Prototype Model—We now have the framework for a prototype model (Fig. 1) that describes how the communications system impacts the overall stability. We are now ready to begin implementing the communications portion so that we can assess its impact on control stability and calculation of the influence matrix "J" based on anticipated network behavior. Participation by Tennessee Valley Authority (TVA), The Electric Power Research Institute (EPRI), some universities, and others will be necessary to prepare a representative case to study impact on stability.
2. Preliminary PHY Layer Modeling—We now have object models for typical communications requirements and protocols that are used by TVA and others. We will need to prepare discrete models for these, in OPNET, to begin migration to a large-scale network prototype.
3. Initial OPNET Integration—We have OPNET running on the four (4) processor host sponsored through the DOE Industrial Technology Program (ITP). We are integrating the discrete models from task 2 into the communications models available in OPNET.
4. First integrated model—We will be completing the integrated models above to verify the model against performance of existing, selected grid communications infrastructure. Then, performing "what-if" scenarios and demonstrating usefulness to industrial partner/owner of the grid being modeled will demonstrated usefulness in implementing grid communications networks.
5. Verification—We have begun to prepare and execute a detailed and rigorous verification strategy ensuring that our approach is accepted in the technical, regulatory, and commercial/industrial communities. The current approach of relating communications system performance to overall control stability has shown significant relevance in discussions with subject matter experts and other stakeholders. These models, first implemented in MATLAB, will be integrated with the OPNET environment for final integrated demonstrations.
6. Publications and Standards—We have one proposed article accepted for publication in the proceedings of an international OPNET conference, and we are

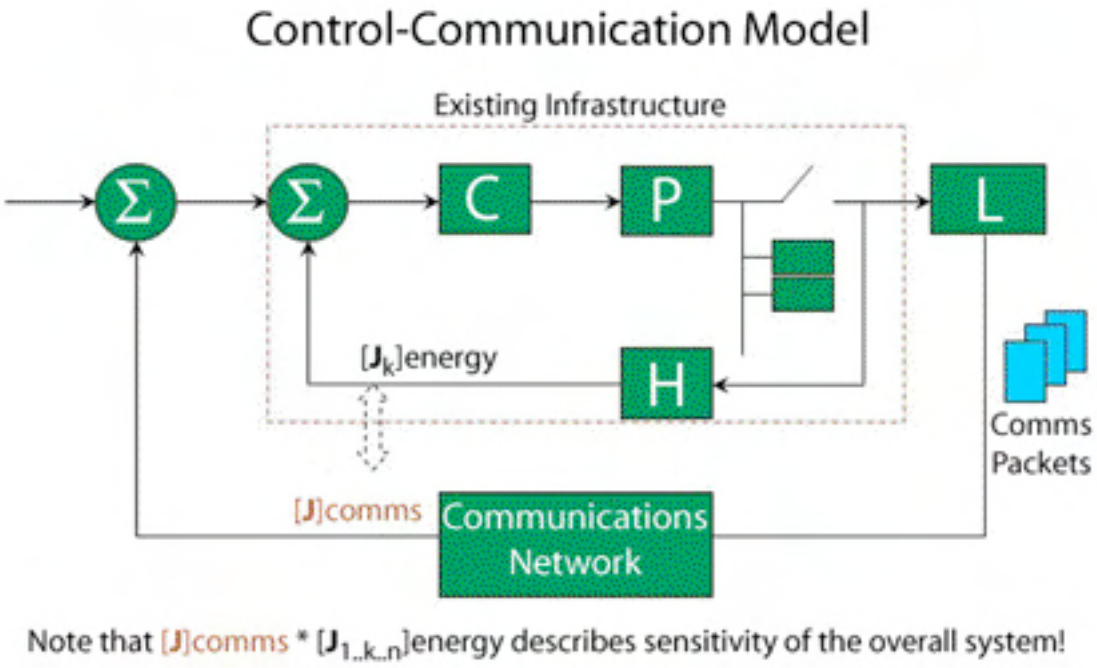

Fig. 1. Outer Communications Loop Impacts Overall Grid Stability—The "Jacobian" matrix contains the influence coefficients that describe how the various performance parameters of the communications network affect control stability.

a partner with Eaton Corporation on a proposal to the DOE-OEA for improving grid reliability and robustness with improved sensors and communication. Team members were invited and are participating in the IEEE 1547.3 standards committee setting key standards for communications in the distributed energy resource architectures emerging on the grid.

Benefits

This project provides the basis for reliable projections of the communications requirements for the required stability. The tools can be used to assess the suitability of existing and developing communications protocols for real-time power grid control. The current models begin to support the key components for an integrated modeling effort to ensure, before implementation, that the performance of a communications network will, in fact, support the required grid measurement and control needs and not contribute to its instability. The Distributed Energy Research (DER) program at DOE will need to be ensured for their communications infrastructure as their architecture matures. The CEIDS and GridWise programs, as mentioned above, can use the initial models developed here to better understand the needs and be able to assess the expected performance from proposed options. Current "can you hear me now" approaches don't allow the playing of the what-if scenarios supported in our program. Continued funding will be needed to move the developments of this project onto the high-performance computing infrastructure of the Oak Ridge National Laboratory and make the tools available to a broader audience. Current implementations will require extensive support from the existing team.

The DOE Office of Energy Transmission and Distribution (OETD) appears to have communication needs for the grid of the future similar to those of the DER Program. Organizations are proposing control architectures and scenarios, but no one has had a tool for assessing/predicting expected performance. Other government agencies have similar complex communication systems, now including a large number of wireless nodes, and will have no way to baseline expected performance (Yoshida 2003). Similar needs have been highlighted at the Department of Homeland Security, DARPA, NRC, and others.

References

Ambrosio, R. 2002. "Internet-Scale Data Acquisition and Control Systems," presented at the DOE/EERE Communications and Controls Conference, Oct. 24–25, 2002; http://www.eere.energy.gov/der/conf_on_comm.html

Buckner, M., and S. Batsell. 2001. "Mobile Ad Hoc Networks," *Sensors Magazine* **18**(1), January 2001.

Consortium for Electric Infrastructure to Support a Digital Society, CEIDS Master Plan; May 23, 2003 (DRAFT).

Lightner, E. 2002. "Distributed Energy and Electric Reliability," presented at the DOE/EERE Communications and Controls Conference, Oct. 24-25, 2002; http://www.eere.energy.gov/der/conf_on_comm.html

Mazza, P. 2005. "The Smart Energy Network: Electricity's Third Great Revolution," Website, Climate Solutions, Olympia, Wash.; http://www.climatesolutions.org/pubs/pdfs/Smart%20Energy%20PDF.pdf

Newman, Sizemore, Carreras, and Lynch. 2002. "Growth and Propagation of Disturbances in a Communication Network Model," *Proceedings of the 35th Hawaii Conference on System Sciences*.

Noecker, N. 2002. "Energy Hub: Integrating the Future," Presented at the DOE/EERE Communications and Controls Conference, Oct. 24–25, 2002; http://www.eere.energy.gov/der/conf_on_comm.html

Yoshida, J. 2003. "War Data Goes Real Time: Middleware Arises to Tame Military Networks," *Electronic Engineering Times*, Page 1, Issue 1279, July 21, 2003.

Flameless Combustion Engines in the Transition to Hydrogen

R. L. Graves,[1] C. S. Daw,[1] R. M. Wagner,[1] J. C. Conklin,[1] and V. K. Chakravarthy[2]
[1]*Engineering Science and Technology Division*
[2]*Computer Science and Mathematics Division*

Advanced internal combustion engines (ICE), fueled by hydrogen and other non-petroleum fuels, represent the nation's greatest mid-term opportunity for reducing petroleum dependence. This project is to research and demonstrate new paths to stretch the efficiency of ICEs toward 60%. Contrary to widespread opinion, combustion engines have approximately the same theoretical potential efficiency as fuel cells. Of the mechanisms that presently hold combustion engines to about 45% peak efficiency, the thermodynamic losses in combustion via high-temperature, propagating flames are prominent. Exploring "flameless" combustion for maximum efficiency will be our focus. Considered thus far for their emissions benefits, new, low-temperature combustion modes have not been studied nor exploited for efficiency benefits to a significant extent.

Advanced ICEs are central to the nation's opportunity for mid-term petroleum savings while fuel cells and hydrogen supply develop. To maximize the benefits, combustion engine efficiency must move beyond present levels. In spite of common misconceptions, there is no fundamental barrier to ICEs reaching 60% efficiency. Our objective here is to define engineering paths to actually achieve this efficiency for both transportation and distributed power generation.

Our research focus is on reducing combustion exergy losses by application of flameless combustion methods. These losses result from the entropy produced by unrestrained chemical reactions (e.g., reactions far from chemical equilibrium in the flame front that dissipate 20–25% of the fuel energy as exhaust heat instead of work). This is one of the largest losses and remaining barriers to substantially higher engine efficiency. Theoretical calculations indicate that if ICE combustion reactions could be slowed and spatially distributed, fuel efficiencies would be enhanced. Our technical approach has focused on three paths:

- Exploitation of recently discovered volumetric combustion modes in piston engines;
- Optimization of time scales of work extraction and combustion reactions; and
- Utilization of 'chemical looping' (oxygen storage to stage the combustion reactions).

A collaborative team of combustion and thermodynamics experts was formed to help coordinate the research. This team consists of ORNL staff and prominent engine researchers from key universities, industry, and Sandia National Laboratory. In December 2004, the team met at ORNL and concurred with our objectives and approach.

To support theoretical calculations and analysis of experimental data, we constructed a set of computer codes for evaluating thermodynamic properties and equilibrium states of gas and gas-solid combustion systems of interest. Although there are commercial combustion codes for similar calculations in certain contexts, none were sufficiently flexible for the desired 2nd Law of Thermodynamics analyses of arbitrary combustion trajectories. These tools are now available for any type of combustion exergy modeling, including parallel models and models of previously unknown types of combustion. A low-dimensional multi-zone ICE model for simulating the reaction and heat transfer processes in non-standard combustion modes was developed. This code extends our capability to analyze experimental data and study novel combustion modes and control strategies. The code is also tailored to interface with commercial engine software that address auxiliary systems such as fuel injection and air handling. A license for Ricardo WAVE software was obtained to provide the latter.

The new analytical tools were initially used for study of the effects of combustion preheat and exhaust gas recirculation on exergy losses, resulting in a concept for a physically realistic isobaric combustor and gas turbine system with approximately 70% efficiency. Chemical looping combustion (CLC), a relatively new concept for staging combustion, was identified to have theoretical efficiency and emission advantages, but numerous technical hurdles. A conceptual embodiment for a CLC engine was developed, and a patent disclosure is in preparation.

Collaborations were established with the University of Wisconsin and Texas A&M University to evaluate global energy distribution in piston-cylinder engines. Our collaborators are utilizing their own models that have been extensively tested and published. The collaboration provides the opportunity to validate our in-house piston-cylinder code and enables a greater variety of approaches to be studied.

Advanced Processes for Nuclear Fuel Microspheres

D. F. Williams,[1] G. D. Del Cul,[1] R. D. Hunt,[1] T. L. White,[2] T. N. Tiegs,[3] and F. C. Montgomery[3]
[1]*Nuclear Science and Technology Division*
[2]*Fusion Energy Division*
[3]*Metals and Ceramics Division*

Better processes are needed to make the particle fuel required for reactors that can create a hydrogen future. At present, toxic solvents are used as heat transfer media to make particle fuel. A solvent-free process that uses microwave heating of the fuel microsphere is being developed in this project. Fuel fabrication steps can be developed inexpensively in a clean environment with non-radioactive surrogates before use with uranium. This can improve nuclear fuels by allowing much more rapid and extensive technical development and simpler initial irradiation testing and post-irradiation examination of the non-fissile fuel materials. Our vision is to develop a new microwave process for making fuel by a combination of mathematical modeling and experimental testing, with hafnia selected as the surrogate particle to develop.

The vision of a hydrogen economy is a primary goal in DOE. High-temperature nuclear fuels are needed for this future. Making high-quality fuel by sustainable and economic processes is a key to a successful fuel technology. A cleaner, more reliable, and more automated process for making microsphere fuel using microwave heating that eliminates all solvents will be a major advance. This project specifically addresses the call for support of Next-Generation Nuclear Systems.

The internal gelation process for making fuel particles can be significantly improved by substituting microwave heating for the toxic solvents now used for heat transfer. Microwave heating of droplets is extremely uniform and rapid, and we expect that (a) the resulting gel-microstructure will be much more uniform than that generated by conventional processes and (b) new materials which require a faster precipitation step will be attained by this method, which can be applied to make inorganic materials that span nearly the entire periodic chart. This process has the potential for many applications, and this project will develop the knowledge needed to design such a process for any number of applications.

Both mathematical modeling of the process and experimental testing is necessary to advance this technology. A combination of microwave energy deposition and heat-transfer/reaction-kinetics modeling is being used to guide the experimental program, interpret the results, and provide a design basis for scale-up. However, the application of microwave methods to micro-drops is a relatively new area. The benefit of this type of heating is the speed and uniformity that can be achieved, most especially for small drops or particles. There is also a degree of complexity in microwave heating that requires we understand, measure, and model the transitions in dielectric susceptibility that occur as we transform the material by processing. Basic information on dielectric response is needed to specify the microwave heating regime, and to optimize the process. The methods we develop to measure and model these changes will permit control of the heating process and the material properties. This is the key piece of information necessary to develop models that will allow this technology to be deployed in an industrial setting.

The following items have been developed: (a) a microwave drop-heating and processing model for microparticle synthesis—including new dielectric measurements on solutions of zirconium, hafnium, and uranium; (b) a prototype cavity design and experimental-rig optimized for microparticle synthesis by microwave heating; (c) a microsphere washing treatment that produces much higher quality hafnia spheres; (d) design and installation of a new apparatus for measurement of the mechanical properties of the microspheres; and (e) design and installation of a continuous feeding system for internal gelation microparticle synthesis. Testing of the prototype cavity with simulant liquids showed that microwave heating was effective and in close agreement with our model predictions. The model and our measurements have also demonstrated that this method of microwave heating can be favorably applied to other continuous heating processes. We are proceeding this year with microwave-driven internal gelation experiments.

We expect that there will be a very significant spin-off into non-nuclear applications for this microwave technology. Catalyst and sorbent particle manufacture by a microwave method for these types of materials will be a significant advance. The potential exists to use microwave-heating for the high-temperature steps needed to make advanced ceramics.

ENGINEERING SCIENCE AND TECHNOLOGY

Seed Money Fund

Novel Pt Support for Proton-Exchange Membrane Fuel Cell Cathode and Anode Active Layer

T. J. Toops[1] and D. A. Blom[2]
[1]*Engineering Science and Technology Division*
[2]*Metals and Ceramics Division*

Fuel cells continue to show great potential as a clean energy source for both mobile and stationary power, but considerable improvements are still necessary to reach this potential, primarily with respect to cost/power ratio. This project details an alternative membrane construction for the proton-exchange membrane fuel cell (PEMFC) that will enable a reduction in the required platinum (Pt) mass, the most costly single component in the PEMFC. The key to this improvement comes from using a continuous array of aligned carbon channels for the Pt support in the electrode. The aligned carbon constitutes the active layer of the membrane assembly and when tested against the current technology demonstrated a six-fold improvement per gram of Pt at peak power. The patent-pending method that was used to synthesize the Pt support allows a high degree of dimensional variability, such that the dimensions can be tuned to reach the optimum fuel cell output in future endeavors.

Introduction

There is a growing interest in the development of alternative power sources in all areas of energy production. A field that has shown remarkable technological progress over the past thirty years is the fuel cell, particularly the proton-exchange membrane fuel cell (PEMFC). Hurdles still exist in each step of this fuel cell system, but one area that requires particular attention is the high cost of using Pt in the active layer of the anode and cathode. The chemical reactions necessary for fuel cells to generate power do not occur at the temperatures of interest (60–120ºC) without a catalyst, and Pt is the most efficient catalyst for both the hydrogen oxidation reaction in the anode and the oxygen reduction reaction in the cathode; there are currently no known cost-effective alternatives to this noble metal. The current target for a competitive PEMFC is $45/kW by 2010, with an additional goal of $30/kW set for 2015. According to an Arthur D. Little study, the current cost of precious metals alone in the present-day fuel cell is $65/kW, an estimated one-fifth of the total cost, which illustrates the necessity of marked improvement in this step alone (Carlson 2001). This project details a Pt support that is geared towards the optimization of the Pt in the fuel cell to derive the optimum power per gram of Pt used.

Technical Approach

PEMFCs are attractive because they can potentially generate more specific power (power normalized to the mass of fuel cell, e.g., W/kg) and power density (power normalized to the cross-sectional area of the electrodes, e.g., W/cm^2) than any other fuel cell. The electrical power is generated through controlled chemical reactions in a stack of fuel cells consisting of bipolar plates, catalyst-containing electrodes, and proton exchange membranes (PEM). As previously mentioned, Pt is the best available catalyst for the hydrogen oxidation reaction at the anode, which proceeds according to the following mechanism:

$$H_2 + 2Pt \rightarrow 2H\text{-}Pt \quad (1)$$

$$2[H\text{-}Pt \rightarrow Pt + H^+ + e^-] \quad (2)$$

$$H_2 \xrightarrow{Pt} 2H^+ + 2e^- \quad (3)$$

The electrons flow out of the anode through an external circuit and then to the cathode, while the H^+ proton permeates through the PEM to the cathode. They then react with O_2 according to the following stoichiometry:

$$O_2 + 4H^+ + 4e^- \xrightarrow{Pt} 2H_2O \quad (4)$$

While the H_2 oxidation reaction and mechanism is well understood, there is still not a well-established mechanism describing the O_2 reduction at the cathode, so only the overall reaction can be accurately displayed. A concern in PEMFCs is overpotential, or the loss of power through interactions that do not generate power, such as electrical resistance, reversible reactions, mass-transfer limitations, etc. In general, the number of steps in a process is proportional to the overpotential associated with the process; for instance, the overpotential in the cathode, a $4e^-$ interaction, is generally an order of magnitude higher than in the anode, a $2e^-$ interaction. Other contributions to overpotential arise from proton mobility, or diffusion, through the electrodes and PEM, and especially the transition between these phases; in fact, recent studies

have shown that the impregnation of the PEM into a small portion of the electrodes lead to a ten-fold improvement in performance because the transfer mobility of reactants was improved (Gottesfeld 1997). This finding highlights the need to consider the diffusional characteristics of the system.

The current membrane electrode assemblies (MEA) use Pt clusters (2–3 nm) dispersed on carbon black supports that have a diameter of about 0.1 μm. Carbon black (CB) is used for its high porosity and high surface area (~150 m^2/g), which enables high power densities. These Pt-coated particles are held together with a binder to constitute a 10- to 60-μm-thick active layer of the anode and cathode. Diffusion is not optimized with these Pt supports since the porous structure is highly irregular and tortuous in carbon black, and the Pt is dispersed throughout the pores. The reactant gases must diffuse into these meandering pores, and the products must diffuse out. The extent that the pore structure effects diffusion is defined as tortuosity, τ:

$$\tau = \text{actual distance molecule travels between two points/shortest distance between two points} \quad (5)$$

Tortuosity is inversely proportional to the effective diffusion of a molecule and can have a dramatic effect on the overall fuel cell efficiency if molecular transport to and from the reaction sites is a limiting factor, such as the case at high loads. In other words, since most of the gas does not diffuse to the center of the carbon black particle, the Pt in the center is not efficiently utilized, so the overall output per gram of Pt decreases. Thus, diffusion is minimized as τ approaches unity.

This project focused on the development and fuel cell demonstration of an alternative support system for this Pt-rich active layer (i.e., the layer where chemical reactions occur). The new technology is based on a recently reported method of aligned carbon nanotubule deposition in the pore structure of anodized alumina, often referred to as the template method (Martin 1996, Kyotani 1996, and Miller 2001). This technique allows the synthesis of an active layer with aligned carbon nanotubules as the Pt support (with outside diameters circa 20 nm), and it results in electrodes comprised of a continuous array of these nanotubules. These aligned nanotubules have theoretical tortuosity of unity for the entire active layer of the electrodes, which minimizes the diffusional constraints of the catalyst support. The fabrication method allows flexibility in controlling the nanotubule diameter (by selection of the alumina pore size), wall thickness (varying deposition time), and location of the Pt particles, either solely on the interior walls, or on all surfaces. This flexibility allows the fine-tuning of the support's pore structure to achieve optimal diffusion, such that the effectiveness of each Pt reactive site would increase. The details of the fabrication are patent pending (ID 1072) and cannot be fully disseminated in this report; however, it should be noted that the process involves inexpensive pyrolysis of hydrocarbons (HC) that deposit carbon nanotubules inside pores of commercially available alumina templates. These nanotubules and their application in the MEA are the fundamental difference between the current PEMFC technology and the one demonstrated in this project. The scope of the project entailed the following steps:

Task 1. Nanotubule Deposition Study
Task 2. Pt Deposition and Alumina Removal
Task 3. Characterization of Pt-coated Nanotube Arrays.
Task 4. MEA synthesis and PEM Fuel Cell testing.

The end result of this project is a direct comparison of the current technology PEMFC against the novel minimal diffusion PEMFC.

Results and Discussion

The deposition rate of carbon on the walls of the alumina pores was fully mapped out for HC pyrolysis on alumina templates, and the rates were verified with high resolution transmission electron microscopy (HRTEM) at ORNL's High Temperature Materials Laboratory (HTML). The HRTEM also verified a constant deposition rate regardless of pore size (20–300 nm); that is, the channel thickness is constant throughout the membrane. Template removal using HF was executed for a wide array of carbon supports, and the method underwent modifications to ensure the integrity of the nanotubular array. It was determined that a minimum wall thickness of 4–5 nm was necessary to ensure the mechanical integrity of the carbon nanotubular array. Using the wet impregnation technique, platinum (H_2PtCl_6 precursor) was added to the nanotubular array both before and after removal of the template. It was determined that Pt deposition before template removal was the best technique to achieve well dispersed Pt crystals; particle size and deposition was verified by HRTEM. Platinum crystals of 2–5 nm were obtained in the carbon arrays with an average particle size of 3 nm, which indicates that approximately one-third of the Pt atoms are surface atoms available for catalytic activity.

Having synthesized the active layer, it was possible to assemble the rest of the MEA with commercially available materials. Nafion® 117 (18 mm thick) was used for the proton exchange membrane, and Toray carbon paper (0.19 mm thick) was used for the gas diffusion layer. The diffusion layer, active layer, and membrane were pressed together at 1250 psig and 150ºC for 5 minutes in a Carver Press with heated platens. This results in a MEA that must be kept under high humidity to minimize disruption, since Nafion® is hygroscopic and is susceptible to curling in transient humidity environments.

To accurately compare the nanotubule array MEA to the current technology, it was necessary to synthesize an

MEA with the current technology, but using the same Pt dispersion technique and MEA assembly protocol. CB with 80-m^2/g specific surface area was used as the catalytic support, and Pt was added using the wet impregnation technique with H_2PtCl_6. HRTEM analysis of the resulting Pt/CB displayed relatively large Pt particle sizes, 5–9 nm, so when comparing the two MEAs all results were normalized to surface Pt. This results in the most accurate comparison, and due to the similarity of the MEA synthesis, allows the comparison to be made where the only variant is the geometry of the Pt support.

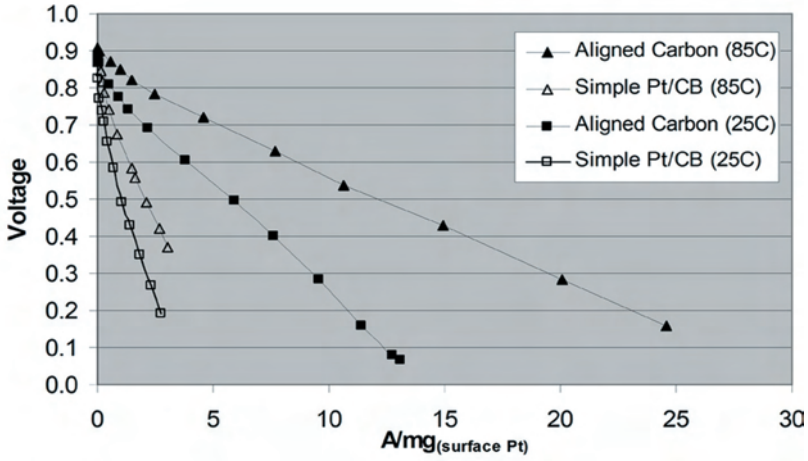

Fig. 1. I-E plot comparing the existing technology Pt support system (Simple Pt/CB) to the improved aligned carbon support. Depicts 6-fold increase in specific current at 0.4 V and 85ºC. Test conditions: 25 or 85ºC, 30 psig O_2, 28 psig H_2, steam saturated at 80ºC, 5-cm^2 cross-sectional area.

Having developed the synthesis technique for the MEAs, fuel cell testing was now possible. A miniature single-cell PEM fuel cell from H_2 Economy was obtained with a cross-sectional area of 5 cm^2. This representative fuel cell consists of a collector plate, a bipolar plate (with a serpentine pathway), and a gasket for each side of the MEA. The fuel cell was easily disassembled, so switching MEAs was trivial. H_2 and O_2 were humidified at 28 and 30 psig, respectively, by passing the gases through a sparger at 10 sccm to achieve saturation and introduced to the fuel cell through heated. The fuel cell was operated both at 25ºC, indicative of startup operation, and the generally accepted maximum output temperature of 85ºC. The most widely accepted test that indicates operation dynamics of a fuel cell is a plot of voltage versus current (an I-E plot) where resistance is applied to draw current. The higher the current is at a given voltage, the better the fuel cell is operating; that is, overpotential is minimized. The fuel cell was equipped with a resistor bank that allows application of a resistance from 0.2 to 10^6 Ω. As shown in Fig. 1, the aligned carbon support has considerably better performance than the Pt/CB electrode; at 85ºC and 0.4 V, the current generated for the novel support is 6 times greater than the Pt/CB support. Similarly, the maximum work from the aligned carbon MEA is 6.4 versus 1.1 $W/g_{(surface\ Pt)}$ for the Pt/CB MEA. These results are very promising and satisfy the proof of principle needed for the patent technology; however, we believe there is still room for further improvements that were unable to be addressed at this time. The pending follow-on funding should allow us to bring this potential to realization as well.

Benefits

Improvements in the PEMFC is a key thrust to DOE's Energy Efficiency and Renewable Energy (EERE) and this project ties directly into this area which is the likely prime mover for FreedomCar. It is relevant to the energy resources and the environmental quality missions of DOE. Many other federal agencies are investigating the usefulness of PEMFCs. The primary barrier of which is their high cost. If this success aids the implementation of PEMFCs as a viable power source, multiple other federal agencies (Department of Defense, Department of Transportation, etc.) could benefit.

The results of this project have been disseminated throughout ORNL, and Tim Armstrong (ORNL's representative for EERE's Hydrogen, Fuel Cells and Infrastructure Technologies Program) further distributed the results to DOE Headquarters. The new project has been included in ORNL's Annual Operating Plan FY 2005 that is currently pending Congressional action. Other contact has been made with industry, although the proprietary nature of the project tends to inhibit full cooperation; however, a non-disclosure agreement is in place with United Technologies Research Center.

References

Carlson, E. J., J. Thijssen, S. Sriramulu, G. Stevens, and S. Lasher. August 2001. Ref 49739, SFAA No. DE-SCO2-98EE50526, Topic 1-Subtopic 1C.

Gottesfeld, S., and T. A. Zaodzinski. 1997. In *Advances in Electrochemical Science and Engineering* **5**, 195, R. C. Alkire, H. Gerischer, D. M. Kolb, C. W. Tobias (eds.), Wiley-VCH, Weinheim, Germany.

Martin, C. R. 1996. *Chem. Mater.* **8**, 1739.

Kyotani, T., L.-F. Tsain, and A. Tomita, *Chem. Mater.* **8**, 2109 (1996).

Miller, S. A., V. Y. Young, and C. R. Martin. 2001. *J. Am. Chem. Soc.* **123,** 12335.

High-Speed Decay Lifetime Analysis Using Field-Programmable Gate Arrays

D. D. Earl
Engineering Science and Technology Division

This project aimed to develop a high-speed, user-configurable circuit for performing high-speed computing of exponential rise and decay lifetimes. For a diverse range of sensing techniques (such as phosphor thermometry, molecular fluorescence lifetime spectroscopy, etc.), the speed at which this mathematical operation can be performed is often the key factor limiting a sensor's achievable measurement rate. Because of the varied analysis methods associated with decay-rate measurements and the low-volume demands of the average research consumer, a generalized, user-configurable, lifetime measurement, digital signal processing (DSP) circuit suitable for laboratory use did not exist before this research. To the author's knowledge, we are the first group to demonstrate a DSP, configurable though VLSI Hardware Description Language, that performs high-speed, single-pulse lifetime measurements using field programmable gate arrays (FPGAs). Measurements on simulated phosphor thermometry data revealed a waveform analysis time of 10 microseconds and a lifetime measurement accuracy of 7% or better (depending on averaging). Application to other sensing techniques is anticipated as a future use of this technology.

Introduction

Computing the lifetime of an exponentially rising or decaying signal is a common calculation associated with various non-contact measurement techniques. For a diverse range of sensing techniques (such as phosphor thermometry, molecular fluorescence lifetime spectroscopy, etc.), the speed at which this mathematical operation can be performed is often the key factor limiting a sensor's achievable measurement rate. Unfortunately, it is this limitation that prohibits decay-rate sensors from investigating and monitoring highly dynamic processes. The investigation of some of these dynamic processes (i.e., ultra-fast surface heating/cooling, lattice energy exchange mapping, etc.) represents some of today's most exciting and promising research areas. Because of the varied analysis methods associated with decay-rate measurements, and the low-volume demands of the average research consumer, a generalized, user-configurable lifetime measurement DSP circuit suitable for laboratory use did not exist at the start of this research. We endeavored to develop the first DSP, written in VLSI Hardware Description Language, to realize high-speed, user-configurable, single-pulse lifetime measurements using field programmable gate arrays (FPGAs). By targeting low-cost, re-programmable, and commercially available FPGA prototyping boards, we aimed to provide a flexible, high-speed measurement platform accessible to researchers in a variety of fields. The results of these efforts and the immediate application of the developed technology to established sensing techniques, based on decay lifetime measurements, are presented and discussed in this report.

Technical Approach

Exponentially rising or decaying lifetime measurements are a common calculation associated with various measurement techniques. Phosphor thermometry, for example, accurately measures surface temperature by analyzing the fluorescent decay lifetime of certain temperature-sensitive phosphor coatings. Unfortunately, the mathematics associated with an exponential fit to real data can be computationally challenging, especially when signals exhibit a superposition of differing decay lifetimes. The speed at which this mathematical operation can be performed is often the key factor limiting a sensor's achievable real-time measurement rate. To provide the necessary computational power, without limiting data analysis options, a PC-based data acquisition system is often the only feasible option for laboratory investigations. Unfortunately, the sluggish measurement rates of a PC-based system (<10 measurements/second) limit the decay-rate sensor to monitoring only slowly varying or static processes. With much of today's material research and sensor development involving highly dynamic processes, an improved data-analysis platform is needed to enhance the applicability and potential of these unique sensing techniques.

Using field programmable gate arrays, it is possible to develop a parameterized DSP algorithm, written in VLSI Hardware Description Language (VHDL), that can realize high-speed, user-configurable lifetime measurements. Because FPGAs are re-configurable microcircuits that can be programmed (and reprogrammed multiple times), it is possible to realize the complex digital circuitry required for this type of calculation. Although FPGAs are generally slower than application-specific ICs (ASICs), they still

provide significant hardware acceleration (1000–10,000×) over PC-based systems while also permitting design modifications. The high computational speed and inherent design flexibility of an FPGA-based data analysis system made it the ideal platform for enabling decay-rate sensors to investigate dynamic processes. The details and results of this development are described in the following section.

Results and Discussion

An Altera DSP development board was used as the platform for developing the high-speed decay lifetime analysis system. Although the development board provided many multi-purpose inputs and outputs, additional circuitry was needed to condition input signals from typical optical detectors and output signals to related instruments. Therefore, an instrument was built to house all of the periphery components, and the completed instrument is shown in Fig. 1.

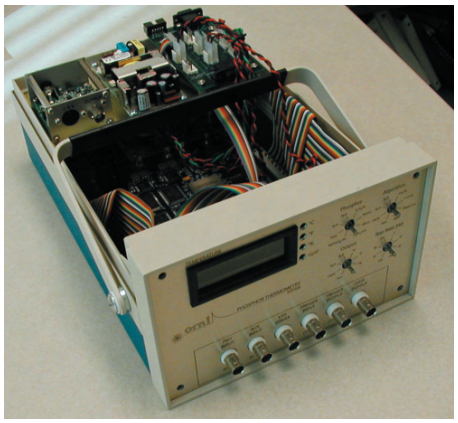

Fig. 1. High-Speed Decay Lifetime Measurement System.

The system was capable of being configured for a number of sensing applications but was initially targeted at phosphor thermometry measurements only. This decision was made because of the ease of access to all of the detectors and data related to this measurement technique. The completed hardware was first used with a Hamamatsu PMT signal that produced a 0–1 volt signal in response to a exponentially decaying optical signal. Unfortunately, the early results revealed a deficiency in the Altera prototype board associated with the data acquisition circuitry and prohibited the direct measurement of the PMT signal. Apparently, the Altera board was improperly designed and possessed an A/D circuit that could only digitize voltages between 1 and 2 volts. Efforts to offset the PMT voltage without distorting the high-speed signal were not successful. As a workaround, the PMT data was first recorded by an oscilloscope and then uploaded to the on-board memory in the Altera FPGA. This workaround allowed us to expose the chip to a very true representation of the real world signal without further development of the hardware. The result was a measurement of the lifetime using an exponential fit routine previously written in VHDL and downloaded into the FPGA. The fit was performed on ten waveforms (each an average of 16 acquired signals) taken at the same temperature and using a fitting region that encompassed all of the signal lying between 10% and 90% of the peak inverted signal. The average measured lifetime was 12.6 msec with a standard deviation of 0.9 msec. This equated to a drift of about 7% between measurements. Although this error is much higher than desired, the error appeared to be strongly tied to the varying noise in the waveform. If a greater number of averages of the acquired signal had been performed, as is commonly done in phosphor thermometry, it is very likely that the standard deviation would have been reduced.

With additional simulated data, it was confirmed that the shortest lifetime measurement that could be measured was 500 nsec, which required a computation time of approximately 10 microseconds (when driving the FPGA through a PLL with a five time multiplied clock). This means that the measurement rate for the circuit is approximately 10,000 samples per second (with no averaging). This high-speed sample rate, combined with the flexibility of the technology, should result in an excellent platform for the future evaluation of high-speed temperature processes.

Benefits

With future improvements to the Altera prototype board's A/D offset, this technology could have immediate application to high-speed and 2-D phosphor thermometry research. Agencies such as DARPA, NASA, and DOE have repeatedly expressed interest in making high-speed, non-contact measurements of high-temperature environments and surfaces (i.e., in situ turbine blade measurements, real-time steel fabrication diagnostics, high-accuracy wing surface temperature measurements, etc.). A good working relationship with NASA and DOE sponsors will be leveraged in the future to identify immediate needs and applications.

High Effective Hydrogen Storage Density

B. S. Richardson[1] and J. F. Birdwell[2]
[1]*Engineering Science and Technology Division*
[2]*Nuclear Science and Technology Division*

Proof-of-principle testing has been performed to evaluate the efficacy of recycling water from a system consisting of a sodium borohydride hydrolysis reactor and a power generator (fuel cell or internal combustion engine). The ultimate goal of the project was to demonstrate that sufficient quantity of water can be recovered from the hydrogen-releasing reaction and combined with water produced by hydrogen oxidation during power generation so that no additional water is required to sustain the reaction. Preliminary experiments were performed to quantify the reaction rate and to verify the suitability of various catalysts for use in water recycle tests. Results of these experiments were used to design two reactors that were used to measure the amount of water that could be recovered for recycling. Proof-of principle of the water recycle concept was demonstrated in bench-top experiments, showing that sufficient amounts of water can be recovered to significantly increase the effective hydrogen storage density.

Introduction

The objective of this project was to conduct proof-of-principle testing demonstrating recycle of both unreacted and reaction product water from the hydrolysis of sodium borohydride such that no additional water would be required to sustain the reaction. The ability to achieve the stated objective is key to the feasibility of a hydrogen generation system based on hydrolysis of alkaline borohydrides. The hydrogen-derived power system concept is based on the coupling of a sodium borohydride reaction system, which releases hydrogen, with a fuel cell or internal combustion engine, in which the hydrogen is oxidized to water in the process of generating energy. The concept is further based on the hydrolysis of sodium borohydride in aqueous solution, in which water is present in excess of the stoichiometric amount required to accomplish the reaction. It is proposed that, by recovering the unreacted water fraction and by recovering the water produced by the oxidation of reaction-product hydrogen, only sodium borohydride needs to be added to the reactor to refuel the system. In this manner, the effective hydrogen storage density of the power system is double the hydrogen fraction in sodium borohydride, since equal quantities of hydrogen are released from the borohydride and reactant water, as shown in Eq. (1).

$$H_2 \text{ Generation: } NaBH_4\,(aq) + 2H_2O \rightarrow 4H_2 + NaBO_2\,(aq). \quad (1)$$

Enabling objectives were quantification of the reaction rate and evaluation of reaction catalysts. Meeting these objectives provided the design basis for the proof-of-principle water recycle experiments.

The hydrolysis reaction takes place spontaneously according to Eq. (1) but does not proceed to completion due to the increasing pH of the reaction solution. This increase in pH results from the formation of the strongly basic metaborate ion. Therefore, the spontaneous reaction can be suppressed by the addition of base to the starting solution. Conversely, the reaction can be accelerated by the addition of an acid to the system. Alternatively, the reaction can be accelerated and sustained to completion by the use of metal-salt catalysts. Ruthenium catalyst was selected for use in the reported work based on previously reported favorable results using ruthenium chloride (Brown 1962).

In actual practice, the salt produced in the reaction of Eq. (1) is hydrated, with the number of water molecules of hydration determined by the temperature at which the exothermic reaction occurs. If operated at sufficiently high temperature (>105°C), the reaction product is a hemihydrate ($NaBO_2 \cdot 0.5H_2O$). The rationale behind the proposed effort is that if the reaction is operated at sufficiently high temperature, and sufficient excess water present in the vapor product stream is recovered by condensation, and sufficient water is recovered from the power generation step, then there will be no need for addition of reagent water. This is feasible since the hydrogen contributed to the process by the hydrolysis of sodium borohydride is converted to water during power generation, resulting in a net production of water across the complete system. If successful, the effective hydrogen storage density is approximately 21%, based on the need to replace only the sodium borohydride reagent (which is approximately 10.5% hydrogen by weight), and based on the contribution of one-half the hydrogen output from reagent water.

Technical Approach

As stated previously, the spontaneous hydrolysis reaction can be suppressed by the addition of a base to the feed solution. Base suppression is overridden by the use of a catalyst; hence, the reaction can be controlled by adding or removing catalyst from the reaction. Therefore, the most desirable reactor configuration is the one that allows rapid contact and separation of catalyst and reactants. This is most easily accomplished in a flow-through reactor, whereby the reaction is initiated by starting the flow of reactants and stopped simply by suspending the flow of reactants.

Two sets of experiments were performed in support of reactor design. In the first, the effectiveness and physical stability of ruthenium attached to two different substrates, carbon and alumina, were evaluated. After selecting a catalyst form based on test results, hydrolysis rate determinations were made as a function of reaction temperature.

Catalyst Test

An issue identified in preliminary testing was the stability of the catalyst material. In these tests, some breakage of a catalyst consisting of ruthenium on carbon chips was observed. It is hypothesized that breakage was due to the rapid evolution of gas inside catalyst micropores. As an alternative, use of ruthenium adsorbed onto alumina spheres was investigated. Alumina spheres loaded with 1% and 2% (by weight) ruthenium were obtained. A quick examination of the effectiveness of these catalysts found that the rate of hydrogen generation achieved using the less loaded alumina was extremely low, and this catalyst was dropped from consideration.

Four samples of the 2% ruthenium on alumina catalyst were weighed and placed into wire mesh packets. Each packet was placed into a beaker containing 25 wt % aqueous sodium borohydride solution. After reaction, each packet was removed from its beaker, was thoroughly rinsed with demineralized water, and was dried in a laboratory furnace. Each catalyst sample was weighed to determine loss of fines due to breakage, after which each packet was opened and the catalyst was inspected visually. A similar procedure was performed with four samples of ruthenium catalyst adsorbed onto carbon.

Rate Testing

Prior rate evaluations using ruthenium on carbon were performed using a batch reactor configuration with no control of the reaction temperature. In order to determine rate under flow conditions, rate determinations were performed using a column packed with a thin layer of catalyst such that complete conversion of reactants was not achieved. In this manner, the reactants are not depleted to such an extent that the rate is inherently controlled by either reaction kinetics or the rate of diffusion of reactants to the catalyst surface. (Results from the previous batch reaction evaluations indicated that the rate was not affected by changes in the initial feed concentration; hence, the rate expression is zero order with respect to concentration.)

The rate of hydrogen evolution was measured over a range of flow rates to determine if the rate controlling mechanism was diffusion or catalyst-surface related. To facilitate calculation of temperature-dependent rate constant, data (Fig. 1) were collected at various temperatures (nominally 25°C, 30°C, and 35°C), which were maintained by submerging the reactor in a temperature-controlled water bath. Hydrogen evolution was measured by water displacement. Experiments were performed both with and without preheating of the feed to the reaction temperature.

Reactor Design

Two different reactors were fabricated and tested. The reactor systems included the reactor, a pump, and a vessel to catch the reaction by-products. The first reactor was made from a 4-in.-long, 1-in.-diameter stainless steel tube, with press-fit stainless steel top-end cap and mounted onto a stainless steel catch vessel using a compression

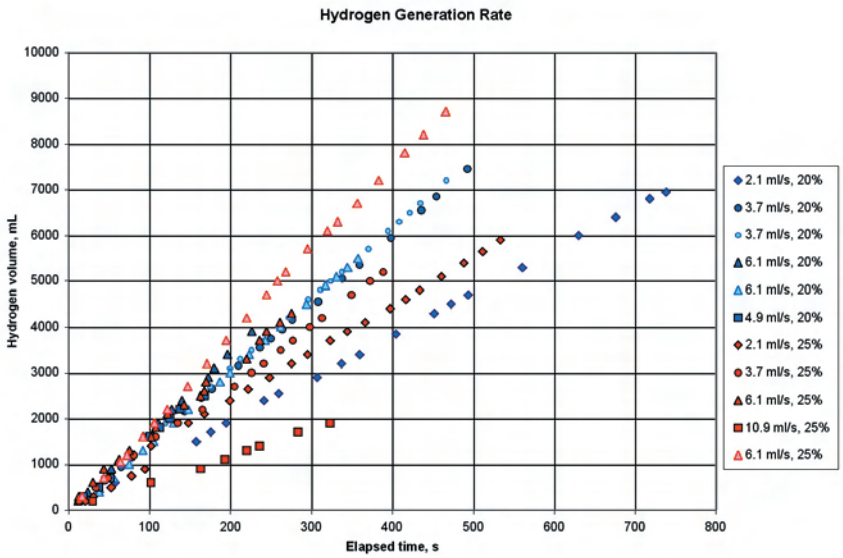

Fig. 1. Hydrogen generation rate data using a differential reactor.

fitting. The second reactor was made from 3.5-in. × 1-in.-diameter polycarbonate tubing, mounted inside a 2-liter polycarbonate catch vessel. The amount of catalyst placed in the reactors was based upon the results of the rate testing. The target power output chosen for these experiments was in the 200- to 500-W range.

Water Recovery Testing

Water recovery determinations were made only for the reaction portion of the previously described power generation system on the basis that reactor water recovery is the limiting factor. A reactor system consisting of a feed container, metering pump, packed-bed reactor, product catch tank, condensate collection tank, and desicant bed was used. The reactor and product catch tank were insulated to assist in maintaining an elevated reaction temperature using only the heat released by the reaction. The condensate collection container was submerged in an ice bath. The desicant bed served as both a final water trap and an indicator of the effectiveness of the ice bath in condensing water from the product stream.

Tests were performed after first weighing all system components. The feed and condensate collection vessels were placed on weigh tables in order to obtain real-time mass measurements. Water recovery efficiency determinations were made by recording feed and condensate masses at the start and end of a period of steady-state reactor operation, and comparing the mass of water collected to that which should be present in the product based on reaction stoichiometry.

Results and Discussion

Catalyst Test

Qualitative evaluation of catalyst performance obviated the need for quantitative analysis. Alumina catalyst spheres were observed to fracture readily during the evolution of hydrogen gas. Examination of the fractured spheres indicated that ruthenium was not loaded uniformly through the microporous sphere structure, the black coloration indicating the presence of ruthenium was absent from the majority of the spheres' cross sections. While some breakage of carbon catalyst pieces was observed, the weight loss was minimal. Since development of an optimal catalyst was not within the scope of the proposed work, the decision was made to proceed with rate and water recovery testing using the carbon-supported ruthenium catalyst.

Rate Testing

Rate determinations indicated an increase in reaction rate with increased temperature. Changes in feed flow rate did not result in any observed change in hydrogen evolution rate. The latter observation indicates that the rate of diffusion of reactants to catalyst sites does not limit the rate of hydrogen production, nor is it likely that rate is controlled by the rate at which products are carried away from the catalyst. Results from prior batch tests indicated no change in reaction rate in response to increased reactant concentration in the feed solution. These previous results did indicate an increase in the rate of gas formation in response to increased loading of catalyst on the substrate. Indications that the rate of hydrogen evolution is affected only by reaction temperature and catalyst loading imply that the rate of the process is controlled by the rate of reaction at the interface and the availability of reaction sites.

Using the rate data obtained and estimating the reaction activation energy using the heat of reaction, a rate constant was determined. This value was used to calculate the quantity of catalyst required to achieve complete conversion of reactants over a range of flows to be used in water recovery tests and at a reaction temperature sufficiently high to result in the production of the hemihdyrate form of sodium metaborate.

Water Recovery Testing

Three separate sets of water recovery experiments, each consisting of multiple, distinct reaction cycles, were performed. In the first set of experiments, the reactor housing and the product catch vessel were made from stainless steel. This proved problematic, as the considerable mass of the system resulted in the need to operate for an extended period of operation in order to generate the heat required to attain the desired system test temperature. Subsequent tests were performed using a polycarbonate reactor and product collection vessel, to minimize system heat capacity. In all tests, the reactor and product collection tank were insulated to minimize heat loss, thereby enhancing vaporization of unreacted water.

Water recovery varied from cycle to cycle, with recovery percentages ranging from just over 60% to over 93% of the total water available. Assuming the efficiencies of recovering unreacted water from the reactor product stream and recovering product water from the fuel cell are equal, and the use of a 25 wt % $NaBH_4$ feed solution, approximately 81% recovery is required to eliminate the need for the addition of supplemental water. Based on this value, the results of the experiments are mixed when recovering sufficient water for full recycling (no additional water added) is the criterion for success. Lower efficiency results correspond to tests during which temperature indications at the reactor outlet and from the product collection vessel were lower than desired. This condition is inherent in the design of the test assembly. If a desired reaction temperature is not reached relatively quickly, an appreciable mass of water accumulates in the product

collection tank. This mass serves as an additional sink for heat generated by the reaction, making attainment of the target reaction temperature increasingly difficult. In actual practice, the problem can be mitigated by addition of instrumentation and equipment to drain start-up water from the product collection chamber. In addition, the design and materials of construction of the reactor system can be optimized to reduce the energy required to reach the target reaction temperature, thereby accelerating attainment of the desired operating temperature. These corrective actions were not pursued during performance of the seed money project due to time and cost constraints, and because the problem did not preclude successful demonstration of the proposed concept.

Benefits

The proposed hydrogen storage concept, based on using sodium borohydride, has the potential for reaching 21 wt % storage of hydrogen, thus exceeding the current Department of Energy objective by a factor of 3.5, and the automobile industry target of 12 wt % H_2 by approximately 75%. This research will position Oak Ridge National Laboratory for potential contributions to the DOE Hydrogen, Fuel Cells, and Infrastructure Technologies Program and the FreedomCAR and Hydrogen Initiative Program (expansion of the FreedomCAR Program), as well as Department of Defense program offices. In addition, there is the potential for cooperative efforts with commercial companies that are currently investigating sodium borohydride as a hydrogen source.

References

Brown, H. C., and C. A. Brown. 1962. *Journal of American Chemical Society* **84**, 1493–1494.

Super-Hydrophobic Nanopost Glass

B. R. D'Urso and J. T. Simpson
Engineering Science and Technology Division

A superhydrophobic surface is a hydrophobic material enhanced by surface nanostructure. Energetically, water prefers to bind to itself instead of the superhydrophobic surface so strongly that a layer of air separates most of the interface between the water and superhydrophobic surface. We have demonstrated a superhydrophobic surface made of glass. Superhydrophobic materials have numerous potential applications including drag reduction for watercraft, water-repellent surfaces, and improved energy efficiency.

Introduction

For simple flat solid materials, the interaction of water and the material can be classified as hydrophilic or hydrophobic. This can be quantified by examining the contact angle of a drop of water with the surface. The contact angle is the interior angle at which the surface of the water drop meets the solid surface. If the contact angle is less than 90 degrees, the material is said to be hydrophilic and indicates that the liquid prefers to bind to the surface more than itself. If the contact angle is greater than 90 degrees, the material is said to be hydrophobic and indicates that the liquid prefers to bind to itself more than the surface. This 90 degree point is the point at which the liquid has no preference to whether it binds to itself or binds to the surface. The largest water contact angle obtained on a simple flat material is approximately 120 degrees, which occurs for a fluorinated polymer (Teflon®) surface. In principle, the most hydrophobic flat surface would consist of close-packed CF_3 Groups (Nishino 1999).

Materials having a larger water drop contact angle can be created by structuring the surface. If the contact angle exceeds 150 degrees, the surface is described as superhydrophobic. The surface of the lotus leaf is a naturally occurring example of a superhydrophobic surface. The lotus leaf surface consists of a waxy material with micron-scale protrusions and nanometer-scale roughness. The surface structure amplifies the hydrophobic nature of the waxy surface (Barthlott 1997).

Superhydrophobic surfaces display surprising properties, such as dewetting, where water rolls off the surface leaving it completely dry. Pinning of water drops on a superhydrophobic surface may be so weak and drop rolling friction so reduced that it is difficult to balance a drop on the surface. Drops of water impacting a superhydrophobic surface appear to bounce off like rubber balls.

Technical Approach

The lotus leaf can serve as a model for synthetic superhydrophobic surfaces. As with the Lotus leaf, synthetic superhydrophobic surfaces generally require a surface structure with protrusive features or high-aspect-ratio roughness. The surface may then be coated with a hydrophobic material such as a fluorinated polymer. Teflon AF®, an amorphous form of Teflon® which can be applied to a surface in solution, is a commonly used hydrophobic surface coating. The combination of the structured protrusive surface features and the hydrophobic coating creates a superhydrophobic surface.

When water is placed on a superhydrophobic material, it is ideally suspended on the tips of the protrusive features, leaving a layer of air separating most of the material from the water. The size scale of the surface features is critical in determining the pressure tolerance of the material. The finer the scale of the features, the more pressure can be applied to the water before it penetrates into the structure. Pressure tolerance is important for use underwater and for resisting wetting by rapidly moving water drops.

We chose to make a superhydrophobic surface starting with glass because it is easily worked with, has well-characterized properties, and can potentially be used in circumstances where optical transparency is important, for example on windshields.

Results and Discussion

We successfully created several new superhydrophobic surfaces on glass. A drop of water on one of these surfaces is shown in Fig. 1. As expected, the surfaces are so superhydrophobic that it is difficult to balance a drop of water on the surface. In order to take the photograph in the figure, the tip of the pipette used to produce the drop of water had to be left in contact with the drop to hold it in place.

Characterizing highly superhydrophobic materials is challenging because the usual method of characterizing

Fig. 1. A photograph of a drop of water on a superhydrophobic surface, illuminated from behind. The volume of the drop is approximately one microliter. The vertical tube in the upper right is the tip of a pipette holding the drop in place.

a surface, measuring the contact angle, is a poor measure of the superhydrophobic surface. The difficulty is that as the binding energy of the drop of water and the surface approaches zero, the contact angle approaches 180 degrees, where the measurement process essentially breaks down. The contact angle is measured by photographing the profile of the drop and fitting it to a known drop shape. The difficulties can be seen even in the simplest case, in the absence of gravity. To measure the contact angle, the radius of the drop and the distance from the center of the drop to the substrate must be determined. When the contact angle is near 180 degrees, even a small error in determining the distance to the substrate may result in a large change in the measured contact angle. The lighting angle, camera angle, substrate curvature, and reflections off the substrate can all lead to significant uncertainty in the substrate position. When all these problems are considered, it appears unlikely that the contact angle can be directly measured with an uncertainty smaller than 5 to 10 degrees with a contact angle near 180 degrees. Unfortunately, this uncertainty is too large to allow comparison between high-performance superhydrophobic surfaces.

Our superhydrophobic materials had visual contact angles too close to 180 degrees to use the standard contact angle methodology. So, in order to quantify the quality of our superhydrophobic materials, we employed the use of a state-of-the-art micro-balance to measure the "stickiness" of water drops on our material surfaces. This device was capable of consistently measuring micrograms of weight (which could then be converted to an associated force). By lowering water drops onto the microbalance surface (via a pipette) and then carefully measuring the force required to remove the drops from the surface, we determined the stickiness of our materials. These stickiness force measurements were then converted into equivalent contact angle measurements. Depending on the particular material measured, we calculated equivalent contact angles ranging from 175 degrees to 179.9 degrees. Based on these results, the superhydrophobic materials made as a result of this seed project appear to be of higher quality and performance than any other superhydrophobic material yet reported in the literature.

Benefits

Superhydrophobic surfaces exhibit properties with many potential applications. The most obvious property of the surface is dewetting, where water rolls off the surface leaving it completely dry. This could be used for windshields in rain, for anti-condensation coatings in refrigerators and heat pumps, etc. Superhydrophobic surfaces can also be self-cleaning. The reduced friction of water drop movement on the surface may be useful for droplet-based microfluidics applications, especially when combined with electrowetting on dielectric (EWOD), where the superhydrophobic property can be effectively turned on and off electrically to manipulate droplets. The most demanding potential application is viscous drag reduction, where a superhydrophobic surface on a watercraft could lead to reduced drag in bulk water. The applications for a drag-reducing surface are extremely broad, ranging from surface water craft to torpedoes to submersible watercraft. The possible fuel savings from decreasing drag on watercraft by even a few percent would of enormous interest to DOE and the Navy.

References

Nishino, T., et al. 1999. "The Lowest Surface Free Energy Based on -CF3 Alignment," *Langmuir* **15**, 4321.

Barthlott, W., et al. 1997. "Purity of the Sacred Lotus, or Escape from Contamination in Biological Surfaces," *Planta*. **202**, 1.

Development of Innovative Triboluminescence Approach for Low- and Hyper-Velocity Impact Damage Sensing

S. W. Allison and S. M. Goedeke
Engineering Science and Technology Division

The foundation for development of triboluminescent (TL) impact sensors using phosphor materials is described here. Though a variety of uses are envisioned, the present effort targeted a potential space structures application where impacts ranging from a few m/s to about 10 km/s are expected. The basis of the method is that triboluminescent phosphor coatings emit light when struck by projectiles. To investigate the effects at the higher speeds, tests were performed at a hypervelocity gun facility at NASA Marshall Space Flight Center in Huntsville, Alabama. These tests showed preliminary evidence of light emission at a velocity of 6 km/s. To address possible effects of the radiation environment of space on the triboluminescent material, a series of samples were irradiated at Alabama A&M University's Center for the Irradiation of Materials. Spectral analysis, thermal cycling analysis, and low-velocity impact studies quantified the response. To summarize, increases in dose affected the triboluminescence in several ways. However, the effects could be reversed somewhat with thermal annealing.

Introduction

Structures in space are subjected to wide temperature swings, ionizing radiation, and orbital debris. Of these, orbital debris can have the most immediate and catastrophic influence on a space mission. This debris may be very small and difficult to detect as it approaches the structure; but, in near-earth orbit, this material can be traveling up to 10 km/s. At these velocities, even the smallest particles have high impact energy. An embedded sensor that could detect the location and severity of impacts on the structure could be used to determine the remaining life of that structure and direct repair missions.

In a similar light, President Bush announced recently a new initiative for Americans to return to the Moon and go to Mars during the first third of the 21st century. For this effort, one needed technology is a computer-based collision detection system for high-speed space debris. One way to create these sensors is to use triboluminescent coatings comprised of phosphor as the active element for the impact detection system. Triboluminescence is a phenomenon that has been known for centuries and is the emission of light due to crystal fracture at the microscopic level. To develop this technology into a useful sensor, some initial steps must be taken. The results summarized in this report are the first actions toward this goal.

Technical Approach

For low-velocity triboluminescence, a simple drop tower may be utilized in which a steel ball falling a known distance onto a sample produces the emission. Previous tests at ORNL using a drop tower similar to that described in Womack 2004 showed a well-behaved dependence of triboluminescence signal with impact energy. This served as justification to proceed with the subsequent hypervelocity tests at the NASA facility.

The hypervelocity gun installation is designed to accelerate projectiles to speeds expected of orbital debris. It is thus a perfect test bed for exploring and developing impact sensing concepts. Only slight modification to the usual NASA test apparatus was necessary for triboluminescence testing. The standard aluminum targets were painted with ZnS:Mn phosphor. Photodiodes situated inside the gun bore but out of the projectile path viewed the front and back impact areas, converting the emission into its electrical analog. This signal was amplified and recorded on a digital oscilloscope. Further technical details are contained in Bergeron 2004 and Bergeron 2005.

For a material to be qualified for space applications, it must survive the radiation environment. In order to gain a better understanding of the effect of radiation on triboluminescent coatings, tests were conducted at the Center for Irradiation of Materials at Alabama A&M. The radiation source was a 3-MeV proton beam accelerator. Once irradiated, the spectrum of each sample was determined. Next, the samples were placed into a calibration furnace and the fluorescent decay time was measured as a function of temperature.

Results and Discussion

Initial drop tower testing with ZnS:Mn powder showed that impact energies greater than 50 mJ produced light proportional to energy. Above 200 mJ the effect was less pronounced. This test was repeated with painted aluminum samples, and it was found that the response is linear out to 600 mJ. This increase could be caused by a number of factors. First, in the powder form, material may be pushed away from the impact zone at higher velocities

before impact due to air convection. Second, the aluminum substrate may be absorbing some of the impact energy.

At high velocities, the data collection was more complicated because of the large amount of background light produced by the gun. Another factor complicating the measurement is survival of the phosphor coating. Two series of tests were performed. The first used a ceramic binder, Cotronics Resbond 793, selected for its high-temperature survivability. This binder proved to be very brittle and was widely scattered after impact. On one test, the projectile missed the painted area of the target and the paint came off large sheets instead of a widely spread powder. It is interesting to note that no light was detected for the shot that missed the painted area, but light was detected when the painted area was struck by the projectile. A second series of tests was performed using poly (phenyl methyl) siloxane (PPMS) binder. For this test series, a blinder was added to the light detector to minimize the background light from the gun. It was found that PPMS stayed attached to the substrate in areas away from the impact. Near the impact, most of the phosphor coating was spalled from the surface. These tests were also limited by the accuracy of the gun to place the projectile in the coated area viewed by the baffled light detector. Figure 1 shows the major result. In this case the coating was viewed from the opposite side of the impact. The signal appears to show two excitations, one on impact and another possibly due to a secondary shock wave traveling through the material. Further testing is needed to clarify this result.

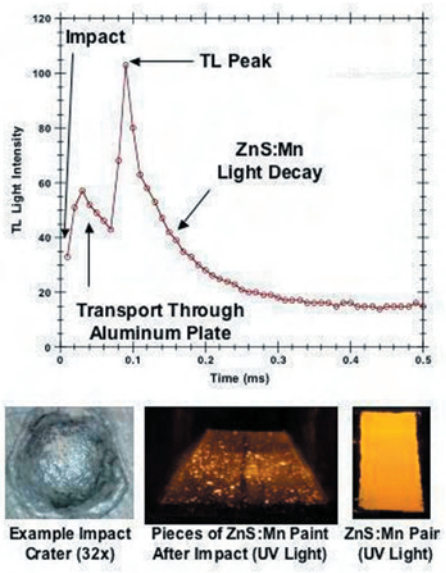

Fig. 1. Example data from hypervelocity test.

With regard to radiation effects, the emission spectra showed no change other than overall brightness which decreased with exposure dose. Also, as the dose increased, the decay time of the phosphor decreased (Hollerman 2004). The temperature measurements showed that at about 175ºC the decay time changes began approaching the unirradiated sample values. This is due to annealing of the proton damage. It was verified by a second set of data for which the decay time of lower-dose samples increased and followed the unirradiated curve at about 175ºC.

Benefits

The low-velocity triboluminescence characteristics are of use also to the development of impact sensors for hydrogen storage tanks. This could enable a health monitoring system on future fuel cell automobiles to be developed. The hypervelocity results are clearly applicable to manned space flight and the future goals of NASA. Perhaps the most interesting results are those found from the proton irradiation studies. These tests showed that radiation produces an effect. The tests also showed that limited amounts of damage can be annealed from the phosphor. The radiation dependence may also be seen as an opportunity for use in radiation sensing. In conclusion, the project adds to the number of possible sensors uses of phosphors. The usefulness of thermographic phosphors now includes not only sensing of temperature, heat flux, and coatings health but now impact and radiation.

References

Bergeron, N. P., W. A. Hollerman, S. M. Goedeke, F. N. Womack, S. W. Allison, and D. L. Edwards. May 2004. "Development of Triboluminescence Sensors for Hypervelocity Impact," Proceedings of the 50th International Instrumentation Symposium of the ISA, San Antonio, Texas.

Bergeron, N. P., S. M. Goedeke, W. A. Hollerman, C. I. Muntele, S. W. Allison, and D. Ila. February 2005. "Evidence of Annealed Proton Damage from a ZnS:Mn-Based Phosphor Paint," to be presented at the Proceedings of the Space Technologies and Applications International Forum, Albuquerque, New Mexico.

Hollerman, W. A., S. M. Goedeke, N. P. Bergeron, C. I. Muntele, S. W. Allison, and D. Ila. October 2004. "Effects Of Proton Irradiation On Triboluminescent Materials Such As Zns:Mn," 18th Annual International Conference on the Application of Accelerators in Research and Industry, Fort Worth, Texas.

Womack, F. N., N. P. Bergeron, S. M. Goedeke, W. A. Hollerman, and S. W. Allison. 2004. "Measurement of Triboluminescence and Proton Half Brightness Dose for ZnS:Mn," *IEEE Transactions On Nuclear Science* **51**(4), 1737–1741.

Development of a Rich Air/Fuel-Ratio Sensor Correction System

B. H. West, M. D. Kass, and S. P. Huff
Engineering Science and Technology Division

Automotive universal exhaust gas oxygen (UEGO) sensors are being used in emission control research to provide fast response information about air:fuel ratio (AFR). These sensors were initially developed for spark-ignition gasoline engines but are commonly used now in diesel research. Spark-ignition (homogeneous charge) engines operate at the chemically correct (stoichiometric) AFR (14.5:1) most of the time, whereas diesels normally operate lean (AFR ranges from ~20:1 at full load to over 100:1 at idle). Because some near-term diesel exhaust emission controls (lean NOx traps) require periodic rich excursions (AFR<14.5:1), UEGOs are commonly used to monitor the AFR. Experiments at ORNL with UEGOs in the exhaust of diesels uncovered a problem with sensor accuracy in the rich regime. This seed money project focused on developing a simple system to overcome biasing of these sensors to provide more accurate AFR information for operating engines. A system consisting of critical flow orifices, pumps, and an oxidation catalyst was assembled and evaluated on the bench using a wide range of simulated rich exhaust gas mixtures. By controlling the mass flows of simulated exhaust and excess air and reacting the mixed gases over a heated oxidation catalyst, we were able to produce a lean mixture for the UEGO from which the initial rich AFR can be determined. The feasibility of this system was proven, and follow-on funding from DOE has been secured to improve the system and improve the understanding of the sensor bias and possibly explore means to improving the sensors for diesel use. Also, UT-Battelle, LLC, has elected to retain title to an invention using the method described herein.

Introduction

In order to reduce nitrogen oxide (NOx) emissions produced by internal combustion engines, catalysts are often utilized to convert NOx to elemental nitrogen. Conventional catalysts, used on modern gasoline-fueled vehicles, require the exhaust chemistry to be maintained at the stoichiometric air:fuel ratio (AFR) corresponding to complete combustion. Theoretically, the combustion products formed during the stoichiometric combustion reaction would be elemental nitrogen, CO_2, and H_2O (neither oxygen nor unburned hydrocarbons would be present). As the exhaust chemistry for these stoichiometric engines drifts slightly lean or slightly rich of the target AFR, the oxygen sensor feedback signals the engine control computer to make small adjustments to the fuel flow to maintain the stiochiometric AFR, enabling the optimal reduction of NOx and simultaneous oxidation of carbon monoxide (CO) and hydrocarbons (HC) in the three-way exhaust catalyst. A similar catalyst technology is now being adapted to the control of emissions from diesel engines, although the new technology (NOx adsorber catalysis) also contains a sorbent that will store NOx during lean (excess oxygen) operation, since NOx cannot be readily reduced under oxidizing conditions. In contrast to stoichiometric gasoline engine operation, diesel engines normally run under lean conditions. To meet proposed emission regulations for diesel engines, several promising after-treatment systems have been developed which demonstrate good NOx conversion efficiencies; however, they need to be regenerated periodically under rich exhaust conditions.

Regeneration is effected by a momentary rich excursion obtained by direct injection of diesel fuel or other reductant into the exhaust in concert with intake air throttling, or by coupling throttling with manipulation of the fuel injection events. Normal lean operation for a diesel is within the range of about 20:1 AFR at high load to over 100:1 at light loads. For diesel fuel the stoichiometric AFR is 14.5:1. Conventional wide-range UEGO (universal exhaust gas oxygen) sensors are fairly accurate at measuring AFR under lean conditions (AFR>14.5) but have been shown to be unreliable for rich operation (AFR < 14.5) due to interference (or biasing) from the various reductant or fuel-derived species in the rich exhaust.

Optimal operation of NOx adsorbers (and other emission control technologies) requires precise measurement of the AFR. Unfortunately, because UEGO sensors are affected by rich exhaust species such as hydrogen, CO, and HC compounds, the sensor readout is biased and the resulting AFR is incorrect. This project focused on developing a simple system to overcome biasing of these sensors to provide more accurate AFR information for operating engines. The objectives were to (1) perform a feasibility study showing that novel arrangement of critical flow orifices and a catalyst can be

used to accurately measure AFR during rich operation and (2) understand how interfering species influence sensor performance. Successful demonstration is expected to lead to follow-on funding from DOE to improve the system and to enable sensor use in diesel engines.

Technical Approach

A UEGO sensor consists of three basic components: (1) a cavity separated from the exhaust by a diffusion passage, (2) a heated exhaust gas oxygen (HEGO) sensor that detects the presence of oxygen, and (3) a pumping cell that can pump oxygen into or out of the cavity based on the polarity of current applied to the pump. The sensor determines the AFR by how much oxygen needs to be pumped into or out of the cavity, as determined by the magnitude of the current applied, to maintain a stoichiometric condition inside the cavity.

During lean (excess oxygen and little to no HC or CO present) operation of the wide range UEGO sensor, the AFR is determined by measuring the level of oxygen in the exhaust. Exhaust gas passes through the diffusion passage and into a cavity in contact with a solid-state electrolyte, typically zirconia. The oxygen molecules are pumped out of the cavity through the electrolyte by applying a current across the pump. The current required to pump all the oxygen out of the cavity is proportional to the excess oxygen in the exhaust, which in turn is proportional to the AFR during lean conditions.

During rich combustion, excess fuel species (HC, CO, and H_2) are present in the exhaust. Under these conditions, the AFR is proportional to the amount of oxygen required to complete the oxidation of the excess fuel species. To measure AFR under these conditions, the sensor electrochemically pumps oxygen from the atmosphere to the cell. Ideally this oxygen reacts with the remaining fuel components to form H_2O and CO_2. The current required to pump in enough oxygen to fully react the excess fuel species is used to determine AFR ratio during rich operation. This approach, while theoretically accurate, is subject to errors associated with the different diffusion rates of the rich species (i.e., H_2 has a much higher diffusion rate, while the diffusion rates for CO and the various HC species are lower). This effect is empirically accounted for and corrected for SI engines, but not for diesel engine operation.

A bench apparatus was constructed to measure rich AFR using the same fundamental principles as the UEGO, but on a larger scale. The design takes advantage of the UEGO's fast response and accurate sensing in the lean regime but avoids problems associated with diffusion of different species through the sensor. In practice the apparatus will take a fixed mass flow rate sample of raw exhaust, mix it with a fixed mass flow rate of clean air, react the remaining fuel components and oxygen to completion across an oxidation catalyst at high temperature, then flow this new lean sample over a UEGO. For the experiments described herein, simulated exhaust mixes with known CO, H_2, and HC concentrations were used instead of raw engine exhaust. For well-defined, known concentrations of fuel species, the theoretical rich AFR is known. The raw, indicated AFR for each mix was measured with one UEGO, while a second UEGO measured the resulting lean AFR of the mix after the oxidation catalyst. Given the relationship between the mass flow of rich exhaust and mass flow of air, the lean measurement was then used to calculate the corrected AFR.

Results and Discussion

An apparatus as described above was successfully assembled and evaluated. A wide range of rich and lean gas mixes were blended and sampled by the apparatus, providing the raw indicated AFR and lean AFR. The lean AFR was used to calculate a corrected AFR. Results of these experiments are shown in Fig. 1. Solid symbols denote the raw, indicated AFR of the blended gas, while the open symbols denote the corrected AFR. As expected at the onset, H_2 has a significant effect of biasing the sensor output rich (that is, indicated AFR is richer than the actual AFR), while CO or HC alone tend to bias the sensor lean. While the families of datasets are for various H_2 concentrations, the CO and HC were also varied in these experiments. In discussions with a sensor manufacturer we have found that they are aware of the problem and design the sensor for the H_2/CO mix commonly found in spark ignition (SI) engines. HC levels in SI engines are typically very low, and the species are of relatively low molecular weight. In the diesel application, the number and molecular weight of HC species are much higher, and total HC concentration can be much higher. Note in Fig.1 that certain gas mixtures yielded raw indicated AFRs that fall on or very close to the 1:1 line (solid symbols, uncorrected). Close inspection of these data reveals a CO:H_2 ratio of 2 or 3 with very low HC concentration, conditions typical of SI engines.

We are very pleased with the results of this project. We have successfully constructed an apparatus for measuring actual AFR in our operating engine experiments, and we have obtained follow-on funding from our DOE sponsor to further refine the design and research the sensor biasing issue. Accurately determining AFR in our ongoing NOx adsorber research is critical to improving the value of the data and the understanding of the catalyst function with various fuel-derived species (reductants).

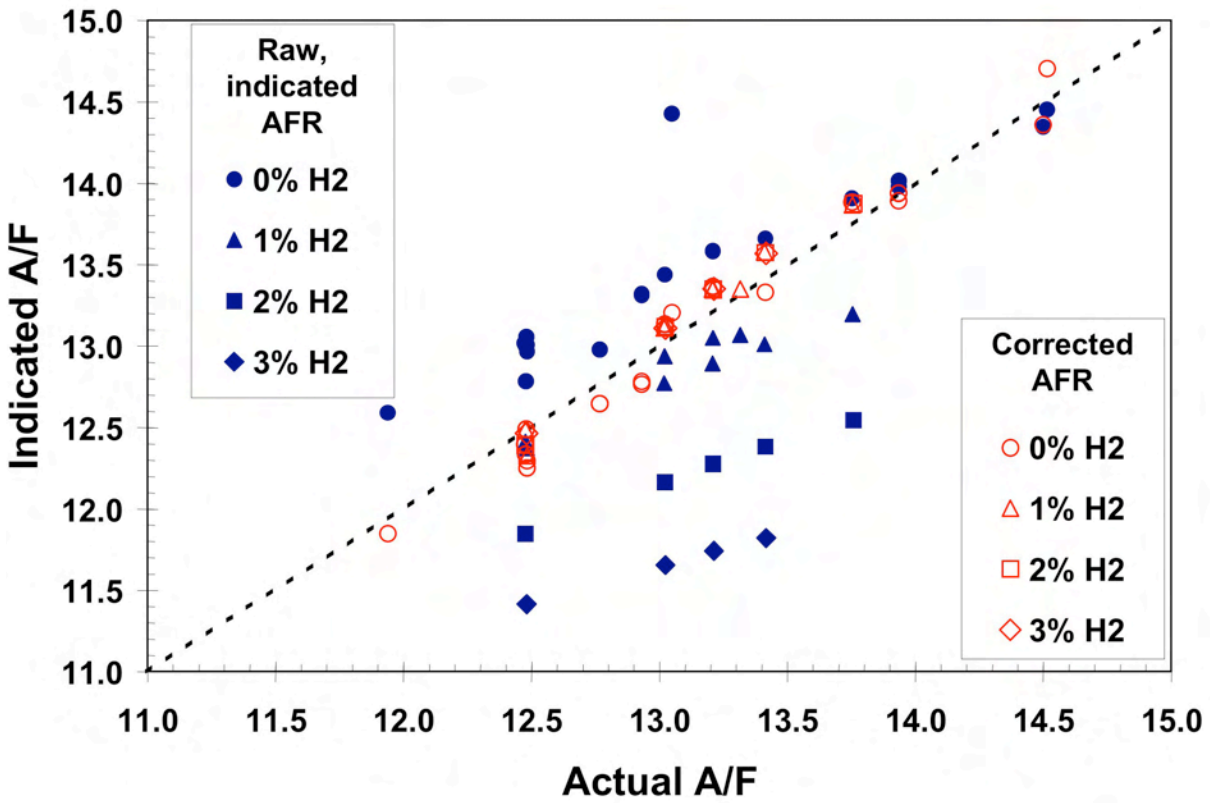

Fig. 1. Indicated Air:Fuel ratio (AFR) vs actual AFR. Raw indicated AFR (solid symbols) measured in simulated exhaust containing known concentrations of CO, H_2, or HC. Corrected AFR (open symbols) calculated from AFR measured after addition of excess air and oxidation of fuel species. Note that for zero H_2 cases, the raw sensor response is biased lean, while increasing H_2 biases the sensor rich. Each open symbol corresponds to a solid symbol data point that has been corrected.

Benefits

As noted above, we have secured follow-on funding from DOE to refine the design and further explore the sensor biasing issue. The benefits to our DOE sponsor are an improvement in the quality of data we will acquire from our ongoing NOx adsorber research programs. In researching the effectiveness of various regeneration strategies, it is critical that the strategies being studied both provide the catalyst with similar stoichiometry. Using this apparatus, we can accurately measure AFR and determine the most effective species for regeneration.

Measurement of Species Distributions in Operating Fuel Cells

W. P. Partridge,[1] T. J. Toops,[1] J. E. Parks,[1] and T. R. Armstrong[2]
[1]*Engineering Science and Technology Division*
[2]*Metals and Ceramics Division*

Measurement and understanding of transient species distributions across and within fuel cells is a critical need for advancing fuel cell technology. The Spatially Resolved Capillary Inlet Mass Spectrometer (SpaciMS) instrument has been applied for in situ measurement of transient species distributions within operating reactors, including diesel catalyst, air-exhaust mixing systems, and non-thermal plasma reactors. The work described here demonstrates the applicability of this tool to proton exchange membrane (PEM) and solid oxide fuel cells (SOFC) research. Specifically, we have demonstrated SpaciMS measurements of (1) transient species dynamics across a PEM fuel cell (FC) associated with load switching, (2) intra-PEM species distributions, and transient species dynamics at SOFC temperatures associated with FC load switching.

Introduction

Modeling efforts have suggested spatial non-uniformities in both species and temperature within operating fuel cells. Such distributions have significant impact on fuel cell performance including mechanical integrity, reactants and products management, and efficiency. However, little in situ spatially resolved measurements are available to assess model predictions. In addition to spatial non-uniformities, temporal non-uniformities may exist as concentration and thermal waves within operating devices. ORNL's expertise in the development and application of minimally invasive diagnostics for species and temperature measurement are believed applicable to elucidate these phenomena.

The Fuels, Engines, and Emissions Research Center (FEERC) at Oak Ridge National Laboratory (ORNL) has been developing diagnostic techniques primarily for the advancement of diesel engine catalysis both in terms of operating efficiency and emissions reduction. Two tools that could be very beneficial to fuel cell diagnostics are the SpaciMS and the phosphor thermography (PhosphorT) instruments. Both of these tools are based on nonreactive and nonconducting, minimally invasive physical probes uniquely applicable for probing intra-fuel cell chemistry.

The SpaciMS capillary inlet system is minimally invasive both in terms of its size, ca. 200-µm OD, and sampling rate, ca. 10 µL/min. The glass capillaries are both nonreactive and nonconducting and can be inserted into small reactor channels and around corners. The capillaries transport the extracted sample from the sample location to a mass spectrometer (MS), where standard electron ionization mass specific detection is performed. This allows for broad species analysis including O_2, CO_2, H_2S, SO_2 and various hydrocarbons, as well as H_2, which is critical to fuel cell technology. Temporal resolution is largely dictated by capillary length; we have achieved ca. 30 Hz and 1 Hz temporal resolution using 1- and 2.5-m-long capillaries, respectively. The ability of this instrument to accurately quantify hydrogen concentration distributions is unique and attributable to the specific MS type. Our experience with applications of the SpaciMS is also unique and broad, including first measurements of in-cylinder H_2 generation from diesel engines, and intra-catalyst species distribution measurements. Species distributions throughout a fuel cell stack could be resolved by translation of the SpaciMS probe, or sampling via separate capillaries positioned throughout the stack. This could provide data critical to understanding fundamental device chemistry, improving performance and validating models, for instance, monitoring of fuel conversion and consumption throughout the stack and identifying the most effective areas as well as local effect on flow conditions.

Despite its success for elucidating automotive catalyst chemistry, fuel cell applications offer additional challenges. Automotive catalyst environments are typically 300–450°C, non-condensing, with at most typically few percent levels of hydrogen. There are many different types of fuel cells, and many different fuel cell issues in need of SpaciMS measurements as generally discussed above. For instance, some fuel cells operate at relatively low temperatures, while others operate at high temperatures; some fuel cell environments are condensing, while others are not; some fuel cells use pure H_2, others use mixtures, and others incorporate the reforming function into the stack, for example, to convert methane to H_2. For fuel cells that use pure H_2, there may be challenges to measuring small concentration changes on such a large baseline. Solid oxide fuel cells operate at high temperatures, 800–1000°C; this will affect both the mechanical nature of the capillary physical probe, as well as the sample density and

thus signal level. Proton exchange membrane (PEM) fuel cells have condensing environments, which increases the probability of blocking the capillary sample probe. The SpaciMS is applicable to both a broad range of fuel cell types and issues. The proof of principle defined in this proposal is not limited to a single fuel cell type but rather establishes a foundation upon which we plan to build a broad fuel cell R&D program.

This project addresses (1) measuring concentration gradients across fuel cells and (2) measurements at high temperatures indicative of SOFCs. Methods to mitigate water clogging of sample capillaries are not investigated in this proposal. Nevertheless, the proposal will establish the ability of the SpaciMS to make measurements critical to fuel cell research for a broad range of fuel cell types. There is currently no sponsor support to demonstrate the tasks described in this proposal.

The project objectives were fully realized. Intra-PEM SpaciMS measurements were demonstrated in addition to the original project objective list.

Technical Approach

The SpaciMS was applied to measure transient species concentration distributions associated with fuel cell operation. A 3-stack, 34-W commercial PEM fuel cell was used to create the PEM test environment. A resistive load bank was used to create load variations. The anode reactant conditions were 100 sccm, 35% H_2, 35% Ar, 30% H_2O, 22 psig. The cathode reactant conditions were 100 sccm, 14% O_2, 56% Ar, 30% H_2O, 25 psig. For intra-PEM SpaciMS measurements, four capillaries were installed along both the anode and cathode flow paths; small grooves to house the sample capillaries were milled into both sides of a single bipolar plate, and the capillaries were sealed in place with silicone. Capillaries were installed in the inlet manifold and at ca. 0.15, 0.46, and 0.78 along the serpentine flow paths.

To demonstrate SpaciMS measurements at SOFC temperatures, the PEM exhaust streams were heated to 900°C. To effect sample heating, each exhaust stream was passed through a 4.25-ft length of 1-mm-ID tubing contained in a tube furnace at 900°C. SpaciMS sampling capillaries were inserted into the heated tubes, and positioned to sample ca. 8-in prior to the heated tube's exit from the furnace; that is, the sample location was within the 900°C furnace.

Results and Discussion

Measurements were made of PEM exhaust species concentration as the FC load was switched. Fuel cell output was varied from 0.02 to 0.95 W. Distinct step changes in H_2, O_2, H_2O, and Ar concentrations were observed to accompany load step changes. In general increasing load resulted in greater H_2 and O_2 depletion. Argon diluent concentrations increased with H_2 and O_2 consumption on both the anode and cathode sides, respectively. High water loading conditions could challenge the capillary sampling system resulting in partial transient capillary occlusion or, in the worst case, capillary clogging; transient occlusion events resulted in high frequency dynamics on the pressure and non-water species traces, and a longer-term water concentration dynamic as the excess water was removed from the capillary. Water blocking of the capillary stopped sample flow and caused the SpaciMS to go to high vacuum; this type of water clogging can often be reversed by reverse flow of N_2 through the sample capillary. Water-induced dynamics were most prevalent on the cathode (O_2) side at high load conditions. This is as expected since cathode-side water concentration should be highest at high-load conditions. Low-frequency variations in both species concentrations and FC output were observed even at a steady-load condition. These are apparently due to transient local reactant depletion or passivation, for example, local water condensation.

Measurements of dynamic species concentrations at SOFC temperatures posed little additional challenges. The higher temperature environment results in fewer molecules in the MS due to decreased sample density and increased capillary resistance, because of the greater sample temperature and correspondingly small mean free path. These effects posed no great measurement challenge, as evidenced by the signal-to-noise ratio of the high-temperature measurements relative to the lower-temperature (PEM-out) measurements. Certainly at SOFC-typical temperatures, quartz sample capillaries become fragile because the polyimide coating burns off at temperatures above ca. 400ºC. This is not a problem as long as sufficient care is taken (e.g., minimize vibrations and rough surfaces contacting the capillaries). In fact, we demonstrated that bent sample capillaries and even those bent against a sharp metal edge do not break when the polyimide is removed. We had intended to investigate stainless-steel (SS) capillaries and/or crimped SS large-bore capillaries, and their comparison to quartz capillaries. We were unable to perform this work.

Intra-PEM species measurements have always been perceived as the most challenging SpaciMS application due to the condensing nature of the environment, specifically due to the expected high probability for capillary clogging by liquid water. We initially planned to mitigate water clogging by housing the sample capillary in a heated and insulated SS sleeve. However, due to time and funding limitations, bare quartz (185-µm OD, polyimide coated) capillaries were used. The method of capillary-probe installation via milled grooves with silicone sealing resulted in leak-free probe access. Despite our expected difficulties, we experienced no water-clogging problems

with any of the intra-PEM capillaries. This is notable particularly because realistic water concentrations were used. In fact, the water-associated sampling challenges were strictly confined to the capillaries outside the PEM. The intra-PEM SpaciMS measurements resolved O_2 depletion and maldistribution as shown in Fig. 1. Figure 1 shows the oxygen concentration at five locations through the PEM, with the FC operating at five different load conditions. The measurements made at 0L, 0.15L, 0.46L and 0.78L, where L is the serpentine pathlength, used capillaries installed in the PEM. The measurement at 1L used a capillary positioned outside the PEM in the FC exhaust stream. Figure 1 indicates monotonically increasing oxygen consumption along the PEM cathode flow path within the PEM. For all loads investigated, the PEM out oxygen concentration is greater than that at the 0.78L intra-PEM location. It is important to realize that these measurements were taken on one cell of a three-parallel-cell PEM. Since separate measurements indicated no air leaks, the behavior of Fig. 1 indicates that other parallel (not instrumented/measured) MEAs are less efficient than the instrumented MEA; because those other MEAs are less efficient, they use less oxygen than the instrumented cell and increase the exhaust concentration. For instance at 980 mW, the instrumented cell is exhausting ca. 0% oxygen, but the two parallel cells are exhausting some combination of oxygen concentration that averages to ca. 8%. This further demonstrates the need for measurement of intra-PEM FC species distributions. Figure 1 also shows significant oxygen consumption at the 980-mW case, with the oxygen being depleted somewhere between the 0.15L and 0.46L locations; that is, in this case, the back 54 to 85% of the flow path is inactive due to an oxygen limited condition. At all locations the oxygen consumption increases with increasing FC output.

SpaciMS measurements of transient species concentration were demonstrated

(a) across a PEM FC
(b) at SOFC-typical temperatures
(c) within a PEM FC

Benefits

The research is consistent with DOE missions to increase energy efficiency, reduce dependence on foreign oil, and improve environmental quality. The DOE Hydrogen programs promote broad fuel cell deployment for both stationary and mobile power generation and promise to have positive impacts on all of these DOE mission areas. This project has demonstrated a tool capable of providing measurements that are critical for fuel cell technology development and hence applicable to forwarding the DOE mission. This diagnostic capability is beneficial to multiple other federal agencies (DOD, DOT, etc) that are investigating fuel cells.

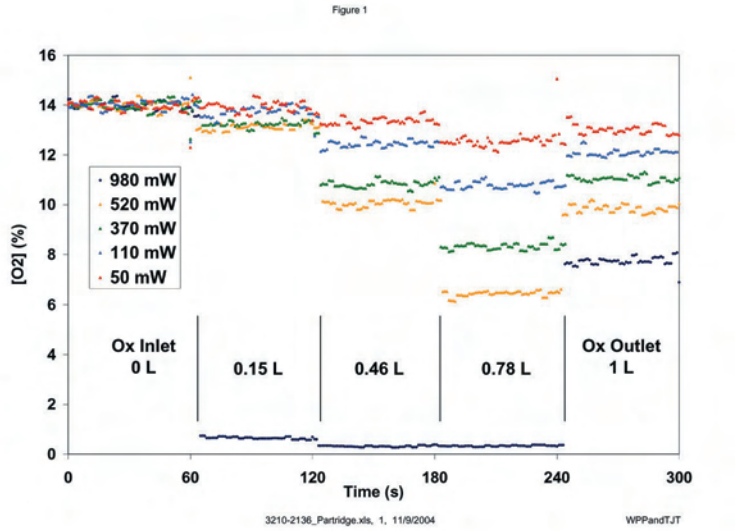

Fig. 1. Intra-PEM SpaciMS measurements of O_2 consumption and maldistribution.

Optically Manipulated Microelectronics Artificial Retina

Z. Hu and T. Thundat
Life Sciences Division

Retinitis pigmentosa (RP) and age-related macular degeneration (AMD) are two common retinal degenerative diseases that have caused blindness for millions of people worldwide. The objective of this project to study the possibility and feasibility of building a novel optoelectrical artificial retinal (AR) prosthetic device that integrates an optical sensor, electrical circuitry, and a stimulation electrode into one unit, forming a high-resolution (>10,000-pixel) imaging device for vision improvement. This complete system-on-chip approach, a thin (~25-μm-thick) disc-like (~ 4-mm-diam) device, is suitable for either epiretinal or subretinal implantation in vision-deficient patients.

In order to address the great need of retinal prosthesis, DOE launched a research project (DOE Lab 01-14) in 2000 for the purpose of developing an artificial retina. ORNL, the leading DOE laboratory on this project, teamed with the University of Southern California (USC), University of California Santa Cruz (UCSC), North Carolina State University (NCSU), Second Sight, LLC, and four other DOE laboratories—ANL, LLNL, LANL, and SNL. The DOE team proposed and is currently working on a retinal prosthesis device using a "one-pixel-one-electrode" design approach in which every electrode needs one wire from outside the eye. The key limitation of this approach is the extreme difficulty and challenge of packing a high-density electrode array into such a small area (~ 5-mm diam). The current highest array density is 60 electrodes, in which the size of each electrode and its connection wire are already less than 200 μm. Given the very restrictive eye structure and the physical size of the electrodes, it is very unlikely much higher numbers of electrodes (>100 electrodes) could be packed into the eye without introducing other significant problems such as losing flexibility and space.

To address these issues that hinder our ability to achieve high-quality and high-resolution visual stimulation, we have proposed a semiconductor-based thin and flexible chip that could contain a large array (>10,000) of photo diodes and field effect transistors (FET) and other microelectronic circuits which is powered by one pair of DC/AC biases between the chip and human body. The key advantage of our design is that each stimulation pixel is self-contained, and there is no need of having a large number of wires (only two wires are needed) from outside the patient's eye. In order to know if this new approach would work, we first needed to answer the following questions: (1) could our proposed circuit be fabricated and also provide the required functionality; and (2) would the fabricated chip still function properly after being thinned down to ~25 μm.

To answer the first question, we designed and built a 100-pixel array model (4.5 in. × 6 in. × 1 in.) using off-the-shelf parts in which 100 photodiodes were placed on one side of a printed-circuit (PC) board and 100 LEDs with FET amplification circuits were on another side of board which was powered by four D-size batteries. When a light pattern was projected on the photodiode side of board, the amplified LEDs reproduced the same light spot pattern and correspondingly mimicked the light intensity on the back side of the PC board. Additionally, we also tested the circuit with one DC power and one AC single and obtained desirable results. Then the tested circuit was successfully transferred into a chip layout using integrated circuit (IC) design software. Limited by the current funding, we could not pursue actual fabrication as each fabrication run would cost about $30K. Nevertheless, our work has already proved the feasibility of the proposed circuit design concept that had met the original objective of this seed money project.

Additional efforts was devoted to determining whether any commercially fabricated IC chip and silicon wafer could be thinned down to ~25 μm from original 300 μm. Two thinning methods were tested: chemical mechanical polishing (CMP) and deep reactive ion etch (DRIE). Both methods demonstrated the possibility of thinning down the IC chips and silicon wafers. Several commercially fabricated IC chips have been thinned down to about 70 μm and some silicon samples have been thinned done to about 40 μm which have already exhibit certain flexibility. For DRIE, we have been able to obtain up to 1-μm/minute etching rate, but the etching rate dramatically decreased when the sample chamber became hot even when we were under a 5-minute-etching/5-minute-cooling operation pattern. If there is a cooling stage in our DRIE system, it would overcome this problem and also prevent the possible thermal damage caused by the high temperature during ion etching.

During work on this project, we filed an invention disclosure titled "Direct view imaging & displaying electronic system" (ID 1465, S-105,064) with the ORNL IP office. In this disclosure, we described a novel fully integrated imaging and display system which completely changed the structure framework of existing imaging and display systems such as a digital camera. The described device borrowed the same concept from our original artificial retina proposal and could be made by the standard CMOS process at rather low costs with ultrahigh anti-dilution display pixel resolution (<100 μm/pixel) with unlimited theoretical display area, high pixel density, low power consumption, possible full-bandwidth light sensing spectrum (from UV to IR), lightweight, easy to assemble and integrate to other imaging system (such as a telescope), and very thin (silicon wafer thickness 300–500 μm). Possible applications of this device could be found in many areas for both civilian and military purposes. Besides DOE, this device might find many application in areas of anti-terrorism, defense, and scientific research in other federal departments such as DHS, DOD, NASA, NIH NRC, EPA and other federal agencies.

Mesoscopic Fluidic-Based Actuators

J. F. Jansen and L. J. Love
Engineering and Science Technology Division

Miniaturization of actuation to the mesoscopic scale (characterized as being in the "sugar cube–to–fist size") promises to enable new classes of systems in medical instruments for future military and aerospace systems. However, existing approaches to miniaturization of actuation technologies have limited performance due to fundamental physical limitations based on scaling laws. While fluidic devices scale well into the mesoscopic domain, preliminary analysis suggests the potential for forces and displacements up to several orders of magnitude greater than existing meso-scale actuation technologies are possible. Our primary scientific challenge will to be to develop the scaling laws and to experimentally verify that fluidic actuators can be controlled at the mesoscopic scale at the required performance levels.

Applications such as robotic surgery needs actuators that have the performance of hydraulics but in the sugar cube–to–human fist size. This size range is in the mesoscopic domain, and hydraulic actuators in this regime will be called mesoscopic fluidic actuators (MFAs). Actuation through controlled fluid displacement is actually one of the oldest forms of actuation; however, very few researchers have explored the general merit of this form of actuation at the meso-scale. There are many advantages to scaling of fluidic devices in terms of movement of small amounts of materials. However, it is our contention that there are likewise many advantages to scaling fluidic systems in terms of actuation.

Some of our concerns when trying to understand how systems scale into this domain are (1) when laminar flow and capillary forces dominate in the transmission of a fluid, (2) when the basic orifice equation changes from the turbulence assumptions, and (3) when the rubbing friction of seals against the wall dominates over the frictional forces due to fluid pressure in an actuator as well as other physical phenomenon. Our primary scientific challenge will be to develop the scaling laws and to experimentally verify that fluidic actuators can be controlled at the required mesoscopic-scale performance levels. Based on the flow requirements, any flow control valve would have to overcome fluid forces of just a few ounces with displacements in the 10-μm to 100-μm range and would have to fit inside a packaging volume of less than 1/8 to 1/16 of a cubic inch. The overall length of this MFA is less than 1 inch.

Many mesoscopic applications require working fluids that are benign to humans such as water or saline solutions (e.g., robotic surgery where any leak of the fluid will be harmless to the patient since saline solutions are routinely used in surgery). However, water or saline as a working fluid presents serious problems in the control of precision fluidics. In addition to the numerous implementation issues in pumping a fluid with poor viscosity, a major control challenge is associated with the effective fluid stiffness caused by poor aeration of this fluid. In addition to the fluid concerns, the higher-than-normal actuator friction will provide another major nonlinearity.

To guarantee that the physics associated with the construction of a MFA is understood, each individual technology associated with it must be tested. Currently we have focused on the development of three test beds that have or will demonstrate the basic technology necessary for MFAs to become a reality. These three are the electric-motor test bed (used to control the flow control valve), the flow-control-valve test bed, and a test bed demonstrating the integration of position sensing on the miniature hydraulic cylinder. The electric motor and the integration of a position sensor on a miniature hydraulic cylinder have been demonstrated. The test bed of the hydraulic control valve has been designed and is currently being constructed. In addition, rotational hydraulic cylinders with integrated LVDT sensing are currently under development and are based on modifications of our current linear designs. Challenges associated with these three test stands have mainly been working at these small dimensions and how one makes port connections.

The primary beneficiary of this project will be the Defense Advanced Research Projects Agency, Defense Science Office in supporting the Operating Room of the Future.

ENVIRONMENTAL SCIENCE AND TECHNOLOGY

Director's R&D Fund

Genomic Characterization of Belowground Ecosystem Responses to Climate Change

S. P. DiFazio,[1] L. E. Gunter,[1] C. C. Brandt,[1] J. C. Schryver,[2] R. J. Norby,[1] and J. Zhou[1]
[1]*Environmental Sciences Division*
[2]*Computer Science and Mathematics Division*

Many analyses of terrestrial ecosystem response to global climate change conclude that knowledge of belowground processes is fundamental to predicting the direction and effects of that change. However, these processes remain poorly understood because outdated and laborious methodologies are being applied to highly complex and heterogeneous biological systems. We have developed a quantitative, species-specific, real-time PCR assay to analyze the relative abundance of individual plant species included in the Old-Field Community Climate and Atmospheric Manipulation (OCCAM) Facility at ORNL. This molecular assay can be used to quickly and accurately measure total root abundance, and will thus facilitate a mechanistic understanding of belowground communities. In addition, we have developed an oligonucleotide microarray to query microbial genes involved in nitrogen cycling. This has provided a tool that will give an unprecedented view of microbial functional community dynamics. Finally, we have developed a new methodology for analyzing the challenging multidimensional datasets that result from studies such as this.

Introduction

Belowground processes play a key role in determining the trajectory of climate change and its impact on terrestrial ecosystems. In particular, the longevity of fine roots and plant litter and soil respiration rates will be major factors in determining the degree to which belowground systems will serve as a net source or sink of carbon as the climate changes (Norby and Jackson 2000; Zak et al. 2000). Microbial activity in the zone immediately surrounding plant roots (the rhizosphere) is particularly important because this is where much of the nutrient cycling activity takes place in the soil, and it is therefore the primary zone of interaction between plants and the microbes that control nitrogen availability (Lynch 1990; McCully 1999). The structure and function of rhizosphere communities can vary tremendously among roots of different plant species (McCully 1999; Bergholz et al. 2001; Tiquia et al. 2002), and one might also expect that above-ground perturbations of plants would affect the rhizosphere due to changes in production of fine roots and/or exudates (Schloter et al. 2000).

Recent advances in genomic technology make it possible to comprehensively and systematically study uncultivated microorganisms at the genomic scale. We have therefore used microarray techniques to query functional microbial diversity in soil systems. Microarrays (or microchips) are a powerful genomic technology that offers a number of advantages, including high throughput, broad range of detection, large capacity, and high sensitivity (Shalon et al. 1996; Guschin et al. 1997). Microarray hybridization–based detection systems are therefore ideal tools for analyzing the structure, composition, and function of microbial communities.

Much like microbial responses, plant root dynamics remain poorly understood due to substantial methodological constraints. Most importantly, none of the existing methods are capable of distinguishing the fine roots of different species, because these generally lack diagnostic morphological characteristics. Therefore, none of the existing methods can accurately quantify interspecific interactions and competitive outcomes belowground. We have developed a technique for rapid quantification of total root mass that can be applied to soil cores using species-specific quantitative real-time PCR (QRT-PCR) to estimate the abundance of roots of each of seven plant species involved in the Old-Field Community Climate and Atmospheric Manipulation (OCCAM) study at Oak Ridge National Laboratory. The general principle of the assay is that the rate of PCR amplification is related to the abundance of template DNA in the amplification reaction, which in turn is proportional to the quantity of roots in the original sample. Species-specific fingerprinting assays have been developed for tree roots from environmental samples (Jackson et al. 1999; Linder et al. 2000; Brunner et al. 2001), but to our knowledge there are no quantitative techniques for root identification. This technique will complement and significantly extend existing methodologies for assaying root abundance and growth.

Technical Approach

Plant Species. Seedlings of seven species typical of old field ecosystems involved in the OCCAM experimental site (http://warming.ornl.gov/OCCAM.html) were grown from seed in potting mix at the site and transplanted into plots in July 2002 and April 2003. These include broomsedge (*Andropogon virginicus* L.), a caespitose

C4 bunchgrass; orchardgrass (*Dactylis glomerata* L.), a C3 bunchgrass; meadow fescue (*Festuca eliator* Huds.), a C3 bunchgrass; sericea (*Lespedeza cuneata* (Dumont) G. Don), a shrubby nitrogen-fixing perennial; ribgrass (*Plantago lanceolata* L.), an herbaceous annual C3 dicot; red clover (*Trifolium pratense* L.), an herbaceous nitrogen-fixing perennial; and goldenrod (*Solidago canadensis* L.), an herbaceous perennial.

DNA Extraction from Roots. Roots were collected from pure species plots grown in the greenhouses at ORNL or at the OCCAM field site using root cores. After collection, roots were separated from the soil matrix by floating and washing in a series of mesh screens (20–60 mesh) to catch fine roots as well as coarse ones. Roots were then lyophilized and macerated by a ball-mill, followed by DNA extraction using the DNeasy Plant Mini Kit (Qiagen).

Species-Specific PCR assays. Species-specific PCR amplification primers were selected from nuclear gene sequences in GenBank in order of the following preference: (1) genomic DNA sequence for coding region; (2) random genomic DNA sequence; (3) complete cDNA sequence; or (4) EST sequence. PCR reactions of genomic DNA mixtures were performed by combining equivalent volumes of concentrated stock (50 ng/µl) of each species plus a calf thymus standard to a final single species concentration of 6.25 ng/µl. Final concentration per reaction was 25 ng each species. For these reactions, pure species standards ranging in concentration from 25.0 mg to 2.5 ng (5 orders of magnitude) were used.

Quantitative RT-PCR Using Reference Samples. QRT-PCR was performed using the iCycler® thermocycler (BioRad) with a double-strand DNA binding dye SYBR® Green for detection of the PCR product (Huang et al. 2001; Gentle et al. 2001) to estimate relative abundance of each species. Each QRT-PCR reaction was performed in duplicate. We initially developed assays for standard PCR using known quantities of purified template DNA from each species. We then amplified DNA mixtures of known template concentration and finally tested tissue mixtures of all of the different species. We then derived calibration curves to relate the number of cycles required to reach exponential amplification (the CT value) to root biomass in the initial samples.

Microbial Sample Collection and DNA Extraction. A total of 72 30-cm-deep core soil samples were taken. Three cores were taken from each half plot (24 half-plots in all). Samples were stored in Ziploc bags on ice until they were transported back to the lab. Once in the lab, samples were sieved to separate the soil from the plant material, and the sieved soil samples (ca. 140 g per sample) were transferred to sterile Whirl-Paks, quick-frozen on liquid nitrogen, and stored on dry ice until they could be moved to an ultralow (–80ºC) freezer for long-term storage.

Approximately 3 g of soil from the three cores in each half-plot were mixed together to give a composite sample for each of the 24 half-plots. Total community genomic DNA was isolated from each of the composite half-plot samples using a commercial soil extraction kit, the protocol for which has been modified and optimized in the Zhou lab.

Microbial Gene Isolation and Sequencing. To ensure the functional diversity of the root-associated microbial community is represented on the Functional Gene Arrays, samples from OCCAM plots were sampled via clonal libraries. Selected functional genes were amplified from nucleic acids extracted from the root-associated soil with previously used degenerate PCR primers. Amplified products were purified, cloned, and sequenced.

Construction of Functional Gene Microarray. A Functional Gene Array (FGAII) was designed and printed. The FGAII contains 5298 unique and group nitrogen cycle gene-specific DNA probes, each 50 nucleotides in length (Table 1). A new software program, CommOligo, was developed and used for probe design. Up to three probes with no obvious potential for cross-hybridization were selected for each gene and added to the array. The resultant collection of oligonucleotide probes span the diversity of all published nitrogen metabolism genes as well as nitrogen metabolism genes from in-house clone libraries (Table 1).

Microarray Analysis. We adapted a new technique for microarray analysis that has substantial advantages over other typically used clustering algorithms such as Principal Components Analysis (PCA). This technique, originally developed by Roweis and Saul (2000), is locally linear embedding (LLE). LLE computes an embedding with global coordinates in a low-dimensional space that preserves the local structure present in the high-dimensional space. LLE has an advantage over many nonlinear data analysis techniques such as neural networks in that it is deterministic, computationally efficient, and requires only the specification of the neighborhood size. The LLE algorithm has three major steps. First, using a distance matrix, it selects the k-nearest neighbors of each data point. Next, each data point is reconstructed using linear weights estimated from each of its selected neighbors. Finally, the global embedded coordinates are computed. The low-dimensional coordinates are chosen to minimize the predictive error of the data point locations in high-dimensional space using the same weight matrix generated in the second step. Although the second step is linear, the linear computations are confined to neighborhoods defined in the first step, whereas the estimation of the global coordinate in the embedded space is nonlinear. Thus LLE provides a substantial advantage over PCA and other strictly linear techniques.

Table 1. Nitrogen Cycle Genes and the Cognate Probes Represented on FGAII

		Number	Number of Probes		
Gene Category	Gene/Target	of Genes*	Unique	Group	Total
Nitrogen Fixation	nifD	30	78	0	78
	nifH	440	1147	0	1147
Nitrogen Fixation Total		**470**	**1225**	**0**	**1225**
Nitrogen Metabolism	amoA	32	81	53	134
	amoA/pmoA	1	2	1	3
	amoB	8	20	7	27
	amoC	2	4	6	10
	gdh	82	235	0	235
	hao	2	6	2	8
	urease	141	380	817	1197
	other	49	137	16	153
Nitrogen Metabolism Total		**317**	**865**	**902**	**1767**
Nitrogen Reduction	narB	8	24	27	51
	narG	191	501	156	657
	nasA	57	161	59	220
	nasD	1	3	0	3
	niiA	1	3	0	3
	nir	2	2	0	2
	nirA	3	9	1	10
	nirB	2	6	0	6
	nirD	1	3	0	3
	nirK	127	309	75	384
	nirS	136	364	92	456
	norB	45	124	8	132
	norZ	1	1	0	1
	nosD	1	3	0	3
	nosZ	111	292	83	375
Nitrogen Reduction Total		**687**	**1805**	**501**	**2306**

* Indicates the number of different DNA sequences represented by unique probes on the FGA.
These figures do not include the ~6,000 sequences represented by group probes.

Results and Discussion

DNA Extraction Efficiency. The extraction protocol used on these samples was most efficient for Trifolium (average 0.25% recovery) and least efficient for Andropogon (average 0.06%) (Fig. 1). The correlation between varying amounts of starting biomass and extracted DNA is $R^2 > 0.90$ for all species except *Andropogon* (0.6126) and *Lespedeza* (0.8829) (Table 2). The failure to gain quantitative yields of *Lespedeza* roots is probably due to the mixture of woody roots with fine roots. Future studies should analyze these classes of roots separately. Furthermore, the low correlation between *Andropogon* DNA yields and starting material were most likely due to early senescence of the *Andropogon* roots, since the above-ground portions of the plants were senescent at the time of root collection. Care should be taken to collect all roots when plants are actively growing to minimize the presence of senescent roots in the samples. This can be challenging for plant populations with large phenological variation, so an alternative approach is to segregate apparently senescent roots from live roots and develop a correction factor.

PCR Specificity. PCR primers were designed with a Tm between 55 and 60°C. Since we hoped to be able to amplify the seven species with one annealing temperature, we ran a series of tests with gradient PCR to determine the optimal temperature for all species. Low stringency of annealing temperatures below 57.5°C produced artifactual bands in *Andropogon* (AvPhyB) and *Fescue* (FPE2) primers and signal strength was diminished at temperatures above 59.4°C in *Dactylis* (DGE2); therefore, a 58°C annealing temperature was determined to be the most optimal for all species. Initial amplification of primers with target and non-target species shows that the products are highly specific to a single species, even differentiating between different species of *Trifolium* that occurred in the same plot.

Quantitative PCR. A series of amplification experiments with pure species, DNA mixtures, and tissue mixtures were made to test efficiency of amplification for various templates. Dilutions of templates (1:10) from 5-, 10-, and 20-mg extracts were amplified as unknowns with serial dilution of known concentrations of the same species as the standard. Standard concentrations ranged over 5 orders of magnitude, from 25 mg to 2.5 ng starting tissue, although concentrations at the lower end and higher end of the range often did not amplify. In all cases at least three concentrations of standard were used in analysis of amplification efficiency. Although trends for all pure species were as expected (increased template concentration is associated with lower threshold cycle), the coefficient of variation was relatively low for *Festuca* (0.84), suggesting that further optimization of primer sequences and PCR conditions is required (Fig. 1).

When equivalent amounts of concentrated DNA from each species were mixed and amplified with pure species as a standard, each species amplified without apparent interference from the presence of other species in the mixture, except for *Solidago* (Fig. 1). Despite repeated attempts, higher concentrations of *Solidago* template in mixtures exhibited elevated threshold values than

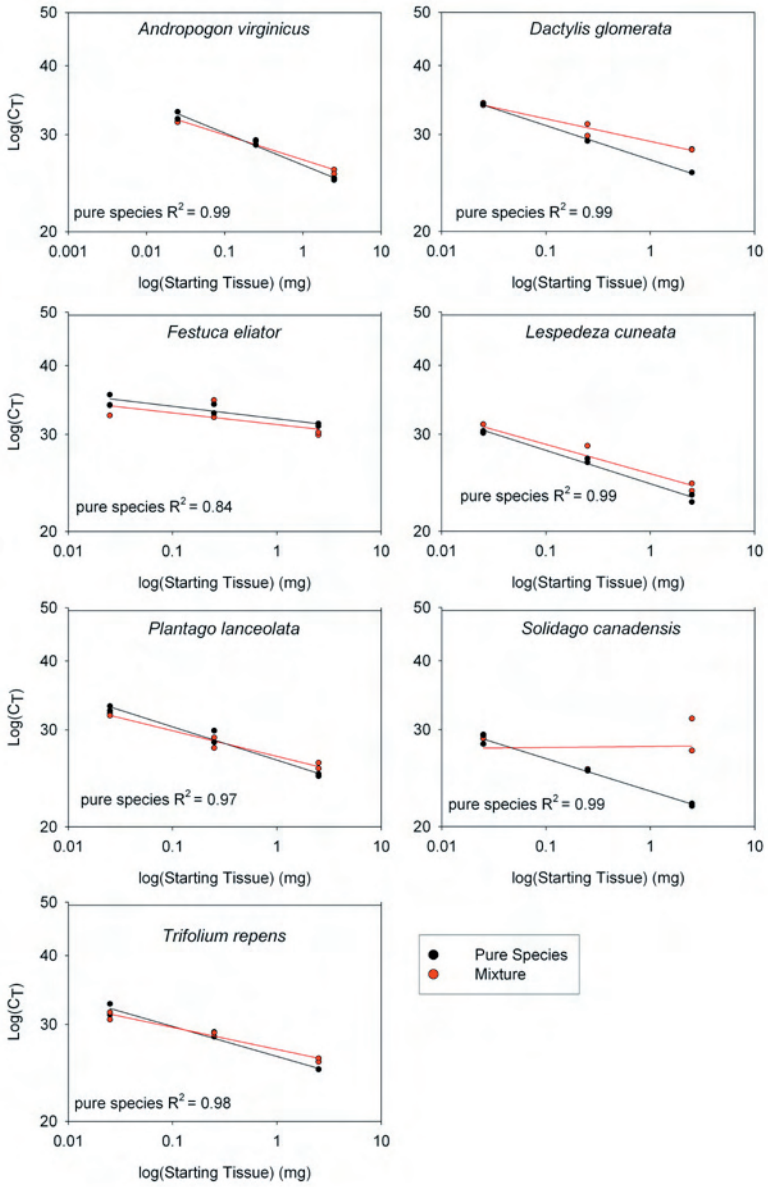

Fig. 1. Log-linear threshold cycle (CT) of mixtures containing equivalent quantities of template from seven OCCAM species plus calf thymus DNA standard. Serial dilutions of pure species are used as standards for the mixtures.

Table 2. Coefficients of variation (R^2) for DNA yield of extractions of 5, 10, 15, 20, and 25 mg of lyophilized root tissue

Species	R^2
Andropogon	0.61
Dactylis	0.94
Festuca	0.96
Lespedeza	0.83
Plantago	0.92
Solidago	0.97
Trifolium	0.99

expected and were associated with weak or non-amplification events.

Microbial Functional Gene Diversity. Sequencing revealed substantial spatial variation in functional genes across the OCCAM plots. For example, sequences from plot 5 were substantially differentiated from sequences in plot 12. In addition, 84% of the OCCAM sequences had less than 85% similarity to sequences in GenBank.

Microarray Analysis. The LLE method was tested on marine sediment samples analyzed with FGAs containing 1473 gene probes (Zhou and Wu, personal communication). The marine data set contained 12 experimental treatments and 8 to 10 replications of each treatment for a total of 106 arrays. The experimental design was a 6 × 2 factorial with samples taken from depths of 11, 9, 7, 5, 3, and 1 ft at two locations.

Both LLE and PCA provided suitable low-dimensional representations of embeddings in high-dimensional nonlinear manifolds, when analyzing a set of differentially expressed genes. The best LLE solution accounts for significantly more sample variance (79.7%) than the related PCA solution (62.2%). Quantitative measures also indicate that both the LLE and PCA are able to achieve a partial separation of samples in two-dimensional space based on depth class and location. The LLE solution appears to provide a better separation of samples.

Benefits

Our results demonstrate that genomic techniques can substantially enhance the resolution and informativeness of ecological studies. We developed a method that allows quantification of roots of different species in mixtures collected from the field. The microbial results demonstrate that substantial yields of microbial DNA can be obtained from field samples. Furthermore, spatial variation is such that extensive sampling is required to capture the diversity present at a typical field site, even in the case of an apparently uniform site like that of the OCCAM experiment. Furthermore, the high frequency of novel sequences in the clone libraries points out one of the shortcomings of the microarray approach: diversity must be assessed by sequencing before arrays can be applied in a new setting. To further explore the benefits and challenges

of the techniques developed in this LDRD project, we have submitted four proposals to pursue ecosystem genomics research through the PER scaling program. Thus far we have been successful with one major project awarded funding over three years. We will also submit a continuation of the plant work to the PER program for the OCCAM study as well as the Throughfall Displacement Experiment. Therefore, the techniques and approaches developed in this LDRD project have substantially enhanced DOE's capabilities in environmental research.

References

Bergholz, P. W., C. E. Bagwell, and C. R. Lovell. 2001. "Physiological diversity of rhizoplane diazotrophs of the saltmeadow cordgrass, Spartina patens: Implications for host specific ecotypes," *Microb. Ecol.* **42**, 466–473.

Brunner, I., S. Brodbeck, U. Buchler, and C. Sperisen. 2001. "Molecular identification of fine roots of trees from the Alps: reliable and fast DNA extraction and PCR-RFLP analysis of plastid DNA," *Mol. Ecol.* **10**, 2079–2087.

Gentle, A., F. Anastosopoulos, and N. A. McBrien. 2001. "High-resolution semi-quantitative real-time PCR without the use of a standard curve," *Biotechniques* **31**, 502–508.

Guschin. D., B. Mobarry, D. Proudnikov, D. Stahl, B. Rittmann, and A. Mirzabekov. 1997. "Oligonucleotide microchips as genosensors for determinative and environmental studies in microbiology," *Appl Environ Microbiol.* **63**, 2397–2402.

Huang, J., F. J. DeGraves, D. Gao, P. Feng, T. Schlapp, and B. Kaltenboeck. 2001. "Quantitative detection of Chlamydia spp. by fluorescent PCR in the LightCycler," *Biotechniques* **30**, 150–157.

Jackson, R. B., L. A. Moore, W. A. Hoffmann, W. T. Pockman, and C. R. Linder. 1999. "Ecosystem rooting depth determined with caves and DNA," *PNAS* **96**, 11387–11392.

Linder, C. R., L. A. Moore, and R. B. Jackson. 2000. "A universal molecular method for identifying underground plant parts to species," *Mol. Ecol.* **9**, 1549–1559.

Lynch, J. M. 1990. "Some consequences of microbial rhizosphere competence for plant and soil," pp. 1–10 in *The Rhizosphere*. John Wiley and Sons, Chichester.

McCully, M. E. 1999. "Roots in soil: Unearthing the complexities of roots and their rhizospheres," *Annu Rev Plant Physiol Plant Mol Biol* **50**, 695–718.

Norby, R., and R. Jackson. 2000. "Root dynamics and global change:seeking an ecosystem perspective," *New Phytol.* **147**, 3–12.

Roweis, S. T., and L. K. Saul. 2000. "Nonlinear dimensionality reduction by locally linear embedding." *Science* **290**, 2323–2326.

Schloter, M., M. Lebuhn, T. Heulin, and A. Hartmann. 2000. "Ecology and evolution of bacterial microdiversity," *FEMS Microbiol. Rev.* **24**, 647–660.

Shalon, D., S. J. Smith, and P. Brown. 1996. "A DNA microarray system for analyzing complex DNA samples using two-color fluorescent probe hybridizatroin," *Genome Res*. **6**, 639–645.

Tiquia, S. M., J. Lloyd, D. A. Herms, H. A. J. Hoitink, and F. C. Michel, Jr. (2002). "Effects of mulching and fertilization on soil nutrients, microbial activity and rhizosphere bacterial community structure determined by analysis of TRFLPs of PCR-amplified 16S rRNA genes," *Appl. Soil Ecol.* **21**, 31–48.

Zak, D. R., K. S. Pregitzer, J. S. King, and W. E. Holmes. 2000. "Elevated atmospheric CO2, fine roots, and the response of soil microorganisms: a review and hypothesis," *New Phytol.* **147**, 201–222.

Intelligent Consequence Management for Energy Assurance

J. Sorensen,[1] O. Franzese,[2] F. Southworth,[2] B. Bhaduri,[3] and C. Liu[3]
[1]*Environmental Sciences Division*
[2]*Engineering Science and Technology Division*
[3]*Computational Sciences and Engineering Division*

This project developed a prototype system to demonstrate the feasibility of intelligent consequence management for energy security. An intelligent consequence management system utilizes state-of-the-art sensor technology and wireless communications coupled to real-time simulation and decision support models that will greatly enhance management of crises in rapidly unfolding events. The real time system developed was for evacuation management. Two technical achievements were realized. The first was the development of a dynamic traffic assignment–based evacuation code. The second was a prototype of an evacuation feasibility tool to assess the time required to evacuate an area at risk on a local level with coverage of the entire country.

Introduction

We have a vision of an intelligent consequence management system that utilizes state-of-the-art sensor technology and wireless communications coupled to real-time simulation and decision-support models that will greatly enhance management of crises in rapidly unfolding events. Among the properties of advanced consequence management are the following:

- New sensor networks or links to existing sensor networks designed to detect and monitor the threats of concern.
- High-speed communications and data exchange.
- Real-time simulation models running on high-speed machines.
- Advanced decision support tools that can process data and simulation outputs into a format useful to decision-makers.

Evacuation is the primary protective action for many natural and technological hazards and many terrorist events. It can be an extremely rapid action for acute hazards such as flash floods, wildfires, sudden volcanic eruptions, localized tsunamis, or hazardous material releases. It can be an extended action for slow onset events such as hurricanes, riverine floods, and distant tsunamis. To illustrate the utility of intelligent consequence management, we concentrated our efforts on developing a prototype of a real-time evacuation model.

Technical Approach

Previously evacuation models used static traffic assignment (or static allocation of flows to different paths) that assume that the conditions of the network at the beginning of the simulation prevail throughout the evacuation. A better representation of the problem of determining the optimal a priori evacuation paths would be a dynamic network flow model. In dynamic networks, the state of the system changes over time. That is, as people move through the network over time, the traversal times determine how long each unit of flow spends traversing any given link while the capacities restrict the rate of flow on that link. Capacities along the link are recaptured as the flow moves out of the link. Dynamic traffic assignment also provides a better linkage between the traffic assignment and simulation models so the dynamics of traffic flow —namely, the route selection process— is more accurately modeled than in models that rely on static assignments. The first goal to achieve was the development of a dynamic evacuation model.

The second major challenge in using a real time evacuation model is collecting data required by the model. First a link/node traffic network needs to be constructed. Second daytime and nighttime populations need to be assigned to network loading points. ORNL has automated these processes through an integration of transportation and populations modeling systems.

Results and Discussion

A prototype dynamic assignment model was developed at ORNL prior to the development of real time traffic monitoring (Southworth et al. 1992) for vehicular networks. An experimental application to use traffic data was also developed (Janson and Southworth 1992). This code has been recently integrated with simulation code ESIM to produce a dynamic evacuation code called DSIM. In each time period of the simulation, new traffic assignments are calculated that are based on the distribution of traffic in the previous time period. Predictions of future traffic behavior are based on current traffic patterns, which are continuously updated at discrete time periods.

The DSIM code more closely simulates driver behavior in congested traffic than a static model. If people encounter stalled traffic, they will take an alternative route based on their knowledge of the area, maps, or traffic guides. Seeking alternative routes that represent underutilized capacity decreases the time needed to evacuate. The dynamic assignment makes it feasible to use real time traffic sensor data to drive the model. The real-time data would be supplied by sensors that assess travel times and flows along the different links on the network as well as queues at chocking points.

A comparison of the static and dynamic codes is found in Fig. 1. The latter predicts lower evacuation times—about 3 hrs 8 minutes against 4 hrs 13 minutes for the static assignment—because it better captures the drivers behavior (e.g., avoidance of congested areas if there are alternative routes to the same destination). Figure 1 shows, as a function of time of day (evacuation starts at 22:00), the percentage of the evacuating population that has exited the Protective Action Zone and is no longer at risk. Although at the beginning of the evacuation both static and dynamic assignments predict almost the same clearance pattern, once the network starts getting congested, the latter is able to use excess capacity to achieve 100% clearance earlier (01:08 vs. 02:13).

A first approximation of the evacuation network is derived from national data bases containing geocoded highway and road data. Two sources of information are used to determine the topology and geometric characteristics of the transportation network within the areas at risk. The first one comprises publicly available databases that are enhanced with the North American Inter-modal Freight Network Model, a national GIS database created at ORNL as part of the Bureau of Transportation Statistics (US DOT) Commodity Flow Survey (Southworth and Peterson 2000). The second source, which complement this database, is a probabilistic model that assigns attributes to segments of roadways (such as, for example, speed limit, number of lanes, and others) where this information is not available.

The probabilistic model was developed using information contained in the FHWA Highway Performance Monitoring System (HPMS) database. This is a national-level highway database that includes use, performance, and operating characteristics information on all public roads. For each state and each roadway class within that state, it is possible to build a probability distribution of traffic parameters characteristics, which can then be used in conjunction with Monte Carlo simulation techniques to generate those network attributes that are not contained in other databases.

This is linked to a high-resolution (90 m) population distribution data (LandScan USA) for the United States as part of the ORNL LandScan global population project. LandScan USA is more spatially refined than the resolution of block-level census data and includes demographic attributes (age, sex, race). The model includes development of an "ambient population" (average over 24 hours) for global LandScan and development of spatial distributions for "residential or nighttime population" as well as for "daytime population" as part of LandScan USA. Locating daytime populations requires not only census data, but data on places of work, journey to work, and other mobility factors. The combination of both residential and daytime

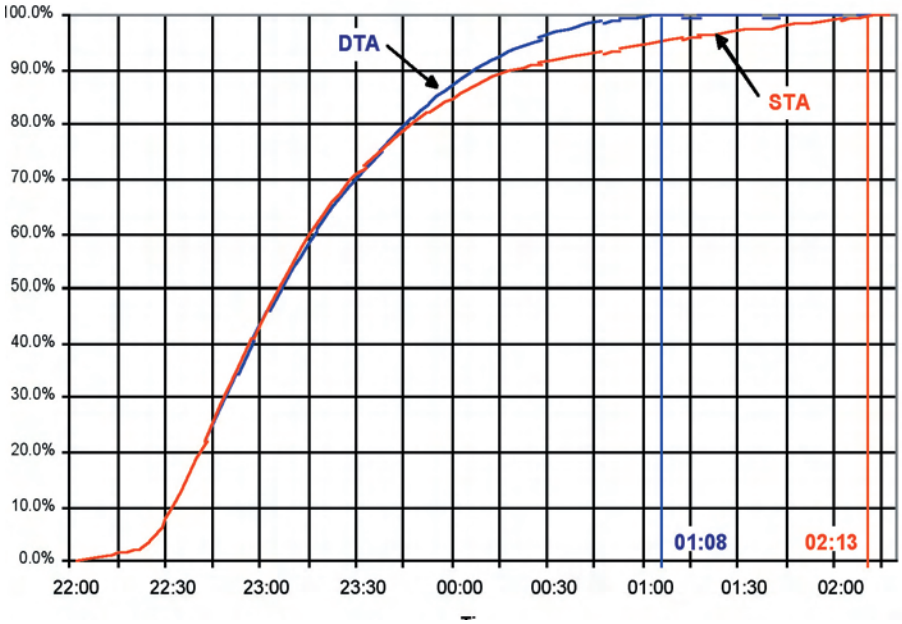

Fig. 1. Traffic Simulation Results: Population Clearance for Static and Dynamic Traffic Assignments.

populations will provide the best estimate of who is potentially at risk and would need to evacuate. Because of the fine spatial detail, population can be assigned to loading points on the transportation network.

For the ICM system, we use a GIS environment that was built at ORNL based on ESRI (Environmental Systems Research Institute, Inc.) MapObjects. The GIS environment is used primarily for input and display of large volumes of data and results but also has components that help build the topology and attributes of the transportation network for those cases in which this information cannot be extracted from existing databases.

The new dynamic modeling capability has been linked to ARCVIEW GIS to visualize the simulation results. The evacuation routes have been layered over an aerial photographic view of the test site around Richmond, Kentucky. The number of vehicles evacuating are depicted as small dots traveling over the network at the speeds predicted by the model. If bottlenecks occur, the dots begin to queue on the network and the density indicates the level of congestion. Other model parameters can be displayed as graphs or charts showing traffic speed, number of vehicles on a link, capacity utilized, and number of vehicles clearing a link.

Benefits

This LDRD effort has positioned ORNL as a leader in consequence management and situational analysis simulation for homeland security. Based on our work, DARPA has funded ORNL to become part of the Pentagon Immune Buildings Program. In that effort, we will build an evacuation model of the Pentagon.

ORNL has been asked to submit proposals to two Department of Homeland Security Office of Science and Technology programs. The first is to help support the training simulation program that is a joint effort between the Emergency Preparedness and Response Portfolio and the Advanced Computing Portfolio. The second is to support the Biological Warning and Incident Characterization System (BWIC) program that is part of the Biological Portfolio.

References

Janson, B., and F. Southworth.1992. "Estimating departure times from traffic counts using dynamic assignment," *Transportation Research* **26b**, 3–16.

Southworth, F., B. Janson, and M. Venigalla. 1992. DYMOD: Toward real time dynamic traffic routing during mass evacuation. Managing Risk With Computer Simulation, San Diego, Calif., Computer Simulation Society.

Southworth, F., and B. E. Peterson. 2000. "Intermodal and international freight network modeling," *Transportation Research* **C8**, 147–166.

ENVIRONMENTAL SCIENCE AND TECHNOLOGY

Seed Money Fund

Permeable Environmental Leaching Capsules (PELCAPs) for Nondestructive In Situ Evaluation of Contaminant Immobilization Techniques in Soil

B. P. Spalding and S. C. Brooks
Environmental Sciences Division

Permeable environmental leaching capsules (PELCAPs), which encapsulate radioisotope-spiked soil samples within a water-permeable polyacrylamide matrix, were developed and tested in situ in groundwater as method to measure immobilization of contaminants. Groups of PELCAPs were retrieved and replaced in ground and surface waters many times during which they were assayed for contaminants nondestructively using gamma spectroscopy. As a proof of principle, soils contained in PELCAPs were labeled with two radioisotopes (strontium-85 and cesium-134) and were leached in both laboratory tests as well as in situ with ground and stream waters at Oak Ridge field sites. In situ retention of both isotopes within PELCAPs, containing thermally treated soil with high degrees of radioisotope immobilization, has been demonstrated for six months in field tests. Untreated soils, readily leached strontium-85 in the field, while the soil, physically retained in the polymer matrix, maintained its cation exchange properties.

Introduction

Although many promising techniques for in situ immobilization of hazardous and radioactive contaminants in soil have been developed, comparative evaluation of several techniques at several sites or of several techniques over a range of groundwater conditions remains extremely costly and difficult to demonstrate in the field due to the destructive and expensive nature of repeated soil and groundwater sampling. The objective of this investigation was to develop and demonstrate an inexpensive, direct, and effective in situ technique to monitor soil contaminant immobilization non-destructively in the field using radioisotope-spiked soil contained within PELCAPs. The PELCAP technical approach has potential advantages for the assessment of induced and/or natural contaminant availability within soils including:

- Nondestructive measurement of the amount of immobilized contaminant in a soil over time thereby avoiding the necessity for repeated, costly, and destructive soil sampling,
- Direct comparison of several immobilization treatments, including a no-treatment control, under identical field conditions within the same well,
- Internal calibration of PELCAP leaching relative to specific reference tracers (^{85}Sr and ^{134}Cs) which have well-characterized environmental leaching behavior,
- Accelerated evaluation of remedial alternatives by deploying PELCAPs in uncontaminated regions of a site avoiding masking by continued contaminant flux, and
- Correlation of PELCAP behavior with widely-accepted laboratory selective extraction and isotopic dilution protocols.

Technical Approach

This PELCAP soil contaminant availability research encompased five research tasks:

(1) Develop a polymer matrix for PELCAPs from which ^{85}Sr and ^{134}Cs freely diffuse with coefficients similar to those found in water; (2) Develop PELCAPs which retain soil particles greater than 0.1 μm; (3) Demonstrate that available forms of radionuclides in soil within PELCAPs leach similarly to unencapsulated soil during laboratory sequential extractions; (4) Demonstrate that soil immobilized forms of radionuclides in PELCAPs behave similarly when leached in situ in field groundwater as when leached by laboratory methods; and (5) Establish the methodology for PELCAP contaminant availability analysis, PELCAP durability for extended field deployment, and precision of PELCAP performance under field conditions.

A standard polymer formulation (15.0% acrylamide, 0.3% methylene-bis-acrylamide, 0.2% tetramethylethyle nediamine, and 0.18% ammonium persulfate in water) for preparing PELCAPs in a polyacrylamide matrix was selected and tested using laboratory sequential extractions with ^{134}Cs and ^{85}Sr spiked soils. Two grams of a standard soil, sieved to <100 mesh, were weighed into a cylindrical mold (a cut-off 10-mL plastic syringe with the plunger as the base) with 3.0 mL of the freshly-prepared polymer solution; the contents (soil suspended in the solution) were mixed with a stainless steel spatula intermittently until the mixture set to a gel usually within 20 minutes. Bulk samples (300 grams each) of one well characterized soil were spiked with either ^{85}Sr or ^{134}Cs to a nominal activity about 0.1 μCi/g using excess tapwater with stirring and final drying at 110°C and remixing by sieving to <100 mesh again. Thermal treatment of the radioisotope-spiked

soil was carried out by heating 30 g subsamples in Pt crucibles at 1000°C for 24 hours; following cooling to ambient temperature, thermally treated soils (colored red but still unsintered and non-cohesive powders) were sieved again to <100 mesh. Six replicate PELCAPs of each treatment/isotope combination were prepared so that statistically valid estimates of sample isotope retention variance in the field could be obtained. Two suites of 54 PELCAPs each (six replicates of 9 types: spiked with either or no isotope, with or without soil, and with either untreated or thermally-stabilized soils) were deployed in both stream water and groundwater. Each PELCAP was retained in a perforated 20-mL snap-top polyethylene vial which, inturn, was restrained in a plastic testtube rack for submersion in either a stream pool or groundwater collection sump on the Oak Ridge site. Additional suites of PELCAPs were prepared for laboratory sequential extractions (Spalding 2001); sequential extractions were also carried out on equivalent amounts of soil without encapsulation in polyacrylamide. Diffusion coefficients of both ^{85}Sr or ^{134}Cs in the polymer cylinders, without soil, were measured for tapwater leaching using the established method for specimens in such cylindrical geometries (ANS 2003). Cation exchange capacity of both the untreated and thermally-treated soil was measured using ^{85}Sr-spiked 0.1N SrCl2 (Francis and Grigal 1971).

Results and Discussion

The sequential extraction behaviors of these radioisotopes from encapsulated soils and from the same but non-encapsulated soils were quite similar. Initially, the extraction sequence (Spalding 2001) was applied with 1-hour intervals between the four successive extractions of each of the solutions (water, 0.1N CaCl2, and 0.2N HCl); however, a 24-hour equilibration for each successive extraction was found necessary to yield extraction profiles similar to those of the un-encapsulated soils. This similarity of soil extractive behavior, whether polymer-encapsulated or not, provides evidence for the inertness of the polymer itself to radioisotope adsorption as well as stability of the polymer to the extraction reagents. Our measurements of diffusion coefficient for both isotopes (ANS 2003) from cylindrical polyacrylamide PELCAPs without soil into tapwater or 0.1N CaCl2 were similar (10^{-6}–10^{-7} cm^2/s) to those in aqueous solution at room temperature. Measurement of soil cation exchange capacities (Francis and Grigal 1971), with or without encapsulation in PELCAPs, were found to be similar (about 10 milliequivalents (+)/100 g for the untreated soil); soil contained in PELCAPs and subjected to six months of in situ leaching in groundwater, was found to exhibit this same cation exchange capacity after use. This finding supports the conclusion that the polymer gel remained inert yet very permeable to ionic species and did not interfere with the cation exchange properties of the soil either immediately on encapsulation in polymer or in the long term during field leaching.

The natural in situ leaching of the isotopes from PELCAPs by natural waters in the field required several months to reach unchanging retention fractions (Fig. 1) but ultimately exhibited similar retention fractions for the isotope-spiked soils as in laboratory-extracted PELCAPs. The behavior of the soils in PELCAPs, summarized in Fig. 1, established a number of the hypotheses proposed by this LDRD SEED project. Firstly, all solid soil constituents were retained in the PELCAPs during six month's suspension in turbulent stream water. The strongly particulate reactive ^{134}Cs, was completely retained in the PELCAPs containing either untreated or thermally-treated soil. All PELCAPs also retained their physical integrity over the six month deployment and appeared on visual inspection to be similar in clarity and elasticity to their original condition. Secondly, ^{134}Cs and ^{85}Sr were readily leached from PELCAPs without soil within 3 days of in situ leaching. Thus, the PELCAPs polymer was excellent at retaining soil particles while remaining inert during aqueous leaching by ionic diffusion through the gel. Thirdly, ^{85}Sr in untreated soil behaved as expected for a cation-exchangeable species in soil. Over several months, the dissolved cations in stream water replaced most, but not all, of the ^{85}Sr resulting in an expected degree of equilibration over time given the soil's cation exchange capacity and the concentration of dissolved cations in stream water (Spalding and Spalding 2001). Some of the

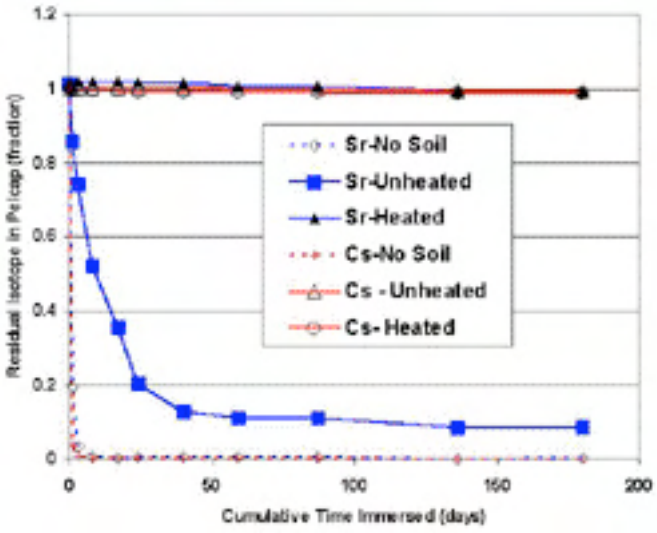

Fig. 1. Retention of ^{85}Sr and ^{134}Cs during six months of in situ leaching by stream water using polyacrylamide-based permeable environmental leaching capsules (PELCAPs) containing soil, thermally-stabilized soil, or no soil (polymer only).

spiked ^{85}Sr (about 8%) in the untreated soil appeared to be naturally attenuated and remained strongly adsorbed to the soil. Fourthly, simple thermal treatment of soil at 1000°C for one day resulted in the complete immobilization of either ^{85}Sr or ^{134}Cs for up to 6 months of in situ leaching in stream or ground water. Although previous work on laboratory thermal treatment using sequential extraction methods has found these isotopes to be strongly adsorbed to soil following such thermal treatment (Spalding 2001), this is the first demonstration of the persistent stability of that immobilization employing the natural continuous leaching afforded by stream and ground waters in situ.

Benefits

The PELCAP soil contaminant availability methodology is applicable to DOE's mission to predict the impacts of long-term stewardship of its waste disposal sites and practices. By providing a low-cost methodology to assess long-term performance of contaminated soil, whether natural or imposed by remediation methods, these research findings should enable DOE managers to make judicious choices in selecting remedial actions. Because the PELCAP methodology involves nondestructive and repeated analyses of soil samples at various times, large cost savings can accrue over traditional destructive sampling methods. This PELCAP soil contaminant availability methodology should also be applicable to the U.S. EPA and the DoD, Strategic Environmental Research and Development Program.

References

American Nuclear Society (ANS). 2003. Measurement of the leachability of solidified low-level radioactive wastes by short-term test procedure. ANSI/ANS-16.1-2003. American Nuclear Society, La Grange Park, IL., 33 pp.

Francis, C. W., and D. F. Grigal. 1971. A rapid and simple procedure using ^{85}Sr for determining cation exchange capacities of soils and clays. *Soil Sci.* **112**: 17-21.

Spalding, B. P. 2001. Fixation of radionuclides in soil and minerals by heating. *Enviorn. Sci. Technol.* **35**: 4327–4333.

Spalding, B. P., and I. R. Spalding. 2001. Chemical equilibria model of strontium-90 adsorption and transport in soil in response to dynamic alkaline conditions. *Enviorn. Sci. Technol.* **35**: 365–373.

Construction of a Gene-Prediction Algorithm in *Populus:* Adding a New Dimension to Complex Biology

L. E. Gunter[1] and F. W. Larimer[2]
[1]*Environmental Sciences Division*
[2]*Life Sciences Division*

The goal of this proposal was to create a unique annotation resource for the *Populus* genome sequencing effort. We developed *Populus*-specific models for the functional analysis of genes using novel information contained in a library of full-length cDNA clones derived from various *Populus* tissues. A collection of accurately characterized, full-length cDNA sequences allowed us to develop a proof of principle for automated gene-prediction algorithms that are critical for recognition of *Populus* genes. The design and implementation of a precise gene-prediction tool for the annotation of the *Populus* genome will open new avenues of functional genomics at ORNL.

Introduction

In September 2004, the DOE-JGI and ORNL in collaboration with Genome Canada-Genome BC, the Umeå Plant Sciences Center, and the University of Ghent released the genome sequence of *Populus trichocarpa* which was sequenced to an 8.6X depth and which is now publicly available. The goal of this project was to fully exploit the opportunity afforded by the whole-genome sequencing effort by designing and testing a novel annotation tool that will establish ORNL as a leader in *Populus* functional genomics. The development of this type of informatics tool will furnish us with a resource that will enhance the laboratory's ability to address future DOE missions in functional genomics of *Populus* and increase the scientific and technical vitality and visibility of ORNL through securing a national and international role in *Populus* genomics. This knowledge could have profound implications for carbon management issues related to long-lived perennials, conversion of biomass to fuels and products, and the deployment of plant-based systems for phytoremediation. The objectives of this research were to (1) provide sequence input of unique *Populus* structural genes to gene-prediction models and (2) design a customized version of Grail-EXP to provide unique and consistent exon finding and gene model algorithms for *Populus*.

Technical Approach

A large collection (~2000) of full-length cDNAs from libraries derived from a variety of tissues of *Populus trichocarpa* "Nisqually-1" were sequenced using dye terminator chemistry, then assembled into full-length reads. Raw sequence data files were analyzed to assign quality scores to sequenced fragments prior to assembly. Only nucleotides assigned a quality score of Q40 with a 2X or greater coverage were used to assemble full-length cDNA sequences that were used to train the gene-prediction algorithm.

In order to train ab initio gene prediction algorithms, ESTs and full-length cDNAs were aligned. Approximately 250,000 *Populus* ESTs were assembled from existing libraries (e.g., xylem, phloem, cork, root, stress treatments, sapwood-heartwood transition zone, subtracted libraries, etc.). This EST resource was clustered into a 20,000 unigene set which contained over 4000 in silico full-length sequences. The in silico set was manually curated and reduced to an 1112 FL EST that was used to train the ab initio gene calling algorithms. The remaining ESTs were used to verify the predicted gene models.

Populus cDNA sequences and EST assemblies were then aligned with genomic draft sequence. High-quality alignments (99% identity and greater) were use to create profiles of exon size and number distribution, coding exon hexamer distribution, intron-size distribution, intron hexamers, and splice-site structure were derived. The Grail EXP6 training module computed the non-coding (intron) frequencies for both 5bp-windows and 6bp-windows from the poplar intron sequence. The coding (cds) frequencies for both "window5" and "window6" from the poplar coding sequence (exons) were also determined. Both the non-coding and coding transition probabilities for Markov chains were calculated from the coding/non-coding frequencies, and transition probabilities are used to calculate the log10 preference files. Initially, the frequency and probability for both high-*gc* and low-*gc* content were assumed to be equal. The donor, acceptor, and start matrix were directly derived from the training set cDNAs and ESTs sampled.

Results and Discussion

Over 2000 full-length poplar cDNAs have been identified from the libraries, sequenced, and assembled in partnership with Genome Canada. These full-length cDNA sequences were aligned to the poplar assembly. High-quality alignments (99% identity) were use to create profiles for coding sequence, intron sequence, and splice-junction frequencies. GRAIL-EXP6 produced 42,169 total gene models, which represent 35,922 distinct loci (Table 1). GRAIL-EXP6 models splice variants. Of the 35,922 distinct loci, 4,542 (12.6%) were represented by two or more splice-variant models (10,789 total).

Both the full-length cDNAs and in-silico cDNAs were used to create the basal annotation for the assembled genome using several gene models. These were GRAIL-EXP6 from ORNL, EUGENE from the University of Ghent, and FgenesH from JGI. In addition, Genewise was used to identify general open reading frames. All *Populus* EST data, along with EST data from other organisms (mainly Arabidopsis and rice), were used to validate the ab initio gene models. In total, each algorithm produced between 27,000–45,000 models. The filtered model set contains 58,000 gene models, with Eugene producing 31,045 unique models (39.8%), FgenesH producing unique 30,465 models (39.0%), GRAIL-EXP6 producing 11,179 unique models (14.3%), and Genewise producing 5,392 unique models (6.9%)

Table 1. The trained modeler results from GRAIL-EXP for the full poplar assembly. LG = linkage group

Scaffold	All	Distinct	Variants	One-exon gene
LG_I	3149	2682	350	690
LG_II	2888	2385	385	651
LG_III	1923	1614	220	458
LG_IV	1344	1137	155	296
LG_V	1726	1458	202	393
LG_VI	1998	1686	239	457
LG_VII	1307	1062	158	293
LG_VIII	2142	1776	263	452
LG_IX	1692	1419	212	366
LG_X	2460	2029	315	544
LG_XI	1119	929	118	283
LG_XII	1177	1000	141	295
LG_XIII	1161	951	131	283
LG_XIV	1501	1264	174	308
LG_XV	1064	936	98	253
LG_XVI	1209	1022	137	291
LG_XVII	404	355	40	108
LG_XVIII	1181	1003	137	254
LG_XIX	844	730	80	233
unmapped	11880	10484	987	4105
Total	**42169**	35922	4542	11013

Approximately 30% of all models have EST support. Gene models per linkage group ranges from 404 to 3149; 11,880 gene models remain in non-assembled, non-mapped regions of the genome. This preliminary set of gene models and annotations is available through JGI's Populus Genome Browser (Fig. 1) and will be refined through further analysis and manual curation.

Summary and Benefits

We were ultimately successful in developing *Populus*-specific gene models by training GRAIL-EXP6 from novel information contained in the sequenced library of 2000 full-length cDNA clones. Models were validated with EST data from *Populus* and other closely related organisms. These models are essential for continuing work in *Populus* functional genomics. The completed sequence from the *Populus* genome is an invaluable resource, not only to the forest research community, but also to plant biologists the world over. However, just as the Arabidopsis and Human Genome communities have found, whole-genome sequence alone is of little utility to most researchers unless it is supplemented with high-quality annotation. To capture the wealth of information connecting plant genome structure, gene family diversity and plant development, detailed knowledge of (1) genome structure and evolution, (2) gene architecture and (3) structural elements controlling transcription derived from known gene sequences is essential. For this, accurate gene identification is fundamental. Designation of orthologs vs paralogs will be greatly enhanced by working hypotheses of genome evolution. Finally, functional genomics efforts, including the design of whole-genome microarrays and large-scale knock-out/knock-in mutagenesis programs, will depend on the accurate and complete annotation of the genome database. Accurate gene prediction models and annotation of the *Populus* genome are of interest to DOE-BER and NSF-PGP in the following areas of interest: (1) functional genomics studies identifying and categorizing complete gene families in *Populus*; (2) comparative and evolutionary genomics work among three moderately related species with strongly contrasting characteristics, *Arabidopsis thaliana*, *Medicago truncatula*, and *Populus trichocarpa*; and (3) *Populus* biology related to the forest products industry, bio-based energy, phytoremediation, and ecosystem sciences. The success of this project and our collaboration in general on the Poplar Genome sequencing

project has contributed to new funding over the next year from the DOE Office of Science BES and NSF-Plant Genome programs.

References

U.S. Department of Energy Joint Genomes Institute (JGI). Populus trichocarpa genome. Available http://genome.jgi-psf.org/Poptr1/Poptr1.home.html.

JGI. Populus trichocarpa v. 1 genome browser. Available October 29, 2004, http://genome.jgi-psf.org/cgi-bin/browserLoad/4177ba9d4a16e57e4f54c7c6.

Minimum Required Migration Distances: A New Tool for Estimating Climate Change Impacts

W. W. Hargrove[1] and F. M. Hoffman[2]
[1]*Environmental Sciences Division*
[2]*Computational Science and Mathematics Division*

We describe a new technique to quantify and map the impact of any specified scenario of climatic change on adapted communities living within the affected area. Analysis is based on a determination of the minimum straight-line distance that the affected community would have to move geographically after the climatic shift in order to return to the same combination of environmental conditions that it had before the change. The minimum required migration distance is used as an analog of the likelihood of local extinction of that community. MRM analysis can be used as a conservation planning tool as well as mapping severity of impact. Standard GIS tools can be used to perform the MRM severity analysis.

Introduction

While the development of global climate simulations is an active area of research, there has been little investment in tools that can estimate the consequences or severity of predicted changes. We have conceived a new type of climate change impact analysis: the minimum migration distances and directions, which will be required for communities to return to optimum conditions following predicted climate change. Consider a plant community that is adapted to growing in cold mountaintop ecoregions. Under climatic warming, this species will be forced to migrate to higher elevations until it runs out of proper local habitat. If the closest mountaintop conditions, which remain, are geographically distant, it is unlikely that this plant community will successfully complete the migration and survive the climatic changes.

This minimum required migration (MRM) distance is a surrogate for the probability of local extinction for specialized communities. Specialized communities have a higher extinction risk in areas where long straight-line Euclidean dispersal distances would be required to find the same pre-change environmental conditions. If the same initial conditions are available only a short geographic distance away, then the risk of extinction is much lower.

The MRM analysis is ecoregion-based. In a given change-through-time scenario, all geographic locations that undergo an environmental change will be considered. At each location, the ecoregion classification is known, both before and after climate change. The straight-line distance required to reach the closest future occurrence of the former ecoregion will be mapped as the MRM distance. Locations changing to or from a unique ecoregion type have no surrogates, and therefore have an infinite MRM distance. Locations not changing have an MRM distance of zero and are not at risk. Since these calculations must be performed for each cell in the map, the process is computationally intensive.

Two maps can be produced per change scenario, one indicating MRM distance and one indicating the compass direction of the MRM. For climatic warming, the direction of MRM will usually be toward the poles but may, in some locations, be mediated by strong local physiographic effects, prevailing wind, or water circulation.

MRM utilizes a multivariate statistical clustering technique to generate the before- and after-change ecoregions upon which the analysis is based (Hargrove, Hoffman and Sterling 2001; Hargrove, Hoffman, and Law 2003; Hargrove and Hoffman 2004a, 2004b). This ecoregionalization method begins with GIS layers describing conditions both before and after a climatic shift. These conditions are used as multivariate descriptors of the climatic environment at each location in the map. Using a supercomputer, all cells in the before and after maps are subjected to an iterative clustering procedure. The number of ecoregions to be found is specified by the user. When fewer than a specified number of map cells changes assignment from the last iteration, the process converges on an ecoregion classification. When used on a chronosequence of maps, we call this technique multivariate spatio-temporal clustering (MSTC) (Hargrove and Hoffman 2003, Hargrove and Hoffman 2004a). Used in this way, MSTC divides both the before- and after-change maps into a single common set of ecoregions. This common assignment of ecoregions makes it possible to determine where the geographically closest conditions are in the future to those formerly in this location in the past.

Methods

We calculated MRM distances and directions within the lower 48 United States under both the CCC and the

Hadley UKMO forecasts for the year 2099. These two alternative future scenarios were selected, prepared, downscaled, and used as the basis for the last U.S. National Assessment of climate change impacts. We produced a common ecoregionalization having 100 quantitative ecoregions within the present and both alternative future U.S. maps.

We characterized environments in terms of the combination of 25 variables. The factors included elevation, maximum, mean, and minimum annual temperature, monthly precipitation, several soil parameters, number of frost-free days, and solar aspect and input. Each of these layers represents a data map which was developed for the continental United States, at a resolution of 1 km^2. There are over 7.8 million map cells in each of the 25 layers. For a more detailed description of the data development methods, see Hargrove and Hoffman (2004b).

The VEMAP program made downscaled yearly data sets for these models available for the period between 1994 and 2099 at 0.5-degree spatial resolution for the continental United States. Sixteen of 25 the environmental conditions were altered to represent the conditions forecast to occur within the United States in the year 2099 by each model. We calculated differences between the present and each future scenario at 0.5-degree resolution and then applied these differences to the 1-km^2 data. In this way, high-resolution local climatic effects were retained in the predictions. MSTC was then used to find the 100 most different common environmental combinations across this set of three maps. Future ecoregion patches that potentially represent sanctuary endpoints for MRMs from large areas are important to identify from a conservation perspective. If such areas were destroyed, the distance of MRMs from a large number of cells would increase, increasing the likelihood of local extinction within large areas of the map. Such areas are important not because of their conservation value today, but because of the potential value that they will have as refugia in the future.

Results

MRM distances follow a negative exponential frequency distribution, with many short MRM distances and only a few very long MRM distances. When graphed as a cumulative frequency distribution, the CCC 2099 scenario rises faster, indicating that it is more severe (i.e., more longer MRM distances and therefore higher likelihood of extinction of local communities) than the Hadley 2099 scenario. The CCC scenario also reaches a higher cumulative plateau, showing that it predicts changes over a greater area than does the Hadley prediction. Such a graphical depiction makes clear the relative severity of impact of multiple scenarios over a particular geographic area.

Ecoregions adjacent to changing areas are the major potential recipients of MRM dispersers. For both scenarios, ecoregions in MT, ND, MN, IA, IL, IN, OH, and the Northeast potentially receive the most MRMs. In addition to these, the Mississippi Valley ecoregion is predicted to potentially receive many MRMs in the CCC scenario, while FL and the coastal plain potentially receive many MRMs in the Hadley scenario. These regions flank significant areas of change in each case.

Large discrete portions of ecoregions are likely to receive more MRMs than smaller areas, especially ones with longer shared borders (Hargrove and Hoffman 1999). The metric of conservation interest is value per unit area, since these are the terms of protection effort, remediation, or acquisition. We divided the number of cells whose MRMs are potentially ending up in each discrete portion of each ecoregion by the number of cells there in order to get a value per unit area.

Areas in which cells potentially receive MRMs from many cells are very localized and differ substantially between the two scenarios. Under the CCC scenario in the eastern United States, parts of the NC and VA mountains, the southern Smoky Mountains, part of southern WV, and areas flanking Chesapeake Bay are important future refugia, among others. In the western United States, the CCC scenario predicts numerous localized future refugia in the CO Rockies, western UT, and northeastern WY/ southeastern MT, as well as others. Future refugia are absent from a significant portion of the map, which under this scenario change dramatically into ecoregions having no counterpart in the present United States.

According to the Hadley scenario in the eastern United States, several areas within the Piedmont are identified as significant refugia, along with isolated areas in the Mississippi Valley and Sabine River Valley. The northern Ozarks are identified as a large potential future refuge, as are several areas in northern WI. In the western United States, the Hadley prediction results in future refugia scattered throughout the eastern Rockies, the arable parts of UT, and western WY. The central valley of CA is also a refuge under the Hadley scenario, as is the Olympic peninsula of WA.

Discussion

Locations of future refugia will be particularly sensitive to the downscaling methods that are used as well as to the scenario of change. Some areas indicated as important future refugia may be artifacts of the differences between resolution of the downscaled predictions and the native 1-km^2 environmental data sets.

MRM considers straight-line shortest migration distances only. There is no consideration of potential connectivity or the actual route required for such a

migration, although this has been shown to be important (Hargrove, Hoffman and Efroymson 2004), nor is there consideration of minimum patch sizes (although patches are largely due to the continental scale of the analysis). Thus, MRM probably underestimates the risk of extinction in some cases.

Prediction of locations of future refugia will be of interest to NGO conservation groups as targets for preservation. However, such preservation will be unorthodox. It is not the current environmental conditions or current biota that makes such parcels valuable but their geographic location and the predicted future environmental conditions that they will have. Thus, such preservation will not entail the protection of the biota currently inhabiting these parcels. After all, the preservation plan is for this biota to go extinct locally and to be replaced by incoming MRMs. All that is necessary for this kind of protection is to ensure that the parcel is left available for native biota and is not developed or used for agricultural purposes. Under this new view, the location and acquisition of lands to be protected is not being viewed as a static problem but rather as a dynamic process.

Benefits

Having the MRM distance and direction maps for forecasts from the two leading GCM models used in the last IPCC analysis should help position ORNL for the next round of IPCC analyses, as well as the upcoming U.S. National Assessment.

References

Hargrove, W. W., and F. M. Hoffman. 1999. "Using multivariate clustering to characterize ecoregon borders," *Computers in Science and Engineering* **1**(4), 18–25.

Hargrove, W. W., and F. M. Hoffman. 2003. "An analytical assessment tool for predicting changes in a species distribution map following changes in environmental conditions," Proceedings, GIS/EM4 Conference, Banff, Alberta, Canada, Sept. 2–8, 2000. CD-ROM, ISBN: 0-9743307-0-1.

Hargrove, W. W., and F. M. Hoffman. 2004a. "The potential of multivariate quantitative methods for delineation and visualization of ecoregions," *Environmental Management* (in press, special ecoregions issue).

Hargrove, W. W., and F. M. Hoffman. 2004b. *A Flux Atlas for Representativeness and Statistical Extrapolation of the AmeriFlux Network*, ORNL/TM-2004/112. Available at http://geobabble.ornl.gov:/flux-ecoregions.

Hargrove, W. W., F. M. Hoffman, and R. A. Efroymson. 2004. "A practical map-analysis tool for detecting potential dispersal corridors," *Landscape Ecology* (in press).

Hargrove, W. W., F. M. Hoffman, and B. E. Law. 2003. "New analysis reveals representativeness of the AmeriFlux network," *Eos* **84**(48), 529–535.

Hargrove, W. W., F. M. Hoffman, and T. L. Sterling. 2001. "The do-it-yourself supercomputer," *Scientific American* **256**(2), 72–79.

Hoffman, F. M., W. W. Hargrove, D. J. Erickson, III, and R. Oglesby. 2004. "Using clustered climate regimes to analyze and compare predictions from fully coupled general circulation models," *Earth Interactions* (in press).

Sounds of Rapids as an Attractant for Migratory Fish

C. C. Coutant, M. S. Bevelhimer, and A. M. Fortner
Environmental Sciences Division

Migratory fish such as salmon lack natural migratory cues at hydropower dams and reservoirs. We hypothesized that underwater sounds of rapids could guide migrants. Laboratory preference-avoidance experiments were conducted. A variety of sounds were played at one arm of a "Y-maze" tank and location of juvenile rainbow trout recorded by video. In 173 trials with 32 fish, there was large individual variation in fish responses, such that fish did not show a general attraction to natural sounds of rapids or repulsion from sounds of dams. Sound transmission through the tank confounded transmission through water, necessitating re-design of experiments.

Wild populations of migratory fishes like salmon have been declining due to many factors, including hydropower dams and reservoirs built on their river and stream migration routes. Reservoirs do not have many of the natural features of rivers and streams, and thus some of the presumed natural cues for migration and orientation are missing. Artificial guidance to dam bypasses is often needed. We hypothesized that the sound of rapids in a natural river could be a natural directional cue that might be artificially reproduced to aid passage. Thus, the objective of this research was to determine if natural sounds of rapids would attract juvenile fish. As a corollary, we tested the hypothesis that artificial sounds of an operating dam would repel fish.

Preference-avoidance experiments were conducted in the laboratory in an adaptation of the classical "Y-maze" behavioral test. Existing laboratory stream channels were modified to form a large U. Sounds were recorded on laptop computer from natural rapids and near Melton Hill Dam and played by underwater speaker into an end of one of the two arms. Juvenile rainbow trout obtained locally were used as surrogates for salmon, and were placed at the bottom of the U at the start of each trial, giving a choice of the arm with sound or without it. A digital video system above the experimental tank was used to observe the behavior of fish. The instantaneous position of each fish every 30 seconds of a 30-min trial was recorded, and the average position and average activity level of the fish was calculated. Standard statistical tests were applied. If the fish spent a greater amount of time in the arm with the speaker, it was determined that the fish was attracted to the sound, and vice versa.

Results indicated that in 173 trials with 32 fish, there was a large individual variation in fish responses, such that overall, fish did not show a general attraction to natural sounds or repulsion from sounds of dams. Some individuals showed strong responses, while others did not. During tests, we noticed sound transmission by the tank itself, which confounded the sound dampening with distance along the length of the channel. Detailed sound measurements in the tank identified lateral and vertical variations in sound intensity. Because fish were often near the bottom or sides of the tank, especially when not actively swimming, they may not have been able to discern the longitudinal sound gradient. The experimental tank requires redesign to minimize tank-transmitted sound.

Although inconclusive so far, the experiments still offer promise of identifying cues for fish behavior that can be used for attraction or repulsion at energy facilities to aid migrations or avoid dam-related damages.

Development of a Novel Method for Rapid Cellular Material Extraction and Separation in Air

M.-D. Cheng
Environmental Sciences Division

High-quality extraction of nucleic materials from a cell takes time, and subsequent purification of the materials requires elaborated treatment. Through tedious extraction and purification, one anticipates obtaining high-quality cellular fragments for genetic analysis and reduction/elimination of false positives. Our technique utilizing laser-induced shock wave coupled with aerosol-based separation is expected to enhance rapid extraction of genetic fragments from living cells and improve the purity of extracted materials.

Several methods exist for breaking up cells and releasing intracellular materials. Ultrasonic wave has been employed to disrupt the bacterial and fungal cells, but it could generate tremendous heat that can destroy organelles and alter the configuration of biological molecules. It has been common practice to suspend cells in liquid buffers and introduce lysing chemicals into the buffers, where chemical lysis is effective, but it contributes to the cost, contamination, and complexity of analysis and creates a problem of disposal of additional chemical waste, especially in situations in which many samples must be analyzed. High-throughput genetic analysis and positive identification of biological aerosols can be substantially enhanced, if high-quality cell lysis and fragment separation can be achieved in the air in real time.

During FY 2004, we investigated the physics of laser-induced shock wave and techniques to confine and focus the shock wave for cell lysing purposes. We characterized the microbial cells that we will use as the test agent and evaluated the fragments that were generated by the shock wave. The shock wave measurement was made under 1-atm pressure and temperature conditions with two experimental configurations—with and without a confinement cell. In either case, we found the traveling velocity of the shock wave decreases approximately by about 30% within some 10 microseconds after it was initiated, which translates into a decrease in the Mach number from 7 to 5. The pressure at the shock wave front was estimated to be about 31 atm. The pressure propagation appears to be isotropic as we could not detect differences at several spherical angles. The pressure front has a thickness about 4 mm; under this condition sharp wave propagation is created to lyse the biological cell structure.

Shewanella oneidensis MR-1 cells were used as the test agents. The choice was simply convenience. The gene sequence of *Shewanella oneidensis* MR-1 cells was mapped in other projects led by a colleague, Dr. Thompson in ESD. Such information will prove useful for comparison for this project in FY 2005. The microbial cells were dispersed by a nebulizer. The size measurement of the uninterrupted MR-1 cells by an aerodynamic particle-size spectrometer showed 2.1–2.4 μm, which is consistent with the microscopic measurement obtained by Dr. Thompson's group.

After shock-wave lysing, the size distribution of the cell fragments appears to be multi-modal, with multiple modes spanning from 20 to 800 nm. It was difficult to verify the multi-modal results because the spectra are statistically weak due to low-cell-density count. The size spectra of fragmented cells overlapped the size distribution that resulted from the residual nanoparticles in the air stream. We are investigating means to reduce the background nanoparticles. Work is also ongoing to assemble a new type of biological aerosol nebulizer that can remove foam from the aerosol stream that can substantially increase the airborne cell density and thus the spectral identification issues. We will also further evaluate the quality of the lysing fragments in FY 2005 and continue to improve our fragment separation technique.

Environmental Isotope Forensics of Perchlorate Contamination

J. Horita,[1] B. Gu,[2] G. M. Brown,[1] N. C. Sturchio,[3] and J.-K. Böhlke[4]
[1]*Chemical Sciences Division*
[2]*Environmental Sciences Division*
[3]*University of Illinois at Chicago*
[4]*U.S. Geological Survey, Reston*

Perchlorate ($ClO4^-$) contamination is threatening nation's drinking and irrigation water supplies in more than 24 states, and the number of the cases is rapidly growing. However, aside from obvious large-scale anthropogenic sources (rocket fuel plants, air force bases, etc.), the source of this contamination is not always identifiable. Variations in the abundances of natural stable isotopes of perchlorate (Cl-^{35}Cl and ^{37}Cl: O-^{16}O, ^{17}O, and ^{18}O) hold a great promise not only in identifying possible sources of perchlorate (man-made or natural) but also in measuring the success of in situ remediation. The goal of this project is to establish science and technology bases, which will enhance significantly the environmental forensics of perchlorate contamination.

Perchlorate contamination is one of the most challenging environmental problems that the nation is currently faced with. One of DOE's missions is to improve the overall quality of our environment, particularly those associated with the various DOE sites. The perchlorate contamination has been identified at sites under the jurisdiction of many federal agencies (DOE, Department of Defense, contractors, etc.). The case of perchlorate contamination is increasing rapidly beyond the boundary of these federal sites, and the areas and regions affected are expanding rapidly. With toxicological effects of perchlorate (cancer and brain development problem), this is becoming one of the most urgent issues to U.S. Environmental Protection Agency. Source identification as well as remediation of the contamination is posing great challenges. Innovative science and technology expected from this project is very likely to contribute significantly to the forensics, particularly the source identification, of perchlorate contamination across the United States.

Building on the ORNL's innovative technologies of bifunctional anion-exchange resins for selective removal of $ClO4^-$ from groundwaters and of an effective recovery method of sorbed $ClO4^-$ from the resins, we have established an extraction-purification method for traces (ppb to tenth of %) of perchlorate in salts and groundwaters. In collaboration with N. C. Sturchio (University of Illinois, Chicago) and J.-K. Böhlke (USGS, Reston), highly accurate analytical methods were developed for determining oxygen (^{16}O, ^{17}O, and ^{18}O) and Cl (^{35}Cl and ^{37}Cl) isotope ratios of purified perchlorate. Using these innovative methods, we clearly established that perchlorate of man-made (reagents) and natural origins (Chilean nitrate deposits) have distinct Cl and O isotope ratios. Then, we conducted a "proof-of-principle" case study at field sites, where their perchlorate contamination is clearly of anthropogenic origin (Air Force base and chemical plant). Our isotopic study unambiguously confirmed their anthropogenic origins. This demonstration opened up a great opportunity for conducting forensic studies of perchlorate contamination of unknown origins and for monitoring the extent of natural and accelerated attenuation of perchlorate in contamination sites. In FY 2004, we presented our results at several national and stakeholder meetings and received several inquiries regarding our capability and readiness for real isotope forensic studies. In early FY 2005, we plan to conduct a case study in West Texas, where high (>50 ppb) concentrations of perchlorate of unknown origin were detected in groundwaters.

Developing a High-Throughput, Laser-Based Technique for Quantifying the Elemental Composition of Wood: Applications in the Forest Products Industry

M. Z. Martin,[1] S. D. Wullschleger,[1] and T. G. Rials[2]
[1]*Environmental Sciences Division*
[2]*Forest Products Center, University of Tennessee*

In this research, we have undertaken the design and evaluation of a laser-induced breakdown spectroscopy (LIBS) system capable of rapid, accurate, and simultaneous elemental analysis in wood. A laser beam, focused onto the surface of the sample, evaporates small amounts of the material and simultaneously excites a plasma discharge. The analysis of the emitted element-specific spectral lines permits the direct determination of the atomic composition of substances. The LIBS technique has been used in two separate, but complementary proof-of-principle investigations to explore potential applications of this technology in the forest products industry. The first of these investigations will use LIBS to assess the quantification of four different chemical treatments of wood, whereas the second will use LIBS to investigate adhesive bondlines at the wood-resin interface in wood composites. Our efforts have focused not only on demonstrating the application of LIBS as a tool for use in the forest products industry, but will also address multivariate analysis in wood and engineered wood composites.

The forest products industry, which encompasses the production of wood, pulp, paper, and engineered wood products, ranks among the top 10 manufacturing industries in the United States. The relative composition of these components varies with plant species, management, and growth environment, but typically is 30:40:25% (Tuskan et al. 1999). The trace elements silica, calcium, sulfur, potassium, manganese, and phosphorus can also be found in wood, as can heavy metals. The presence of lead, chromium and other heavy metals in wood have been used for decades in the field of dendrochemistry to document the presence of pollutants in the soil and aerial environment.

Some research has shown that the inorganic component can impact pulping chemistry and impart poor photo-yellowing resistance to paper. In addition, considerable work has shown that metal cations can affect the mechanism of thermal decomposition of wood and biomass, which directly influences the composition of bio-oil products from pyrolysis.

Numerous techniques have been examined for determining the structural composition of wood, and several high-throughput spectroscopic tools have emerged that provide information on chemical, physical, and mechanical properties of wood and wood products (Tuskan et al. 1999, Rials et al. 2002). Such work has focused almost exclusively on organic constituents of wood, neglecting the inorganic trace elements. Therefore, one of the major objectives of our study will be to link elemental analysis using LIBS, standard analytical techniques (i.e., AAS), and multivariate statistics.

We have made good progress on this research project. The studies were done on preservative treated wood that is used in construction of decks, fences, and residential applications. The preservatives used are chromated copper arsenate (CCA) and ammoniacal copper zinc arsenate (ACZA). These samples have been tested using near infrared spectroscopy (NIR) and atomic absorption spectroscopy (AAS). We obtained 165 samples of different powdered wood samples from our collaborators at the University of Tennessee Forrest Products Center. A variety of wood types such as ACZA treated Douglas fir, CCA treated eastern hemlock, CCA treated hemlock fir, and ACQ-B treated hemlock firs were obtained.

We have been able to optimize the pelletization of these powdered samples. This optimization of the wood pellets made it possible to consistently sample the pellets. Laser-induced breakdown spectroscopy (LIBS) technique was performed on 85 samples and principle component analysis (PCA) and partial least squares (PLS) regression was performed on the LIBS data. The principle component analysis has shown very good comparison to Cu, Zn, and As present in these samples, and the coefficient of regression has been calculated to be 0.992–0.998 for the three elements and the standard deviation is <3% in each case. The results highlight the potential for this technique to predict the concentration, as well as identify the type, of inorganic preservatives present. These results have been presented in an invited talk at the Third International Conference on Laser Induced Plasma Spectroscopy and Applications held September 28–October 1, 2004, in

Torremolinos (Málaga). The invited talks will then be published in full length in the journal, Spectra Chimica Acta which is a leading spectroscopy journal. A very good correlation for PCA principal component analysis is used to observe any clustering and/or separation in the sample sets.

References

Rials, T. G, S. Kelley, and C-L. So. 2002. "Use of advanced spectroscopic techniques for predicting the mechanical properties of wood composites." Wood and Fiber *Sci.* **34**(3): 398–407.

Tuskan G., et al. 1999. "Two high-throughput techniques for determining wood properties as part of a molecular genetics analysis of hybrid poplar and loblolly pine." Applied Biochemistry and Biotechnology 77-79: 55–65.

Using Live-Cell Imaging Technologies to Probe Molecular Interactions between Bacterial Cells and Heavy Metals

D. K. Thompson,[1] M. Doktycz,[2] S. D. Brown,[1] and J. Morrell[2]
[1]*Environmental Sciences Division*
[2]*Life Sciences Division*

High-resolution imaging of cell surface structure and molecular interactions in real time and under physiological conditions will be essential for solving structure-function questions in the post-genomics era. The overall objective of this project is to investigate the feasibility/utility of live cell imaging techniques in exploring microbial cell surface structure and morphology under heavy-metal stress conditions and dissecting the molecular interactions involved in metal uptake and/or resistance. The research focuses on three tasks: (i) atomic force microscopy (AFM) to characterize the morphology and cell surface structure of *Shewanella oneidensis* cells in the presence of heavy metals (Task 1), (ii) fluorescence microscopy to investigate in vivo protein localization and expression dynamics (Task 2), and (iii) development of an assay for examining cell surface receptor–siderophore binding (Task 3).

To develop effective bioremediation strategies for the cleanup of contaminated DOE sites, fundamental knowledge is needed on microbe-metal interactions and the ability of metal-reducing microorganisms to survive in relevant contaminated environments. Understanding how organisms respond to their environment requires the ability to observe molecular events in live cells in real time. Characterization of the interaction between *S. oneidensis* and heavy metals beyond that of a snapshot genomics view will require new, innovative approaches capable of probing single cells at molecular-scale resolution. The technical objectives of this project include (i) developing robust cell-mounting techniques enabling live cell imaging in *Shewanella*; (ii) developing the capability of producing reporter gene fusions encoding tagged proteins for in vivo visualization; and (iii) validating a novel technique for investigating cell surface receptors. The scientific goals are (i) to determine whether morphological changes occur on the surface of *S. oneidensis* cells in the presence of metals; (ii) to determine temporal and spatial localization patterns for proteins up-regulated in response to metals; and (iii) to demonstrate siderophore-cell surface receptor binding.

This project utilizes various imaging techniques. AFM is a relatively new method for biological imaging that produces a high-resolution topographical map of a cell surface using a cantilever-mounted probe tip. AFM is ideally suited for imaging cell-metal interactions at the cell-surface level in real time and under physiological conditions. Fluorescence microscopy methods will be used to investigate protein expression dynamics/localization and protein-protein interactions within live *S. oneidensis* cells in response to strontium (Sr^{2+}). While Task 3 requires little imaging, its ultimate usefulness for future imaging experiments will be in the development of methods for attaching siderophores to surfaces, demonstration of which will lend credence to future grants proposing to measure binding forces between an individual siderophore ligand and cell surface receptor protein by attaching siderophores to an AFM cantilever tip.

The goal of Task 1 is to investigate the cell surface morphology of *S. oneidensis* MR-1 cells grown in the presence of strontium using AFM. In preparation for AFM, *S. oneidensis* cells were grown in liquid medium containing 0, 50, 100, or 150 mM Sr^{2+} and investigated for gross morphological defects using light microscopy. We observed that cells grown in the presence of high Sr^{2+} (100–150 mM) were more elongated than cells grown at lower concentrations. This elongated morphology was also observed for cells grown on solid medium containing Sr^{2+}.

Methods for stably immobilizing *S. oneidensis* cells for AFM imaging were investigated. For these experiments, MR-1 was grown on agar plates containing varying amounts of Sr^{2+} at 30ºC. Cells were suspended in 0.5 ml phosphate buffer, and approximately 100 µL of the cell suspension was applied to a gelatin-coated mica disk and incubated for 10 min at room temperature to promote attachment. After incubation, the mica disk was rinsed in water to remove unattached cells and then dried for AFM imaging. This technique proved to be reproducible and effective for immobilizing *S. oneidensis* cells for imaging studies. Technical objectives for Task 1 were accomplished in the first funding period.

In addition, we have imaged MR-1 cells grown in complex medium containing 0 or 50 mM $SrCl_2$ for 6 days. In previous growth studies, we observed the formation of a precipitate in cell cultures grown for several days

in the presence of 50 mM $SrCl_2$. Cells were prepared for AFM imaging to determine whether this precipitate was associated with the cell surface. Unexpectedly, we found that MR-1 cells grown for 6 days in the presence of $SrCl_2$ appeared to have rather large "bumps" when imaged by AFM. Moreover, these structures seemed to be internal and often localized at the ends of the cells. In contrast, these structures were absent or less prominent in cells grown in growth medium lacking $SrCl_2$. Higher magnification images of the cells did not reveal any obvious signs of precipitate associated with the surface. Based on these very preliminary observations, it is tempting to speculate that the cells may be sequestering strontium internally. More testing is needed to examine the cell surface more closely as well as to determine the nature of the internal structures and the conditions that cause their formation.

We have obtained the appropriate plasmid constructs for creating GFP (green fluorescent protein)- and YFP (yellow fluorescent protein)-target protein fusions (Task 2). Cloning of target MR-1 genes into these reporter constructs is currently in progress. To test if *S. oneidensis* proteins could be fused to the GFP protein and imaged successfully in MR-1, we initially targeted the *so3585* gene (encodes a putative azoreductase), which has been cloned into the Gateway® pDONR221 vector. pENTR*so3585* plasmid DNA was then used as a substrate in a LR Gateway® reaction with a modified destination plasmid (pJM28) to create the pJM*so3585-gfp* expression vector. The pJM*so3585-gfp* expression vector has been transformed into *E. coli* DH5α and strain β2155 for introduction into *S. oneidensis* MR-1 via conjugation. MR-1 and *E. coli* strains that both contain pJM*so3585-gfp* and wild-type strains will be examined using confocal microscopy once MR-1 exconjugants are obtained.

NUCLEAR SCIENCE AND TECHNOLOGY

Director's R&D Fund

Breakthrough Multi-Megawatt Space Reactor Power System Design

A. L. Qualls,[1] E. D. Blakeman,[1] S. R. Greene,[1] S. H. Kim,[1] J. O. Johnson,[1]
J. S. Neal,[1] K. W. Childs,[3] J. C. Conklin,[2] and P. J. Otaduy[2]
[1]*Nuclear Science and Technology Division*
[2]*Engineering Science and Technology Division*
[3]*Computational Sciences and Engineering Division*

A Space Reactor Power System (SRPS) Optimization Tool has been developed that uses evolutionary computational algorithms called genetic algorithms (GA) to optimize the design of SRPS subsystems for a nuclear electric propulsion (NEP) space vehicle. The tool works in conjunction with the Nuclear Electrical Vehicle Optimization Tool (NEVOT), which was jointly developed by Oak Ridge National Laboratory, Marshall Space Flight Center, and Arnold Engineering Development Center as part of the Tri-Lateral Alliance. The ORNL SRPS Optimization Tool has been used by ORNL to produce a pre-conceptual design of a multi-megawatt space reactor power system, which was chosen by DOE as the baseline concept for the multi-megawatt NEP design study under the DOE Space Reactor Technology Program. The methodology and toolset developed under the LDRD program is presently being used at ORNL on several ongoing research programs and is being proposed for use on others. Although the tool was developed for a space power application, the methodology can be applied to any multi-discipline, multi-objective optimization problem and additional applications are being pursued.

Objective

The objectives of this work were to (1) develop a breakthrough methodology for designing multi-discipline, multi-objective engineering systems; (2) to re-establish ORNL as a leading center for the design and development of multi-megawatt Rankine Space Reactor Power Systems (SRPS); and (3) to pilot the Tri-Lateral Alliance with Arnold Engineering Development Center and Marshall Space Flight Center.

Technical Approach

The SRPS Optimization Tool employs detailed subsystem design codes in conjunction with a genetic algorithm (GA) optimization tool to produce self-consistent, optimized, detailed SRPS designs. Design codes for the reactor, the shield, the power conversion systems, and the heat rejection system have been developed to perform addition system design and analysis after the distinguishing features of the system are selected by the GA. The optimal combination of subsystem designs are evolved by the GA methodology by removing designs with poor evaluations from the solution population and repopulating the design population with combinations and mutations of the better designs. Over many successive generations, only the best solutions remain.

The power of the methodology is that (1) the systems are created without sequential design information, which removes design bias and allows novel approaches to be investigated; (2) the algorithm does not require modification to search for optimal solutions to different missions with different constraints or with different definitions of fitness; (3) more sophisticated analyses, models, and approaches can be easily included into the methodology as they become available; and (4) the results are detailed, self-consistent designs of optimized integrated SRPS subsystems. These features make the SRPS Optimization Tool a flexible and powerful tool for performing subsystem trades studies and optimization for a broad range of design problems.

Figure 1 shows the inter-relation between various segments of the software that make up the ORNL SRPS Optimization Tool and NEVOT. Subsystem design modules (in this case the SRPS, Electric Propulsion and Vehicle subsystems) are independent codes executed under the integration software, or Wrapper. The Wrapper defines how the subsystems inter-relate, which is derived from the general description of the system being optimized. The Wrapper also controls the sharing of information between subsystem design modules. The Genetic Algorithm Executive controls the optimization process and selects the features of each system design, which are the inputs into the subsystem design modules. The ability of each system to meet the mission requirements is estimated and input into the fitness evaluation. System characteristics that are to be optimized (i.e., mass, cost, reliability, etc.) are also input into the fitness evaluation. Some combination of the mission fitness and optimization parameters is used to create an estimate of the overall system fitness. The fitness of each system relative to the entire population determines its probability of survival. After iterating through many generations, the best system designs remain. The better

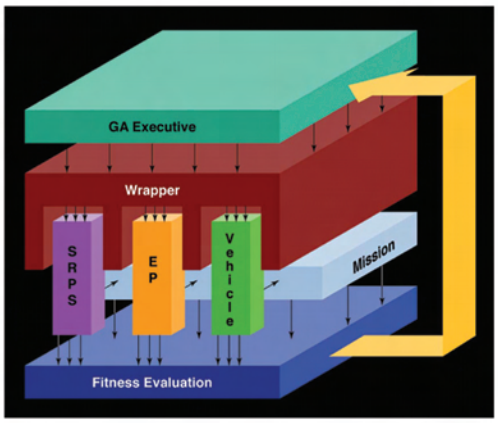

Fig. 1. Graphic representation of the evaluation methodology used in the ORNL SRPS optimization tool as extended to NEVOT.

solutions are saved for later examination to determine why they are superior. The ORNL SRPS Optimization Tool uses this exact methodology with reactor, shield, power conversion, and heat rejection subsystem design modules. When the SRPS Optimization Tool is run in conjunction with NEVOT, the SRPS can itself be optimized within the broader vehicle optimization.

Results

The SRPS Optimization Tool uses design modules that have either a sophisticated engineering design algorithm or a realistic physics evaluation of each subsystem. The liquid-metal reactor module is derived from a modified version of the ALKASYS Design code (Moyers 1987). The liquid-metal Rankine power conversion module and the heat rejection module are derived from programs developed to predict Nuclear Electric Propulsion subsystem performance and mass developed by NASA. The potassium power conversion system design code (Johnson 1993) and the heat rejection system design code (Moriarity 1993) were upgraded and modified to operate at lower power; however, they are largely unchanged. Shield and Brayton system power conversion design modules were written from first principles at ORNL.

Extensive module integration software was written to allow the design modules to interact with one another, to allow different levels of sophistication to be used in an evaluation (which permits the algorithm to quickly scope down to better solutions with simple models before using more computational intensive algorithms for fine tuning the designs), and to modify design requirements and constraints. Remote computing capability has also been included in the tool so that ORNL can collaborate with area experts (and their design codes) in real time over the internet.

Benefits

Designs created within the optimization tool are not derived through an iterative sequential design approach. They are evaluated after being created. By developing the optimization tool without engrained sequential design logic, it has more flexibility to design and combine subsystems, which allows it to find new and unique design solutions. This project has exposed many ORNL researchers to this new and powerful optimization methodology. Because the approach can be applied to any multi-objective, multi-discipline design and optimization problem, it is thought that our LDRD project experience will continue to enhance our abilities to support the broader DOE mission.

The ORNL SRPS Optimization Tool places ORNL in the advantageous position of having updated design and evaluation tools (and recent experience using them) for the systems presently under evaluation for the ongoing SRPS development work sponsored by DOE and NASA in response to the President's Vision for Space Exploration. The tools and techniques developed by ORNL researchers are being used to perform system trade studies for ongoing space power programs (DOE-NE and DOE-NR), and the tools have generated interest from other potential sponsors (JPL).

Finally, part of the purpose for engaging in this project was to establish stronger ties to the NASA community and to enhance our reputation as a space power design center. While it is difficult to accurately assess our success in this area, it seems fair to say that our recent successes in the space power program can be at least in some part be attributed to our involvement in this LDRD project over the past two years.

References

Eldred, M. S., et al. *DAKOTA, A multilevel parallel object oriented framework for design optimization, parameter estimation, uncertainty quantification and sensitivity analysis*, Version 3.1 Users Manual.

Moyers, J. C., and J. P. Nichols. 1987. *ALKASYS. A Computer Program for Studies of Rankine-Cycle Space Nuclear Power Systems*, ORNL/TM-10427.

Johnson, G. A. 1993. *Potassium-Rankine Power Conversion Subsystem Modeling for Nuclear Electric Propulsion (Task Order 10)*, NASA Contractor Report CR-191134.

Moriarity, M. P. 1993. *Heat Pipe Cooled Heat Rejection Subsystem Modeling for Nuclear Electric Propulsion (Task Order 18)*, NASA Contractor (Rockwell International) Report CR-191132, 1993.

NUCLEAR SCIENCE AND TECHNOLOGY

Seed Money Fund

Development of a Three-Dimensional Radioisotope Depletion Method Using Monte Carlo Transport

M. D. DeHart,[1] L. M. Petrie,[1] and S. M. Bowman[1]
[1]*Nuclear Science and Technology Division*

Accurate calculation of the depletion of nuclear materials requires careful determination of the neutron flux density and spectrum in the regions of interest. Increasing complexity in reactor designs, evolutionary concepts, and non-reactor applications such as safeguards, security, and nonproliferation are beginning to require robust geometrical modeling capabilities to capture neutron transport for complex configurations. Monte Carlo transport methods offer the type of flexibility needed for such applications but present other difficulties not encountered in deterministic transport methods. The objective of this project is the development of a prototypic code sequence to perform Monte Carlo-based depletion. As part of this effort, approaches will be developed to relate the stochastic uncertainty of the Monte Carlo method to the uncertainty in isotopic predictions, minimize uncertainty via variance reduction, and reduce the computational effort associated with burnup-dependent iterations. To date, both the KENO V.a and KENO VI Monte Carlo transport codes have been adapted to work within a depletion code sequence; comparisons with other methods and measured data show excellent agreement.

This project seeks to implement the Monte Carlo transport codes KENO V.a and KENO VI within the TRITON depletion driver module of the criticality safety analysis computer software system, SCALE, and to study and implement methods to improve the efficacy of iterative depletion based on Monte Carlo transport solutions. Error propagation from the results of Monte Carlo simulations will become a key attribute of such a system.

To date, the KENO V.a Monte Carlo transport codes have been integrated within the TRITON control module of SCALE and undergone significant testing and validation. KENO V.a provides a relatively fast transport solution that allows depletion calculations to be performed on about the same timescale as two-dimensional deterministic methods. More recently, a new version of TRITON has been developed to support KENO VI depletion. Although slower than KENO V.a for a given problem, KENO VI provides a very robust geometry package that allows calculations to be performed for practically any configuration. This will be important in complicated configurations encountered in advanced reactor design concepts.

For both transport codes, the SCALE utility codes KMART and KMART6, originally developed to post-process KENO calculations, have been adapted to provide collapsed cross sections and fluxes required by TRITON for setting up ORIGEN-S depletion calculations. Restart capabilities of the KENO codes have been used to provide an improved starting source for each depletion step, further improving calculation times. Ongoing R&D work seeks to study and implement methods using variance reduction techniques to improve the efficacy of iterative depletion based on Monte Carlo transport solutions. Error propagation from the results of Monte Carlo simulations will become a key attribute of this system.

Performance of both depletion sequences is being assessed by comparison to two-dimensional results obtained using deterministic transport methods and by direct comparison to measured spent fuel data. Results show excellent agreement with other codes and data. Numerical experiments with three-dimensional configurations demonstrate the effect of axial leakage and spectral hardening that cannot be captured using two-dimensional methods. Uncertainties in the prediction of isotopic concentrations have been found to be much smaller than originally anticipated.

Both the Nuclear Regulatory Commission and the U.S. Air Force have a strong interest in this work. These organizations are felt to be only a few of the broad set of potential users for the results of this work. Additional organizations that may find this work of value include the National Nuclear Security Administration; Office of Nuclear Energy, Science and Technology; Office of Science; and the Office of Civilian Radioactive Waste Management within the Department of Energy (DOE). Outside the DOE, other organizations and agencies that would potentially benefit from the results of this work include the Department of Homeland Security, the Department of Defense, and the National Aeronautics and Space Administration.

PHYSICS

Director's R&D Fund

Detector Development for Fundamental Neutron Physics at the HFIR and Spallation Neutron Source

G. Greene[1,2] V. Cianciolo,[1] K. Rykaczewski,[1] R. Grzywacz,[1,2]
W. M. Snow,[3] D. Bowman,[4] S. Penttila,[4] and W. S. Wilburn[4]
[1]*Physics Division*
[2]*University of Tennessee*
[3]*Indiana University*
[4]*Los Alamos National Laboratory*

Low-energy, cold neutrons have been employed in a wide variety of investigations that shed light on important questions in particle and nuclear physics. These include such issues as the determination of fundamental constants, enhancing our understanding of fundamental symmetry violations, and exploring the nature of physics beyond the standard model. Experiments in this field have traditionally been carried out at high flux reactors with dedicated cold sources. While this continues to be the source of choice for many experiments, there is an important class of measurements that can best be carried out at pulsed source. However, such pulsed neutron experiments have not generally been attempted due to flux limitations. The SNS, which will provide pulsed neutron beams more than an order of magnitude more intense than existing sources, will allow ORNL to become the world leader in this area of research. The work performed in this LDRD project concerned a variety of activities that were aimed at the development of world-class expertise within ORNL staff as well as the development of detector technology that will allow significant science to be carried out at the Fundamental Neutron Physics Beamline at the SNS. Research activities were directed towards the detailed design of a new type of neutron decay spectrometer for the measurement of a complete set of correlations in neutron beta decay.

Introduction

Low-energy neutrons have been employed in a wide variety of investigations, which lie at the heart of important issues in particle physics, nuclear physics, and cosmology. These include the elucidation of crucial questions in areas such as (1) the nature of time reversal non-invariance and the origin of the cosmological baryon asymmetry; (2) the nature of the electroweak theory and the origin of parity violation; and (3) the nature and detailed description of the weak interaction between quarks. Experiments have been most effectively carried out at high flux reactors with dedicated cold sources. Such continuous beam sources provide the very highest time-averaged fluxes of cold neutrons. Specifically, the Institut Laue-Langevin, the Petersburg Nuclear Physics Institute, and the NIST Cold Neutron Research Facility have had productive programs in this field. This work has not been pursued at HFIR due to the absence of cold source as well as logistical problems such as the absence of a guide hall. With the HFIR upgrade nearing completion, ORNL will soon have a source which will provide the highest continuous flux of cold neutrons in the United States and will have a capability comparable to the ILL.

While reactors continue to be the source of choice for some experiments, it has recently been recognized that there is an important sub-class of experiments that can significantly benefit from the pulsed nature of spallation sources. Pulsed cold neutron experiments were not aggressively pursued as there were no cold beams available for fundamental physics. Only recently has this changed with the development of a cold neutron beam line for such work at LANSCE. Notwithstanding the very significant advantages of a pulsed source, the relatively low flux at LANSCE implies that its utility for this field will be limited. The SNS, with an anticipated flux that is ~20 times that of LANSCE, totally changes the prospect for fundamental physics with pulsed cold neutrons. Indeed, the SNS will be the source of choice for a significant fraction, likely even most, of this work in the future.

In 2004, the DOE Office of Science approved and allocated funding for a "Fundamental Neutron Physics Beamline" (FNPB) at the SNS. The FNPB is a $9.2M M.I.E. project that will accommodate a number of experiments in the field of nuclear and particle physics with cold neutrons. This facility will be operated as user facility with allocation of beam time based on a proposal- driven, peer review process. A user group of more than 60 physicists from more than 20 institutions have expressed their interest in using this facility for their research.

At present, notwithstanding considerable enthusiasm within the Laboratory, ORNL has no research program in fundamental neutron physics and there is relatively

little experience among the Physics Division staff in this field. The major use of these LDRD funds was to begin a research program in the field of fundamental neutron physics that will allow ORNL to be active participant in the emerging national research program at the SNS.

Technical Approach

One of the most important applications of low-energy neutrons for the study of basic nuclear and particle physics lies in the detailed study of the beta decay of the free neutron. Because the weak interaction in the neutron is "unencumbered" by the nucleon-nucleon interactions present in nuclei, accurate measurements of the parameters that describe neutron decay can provide precise information about the fundamental "constants" of the weak interaction. Of particular interest is the extraction of the weak vector coupling constant g_V which can be obtained by measurement of the neutron lifetime and the neutron decay correlations. Because this quantity is also accessible from measurements in special nuclear decays, from pion decay, and can be obtained indirectly from kaon decay, a precise measurement from the simple case of the neutron provides a test of a multitude of important theoretical concepts including the universality of the weak interaction and the unitarity of the Cabbibo-Kobayashi-Moskawa matrix. Because there are a number of outstanding discrepancies among the data from which g_V can be extracted, new neutron measurements are particularly interesting (Gould et al. 2001).

The work supported by this LDRD funding concerned the development of a detector capable of providing a highly accurate measurement of the correlations in neutron beta decay. The experiment consists of an arrangement of electric and magnetic field which guide the decay electrons and protons to segmented silicon detectors. Figure 1 gives a schematic of the decay correlation apparatus.

The current research concerned the refinement of three aspects of the complete detector:

(a) *Develop silicon detectors capable of detecting both decay protons and decay electrons from neutron beta decay.*

We have been pursuing a new concept for a neutron decay detector based on a silicon detector that has the following properties:

1. It must be thick enough (>2 mm) to completely stop electrons with energies up to ~750 keV.
2. It must have a thin entrance "window" that will produce an energy loss of <5 keV to allow detection of low-energy protons.
3. It must be pixilated to allow position-sensitive detection with a resolution of ~1 cm.
4. It must have low noise (few keV).

(b) *Develop a data acquisition system for a neutron beta decay experiment.*

The requirements of the data acquisition system for the neutron beta decay experiment are rather stringent. We require a system that

1. has a timing resolution of ~1 ns for electrons of energies of several tens of keV,
2. has memory "depth" of tens of microseconds,
3. is affordable enough to allow ~200 channels, and
4. allows preprocessing for event recognition to reduce data rates to tractable levels.

(c) *Perform simulations of charged-particle trajectories to allow development of a detailed design for a neutron beta decay spectrometer.*

The neutron beta decay spectrometer consists of a superconducting magnet and a high-voltage electrode structure that will allow detection of decay electrons and protons with essentially unit efficiency (Wilburn 2004). To ensure this stringent requirement, it is necessary to carry out Monte Carlo simulations for a variety of detector geometries.

Results and Discussion

(a) *Develop silicon detectors capable of detecting both decay protons and decay electrons from neutron beta decay.*

We have constructed and tested two prototype detectors that duplicate the behavior of single pixels of the final detector. These detectors have the required area (~2 cm), are thick (~5 mm), and are liquid nitrogen cooled to allow low noise. In addition these prototypes have thin "entrance windows" which should allow the requisite small energy loss for protons. These prototype detectors have been tested with radioactive sources and a previously existing data acquisition system and have demonstrated all the requirements for one pixel of the final detector. In addition, the two "single-pixel" detectors can now be used with radioactive sources to test the suitability of the new data acquisition system. Such tests require coincident detection from at least two pixels.

In addition to the single-pixel detectors, a segmented detector with 9 pixels has been fabricated to our specifications and procured. While this detector is not of sufficient size for a final beta decay detector, it does provide proof of principle that a suitable detector is quite feasible.

(b) *Develop a data acquisition system for a neutron beta decay experiment.*

In concert with a commercial firm we have designed a 100-MHz, 12-bit modular data acquisition system that

should meet all of the requirements for the neutron beta decay experiment. The system is a significant extension of an existing ORNL 40-MHz system. The new system has an on-board programmable digital signal processor on board which will allow sophisticated event recognition to be employed. At a per-channel cost of <$1K, the system is affordably scalable to the requisite ~200 channels. Two modules with a total of 32 channels have been procured for test purposes. These modules, in combination with the two single-pixel detectors, will allow the development and testing of detailed data acquisition software for the final experiment.

(c) Perform simulations of charged-particle trajectories to allow development of a detailed design for a neutron beta decay spectrometer.

Using a combination of Monte Carlo simulations, analytic solutions, and scaling arguments, we have identified magnetic field and electrode geometries that satisfy the two major requirements for the spectrometer. These are the uniformity of the electric field in the decay volume and the maintenance of adiabaticity in the region where the electric and magnetic fields are spatially varying. We have established that the range of appropriate geometries is sufficiently broad to allow considerable flexibility in the final design of the actual spectrometer.

Benefits

The research carried out under this LDRD has clearly established the feasibility of a neutron beta decay experiment at the SNS. In so doing we have also developed a degree of expertise at ORNL that will allow us to credibly take a leadership role in the developing program of research at the fundamental neutron physics beamline at the SNS.

References

Gould, Greene, Plasil, and Snow (eds.). 2001. "Fundamental Physics with Pulsed Neutron Beams," Proceedings of the Workshop on Fundamental Physics with Pulsed Neutron Beams, Research Triangle Park, NC, World Scientific.

Wilburn, W. S., et al. 2004. "Measurement of Neutron Decay Parameters—The abBA Experiment," Proceedings of the International Conference on Fundamental Physics with Cold Neutrons, Gaithersburg, Maryland (to be published in the NIST Journal of Research).

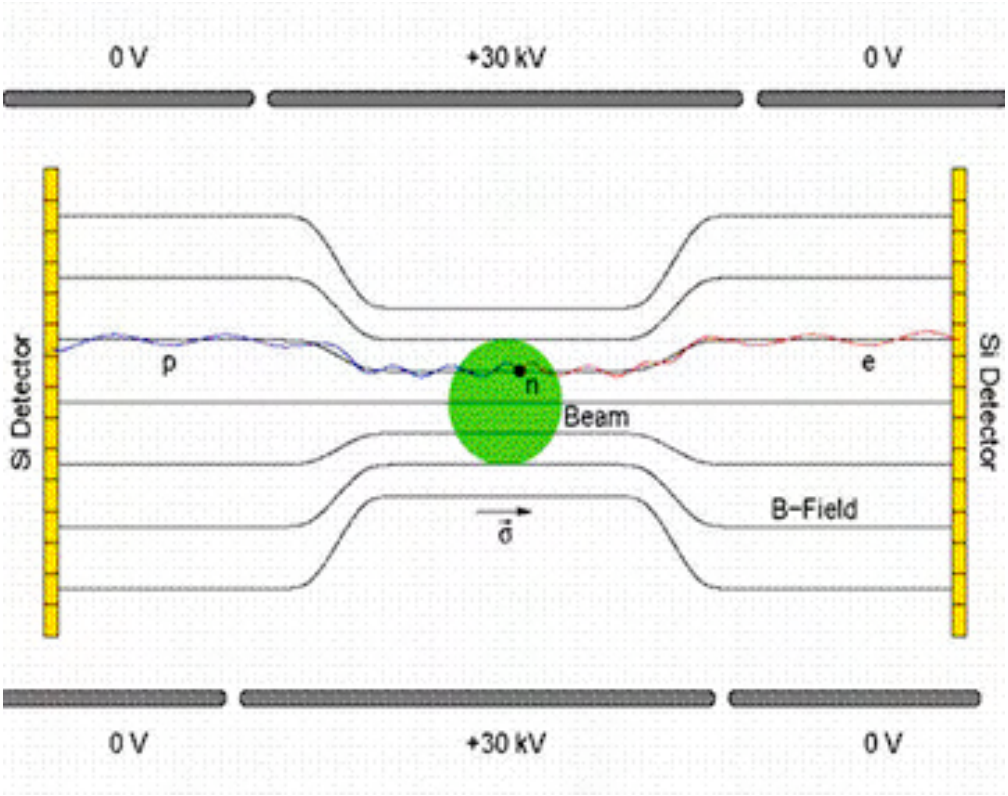

Fig. 1. Schematic of experimental apparatus capable of precisely measuring (0.1%) all four time-reversal invariant a neutron decay correlation parameters. In this LDRD project we developed key enabling technologies for such an experiment: thick silicon sensors with thin entrance windows; an appropriate electrode/magnet design; and a low-noise, precision timing data acquisition system.

Three-Dimensional Neutron Structural Microscopy: Design and Demonstration

B. C. Larson,[1] G. E. Ice,[2] J. D. Budai,[1] J. Z. Tischler,[1] C. R. Hubbard,[2] and S. A. Spooner[3]
[1]*Condensed Matter Sciences Division*
[2]*Metals and Ceramics Division*
[3]*Condensed Matter Sciences Division, Retired*

The goal of this project was to design and demonstrate critical aspects of neutron-based, three-dimensional (3D) structural microscopy in order to enhance neutron science and advanced materials characterization capabilities at ORNL. When fully developed, 3D neutron microscopy will enable nondestructive, spatially resolved investigations of the local crystal structure, lattice orientation, and strain in large-grained, polycrystalline materials. Within this project, we have designed, fabricated, and tested achromatic neutron-beam focusing mirrors, and we have made proof-of-principle demonstrations of 3D spatially resolved neutron Laue diffraction. Kirkpatrick-Baez neutron supermirrors were tested using spallation neutrons at the Los Alamos Neutron Science Center (LANSCE) and using reactor neutrons at the Chalk River reactor; a ~1 × 3 mm^2 beam was focused to as small as 90 × 90 μm^2 with a flux gain of ~100. Depth-resolved, white-beam Laue diffraction measurements using a translation-aperture technique were performed at the Intense Pulsed Neutron Source (IPNS) at Argonne National Laboratory and at Chalk River in which it was demonstrated as a proof of principle that structural features could be resolved with 500-μm resolution along the incident beam. The results of this project indicate that 3D neutron structural microscopy with spatial resolution of 50 μm or less in all dimensions can be realized in the future. The successful demonstration of Kirkpatrick-Baez neutron beam focusing in this project has generated widespread interest within the neutron community for applications such as high-pressure, tomography, and small sample sizes; the inclusion of Kirkpatrick-Baez supermirror focusing optics is presently being considered on several SNS beamlines.

Introduction

Although advanced materials processing relies almost entirely on controlling microstructural features such as grain sizes, shapes, strains, and textures, nondestructive, spatially resolved 3D structural probes are still not available for bulk materials on length scales of sub-millimeters to centimeters. Electron or optical microscopy methods that are normally used for determining grain-morphology and crystal microstructure are confined to thin foils or surfaces, and newly developed synchrotron X-ray microdiffraction techniques that provide submicron-resolution 3D structural microscopy are restricted to the so-called mesoscopic length scales of tenths of microns to a few hundred microns. For a full and comprehensive understanding of materials strength, structure, microstructure, and evolution, measurements of grain structure, residual stress, and intra- and inter-granular interactions are needed on all length scales ranging from submicron to macroscopic sizes. Accordingly, the aim of this project was to demonstrate the capability of white-beam (polychromatic) neutron Laue diffraction to overlap with X rays on the few-hundred-microns scale and to extend measurements to fully macroscopic length scales. By extending experience gained in our development of 3D X-ray structural microscopy at the Advanced Photon Source (APS), we have designed and tested prototype high-resolution neutron-beam focusing optics and depth-resolved Laue diffraction techniques on spallation and reactor white neutron beams as proof-of-principle demonstrations of Kirkpatrick-Baez (KB) mirror focusing and translation-aperture 3D neutron structural microscopy. The results demonstrate that the mesoscale-to-macro-scale-range 3D structural studies that are needed to link emerging materials theory and large-scale computer modeling with experimental measurements are now possible. Moreover, it has become clear during this LDRD that neutron focusing optics can have a major impact on neutron science in a wide range of applications in addition to 3D neutron structural microscopy.

Technical Approach

Focusing intense neutron beams to small diameters is the critical first step in developing a method for 3D spatially resolved neutron microbeam diffraction. Our analysis and modeling of non-dispersive (achromatic) KB neutron optics found that mirror focusing can provide increased neutron intensity for beams below 0.5 mm. For example, we calculate that for a ~100-μm-diameter neutron beam, there is a theoretical gain of around 60–100 in flux compared to the best possible performance of guide-tube-based neutron transport with a 100-μm slit. Based on phase-space optics, we predict that focused beams are preferred over slits whenever the distance from the last optical element is greater than 140 times the size of the beam, a condition that exists for many neutron applications. Further, KB supermirror systems operating

near the theoretical limit imposed by the neutron source brilliance can be readily fabricated.

Using ray tracing analysis and modeling, a prototype KB neutron supermirror system was designed and fabricated to focus neutron beams below 100 × 100 μm^2. The figure of the mirrors was tested at the APS metrology laboratory using a long-trace profiler, and active bending was used to shape the flat M~3 neutron supermirrors into good approximations of ellipses. The active bend system was particularly useful for demonstrating a prototype, as it allowed for changes in source and image distances. More advanced systems with the potential for focusing larger divergences and higher intensities onto the sample have been designed within this project as well.

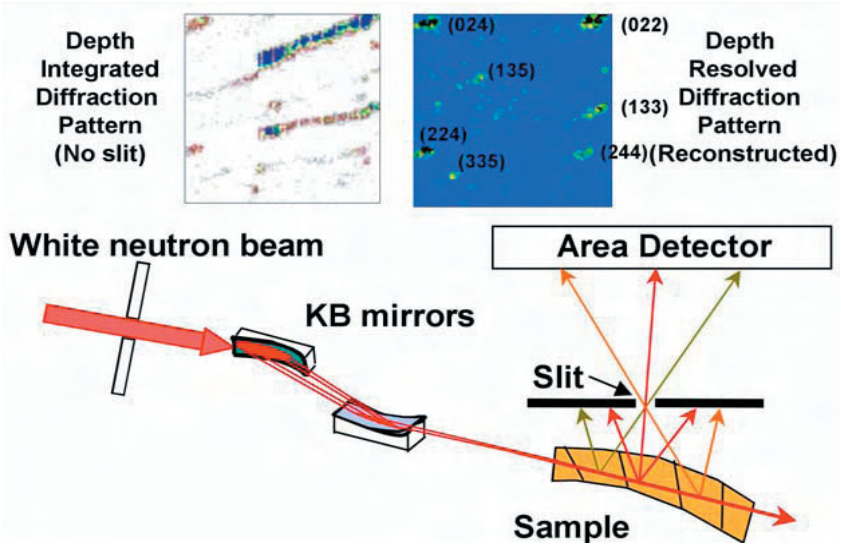

Fig. 1. The lower schematic depicts the essential elements of 3D neutron structural microscopy; the elliptically figured KB mirrors focus the incident white neutron beam at the sample; the sample is translated near the diffracted-beam profiler slit, and a timing area detector collects Laue diffraction patterns. The upper images show Laue diffraction patterns from a bent copper single-crystal plate: (left) full-sample depth-integrated Laue pattern image obtained with slit removed; (right) spatially resolved Laue pattern image reconstructed from sample translation measurements and indexed using analysis software.

The next crucial step (after addressing the focusing optics) towards realizing 3D structural microscopy with neutrons was the ability to depth profile the diffraction patterns along the incident neutron beam path. Using focused beams, two-dimensional (2D) spatial resolution can be achieved simply by translating the sample in directions perpendicular to the focused beam; however, to achieve spatial resolution in the third dimension, depth profiling and subsequent data analysis techniques are required. These techniques were adapted in analogy with our recently developed synchrotron X-ray profiling procedures (Larson 2002). This method involves a slit located close to the sample that functions as a pin-hole camera and establishes the origin point for each diffracted beam, as illustrated in the schematic in Fig. 1. A sample translation stage with an adjustable width cadmium slit system was constructed, and data analysis algorithms were developed. The neutron diffraction depth-profiling capability was tested on unfocused neutron beams through user-proposal experiments carried out on the Single Crystal Diffraction (SCD) beamline at the Intense Pulsed Neutron Source (IPNS) facility at Argonne National Laboratory. Time-of-flight (TOF) Laue diffraction images were recorded on large-area scintillation detectors located perpendicular to the incident neutron beam, as illustrated in Fig. 1. Data analysis software was developed for determining the diffraction angle and the energy of each neutron using the time-delay and x-y position data recorded by the time-resolved 2D detector. Samples examined to demonstrate the principle of the measurements included a cylindrically deformed (bent) copper single-crystal, a stack of copper and niobium single crystal plates (mimicking a two-phase polycrystalline sample), and a copper crystal macroscopically indented on one surface using a cylindrical rod.

The focusing and depth-resolving elements of this project were combined in experiments carried out at the Chalk River reactor facility. Here, a polychromatic neutron beam was focused using the supermirror system and depth-resolved measurements from the indent-deformed copper sample were obtained.

Results and Discussion

The prototype KB mirror system was initially tested on Flight path 5 at LANSCE where an ~100- × 180-μm^2 focus was obtained. In the absence of a real-time camera, the system parameters were optimized by focusing a laser beam set to simulate the trajectory of a neutron beam. In addition to condensing the ~ 1- × 3-mm^2 polychromatic neutron beam cross section by a factor of ~150, the system, as anticipated, showed no evidence for chromatic aberrations from gravitational or other effects. The results of this first measurement were reported (Ice 2004). A subsequent test of the mirror system was performed at Chalk River, where a ~90- × 90-μm^2 focus with an intensity gain of ~100 was demonstrated using real-time imaging on a neutron-sensitive CCD area detector system.

Initial depth-profiling demonstration experiments were carried out using the SCD beamline at the IPNS spallation neutron source. With the depth-resolving slit removed, the Laue diffraction pattern from a bent copper single-crystal plate (2 mm × 9 mm × 10 mm) consisted

of long streaks for each reflection recorded corresponding to the continuous rotation of lattice planes along the incident beam, as illustrated in the left image inset in Fig. 1. With the depth profiling slit in place, diffraction images were collected as the sample -was step-translated parallel to the beam direction. Depth-profiling analysis software developed in this project was then used to reconstruct complete diffraction patterns for each step-length of the beam along the sample; each reconstructed image revealed a pattern of single-crystal diffraction peaks corresponding to the local crystal orientation at a particular spatial position. The reconstructed Laue diffraction patterns were then indexed to determine the crystallographic orientation of the bent Cu crystal along the incident beam with a spatial resolution of 1 mm. In a second demonstration experiment, a mixed stack of 0.5, 1.0 or 2.0 mm thick single-crystal copper or niobium disks was placed in the beam and depth-resolved Laue images were obtained. For this composite sample, the local Cu (fcc) versus Nb (bcc) lattice structure and orientation was identified with a spatial resolution of 0.5 mm. It is important to note that TOF measurements at a pulsed neutron source such as the IPNS provide the energy (and hence d-spacing) of each diffraction peak directly; this greatly aids the indexation analysis. In a third experiment, one surface of a rectangular-shaped copper single-crystal block was cylindrically indented to a depth of 0.5 mm using a 5-mm-diameter steel rod. Measurements made as a function of depth along the beam and as a function of distance below the indent yielded 2D spatially resolved maps of the local lattice rotations (range ~0–5°) inside the deformed sample.

In FY 2004, collaborations with scientists at Chalk River demonstrated an integrated microdiffraction system, which combined all the elements required to perform polychromatic microdiffraction experiments. For these experiments, the monochromator crystal of the Chalk River engineering science beamline was replaced with a neutron supermirror to deflect the beam. Aided by a real-time camera to guide focusing, the KB mirror system produced a very small (~100- × 100-μm^2) beam and depth-resolved measurements determined the local crystal orientation of the cylindrically indented Cu single crystal with ~500-μm spatial resolution along the beam.

The experiments performed in this project successfully demonstrated the capability of neutron Laue diffraction microscopy to provide 3D, spatially resolved maps of the lattice symmetry, chemical structure, and local crystal orientation for both pulsed and reactor neutron sources. These demonstration proof-of-principle experiments indicate that by combining the high intensity of SNS beamlines with enhanced KB focusing optics, it will be possible to develop neutron structural microscopy with spatial resolution less than 50 μm in all three dimensions.

The success of the combined focusing and diffraction demonstration at Chalk River led scientists from the Spallation Neutron and Pressure (SNAP) beamline at ORNL to perform a follow-on experiment at Chalk River using our KB mirrors in which even smaller beams were produced (90 × 89 μm^2) and where diffraction from FeO in a high-pressure-cell sample was detected. This work represented a significant advance over existing neutron-optical systems, as previous experiments (without focusing optics) at LANSCE and the NIST reactor had been unable to detect diffraction signals from this sample due to the severe size restrictions imposed by the pressure cell.

Benefits

This LDRD project will directly benefit DOE neutron sciences and materials programs in a number of ways. First, it has contributed directly to follow-on BES funding at ORNL of an "Advanced Neutron and X-ray Studies of Polycrystalline Deformation Physics," (J. W. L. Pang: PI; G. E. Ice and B. C. Larson: co-PIs) proposal that included neutron 3D structural microscopy as a major new direction for FY 2005 and beyond. Secondly, based on the success of this LDRD and follow-on pressure-cell experiments at Chalk River, inquiries have been received from most of the neutron beamlines presently under development at the SNS, interest has been expressed by scientists at LANSCE at LANL and the ILL at Grenoble, France, and from the general neutron optics community. Current planning at the SNS calls for beamline modifications to ensure that advanced Kirkpatrick-Baez focusing optics will be an option on at least five beamlines at the SNS: SNAP, VULCAN, NOMAD, SCD, and MANDI. Thirdly, the DOE Basic Energy Sciences program office has recently requested a white paper describing the need for future developments in the area of focused neutron beams, and invitations have been received to speak at upcoming neutron science meetings and beamline development workshops indicating a broad interest in neutron-focused beam capabilities. Finally, the results of this LDRD have stimulated conceptual design of new approaches for neutron supermirror focusing that have the potential to increase the angular acceptance (and hence the beam power) of large neutron beams by factors in the range 5–10. Such developments would have a major impact on cost and flexibility of neutron instrumentation considering that guide-tube-based neutron transport is expensive and difficult to upgrade.

References

Larson B. C., W. Yang, G. E. Ice, J. D. Budai, and J. Z. Tischler. 2002. "Three-Dimensional X-ray Structural Microscopy with Submicrometre Resolution," *Nature* **415**, 887.

Ice G. E., C. R. Hubbard, B. C. Larson, J. W .L. Pang, J. D. Budai, S. Spooner, and S. C. Vogel. 2004. "Kirkpatrick-Baez microfocusing optics for thermal neutrons," *Nuclear Instruments and Methods A*, accepted for publication.

Neutron-Rich Radioactive Ion Beam Production with High-Power Electron Beams

J. R. Beene,[1] J. J. Das,[1] W. T. Diamond,[2] J. D. Fox,[3] J. W. Johnson,[1]
D. W. Stracener,[1] and M. Saltmarsh[1]
[1]*Physics Division*
[2]*Chalk River Nuclear Laboratories*
[3]*Florida State University*

This project was an experimental and numerical investigation of the production of neutron-rich radioactive ion beams (RIBs) using high-power electron beams. This concept has never been employed at an operational radioactive ion beam facility, but preliminary investigations indicate that there is potential for producing very high intensities of particularly interesting RIB species at a cost much lower than that of a comparable-performance conventional facility. We have designed, developed, and initiated an experiment designed to measure RIB yields of key species, in a well-understood environment such that relative production rates and approximate absolute rates can be deduced out to very neutron-rich species ($T_{1/2}$ ~1 s). The equipment and experimental concept we have developed can provide a systematic, quantitative experimental evaluation of electron-beam production of neutron-rich species of particular interest to radioactive beam nuclear physics. In order to develop, evaluate the experiment design, and to provide a framework for interpreting the results, extensive numerical studies of electron-beam target interactions were carried out, along with modeling of other experiment components. These numerical tools have been extended and elaborated to provide an evaluation of the relative merit of several possible implementations of electron-beam RIB production at HRIBF.

Introduction

Much of the scientific focus in nuclear physics for the next decade will be on the use of neutron-rich radioactive ion beams (RIB) to explore novel nuclear structure effects associated with weak nucleon binding and address important questions in nuclear astrophysics. The techniques developed will also provide the opportunity for certain critical cross-section measurements of importance to the nuclear safeguards and stockpile stewardship community. ORNL is the site of the Holifield Radioactive Ion Beam Facility (HRIBF) that will provide one of the primary sites at which a RIB physics research community in the United States will be developed and nurtured in anticipation of a next-generation U.S. facility, the Rare Isotope Accelerator (RIA), which is currently expected to be operational sometime after 2015. HRIBF is the only facility in the world now capable of producing high-quality beams of heavy neutron-rich radioactive species accelerated to energies above the Coulomb barrier. Truly remarkable, pioneering science has been done over the last several years at HRIBF using these beams. However the HRIBF in its current form cannot meet the level of performance that will be required of it over the next decade. The HRIBF staff has developed a phased approach to upgrading our facility that fits well with our understanding of possible funding profiles that are acceptable to the DOE Office of Nuclear Physics (DOE-NP). The initial aspects of this strategic plan deal primarily with badly needed improvements in our ability to deliver more hours of RIB to experimenters at higher reliability. However as other facilities in Europe, Canada, and Japan begin to deliver neutron-rich beams, it is critical that we find a way to significantly increase the intensity of our beams. Unfortunately, conventional approaches which provide really significant improvements would involve costs far beyond the DOE-NP guidelines. Fortunately, we have identified a new direction (Diamond 1999) for RIB production using a high-power electron beam which could improve the beam intensity capabilities of the HRIBF by more than two orders of magnitude in critical areas, at a cost that would be acceptable.

Technical Approach

To assess the potential of this concept, we proposed to use a high-power beam of electrons from the Oak Ridge Electron Linear Accelerator (ORELA) to induce photo-fission in a uranium foil target array. Fission products emitted from the uranium foils are stopped in high-pressure helium gas and captured by NaCl aerosol particles entrained in the gas. The flow of aerosol-laden helium transports the fission products over a distance ~20 m where, in the initial implementation of the experiment, they are deposited on a moving tape system and subsequently transported to a shielded position for counting by a system of high-resolution γ-ray detectors in close geometry. Transit times on the order of one second with essentially no chemical-species dependence are expected on the basis of numerical modeling and previous results. Consequently yield measurements of a variety of elements over a wide isotope range extending

to very neutron-rich nuclei can be made. We have also investigated the coupling of the aerosol-laden helium to a skimmer system where the aerosols are separated from the helium and injected into an ion source for subsequent acceleration and mass analysis before γ-counting. Implementation of an ion source and mass analysis system can substantially extend the scope and sensitivity of the studies; however, it introduces a chemical dependence that makes even relative yields of isotopes of different atomic species difficult to compare. Consequently it seemed prudent to concentrate initially on direct measurements of species in the helium jet without ionization and mass analysis. Results of these initial measurements can be used to provide relative normalizations among different atomic species if mass-analyzed measurements are subsequently needed.

We note that it has been possible to assemble an experiment of this complexity at modest cost because of the availability of ORELA, and a diligent canvassing of the North American nuclear physics community for surplus hardware that could be used to assemble our experimental system.

Results and Discussion

A photo-fission target suitable for high-power (at least 10-kW) electron beam irradiation at ORELA was designed, fabricated, and pressure tested to 15 atmospheres. The target is illustrated in Fig. 1. The multi-foil target was designed to contain 20 uranium foils inside a water-cooled housing made from high-purity copper with input and outlet connections for the transport of salt-loaded helium gas. The collection and transport of fission products from this target to a counting station has been checked by a ^{252}Cf source and flowing helium at 10 atmospheres. Preliminary analysis indicates that the transport efficiency is around 40% along a 30-m, 0.75-mm-diameter stainless tube.

ORELA normally operates as a neutron source, with a production target mounted in an evacuated target room ("igloo"). A system to contain our fission-fragment production target, and insert it into the ORELA target room, has been designed and fabricated. The device can be inserted into one of the ORELA neutron beam flight tubes (Flight Tube # 9) so that our uranium target assembly intersects the electron beam between the vacuum window and the neutron production target. The design includes vertical and horizontal position adjustment over a large range. The target can be retracted out of the electron beam line during normal ORELA operation. Since the ORELA target room operates with the air evacuated, the insertion mechanism must maintain the target room vacuum seal. A significant effort was devoted to considerations of remote handling of the target after the experiments are finished.

Our experiment is designed to transport in excess of 109 fission fragments per second per kW of electron

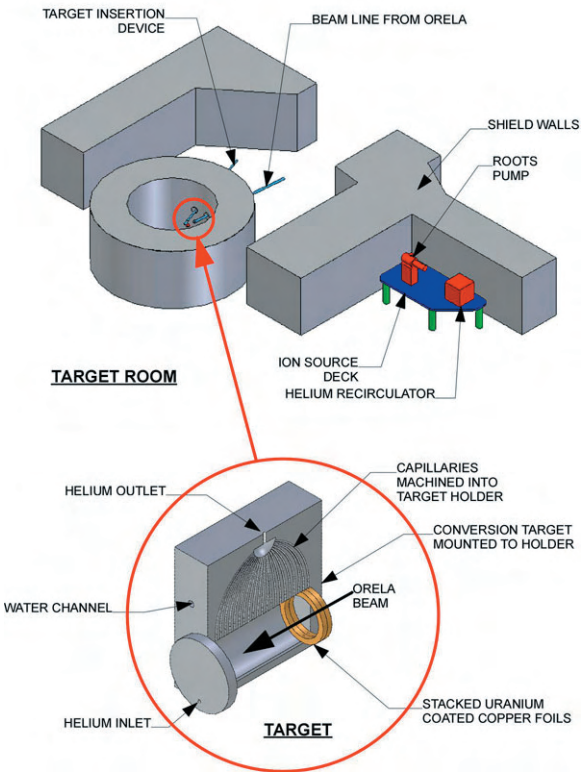

Fig. 1. Schematic representation of the complete experiment concept developed in this project. No detail is shown for the complex target insertion mechanism.

beam from the production target to the analysis system. Consequently, it is necessary to provide the experiment with a well-designed helium recirculation system to avoid release of radioactive materials. A major savings was achieved by locating a complete helium recirculation system at Los Alamos Nuclear Laboratories (LANL) that was surplus to their needs. The system closely matched our requirements. It has been transported to ORNL, refurbished, modified as needed, and the computer control system upgraded.

We spent considerable time and effort on the development of an ion source skimmer that would operate efficiently when fed by a high-pressure helium flow. While we decided not to implement ion-beam mass analysis in the initial experiment, it was still important to identify how this would be accomplished. Our initial efforts to adapt existing HRIBF sources designed to operate at low-background gas pressures were not successful. A survey of the literature, coupled with canvassing of the relevant physics community, indicated that a source that met our needs had been developed at Chalk River Nuclear Laboratory (Schmeing 1987). We were able to obtain a source based on this design for later implementation at ORNL.

A complete experiment, including data acquisition and controls, has thus been designed, fabricated, and tested

and is ready for deployment at ORELA. Unfortunately, no beam time has been available at ORELA this year. We expect that ORELA will become operable. We will be able to obtain beam time shortly after operation commences, and long-delayed experiments are run. We hope that it will be possible to complete our experiment when beam is available.

A significant fraction of the effort supported by this project was devoted to a variety of numerical studies relevant to experiment design, including Monte Carlo studies of beam-target interaction. These studies provide an accurate account of the total fission rate and total energy deposition in a target assembly of arbitrarily complex geometry. As indicated above, measurements made with the gas-jet technique provide accurate relative production yields for different atomic species, as well as different isotopes of a given species. It is desirable to have absolute yields. The efficiency calibrations using the ^{252}Cf source provide a solid basis for establishing an absolute yield scale with reasonable accuracy (factor of two or better). Absolute yields (as a fraction of total fission) for a few isotopes near Z=50 have been measured with mono-energetic photon beams on ^{238}U (DeFrenne 1984). The Monte Carlo treatment of thick-target bremsstrahlung in our experimental conditions allows us to use these photon-beam measurements to establish our absolute yield scale more accurately.

The numerical tools developed, validated and benchmarked for this experiment have broad utility. In an application which we consider to be a part of this project, they were used to provide a detailed numerical evaluation of the merits of several possible implementations of electron-beam RIB production at HRIBF. This work has led to a preliminary HRIBF upgrade concept that will eventually form the basis of a proposal to be submitted to DOE.

The estimates of species isotopic yield distributions from electron-induced fission which provided the motivation for this study were based on excitation-energy systematics and yields from neutron-induced fission at several energies. During the course of this study, much more sophisticated phenomenological predictions (Rubchenya 2003) of photo-fission yields have been obtained, spanning essentially the full range of fission fragment A and Z. If these predictions prove to give an accurate account of our experimental results, they will be extremely useful as a guide to beam development for species very far from stability at a future electron-beam-driven RIB facility.

Benefits

The first phase of the HRIBF upgrade plan discussed in the Background section has just been funded by DOE-NP at a level of $4.7M for FY 04–05. This initial upgrade project does not involve a production accelerator upgrade and hence is not directly coupled to this LDRD project. However, the existence of an R&D program on an innovative direction for RIB production which might eventually be implemented in a later stage was viewed favorably by both program office staff and project reviewers. Therefore, in a very real sense, this LDRD project has already produced a significant return on investment. If this project is successful, we will have an extremely strong case for adding a modest electron accelerator to the upgraded HRIBF complex. The total additional cost of the electron-accelerator addition to the upgrade program would be about $10M. The total upgrade package for the HRIBF, including the electron accelerator, should approach $20M. We have already been awarded the first-phase funding. A second phase funded at about $5M has a high probability. The direction we go with the third phase, and the probability for obtaining funding for it, depends directly on this LDRD project. The modeling tools developed as part of this project have already been used to create a preliminary concept for the implementation of electron-beam produced RIBs at HRIBF, which will be presented to a DOE-NP Science and Technology Review of HRIBF in November 2004. The numerical tools have also been applied to the development of ORNL proposals for active interrogation of special nuclear materials (particularly highly enriched uranium) by electron beams.

References

DeFrenne, D., H. Thierens, B. Proot, E. Jacobs, P. DeGelder, and A. DeClerq. 1984. "Isotopic and elemental yields for the photofission of 235, 238U with 12-30 MeV Photons," *Phys. Rev* **C29**, 1908.

Diamond. W. T. 1999. "A Radioactive ion beam facility using photofission," *Nucl. Instrum. and Methods Phys. Res.* **A432**, 471.

Rubchenya, V. A., and J. Aysto. 2003. "Theoretical Predictions for Neutron Rich Fission Product Yields." EURISOL Research Report and private communication.

Schmeing, H., J. S. Wills, E. Hagberg, J. C. Hardy, V. T. Koslowsky, and W. L. Perry. 1987. "The Chalk River Helium-Jet Ion Source," *Nucl. Instrum. and Methods Phys. Res.* **B26**, 321.

Probing Explosive Nucleosynthesis Through Measurements at the Holifield Radioactive Ion Beam Facility

D. W. Bardayan, J. C. Blackmon, and M. S. Smith
Physics Division

Unstable nuclei play an influential role in many astrophysical processes occurring in exploding stars such as novae, supernovae, and X-ray bursts. To understand these events, we must understand the reactions involving unstable radioactive nuclei. The best way to probe such reactions is by using beams like those available at the HRIBF. We are performing important studies of proton-induced reactions on radioactive fluorine and phosphorus nuclei and neutron-induced reactions on radioactive neutron-rich nuclei. The large detector arrays and the ion beams at the HRIBF are being used to carry out these measurements.

The understanding of the reactions on and structure of unstable nuclei is critical to understanding cataclysmic stellar explosions such as novae, supernovae, and X-ray bursts. The goal of this project is to measure the properties of and reaction rates on several important radioactive nuclei. The information gained will help address issues such as the gamma-ray emission from novae, which is important to understanding results from new space-based telescopes, and of the composition of meteorites, which sample the universe outside the solar system.

In particular, we will study the rate of the $^{18}F + p \rightarrow {}^{15}O + \alpha$ reaction by measuring the rate directly at a variety of energies and by studying the elastic scattering of $^{18}F + p$. We will also study the proton-capture rates of ^{29}P and ^{30}P. These reactions form compound nuclei ^{30}S and ^{31}S, respectively, which we will study via the $^{32}S + p \rightarrow t + {}^{30}S$ and $^{32}S + p \rightarrow d + {}^{31}S$ reactions at the HRIBF. Finally, the transfer of neutrons to heavy neutron-rich radioactive beams will also be studied. This is important because in supernovae, neutron-rich nuclei are processed to even heavier nuclei by a series of neutron captures and beta decays called the r-process. To understand this processing, we must understand the neutron-captures rates on these nuclei, and we will study these rates via measurements of neutron-transfer reactions on radioactive beams at the HRIBF.

Several requirements of the measurements make them difficult, if not impossible, to be studied at other facilities besides the HRIBF. Only at the HRIBF is a ^{18}F beam available with sufficient quality to perform the high-precision measurements necessary for astrophysics. The neutron-transfer studies on r-process nuclei are also only possible at the HRIBF. These studies require beams of neutron-rich nuclei accelerated to energies high enough to overcome the electrostatic repulsion of the positively charged nuclei, and such beams are only available at the HRIBF.

Much progress has been made on the preparation and implementation of these studies. The elastic-scattering rate of $^{18}F + p$ has been measured over a large energy range. A new quantum level in ^{19}Ne was observed for the first time, which significantly affects the $^{18}F + p$ reaction rates. These results have been presented at scientific meetings and published in the *Physical Review*. To study the $^{32}S + p$ reactions, special targets were required. These targets (ZnS) were developed locally and have been used to study levels of interest in $^{30,31}S$. The results from these measurements have been presented at scientific meetings. Finally, the neutron-transfer reactions $^{82}Ge + d \rightarrow p + {}^{83}Ge$ and $^{84}Se + d \rightarrow p + {}^{85}Se$ have been measured at the HRIBF. These are the first neutron-transfer measurement ever made on r-process nuclei. The results from these measurements have been submitted for publication in the *Physical Review*. The techniques developed highlight a roadmap to further studies at future facilities such as the Rare Isotope Accelerator (RIA), a proposed facility endorsed by the Nuclear Science Advisory Committee at the highest priority for future construction in the United States.

The DOE Office of Nuclear Physics supports research in low-energy nuclear physics (e.g., research performed at the HRIBF) with a new component involving reactions of astrophysical interest. This project is central to DOE's desire to continue growth in this area and to develop techniques applicable for use at future facilities such as RIA. This project also advances goals of the National Science Foundation (NSF), which supports nuclear measurements of astrophysical interest mainly through its support of facilities such as at the University of Notre Dame and the National Superconducting Cyclotron Laboratory at Michigan State University.

H^- Laser Stripping Proof-of-Principle Experiment for the Spallation Neutron Source Power Upgrade Proposal

Y. Braiman,[1] S. Henderson,[2] A. Aleksandrov,[2] S. Assadi,[2] J. Barhen,[1] V. Danilov,[2] W. Grice,[1] and Y. Liu[1]
[1]*Computer Science and Mathematics Division*
[2]*Accelerator Systems Division, Spallation Neutron Source Project*

Our group formulated a practical method to achieve H^- stripping with good efficiency using a narrowband laser. Such a scheme would provide a clear path forward for the Spallation Neutron Source (SNS) Power Upgrade by eliminating foil lifetime issues and providing a lower-beamloss approach for charge-exchange injection. The goal of this project is to perform a proof-of-principle experiment to test this promising idea. Our aim is to prove an approach that would point the way towards a viable laser-based charge-exchange injection method, having application at the SNS and other future high-power accelerators under consideration throughout the world.

The Spallation Neutron Source (SNS) utilizes charge-exchange injection to "stack" a high-intensity proton beam in the accumulator ring for short-pulse neutron production. In this process, a 1-msec-long, 1-GeV H^- beam-pulse is transported to a stripping foil located at the injection point of the ring. Both electrons are foil-stripped, and the resulting proton is merged with previously accumulated beam. As the beam power of the SNS accelerator complex is increased from the baseline 1.44 MW to beyond 3 MW as envisioned in the SNS Power Upgrade Proposal, the traditional foil-stripping scheme will become a severe limitation. It is expected that the lifetime of carbon foils at such high beam powers will be too short to be of practical use due to foil damage by extreme temperatures. Furthermore, the use of stripping foils carries undesirable side effects for high-power operation, principally, the uncontrolled beamloss associated with multiple traversals of the foil by the accumulated beam.

We developed a novel approach for laser stripping of a 1-GeV H^- beam that uses a three-step method employing a narrowband laser. In the first step, the beam traverses a strong magnetic field in which the H^- ions are stripped to H^0 ($H^- \rightarrow H^0 + e^-$) by the Lorentz-stripping mechanism. In the second step, the H^0 beam is excited to the $n = 3$ state by colliding a laser beam with the neutral hydrogen beam at an angle chosen to provide the necessary transition frequency in the hydrogen atom's rest-frame. In the final step, the excited hydrogen is readily stripped ($H^{0*} \rightarrow p + e^-$) in a second high-field magnet.

We completed the FY 2004 deliverables outlined in the initial proposal. We have (a) performed experimental parameter optimization including an optimized parameter set, optics design, and beamline insertion layout design; (b) completed design of the magnets, including a complete set of mechanical drawings, and have initiated the procurement of the magnet hardware itself; (c) designed laser beam optics and vacuum chamber, including the actual vacuum hardware, laser optical and diagnostics hardware; (d) completed the laser-beam transport system that brings the laser light to the experimental station in the SNS linac tunnel; and (e) transported laser-light to the experimental station and measured the beam properties. As planned, most of the design portion of this task has been completed, and the procurement of the laser optical hardware is in progress.

For the laser source we are using the third harmonic beam from a Nd:YAG laser with 650 mJ pulse energy (at 1064 nm wavelength), 6–8 ns pulse width, and 30 Hz repetition rate. Frequency-tripled light has been obtained from the laser system, and the required pulse energy of 150 mJ was measured, as were the laser beam profiles. The optical system design that involves multiple stages beginning with the third harmonic output from the laser, which is housed in an auxiliary building outside the SNS linac tunnel and terminating with the laser-particle interaction region inside the vacuum, was verified.

The hardware design, procurements, and commissioning of the laser and laser transport system are all on-track for an experimental test using the accelerated linac beam in summer 2005.

PHYSICS

Seed Money Fund

Development of Readout Electronics Architecture for a Silicon-Strip Vertex Detector Upgrade to the PHENIX Experiment

V. Cianciolo,[1] M. Bobrek,[2] C. L. Britton,[2] W. L. Bryan,[2] K. N. Castleberry,[2] and K. F. Read[1]
[1]*Physics Division*
[2]*Engineering Science and Technology Division*

The Relativistic Heavy Ion Collider (RHIC) at Brookhaven National Laboratory (BNL) smashes particle beams into each other in an attempt to create conditions of energy and density that have not existed since shortly after the Big Bang, thereby melting protons and neutrons into their constituent quarks and gluons. The PHENIX experiment at RHIC has provided an intriguing series of results that has electrified the nuclear physics community. A multi-layer silicon vertex detector would greatly extend PHENIX's scientific impact, and this project focused on the development of a viable concept for the outer layers of such a detector meeting stringent requirements on detector material budget and radiation tolerance, and simultaneously interfacing with a novel BNL strip-pixel sensor and the PHENIX data acquisition system.

Introduction

The PHENIX experiment consists of hundreds of thousands of sensors and corresponding electronics readout channels. Like all high-energy physics detectors, PHENIX is essentially a camera, allowing us to take a "picture" every time two particles in the particle beams smash into each other. RHIC is unique because it collides heavy ions and polarized protons at the highest energies available in the world. With heavy ion collisions we explore matter at extremes of temperature and density that have not existed since a few microseconds after the Big Bang, conditions under which we expect individual quarks and gluons normally trapped inside of protons and neutrons to be briefly liberated in the creation of a new state of matter, the quark-gluon plasma (QGP). With polarized proton collisions, we hope to improve our understanding of the mysterious origin of the proton's spin.

The PHENIX experiment has had four very successful years of data collection, providing an intriguing series of results that has electrified the nuclear physics community (Adcox 2004). The PHENIX collaboration is now considering several detector upgrades in order to take advantage of technological improvements to significantly improve the quality and breadth of possible measurements. A multi-layer Silicon Vertex Detector (SVD) (Heuser 2003) would greatly extend PHENIX's scientific impact, and this project focused on the development of a viable concept for the outer layers of such a detector meeting stringent requirements on detector material budget and radiation tolerance, and simultaneously interfacing with a novel BNL strip-pixel sensor (Li 2004) and the PHENIX data acquisition system (DAQ).

The proposed SVD is designed to measure the distance of closest approach to the collision vertex of individual tracks with a resolution of 30–50 μm, even in the high-multiplicity environment of a head-on heavy ion collision. This would (a) allow identification of heavy quark mesons (those containing *c* or *b* quarks) whose decay vertices are displaced from the collision point by a distance $c\tau \sim 100$–500 μm; (b) improve the measurement of the primary event vertex; and (c) greatly suppress fake-track backgrounds at high transverse momentum (p_T). These measurement improvements would (a) greatly extend the phase space over which heavy-quark particles can be measured, consequently improving our knowledge of the gluon spin structure of the proton; nuclear modifications of parton distribution functions; energy loss of heavy quarks in a hot, dense nuclear medium; and the baseline against which to judge J/Ψ production–a sensitive probe of the possible phase transition to a QGP; (b) improve J/Ψ and Υ mass resolution and allow significant reduction in background muons resulting from light-meson decay; and (c) extend our study of "jet suppression" to much higher p_T. This detector would also improve our ability to measure the orientation of the reaction plane. It will be crucial to measure various observables: correlations, flow, momentum spectra, etc., with respect to a well-determined reaction plane.

The proposed SVD consists of a barrel (four concentric cylinders surrounding the beam axis) and two multi-layer "end caps." During this project we developed a viable concept for the electronic readout of the outer layers of the barrel. These layers will be instrumented with novel silicon strip-pixel detectors developed at BNL which provide two-dimensional information (80 μm × 1 m) with a single-sided process. They will have nearly 400,000 channels in a volume the size of a milk jug. This presents a significant challenge due to power dissipation and data throughput. In addition, the material in the detector must be kept to an absolute minimum: the goal for

the entire detector (sensors, readout electronics, cooling, etc.) is equivalent to 1 mm of silicon per layer, and the sensors themselves are 0.5–0.6 mm! Cost considerations strongly argue for the use of an existing readout chip, but the selected technology must be compatible with both the chosen sensor and the existing PHENIX DAQ, which has bandwidth limitations and latency/buffering requirements. Finally the detector will be subject to a significant radiation dose and must be designed to last for more than ten years.

Technical Approach

Through paper studies and discussions with engineers at Fermi National Accelerator Laboratory, we were able to identify a likely candidate for the main readout chip (SVX4), which provides 128 channels of preamp, analog data buffering and digitization. We developed a testboard and control program with which we verified compatibility of this chip with the PHENIX DAQ. In the process of developing the test protocol, we determined that the SVX4 lacks event-selection (triggering) capability. Calculations determined that this was acceptable for the barrel strip layers, but ensuing discussions with PHENIX colleagues led to improved design for the inner barrel layers which now includes triggering capability. Through discussions with BNL sensor designers, and calculations of the expected dark current versus temperature and radiation dose, we were able to determine that the sensors must be cooled to ~0ºC and require external capacitive coupling to the SVX4. We calculated the power dissipation for the system which allowed specification of conductor thicknesses and showed that data transmission to the DAQ is not a major heat source for either LVDS or optical options. Radiation dose calculations were evaluated and found to be quite uncertain since the rates are not primarily due to beam collisions. Prudence therefore argues for an ASIC implementation of a logic chip required to control several serialized SVX4s. Calculations of the readout electronics thickness showed that without some breakthroughs, the detector will have more than twice as much material as desired. To reduce the required material, we developed a novel bus architecture. We suggested using aluminum instead of copper as the primary conductor, which further reduces the amount of material. One of the big contributors to the detector material budget is the cooling system. There may be a role for ORNL carbon foam; its excellent heat conductivity may allow us to use non-liquid cooling that would simplify construction and reduce material. Calculations showed that the full 8-bit energy information produced by the SVX4 was required, and that to satisfy bandwidth requirements on-board zero-suppression was required. An error-checking algorithm to allow validation of zero-suppressed data was developed.

Results and Discussion

SVX4 readout chip

The strip-pixels will be read out with the SVX4 chip. The 128-channel chip is implemented in the 0.25-µm TSMC process and is inherently rad-hard. We demonstrated compatibility with PHENIX latency and buffering requirements using a testboard and control program we developed to mimic the PHENIX DAQ. During our studies we realized that the SVX4 does not provide event selection or triggering capabilities. Detailed Monte Carlo simulations by PHENIX colleagues showed that this was acceptable. However, it revealed the need to augment the design of the inner barrel layers with the addition of this capability.

The SVX4 chip is designed for the use with an AC-coupled strip sensor, but the strip-pixel sensor is a DC-coupled device. There are several consequences of the difference in coupling. The most important of which is that at room temperature the leakage current temperature is highly temperature dependent, which would result in significant time-dependent pedestal shifts, especially after the sensors are exposed to the expected radiation dose. The leakage current needs to be reduced by cooling the sensors. Explicit AC decoupling of the SVX4 and the sensor is highly recommended via a 128-channel "RC" chip matching the SVX4 pitch.

The power consumption of the SVX4 is 3mW/channel, for a total of over 1 kW for the two strip-pixel layers. This allowed us to specify the cable plant required to deliver the power and the power/ground-plane thickness in the Readout Card (described below).

Sensor Readout Card (ROC) / Readout Bus

Circuit boards hosting the SVX4s are termed readout cards (ROCs), shown in Fig. 1. In addition to twelve SVX4s, each ROC has one custom ROC control chip (RCC). It is possible to implement this chip as either a field programmable gate array (FPGA) or as an application specific integrated circuit (ASIC). Radiation and thickness considerations argue for an ASIC; flexibility argues for an FPGA. The expected radiation dose is highly uncertain because up to now the primary contributor in the PHENIX experimental area has been due to non-collision effects which vary tremendously and are nearly impossible to predict. In the face of this ignorance, we recommend an ASIC implementation and have developed a highly simplified RCC algorithm to reduce risk of non-recoverable algorithm error.

The thickness of the ROC is a critical component of the overall detector material budget. Our studies led to two significant reductions in the detector material budget: (1) one of the sensor metallization layers was redesigned to incorporate a pitch adapter, eliminating the complication and extra material of an external pitch

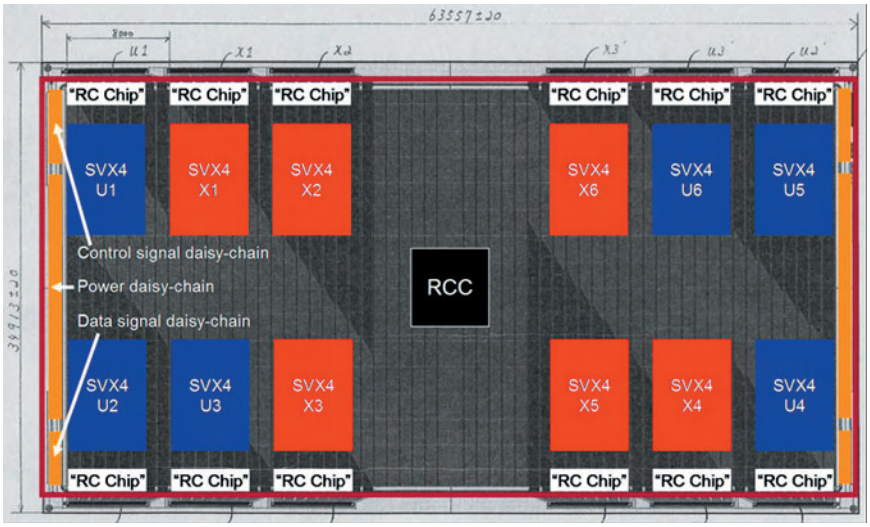

Fig. 1. Suggested layout for PHENIX silicon barrel strip layer ROC/bus shown on top of a strip-pixel sensor (units are μm). The twelve SVX4s together process 1536 channels and dissipate ~5W of power. Five sensor/ROC combinations are connected at the ROC edges to form a ladder – one azimuthal slice of the barrel. The edge connections allow the ROC to also serve as the power/control/signal bus, thus significantly reducing the material budget.

adapter; (2) since the ROCs completely cover the sensor, and since they require ground-planes, power planes and control signal traces, our design daisy-chains those contacts across ROC boundaries to form a bus without any extra material. Five or six ROC/sensor combinations are daisy-chained to form a ladder – one azimuthal slice of the detector. We evaluated the primary trace count on the ROCs. We found it to be dominated by connections from the ladder bus to the RCC and from the RCC to the SVX4s and developed a simplified layout that fits on only two trace layers.

We will use an approach similar to the ATLAS silicon-strip hybrid with aluminum/polyimide flex cable. The thickness is estimated to total 0.42% of a radiation length. The sensors contribute an additional 0.55%. The final significant contribution is from material required to remove heat from the system. A heat management system fabricated from ORNL-developed carbon foam may be significantly thinner than the 0.7% currently estimated.

Pilot Module (PM)

The ROCs need to receive timing and control signals, and they need to send out data. Space limitations at ladder ends (2 × 3 cm) and the inaccessibility of this area both argue to put as little intelligence there as possible. Thus a PM, wire-bonded to the ROC bus at the end of each ladder, will simply drive signals to a remote front-end module (FEM). Signals may be driven off the PM either on copper (by the RCCs themselves) or on optical fiber (with, e.g., the Texas Instruments TLK1501, a very-low- power 16-bit serializer/de-serializer chip). The fiber option is especially attractive because it offers reduced cable plant, lack of electrical connection and consequent grounding concerns, and the ability to put the FEMs in a truly remote location. FEMs are the interface between the ladders and the DAQ. They will be outside the detector acceptance and will have connections between the different pieces of the DAQ and the PMs. They will have on-board intelligence for control (very similar to that developed for the testboard) and data formatting (almost entirely a subset of code developed for previous PHENIX detectors).

Benefits

This project developed a viable plan for construction of a major portion of the proposed PHENIX silicon vertex detector upgrade, making it much more likely that the project can go forward. The development of such a detector is a high priority for one of the major experiments at RHIC, a DOE basic nuclear research facility. In addition, expertise developed at ORNL may be useful in development of silicon-based Compton imagers, potentially useful for applications of interest to NASA and the Department of Homeland Security.

References

Adcox, K., et al. 2004. "Formation of dense partonic matter in relativistic nucleus-nucleus collisions at RHIC: Experimental evaluation by the PHENIX collaboration," submitted to *Nucl. Phys. A.*

Heuser, J., et al. 2003. "Vertex detector upgrade plans for the PHENIX experiment at RHIC," *Nucl. Insrum. Meth.* **A511**, 210–214.

Li, Z., et al. 2004. "Novel silicon strip-pixel detector for PHENIX upgrade," *Nucl. Instrum. Meth.* **A518**, 300–304.

Toward Neutron Star Merger Simulations: Gravitational Waves, Heavy Element Nucleosynthesis, and Gamma-Ray Bursts

C. Y. Cardall,[1,2] M. W. Guidry,[1,2] A. Mezzacappa,[1] and R. J. Toedte[3]
[1]*Physics Division*
[2]*Department of Physics and Astronomy, The University of Tennessee*
[3]*Computer Science and Mathematics Division*

The purpose of this project was to develop a set of computational tools, GenASiS (General Astrophysical Simulation System), aimed at the simulation of neutron star mergers. These cataclysmic events produce several phenomena of high interest in astrophysics. Advanced simulation and analysis tools are needed to shed light on the details of these mergers and their resulting phenomenology. The mutual orbit and final merger of two high-density, self-gravitating bodies moving at high speed calls for adaptive mesh radiation hydrodynamics, a frontier in scientific computing. As initial stages to GenASiS, we made progress on the development of an adaptive mesh neutrino radiation hydrodynamics code, together with analysis and visualization tools. While aspects of the problem proved more challenging than expected, continued building upon this foundation will position us to make significant advances to the state of the art in neutron star merger simulations.

Introduction

A neutron star merger is the cataclysmic finale to the mutual orbit of two neutron stars. A neutron star is the compact remnant of a massive star, left behind after the supernova explosion that follows the end of the star's nuclear burning stages. One of the most extreme objects in nature, a neutron star contains about 1.4 times the mass of the Sun within a radius of only 10 km. While most neutron stars are isolated, a number of neutron star "binaries"—pairs of neutron stars in mutual orbit—have been discovered. Detailed observations indicate that these binaries inspiral slowly towards each other, leading inexorably to their violent collision.

Neutron star mergers are associated with three phenomena of high interest in astrophysics: gravitational waves, heavy element nucleosynthesis, and gamma-ray bursts. First analyses of data from gravitational wave interferometers have appeared recently, cracking open a new observational window on the universe (e.g., Abbott et al. 2004, Takahashi et al. 2004). Neutron star binaries will be one of the primary targets of this new class of observations. The origin of heavy elements produced by rapid neutron capture (the "r-process") is still unknown; neutron star mergers are a leading candidate (Symbalisty and Schramm 1982). These mergers are also proposed as the "central engines" that launch the relativistic plasmas that produce short-time-scale gamma-ray bursts (Meszaros 2002).

A number of groups have performed simulations of neutron star mergers, and various simplifications are typically employed at the current state of the art:

1. Smoothed-particle hydrodynamics is often used instead of more accurate grid-based methods.
2. Realistic equations of state for finite-temperature, dense nuclear matter are avoided by some groups in favor of much simpler polytropic equations of state.
3. Neutrino transport—important for characterizing energy flows from hot, dense nuclear matter—is often ignored entirely, or at best treated with crude schemes.
4. Newtonian gravity, with a simplified treatment of the back reaction from gravitational radiation, is often used instead of full general relativity.
5. Costly nucleosynthesis network calculations are often performed as a "post-processing" on finished simulations, ignoring the possible energy and composition feedbacks that might be followed if nuclear composition changes were incorporated into the main simulation.
6. The dynamics and possible influence of magnetic fields in neutron star mergers have not been the subject of detailed simulations.
7. Often, visualization has been given short shrift in terms of both development of suitable tools and availability of computational resources—an important oversight in a context where physical understanding of complex events requires visual exploration of many different phenomena and their relationships at a range of scales.

As described in the next section, we proposed to develop tools that would help improve upon items 1–3 and 7. Because of our experience with neutrino radiation transport in supernova simulations (Liebendoerfer et al. 2004), we have a particular opportunity to improve

upon simplification 3. This is an important development: Neutrino radiation is one of two leading candidate energy sources in the "central engine" of gamma-ray bursts (e.g., Fryer and Meszaros 2003), and careful simulations will be needed to study this possible mechanism in detail.

Our proposed developments to GenASiS were chosen to advance the state of the art in neutron star merger simulations and begin the building of a longer-term program addressing all the shortcomings in the list 1–7 above. We made significant progress on each of our targeted items 1–3 and 7, but challenges encountered along the way prevented us (in the period covered by this research grant) from bringing the code all the way to the state of maturity on which we had planned.

Technical Approach

GenASiS is an extensible code that will be used to study neutron star mergers with massively parallel simulations on distributed-memory computer architectures. GenASiS uses the MPI library for message passing. It is almost all Fortran 90/95, with an attempt to implement the spirit of object-oriented design to the extent allowed by this language. The word "General" in the acronym GenASiS (General Astrophysical Simulation System) has to do with the extensibility of the code: the ability to implement different options (coordinate systems, equations of state, flux methods, etc.) without having to alter basic elements of the code. This is accomplished with the function overloading capability of Fortran 90/95.

Beyond extensibility and functionality on distributed-memory machines, the key computational capability of GenASiS is adaptive mesh radiation hydrodynamics, a frontier in scientific computing. This capability is called for in the simulation of neutron star mergers, which feature two self-gravitating bodies composed of dense nuclear matter, moving at high speed. The idea of an adaptive mesh is to employ high resolution only where needed in order to conserve memory and computational effort. In this problem, an adaptive mesh would allow much of the "empty space" between the two neutron stars (and to a distant outer boundary) to be handled with low resolution. Radiation transport is so expensive—both in terms of memory and computational demands—that an adaptive mesh is the only way it could be implemented in three spatial dimensions. Adaptive mesh refinement for hydrodynamics had been around for some time, but adaptive mesh refinement for radiation hydrodynamics remains a frontier to which significant contributions can be made. For technical reasons related to the way neutrino radiation is evolved (implicit time differencing), we decided that the cell-by-cell refinement approach of Khokhlov (1998) was the most natural adaptive mesh algorithm to adopt.

Results and Discussion

Before this project began in June 2003, initial development of GenASiS was under way; our goal in this project was to bring GenASiS to a level of development that would permit credible proposals to simulate neutron star mergers. We set ourselves four tasks, three of which were only partially completed:

1. Parallelize our adaptive mesh fluid dynamics code and add a realistic dense nuclear matter equation of state, specifically that of Lattimer and Swesty (1991) (subroutines available at http://www.astro.sunysb.edu/dswesty). The Lattimer-Swesty equation of state was added to the code. Routines were written that partition the mesh in such a way that each processor has its share of spatial zones at each level of refinement, that label the neighboring zones (including "parent" and "child" zones) needed by other processors, and that exchange mesh refinement and coarsening information between all processors at every time step. The actual exchange of fluid variables between processors has not yet been implemented.
2. Include self-gravity by implementing a Poisson solver on adaptive mesh with a finite differencing approach. We finished this task. We worked out the finite differencing of the Poisson equation on an adaptive mesh in coordinates sufficiently general to allow Cartesian, spherical, and cylindrical coordinates to be used. The finite-difference approach requires the solution of a linear system; we implemented the distributed sparse matrix inversion with the Portable, Extensible Toolkit for Scientific computation (PETSc, http://www-unix.mcs.anl.gov/petsc/petsc-2).
3. Add realistic neutrino interactions to our parallel, fixed mesh neutrino radiation transport code; incorporate number and energy transfer to the fluid; and make this portion of the code adaptive. We adopted the Global Arrays library (http://www.emsl.pnl.gov/docs/global/ga.html) to distribute segments of the high-dimensional table of interaction kernels among processors; also each processor uses this library to retrieve the segments it needs. Realistic neutrino emission/absorption, scattering, and pair processes are all in this global table, but so far only emission/absorption are made use of by the neutrino transport solver. We successfully implemented number and energy transfer to the fluid. The distributed transport solver is implemented for a single-level mesh. The overall algorithm and structure of the solver are compatible with an adaptive mesh, but specific implementation for the adaptive mesh has not yet been accomplished.
4. Implement visualization tools for our adaptive mesh using AVS Express toolkit (http://www.avs.com/software/soft_t/avsxps.html). We wrote parallel I/O

routines for GenASiS with the HDF5 library (http://hdf.ncsa.uiuc.edu/HDF5), and also a stand-alone code to transform these files into a form readable by AVS Express. IDL (http://www.rsinc.com/idl) code was written to make plots and animations of fluid variables on the adaptive mesh for test problems in one spatial dimension. AVS Express code for plotting fluid variables on the adaptive mesh was written and demonstrated on two and three dimensional GenASiS data, but this code has not yet been packaged into AVS Express modules easily usable by GenASiS users.

We did not completely finish our projected tasks because of unforeseen difficulties in integrating Eulerian fluid dynamics with self-gravity on an adaptive mesh, experienced in simple gravitational collapse problems with analytic solutions. The adaptive mesh time stepping algorithm in Khokhlov (1998), in which the frequency of update depends on the level of refinement, turned out not to work well in concert with a self-gravity solver. We rewrote the time-stepping and fluid updates to address the entire mesh at once, and this "synchronized" approach works much better on these collapse problems. We also found that our first-order fluid dynamics was inadequate. We implemented a variation of a second-order scheme of Stone and Norman (1992), but the zone-centering variation required by an adaptive mesh appeared to make it unstable. We turned to "central schemes" (e.g., Del Zanna and Bucciantini 2002), which are simple and accurate and feature native zone-centered differencing naturally compatible with adaptive mesh refinement, but were unable to complete the implementation within the time scale of the project.

Benefits

In addition to enabling a program of neutron star merger studies, this work has many benefits to DOE and other agencies. It addresses DOE's need for research in advanced scientific computing. Moreover, neutron star mergers involve interesting nuclear physics issues, including the dense matter equation of state, neutrino interactions, and heavy element (r-process) nucleosynthesis (the subject to be studied by the Rare Isotope Accelerator proposed to DOE). Developments in radiation transport are useful in studies of combustion, climate, and stockpile stewardship—all of interest to DOE. This project also will be relevant to projects undertaken by the National Science Foundation (NSF) and the National Aeronautics and Space Administration (NASA). The NSF is funding the Laser Interferometer Gravitational Wave Observatory that is comprised of two detectors of gravitational radiation from astrophysical sources. Neutron star mergers are expected to be a primary source of gravitational waves, and "templates" computed from simulations that are needed to distinguish gravitational wave signals from noise. The NSF is also funding a Physics Frontier Center for gravitational wave phenomenology at Penn State, to which our work will also contribute. NASA has several orbiting observatories, both active and planned, sensitive to various wavelengths of electromagnetic radiation; these study the enigmatic gamma-ray bursts, of which neutron star mergers are one of two proposed "central engines."

Because of these benefits, there are good opportunities for follow-on funding from DOE, NSF, and NASA. DOE's Office of Science funds relevant research by small groups through the Division of Nuclear Physics and also larger scale initiatives to attack particular science problems through large-scale simulations. At the NSF, which mostly funds individual or small group grants, there is compatibility with programs in several directorates. NASA has funded large computational astrophysics "grand challenge" projects in recent years.

References

Abbott, B., et al. (LIGO Scientific Collaboration). 2004. "Analysis of LIGO data for gravitational waves from binary neutron stars." *Physical Review D* **69**, 122001-1–122001-16.

Del Zanna, L., and N. Bucciantini. 2002. "An efficient shock-capturing central-type scheme for multidimensional relativistic flows. I. Hydrodynamics." *Astronomy & Astrophysics* **390**, 1177–1186.

Fryer, C. L., and P. Meszaros. 2003. "Neutrino-driven explosions in gamma-ray bursts and hypernovae." *Astrophysical Journal* **588**, L25–L28.

Khokhlov, A. 1998. "Fully Threaded Tree Algorithms for Adaptive Refinement Fluid Dynamics Simulations." *Journal of Computational Physics* **143**, 519–543.

Lattimer, J. M., and F. D. Swesty. 1991. "A Generalized Equation of State for Hot, Dense Matter," *Nuclear Physics A* **535**, 331–376.

Liebendoerfer, M., O. E. B. Messer, A. Mezzacappa, S. W. Bruenn, C. Y. Cardall, and F.-K. Thielemann. 2004. "A Finite Difference Representation of Neutrino Radiation Hydrodynamics in Spherically Symmetric General Relativistic Spacetime," *Astrophysical Journal Supplement Series* **150**, 263–316.

Meszaros, P. 2002. "Theories of gamma-ray bursts," *Annual Review of Astronomy and Astrophysics* **40**, 137–169.

Stone, J. M., and M. L. Norman. 1992. "Zeus-2D: A Radiation Magnetohydrodynamics Code for Astrophysical Flows in Two Space Dimensions. I. The Hydrodynamic Algorithms and Tests," *Astrophysical Journal Supplement Series* **80**, 753–790.

Symbalisty, E., and D. N. Schramm. 1982. "Neutron star collisions and the r-process," *Astrophysical Letters & Communications* **22**, 143–145.

Takahashi, H., et al. (TAMA Collaboration and LISM Collaboration). 2004. "Coincidence analysis to search for inspiraling compact binaries using TAMA300 and LISM data," *Physical Review D* **70**, 042003-1–042003-17.

Development of Novel Technology to Synchronize Pulsed, Broad-Area, Semiconductor Lasers

Y. Liu, V. Kireev, and Y. Braiman
Computer Science and Mathematics Division

The objective of this project was to develop a novel method of synchronizing nanosecond-pulsed high-power semiconductor lasers using external optical feedback and beam coupling. Well-established semiconductor laser pulse modulation technology together with our invented pulsed laser transverse/longitudinal modes locking and laser array synchronization and beam combination techniques were employed in the development of this technology. Using an external cavity containing a diffractive grating, we are able to reduce the laser spectrum bandwidth from 5 nm to a single-longitudinal-mode level. The wavelength can be tuned in a range over more than 10 nm. An experimental scheme for frequency locking and beam combination of a broad-area semiconductor laser array has been designed using an external cavity that consists of array collimation, projection lenses, and diffraction grating. It was experimentally demonstrated that all 19 emitters in the array are frequency locked to the single mode with a narrow spectrum bandwidth. The entire array output shows a single transverse mode. The project opened technical opportunities for developing new pulse light sources that have inherently large electrical-optical conversion efficiency, compactness, as well as rich flexibility on pulse duration and repetition rate.

Introduction

Pulse generation in semiconductor lasers is classified into two categories in terms of the pulse duration. For pico-/femto-second pulses, gain switching, Q-switching, and mode locking technologies are conventionally used. Nanosecond pulses in semiconductor lasers can be easily generated by the direct drive current modulation of the laser. In this project, we focus on the synchronization of the nanosecond-pulsed semiconductor lasers. One of the most critical issues of pulsed semiconductor lasers is the limitation of the peak power that can be obtained from the single transverse mode and the narrow spectrum. Even using broad-area semiconductor lasers, the pulse energy is limited below 100 pJ, and the peak pulse power is below tens of watts (Mar 1994, Gee 1998). These values are far less than the outputs of their solid-state counterparts. Meanwhile, synchronization and coherent beam combination of an array of lasers provide a promising method of obtaining high power and high intensity laser outputs. A number of experiments have demonstrated the synchronization of continuous-wave (CW) broad-area lasers by using external optical injection techniques. We have developed several designs of synchronizing CW broad-area semiconductor laser arrays using commercially available high-power laser arrays (Liu 2002). While the injection-locking technique is promising in synchronizing CW laser arrays, it has a number of significant drawbacks in synchronizing nanosecond-pulsed laser arrays for a couple of reasons: (i) due to the extremely small duty ratio ($<10^{-3}$) of the pulse, only very small portion of the injection energy can be used for locking/synchronization of lasers; (ii) a very strong injection power (orders of magnitude higher than in the case of CW lasers) is required in order to lock the peak power of the pulsed laser.

Technical Approach

This project sought to develop and demonstrate a scalable experimental design to lock and synchronize nanosecond-pulsed broad-area semiconductor lasers using external cavity technology. The research progressed along the following three paths which address the specific technical challenges of the project: (i) generation of high-power nanosecond optical pulses in broad-area lasers; (ii) locking of nanosecond-pulsed broad-area lasers; and (iii) development of scalable experimental design to synchronize broad-area laser arrays.

The broad-area laser used in the proof-of-principle experiment is a single-stripe laser diode (Coherent Inc.) with a 100-μm × 1-μm aperture that emits a far-field pattern subtended by 6° × 35°. When operating at a CW mode, the laser lases at a center wavelength of around 808 nm with a threshold of 350 mA. At the driving current of 1.2 A, the laser output measures about 1.2 W with a spectrum bandwidth of about 2 nm. Commercial pulse drivers (BK Precision) were used to drive the laser at the pulse operation mode. These drivers can provide electrical pulses at pulse durations of 5–1000 ns, repetition rates of up to 240 KHz, and peak output currents of up to 40 A. This provided optical pulses with peak powers of more than 40 W. The light output from the broad-area laser was collimated by an AR-coated aspheric lens. A beam splitter and a diffraction grating were placed right

after the collimation lens. Most of the light is reflected from the grating as the first-order diffraction and was fed back to the laser cavity. A part of the laser output was collimated into an optical fiber with a core size of 50 μm for spectrum and temporal waveform measurements. We found that when the laser was operated in a pulse mode, about 50 percent of the laser ourput was collimated into the optical fiber.

The above experiment was scaled up to the synchronization of laser array as schematically shown in Fig. 1. The laser array has a large spacing (500 μm) between the lasing apertures. Since the broad-area laser emitter has a very asymmetric emission aperture (125 μm × 1 μm), the laser output shows different beam qualities along fast and slow axes. In particular, along the slow axis direction, the emission size (125 μm) is much larger than the laser wavelength and the output beam exhibits higher-order modes with multiple lobes in the far-field pattern. In this experiment, we used a cylindrical microlens array to collimate the array output in the slow-axis direction. The separation between each lens was designed to match the laser array. Apart from the beam collimation, the lens array was also used as a beam splitter in the experiment. To this end, we shifted the lens array along the x direction in Fig. 1. When the position of the lens array matched exactly that of the laser, more than 95% of the laser array output was focused in the central lobe. When the lens array shifted 250 μm relative to the laser array, two central lobes appeared at the far field with roughly equal intensities. The ratio between the two main lobes could be continuously tuned from 0.1 to 10 by shifting the lens array along the slow axis. The first part of the array output beam was fed back by an external cavity, and the second part of the array output was employed as the array output. The present experimental design has a number of advantages compared to previous experiments (Pan 1998, Apollonov 1999, Chann 2000, Daneu 2000) using external cavities because of low loss and easy adjustment.

Results and Discussion

Large-amplitude, nanosecond-pulsed current modulations considerably increase linewidth of the broad-area laser (Vasil'ev 2000). The inset box of Fig. 1 shows optical spectra of the broad-area laser at three different operation situations: (A) free-running laser (without external cavity) at CW operation mode; (B) free-running laser at pulse operation mode; and (C) pulse operation mode with the external grating. The average power of the laser at pulse operation mode measures 8 mW for the pulse repetition rate of 100 KHz and the pulse duration of

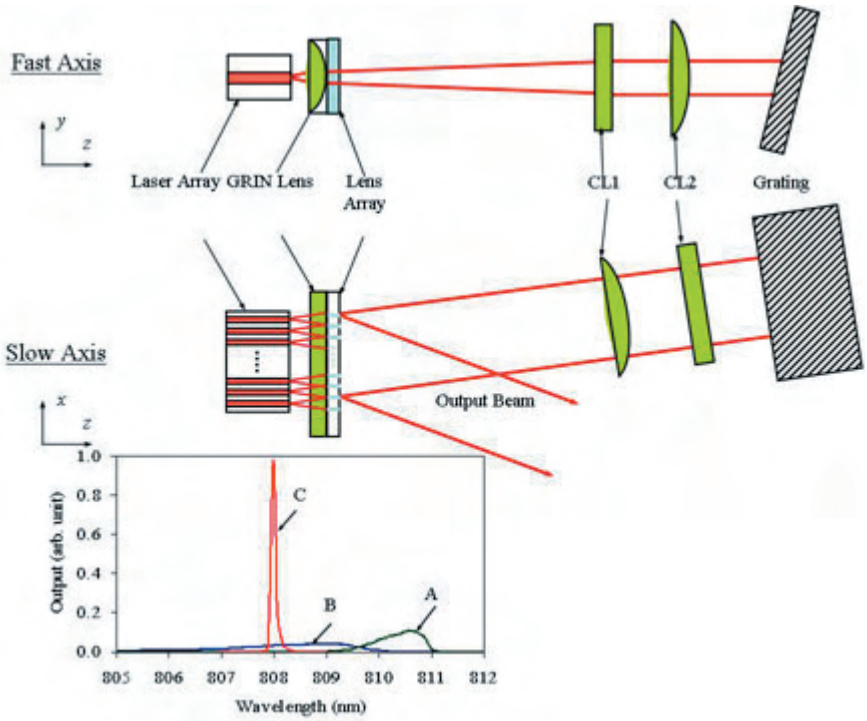

Fig. 1. Schematic of the broad-area laser array synchronization with external cavity configuration. CL: cylindrical lens. Inset box: optical spectra of the broad-area laser at different operation conditions. Curve A: CW operation mode (output ~1 W at 900-mA driving current) without external cavity. Curve B: pulsed operation mode (pulse duration: 7 ns @ 100 KHz) without external feedback. Curve C: pulsed operation mode with the external feedback from grating.

7 ns. The spectrum broadening (up to 5 nm) due to pulse modulation was reduced to a single longitudinal mode level with an external grating feedback as shown in the inset box of Fig. 1. The 3 dB linewidth of the spectrum measured about 0.09 nm, which corresponds to about 40 GHz at the center wavelength of 808 nm. The linewidth was found to show monotonic increase upon the growth of the peak pulse power. Wavelength tunability of the laser has also been demonstrated. In our experiment, the frequency of the pulsed laser was tuned over 10 nm with the external cavity.

Upon the success of locking single pulsed laser, we have designed and conducted the experiment on a 19-emitter laser array using the designed external cavity scheme shown in Fig. 1. At this stage, the experimental design was tested using a laser array operated at CW mode. We demonstrated that all 19 lasers were frequency locked to the single mode with a narrow spectrum bandwidth. The entire array output showed a single longitudinal mode and single transverse mode with the far-field angle close to the diffraction limited angle of a single broad-area emitter without external cavity. Implementation of short external cavity is an important technical issue in the ongoing research in order to lock nanosecond-pulsed laser arrays. One approach is to use a volume Bragg grating that can be employed in a compact configuration. We believe that the proposed approach will result in single-mode, wavelength tunable nanosecond-pulsed light sources with much higher pulse energy and intensity compared to the conventional pulsed semiconductor lasers.

Benefits

The advanced technology developed in the project will open opportunities of building new pulse light sources that have inherently large electrical-optical conversion efficiency and compactness, as well as rich flexibility on pulse duration and pulse repetition rate. This will provide promising options for applications in light material interaction and laser material processing supported by DOE programs. It will also have significant impact on LADAR, optical space communications, and directed-energy applications which are considered by the Department of Defense (e.g., Office of Naval Research, DOD/OSD Joint Technology Office, and Missile Defense Agency) and the National Aeronautical and Space Administration.

References

Apollonov, V. V., S. I. Derzhavin, V. V. Kuzminov, D. A. Mashkovskii, A. M. Prokhorov, V. N. Timoshkin, and V. A. Filonenko. 1999. "Phase-locking of a linear array of high-power laser diodes," *Quantum Electronics* **29**, 839–841.

Chann, B., I. Nelson, and T. G. Walker. 2000. "Frequency-narrowed external-cavity diode-laser-array bar," *Opt. Lett.* **25**, 1352–1354.

Daneu, V., A. Sanchez, T. Y. Fan, H. K. Choi, G. W. Turner, and C. C. Cook. 2000. "Spectral beam combining of a broad-area diode laser array in an external cavity," *Opt. Lett.* **25**, 405–407.

Gee, S., G. Alphonse, J. Connolly, and P. J. Delfyett. 1998. "High-power mode-locked external cavity semiconductor laser using inverse bow-tie semiconductor optical amplifiers," *IEEE J. Sel. Top. Quantum Electron* **4**, 209–215.

Liu, Y., H. K. Liu, and Y. Braiman. 2002. "Injection locking of individual broad-area Lasers in an integrated high-power diode array," *Appl. Phys. Lett.* **81**, 978–980; "Simultaneous injection locking of two broad-area lasers in a high-power diode array driven by a common current source," *Appl. Opt.* **41**, 5036–5039.

Mar, A., R. Helkey, J. Bowers, D. Mehuys, and D. Welch. 1994. "Mode-locked operation of a master oscillator power amplifier," *IEEE Photon. Technol. Lett.* **6**, 1067–1069.

Pan, M. W., D. J. Evans, G. R. Gray, L. M. Smith, R. E. Benner, C. W. Johnson, and D. D. Knowlton. 1998. "Spatial and temporal coherence of broad-area lasers with grating feedback," *J. Opt. Soc. Am. B* **15**, 2531–2536.

Vasil'ev, P. P., I. H. White, and J. Gowar. 2000. "Fast phenomena in semiconductor lasers," *Rep. Prog. Phys*. **63**, 1997–2042.

Development of a Preamplifier for an Imaging Gamma-Ray Detector

J. C. Blackmon,[1] C. L. Britton,[2] W. L. Bryan,[2] V. Cianciolo,[1] P. W. Stankus,[1] A. L. Wintenberg,[2] and G. R. Young[1]
[1]*Physics Division*
[2]*Engineering Science and Technology Division*

An efficient gamma-ray detector that measures both the energy and direction of the incident gamma ray is desired for applications including astrophysics, medical imaging, and homeland security. Some of the most promising concepts for such devices are based on large, highly segmented arrays of silicon or germanium detectors. Such devices require integrated electronics that achieve substantially improved performance over currently available technology. This project focused on the development of front-end electronics with improved resolution for high-capacitance, solid-state devices. Target performance criteria were specified. Design studies were performed. Simulations of one circuit design successfully met or exceeded all performance specifications. Prototype circuits were fabricated for two of the most promising designs and preliminary testing performed.

Introduction

The detection of photons with energies on the order of MeV (gamma rays) is of great interest because they are signatures of the decay of radioactive atomic nuclei. Our understanding of nuclear structure has been advanced in large part owing to improved capabilities in gamma-ray detection. The detection of gamma rays from astrophysical objects has greatly impacted our understanding of the evolution of our galaxy. Many medical imaging techniques are based upon the detection of gamma rays following the introduction of radioactive isotopes to the body. The detection of gamma rays is also of interest for detection of certain radioactive materials for the nuclear safeguards program and homeland security.

Gamma-ray detection is currently performed using large high-purity single crystals of materials such as NaI, Ge, BaF, or LSO that ideally absorb and integrate the full energy of the gamma ray in the crystal. These detectors measure the gamma-ray energy with an efficiency and energy resolution that varies substantially with the material, the size of the crystal, and the gamma-ray energy. However, in all of these approaches, no information on the direction of the incident gamma ray is retained. Currently the only widely applicable way to produce an image of a source of gamma rays is to restrict the field of view of the detector to a fraction of the source at a given time. Good position resolution can only be obtained through a great reduction in field of view of the detector, resulting in a corresponding reduction in sensitivity. For example, this is the approach taken in the SPECT (Single Photon Computed Tomography) technique used for medical imaging and in the INTEGRAL orbiting gamma-ray observatory.

An efficient gamma-ray detector that measures both the energy and direction of the incident gamma ray without collimation would be highly desired for a variety of applications including astrophysics, medical imaging, and homeland security. The most promising concepts for such a device are based upon the tracking of each individual interaction of a gamma ray as it passes through a large, highly segmented detector. Such instruments demand a high number of electronics channels with high resolution for low-energy signals. Current technology does not meet the requirements for resolution, power, and cost per channel. We developed prototype front-end electronics with the goal to demonstrate an approach for meeting these needs.

Technical Approach

The resolution in both gamma-ray energy and direction that is achieved ultimately depends upon the resolution with which each scattered electron is measured, in both energy and position. Obtaining good energy resolution for recoiling electrons is difficult due to the low energy deposited and the large detector area (high capacitance). CMOS integrated circuits have been popular for low-power, small-feature-size detector electronics over the last decade because of the need for tens of thousands of channels of electronics at a reasonable cost (a few 10s of dollars/channel). As an example of a state-of-the-art CMOS preamplifier, we were able to achieve a FWHM of 3.7 keV on a 662-keV gamma peak. However, when applied to low-energy scattered electrons, the energy resolution of the preamplifier is the limiting factor in the resolution with which the incident gamma ray is reconstructed.

One of the main drawbacks to CMOS preamplifiers is the presence of 1/f or flicker noise. Flicker noise is caused by field and mobility variations in the conductive channel of the MOSFET. This noise has a 1/f power spectral density (PSD) and can be characterized for a given process. The problem with flicker noise is that for

high-resolution spectroscopy with solid-state detectors, this noise is problematic at the very frequencies needed for processing the signals from the detectors. However, JFETs have been used for four decades as input devices for high-resolution radiation detectors but are not normally available on CMOS processes. In this project we have developed the first CMOS preamplifier that uses a JFET input device. This preamplifier would ultimately consist of eight individual channels on a single chip and connect to eight discrete or an integrated array of eight JFETs external to the preamplifier chip. This would result in the best of both worlds; low-noise input devices and low-power preamplifier circuitry.

Following the preamplifier, we would also implement the other functions needed in a spectroscopy system: shaping amplifier, peak-detect-and-hold (PDH) and discrimination. The shaping amplifier serves two main purposes—it improves the signal-to-noise ratio of the pulse and produces a pulse shape for which it is easy to find the peak. Typically, shaping times of the order of a microsecond give optimal results. The PDH circuit is used to sample the peak of the pulse and hold that value until it can be digitized. The discrimination function tells that a pulse has occurred and this function is inherent in the PDH—there is logic that indicates that a pulse has been captured, and this information is passed on to the readout control logic.

Once peaks are detected and held, they must be digitized and the data collected. The architecture for this readout process depends upon a number of factors including but not limited to the number of channels, the rate, power and size limitations. For a low-channel-count, low-rate system, the typical solution is to multiplex all channels into a single analog-to-digital converter (ADC), freeing each PDH to process another pulse only after the ADC is finished with that channel. Higher rates can be achieved by breaking the multi-channel system into multiple subsystems operating in parallel. The fastest throughput is obtained by having one ADC per channel, but that is likely impractical for power and/or volume concerns for a system having many channels. We have implemented alternative architectures using analog memories to store analog values (like the output of the PDH) pending digitization. This type of architecture frees the PDH almost immediately to process another pulse. The analog memory holds values awaiting digitization. The size of the analog memory and speed and number of ADCs can then be matched to pulse rate of detector.

In order to fit within budget and time constraints of this proposal, the scope of the electronics development was limited to that of the preamplifier and shaper. These are the crucial components where new technology is required in order to achieve the desired performance. We aimed to design and produce a prototype CMOS chip with an external junction FET preamplifier that demonstrate a new technique that achieves significantly improved performance over other CMOS devices.

Results and Discussion

Design criteria were decided in collaboration with the Gamma and Cosmic-Ray Astrophysics Group at the Naval Research Laboratory that is currently developing segmented detectors for gamma-ray imaging. Most importantly, a noise criterion of 1-keV FWHM for a 0-pF input device was specified, with a noise slope of about 50 eV/pF. An energy range of 10 keV to 1 MeV is required, with an output voltage range of 2–4 V. The input device is to be AC coupled, with both positive and negative polarity input accepted. Finally, the shaping is to be unipolar with a peaking time of 0.5 μs.

We designed a dual-channel preamplifier/shaper with an external FET to meet or exceed these criteria. Simulations were performed for a number of designs using JFETs that are commercially available from InterFet, Inc. of Dallas, TX. InterFet is the major supplier of JFETs for nuclear detection applications. We found that for the input capacitance range of interest, the best performance was achieved using either the 2N6453 or 2N4416A JFETs.

The design and simulated performance for a 0-pF input device with a 2N4416A JFET are shown in Fig. 1. The circuit based on the 2N4416A JFET was found to have better performance with both 0-pF and 20-pF input, but the noise slope was much worse than for the 2N6453 device. The noise for the 2N4416A was 0.44 keV compared to 1.72 keV for the 2N6453 with 0-pF input. With a 20-pF input capacitance, the 2N6453 gave 2.44 keV compared to 2.22 keV for the 2N4416A. For higher input capacitance, the 2N6453 provides better resolution. These design studies indicate a factor of 2 improvement over the current state of the art, but the devices are not predicted to quite meet the required specifications. Nevertheless, prototype 2-channel chips were fabricated using this design, and packaged with the 2N6453 JFETs.

Further design studies were performed to explore ways to reduce the noise slope with the 2N4416A JFETs. Increasing the pulse width is one way to reduce the noise level, and simulations indicate that the noise specifications can be achieved in this way. However, 0.5-μs peaking time is another of the initial specifications, and other approaches were explored. A successful design that is predicted to exceed all the required specifications was finally achieved using dual 2N4416A external FETs for the input. This reduced the noise slope considerably. With 0-pF input capacitance, the noise level was increased to 0.55 keV, but at 20 pF the noise level was reduced to 1.86 keV, a 36% improvement in the noise slope. Prototype 2-channel chips were also fabricated with this design packaged with dual 2N4416A JFETs. Test layouts

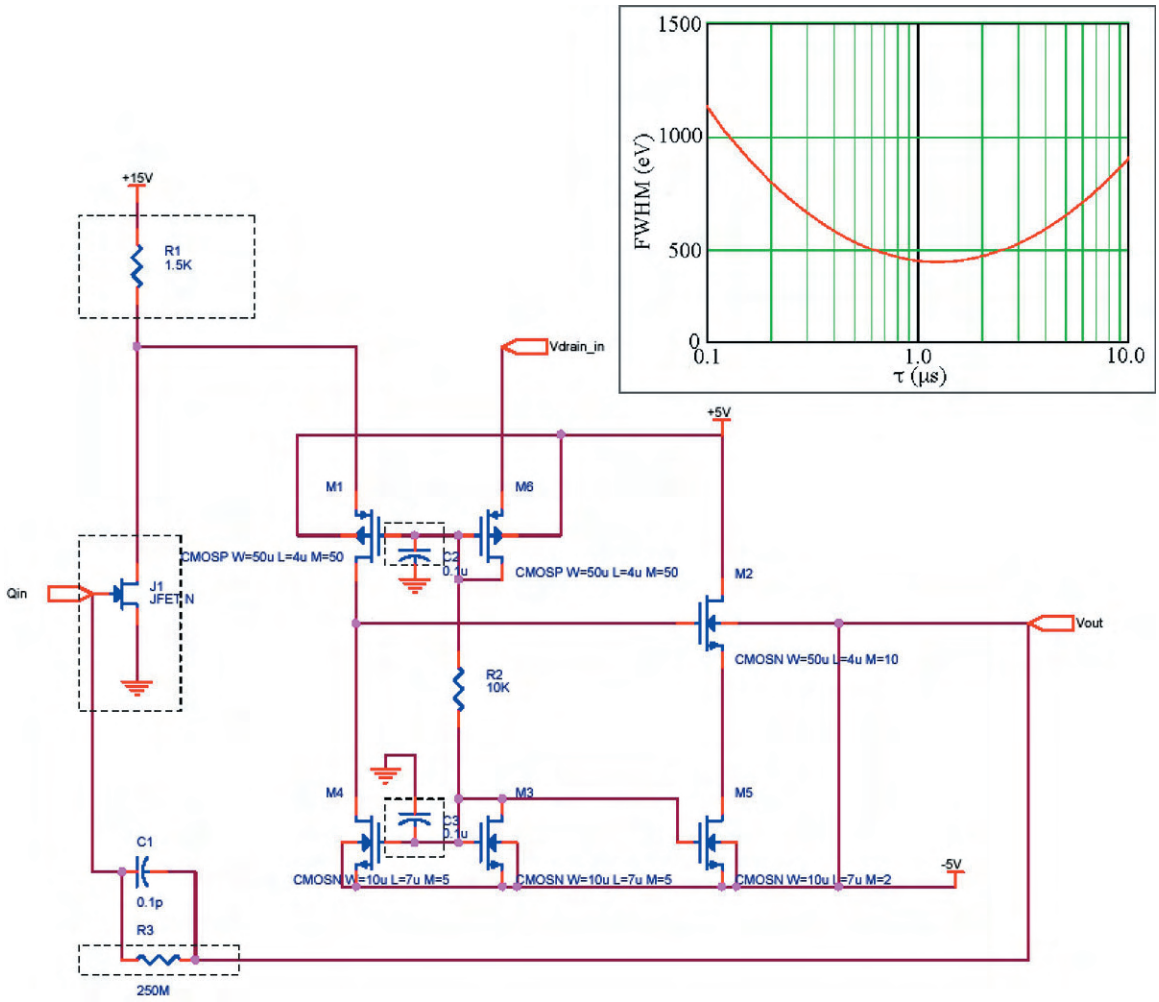

Fig. 1. Schematic of the preamplifier design. The dashed boxes indicate parts of the circuit that are external to the CMOS chip in the prototypes that were manufactured. The inset shows the simulated performance using a single 2N4416A JFET for a no-capacitance input device.

were made, but results from quantitative characterization studies are not yet available.

Benefits

The DOE Office of Science, NASA, and the NIH are all currently funding detector development that should benefit from this technology. Research in gamma-ray astronomy is closely tied to the current research program in nuclear astrophysics in the Physics Division at ORNL. DOE has jointly funded gamma-ray astronomy missions (e.g., GLAST, with NASA) and this research may help position DOE and ORNL to be a partner in the next major gamma-ray astronomy mission. This research may also benefit ongoing research in the area of homeland security.

Development of a Position-Sensitive Neutron Detector for Use at the High Flux Source Facilities: SNS and HFIR

V. Cianciolo,[1] D. Markoff,[2] C. L. Britton,[3] and R. G. Cooper[4]
[1]*Physics Division*
[2]*North Carolina State University*
[3]*Engineering Science and Technology Division*
[4]*SNS Experimental Facilities Division*

At present, there does not exist a high-efficiency, position-sensitive neutron detector that can handle the large fluxes (100 MHz/cm^2) that will be available at HFIR and the SNS. We proposed to develop a prototype detector with these capabilities and with coarse energy resolution. The proposed detector concept expands the segmented ionization chamber design that has successfully been used in a preliminary measurement of the neutron spin rotation in a liquid helium target and builds upon technology currently being developed at ORNL for the SNS. This detector will serve as a prototype beam monitor for a number of experiments proposed for HFIR and the SNS and may find application in more traditional neutron scattering measurements.

The goal of this project is to develop a prototype detector which will be ~100% efficient in the face of the very high neutron fluxes (100 MHz/cm^2) that will be available at HFIR and the SNS. Coarse position resolution (~1 cm^2) and coarse energy resolution (~1Å) are also required for the anticipated primary application as a beam monitor in fundamental neutron physics experiments.

We propose to combine the features of two previous neutron detectors into one detector that satisfies all our requirements. The first detector is a segmented ionization chamber (operating gas: ^{3}He and Ar) with course spatial and energy resolution. Ionization resulting from neutron capture on ^{3}He is detected on a series of charge collecting plates divided transversely and along the beam. Transverse segmentation gives coarse position resolution. Longitudinal segmentation gives energy resolution since the distance a neutron travels in the detector prior to capture is proportional to velocity. That detector is 100% efficient but has insufficient position resolution and is not capable of handling the larger flux that will be available at HFIR and the SNS. The second detector, developed by members of ES&TD, solved the rate limitation and obtained very fine position resolution by integrating a solid neutron converter material into a MicroMegas detector. That detector is limited to only a few percent efficiency because the neutron converters self-absorb the capture products. For applications in which the beam is to be monitored prior to interaction with a target this low efficiency is a design feature. We will use the same basic MicroMegas detector elements but obtain increased efficiency and energy resolution by (a) using ^{3}He as the operating gas instead of using a solid converter and (b) placing several detector modules in series along the beam axis.

NCSU has designed and is constructing the pressure vessel that will hold the detector and the operating gas mixtures under pressure. NCSU has also designed and is constructing a gas handling system. ORNL has fabricated MicroMegas detector plates, constructed printed circuit boards that will readout the detector elements, and has modified firmware necessary to run in self-triggered mode.

Successful development of the proposed neutron detector prototype will result in enabling technology for several fundamental neutron physics experiments proposed for HFIR and the Fundamental Neutron Physics Beamline at the SNS. In addition, a high-rate, high-efficiency detector with good position resolution is very likely to have applications in more traditional neutron scattering measurements.

AUTHOR INDEX

INDEX OF PROJECT NUMBERS

DIRECTOR'S R&D FUND PROJECTS BY INITIATIVE

Neutron Sciences Initiative

Fission to Fusion Initiative

Systems Biology Initiative

Terascale Computing and Simulation Science Initiative